Matthias Kind · Wolfgang Peukert
Heinz Rehage · Heike P. Schuchmann
Editors

Colloid Process Engineering

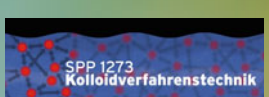

Colloid Process Engineering

Matthias Kind · Wolfgang Peukert
Heinz Rehage · Heike P. Schuchmann
Editors

Colloid Process Engineering

Springer

Editors
Matthias Kind
Institute of Thermal Process Engineering
Karlsruhe Institute of Technology (KIT)
Karlsruhe
Germany

Heinz Rehage
Physical Chemistry II
TU Dortmund
Dortmund
Germany

Wolfgang Peukert
Institute of Particle Technology
Friedrich-Alexander-Universität Erlangen
Erlangen
Germany

Heike P. Schuchmann
Institute of Process Engineering in Life
Section I: Food Process Engineering
Karlsruhe Institute of Technology (KIT)
Karlsruhe
Germany

ISBN 978-3-319-15128-1 ISBN 978-3-319-15129-8 (eBook)
DOI 10.1007/978-3-319-15129-8

Library of Congress Control Number: 2015932657

Springer Cham Heidelberg New York Dordrecht London

Printed on acid-free paper

Springer International Publishing AG Switzerland is part of Springer Science+Business Media (www.springer.com)

Preface

Numerous colloidal systems can be identified in nature. Many synthetic materials which are produced and processed are also colloidal systems. Such systems are always multiphasic and are mostly comprised of submicron particles or nanometer particles. The macroscopic properties of colloidal systems are governed by the microscopic interactions of its dispersed constituents with each other and with the surrounding dispersing medium. The properties of such particle systems are dominated by interfacial effects rather than volume effects because of their huge internal surface.

The focus of *Colloid Process Engineering* is on the handling of colloidal systems in technical processes and about their manipulation by such processes. Many branches in this field may find numerous pathways to rewarding new products with tailor-made properties. The economic success in global competition for any producer is based on the ability to establish products on the market with high and as yet unavailable beneficial properties at a competitive price. To meet these requirements, it is necessary to synthesize products with the targeted property profile through its complex structure as an integrated system. Colloidal systems offer unique opportunities for realizing such tailor-made integrated systemic products. *Colloid Process Engineering* is indispensable for the production of noteworthy amounts of such colloidal systems with relevance to the market.

Colloid Process Engineering is an emerging discipline at the interface between natural sciences, in particular colloidal and physical chemistry, and engineering, in particular chemical engineering. On the one hand, knowledge about molecular interaction and functional molecules is the key to controlling the microscopic interaction. On the other hand, process parameters, such as fluid dynamics, concentration profiles and mechanic forces, are decisive for structure formation and its preservation and functionality during application.

The articles in this book are aimed at scientists, researchers and developers in academia, science and engineering. This book is no true textbook or homogenized monograph. It is, rather, the compilation of the results of a recent cooperative research effort regarding *Colloid Process Engineering*. The effort was funded for six years (2008–2013) by the German Research Foundation.

It comprised an interdisciplinary team of 16 research projects and was carried out at various universities in Germany. Frequent seminars and workshops aimed at homogenizing perceptions, concepts and understanding of what *Colloid Process Engineering* may be about.

The book is structured along the headlines

- Fundamentals and Modeling
- Colloidal Systems with Solid Disperse Phase
- Colloidal Systems with Liquid Disperse Phase
- New Process Routes

The reader may find recent research results about various colloidal phenomena, as well as their scientific interpretation.

In *Fundamentals and Modeling*, answers are given to the questions why and under which conditions small molecules and self-organizing nanoscale particles stabilize emulsions and foams (Pickering effect) or emulsions form a gel. Advanced, non-linear rheological methods are proposed which allow the characterization of the structural parameters of colloidal systems and their changes in time. Furthermore, microscopic and fluid mechanic insights are given as to how colloidal aggregation in turbulent flow comes about and how such flows are to be modeled with up-to-date computational fluid dynamic approaches. The section closes with a chapter about the drying of colloidal systems and addresses the question of how drying affects the structure of a colloidal product.

In *Colloidal Systems with Solid Disperse Phase*, the restructuring of such colloidal systems is treated on a theoretical, an analytical and an experimental basis. Such restructuring may only be possible if an existing structure is destroyed. Therefore, mechanics and breakage of aggregates is addressed in this section as well. A high concentration of the colloidal system and its flow behavior is decisive for some applications. It is shown that weak attraction among the colloidal particles allows for unprecedented concentrations. Finally, formation, characterization, stabilization and post-processing of nanoparticles below 20 nm are addressed in this section. Such particle systems are needed for optoelectronic applications.

In *Colloidal Systems with Liquid Disperse Phase*, surfactants are needed to prevent the disperse phase from coalescing. The dynamics of the adsorption of surfactants at the interface during processing is of particular importance. Detailed and high-resolution measurements reveal that the mechanism of this adsorption comprises competitive effects among the various constitutive components of the system. Vesicles are peculiar, biomimetic liquid-liquid systems, in the sense that the dispersed droplets themselves are also a two-phase liquid-liquid system: They consist of a liquid core surrounded by a liquid shell. A systematic survey of preparation methods and an analysis of the physicochemical parameters required should help the interesting application perspectives of vesicles to become available.

In *New Process Routes*, two exemplary processes regarding the importance of process engineering aspects in the manufacturing of colloidal systems are treated. One of these process routes tracks the manufacturing of nanoscale core-shell particles via an emulsification process, followed by a miniemulsion polymerization for

the creation of a rigid shell. The other process route aims at the manufacturing of an organosol by transferring freshly produced mineral particles from the aqueous phase into the organic phase.

We are convinced that, in total, this spectrum of examples gives a unique insight into some important current frontiers of *Colloid Process Engineering*, and hope that reading these different articles will offer new insights into the world of colloidal process engineering or open the reader's mind to interesting process pathways in the colloidal world.

The editors of this book pay special thanks to Dipl.-Ing. Sebastian Wilhelm, who put a lot of effort into its preparation.

The financial support of DFG (Deutsche Forschungsgemeinschaft) within the priority program SPP 1273 "*Colloid Process Engineering*" is gratefully acknowledged.

Matthias Kind
Wolfgang Peukert
Heinz Rehage
Heike Schuchmann

Contents

Part II Colloidal Systems with Solid Disperse Phase

Part III Colloidal Systems with Liquid Disperse Phase

Part IV New Process Routes

Part I
Fundamentals and Modeling

Colloidal Particles in Thin Liquid Films

Yan Zeng, Sebastian Schön, Adrian Carl and Regine von Klitzing

Abstract This chapter deals with the structuring of Silica nanoparticles in thin liquid films. In the first part of the chapter the particles are kept hydrophilic and their ordering under geometrical confinement in a thin liquid film is described. The thin film is formed between two solid surfaces in Colloidal Probe AFM. The effect of suspension parameters (particle concentration, particle size and salt concentration) and parameters of the outer surfaces (surface potential, roughness and elasticity) on the ordering are studied. In the second part of the chapter the same particles are hydrophobized with short chain amphiphiles. The partially hydrophobic nanoparticles are used to stabilize thin foam films in a *Pickering* foam. A multiscale approach from bulk solution via macroscopic foams, foam bubbles to the adsorption at the free water/air interface is presented in order to understand the stabilisation of Pickering foams.

Keywords Colloidal particles · Thin liquid films · Structural forces · Colloidal probe AFM · Pickering foam

1 Introduction

Nanofluids, which usually refer to suspensions containing nanoparticles, attract scientists and industries since several decades because of their important applications. For instance, they are widely used in ultra polishing of electronic materials, as inks and paint pigments in printing, and as cosmetics, lotions, pharmaceuticals, ceramics, foams, and emulsions. Thus the understanding of the inter-particle surface force is key to manipulating the stability, rheology and other desired properties of the suspensions.

The ordering of the nanoparticles under confinement in thin films and/or at interfaces plays a decisive role for the properties of the macroscopic system like

Y. Zeng · S. Schön · A. Carl · R. von Klitzing (✉)
Stranski-Laboratorium, Institut für Chemie, Strasse des 17. Juni 124, 10623 Berlin, Germany
e-mail: klitzing@chem.tu-berlin.de

M. Kind et al. (eds.), *Colloid Process Engineering*,
DOI 10.1007/978-3-319-15129-8_1

foams or emulsions. The first part of the present chapter presents the effect of geometrical confinement in a thin liquid film on the ordering of of hydrophilic Silica nanoparticles. This ordering takes place perpendicular to the film surface. In the second part about hydrophobized Silica nanoparticles it is rather the ordering at the interface, i.e. lateral to the interface which plays an important role.

In aqueous bulk solution, hydrophilic nanoparticles are homogeneously distributed with a near-field ordering, which is typical for complex liquids. Confining the nanoparticle suspension between two (planar) surfaces leads to the formation of nanoparticle layers parallel to both surfaces (Fig. 1). In other words, the particle density profile oscillates perpendicular to the surface with an exponential decay leveling off far away from the surface. This confinement-induced oscillation can be measured as oscillatory force or structure force in AFM and results from the periodic ordering of confined particles. As shown in Fig. 1 during repulsion the particles are assumed to be ordered in layers. Depletion is induced by the expulsion of one layer leading to a decrease in particle concentration with respect to the particle concentration of the outer bulk reservoir. In the scheme the particles are uncharged and the distance between two maxima corresponds more or less to the diameter of the particles. Oscillatory forces were first described by Israelachvili in pure water solvent by using surface force apparatus (SFA) [15, 17]. The first study of ordering of nanoparticles in thin films can trace back to 1980s. Nikolov [25] found that thinning films of aqueous dispersions of polystyrene latex nanoparticles changes thickness with regular step-wise jump transitions by using reflected light microinterferometry. These observations verified that the stratification of thin liquid films can be explained as a layer-by-layer thinning of ordered structures of colloidal particles formed inside the film. Several papers reported that also particles tend to form periodic ordering during the

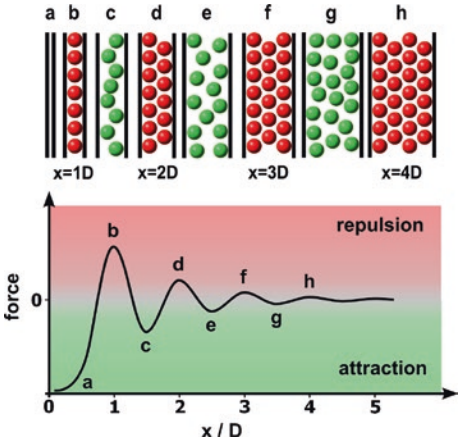

Fig. 1 Scheme which explains the oscillatory forces of suspension of uncharged particles or molecules. The *red* part corresponds to repulsion and the *green* part corresponds to depletion. In the *top row* the ordering of the particles between 2 opposing surfaces is shown and in the bottom the corresponding sequence of oscillatory forces. The distance x between the 2 outer surfaces is given with respect to the particle diameter D. A similar scheme is shown in [16]

approach of confining surfaces by methods like thin film pressure balance [1, 8, 33] and reflectometry [34, 35]. Further, oscillatory forces of nanoparticle suspensions were obtained by the group of Walz and Drelich et al. [9, 28, 36] with Colloidal Probe Atomic Force Microscope (CP-AFM). The CP-AFM was developed by Ducker and Butt [6, 10] in the early 1990s and showed advantage in measuring the complete oscillatory force curves for various systems. Oscillatory forces could be observed for micelles, polymers and particles [2, 4, 5, 20, 21, 23, 24, 26–30, 36–38].

A precise understanding of the effect of confinement on the structuring of nanoparticles, the period of the force oscillation and decay length in relation to the corresponding bulk properties was however still absent. In order to achieve better understanding of the effect of confinement a comparison between the bulk solution and the confined film, was necessary. The first part of the chapter focuses on aqueous suspensions of hydrophilic Silica nanoparticles under confinement. Especially, the confinement effect itself is separated from the effect of outer surfaces' properties.

The second part of the chapter addresses the structuring of hydrophobized nanoparticles in thin liquid films. Therefore the Silica nanoparticles are used as in the first part, but they are hydrophobized by short chain amphiphiles. After hydrophobization the Silica nanoparticles have a strong tendency to adsorb at the air/water interface. They are able to stabilize foams. This type of foam is called Pickering foam. Fundamental differences between a particle stabilized foam and a surfactant stabilized foam are [3]: The adsorption energy is only several kT for surfactants while it can be up to 10,000 kT for particles. The adsorption energy is the highest for particles with a contact angle of 90°. As a consequence the adsorption of particles is almost irreversible for particles, but in dynamic equilibrium for surfactant molecules. The curvature of surfactant stabilized foams or emulsions is determined by the packing parameter. In particle stabilized systems the curvature is mainly determined by the contact angle of the particles with the air(oil) and water phase. The adsorption energy increases with increasing diameter of the particles. Nanoparticles are mostly hydrophobized by salinization or by adsorption of surfactants. Salinization needs a bit effort in terms of preparation and the control of degree of hydrophobicity is quite challenging. Using surfactants means that a dynamic equilibrium exists between surfactant molecules which are adsorbed at the nanoparticles and free surfactants. The free surfactant molecules in turn can adsorb at the air/water interface, which leads to a combined stabilisation by surfactants and particles. Therefore, in the present overview the nanoparticles are hydrophobized with short amphiphilic molecules which are not able to stabilize a foam alone without particles.

2 Part I: Ordering of Hydrophilic Nanoparticles in Aqueous Thin Films

The first part of the chapter focuses on the ordering of silica nanoparticles (diameter: 9–26 nm) in an aqueous suspension confined between a colloidal probe (about 7 μm in diameter) and a planar Silicon wafer. The colloidal probe is glued

to an AFM cantilaver and the force between the two opposing outer surfaces is measured with a CP-AFM. The oscillatory force in dependence of the distance between the two outer surfaces x is fitted with the following equation:

$$f(x) = A \cdot e^{-\frac{x}{\xi}} \cdot \cos\left(2\pi \frac{x}{\lambda}\right) \tag{1}$$

with three parameters: the period λ of the force oscillation, the decay length ξ and the amplitude A. In order to study the effect of confinement the results of the CP-AFM are compared to the results of Small Angle X-ray Scattering (SAXS). The total scattering intensity is a combination of form factor, which describes size and shape of the nanoparticles and the structure factor. The structure factor S(q) is the Fourier transformation of the pair correlation function g(r), i.e. the distribution of the nanoparticles in the suspension. The structure factor is extracted out by dividing the total intensity by the form factor. S(q) has a Lorentzian line shape in dependence of the momentum transfer $q = 4\pi \sin\theta/\lambda$ (θ = scattering angle). It is fitted with

$$S(q) = \frac{S_0\left(\frac{\Delta q}{2}\right)^2}{(q - q_{\max})^2 + \left(\frac{\Delta q}{2}\right)^2} \tag{2}$$

where $q_{\max}$ corresponds to the position of the maximum S_0 of the structure peak intensity, Δq the full width at half maximum of the intensity. In order to check the effect of geometrical confinement the three parameters of the SAXS studies are compared to the three parameters of the CP-AFM experiments: $2\pi/q_{\max}$ is compared quantitatively to λ and correspond to the average distance between the Silica nanoparticles. $2/\Delta q$ is compared quantitatively to ξ and correspond to the range of ordering. Both amplitudes S_0 and A can only be qualitatively compared and correspond to the strength of nanoparticle ordering. In this context the oscillatory force curve measured with a CP-AFM can be considered as a pair correlation function and the structure peak as its Fourier transform. A full description is given in [40]. In the following we will mainly concentrate on the comparison of the distance d between the nanoparticles in bulk suspension (SAXS, $2\pi/q_{\max}$) and under confinement (CP-AFM, λ) for different system parameter.

2.1 Effect of Suspension Parameters

2.1.1 Nanoparticle Concentration

Figure 2 shows force curves for three different concentrations of 26 nm Si particles confined between a Silica colloidal and a planar Si wafer. With increasing concentration the period decreases, indicating a decreasing distance between the nanoparticles.

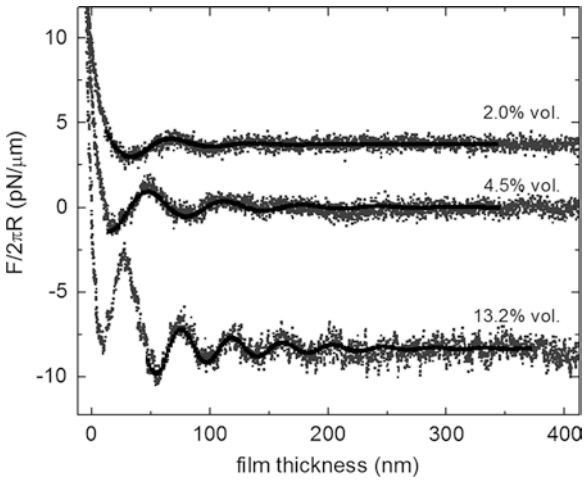

Fig. 2 Experimental curves for F(x) obtained by CP-AFM for suspensions of three different Si nanoparticle (26 nm) concentrations (the data have been vertically offset for sake of clarity). The curves are fitted according to Eq. 1 (*solid lines*). The *thickness* corresponds to the distance between the two outer surfaces. The graph is taken from [18]

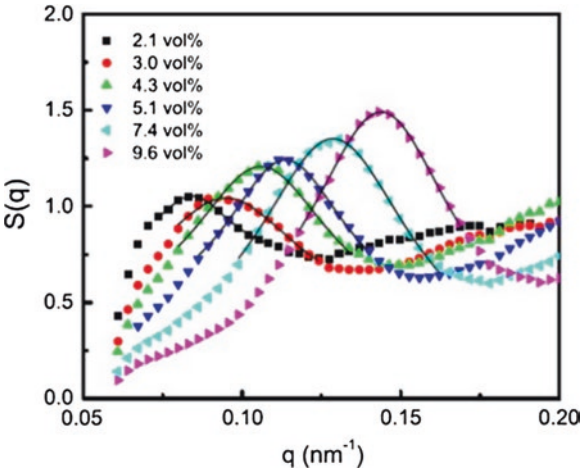

Fig. 3 SAXS structure peak for aqueous suspensions of different Si nanoparticle concentrations. The *solid lines* correspond to fits by Eq. 2. The graph is taken from [40]

The SAXS spectra of the respective dispersions are shown in Fig. 3. The structure peak is shifted to larger q values with increasing concentration indicating again a decreasing distance between the nanoparticles. Figure 4 in the next section shows that the particle distance is the same in bulk and under confinement.

2.1.2 Nanoparticle Size

Figure 4 shows the values for $2\pi/q_{\max}$ (SAXS) and for λ (CP-AFM) for suspensions containing nanoparticles of different sizes (11, 16 and 26 nm).

The graph clearly shows that (1) confining the suspension has no effect on the distance between the nanoparticles for all three nanoparticle sizes and (2) the

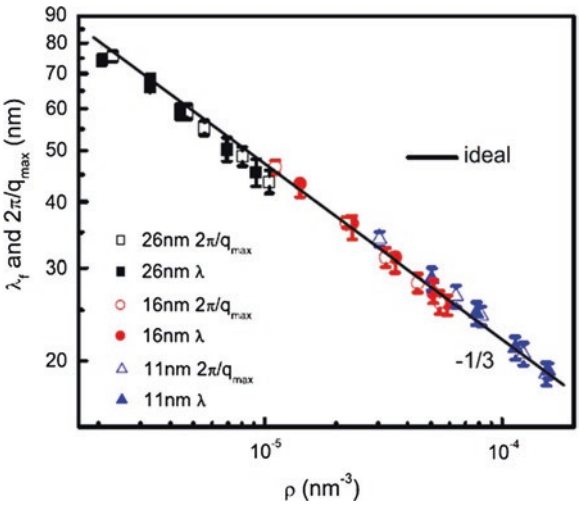

Fig. 4 Comparison between AFM period λ and SAXS $2pi/q_{max}$ for Si nanoparticles of three different sizes (11, 16 and 26 nm) at varying particle number density ρ. The *solid line* is the calculated ideal value of average particle distance in bulk with $d = \rho^{-1/3}$. The graph is taken from [40]

results for the three nanoparticle types fall on a master curve if the distance is considered in dependence of the particle number density ρ. The scaling of the distance with the particle number density shows a simple behavior with $d = \rho^{-1/3}$. In literature often another scaling law is described for charged objects under confinement [25, 26]: The distance between two charged spherical nanoobjects (nanoparticles or micelles) equals the diameter plus twice the Debye length $d = 2(r + \kappa^{-1})$. This law might be valid in a specific case, but cannot be used as generalized law.

2.1.3 Ionic Strength

An increase in ionic strength leads to a decrease in oscillation amplitude due to an increasing screening of the electrostatic repulsion between the nanoparticles. Above an ionic strength of 10^{-3} mol/l no oscillations can be detected anymore. Interestingly, the period of the force oscillation remains the same, but the decay length decreases. In agreement with this, also the position of the structure peak of the SAXS spectra stays constant, but the peak width increases. This might be interpreted as a constant average interparticle distance irrespective of the ionic strength but the position of the particles becomes less defined with increasing ionic strength.

2.2 Effect of Parameters of Outer Surfaces

So far it has been shown that the solution parameters like nanoparticle size and ionic strength have no influence of the general scaling law of the particle distance

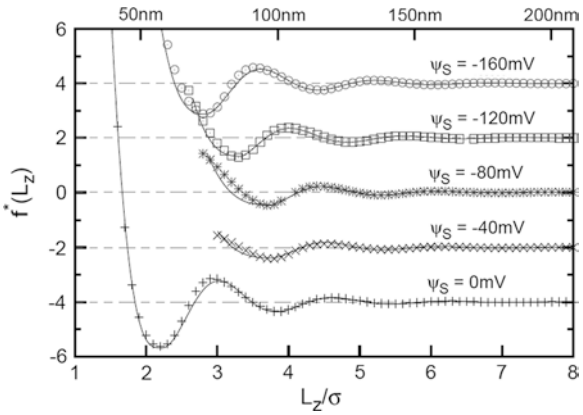

Fig. 5 Results of Monte Carlo simulations with Grand Canonian Potential (GCMC) for the reduced solvation pressure at surface potentials 0, −40, −80 (Silica) and −120 and −160 mV (mica). The *solid lines* are fit functions obtained from Eq. 1. For clarity the curves are shifted along the Y-axis. The abscissa at the *bottom* represents the distance normalized with respect to the diameter of the nanoparticles (26 nm). The graph is taken from [13]

$d = \rho^{-1/3}$ with the particle number density ρ. No confinement effect could be detected. In the following the effect of the properties of the confining outer walls, i.e. the surfaces of the colloidal Si probe and the Silicon wafer on the oscillation period will be presented.

2.2.1 Surface Potential

For modification of the surface potential the surface of the Silicon wafer was replaced by Mica surface. This increases the surface potential from about −70 to about −150 mV. This increases the amplitude of the force oscillation. Due to the electrostatic repulsion between the nanoparticles from the outer walls the strength of particle ordering increases. Monte Carlo simulations showed that the picture is not as simple. A non-monotonous behavior was observed as shown in Fig. 5.

From 0 to −40 mV a decrease in oscillation amplitude was observed and an increase from −40 to −160 mV. The minimum in oscillation amplitude at about −40 mV indicates two opposing effects: with increasing surface potential also the concentration of counterions increases. As mentioned above, an increase in ionic strength leads to a decrease in decay length and therefore to reduced oscillations. This seems to be the dominating effect at low surface potential. The effect of the increasing surface potential which causes a higher strength in particle ordering dominates the results at higher surface potential values.

2.2.2 Surface Roughness

The oscillatory forces only occur if the silica nanoparticles are ordered both perpendicular and parallel to the surfaces over a reasonably long range (e.g. [12]). This means that the surface roughness and therefore the internal roughness between adjacent layers of nanoparticles must be much lower than the period of the force oscillation. An expulsion only occurs if the distance h between the two outer surfaces is commensurable with respect to the oscillation period λ. If the outer surfaces are rough, the distance h between the outer surfaces varies in lateral direction parallel to the outer surfaces and h is not commensurable with respect to the period at all lateral positions. If the precondition for layer expulsion is given only at a few positions in the film, no collective expulsion and thus no oscillatory force will be observed. As an example the roughness of the outer surfaces was increased in a controlled manner by deposition of polymer layers at the outer surfaces [41]. Thereby, both planar Silicon wafer and colloidal probe were modified by physisorption of layers of oppositely charged polyelectrolyte with the so called layer-by-layer technique [7, 39]. With increasing number of double layers of poly (styrene sulfonate) (PSS) and poly(ethylene imine) (PEI) the roughness increases from about 1.2 nm (1 double layer) to 2.2 nm (5 double layers). The layer-by-layer technique modifies the surface roughness without changing the surface potential of a multilayer with the same outermost layer. For instance it is always about −45 mV for PSS terminated polyelectrolyte multilayers irrespective of the number of under-laying polyelectrolyte layers. The oscillatory forces of nanoparticle suspensions with a particle diameter of 26 nm are measured by a colloidal-probe atomic force microscope. Figure 6 shows the respective force curves for different numbers of deposited polyelectrolyte double layers with PSS as terminated layer.

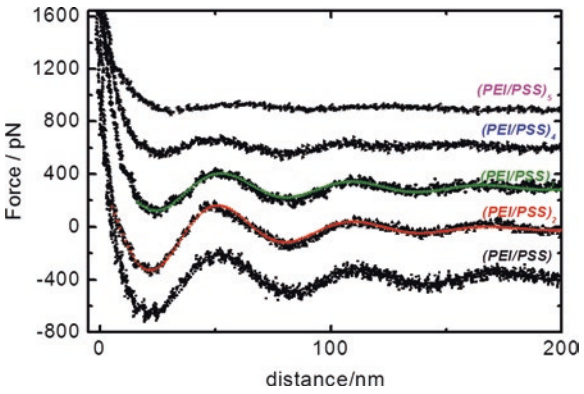

Fig. 6 Force curves measured with a Colloidal Probe AFM. The outer surfaces (Silicon colloidal probe and Silicon wafer) were coated with different numbers of poly(ethylene imine) (PEI, polycation)/poly (styrene sulfonate) (PSS, polyanion) double layers. The *solid lines* correspond to fits by the Eq. 1. Due to sake of clarity the curves are shifted in vertical direction. The polyanion (PSS) was always the outermost layer. The abscissa corresponds to the distance between colloidal probe (microsphere) and the Silicon wafer. The graph is taken from [41]

The period λ, which indicates interparticle distance is not affected by the surface roughness. The corresponding reduction in the oscillatory amplitude and the shift in the phase correlate with an increase in surface roughness. Increasing surface roughness further induces a disappearance of the oscillations. A roughness of a few nanometers on a single surface, which corresponds to about 10 % of the nanoparticle diameter, is sufficient to eliminate the oscillatory force. For instance, only one deposited layer of hyaluronic acid or polyacrylic acid leads to an immediate elimination of oscillations. Both polyanions are known as strong water absorber and their deposition leads to a strong increase in roughness [41].

2.3 Extended Fitting Procedure

Although fitted/simulated and experimental data are in good agreement deviations can be found, especially for smaller surface-to-surface-separation between the outer surfaces and at higher concentrations of the nanoparticles. For instance, Fig. 2 shows the deviation for 13.2 vol % at small separations. Furthermore, the quality of the fits by Eq. 1 depends on the starting point of the fit region. Again the period λ is quite robust against shifts of the starting point but the amplitude and decay-length are strongly affected by the starting point [32].

The commonly used fitting equation for oscillatory structural forces as introduced by Israelachvilli [16] can be extended by introducing an additional term of exponential decaying nature (**B**: strength of the additional term, ξ_2: exponential decay length):

$$f(x) = A \cdot e^{-\frac{x}{\xi}} \cdot \cos\left(2\pi \frac{x}{\lambda}\right) + B \cdot e^{-\frac{x}{\xi_2}} \tag{3}$$

This additional term is able to describe deviations between the common fit equation and data measured for aqueous suspensions of silica nanoparticles, especially at small surface-to-surface—separations and larger concentrations. Figure 7 shows

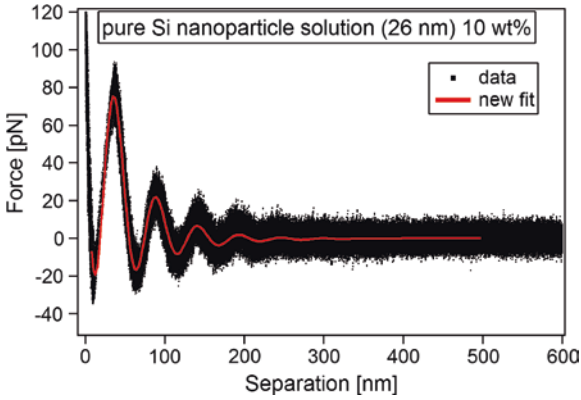

Fig. 7 Fit of experimental data (26 nm Si nanoparticles) with the additional exponential decaying term according to Eq. 3). The experimental data are well fitted down to very small surface-to-surface separations. The abscissa corresponds to the distance between colloidal probe (microsphere) and the Silicon wafer

that the data can be fitted down to very small surface-to-surface separations by Eq. 3.

Furthermore, the extension enables a large increase of the data range accessible for accurate fitting, especially towards small separation. It leads to constant fit parameters irrespective of the starting point of the fit. Therefore, resulting in a strong increase of accuracy for all fit parameter in the system studied here.

So far, the physical meaning of the additional term is not finally clarified. A first assumption might be that the additional electrostatic repulsion introduced by the charged outer surfaces might be taken into account by the extended fitting equation. The experimental data contradict this assumption. With increasing nanoparticle concentration factor B increases, i.e. the additional term becomes more important. On the other hand, with increasing nanoparticle concentration the ionic strength increases due to the increase in counterion concentration. That would lead to a decrease in electrostatic repulsion which is in contrast to the observed effect. An explanation for the additional exponential term in Eq. 3 might be dynamic effects. With increasing approach velocity of both outer surfaces the additional term increases. This might indicate that reorganisation between both surfaces becomes important. So far, an explanation is missing.

3 Stabilisation of Foam Films by Partially Hydrophobic Nanoparticles

3.1 Macroscopic Pickering Foam

Primary n-alkylamines of carbon chain lengths C_5–C_8 were investigated for their effect on the foaming properties of silica nanoparticle suspensions. The system was buffered at a high pH (10.3) where the alkylamines and Silica particles are oppositely charged. Short chain amines were chosen because they do not form stable foams when the corresponding amine solutions are aerated without the addition of silica particles. Similarly, the nanoparticle dispersions show essentially no foamability since the silica particles are very hydrophilic and therefore not surface active. Combining aqueous suspensions of silica nanoparticles and alkylamines show a broad spectrum of foaming behavior, i.e. strong synergistic effects. In the present study 26 nm Silica-nanoparticle were used. With increasing alkylamine concentration the height of the foam stability increases as shown in Fig. 8. Beyond a certain alkylamine concentration the stability decreases. The alkylamine concentration causing maximum foam stability decreases with increasing alkylamine chain length. In order to understand this non-monotonic foam stability behavior the Silica-nanoparticles were studied in suspension and at the air/water interface. In order to understand this non-monotoneous effect of the alkylamine concentration the correlation between foam height, adsorption of the alkyl amine on the Silica nanoparticles and the adsorption of hydrophobized Silica nanoparticles at the air/water interface is studied.

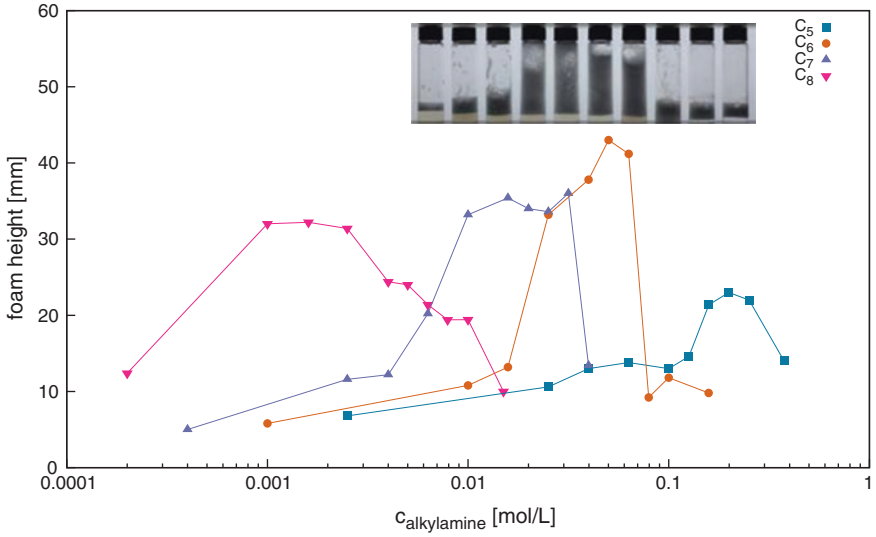

Fig. 8 Foam height of Pickering foams containing Si nanoparticles and alkyl amines with 4 different alkyl chain lengths in dependence of the concentration of alkylamines

3.2 Suspension

To follow the adsorption of the alkylamines onto the silica particles' surface in the bulk, the electrophoretic mobility of the suspensions were measured at different alkylamine concentrations. Figure 9 shows the ζ potential of the silica particles as a function of the alkylamine concentration for different carbon chain lengths. The zeta potential values were calculated from the electrophoretic mobility u of the nanoparticles by

$$\zeta = \frac{u\eta}{\varepsilon_0 \varepsilon_r f(\kappa r)} \tag{4}$$

with η the dynamic viscosity, $\varepsilon_0\varepsilon_r$ the dielectric constant of the medium and $f(\kappa r)$ is the Henry function. Since the Debye length is much shorter (1.5 nm) than the particle radius (13–14 nm) Smoluchowski approximation is applicable.

The bare silica particles in buffer solution have a ζ -potential of about -35 mV. Around a ζ -potential of -25 mV, flocculation of particles is observed for all carbon chain lengths. The other way around, a value of the ζ -potential of -25 mV does not mean automatically flocculation. For instance in presence of multivalent salt but in absence of amphiphiles no flocculation was observed. This means that electrostatic repulsion is not the main reason for flocculation but hydrophobic interactions. Due to cooperative binding of amphiphiles at the Silica particles hydrophobic patches are formed at the particles which drive the flocculation. This assumption is supported by the fact that the alkylamine concentration for

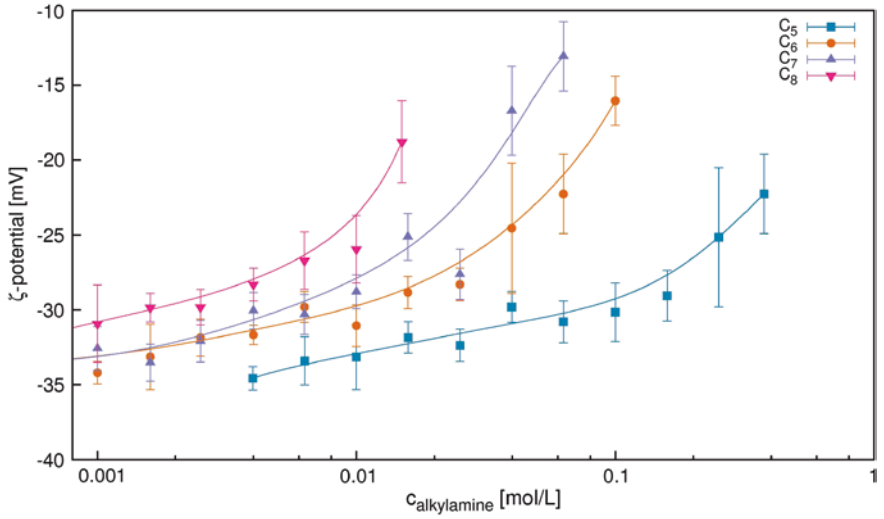

Fig. 9 ζ potential of the silica particles as a function of the alkylamine concentration for different carbon chain lengths

flocculation decreases with increasing alkyl chain length. For all alkyl amines the addition of pyrene showed that the I_1/I_3 ratio drops down at the respective concentration where flocculation occurs. For the two shorter alkyl amine chains (C_5 and C_6) a redispersion at higher alkyl amine concentration could be observed. This might be caused by charge reversal, i.e. positive ζ potential) and the formation of micelles, i.e. increasing re-hydrophilization. The addition of the two longer alkyl amines (C_7–C_8) lead to phase separation and redispersion cannot be observed.

The comparison with the foamability shows that for all alkyl amine concentrations the foam destabilisation starts at the alkyl amine concentration for flocculation. This might be explained by the fact that the flocculation reduces the effective concentration of nanoparticles, which are able to adsorb at the air/water interface.

3.3 Adsorption of Nanoparticles at the Free Air/Water Interface

In order to gain insight on the interfacial properties of the silica/alkylamine suspensions, surface pressure isotherms were recorded. Surface pressure isotherms permit to gain insight into the two-dimensional particle-particle interaction at the air/suspension interface.

As mentioned in the introduction, the difference between a surfactant stabilized foam and Pickering foam is that the particles are much stronger attached to the air/water interface than surfactant molecules. Therefore the system is kinetically

hindered and Gibbs' dynamic equilibrium between the interface and the bulk phase cannot be reached on a reasonable experimental time scale. On contrary, the lateral pressure $\Pi = \gamma_0 - \gamma$ between particles can be measured similar to Π between insoluble amphiphiles; γ_0 corresponds to the surface tension of the pure alkyl amine solution without particles.

Instead of a Langmuir trough the pendant drop technique was used in order to follow the change in surface tension during compression [11, 19]. In comparison with the classical experiment in a Langmuir trough, this technique has been shown to be less susceptible to surface impurities and results in high reproducibility. Because of the droplet geometry, the compression is very uniform, an advantage, since especially for particle layers it has been found that the compression direction may induce unwanted structuring at the interface. In this study, the ratio $R_{drop}/R_{particle} > 100$, so the interface appears flat for a single particle.

Figure 10 shows pressure—area isotherms for two different concentrations of hexylamine. In the experiment the prepared nanoparticle layer of total interfacial area A_0 were compressed under controlled conditions [11, 19]. With increasing alkyl amine the adsorption ability of the particles and therefore the particle concentration at the surface increases. This results in a steeper isotherm for the higher hexyl amine concentration. An insoluble particle layer cannot be compressed infinitely since at a certain number density, the particles form a closely-packed layer at the droplet interface. In Fig. 10, for the higher hexyl amine concentration the collapse can be identified as a kink in the surface pressure curves towards lower values of A/A_0. Further forced compression of the droplet results in surface wrinkling and a non-Laplacian shape of the droplet. The pressure remains constant. With increasing alkylamine concentration, the collapse area fraction increases. Put another way, the amount of adsorbed silica particles increases with increasing alkylamine modification and chain-length, so a compression leads to a close-packed layer at a larger area. With increasing chain length of the alkyl amine this effect becomes even more pronounced, i.e. the area at which the collapse appears increases.

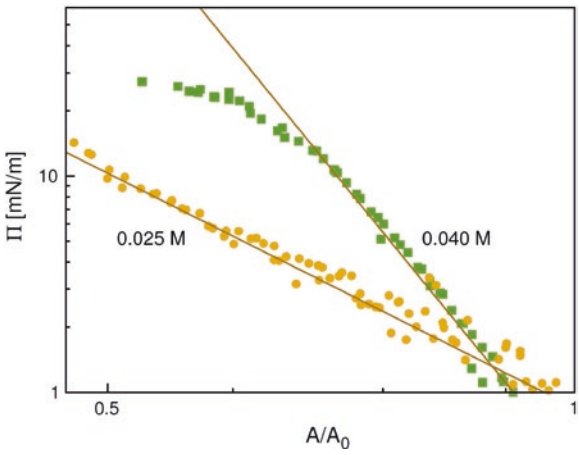

Fig. 10 Surface pressure—area isotherms for two different concentrations of hexylamine. The isotherms are recorded with the pendent drop technique by sucking liquid out of the droplet leading to a decrease in surface area of the droplet. The *solid lines* correspond to fits by $(A/A_0)^E$ with exponent E as fitting parameter

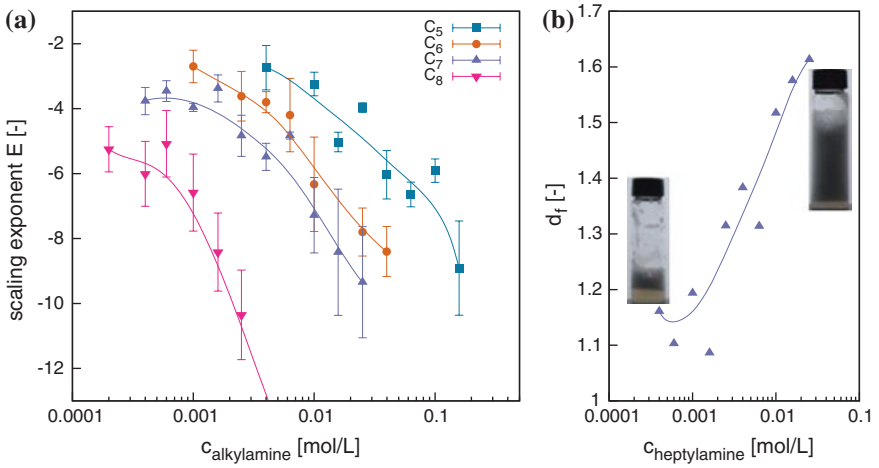

Fig. 11 **a** Scaling exponents E, determined from the power law fits of the experimental data from surface compression as shown in Fig. 10. **b** Hausdorff dimension, determined from Eq. 5 as a function of alkyl amine concentration. The two photos show the foam height at the respective alkyl amine concentrations

The log-log presentation in Fig. 10, shows clearly that the surface pressure scales as power law of the form $(A/A_0)^E$. Figure 11a displays the scaling exponents E that were determined from the power law fits of the experimental data from surface compression. With increasing amine concentration, a steeper build up of the surface pressure during the surface compression is found, which is reflected by a more negative scaling exponent. Qualitatively, an increase in alkyl chain length has the same effect.

Groot and Stoyanov [14] performed simulations on adsorbed nanoparticles. They found a power law behavior for the compression at the interface as well, similar to the present experimental results. In their study, the exponents were varying between −6.5 and −10.5, depending on the structure of the particle aggregates in the layer. Using a scaling argument, they arrived a the following expression for the surface pressure

$$\Pi = \left(\frac{A}{A_0}\right)^{-\left(\frac{d_s+d_f}{d_s-d_f}\right)} = \left(\frac{A}{A_0}\right)^E \tag{5}$$

Herein, d_s is the space dimension, i.e. 2, and d_f is the fractal dimension (Hausdorff dimension) of the 2D aggregated particle cluster. Typical values for Hausdorff dimensions are e.g. 1.44 for diffusion limited cluster aggregation (DLCA) and 1.55 for reaction limited cluster aggregation (RLCA) [22, 31]. Assuming isolated 2D aggregates which were formed by interfacial particle-particle aggregation, an exponent of about −6 is estimated. Close to the two- dimensional sol-gel transition, the system should behave like a percolated network and the corresponding exponent is determined to −9.5 [31].

Figure 11b shows that the Hausdorff dimension increases with increasing alkylamine concentration. The formation of a percolated network leads to a foam stabilisation while single aggregates leads rather to a lower foam height. This explains the increase in stability with increasing alkyl amine concentration.

3.4 Summary, Conclusion and Outlook

The chapter addresses the ordering of Si nanoparticles in thin liquid films. While hydrophilic Si nanoparticles order in the film core perpendicular to the outer film surfaces, partially hydrophobized Si particles can also adsorb at the (fluid) surface of foam films or emulsion films. Lateral ordering becomes important for the stability of the respective macroscopic systems (foams and emulsions).

Hydrophilic particles Confining charged particles in a thin film between two surfaces leads to oscillatory forces which can be measured with a colloidal probe AFM. For uncharged nanoparticles the period λ is constant irrespective of the particle concentration. For charged particles λ scales with $c^{-1/3}$. The scaling behavior of λ is very robust against many parameters related either to the suspension itself like particle size and ionic strength or related to the outer surfaces like surface potential and surface roughness. One of the open questions addresses the effect of nanoparticle charge: What happens at the transition of uncharged to charged particles. How does the scaling law changes from a concentration independent one to $\lambda \propto c^{-1/3}$? It could be shown that the experimental force curves can be fitted with a simple exponentially decaying cosine function (Eq. 1). The limit of this fitting procedure occurs for small surface-to-surface distances. The deviation becomes even more pronounced at high nanoparticle concentrations. A better fit quality is achieved with an additional exponential term (Eq. 3). Here, the physical meaning of the additional term in the fitting procedure is still unclear.

Hydrophobic particles After hydrophobizing the Si nanoparticles with short chain amines, they adsorb to the fluid surface of a foam film. The surface coverage is low, so that particle-particle interactions are negligible. With increasing adsorption of amine, the surface coverage increases and the particles start to form isolated aggregates, floating at the air/solution interface. Upon further increase in amine concentration and hence, a higher particle surface fraction, the particles clusters percolate. With increasing connectivity of the particle network at the bubble interfaces in the foam, the interfaces become more rigid. It has been shown that increased surface rigidity is linked to a deceleration of foam drainage and therefore leads to higher stability of the foam. With further increase in alkyl amine concentration hydrophobic patches on the particles lead to strong hydrophobic interaction and rapid flocculation. The flocculation retracts particles which misses at the interface. This leads to a decreasing foam stability. To summarize, surface aggregation and bulk aggregation of hydrophobized Si nanoparticles counteracts each other in terms of foamability and foam stability. Here one of the open

questions focuses on the effect of surfaces on the formation of aggregates which can obviously bridge two opposing surfaces of a foam film.

Acknowledgments The authors thank the DFG for financial support via the priority program "Kolloidverfahrenstechnik" SPP 1273 (Kl1165/1-3) and the CRG/TR 63 (Sfb) TP 6.

References

1. Basheva ES, Danov KD, Kralchevsky PA (1997) Experimental study of particle structuring in vertical stratifying films from latex suspensions. Langmuir 13(16):4342–4348
2. Biggs S, Burns JL, Yan YD, Jameson GJ, Jenkins P (2000) Molecular weight dependence of the depletion interaction between silica surfaces in solutions of sodium poly(styrene sulfonate). Langmuir 16(24):9242–9248
3. Binks BP (2002) Particles as surfactants—similarities and differences. Curr Opin Colloid Interface Sci 7(1–2):21–41
4. Burns JL, Yan YD, Jameson GJ, Biggs S (2000) Relationship between interaction forces and the structural compactness of depletion flocculated colloids. Colloids Surf A 162(1–3):265–277
5. Burns JL, Yan YD, Jameson GJ, Biggs S (2002) The effect of molecular weight of non-adsorbing polymer on the structure of depletion-induced flocs. J Colloid Interface Sci 247(1):24–32
6. Butt HJ (1991) Measuring electrostatic, vanderwaals, and hydration forces in electrolyte-solutions with an atomic force microscope. Biophys J 60(6):1438–1444
7. Decher G (1997) Fuzzy nanoassemblies: toward layered polymeric multicomposites. Science 277(5330):1232–1237
8. Denkov ND, Yoshimura H, Nagayama K, Kouyama T (1996) Nanoparticle arrays in freely suspended vitrified films. Phys Rev Lett 76(13):2354–2357
9. Drelich J, Long J, Xu Z, Masliyah J, Nalaskowski J, Beauchamp R, Liu Y (2006) AFM colloidal forces measured between microscopic probes and flat substrates in nanoparticle suspensions. J Colloid Interface Sci 301(2):511–522
10. Ducker WA, Senden TJ, Pashley RM (1991) Direct measurement of colloidal forces using an atomic force microscope. Nature 353(6341):239–241
11. Fainerman VB, Kovalchuk VI, Lucassen-Reynders EH, Grigoriev DO, Ferri JK, Leser ME, Michel M, Miller R, Mohwald H (2006) Surface-pressure isotherms of monolayers formed by microsize and nanosize particles. Langmuir 22:1701–1705
12. Gee ML, Israelachvili JN (1990) Interactions of surfactant monolayers across hydrocarbon liquids. J Chem Soc Faraday Trans 86:4049
13. Grandner S, Zeng Y, von Klitzing R, Klapp SHL (2009) Impact of surface charges on the solvation forces in confined colloidal solutions. J Chem Phys 131(15):154702
14. Groot RD, Stoyanov SD (2010) Equation of state of surface-adsorbing colloids. Soft Matter 6:1682–1692
15. Horn RG, Israelachvili JN (1981) Direct measurement of structural forces between 2 surfaces in a non-polar liquid. J Chem Phys 75(3):1400–1411
16. Israelachvili JN (1992) Intermolecular and surface forces. Academic Press, London
17. Israelachvili JN, Pashley RM (1983) Molecular layering of water at surfaces and origin of repulsive hydration forces. Nature 306(5940):249–250
18. Klapp SHL, Zeng Y, Qu D, von Klitzing R (2008) Surviving structure in colloidal suspensions squeezed from 3d to 2d. Phys Rev Lett 100(11):118303
19. Kwok DY, Tadros B, Deol H, Vollhardt D, Miller R, Cabrerizo-Vilchez MA, Neumann AW (1996) Axisymmetric drop shape analysis as a film balance: rate dependence of the collapse pressure and molecular area at close packing of 1-octadecanol monolayers. Langmuir 12:1851–1859

20. McNamee CE, Tsujii Y, Matsumoto M (2004) Interaction forces between two silica surfaces in an apolar solvent containing an anionic surfactant. Langmuir 20(5):1791–1798
21. McNamee CE, Tsujii Y, Ohshima H, Matsumoto M (2004) Interaction forces between two hard surfaces in particle-containing aqueous systems. Langmuir 20(5):1953–1962
22. Meakin P (1984) Diffusion-controlled aggregation on two-dimensional square lattices: Results from a new cluster-cluster aggregation model. Phys Rev B: Condens Matter 29:2930
23. Milling AJ (1996) Depletion and structuring of sodium poly(styrenesulfonate) at the silica-water interface. J Phys Chem 100(21):8986–8993
24. Milling AJ, Kendall K (2000) Depletion, adsorption, and structuring of sodium poly(acrylate) at the water-silica interface. I. An atomic force microscopy force study. Langmuir 16(11):5106–5115
25. Nikolov AD, Wasan DT (1989) Ordered micelle structuring in thin-films formed from anionic surfactant solutions. I. Experimental. J Colloid Interface Sci 133(1):1–12
26. Nikolov AD, Wasan DT (1992) Dispersion stability due to structural contributions to the particle interaction as probed by thin liquid-film dynamics. Langmuir 8(12):2985–2994
27. Piech M, Walz JY (2002) Direct measurement of depletion and structural forces in polydisperse, charged systems. J Colloid Interface Sci 253(1):117–129
28. Piech M, Walz JY (2004) The structuring of nonadsorbed nanoparticles and polyelectrolyte chains in the gap between a colloidal particle and plate. J Phys Chem B 108(26):9177–9188
29. Qu D, Baigl D, Williams CE, Mohwald H, Fery A (2003) Dependence of structural forces in polyelectrolyte solutions on charge density: a combined AFM/SAXS study. Macromolecules 36(18):6878–6883
30. Qu D, Pedersen JS, Garnier S, Laschewsky A, Moehwald H, Klitzing RV (2006) Effect of polymer charge and geometrical confinement on ion distribution and the structuring in semi-dilute polyelectrolyte solutions: comparison between AFM and SAXS. Macromolecules 39(21):7364–7371
31. Robinson JD, Earnshaw JC (1992) Experimental study of colloidal aggregation in two dimensions. I. Structural aspects. Phys Rev A 46:2045
32. Schoen S, von Klitzing R (2014) Simple extension of commonly used fitting equation for oscillating structural forces in case of silica nanoparticle suspensions (in preparation)
33. Sethumadhavan GN, Nikolov AD, Wasan DT (2001) Stability of liquid films containing monodisperse colloidal particles. J Colloid Interface Sci 240(1):105–112
34. Sharma A, Tan SN, Walz JY (1997) Effect of nonadsorbing polyelectrolytes on colloidal interactions in aqueous mixtures. J Colloid Interface Sci 191(1):236–246
35. Sharma A, Walz JY (1996) Direct measurement of the depletion interaction in a charged colloidal dispersion. J Chem Soc Faraday Trans 92(24):4997–5004
36. Tulpar A, Van Tassel PR, Walz JY (2006) Structuring of macroions confined between like-charged surfaces. Langmuir 22(6):2876–2883
37. Uzum C, Christau S, von Klitzing R (2011) Structuring of polyelectrolyte (NaPSS) solutions in bulk and under confinement as a function of concentration and molecular weight. Macromolecules 44:7782–7791
38. Uzum C, Makuska R, von Klitzing R (2012) Effect of molecular architecture on the polyelectrolyte structuring under confinement. Macromolecules 45:3168–3176
39. von Klitzing R (2006) Internal structure of polyelectrolyte multilayer assemblies. Phys Chem Chem Phys 8(43):5012–5033
40. Zeng Y, Grandner S, Oliveira CLP, Thunemann AF, Paris O, Pedersen JS, Klapp SHL, von Klitzing R (2011) Effect of particle size and debye length on order parameters of colloidal silica suspensions under confinement. Soft Matter 7:10899–10909
41. Zeng Yan, von Klitzing Regine (2012) Oscillatory forces of nanoparticle suspensions confined between rough surfaces modified with polyelectrolytes via the layer-by-layer technique. Langmuir 28:6313–6321

Colloidal Gels Formed by Dilute Aqueous Dispersions of Surfactant and Fatty Alcohol

Felix Grewe, Jochen Ortmeyer, Roxana Haase and Claudia Schmidt

Abstract Mixtures of surfactants, fatty alcohol as cosurfactant, and water often form gels, even at high dilution. We have investigated highly dilute samples of the system sodium dodecyl sulfate/cetyl alcohol/water (SDS/CA/D_2O) at varying SDS/CA ratio. Gel-like samples are obtained only at low SDS/CA ratios. The phase structure and the dynamics of the molecules have been determined by a combination of proton and carbon-13 NMR spectroscopy, cryo-transmission electron microscopy, very-small-angle neutron and x-ray scattering, differential scanning calorimetry, rheology, and pulsed gradient spin echo NMR diffusometry. The gel-like character is found to be caused by jammed uni- and multilamellar vesicles.

Keywords Surfactant fatty alcohol water mixture · Vesicle · Lamellar phase · Gel · NMR · Pulsed field-gradient diffusometry · Transmission electron microscopy

1 Introduction

Surfactants show a rich phase behavior in aqueous solutions [10, 27, 41]. There are isotropic micellar solutions, which may contain micelles of different shapes, as well as several types of liquid crystalline phases, for example, cubic, hexagonal, and lamellar ones. In particular, hexagonal and cubic phases of the bicontinuous type have a gel-like character, whereas micellar solutions and also lamellar phases tend to be fluid. In some cases even highly dilute aqueous solutions or dispersions that contain only a few percent of organic components have gel-like properties. This is the case for worm-like micellar solutions, which occur when micelles show a one-dimensional growth leading to very long thread-like aggregates that form an entangled network [6, 11]. But also a two-dimensional growth of micelles to extended lamellar sheets or,

F. Grewe · J. Ortmeyer · R. Haase · C. Schmidt (✉)
Department Chemie, Universität Paderborn, Warburger Straße 100,
33098 Paderborn, Germany
e-mail: claudia.schmidt@uni.paderborn.de

M. Kind et al. (eds.), *Colloid Process Engineering*,
DOI 10.1007/978-3-319-15129-8_2

more commonly, to closed aggregates called vesicles may cause gel-like rheological properties [17]. The rheology of vesicles and disks and its relationship to the microstructure of the phases has been reviewed recently by Gradzielski [18].

The shape of surfactant aggregates depends on the spontaneous curvature of the amphiphilic layer which is controlled by the surfactant packing parameter [23]

$$P = \frac{V}{Al}, \tag{1}$$

which characterizes the shape of a surfactant. A denotes the effective cross-sectional area of the hydrophilic headgroup, and V and l are the volume and length of the hydrophobic tail, respectively. Thus by choosing both the types and amounts of surfactants and cosurfactants in a formulation the phase structure and hence the rheological properties, which play an important role in processing and application of surfactant systems, can be tuned.

In the formulation of pharmaceutical and cosmetic lotions and creams mixtures of surfactants and fatty alcohols are often employed. Due to the large packing parameter of the long-chain alcohol molecules bilayer structures are formed in these systems, for which stable gels may be found even at high dilution. According to the gel-network model by Eccleston [12] lamellar structures, in which layers of water alternate with bilayers of the amphiphiles, are an essential component. The lamellar structures may coexist with crystalline phases and bulk water. A comparison of the lamellar spacings with the rheological properties indicates that thicker interlamellar water layers lead to higher viscosities since the volume ratio of the lamellar phase to the continuous aqueous phase increases with the entrapment of water between the bilayers, resulting in higher viscosities [12].

In this chapter the structure of a dilute gel-forming ternary model system consisting of surfactant, fatty alcohol, and water, which has been investigated by complementary experimental methods, is presented. The combination of rheology, differential scanning calorimetry (DSC), nuclear magnetic resonance (NMR), scattering experiments, and electron microscopy yields a fairly complete structural model and the identification of the essential features that are responsible for the gel character. A particularly versatile technique for the investigation of colloidal surfactant systems is NMR, by which different aspects including chemical composition, phase behavior, molecular dynamics, and diffusion can be studied. Another example for the application of NMR in colloid science is the investigation of the organic layers on colloidal particles, cf. the chapter by Zellmer and Garnweitner on “Small-molecule Stabilization Mechanisms of Metal Oxide Nanoparticles” in this volume or Ref. [24].

2 The Model System SDS/CA/Water

The ternary system consisting of the anionic surfactant sodium dodecyl sulfate (SDS), 1-hexadecanol (cetyl alcohol, CA), and D_2O was used as an example for structural investigations with different methods [16, 19]. The corresponding system

Table 1 Composition of samples (all containing 97 % D_2O)

Label	Mass fraction SDS (%)	Mass fraction CA (%)	γ	Molar ratio CA/SDS
J0	0.0	3.0	0.00	–
J1	0.3	2.7	0.10	10.70
J2	0.5	2.5	0.17	5.97
J3	0.7	2.3	0.23	3.89
J4	0.9	2.1	0.30	2.77
J5	1.2	1.8	0.40	1.78
J6	1.5	1.5	0.50	1.19
J7	1.8	1.2	0.60	0.79
J8	2.1	0.9	0.70	0.51
J9	2.8	0.2	0.93	0.09
J10	3.0	0.0	1.00	0.00

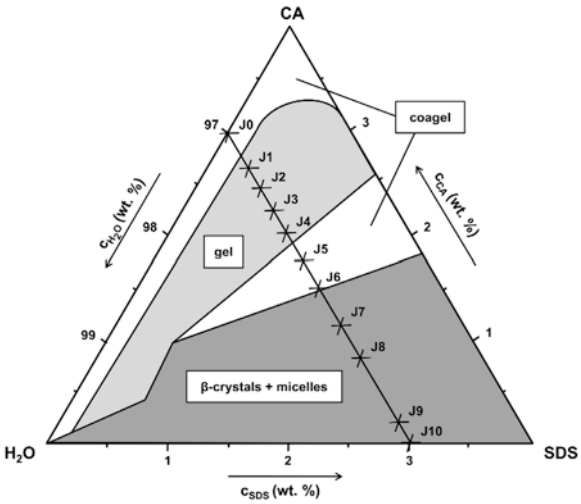

Fig. 1 Phase diagram of the dilute corner of the system SDS/CA/water according to Goetz and El-Aasser [14] after cooling the mixtures from 70 °C to room temperature. The compositions of the samples discussed in this report are shown as crosses. Note that the original phase diagram was obtained for SDS/CA/H_2O [14], whereas the crosses show the mass fractions of samples containing D_2O

with H_2O as solvent is known to forms gels at high dilution and its phase behavior has been studied before [14, 15]. The SDS/CA/water system was chosen to keep the model as simple as possible although it is well known that mixtures of fatty alcohols, for example, of CA and stearyl alcohol (SA), yield more stable gels [1].

A series of eleven samples containing 97 wt% D_2O and varying amounts of surfactant (SDS) and fatty alcohol (CA), as shown in Table 1, was investigated. The ratio

$$\gamma = \frac{m_{\mathrm{SDS}}}{m_{\mathrm{SDS}} + m_{\mathrm{CA}}} \tag{2}$$

denotes the mass fraction of surfactant in the mixture of surfactant and alcohol. The samples were mixed at 70 °C, cooled to room temperature, and stored at room temperature. Figure 1 shows the dilute corner of the phase diagram at room temperature according to Ref. [14] together with the samples investigated here.

Of the innumerable surfactant/alcohol/water systems studied in the past, mainly two others will be drawn on for comparison. The first one is the system SDS/CA-SA/water studied by Awad and coworkers [1] at a water concentration of 89 wt%. These authors used a fatty alcohol mixture with a mass ratio CA:SA = 1:1.18. The second system, investigated by Schipunov [38], contains a varying ratio of the surfactant N-(2-hydroxyethyl)dodecane amide (CMEA) and the fatty alcohol CA, about 90 wt% water, and 1 wt% of the additional surfactant sodium-2-[2-dodecoxyethoxy]-ethyl-sulfate (SLES). We will refer to this system as the CMEA/CA/water system.

3 Phase Behavior

Based on the phase diagram reported by Goetz and El-Aasser for the system SDS/CA/H_2O [14], shown in Fig. 1, samples J1–J4 are expected to be gels, samples J5 and J6 to form a coagel (mixture of gel and alcohol crystals), and samples J7–J9 to contain both micelles and crystals. J10 is a micellar solution of SDS. This will be investigated in the following by different methods. It must be pointed out that the samples may be out of equilibrium. The phases and their structures can be metastable. They may exist for very long times but ageing phenomena may occur as well.

3.1 Macroscopic Appearance

Fatty alcohols are almost insoluble in water. Thus, sample J0 is an unstable dispersion, which separates into an almost neat water phase and white solid alcohol crystals floating on the surface. Samples J1–J8 are white and completely opaque. The ones with higher SDS content (J7 and J8) separate within one week into a clear solution at the bottom and a white phase on top. Sample J9 is almost clear and shows birefringence on shaking, whereas J10 is a clear solution of SDS micelles.

3.2 Rheological Properties

The viscosity of the samples decreases with increasing surfactant (SDS) mass fraction γ in the SDS/CA mixture. At a shear rate of 1 s^{-1} the samples with the highest CA content (J1–J3 of the gel region) have a steady-state viscosity of about 10 Pa s; the value for sample J4 is already about 50 % lower and the viscosity decreases further with increasing γ. For samples J1–J6 the steady-state viscosity was measured as a function of shear rate in the range of 1–10 s^{-1} and the samples were found to be shear-thinning.

In Fig. 2 the storage and loss shear modulus (G' and G'') and the complex viscosity ($|\eta^*|$) of sample J1 are shown. The rheological measurements were performed at slightly elevated temperature to achieve good temperature stability. In the frequency range investigated the storage modulus is larger than the loss

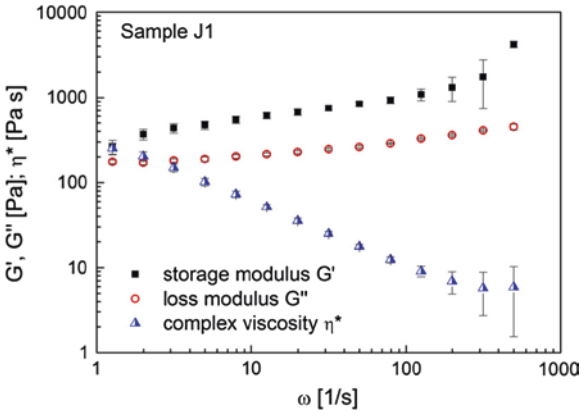

Fig. 2 Storage modulus, loss modulus, and complex viscosity of sample J1 at 30 °C

modulus and both moduli show only a weak frequency dependence. This behavior is characteristic of a gel. Samples J1–J5 show a similar behavior. Thus, rheologically all these samples are gels. Samples J1 and J2 have the highest storage modulus of all samples (2000 Pa s at a frequency of 1 Hz). Amplitude sweep experiments, in which the complex modulus is measured as a function of deformation, show that both the extent of the linear viscoelastic regime and the cross-over point of G' and G'' decrease with increasing SDS content. In other words, the gels with a higher CA/SDS ratio are stronger.

3.3 Thermal Phase Transitions

Since samples were prepared by cooling from 70 °C some of them, in particular the gel-like ones, are in a quenched non-equilibrium state. For the formation and for the long-term stability of these quenched structures the dynamic state of the molecules is important. The alkyl chains of the fatty alcohol and of the surfactant can be in a frozen or in a mobile state. Transitions between phases differing in alkyl chain dynamics can be revealed by DSC measurements. Before presenting the thermal transitions of the SDS/CA/water samples the phase behavior of fatty alcohols, the major component of the gel-like samples, will be reviewed briefly.

The polymorphism of fatty alcohols has been known for a long time. Three phases have been reported [2, 9, 26, 34, 35]. At high temperatures a hexagonal or rotator phase may exist, which is ususally denoted by α but also by R'_{II} [33] because of its similarity to the R_{II} phase of *n*-alkanes. At lower temperatures an orthorhombic phase (β or β_1) or a monoclinic phase (γ or β_2) is found for alcohols with odd or even number of carbon atoms, respectively. The transition temperatures depend on the purity of the samples; hydration, in particular, causes a stabilization of the α phase by shifting the melting temperature upwards and at the same time lowering the transition temperature to the low-temperature phase [14, 26]. For cetyl alcohol of high purity only a single peak is seen in calorimetric measurements upon heating; the transition at 322.2 K may be close to a triple

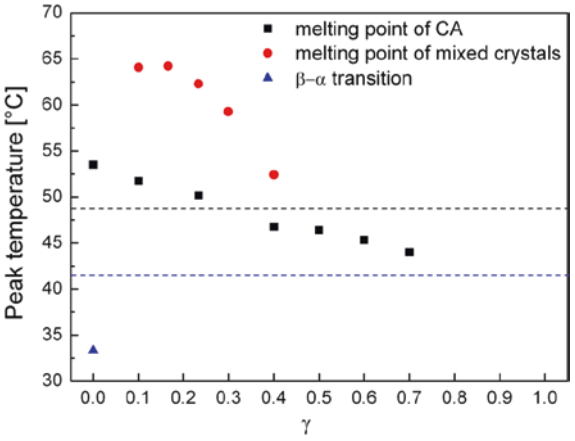

Fig. 3 Transition temperatures obtained by DSC for the samples of Table 1. The *dotted lines* represent the transition temperature (41.5 °C) and the melting point (48.7 °C) of neat CA

point of the melt and the two crystalline phases β and α [34]. On cooling, however, at first the transparent crystals of the α phase separate from the melt before the opaque crystals of the β phase appear at lower temperature [26]. Thus two peaks can be seen by differential scanning calorimetry (DSC) upon cooling.

The crystalline phases consist of stacked bilayers of alcohol molecules, which are either in a tilted (γ) or perpendicular orientation (α and β) with respect to the plane of the bilayers. A similar stacking of bilayers is found in lamellar liquid crystals but in this case the structure is swollen in a one-dimensional fashion by water and/or oil. Depending on whether the surfactant and cosurfactant chains are in a conformationally disordered molten or an extended rigid state, the lyotropic liquid crystalline phase is called L_α or L_β phase, respectively. The L_β phase is also known as gel phase. This nomenclature is also used for lipids. Concerning the surfactant/fatty alcohol/water systems considered here, it must be pointed out that the swelling of α crystals with water results in an L_β phase.

Using DSC, one or two transitions are found for the dilute aqueous dispersions of fatty alcohol/surfactant mixtures, depending on the mass fraction of the surfactant γ. This is shown in Fig. 3 for the system SDS/CA/D_2O (97 wt% D_2O). The transition temperatures depicted in Fig. 3 correspond to the peak temperatures of the second heating run after a previous heating and cooling cycle. It must be emphasized that the dispersions are not in thermodynamic equilibrium and plots as the one in Fig. 3 do not represent a phase diagram. Qualitatively the same behavior, namely, two transitions at low surfactant content which merge into only one transition at higher surfactant content, is found when CA is replaced by the shorter myristyl alcohol (*n*-tetradecanol) [19] and also in the system CMEA/CA/water [38].

The transitions of neat CA (measured upon cooling where the α modification is formed) are shown as dotted lines in Fig. 3. The two transitions observed for the dispersion with $\gamma = 0$ (SDS-free) correspond to those of hydrated CA and are assigned to the β-to-α transition and to the melting point of the α phase. When

SDS is added the β-to-α transition is no longer seen, probably because it is shifted to even lower temperatures. The main effects of replacing more and more CA by SDS are (i) a decreasing temperature of the melting transition of CA α crystals due to the incorporation of some SDS molecules, and (ii) an additional phase transition at higher temperatures, which is assigned to the melting of a water-swollen phase of bilayers consisting of CA and SDS. Due to the immobility of the chains (cf. Sect. 4) this new phase is a gel phase, L_β. Its melting point decreases with increasing SDS mass fraction. The decrease of both transition temperatures upon addition of SDS can be explained by the higher mobility of the shorter SDS chains. Based on the low transition enthalpy of the transition at lower temperature, which was not observed at all for some samples of the system containing myristyl alcohol, we may conclude that only a small amount of the alcohol-rich phase with the low melting point is present. Whether or not this crystalline phase is present may depend on the conditions of sample preparation.

Although the transition temperatures of the CMEA/CA/water system [38] exhibit a striking similarity there is also one difference in comparison to SDS/CA/water. By polarizing microscopy and Raman microscopy the low-temperature transition of CMEA/CA/water could be assigned to the melting of needle-shaped CMEA-rich crystals. In other words, the surfactant, not the alcohol is the main component of the crystals with the low melting temperature. The high content of CMEA in these crystals is probably due to the poor solubility of this surfactant in water, in contrast to SDS. For CMEA/CA/water the transition at higher temperature coincides with the disappearance of vesicle-like structures, which show Maltese crosses in polarizing microscopy with crossed polarizers and are rich in CA according to Raman microscopy. The small amount of SLES present in the CMEA/CA/water system may control the phase behavior to a large extent by playing a role similar to SDS. The influence of SLES is also evident from the presence of the high temperature transition of the CMEA/CA/water system in the absence of CMEA. In SDS/CA/water (cf. Fig. 3) this transition is absent at $\gamma = 0$ since no surfactant is present.

Based on the properties described so far, samples J1–J3 can be clearly considered as gels, samples J4–J6 are less well defined and samples J7–J8 macroscopically separate into two phases consisting of micelles and crystals. Sample J9 may contain very few dispersed crystals, while J10 is a one-phase micellar solution.

4 NMR

NMR spectroscopy on ^{1}H, ^{2}H, and ^{13}C nuclei offers many possibilities to study gel-like systems. Both high-resolution and solid-state NMR can be used to obtain complementary information. In addition, diffusion measurements by pulsed field gradient NMR can be employed to study structural aspects.

4.1 ^1H NMR Spectroscopy

High-resolution proton NMR spectroscopy can be used to obtain an overview on the phase behavior. The linewidth and the presence or absence of peaks provides information on the dynamic state of the chain molecules. As an example, the proton spectra of the different samples of SDS/CA/D_2O obtained at 30 and 70 °C, which are shown in Fig. 4, are discussed [19]. The signal of D_2O, which has a temperature dependent resonance frequency, was used as lock signal and chemical shift reference. Therefore the other signals have temperature-dependent chemical shifts. The signal intensities of all spectra are scaled to obtain equal heights of the large CH_2 peaks, which occur at about 1.3 and 1.7 ppm in the spectra at 30 and 70 °C, respectively.

The top rows in each set show the spectra of an aqueous solution containing 3 wt% SDS (sample J10 with $\gamma = 1$), which is well above the critical micelle concentration of 0.2 wt% [5]. Most of the methylene groups have similar chemical shifts and contribute to one single unresolved peak but the signals of the methyl group and the α- and β-methylene groups are well resolved *J* multipletts. The high resolution proves that the aggregates are small and have short correlation times of rotation.

A comparable resolution is found for both SDS and CA signals when only a small fraction of SDS is replaced by CA (sample J9 at 30 °C as well as samples J9 and J8 at 70 °C). These are the transparent samples. Since pure CA is insoluble in water, yielding no signal for sample J0 (spectrum not shown), the presence of highly resolved CA signals in samples J9 and J8 makes evident that CA is incorporated into the SDS micelles, which are small and rotating quickly. As the fraction of CA is increased the signals broaden at first, indicating a growth of the aggregates, which leads to a loss of their rotational freedom (J8–J6 at 30 °C). The growth of the aggregates is due to a change in curvature resulting from the increase of the average surfactant packing parameter *P* [23] as more and more of the anionic surfactant SDS, which has a large effective head group, is replaced by CA, which has a very small headgroup.

As γ is further decreased the signals disappear almost completely (J4–J1 at 30 °C) due to chain freezing. The poor signal-to-noise ratio observed for the samples in the gel regime shows that only a very small fraction of the chains is not frozen. Furthermore, the shape of the CH_2 peak of samples J8–J3 indicates the presence of several phases in which the components have slightly different chemical shifts. This proves the multi-phase structure also of mixtures which do not show a macroscopic phase separation.

The comparison of the spectra at 30 and 70 °C shows that samples with high γ show almost no temperature dependence, whereas a large increase in the signal intensity is found at higher temperature for the samples with higher CA content (low γ), indicating that most alkyl chains have melted. The melting sets in at 55 °C at the lower phase transition observed by DSC, but only for a small fraction of the chains. Most chains begin to melt at the upper transition. However, even at 70 °C

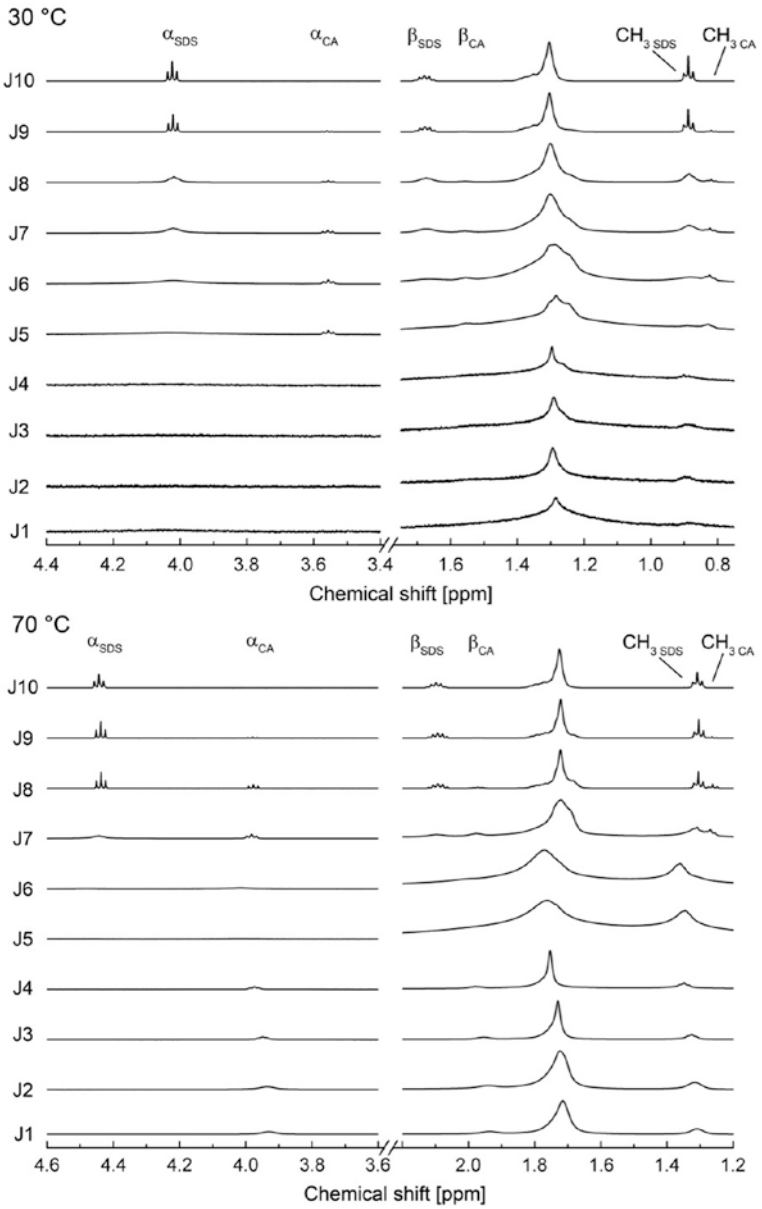

Fig. 4 ^{1}H NMR spectra at 30 (*top*) and 70 °C (*bottom*). Within each series of spectra the mass fraction of SDS (γ as given in Table 1) decreases from top to bottom

not all of the theoretical signal intensity is found either due to incomplete melting or macroscopic phase separation which leads to accumulation of some components outside of the active volume of the NMR coil. For the CMEA/CA/water

system at $\gamma = 0.4$ it was also found that very little signal can be detected at the lower phase transition and most of the proton signals appear only above the upper phase transition temperature [38].

4.2 ^{13}C Spectroscopy

Proton NMR is a tool that is easy to use for the investigation of mobile components and the detection of chain melting but its use for a more detailed investigation of the rigid fraction is limited to a line width or second moment analysis in order to compare completely immobilized chains from rotating ones in rotator phases [4]. Complementary information on the solid fraction can be obtained by high resolution solid-state NMR which is routinely available for ^{13}C, using magic angle spinning (MAS), cross polarization (CP), and dipolar decoupling of protons [37, 39]. The large chemical shift range of ^{13}C yields well resolved spectra with signals from the different components. Hence, the presence or absence of components in solids and solid-like phases can be determined. Moreover, the signals of all-trans chains and disordered chains, which are separated by about 2–3 ppm due to the γ-gauche effect can be distinguished [22].

Both for the SDS/CA/water and the CMEA/CA/water systems, the all-trans signal disappears above the upper phase transition temperature. The signal of disordered chains is usually of lower intensity since cross-polarization, which requires a dipolar coupling between ^{1}H and ^{13}C nuclei, is less efficient for mobile chains. Cross-polarization breaks down completely for liquid-like chains with isotropic mobility since the dipolar coupling is averaged to zero. Highly mobile chains can be observed better by using direct carbon excitation instead of cross-polarization.

^{13}C NMR spectroscopy can also be used to investigate the long-term stability of gels. Since the gels are often metastable, a common ripening or ageing effect is the formation of crystals. As an example, in Fig. 5 ^{13}C CP/MAS NMR spectra of sample J1 of the SDS/CA/water system immediately after preparation as well as 14 and 29 days later are shown. The increase of the cross-polarized signal resulting from rigid chains is clearly recognized.

4.3 ^{2}H NMR Spectroscopy

^{2}H NMR spectroscopy using D_2O as a probe is widely used to study the phase behavior of more concentrated surfactant systems [7, 41] but provides less information for very dilute systems, in which the residual quadrupole coupling resulting from the anisotropic motion of water molecules next to the bilayers is smaller than the line width. In favorable cases, when the domains of a lamellar phase are large and free of defects which lead to curved bilayers, quadrupole

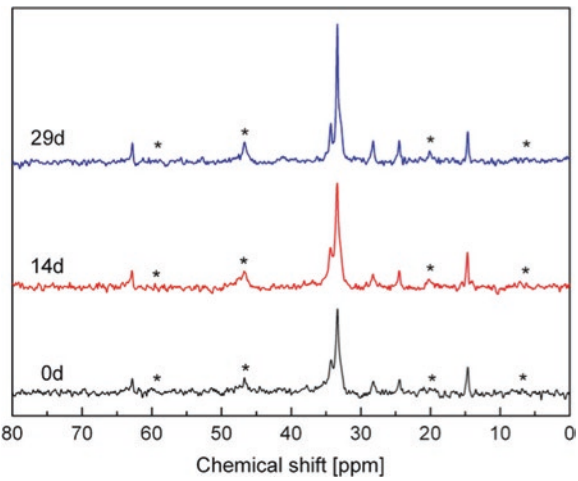

Fig. 5 ^{13}C CP/MAS NMR spectra of sample J1 immediately after preparation, 14 and 29 days later. Rotational side bands are labeled with *asterisks*

splittings have been observed in aqueous solutions containing as little as 10 wt% surfactant [25]. At even lower concentrations there are usually no resolved splittings, in particular, since vesicles prevail in dilute systems, and water diffusion along the curved bilayers leads to motional averaging and a collapse of the splitting to a single isotropic peak. Therefore, the D_2O signal provides little information on the phase structure of very dilute systems. However, the use of a selectively deuteriated surfactant or cosurfactant, though expensive, can be an alternative if the concentration of the deuteriated species is not too low. Due to the large spectral width, the signal-to-noise ratio is low and long measurement times are required.

For the more concentrated CMEA/CA/water system investigations with deuteriated components have been carried out at $\gamma = 0.4$ [38]. When 50 % percent of CA is replaced by α-deuteriated stearyl alcohol a large quadrupole splitting of approximately 28 kHz, consistent with a rotator phase, is observed. At the upper phase transition temperature of about 315 K, where the chains melt, the splitting is reduced to about 19 kHz and decreases to about 14 kHz at 330 K. This shows that the system passes through a lamellar liquid-crystal L_α phase before the isotropic phase, recognized by the appearance of an intensive single peak, begins to form at 328 K. When 50 % of CMEA is replaced by an analogue containing a deuteriated hydroxy ethyl group (two different CD_2 groups) a reduced splitting, which shows a continuous decrease with increasing temperature, first occurs above the lower transition temperature. Most interestingly, after several months, the signal of the deuteriated stearyl alcohol had "disappeared" at room temperature, most likely meaning that due to crystallization the splitting was increased to a value larger than the measured spectral range of 60 kHz [38]. These observations illustrate that ^{2}H NMR spectroscopy can also be a useful tool to investigate phase transitions and molecular dynamics in rather dilute systems.

4.4 Rheo-NMR Spectroscopy

In the dilute region of bilayer-forming systems vesicles are very common, in particular when shear is applied during mixing. Vesicles also exist in the SDS/CA/water system, cf. Sect. 6. In more concentrated systems containing 35–60 wt% surfactant ^{2}H NMR spectroscopy under shear, so-called rheo-NMR [8, 20], has been used to detect vesicles and their formation or destruction in situ [29, 30, 36]. At high water content, as mentioned before, there is neither a resolved splitting (for layered structures) nor a noticeable line-broadening (in the case of vesicles) and ^{2}H rheo-NMR spectroscopy using D_2O as probe molecule fails. Using deuteriated surfactant is no alternative in this case since the expected signal-to-noise ratio is very low and diffusion of the deuteriated species is too slow for vesicle formation to have a significant effect on the spectral lineshape as the motional regime of $\tau_c \approx 1/\Delta\nu$ (where τ_c denotes the correlation time of reorientations due to diffusion and $\Delta\nu$ is the quadrupole splitting) is not reached.

On the other hand, ^{1}H NMR was found to be very sensitive to the structures in the dilute SDS/CA/water system and should provide information on the effect of shear in such dilute gel-forming systems. In particular, it should be possible to follow the processes of chain melting and freezing, which depend on the composition of the phases present and therefore on the mixing protocol. As a first step towards such investigations a prototype ^{1}H rheo-probe was built as part of this project [19].

In Fig. 6 some spectra obtained with the ^{1}H rheo-probe are shown [19]. In the top and center the spectra of samples J9 (micellar solution) and J1 (gel) in comparison with the high-resolution spectra illustrate the limited resolution of the solid-state spectrometer used. Nevertheless, the liquid and gel samples can be distinguished. Due to the low signal-to-noise ratio of the alkyl chain signal of the gel sample the peak resulting from residual protons in water and a background signal from the Teflon coil support appear enlarged. Nevertheless, as shown at the bottom of Fig. 6, the chain melting in the gel sample can be clearly detected with the rheo-probe. The very first experiments under shear have not yet shown a change of the NMR spectrum and further investigations at variable temperatures and compositions should be performed.

4.5 NMR Diffusometry

Pulsed field gradient NMR is an established tool for the investigation of self-diffusion, which is very sensitive to the structure of surfactant systems [3, 13, 31, 40]. As an example results obtained for the system SDS/CA/water are shown in Fig. 7. Previous investigations of this system by NMR diffusometry gave similar results [15]. The data presented in Fig. 7 were obtained from echo decay curves measured using the pulsed gradient spin echo technique [40] with trapezoidal magnetic field gradients of varying amplitude at 30 °C. The diffusion time Δ (more precisely,

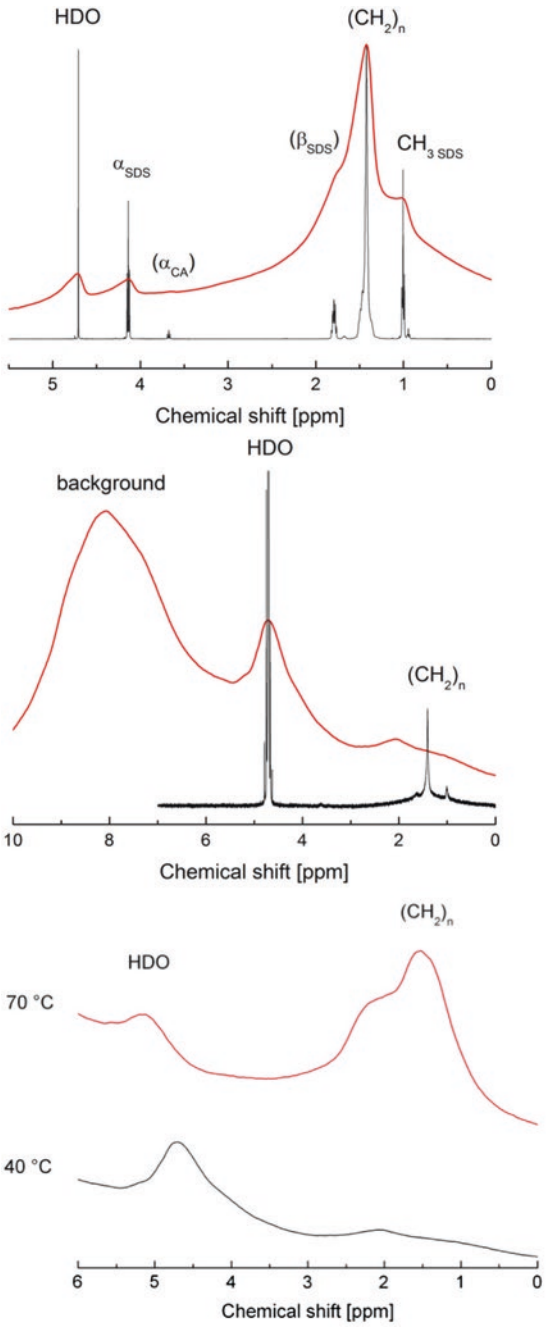

Fig. 6 ^{1}H NMR spectra obtained with a prototype of a rheo-NMR probe for proton measurements. *Top* and *center*: Spectra of samples J9 (micellar solution) and J1 (gel) in comparison with high resolution ^{1}H NMR spectra. *Bottom*: Spectra of sample J1 at 40 and 70 °C. Despite the poor resolution of the rheo-probe and a background signal from the coil support made of Teflon the difference between rigid and fluid alkyl chains can be clearly recognized

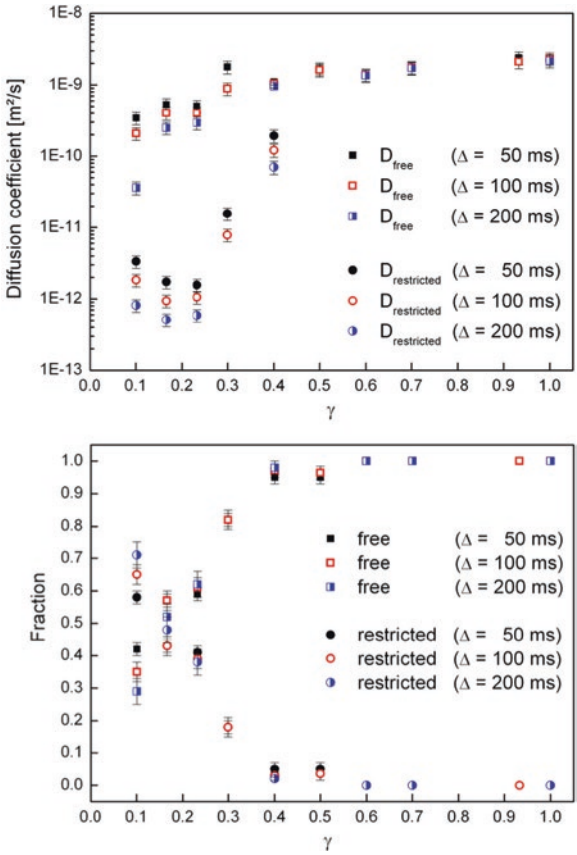

Fig. 7 Diffusion coefficients of free and restricted water molecules for different diffusion times Δ (*top*) and fractions of free and trapped water molecules (*bottom*)

the delay between the gradient pulses) was kept constant in each experiment. The echo decay curves of the water signal were analyzed using the most simple model assuming two populations of water with different self diffusion coefficients D. The two populations with a higher and a lower diffusion coefficient correspond to "free" water, which can diffuse more or less unhindered, and to "trapped" water which is severely restricted in its diffusion because it is enclosed within vesicles or between bilayers. A possible exchange between the two populations was not taken into account. In Fig. 7 the two diffusion coefficients (top) and the fractions of the two populations (bottom) are shown. For samples with a high mass fraction γ of SDS only one population of free water with a high diffusion coefficient is found. The values of this diffusion coefficient are independent of Δ which is typical for free diffusion. The diffusion coefficients of the samples in the micellar region are consistent with the literature value of pure HDO which is between 2.14 and 2.43 $\times$ 10^{-9} m^2 s^{-1} at 25 °C [42]. With increasing amount of CA (decreasing γ) D decreases indicating an increasing obstruction by larger aggregates. Starting from $\gamma = 0.4$ (sample J5) the echo decay curves can no longer be fitted with a

single diffusion coefficient and the apparent diffusion coefficients decrease with increasing diffusion time Δ, indicating restricted diffusion. In the gel regime, as γ gets smaller, diffusion gets slower and the fraction of slowly diffusing water molecules (cf. bottom of Fig. 7) increases to more than 50 %.

5 Scattering Methods

Small angle X-ray and neutron scattering techniques also yield structural information. Small angle X-ray scattering (SAXS) can be used to obtain information on the period of layer stacking. The structures of crystals can be investigated with wide-angle X-ray diffraction. Small angle neutron scattering (SANS) can provide information on aggregate shapes.

5.1 SAXS

Figure 8 shows small-angle X-ray scattering intensities as a function of the modulus of the scattering vector Q for samples in the gel region of the SDS/CA/water system [19]. Two peaks (1st and 2nd order) corresponding to a distance of about 4.5 nm, which amounts to approximately twice the length of a CA molecule, can be recognized. The distance decreases with increasing γ and approaches twice the length of an SDS molecule at high γ. The shoulder observed for some of the samples, which develops into a second peak at higher γ (not shown), gives additional evidence of the multi-phase structure of the samples. The instrument used to obtain the data shown in Fig. 8 did not allow for the detection of peaks at even lower scattering vectors. Measurements on the SDS/CA-SA/water system, which

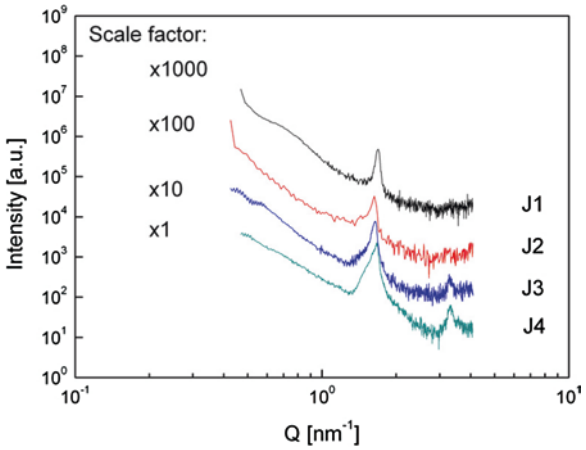

Fig. 8 Small angle X-ray scattering of the gel samples J1 to J4 at room temperature

was investigated at a higher concentration (89 wt% water) have shown several orders of peaks at lower Q values corresponding to a lamellar order with a period of 26 nm [1]. The broad peaks which can be recognized in Fig. 8 below $Q = 1\,\mathrm{nm}^{-1}$ and the increased intensities at the beginning of some curves may correspond to higher orders of lamellar correlation peaks.

5.2 Neutron Scattering

Results obtained by very-small-angle neutron scattering (V-SANS) performed with the KWS-3 instrument at the FRM II research reactor in Garching/Munich on some of the samples of the SDS/CA/water system are shown in Fig. 9. The observed Q^{-2} dependence is consistent with vesicular structures which have a bilayer thickness much smaller than the radius of the D_2O-filled core. In this case the scattering of the shells becomes identical to the scattering of extended lamellar sheets [32].

The scattering curves of samples of the gel region, shown in Fig. 9, show a more or less pronounced shoulder between 0.07 and 0.22 nm^{-1}. This feature can be interpreted as a smeared correlation peak caused by periodic lamellar structures. It occurs in a similar range of Q values as the peaks observed for the more concentrated SDS/CA-SA/water system investigated by X-ray scattering [1]. For sample J3 the lamellar correlation peak corresponds to a periodic distance of 39.3 nm, which is higher than the value observed for the more concentrated system with a mixture of the alcohols CA and SA. There is no obvious trend in position or shape of the correlation peak for samples with different γ. This may be due to the fact that the applied protocol of sample preparation does not ensure a fully reproducible structure of the samples.

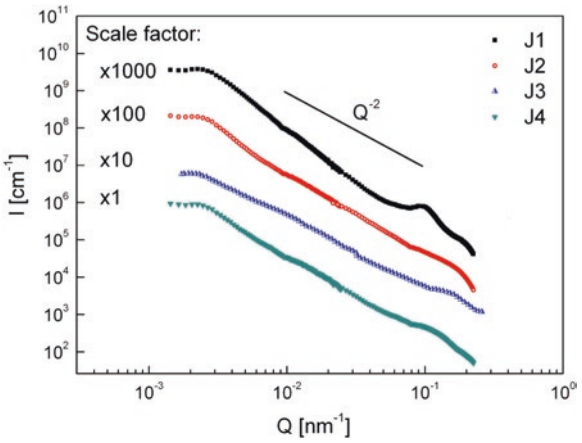

Fig. 9 V-SANS of the gel samples J1 to J4

In addition to the lamellar correlation peak, a very weak shoulder can be seen between 0.9×10^{-2} and 2.5×10^{-2} m^{-1} in Fig. 9. This Q range corresponds to distances between 0.25 and 0.67 μm, which matches the most frequent vesicle diameters.

6 Transmission Electron Microscopy (TEM)

Sample images obtained by microscopic techniques provide the most direct information on sample structures. However, care must be taken not to interpret artifacts resulting from sample preparation. Specimens for cryo-TEM must be very thin and vesicular structures with diameters larger than about 1 μm will collapse. Blotting leads to a change of concentration which may result in a change of aggregate structures.

In Fig. 10, cryo-TEM images of two samples of the SDS/CA/water system are shown. Because of the poor contrast, image tracing was used to visualize the most prominent features, which were statistically analyzed. Both samples, J3 of the gel region and J6 of the multiphase region, show vesicular structures. While those of

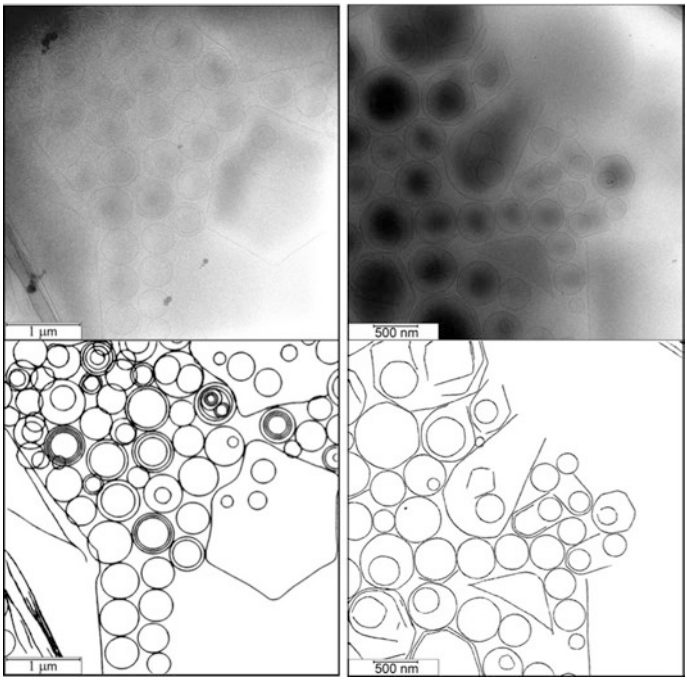

Fig. 10 Cryo-TEM images of sample J3 (gel) and J6 (multi-phase region) (*top*) and contours of the aggregates obtained by image tracing (*bottom*)

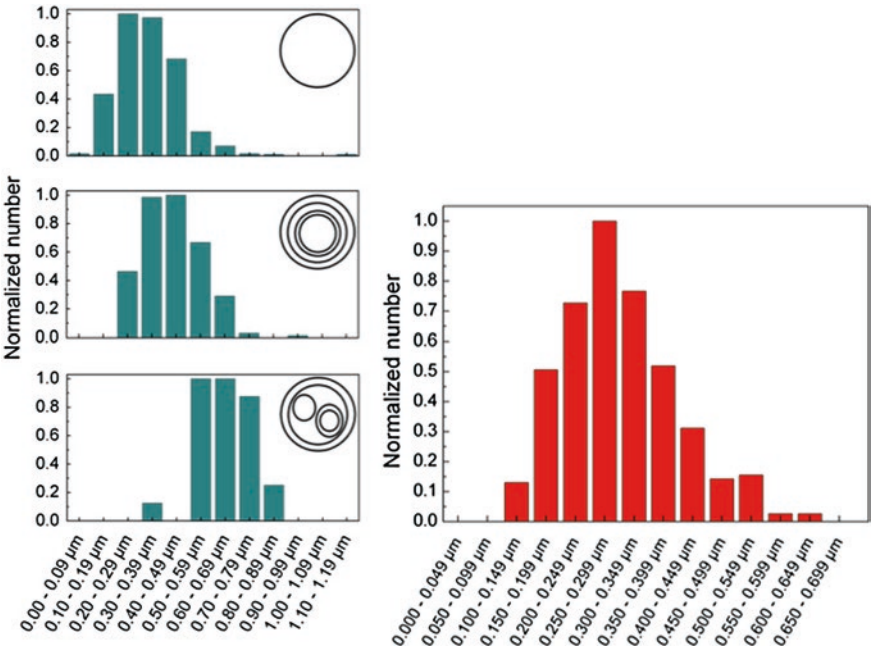

Fig. 11 Distribution of vesicle diameters for samples J3 (*left*) and J6 (*right*)

Table 2 Vesicle statistics

Sample	Vesicle type	Relative abundance	Average diameter (µm)
J3	ULV	1.00	0.33
J3	MLV	0.38	0.43
J3	MVV	0.04	0.65
J6	ULV	1.00	0.30
J6	MLV	0.08	0.45
J6	MVV	–	–

sample J3 appear only slightly darker than their surroundings and multiple layers can be recognized, the ones of sample J6 have much darker cores and usually only a single layer at the perimeter can be recognized.

The distributions of the vesicle diameters obtained for the two samples are shown in Fig. 11. For the gel-like sample J3 a distinction is made between unilamellar (ULV), multilameller (MLV) and multivesicular vesicles (MVV). In Table 2 the average diameters of the different types of vesicles and their relative abundance for a total vesicle count of 903 (J3) and 357 (J6) are summarized. The average vesicle diameters are consistent with the position of the weak shoulder

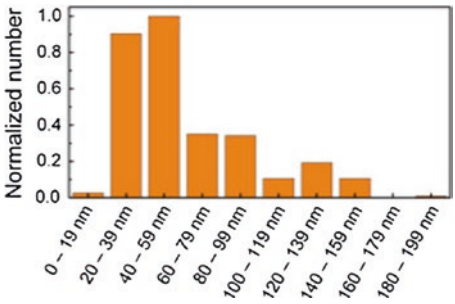

Fig. 12 Distribution of distances between neighbouring bilayers in sample J3

observed at intermediate Q values by SANS. Figure 12 shows the distribution of the distance between bilayers in multilamellar vesicles. The lamellar distances determined by the analysis of the cryo-TEM images of sample J3 are in good agreement with the lamellar correlation peak observed by SANS corresponding to a periodic distance of 39.3 nm.

7 Discussion

The results found by different experimental methods for the SDS/CA/water system presented here and for similar systems provide evidence that the gel phases contain a large volume fraction of vesicles, which can be of the multilamellar type. The amphiphilic molecules which form the bilayers have frozen alkyl chains making the vesicles fairly rigid. The gel character does not result from a connected network as in the case of, for example, entangled worm-like micelles but from the jamming of the vesicles due to their large volume fraction. The gelling phenomenon of vesicles is similar to the glass transition of colloidal dispersions which occurs at a volume fraction of about 58 % for hard spheres [21]. The gels discussed here may contain additional crystals or planar lamellar structures as well, but their influence on the rheological properties is probably small. Such a gel state of densely packed multilamellar vesicles has also been reported, for instance, for a cat-anionic fluoro/hydrocarbon surfactant system [28].

In the following, the volume fraction of vesicles in the SDS/CA/water system is estimated in order to verify the gel model of jammed vesicles. Sample J3 with $\gamma = 0.23$ (cf. Table 1), for which the required experimental data are available, will be considered. The two water populations found in the gel regime have been assigned to water that is trapped inside of vesicles or between bilayers and to almost pure water. The volume fractions of these two water populations can be estimated from

$$\phi_{\text{bilayer}}^{(\text{sample})} = f\phi_{\text{bilayer}}^{(\text{ves})} + (1-f)\phi_{\text{bilayer}}^{(\text{aq})}, \tag{3}$$

where f and $1-f$ are the volume fractions of the vesicle "phase" and the continuous water "phase", while $\phi_{\text{bilayer}}^{(\text{sample})}$, $\phi_{\text{bilayer}}^{(\text{ves})}$, and $\phi_{\text{bilayer}}^{(\text{aq})}$ denote the volume fractions of bilayers in the whole sample, in the vesicle phase, and in the water phase, respectively. The total volume fraction of bilayers in the sample can be replaced by the combined volume fractions of SDS and CA if the small amounts of SDS and CA in the aqueous continuum and in crystals are neglected. With the densities $\rho_{D_2O} = 1.1\ \text{g cm}^{-3}$, $\rho_{\text{SDS}} = 1.0\ \text{g cm}^{-3}$, and $\rho_{\text{CA}} = 0.81\ \text{g cm}^{-3}$, the mass fractions given in Table 1 can be converted to volume fractions. For sample J3 a combined volume fraction of SDS and CA of 3.9 % results, which is taken as the average volume fraction of bilayers in the whole sample, $\phi_{\text{bilayer}}^{(\text{sample})}$. Taking the lamellar period of the crystals obtained by X-ray scattering as an estimate of the bilayer thickness, $d_{bilayer} = 4.5$ nm, and the average distance of bilayers determined by TEM as an estimate of the lamellar period, $d = 61.1$ nm, the volume fraction of bilayers in the vesicles is approximately $\phi_{\text{bilayer}} = d_{\text{bilayer}}/d = 7.4\,\%$. Since the volume fraction of bilayers in the aqueous continuum is zero Eq. 3 yields $f = 53\,\%$. Taking into account that part of the volume in the vesicle phase is occupied by bilayers, the fraction of water in the vesicle phase amounts to 51 %. This value can be compared with the fraction of trapped water determined by the diffusion experiments, which is about 40 % for sample J3 (cf. Fig. 7). Given the simplicity of the models used in fitting the diffusion data and for the structure the agreement with the calculated value is very good. Furthermore, the volume fraction of 53 % for the vesicles is quite close to the volume fraction of 58 % at which the colloidal glass transition of hard spheres is found. These findings support the model of jammed vesicles.

The large volume fraction of vesicles required for a gel to form can be achieved at a low combined volume fraction of surfactant and cosurfactant only if the distance between single bilayers in multilamellar vesicles is sufficiently large. Hence, if the swelling of lamellar aggregates is not sufficient the aggregates will be too compact and their volume fraction will not be large enough to cause jamming. The comparison of the TEM images of samples J3 and J6 depicted in Fig. 10 suggests indeed that the vesicles of sample J6, which is not in the gel regime, have much more compact cores than the vesicles of the gel sample J3. From the diffusion results, which yield a very small fraction of only about 5 % of trapped water in sample J6, one may conclude that the vesicle cores of this sample consist mainly of bilayers and very little water. This structural difference is in good agreement with the different rheological properties of these two samples.

Different experimental techniques, such as the DSC and NMR investigations presented above, have shown that the gels contain bilayers with frozen alkyl chains. Rigid molecules are not only important for the rigidity of the vesicle membranes but also for the long-term stability of the metastable gels. If the mobility of the molecules forming the bilayers gets too high diffusion of the molecules will lead to the formation of the thermodynamically stable crystalline phases. A chain length mismatch of the alcohol molecules as in the commonly used mixtures of cetyl and stearyl alcohol helps to prevent crystallization [1].

The DSC investigation of the SDS/CA/water and similar systems suggests that a large difference between the melting point of stable hydrated crystals and the melting point of the (metastable) L_β phase is required for gels to form. If the difference in melting points is too small the L_β structure cannot be quenched to temperatures sufficiently far below its own melting point and thermodynamically stable crystals will form instead. The formation of the gel phase appears to be kinetically controlled. On the other hand, it has also been suggested that the presence of larger fractions of the ionic surfactant leads to a higher ionic strength of the aqueous solution between the bilayers and therefore to a screening of their electrostatic repulsion and thus to a collapse of the bilayers, which enables the formation of crystals and leads to phase separation [14].

8 Conclusion

In order to obtain stable gels from aqueous dispersions of bilayer-forming surfactant/cosurfactant mixtures the following aspects should be considered. The formulation should form an L_β phase with a high melting temperature. This requires the presence of sufficiently long alkyl chains. The chain melting temperature can be most easily determined by DSC or NMR measurements. For the bilayers to form vesicles a certain amount of surfactant is required to introduce some defects and to tune the bilayer curvature. A high degree of swelling of the bilayers with water must be possible in order to obtain a high volume fraction of aggregates, in which most of the water is trapped. This can be verified by NMR diffusometry. The chain melting temperature and the volume fraction of trapped water appear to be the most important parameters that should be optimized.

Acknowledgments We thank Vitaliy Pipich, Martin Schneider and Günter Goerigk for help with the neutron scattering experiments performed with the JCNS (Jülich Centre of Neutron Science) instrument KWS-3 at the FRM II research reactor in Garching/Munich, Frank Polzer for the cryo-TEM experiments, Daniel Topgaard and Stefanie Eriksson for help with the pulsed field gradient diffusometry performed at Lund University, Hans Egold and Karin Stolte for the high resolution proton NMR measurements, and the students Johannes Brinkmann, Svenja Marl, Dagmar Moritz, Matthias Hoffmann, Malte-Ole Schneemann, Alexei Schwarz, Nikolai Sitte, Viktor Warkentin, Daniel Wiegmann, and Martin Wiesing for their support. This project was funded by Deutsche Forschungsgemeinschaft, priority program SPP 1273.

References

1. Awad TS, Johnson ES, Bureiko A, Olsson U (2011) Colloidal structure and physical properties of gel networks containing anionic surfactant and fatty alcohol mixture. J Dispersion Sci Technol 32:807–815
2. Abrahamsson S, Larsson G, von Sydow E (1980) The crystal structure of the monoclinic form of *n*-hexadecanol. Acta Cryst 13:770–774

3. Åslund I, Medronho B, Topgaard D, Söderman O, Schmidt C (2011) Homogeneous length scale of shear-induced multilamellar vesicles studied by diffusion NMR. J Magn Reson 209:291–299
4. Andrew ER (1950) Moleculer motion in certain solid hydrocarbons. J Chem Phys 18:607–618
5. Berr SS (1987) Solvent isotope effects on alkyltrimethylammonium bromide micelles as a function of alkyl chain length. J Phys Chem 91:4760–4765
6. Berret J-F (2004) Rheology of wormlike micelles: equilibrium properties and shear-banding transitions. In: Weiss RG, Terech P (eds), Molecular gels. Materials with self-assembled fibrillar networks. pp. 667-720
7. Blackburn JC, Kilpatrick PK (1992) Using deuterium NMR lineshapes to analyze lyotropic liquid crystalline phase transitions. Langmuir 8:1679–1687
8. Callaghan PT (1999) Rheo-NMR: nuclear magnetic resonance and the rheology of complex fluids. Rep Prog Phys 62:599–670
9. Chapman D (1956) Infra-red spectroscopy applied to studies of polymorphism. Spectrochim Acta 11:609–617
10. Chevalier Y, Zemb T (1990) Structure of micelles and microemulsions. Rep Prog Phys 53:279–371
11. Dreiss CA (2007) Wormlike micelles: where do we stand? Recent developments, linear rheology and scattering techniques. Soft Matter 3:956–970
12. Eccleston GM (1990) Multiple-phase oil-in-water emulsions. J Soc Cosmet Chem 41:1–22
13. Ferreira TM, Bernin D, Topgaard D (2013) NMR studies of nonionic surfactants. Annu Rep NMR Spectrosc 79:73–127
14. Goetz RJ, El-Aasser MS (1990) Dilute phase behavior of cetyl alcohol, sodium lauryl sulfate, and water. Langmuir 6:132–136
15. Goetz RJ, Khan A, El-Aasser MS (1990) FT PGSE NMR investigations of the supramolecular structure of a dilute gel phase. J Colloid Interface Sci 137:395–407
16. Grewe F, Polzer F, Goerigk G, Topgaard D, Schmidt C Structure of dilute aqueous surfactant/cosurfactant emulsions (in preparation)
17. Gradzielski M (2003) Vesicles and vesicle gels—structure and dynamics of formation. J Phys Condens Matter 15:R655–R697
18. Gradzielski M (2011) The rheology of vesicle and disk systems—relations between macroscopic behaviour and microstructure. Curr Opin Colloid Interface Sci 16:13–17
19. Grewe F (2013) Structures of aqueous surfactant systems: a study of binary micellar solutions and ternary surfactant/fatty alcohol/water emulsions. Doctoral thesis, Universität Paderborn
20. Grabowski DA, Schmidt C (1994) Simultaneous measurement of shear viscosity and director orientation of a side-chain liquid-crystalline polymer by rheo-NMR. Macromolecules 27:2632
21. Hunter GL, Weeks ER (2012) The physics of the colloidal glass transition. Rep Prog Phys 75:066501
22. Ishikawa S, Ando I (1992) Structural studies of dimyristoylphosphatidylcholine and distearoylphosphatidylcholine in the crystalline and liquid-crystalline states by variable-temperature solid-state high-resolution ^{13}C NMR spectroscopy. J Mol Struct 271:57–73
23. Israelachivili JN, Mitchell DJ, Ninham BW (1976) Theory of self-assembly of hydrocarbon amphiphiles into micelles and bilayers. J Chem Soc Faraday Trans II 72:1525–1568
24. Kube M, Erler J, Peuker U, Schmidt C Thermal decomposition of ricinolic-acid-stabilized zinc oxide nanoparticles studied by FTIR and NMR spectroscopy (in preparation)
25. Kratzat K, Schmidt C, Finkelmann H (1994) A doubly branched nonionic oligooxyethylene V-amphiphile: effect of molecular geometry on liquid-crystalline phase behavior, 3. J Colloid Interface Sci 163:190–198
26. Lawrence ASC, Al-Mamun MA, McDonald MP (1967) Investigation of lipid-water system. Part 2. Effect of water on the polymorphism of long chain alcohols and acids. J Chem Soc Faraday Trans I 63:2789–2795
27. Laughlin RG (1994) The aqueous phase behavior of surfactants. Academic Press, London

28. Long P, Hao J (2010) A gel state from densely packed multilamellar vesicles in the crystalline state. Soft Matter 6:4350–4356
29. Lukaschek M, Müller S, Hasenhindl A, Grabowski DA, Schmidt C (1996) Lamellar lyomesophases under shear as studied by deuterium nuclear magnetic resonance. Colloid Polym Sci 274:1–7
30. Müller S, Börschig C, Gronski W, Schmidt C, Roux D (1999) Shear-induced states of orientation of the lamellar phase of $C_{12}E_4$/water. Langmuir 15:7558–7564
31. Medronho B, Brown J, Miguel MG, Schmidt C, Olsson U, Galvosas P (2011) Planar lamellae and onions: a spatially resolved rheo-NMR approach to the shear-induced structural transformations in a surfactant model system. Soft Matter 7:4938–4947
32. McKelvey CA, Kaler EW (2002) Characterization of nanostructured hollow polymer spheres with small-angle neutron scattering (SANS). J Colloid Interface Sci 245:68–74
33. Métivaud V, Lefèvre A, Ventolà L, Négrier P, Moreno E, Calvet T, Mondieig D, Cuevas-Diarte MA (2005) Hexadecane ($C_{16}H_{34}$) + 1-hexadecanol ($C_{16}H_{33}OH$) binary system: crystal structures of the components and experimental phase diagram. Application to thermal protection of liquids. Chem Mater 17:3302–3310
34. Mosselmann C, Mourik J, Dekker H (1974) Enthalpies of phase change and heat capacities of some long-chain alcohols. Adiabatic semi-microcalorimeter for studies of polymorphism. J Chem Thermodynamics 6:477–487
35. Meyer JD, Reid EE (1933) Isomorphism and alternation in the melting points of the normal alcohols, acetates, bromides, acids and ethylesters from C_{10} to C_{19}. J Am Chem Soc 55:1574–1584
36. Medronho B, Shafaei S, Szopko R, Miguel MG, Olsson U, Schmidt C (2008) Shear-induced transitions between a planar lamellar phase and multilamellar vesicles: continuous versus discontinuous transformation. Langmuir 24:6480–6486
37. Pines A, Gibby MG, Waugh JS (1973) Proton-enhanced NMR of dilute spins in solids. J Chem Phys 59:569–590
38. Schipunov E (2014) Untersuchung strukturierter Tensidsysteme. Doctoral thesis, Universität Paderborn, 2013 (Der Andere Verlag)
39. Schaefer J, Stejskal EO (1975) Carbon-13 nuclear magnetic resonance of polymers spinning at the magic angle. J Am Chem Soc 98:1031–1032
40. Söderman O, Stilbs P (1994) NMR studies of complex surfactant systems. Prog Nucl Magn Reson Spectr 26:445
41. Tiddy GJT (1980) Surfactant-water liquid crystal phases. Phys Rep 57:1–46
42. Weingärtner H (1982) Self diffusion in liquid water—a reassessment. Zeitschr Phys Chem 132:129–140

Resolved Numerical Simulation of Particle Agglomeration

M. Ernst and M. Sommerfeld

Abstract In numerous technical applications collisions between fine particles results in the formation of agglomerates, as for example in colloidal systems. The process of agglomerate formation is rather complex and depends on quite a number of interaction phenomena, such as particle collision rate, fluid dynamic interaction between colliding particles and molecular attraction as well as electrostatic repulsion of the particles. For analysing agglomeration in great detail and for predicting the resulting agglomerate structure the Lattice-Boltzmann method was extended and applied for simulating the motion of resolved primary particles exposed to various flow situations. The temporal variation of agglomerate morphology was characterised using the sphericity, the radius of gyration and the porosity of the convex hull. Two situations were considered where collision and agglomeration are induced by differential settling of a cluster of particles having a pre-scribed size distribution and primary particles are moving in a shear layer whereby also inter-particle collisions are being enforced. For both situations the importance of hydrodynamic interaction in the agglomeration process is emphasised.

Keywords Direct numerical simulation · Lattice Boltzmann method · Resolved particles · Hydrodynamic interaction · Agglomeration · Morphological characterisation

1 Introduction

In dense fluid-particle flows such as colloidal systems, inter-particle collisions followed by a possible agglomeration of the primary particles will determine the morphology of the produced particles and also their further transport within

M. Ernst · M. Sommerfeld (✉)
Mechanische Verfahrenstechnik, Zentrum für Ingenieurwissenschaften,
Martin-Luther-Universität Halle-Wittenberg, 06099 Halle (Saale), Germany
e-mail: martin.sommerfeld@iw.uni-halle.de

M. Kind et al. (eds.), *Colloid Process Engineering*,
DOI 10.1007/978-3-319-15129-8_3

the system. If the fine particles are well dispersed in a colloidal system, they are characterised by an extremely large surface area in relation to their volume. This leads to an increasing importance of various short-range phenomena. The molecular attraction and electrostatic repulsion of particles, often summarised to an effective interaction potential, has a direct influence on the adhesion of colliding particles. If the resulting adhesive forces are strong enough, particles tend to agglomerate with each other forming complex-shaped particle clusters. Apart from that, the hydrodynamic interaction between approaching particles causes, for example, that not all potential collision partners mandatorily collide with each other since the displacement of the fluid during the approach of particles may lead to a deflection, especially at small particle Reynolds numbers. Moreover, the flow in the direct surrounding of a moving agglomerate causes a rotation, restructuring or breakup of the agglomerate structure. This, in turn, has consequences on the directly surrounding fluid.

It becomes obvious that the modelling of all these effects in the framework of the very efficient Stokesian dynamics ([33] and references therein) and discrete particle methods ([31] and references therein) is still a big challenge. Flow simulations with fully resolved particles constitute a feasible way for analysing agglomeration phenomena in turbulent colloidal systems accounting for the short-range phenomena discussed above, especially with regard to the hydrodynamic interaction prior to inter-particle collisions. In this context, the term "fully resolved" means that the curved shape of the particle surface or an agglomerate is re-constructed by the numerical grid. Here, the focus is on the accurate representation of the particle-fluid interface as well as the boundary layers.

In recent years, several methods have been developed for simulating the transport of fully resolved freely moving particles in laminar and turbulent two-phase flows. Methods like fictions domain [17], finite difference [38], finite element [26], immersed boundary [36] as well as interface tracking [6] are only a few examples of established simulation approaches. Nevertheless, all methods mentioned above face the same problem: the limitation is that transient computations of a time-varying particle-fluid interface of moving resolved particles require a significant amount of computational time.

An alternative approach for describing the motion of fully resolved particles is based on the Lattice-Boltzmann method (LBM). The LBM has emerged to be a powerful method for numerically calculating dispersed two-phase flows for two reasons: the method's robustness and its numerical efficiency being the result of the local character of the governing equations [23, 24]. Simulation results obtained by the LBM for steady fluid flow around rigid agglomerates have been recently compared with results computed by a finite element method and Stokesian dynamics [2, 30]. Contrary to previous LBM-based studies [9, 16, 34], particle-particle collisions need to be fully resolved in order to investigate agglomeration processes in great detail.

The main objective of this work is to investigate the transport, collision and agglomeration behaviour of fully resolved particles in turbulent fluid flows.

The applicability of the present LBM to colliding point-particles suspended in homogeneous isotropic turbulence has been recently demonstrated by Ernst and Sommerfeld [13]. In this context, the direct numerical simulation of an unsteady turbulence field is realised by applying a spectral forcing scheme. As a further step, flow-induced collision and agglomeration of resolved particles should be examined in order to understand the influence of the short-range hydrodynamic interaction between approaching particles at different particle Stokes and Reynolds numbers.

The purpose of this contribution is to demonstrate the applicability of the present LBM for agglomerating particles. For this purpose, the agglomeration inside a cluster of both mono- and poly-dispersed spherical particles is analysed. In doing so, two situations are considered: settling particles in quiescent fluid as well as moving particles in a shear layer whereby inter-particle collisions are being enforced. Based on that, an investigation of the growth and transport of these agglomerates is supposed to provide an insight into small-scale processes, which might be crucial for industrial applications such as crystallisation problems.

This paper is organised as follows. In the subsequent section, the numerical method including the governing equations for the fluid as well as the treatment of moving solid-fluid boundaries required for the direct numerical simulation of fully resolved particles is presented. In Sect. 3, the characterisation of the agglomerate morphology is introduced by means of different structural parameters. Afterwards, in Sect. 4, the transient evolution of the agglomeration behaviour of a cluster of 50 settling spheres as well as the characterisation of resulting complex-shaped agglomerates is described. Secondly, in Sect. 5, the influence of fluid viscosity, particle inertia and pre-scribed particle size distribution on the agglomeration progress in laminar shear layers is investigated. And finally, in Sect. 6, the most prominent findings of this study are summarised, and an outlook on further investigations is given.

2 Description of the Lattice Boltzmann Method

In the following paragraphs, the applied numerical methods which are used for modelling the motion and agglomeration of primary particles are briefly described. This includes the basic equations of the Lattice-Boltzmann method as well as the LBM-based treatment of fully resolved particles. For this purpose, the consideration of curved no-slip particle boundaries (Sect. 2.2.1), the determination of flow-induced forces and torques acting on particles (Sect. 2.2.2) and the motion of solid-fluid boundaries over equidistant grids (Sect. 2.2.3) are described. Since particles may collide with each other explanations follow about the computation of flow-induced particle forces below the resolution limit of the finite grid during the approach of particles (Sect. 2.2.4) as well as the detection and modelling of the agglomeration of particles (Sect. 2.2.5).

2.1 Lattice-Boltzmann Method

The Lattice-Boltzmann method is a numerical scheme for fluid simulations which originated from molecular dynamics models such as the lattice gas automata. In contrast to the prediction of macroscopic properties such as mass, momentum and energy by solving conservation equations, e.g. the Navier-Stokes equations, the LBM describes the fluid behaviour on a so-called mesoscopic scale [7, 19]. The basic parameter in the Boltzmann statistics is the distribution function $f = f(\boldsymbol{x}, \boldsymbol{\xi}, t)$, which represents the number of fictitious fluid elements having the velocity $\boldsymbol{\xi}$ at the location $\boldsymbol{x}$ and the time t. The temporal and spatial development of the distribution function is described by the Boltzmann equation in consideration of collisions between fluid elements.

In this study, the Boltzmann equation is solved with the help of a single relaxation time collision operator approximated by the Bhatnagar-Gross-Krook (BGK) approach [1]. Here, the relaxation of the distribution function to an equilibrium distribution is supposed to occur at a constant relaxation parameter τ. The substitution of the continuous velocities in the Boltzmann equation by discrete ones leads to the discrete Boltzmann equation, where $f_{\sigma i} = f_{\sigma i}(\boldsymbol{x}, t)$. The number of available discrete velocity directions σi that connect the lattice nodes with each other depends on the applied model. In this work, the D3Q19 model is used which applies for a three-dimensional grid and provides 19 distinct propagation directions. Discretising time and space with Δt and $\Delta \boldsymbol{x} = \boldsymbol{\xi}_{\sigma i}\, \Delta t$ yields the Lattice-Boltzmann equation:

$$f_{\sigma i}^{**} - f_{\sigma i} = -\frac{\Delta t}{\tau} \underbrace{\left(f_{\sigma i} - f_{\sigma i}^{\mathrm{eq}}\right)}_{f_{\sigma i}^{\mathrm{neq}}} \tag{2.1}$$

where $f_{\sigma i}^{**} = f_{\sigma i}(\boldsymbol{x} + \Delta \boldsymbol{x}, t + \Delta t)$. The term in brackets on the right-hand side of Eq. (2.1) corresponds to the non-equilibrium part of the distribution function with $f_{\sigma i}^{\mathrm{neq}} = f_{\sigma i}^{\mathrm{neq}}(\boldsymbol{x}, t)$. During the propagation step, information is transported along the discrete lattice directions—left-hand side of Eq. (2.1)—followed by the collision step—right-hand side of Eq. (2.1). The discretised equilibrium distribution $f_{\sigma i}^{\mathrm{eq}}$ and the appropriate weighting factors $\omega_{\sigma i}$ for the D3Q19 model are given below:

$$f_{\sigma i}^{\mathrm{eq}} = \omega_{\sigma i} \rho \left[1 + \frac{3\, \boldsymbol{\xi}_{\sigma i} \boldsymbol{u}}{c^2} + \frac{9 (\boldsymbol{\xi}_{\sigma i} \boldsymbol{u})^2}{2 c^4} - \frac{3 \boldsymbol{u}^2}{2 c^2} \right] \tag{2.2}$$

$$\omega_{\sigma i} = \begin{cases} 1/3; & \sigma = 0,\ i = 1 \\ 1/18; & \sigma = 1,\ i = 1 \ldots 6 \\ 1/36; & \sigma = 2,\ i = 1 \ldots 12 \end{cases} \tag{2.3}$$

Here, $\boldsymbol{u} = \boldsymbol{u}(\boldsymbol{x}, t)$ and $\rho = \rho(\boldsymbol{x}, t)$ are the local fluid velocity and density. The grid constant c can be defined as the ratio of spatial and temporal discretisation.

Depending on the resolution of the numerical grid, the relaxation time parameter can limit the maximum Reynolds number. A more detailed description of the basic principles of the LBM can be found in previous publications [11–13, 21] as well as in Crouse [8], which also gives details on the implemented tree data structure.

2.2 Treatment of Fully Resolved Particles

In the present contribution, particles (i.e. primary particles as well as agglomerates) are fully resolved by the numerical grid whereby details of the flow around the particles are captured and the forces on the particles follow from the boundary condition of the LBM. These forces are used to update the particle position within the stationary equidistant grid. This approach also implies that the presence of particles and agglomerates affect the flow field and the fluid dynamic interaction between the particles (i.e. primary particles and agglomerates) is captured automatically.

2.2.1 Solid-Fluid Boundary Condition

In order to resolve the curved surface of complex-shaped particles with a structured mesh, the exact position of the particle surface within a cell is considered. There are several methods in the literature for describing a curved wall with a no-slip boundary condition in the frame of the LBM, e.g. [3, 18, 27]. Due to their applicability on moving boundaries, an extrapolation scheme proposed by Guo et al. [18] is used for the present treatment of particles.

The basic idea of the scheme above is to decompose the numerical grid into two parts. As shown in Fig. 1, all nodes that are lying within a particle structure are marked as solid nodes (grey grid cells), whereas nodes outside the particle are marked as fluid nodes (white grid cells). It is important to accentuate that in the present LBM, fluid information and particle properties are stored by definition at the grid nodes, while grid cells represent their associated control volumes. The position for any type of grid nodes is always located at the front left bottom vertex within the cubic grid cells. According to Fig. 1, the link between the fluid node $\boldsymbol{x}_F$ and the solid node $\boldsymbol{x}_S$ intersects the physical boundary at the point $\boldsymbol{x}_W$. The fraction of the intercept on the fluid side is given below:

$$q = \frac{|\boldsymbol{x}_F - \boldsymbol{x}_W|}{|\boldsymbol{x}_F - \boldsymbol{x}_S|} \tag{2.4}$$

Hence, the parameter $q_{\sigma i}$ indicates the relative distance between the particle surface and the next fluid node in σi-direction (cf. Fig. 1). Note that for finishing the propagation step of the fluid at $\boldsymbol{x}_F$, the post-relaxation distribution function at the solid node $f^*_{\sigma i}(\boldsymbol{x}_S, t)$ is needed and defined in the following way:

$$f^*_{\sigma i}(\boldsymbol{x}_S, t) = f^{\mathrm{eq}}_{\sigma i}(\boldsymbol{x}_S, t) + \left(1 - \frac{\Delta t}{\tau}\right) f^{\mathrm{neq}}_{\sigma i}(\boldsymbol{x}_S, t) \tag{2.5}$$

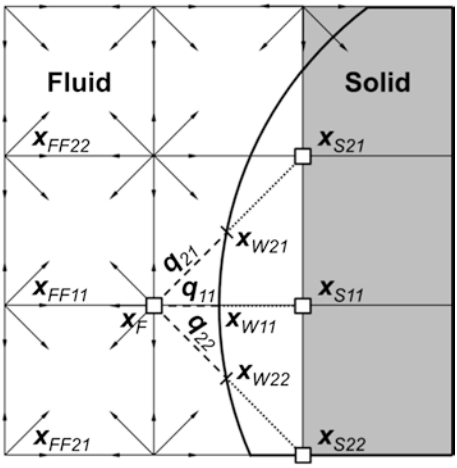

Fig. 1 Schematic two-dimensional drawing of the curved boundary condition in the LBM: the numerical grid is divided into fluid cells (*white grid cells*) and solid cells (*grey grid cells*). The effective contour of the curved obstacle (*bold solid line*) is discretised by the distribution functions (*black arrows*). The relative distance between the fluid node and the curved particle surface is weighted through the parameter $q_{\sigma i}$ (*dashed lines*). Please note that grid nodes (*small open squares*) are always located at the front left bottom vertex within the cubic grid cells

where $f_{\sigma i}^{\mathrm{eq}}(\boldsymbol{x}_S, t)$ and $f_{\sigma i}^{\mathrm{neq}}(\boldsymbol{x}_S, t)$ is the equilibrium and non-equilibrium part of $f_{\sigma i}(\boldsymbol{x}_S, t)$, respectively. The equilibrium part $f_{\sigma i}^{\mathrm{eq}}(\boldsymbol{x}_S, t)$ is approximated by a fictitious definition specified as follows:

$$f_{\sigma i}^{\mathrm{eq}}(\boldsymbol{x}_S, t) = \omega_{\sigma i}\left[\rho_P + \rho\left(\frac{3\boldsymbol{\xi}_{\sigma i}\boldsymbol{u}_S}{c^2} + \frac{9\,(\boldsymbol{\xi}_{\sigma i}\boldsymbol{u}_S)^2}{2c^4} - \frac{3\boldsymbol{u}_S^2}{2c^2}\right)\right] \tag{2.6}$$

Here, ρ_P and $\boldsymbol{u}_S$ are the density and velocity at the solid nodes $\boldsymbol{x}_S$, whereas ρ is the fluid density at $\boldsymbol{x}_F$. The velocity $\boldsymbol{u}_S$ is determined by a linear extrapolation as a function of q:

$$\begin{aligned} \boldsymbol{u}_S &= \boldsymbol{u}(\boldsymbol{x}_W) + (q-1)\boldsymbol{u}(\boldsymbol{x}_F) + (1-q)\tfrac{2\boldsymbol{u}(\boldsymbol{x}_W)+(q-1)\boldsymbol{u}(\boldsymbol{x}_F)}{1+q}, && q < 0.75 \\ \boldsymbol{u}_S &= \tfrac{\boldsymbol{u}(\boldsymbol{x}_W)+(q-1)\boldsymbol{u}(\boldsymbol{x}_F)}{q}, && q \geq 0.75 \end{aligned} \tag{2.7}$$

The non-equilibrium part $f_{\sigma i}^{\mathrm{neq}}(\boldsymbol{x}_S, t)$ can be approximated by the non-equilibrium part of the distribution function at the fluid nodes $\boldsymbol{x}_F$ and $\boldsymbol{x}_{FF}$:

$$\begin{aligned} f_{\sigma i}^{\mathrm{neq}}(\boldsymbol{x}_S, t) &= q_{\sigma i} f_{\sigma i}^{\mathrm{neq}}(\boldsymbol{x}_F, t) + (1-q_{\sigma i}) f_{\sigma i}^{\mathrm{neq}}(\boldsymbol{x}_{FF}, t), && q < 0.75 \\ f_{\sigma i}^{\mathrm{neq}}(\boldsymbol{x}_S, t) &= f_{\sigma i}^{\mathrm{neq}}(\boldsymbol{x}_F, t), && q \geq 0.75 \end{aligned} \tag{2.8}$$

Using $q_{\sigma i}$, particles are fully resolved by the numerical grid. As a consequence, details of the flow around the particles are captured, and the forces on the particles follow from the wall boundary condition of the LBM (i.e. bounce-back).

2.2.2 Particle Motion

Modelling particle motion requires two things: firstly, solving Newton's second law for translation and secondly, solving Euler's equations for rotation. The forces and torques which cause a change of position arise from fluid-particle interaction and are obtained by the LBM. Flow-induced forces and torques acting on particles can be determined by balancing the momentum of the fluid at the particle surface. The difference of the fluid momentum before and after a wall contact yields the local force $\boldsymbol{F}_{\sigma i}$. Local torques $\boldsymbol{T}_{\sigma i}$ follow from local forces and their distance to the centre of rotation $\boldsymbol{x}_R$:

$$\boldsymbol{F}_{\sigma i}(\boldsymbol{x}, t + \Delta t/2) = \frac{\Delta V}{\Delta t}\left(f_{\sigma i}(\boldsymbol{x}, t + \Delta t) - f^*_{\sigma i}(\boldsymbol{x}, t)\right)\boldsymbol{\xi}_{\sigma i} \tag{2.9}$$

$$\boldsymbol{T}_{\sigma i}(\boldsymbol{x}, t + \Delta t/2) = (\boldsymbol{x} - \boldsymbol{x}_R) \times \boldsymbol{F}_{\sigma i}(\boldsymbol{x}, t + \Delta t/2) \tag{2.10}$$

where $f^*_{\sigma i}(\boldsymbol{x}, t)$ is the discrete post-relaxation distribution function taken before the propagation. Summarising all local forces and torques along the obstacle surface, respectively, leads to the total force $\boldsymbol{F}$ or torque $\boldsymbol{T}$:

$$\boldsymbol{F}(t + \Delta t/2) = \sum_x \sum_{\sigma i} \boldsymbol{F}_{\sigma i}(\boldsymbol{x}, t + \Delta t/2) \tag{2.11}$$

$$\boldsymbol{T}(t + \Delta t/2) = \sum_x \sum_{\sigma i} \boldsymbol{T}_{\sigma i}(\boldsymbol{x}, t + \Delta t/2) \tag{2.12}$$

For validating the flow-induced forces acting on a particle, the drag coefficient of single spherical particles fixed in space was calculated for a wide range of particle Reynolds numbers (i.e. 0.3–480) and compared to experimental data. The simulations captured the main features of the flow structure around the sphere. Furthermore, the drag coefficient was predicted with reasonable accuracy [10, 21].

The particle motion is calculated in a Lagrangian frame of reference, which considers a discrete resolved particle travelling in a continuous fluid medium. The changes of the position and angular displacement of the particle, $\boldsymbol{x}_P$ and $\boldsymbol{\varphi}_P$, as well as the translational and angular components of the particle velocity, $\boldsymbol{u}_P$ and $\boldsymbol{\omega}_P$, are calculated by solving a set of ordinary differential equations (ODEs) along the particle trajectory:

$$\boldsymbol{F} + \boldsymbol{F}_{\text{ext}} = m_P \frac{\mathrm{d}\boldsymbol{u}_P}{\mathrm{d}t} \tag{2.13}$$

$$\boldsymbol{T} = \boldsymbol{J}_P \cdot \frac{\mathrm{d}\boldsymbol{\omega}_P}{\mathrm{d}t} + \boldsymbol{\omega}_P \times (\boldsymbol{J}_P \cdot \boldsymbol{\omega}_P) \tag{2.14}$$

$$\boldsymbol{u}_P = \frac{\mathrm{d}\boldsymbol{x}_P}{\mathrm{d}t} \tag{2.15}$$

$$\boldsymbol{\omega}_P = \frac{\mathrm{d}\boldsymbol{\varphi}_P}{\mathrm{d}t} \tag{2.16}$$

Here, m_P is the particle mass, $\boldsymbol{J}_P$ the moment of inertia of the particle and dt the time step of the Lattice-Boltzmann scheme. Therefore, fluid flow and particle motion are calculated with the same temporal discretisation. Moreover, the particle variables are updated during each LBM iteration step realising a fully transient simulation.

Besides the flow-induced forces and torques acting on a particle, $\boldsymbol{F}$ and $\boldsymbol{T}$, external forces can also be considered in the equation of motion. Under consideration of particle acceleration due to gravity, Eq. (2.13) can be modified in this way:

$$\boldsymbol{F} + (\rho_P - \rho) V_P \boldsymbol{g} = m_P \frac{\mathrm{d}\boldsymbol{u}_P}{\mathrm{d}t} \tag{2.17}$$

where V_P is the volume of the particle, and $\boldsymbol{g}$ represents the gravitational acceleration. In order to calculate the particle motion, the integration of Eqs. (2.13–2.16) is performed with the help of a forward Euler scheme. The linearized form of the ODEs for translational motion is given below:

$$\boldsymbol{u}_P(t) = \frac{\boldsymbol{F}(t - \Delta t) + \boldsymbol{F}_{\mathrm{ext}}(t - \Delta t)}{m_P} \Delta t + \boldsymbol{u}_P(t - \Delta t) \tag{2.18}$$

$$\boldsymbol{x}_P(t) = \frac{\boldsymbol{u}_P(t - \Delta t) + \boldsymbol{u}_P(t)}{2} \Delta t + \boldsymbol{x}_P(t - \Delta t) \tag{2.19}$$

The arbitrary rotation of rigid particles is described in the following equations. In this context, the mathematical concept of quaternions is used to represent the angular displacement of the particle within the three-dimensional space [22]. Apart from a higher computational accuracy and efficiency, the main advantage over ordinary rotation matrices is that the solution of quaternions allows an enhanced stability of the numerical solution as a result of non-existent singularities.

$$\omega_{P,x}(t) = \frac{1}{J_{P,xx}} \left[T_x + \left(J_{P,yy} - J_{P,zz} \right) \omega_{P,y}(t) \omega_{P,z}(t) \right] \Delta t + \omega_{P,x}(t - \Delta t) \tag{2.20}$$

$$\omega_{P,y}(t) = \frac{1}{J_{P,yy}} \left[T_y + \left(J_{P,zz} - J_{P,xx} \right) \omega_{P,z}(t) \omega_{P,x}(t) \right] \Delta t + \omega_{P,y}(t - \Delta t) \tag{2.21}$$

$$\omega_{P,z}(t) = \frac{1}{J_{P,zz}} \left[T_z + \left(J_{P,xx} - J_{P,yy} \right) \omega_{P,x}(t) \omega_{P,y}(t) \right] \Delta t + \omega_{P,z}(t - \Delta t) \tag{2.22}$$

$$\boldsymbol{\varphi}_P(t) = \frac{\boldsymbol{\omega}_P(t - \Delta t) + \boldsymbol{\omega}_P(t)}{2} \Delta t + \boldsymbol{\varphi}_P(t - \Delta t) \tag{2.23}$$

The linearization of the previously mentioned ODEs can be applied since in the present studies the time step Δt which is the same for fluid flow and particle motion is several times smaller than the particle response time τ_P. Accordingly, the ratio $\Delta t/\tau_P$ lies in between $[6.17 \times 10^{-6}, 2.5 \times 10^{-3}]$. Furthermore, the equation

of motion is solved simultaneously for all tracked particles after the time step of the fluid flow is completed.

2.2.3 Moving Solid-Fluid Boundary

Since a Lagrangian frame of reference is realised, particles may move freely through the fluid domain. As a consequence of the particle treatment, a change in particle position involves state modifications of the numerical grid and of the boundary conditions. On the one hand, for situations where a particle is moving over a stationary grid, nodes that are overlapped by the particle during a time step are switched from fluid to solid status. On the other hand, nodes that are behind a particle and previously marked as solid may be switched to fluid nodes once they are located inside the fluid domain. Figure 2 demonstrates the procedure of switching the cell state from fluid to solid and vice versa with the help of the boundary motion of a disc over a two-dimensional grid.

For the initialisation of new fluid nodes, all 19 equilibrium and non-equilibrium distribution functions of each node are reconstructed through an extrapolation method, proposed by Caiazzo [5]. The so-called refill method consists of four substeps. At first, the fluid velocity and density of a new fluid node is obtained by extrapolation from the closest fluid neighbour nodes. The corresponding equilibrium distribution can be calculated in a second step with [25]:

$$f_{\sigma i}^{\mathrm{eq}} = \omega_{\sigma i}\widetilde{\rho}\left[1 + \frac{3\boldsymbol{\xi}_{\sigma i}\widetilde{\boldsymbol{u}}}{c^2} + \frac{9\left(\boldsymbol{\xi}_{\sigma i}\widetilde{\boldsymbol{u}}\right)^2}{2c^4} - \frac{3\widetilde{\boldsymbol{u}}^2}{2c^2}\right] \tag{2.24}$$

where $\tilde{\rho}$ and $\widetilde{\boldsymbol{u}}$ are extrapolations of the fluid density and velocity at the reconstructed fluid node. In the third step, the non-equilibrium part of the distribution function at the new fluid nodes is determined from the non-equilibrium part of the neighbour nodes by extrapolation [5]. Consequently, both the equilibrium and

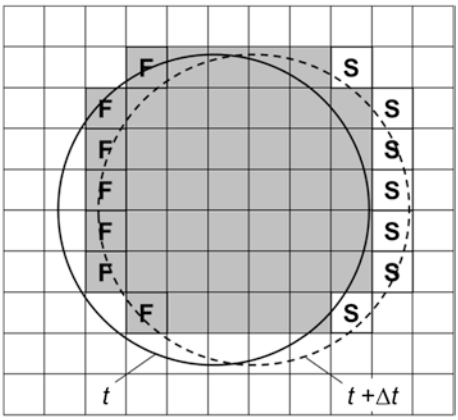

Fig. 2 Motion of a spherical particle over the structured regular mesh from time level t to $t + \Delta t$, in analogy to Seo and Mittal [32]: the switching from fluid to solid status, denoted by S, and from solid to fluid status, denoted by F, is illustrated in a two-dimensional view for the sake of simplification

non-equilibrium parts are used to initialize the missing distributions according to Eq. (2.1). Thömmes et al. [35] recently demonstrated the applicability of this procedure by simulating LBM-based multiphase flows with free surfaces.

2.2.4 Missing Fluid Distribution Functions

During the approach of particles, the distance between particle surfaces falls below the resolution limit of the finite grid after a particular stage. This leads to a non-physical force acting on the particles because fluid nodes are missing in the gap between the particle surfaces and, hence, the momentum balance of the fluid is incomplete at the particle surface. Figure 3 illustrates this scenario where the missing fluid distribution functions at the particle nodes are shown (see dashed and dotted arrows). Consequently, a realistic flow-induced force acting on each particle against the direction of the approaching particles cannot be obtained. This, in turn, has consequences for the underlying agglomeration event whereby both collision partners artificially stick together.

However, one focus of this work addresses the investigation of inter-particle collisions up to point contact using fully resolved particle surfaces. For that reason, a reconstruction scheme for missing fluid distribution functions had to be developed in order to avoid the non-physical approach of particles below the discretisation limit of the fluid. While the particles are moving in close neighbourhood, temporal so-called non-fluid nodes with fluid properties are dynamically generated at the solid nodes within the opposite collision partner if the gap width between the particle surfaces is smaller than the spatial discretisation Δx. The positions of those nodes correspond to the positions of the missing fluid distribution functions which are exemplary depicted in Fig. 3. Non-fluid nodes are generated newly and only on demand prior to the computation of the momentum balance of the fluid at the particle surface for each time step. Hence, the temporary

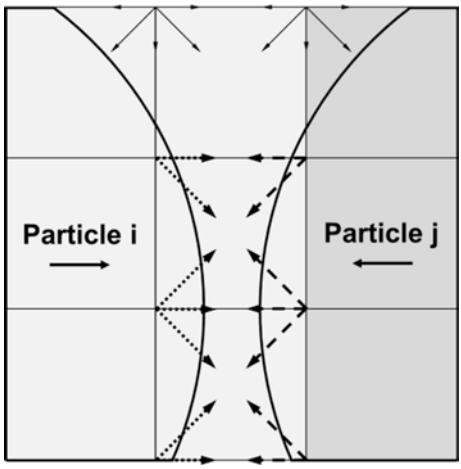

Fig. 3 Schematic sketch of two approaching particles, i and j, where the flow in the gap between both particles is no longer fully resolved by the numerical grid: *dashed arrows* represent those distribution functions at the nodes of particle j that are missing for the momentum balance of the fluid along the surface of particle i. *Dotted arrows* belong to particle j. Please note that grid nodes are always located at the front left bottom vertex within the cubic grid cells

switchover from solid nodes to non-fluid nodes (i.e. solid nodes with fluid properties) has no effect on the effective particle shape.

Under consideration of moving no-slip solid-fluid interfaces, the initialisation of these artificial nodes is done by reconstructing the fluid velocity at the particle surface. Here, the fluid velocity equals to the local surface velocity of the particle at its surface. Accordingly, the missing distribution functions can be determined on the basis of an equilibrium distribution in analogy to Eq. (2.2) by introducing the particle velocity:

$$f_{\sigma i} = \omega_{\sigma i}\rho\left[1 + \frac{3\,\boldsymbol{\xi}_{\sigma i}\boldsymbol{u}_P}{c^2} + \frac{9(\boldsymbol{\xi}_{\sigma i}\boldsymbol{u}_P)^2}{2c^4} - \frac{3\boldsymbol{u}_P^2}{2c^2}\right] \tag{2.25}$$

Therefore, the momentum balance of the fluid distribution functions at the particle surface is now fulfilled in any case. Nevertheless, the resolution of the fluid is limited. As already indicated, the physical lubrication cannot be completely simulated when particles are in close neighbourhood. The portion of lubrication that is not directly resolved by the numerical grid has to be modelled by an empirical approximation. For that reason, a pair-wise sub-grid repulsion force acting on all involved particles may be introduced [15, 28]. Please note that in the present studies, however, only the part of lubrication is considered, which is directly resolved by the numerical grid.

2.2.5 Inter-particle Collision and Agglomeration

If repulsive short-range phenomena such as hydrodynamic interactions before a collision are too weak to change the trajectory of the approaching objects, particles may collide with each other in the further progression of their relative movement. In the present analyses, a collision means the agglomeration of the involved collision partners in any case. Here, the detection of particle-particle collisions is performed by using a deterministic hard-sphere collision model. This model assumes that collisions are binary and quasi-instantaneous. Furthermore, the contact between two solid particles occurs in a single point. In order to determine whether a collision takes place, an event-driven collision detection algorithm is applied. Details on the implemented deterministic collision model with the LBM as its basis were recently published by Ernst and Sommerfeld [13].

In general, collision pairs can consist of primary particles or primary particles and agglomerates or agglomerates and agglomerates. The molecular attraction between the particles, and consequently, the resulting adhesion is assumed to be strong enough for particles to always stick together and form agglomerates. Apart from the agglomeration of particles, the restructuring or breakup of formed agglomerates is not considered.

The determination of post-agglomeration velocities of the resulting agglomerate is based on the laws of a perfectly inelastic collision considering conservation of both translational and angular momentum. Therefore, the new translational

velocity components of the formed agglomerate $\boldsymbol{u}_A$ are calculated in terms of the pre-collision velocity components, $\boldsymbol{u}_{P1}$ and $\boldsymbol{u}_{P2}$:

$$\boldsymbol{u}_A = \frac{m_{P1}\boldsymbol{u}_{P1} + m_{P2}\boldsymbol{u}_{P2}}{m_A} \tag{2.26}$$

where the mass of the agglomerate m_A equals to the sum of both agglomeration partners, m_{P1} and m_{P2}. In analogy to the conservation of translational momentum, the new angular velocity components $\boldsymbol{\omega}_A$ of the formed agglomerate are determined under consideration of the law of conservation of angular momentum:

$$\omega_{Ax} = \frac{I_{P1xx}\omega_{P1x} + I_{P2xx}\omega_{P2x}}{I_{Axx}} \tag{2.27}$$

$$\omega_{Ay} = \frac{I_{P1yy}\omega_{P1y} + I_{P2yy}\omega_{P2y}}{I_{Ayy}} \tag{2.28}$$

$$\omega_{Az} = \frac{I_{P1zz}\omega_{P1z} + I_{P2zz}\omega_{P2z}}{I_{Azz}} \tag{2.29}$$

with the moments of inertia I_{xx}, I_{yy} and I_{zz} of both colliding particles, 1 and 2, as well as the agglomerate A around the axes of coordinates (x, y, z) which are fixed in space [20]. The centre of mass $\boldsymbol{x}_A$ represents the weighted average of the position vector $\boldsymbol{x}_P$ of all agglomerated primary particles and marks at the same time the characteristic position of the agglomerate.

3 Morphological Characterisation of Agglomerates

For analysing the temporal evolution of agglomeration and to compare agglomerates obtained under different conditions information on the agglomerate morphology is required. The obtained agglomerate properties are the basis for evaluating the flow behaviour represented by aerodynamic coefficient [12], for example. Furthermore, correlations between adequate structure parameters and flow characteristics of agglomerates can be developed.

Fundamental agglomerate properties are the number of primary particles as well as volume and surface area which provide the basis for calculating further quantities such as volume specific surface and sphericity. In this study, the sphericity ψ of an agglomerate is defined according to Wadell [37] as the ratio of the surface area of the volume equivalent sphere A_{VES} considering the total number of agglomerated primary particles n_{PP} and the total surface of the given agglomerate A_{Agg}:

$$\psi = \frac{A_{VES}}{A_{Agg}} = \frac{\pi d_{VES}^2}{\pi \sum_{i=1}^{n_{PP}} d_{Pi}^2} = \frac{\left(\sum_{i=1}^{n_{PP}} d_{Pi}^3\right)^{2/3}}{\sum_{i=1}^{n_{PP}} d_{Pi}^2} \tag{3.1}$$

The disadvantage of the sphericity is that information neither about the spatial dimensions nor about the agglomerate structure is included. A measure of the absolute agglomerate size is the interception radius R_o which corresponds to the largest extension of the agglomerate with respect to its centre of mass. An indicator of the mass distribution inside the agglomerate is the radius of gyration R_g or the fractal dimension which is not considered here. In the present analysis, R_g is determined by calculating the root mean square of the distance of each primary particle to the centre of mass of the agglomerate:

$$R_g = \sqrt{\frac{1}{n_{PP}} \sum_{i=1}^{n_{PP}} \left| \boldsymbol{x}_{P,COM} - \boldsymbol{x}_{P,i} \right|^2} \tag{3.2}$$

Another property characterising the compactness of agglomerates is the porosity ε. In this study, it is quantified by the ratio of the void-space V_V and the displaced volume V_D of the agglomerate:

$$\varepsilon = \frac{V_V}{V_D} = \frac{V_V}{V_S + V_V} = 1 - \frac{V_S}{V_H} \tag{3.3}$$

where the displaced volume corresponds to the sum of void space V_V plus the solids volume V_S. In this study the volume displaced by the agglomerate is assumed as the volume of the convex hull around the agglomerate V_H [12, 14]. This is more realistic then using a sphere enwrapping the agglomerate.

4 Agglomeration During Sedimentation

As a first example demonstrating agglomerate growth the sedimentation of a group of 13 particles with different diameters in quiescent liquid was considered. The mean particle diameter is 50 μm and the size variation in the cluster is ±20 %. The computational domain, a vertical channel with quadratic cross-section (dimensions 0.3 mm × 0.3 mm × 5 mm), is discretised by 135,000 computational cells. In terms of the mean particle diameter the computational domain has the dimensions of $6 \cdot d_p \times 6 \cdot d_p \times 100 \cdot d_p$. The resolution of the mean particle diameter is 5 cells.

Initially, the particles were placed in a cluster without contact at the top of the computational domain (Fig. 4a). Then the particles were released and allowed to sediment. During this sedimentation process, touching particles were assumed to stick together and form an agglomerate which continues to sediment as one entity and was permitted to rotate freely. The colour coding of the particles is selected in such a way that those particles forming agglomerates in a later stage have identical colour. The uncoloured particles (grey) do not form agglomerates. Figure 4b shows an interim scenario of the sedimentation process with the trajectories of the primary particles which form agglomerates. Please note that non-agglomerated

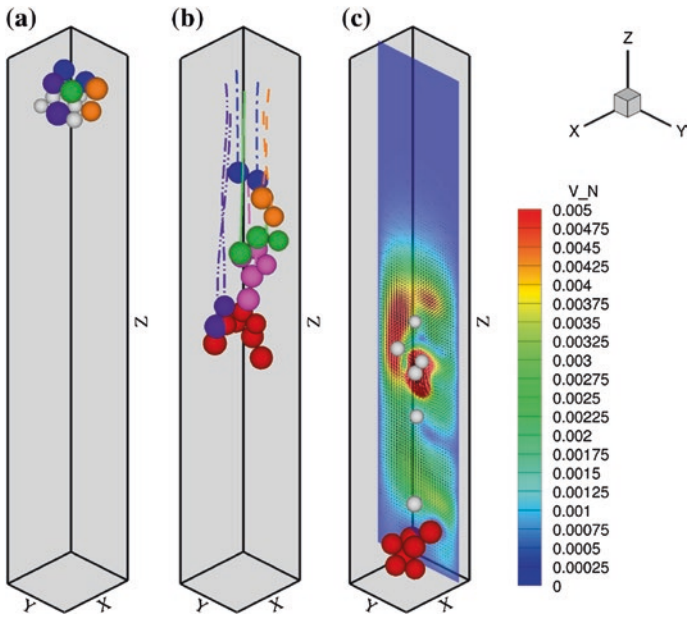

Fig. 4 Simulation of sedimentation and agglomeration of a cluster of poly-disperse particles in a vertical channel, **a** initial particle cluster, **b** interim stages of sedimentation and agglomerate formation with particle trajectories, **c** final stage of sedimentation with induced instantaneous flow field

particles are not shown in Fig. 4b. The depicted agglomerates indicate the agglomeration history. Initially only doublets are formed and during the second period these doublets form larger agglomerates. The orange particles and the single green particle form the green triplet and the blue doublet and the green triplet form the pink agglomerate. Finally the violet doublet and the pink agglomerate form one large agglomerate with 7 primary particles. This large agglomerate, after all, sediments much faster than the remaining primary particles and approaches the bottom wall. Figure 4c shows the final simulation stage including also a vertical plane of the induced fluid velocity field visualised by colour coding.

For the sedimentation of the 13 primary particles and the resulting agglomerates also the sedimentation velocity versus height was evaluated from the simulations. Since only 7 particles are involved in agglomeration just their results are depicted in Fig. 5. Initially, the settling velocity increases for all particles yielding a slow change of height. Although, different sized particles are included in the cluster, initially all particle sediment as a group with about the same velocity. In a later stage, after a settling velocity of 0.03 m/s is reached, the relative motion between the particles increases (i.e. spread of the lines in Fig. 5) resulting in collisions between them. First particle 2 and 7 collide forming agglomerate 14. Of course at this stage there is a large velocity difference between the involved primary particles. The initial velocity of the new agglomerates lies always between those of the involved collision partners. The different spatial location upon

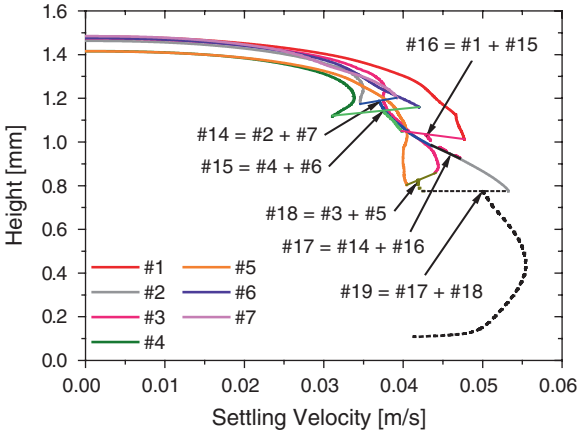

Fig. 5 Correlation between particle/agglomerate location and settling velocity (the numbers indicate primary particle and agglomerates, the occurrence of an agglomeration is indicated by connecting the respective end points by a *straight line*)

collision results from the finite size of the primary particles. Then particle 4 and 6 collide with a large relative velocity forming agglomerate 15. This agglomerate collects then other primary particles (No. 1). The last collision between two primary particles (No. 3 and 5) forms agglomerate 18. It is also observed that the formed agglomerates are rapidly accelerating yielding an increasing sedimentation velocity. Finally, one large agglomerate (No. 19) with 7 primary particles is formed. When approaching the bottom wall this agglomerate is decelerated due to the fluid dynamic interaction with the wall.

A hydrodynamic interaction between colliding particles may be also identified resulting in a deceleration just prior to collision (e.g. particle 2 and 7 and particle 4 and 6). Naturally, all the produced agglomerates are allowed to rotate freely (see Fig. 4). These results demonstrate that based on the Lattice-Boltzmann simulations a detailed analysis of the micro-structure in sedimenting particle clusters is possible. The agglomerates formed during the sedimentation process may be also characterised with respect to structural parameters, such as, porosity, radius of gyration or fractal dimension Ernst et al. [14]. This has been done by Ernst et al. [14] for a cluster consisting initially of 50 primary particles.

5 Agglomeration in Shear Flows

In addition to the formation of agglomerates inside settling particle clusters, the agglomeration of resolved particles in laminar shear flows is analysed. Apart from the fluid viscosity, the influence of both the particle inertia and the pre-scribed particle size distribution on the agglomeration process is investigated successively. At first, the numerical setup applied for different simulations is briefly described. Secondly, the transient evolution of the agglomeration process is introduced. Finally, the morphology of the growing agglomerates is characterised by means of different structural parameters.

Table 1 Fluid and particle properties modified in the different simulations

Case	η (Pa s)	$d_P/\Delta x$	ρ_P/ρ	$\Delta t/\tau_P$	Re_P	St
R-M	1.0×10^{-3}	6.0	2.5	1.0×10^{-3}	1.0	1.4
R-P	1.0×10^{-3}	6.0 ± 1.8	2.5	1.0×10^{-3}	1.0	1.4
D1-M	1.0×10^{-3}	6.0	1.0	2.5×10^{-3}	1.0	0.6
D2-M	1.0×10^{-3}	6.0	5.0	2.5×10^{-3}	1.0	2.8
D1-P	1.0×10^{-3}	6.0 ± 1.8	1.0	5.0×10^{-4}	1.0	0.6
D2-P	1.0×10^{-3}	6.0 ± 1.8	5.0	5.0×10^{-4}	1.0	2.8
V1-M	1.0×10^{-2}	6.0	2.5	1.0×10^{-3}	0.1	0.1
V2-M	1.0×10^{-4}	6.0	2.5	1.0×10^{-3}	10.1	13.8
V1-P	1.0×10^{-2}	6.0 ± 1.8	2.5	1.0×10^{-3}	0.1	0.1
V2-P	1.0×10^{-4}	6.0 ± 1.8	2.5	1.0×10^{-3}	10.1	13.8

Reference setup (*R*), different density ratios (*D1* and *D2*) and dynamic viscosities (*V1* and *V2*) with mono- (*M*) and poly-disperse (*P*) size distributions of the primary particles

5.1 Numerical Setup

The simulations are performed in a horizontal channel with a rectangular cross-section of 12.5 $\bar{d}_P$ in height and 10.0 $\bar{d}_P$ in the width. The channel length is 83 1/3 $\bar{d}_P$, where $\bar{d}_P$ is the mean diameter of the primary particles. As a result, the cross-section is discretised with 75 × 60 grid cells. The channel height has 500 grid cells, yielding in total 2.25 million cells. The shear flow is induced by a moving upper wall having a positive velocity and a lower wall which is at rest. Besides the opposed inflow and outflow boundaries in stream-wise direction, the flow field is restricted by artificial moving side walls. The velocity on the walls is initialised by the imposed flow at the corresponding position of the next neighboured fluid node. The nodal velocity at the inlet is defined by $\boldsymbol{u}(x_z) = \dot{\gamma} \boldsymbol{x}_z \boldsymbol{e}_x$, where x_z is the vertical z-coordinate and $\boldsymbol{e}_x$ the unit vector in the stream-wise x-direction. In all simulations, the fluid density ρ is 1000 kg/m^3 and the shear rate is set to $\dot{\gamma} = 560$ 1/s.

For insuring different hydrodynamic interaction prior to particle-particle collisions in the individual runs, various dynamic fluid viscosities η and particle material densities ρ_P were used. The corresponding fluid and particle properties are summarized in Table 1. In the present study, the particle Reynolds number Re_P and the particle Stokes number St are defined by $Re_P = \dot{\gamma} \bar{d}_P^2 \rho/(2\eta)$ and $St = \tau_P \bar{u}_{Px}/\bar{d}_P$, respectively, in which τ_P is the particle response time with $\tau_P = \rho_P \bar{d}_P^2/(18\eta)$, and $\bar{u}_{Px}$ the mean stream-wise initial velocity of all primary particles. This velocity corresponds to the undisturbed fluid velocity at the particle initial location as described below. As shown in Table 1, Re_P and St vary between [0.1, 10.1] and [0.1, 13.8], respectively.

According to Table 1, the effect of the particle density and dynamic viscosity is investigated in each category (R, D and V) with three different values. Furthermore, these categories are subdivided additionally into groups with mono- (M) and poly-disperse (P) size distributions of the spherical primary particles.

The mean diameter $\bar{d}_P$ is resolved in all runs with $\bar{d}_P/\Delta x = 6$ grid cells. In case of the poly-disperse size distribution, $\bar{d}_P$ varies with ± 30 %, having a constant probability.

At the beginning of the simulations, the positions of the centres of masses of the primary particles, which are placed randomly inside the cluster, are identical for all analysed configurations regardless of a mono- or poly-disperse size distribution. The cluster is positioned near to the inflow boundary and consists of 50 non-overlapping primary particles. As shown in Fig. 6, the centre of mass of the cluster has a slight negative offset with regard to the horizontal centre line of the channel by virtue of the slip-shear lift force acting on the particles during the simulations. Initially, the velocity of the primary particles equals the local undisturbed fluid velocity at the position of the particle centres. In the present studies, both gravity and Brownian motion have not been taken into account. To avoid multiple collisions during one time step, the applied time steps are small, i.e. $\Delta t/\tau_P$ varies between $[5.0 \times 10^{-4}, 2.5 \times 10^{-3}]$. Finally, the motion of resolved no-slip solid-fluid boundaries as well as the collision and agglomeration of particles follows the same methods and assumptions mentioned in Sect. 2.

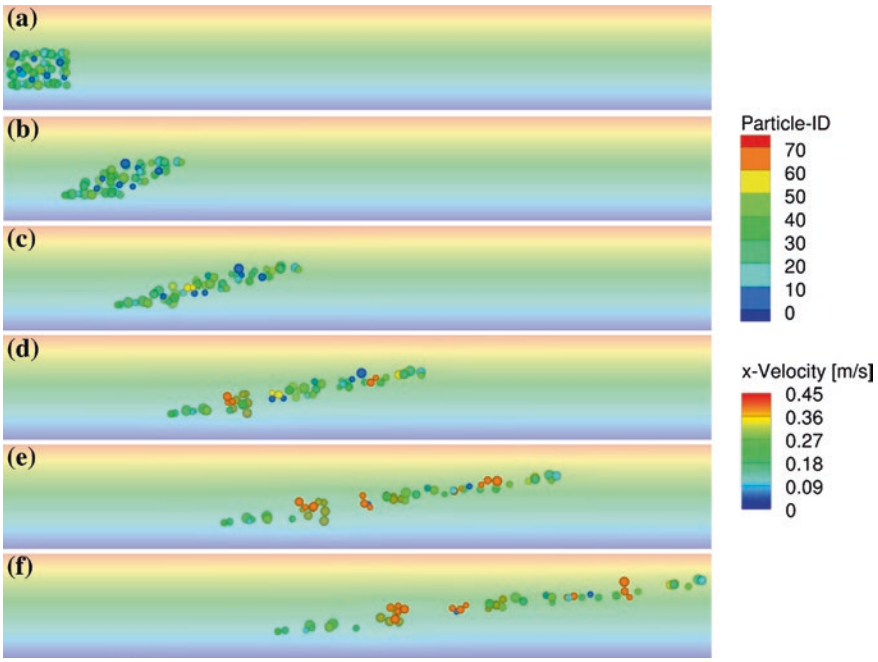

Fig. 6 Snapshots of the fluid velocity field (*see colour scale*) and particle cluster distribution with the poly-disperse size distribution at $Re_P = 1.0$ and $St = 1.4$ (Case R-P) at various instants of time; from *top* to *bottom*: $t/t_{\text{tot}} = 0.0$ (**a**), 0.2 (**b**), 0.4 (**c**), 0.6 (**d**), 0.8 (**e**) and 1.0 (**f**). Spheres of the same colour have formed an agglomerate. Cut through the centre of the three-dimensional domain

5.2 Transient Growth of Agglomerates

In the following, the transient growth of agglomerates in a shear flow is investigated through LBM simulations. Colliding particles are again assumed to form a rigid agglomerate which is not allowed to deform or breakup. The colour coding of the particles depicted in Fig. 6 is the same as in the previous section, i.e. primary particles having an identical colour belong to the same agglomerate. Figure 6a–f show six temporal stages of a typical shear-induced agglomeration process considering a poly-dispersed size distribution of primary particles; e.g. case R-P in Table 1.

At the beginning of the simulation, particles are located in a cuboid-shaped cluster (see Fig. 6). Due to their different positions inside the shear layers, upper primary particles are moving faster than the lower ones. This leads to an increasing deformation of the original particle arrangement whereby collisions between particles are being enforced (Fig. 6b). As shown in Fig. 6c–d, the quick formation of doublets and triplets are the basis for a rapid growth of agglomerates. The red-coloured agglomerate, for example, in the lower part of Fig. 6d starts to rotate freely in order to re-balance its orientation with respect to the modified centre of mass and the sustained changes of the shear-induced particle forces. In the further progression of the simulation, this rigid agglomerate collides with other primary particles and agglomerates (see Fig. 6e–f). Finally, as depicted in Fig. 6f, several agglomerates consisting of three and more primary particles are being formed.

Apart from the flow-induced drag force, moving particles experience an additional transverse lift force due to the non-uniform relative velocity between shear-layers and particles [29]. The resulting non-uniform pressure distribution around the resolved particle surface leads to a lift force which acts towards the direction of higher slip velocity. Figure 6 illustrates this behaviour by means of the horizontal offset between the initial and final positions of the upper particles shown in Fig. 6a–f.

A simple measure of the growth of agglomerates can be obtained by counting both the total number of particles/agglomerates N_P which remain in the fluid domain and, as a counterpart, the total number of primary particles bonded in agglomerates N_A^{PP}. Please note that here the term “particles” implies primary particles as well as agglomerates. Figure 7 reflects the growth of agglomerates observed during the simulations of the Cases R and D specified in Table 1 considering mono- as well as poly-disperse size distributions of the primary particles.

In case of equal-sized primary particles, the number of particles in the domain decreases during the first half of the calculation period to the same extent independently of the particle Stokes numbers examined (see Fig. 7a). This behaviour may be explained by the fact that during the early stage of the simulation, particles with different response behaviour collide with similar small relative velocities. In this context, the inertia of both agglomeration partners plays only a subordinate role with respect to the hydrodynamic interaction between fluid and particles. However, at $t > 0.01$ s, the number of remaining

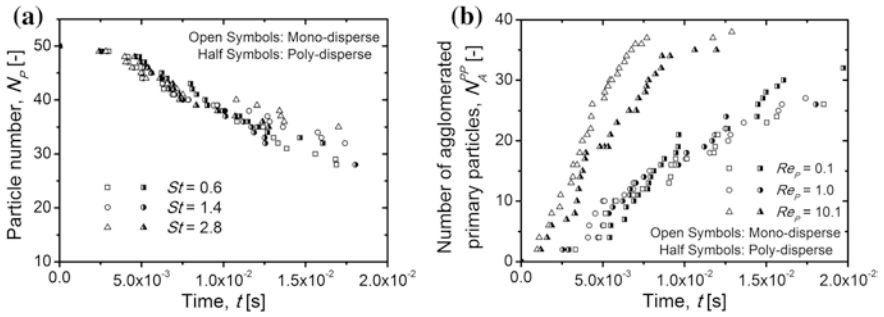

Fig. 7 Temporal development of **a** the total number of particles N_P considering primary particles as well as agglomerates and **b** the total number of primary particles included in agglomerates N_A^{PP} with the particle Stokes number St as a parameter taking into account both mono- and poly-disperse size distributions (Table 1: Cases R and D)

particles decrease noticeably slower with increasing St; see Fig. 7a. Due to the larger inertia, formed agglomerate structures need more time for angular acceleration caused by the shear gradient in the fluid flow. This in turn leads to a slower agglomeration progress since collisions with other neighbouring particles occur slower in comparison to smaller particle Stokes numbers. Consequently, for larger times, the number of primary particles collected in agglomerates decreases with increasing Stokes number (Fig. 7).

In contrast, particles with poly-dispersed size distribution agglomerate in a shorter interval of time (see Fig. 7a) and the agglomeration progress is largely completed at about $t = 0.013$ s. Thereafter, primary particles are being captured only sporadically (see also Fig. 7b). Here, different particle Stokes numbers have only a marginal impact on the agglomeration process. In addition, the decrease of particle number exhibits fewer fluctuations in comparison to setups with equal-sized particles. This hypothesis is reflected by an almost linear slope formed by the individual agglomeration events depicted in Fig. 7b (i.e. number of primary particles in an agglomerate).

Apart from particle number statistics shown in Fig. 7, the time-dependent change of the particle number N_A^{PP} can be used to evaluate the agglomeration frequency f_A^{PP} which is defined as:

$$f_A^{PP} = \frac{\mathrm{d}N_A^{PP}}{\mathrm{d}t} \tag{5.1}$$

For the following analyses, the mean time between two successive agglomeration events τ_A^{PP}, also referred to as agglomeration time, is used instead of f_A^{PP} by applying the following relation:

$$\tau_A^{PP} = \frac{1}{\left\langle f_A^{PP} \right\rangle_A} \tag{5.2}$$

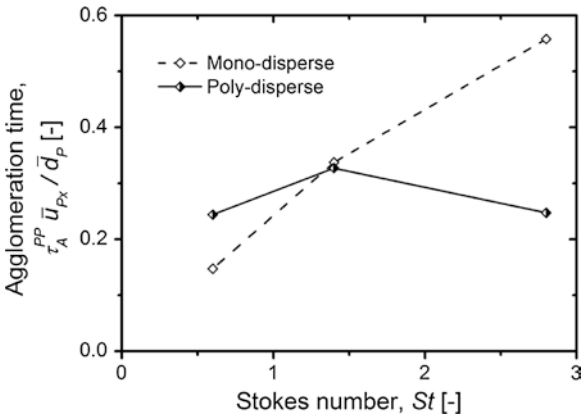

Fig. 8 Agglomeration time τ_A^{PP} normalised by the particle advection time scale $\bar{u}_{Px}/\bar{d}_P$ as a function of both the particle Stokes number St and the considered particle size distribution

where $\langle\cdot\rangle_A$ is the agglomerate average operator. The agglomeration times obtained by the data represented in Fig. 7b are depicted in Fig. 8.

Due to the increasing delay in rotational acceleration with growing Stokes number, τ_A^{PP} increases in case of equal-sized particles continuously with increasing inertia of the particles, whereas τ_A^{PP} has a slight maximum considering a particle size spectrum at about $St = 1.4$. It becomes apparent that the particle size distribution has a direct impact on the particle inertia-induced agglomeration process while retaining the particle Reynolds number at $Re_P = 1.0$. The difference between the agglomeration times for mono- and poly-disperse systems is the result of particle/agglomerate inertia effects and a hydrodynamic interaction between collision partners, particularly when small and large particle (i.e. agglomerates) collide. Hydrodynamic interaction implies that with decreasing St the agglomeration frequency is reduced and hence the agglomeration time increased (i.e. with respect to the mono-disperse results). The opposite occurs for increasing St, the agglomeration frequency increases and the agglomeration time is reduced. This is directly reflected by the result in Fig. 8 comparing the poly- with the mono-disperse results.

In addition to St, the growth of agglomerates is analysed with the help of various particle Reynolds numbers Re_P which spread in the present study over three orders of magnitude; i.e. cases R and V in Table 1. As shown in Fig. 9a, the time-dependent development of the particle number N_P for small and intermediate particle Reynolds numbers (i.e. $Re_P = 0.1$ and 1.0) behaves similar to the results presented in Fig. 7a and is almost independent from the size distribution of the primary particles. The situation is however different if the particle Reynolds number becomes larger than unity. According to Fig. 9a, b, a clear distinction between both considered setups can be recognized in which equal-sized primary particles agglomerate faster than those with a diameter spectrum (see also Fig. 10). At a later stage of these two simulations, only a few agglomerations are occurring since 70 % of the primary particles (i.e. $N_A^{PP} > 35$) are already incorporated in various agglomerate structures. Consequently, the slopes of the triangle-shaped symbols

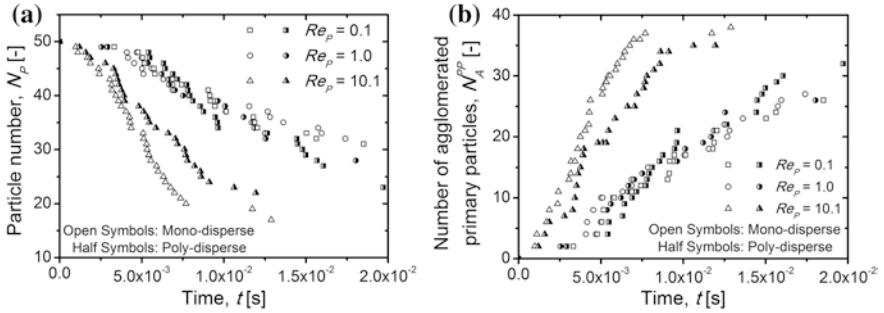

Fig. 9 Influence of the particle Reynolds number Re_P on the temporal development of **a** the total number of particles N_P considering both primary particles and agglomerates and **b** the total number of agglomerated primary particles N_A^{PP} with the particle size distribution as a parameter (Table 1: Cases R and V)

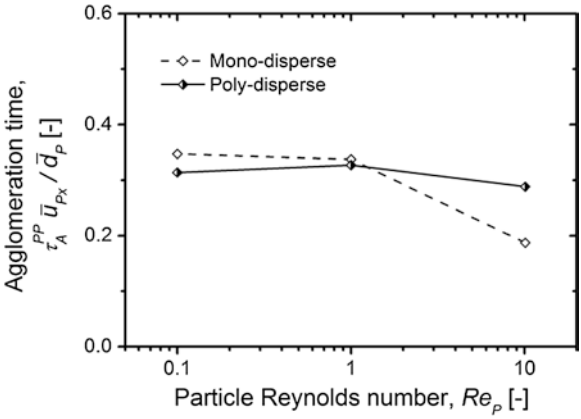

Fig. 10 Mean time between two successive agglomeration events τ_A^{PP} observed in the cases R and V and plotted against the particle Reynolds number Re_P with the particle size distribution as a parameter: Note that τ_A^{PP} is normalised by the time scale of the particle advection $\bar{u}_{Px}/\bar{d}_P$

($Re_P = 10.1$) depicted in Fig. 9b are no longer in-line at $t > 0.008$ s (open symbols, mono-disperse) and $t > 0.009$ s (half-filled symbols, poly-disperse), respectively.

Figure 10 illustrates the resulting agglomeration times τ_A^{PP} based on the data depicted in Fig. 9b. In case of mono-disperse primary particles, τ_A^{PP} decreases with increasing particle Reynolds number in which the relative deviation between the largest and the two smaller Re_P is clearly pronounced. Increasing particle Reynolds number implies growing particle inertia, whereby the agglomeration frequency is increased and the agglomeration time reduced accordingly. For a spectrum of primary particle sizes the agglomeration time remains almost constant, just near $Re_P = 1.0$ a small maximum of τ_A^{PP} may be identified. Consequently, τ_A^{PP} becomes larger than the values for mono-sized particles in the case of $Re_P > 1.0$. Therefore, it can be concluded that here the hydrodynamic interaction prior to inter-particle collisions, especially if small and large particles are involved, yields higher agglomeration times and hence a reduction of agglomeration frequency.

5.3 Morphological Characterisation

In addition to the statistics of the total number of both remaining and agglomerated particles as well as the agglomeration time scale, the morphology of agglomerates is characterised by means of different structural parameters. For that all agglomerates existing at the end of the simulation are considered. Referring to Sect. 3, the sphericity Ψ of a given agglomerate (Eq. 3.1) is calculated as the ratio of the surface area of the volume equivalent sphere of the agglomerates to the surface area of all primary particles involved in the agglomerate. In this context it has to be taken into account that information neither about the agglomerate structure nor about the spatial dimension can be derived from Ψ [14]. Figure 11 shows the sphericity of all agglomerates formed during the respective simulations specified in Table 1 in dependence of the volume equivalent diameter of the agglomerate d_{VES}, normalised by the mean diameter of all introduced primary particles d_p.

As a result, the sphericity decreases roughly in an exponential way with increasing number of primary particles per agglomerate represented by its appropriate d_{VES} (see Fig. 11). This behaviour has been expected since according to Eq. (3.1) the surface area of the volume equivalent sphere increases during the growth of agglomerates slower than the total surface of the linked primary particles. Moreover, in case of equal-sized primary particles (Fig. 11: *open symbols*), all evaluated agglomerates have by definition the same sphericity for the appropriate d_{VES} independently of the analysed St and Re_P. On the other hand, it becomes evident that in case of a poly-disperse particle size distribution the sphericity deviates from its comparative case with equal-sized primary particles. Attention will be drawn here especially to the range between $1.0 < d_{VES}/d_P \leq 1.4$ where Ψ scatters around 0.80 for different d_{VES} (see Fig. 11). Here, each of the half-filled symbols represents a doublet consisting of two different-sized particles. However, it is worth emphasising that the sphericity of agglomerates formed by equal-sized

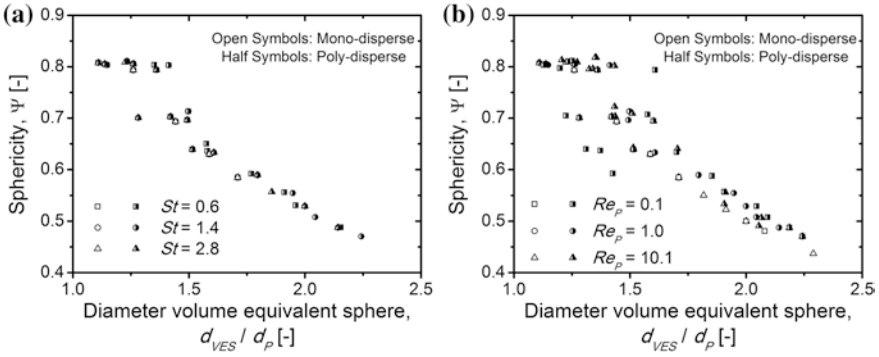

Fig. 11 Comparison of the sphericity of agglomerates as a function of the normalised diameter of the volume equivalent sphere with **a** the particle Stokes number St and **b** the particle Reynolds number Re_P as a parameter considering both mono-disperse (*open symbols*) and poly-disperse (*half-filled symbols*) size distributions of the primary particles

primary particles is overall smaller than the comparable case with a size spectrum of the primary particles (i.e. values of Ψ for $d_{VES}/d_P > 1.5$). This resulted from the fact that small and, thus, less inertial particles may change their original path due to the hydrodynamic interaction when approaching other neighboured particles. Consequently, those particles are collected to a lesser extent by agglomerates, which leads in turn to larger sphericities. Nevertheless, neither different particle Stokes numbers nor various particle Reynolds numbers have a recognizable trend in the sphericity of growing agglomerates. However, for the poly-sized system a larger scatter of the sphericity depending on Re_P is observed compared to the results for different St.

A measure of the mass distribution inside agglomerates is the radius of gyration R_g which is calculated with the help of the distance of each primary particle to the centre of mass of the agglomerate (see Eq. 3.2). At the beginning of the simulations, the agglomerates only consist of two or three primary particles. At this stage, the compact structure of agglomerates leads to small R_g values (see Fig. 12). In case of a doublet consisting of equal-sized particles (i.e. $d_{VES}/d_P = 1.26$), the ratio R_g/r_P is about 1.0. The resulting centre of mass coincides therefore with the contact point between both particle surfaces and the radius of gyration equals to the radius r_P of a primary particle. For doublets which consist of primary particles with different diameters (i.e. $d_{VES}/d_P < 1.42$), the ratio R_g/r_P fluctuates around 1.0. Due to the collision with other particles, the resulting agglomerates grow in all spatial directions, indicated by a rapid increase of R_g. The strip formed by the different-shaped symbols depicted in Fig. 12a, b follows an almost linear increase of the radius of gyration under consideration of a discrete scattering range. Again a clear trend of R_g with respect to St and Re_P cannot be identified. However, the data with Re_P as a parameter show a larger variation than those using the Stokes number.

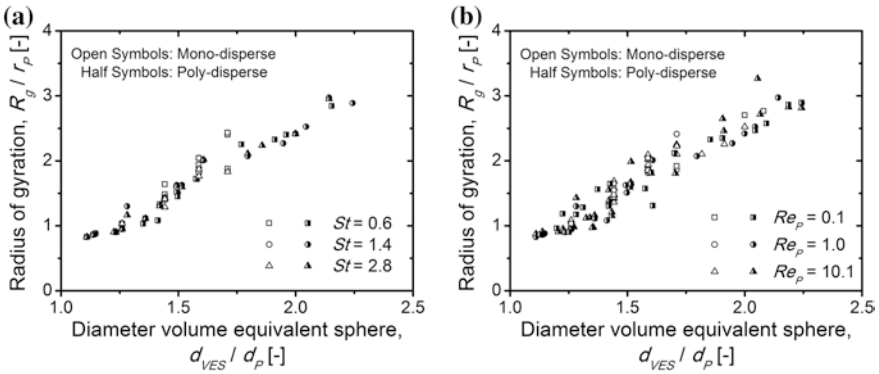

Fig. 12 Development of the normalised radius of gyration with **a** the particle Stokes number St and **b** the particle Reynolds number Re_P as a parameter depending on the normalised diameter of the volume equivalent sphere. For comparison purposes, mono-disperse (*open symbols*) and poly-disperse (*half-filled symbols*) particle size distributions are taken into consideration

The structures of cluster-cluster (C-C) and particle-cluster (P-C) fractal-like agglomerates have been investigated by Brasil et al. [4]. In the applied numerical scheme, simplified models based on the Langevin dynamics have been used in which the hydrodynamic interaction between fluid and particles is not accounted for. As a result, the theoretical number of equal-sized primary particles N_A^{PP} in agglomerates scales approximately with the radius of gyration R_g as follows [4]:

$$N_A^{PP} = k_f \left(\frac{R_g}{r_P} \right)^{D_f} \tag{5.3}$$

where r_P is the mean radius of all introduced primary particles, k_f the structural coefficient and D_f the fractal dimension of the agglomerate. The fractal pre-factors k_f and D_f for both C-C and P-C agglomerate populations are summarised in Table 2. By comparing the present LBM-based results with the numerical predictions shown in Fig. 13 it becomes apparent that the number of primary particles per agglomerate can be estimated only to some degree with the help of the cluster-cluster agglomeration model. Accordingly, viscous forces have a non-negligible impact on the motion of approaching particles in the analysed cases which requires a more specific attention for the prediction of agglomerate sizes using R_g.

Table 2 Fractal pre-factors k_f and fractal dimension D_f used for the prediction of cluster-cluster (C-C) and particle-cluster (P-C) agglomerates [4]

Method	k_f	D_f
C-C	1.27 ± 0.07	1.82
P-C	0.51 ± 0.02	2.75

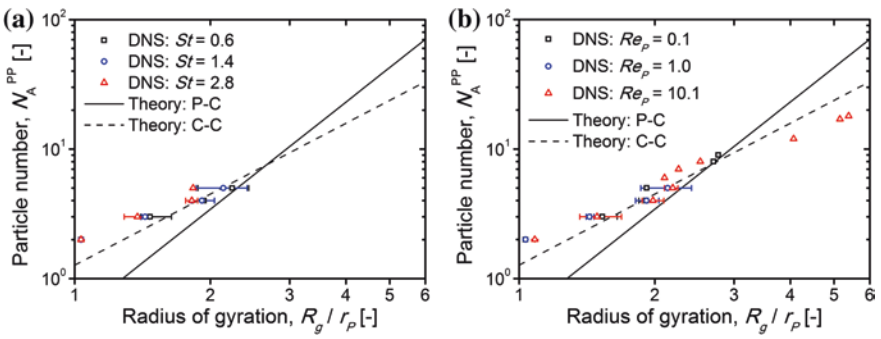

Fig. 13 Number of equal-sized primary particles N_A^{PP} per agglomerate as a function of the averaged radius of gyration including its extreme deviation (*horizontal bars*) as well as **a** the particle Stokes number *St* and **b** the particle Reynolds number *Rep*. Results obtained by LBM-based direct numerical simulations (DNS, *open symbols*) and numerical predictions for agglomerates formed by particle-cluster (P-C, *solid line*) and cluster-cluster (C-C, *dashed line*) collisions based on Langevin dynamics [4]

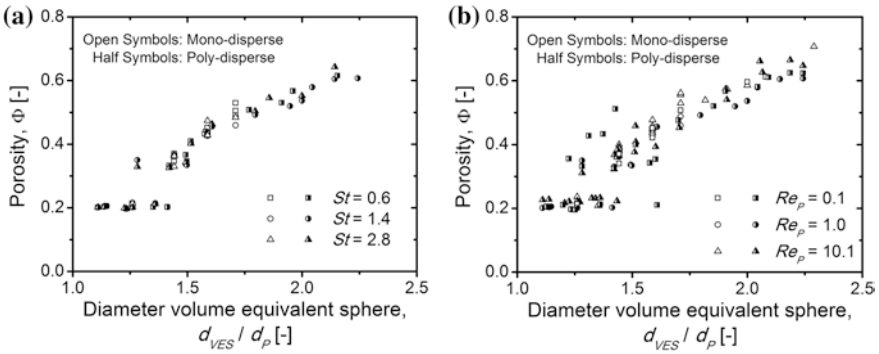

Fig. 14 Porosity distribution of agglomerates resulting from simulations with different **a** particle Stokes numbers *St* and **b** particle Reynolds numbers Re_P plotted against the normalised diameter of the volume equivalent sphere in dependence on the initial particle size distribution (*open- and half-filled symbols*)

Apart from the radius of gyration, the porosity is utilised as a second morphological parameter. In the present study, the porosity ε given by Eq. (3.3) is determined based on the convex hull around the agglomerate [12, 14]. As shown in Fig. 14, compact structures such as doublets and triplets, which were formed at the initial stage of the simulations, have a small porosity. With increasing size of the agglomerates and, thus, increasing number of primary particles, the porosity increases rapidly approaching a value of about 0.625 (see Fig. 14). In this region, fluffy-structured agglomerates are shaped as a result of collisions with other particles (i.e. primary particles as well as agglomerates) yielding larger porosities. In analogy to the radius of gyration, the porosity of the formed agglomerates does not show any clear trends with respect to the considered *St* and Re_P as well as the prescribed particle size distribution. Also here the scatter of the data is larger when considering Re_P as a parameter.

6 Conclusions

The Lattice-Boltzmann method has been extended and refined for allowing the simulation of moving resolved particles, including their collision and agglomeration. The methods applied for treating a moving solid-fluid interface and the approach of particles below the resolution limit of the numerical grid are essential for doing such simulations. A thorough validation of these methods was introduced by Ernst et al. [14]. In this work the agglomeration process of primary particles has been analysed in detail for two scenarios, namely agglomeration in a cluster of sedimenting particles and in a group of particles being introduced in a linear shear flow. Special emphasis was put on the importance of hydrodynamic interaction on the collision and agglomeration of particles. For a small group of

sedimenting particles the particle velocity change due to hydrodynamic interaction just prior to collision could be identified. In a plane shear layer the influence of hydrodynamic interaction on agglomeration could be demonstrated by comparing agglomeration times for mono- and poly-disperse systems. Thereby, it was shown, that hydrodynamic interaction is more important in poly-disperse particle systems, mainly as a result of the collision between primary particles and agglomerates. The analysed structural parameters for agglomerates did not reveal any clear trends with regard to hydrodynamic effects, by considering both the Stokes number as well as the particle Reynolds number.

Especially however, for the shear-layer case the interaction between colliding particles is rather complex and therefore, requires further analysis of the translational and rotational behaviour of the interaction between primary particles and agglomerates just prior to contact. In addition to the sub-grid hydrodynamic interaction which is also referred to as lubrication, future work aims at incorporating the interaction potential resulting from electrostatic repulsion and molecular attraction. For incorporating such short range interaction effects, however, additional models have to be developed.

References

1. Bhatnagar PL, Gross EP, Krook M (1954) A model for collision processes in gases. I. Small amplitude processes in charged and neutral one-component systems. Phys Rev 94:511–525
2. Binder C, Feichtinger C, Schmid H-J, Thürey N, Peukert W, Rüde U (2006) Simulation of the hydrodynamic drag of aggregated particles. J Colloid Interface Sci 301:155–167
3. Bouzidi M, Firdaouss M, Lallemand P (2001) Momentum transfer of a Boltzmann-lattice fluid with boundaries. Phys Fluids 13:3452–3459
4. Brasil AM, Farias TL, Carvalho MG, Koylu UO (2001) Numerical characterization of the morphology of aggregated particles. Aerosol Sci 32:489–508
5. Caiazzo A (2008) Analysis of lattice Boltzmann nodes initialisation in moving boundary problems. Prog Comput Fluid Dyn 8:3–10
6. Chen F, Hagen H (2011) A survey of interface tracking methods in multi-phase fluid visualization. In: Middel A, Scheler I, Hagen H (eds) Visualization of large and unstructured data sets—applications in geospatial planning, modeling and engineering, vol 19. Dagstuhl Publishing, Germany, pp 11–19
7. Chen S, Doolen GD (1998) Lattice Boltzmann method for fluid flows. Annu Rev Fluid Mech 30:329–364
8. Crouse B (2003) Lattice-Boltzmann Strömungssimulationen auf Baumdatenstrukturen. Doctoral thesis, Technische Universität München
9. Derksen JJ (2012) Direct numerical simulations of aggregation of monosized spherical particles in homogeneous isotropic turbulence. AIChE J 58:2589–2600
10. Dietzel M, Sommerfeld M (2010) LBM simulations on agglomerate transport and deposition. AIP conference proceedings, vol 1207, pp 796–801
11. Dietzel M, Ernst M, Sommerfeld M (2011) Application of the Lattice-Boltzmann-method in two-phase flow studies: from point particles to fully resolved particles. In: Proceedings of ASME-JSME-KSME 2011 joint fluids engineering conference, vol 1, Symposia—Parts A, B, C, and D, Paper No. AJK2011-04033, pp 1697–1707 (2011)
12. Dietzel M, Sommerfeld M (2013) Numerical calculation of flow resistance for agglomerates with different morphology by the lattice-Boltzmann method. Powder Technol 250:122–137

13. Ernst M, Sommerfeld M (2012) On the volume fraction effects of inertial colliding particles in homogeneous isotropic turbulence. J Fluids Eng 134:#031302
14. Ernst M, Dietzel M, Sommerfeld M (2013) A lattice Boltzmann method for simulating transport and agglomeration of resolved particles. Acta Mech 224:2425–2449
15. Feng Z-G, Michaelides EE (2005) Proteus: a direct forcing method in the simulations of particulate flows. J Comput Phys 202:20–51
16. Gao H, Li H, Wang L-P (2013) Lattice Boltzmann simulation of turbulent flow laden with finite-size particles. Comput Math Appl 65:194–210
17. Glowinski R, Pan TW, Hesla TI, Joseph DD, Periaux J (2001) A fictitious domain approach to the direct numerical simulation of incompressible viscous flow past moving rigid bodies: application to particulate flow. J Comput Phys 169:363–426
18. Guo Z, Zheng C, Shi B (2002) An extrapolation method for boundary conditions in the lattice Boltzmann method. Phys Fluids 14:2007–2010
19. He X, Luo L-S (1997) Theory of the lattice Boltzmann method: from the Boltzmann equation to the lattice Boltzmann equation. Phys Rev E 56:6811–6817
20. Hölzer A (2007) Bestimmung des Widerstandes, Auftriebs und Drehmoments und Simulation der Bewegung nichtsphärischer Partikel in laminaren und turbulenten Strömungen mit dem Lattice-Boltzmann-Verfahren. Doctoral thesis, Martin-Luther-Universität Halle-Wittenberg
21. Hölzer A, Sommerfeld M (2009) Lattice Boltzmann simulations to determine drag, lift and torque acting on non-spherical particles. Comput Fluids 38:572–589
22. Kuipers JB (2002) Quaternions and rotation sequences. Princeton University Press, Princeton
23. Ladd AJC (1994) Numerical simulations of particulate suspensions via a discretized Boltzmann equation. Part 1. Theoretical foundation. J Fluid Mech 271:285–309
24. Ladd AJC (1994) Numerical simulations of particulate suspensions via a discretized Boltzmann equation. Part 2. Numerical results. J Fluid Mech 271:311–339
25. Lallemand P, Luo LS (2003) Lattice Boltzmann method for moving boundaries. J Comput Phys 184:406–421
26. Maury B (1999) Direct simulations of 2D fluid-particle flows in biperiodic domains. J Comput Phys 156:325–351
27. Mei R, Yu D, Shyy W, Luo LS (2002) Force evaluation in the lattice Boltzmann method involving curved geometry. Phys Rev E 65:#041203
28. Nguyen NQ, Ladd AJC (2002) Lubrication corrections for lattice Boltzmann simulations of particle suspensions. Phys Rev E 66:#046708
29. Saffman PG (1965) The lift on a small sphere in a slow shear flow. J Fluid Mech 22:385–400
30. Schlauch E, Ernst M, Seto R, Briesen H, Sommerfeld M, Behr M (2013) Comparison of three simulation methods for colloidal aggregates in Stokes flow: finite elements, lattice Boltzmann and Stokesian dynamics. Comput Fluids 86:199–209
31. Schutte KCJ, Portela LM, Henkes RAWM (2013) A numerical study on the formation and break-up of particle agglomerates. In: Proceedings of 8th international conference on multiphase flow, Paper No. ICMF2013-731, pp 1–12
32. Seo JH, Mittal R (2011) A sharp-interface immersed boundary method with improved mass conservation and reduced spurious pressure oscillations. J Comput Phys 230:7347–7363
33. Seto R, Botet R, Briesen H (2011) Hydrodynamic stress on small colloidal aggregates in shear flow using Stokesian dynamics. Phys Rev E 84:#041405
34. Ten Cate A, Derksen JJ, Portela LM, Akker HEA (2004) Van den: fully resolved simulations of colliding monodisperse spheres in forced isotropic turbulence. J Fluid Mech 519:233–271
35. Thömmes G, Becker J, Junk M, Vaikuntam AK, Kehrwald D, Klar A, Steiner K, Wiegmann A (2009) A lattice Boltzmann method for immiscible multiphase flow simulations using the level set method. J Comput Phys 228:1139–1156
36. Uhlmann M (2005) An immersed boundary method with direct forcing for the simulation of particulate flows. J Comput Phys 209:448–476
37. Wadell H (1935) Volume, shape and roundness of quartz particles. J Geol 43:250–280
38. Zhang Z, Prosperetti A (2005) A second-order method for three-dimensional particle simulation. J Comput Phys 210:292–324

Small-Molecule Stabilization Mechanisms of Metal Oxide Nanoparticles

S. Zellmer, C. Grote, T.A. Cheema and G. Garnweitner

Abstract The stabilization of nanoparticles to prevent agglomeration is of great importance for their application. To achieve long-term stable particle dispersions that can be stored and processed, and to clarify stabilization mechanisms in detail, the stabilization of metal oxide nanoparticles with small molecules was investigated. Particularly, the adsorption of the stabilizer and thereby the dynamic and kinetic processes on the surface of the metal oxide nanoparticles are essential for the stabilization process. Within this project, particle-stabilizer-solvent-interactions for different particle systems, ITO and ZrO_2, were described and influences of the chain length, the stabilizer concentration as well as the binding strength between stabilizer and surface were investigated and modeled. The developed model enables a prediction of the efficiency of the systems and about optimized combinations of stabilizer-particle-solvent systems.

Keywords Metal oxide nanoparticles · Colloidal stability · Stabilization mechanisms · Steric stabilization · Non-aqueous sol-gel synthesis

1 Introduction

Based on their unique properties, metal oxide nanoparticles are used in a variety of applications. ITO nanoparticles, for example, belong to the class of transparent conducting oxides (TCO) and show promise in the field of printable electronics for cheap and reliable polymer-based flexible touch-panels as well as displays [1–3]. As another example, ZrO_2 nanoparticles are highly attractive for ceramics,

S. Zellmer (✉) · C. Grote · T.A. Cheema · G. Garnweitner
TU Braunschweig, Institut für Partikeltechnik, Volkmaroder Str. 5,
38104 Braunschweig, Germany
e-mail: s.zellmer@tu-bs.de

G. Garnweitner
e-mail: g.garnweitner@tu-bs.de

M. Kind et al. (eds.), *Colloid Process Engineering*,
DOI 10.1007/978-3-319-15129-8_4

coatings, electronic devices, thin film capacitors and composites because of their enhanced mechanical and dielectric properties [4–13].

To process and utilize these materials in different fields, the nanoparticles must be stabilized to prevent agglomeration. The combination of attractive interactions, such as van der Waals forces, and repulsive interactions determines whether the particles will agglomerate. These repulsive interactions can be achieved by steric repulsion via the adsorption of organic molecules on the particle surface or electrostatic repulsions caused by surface charges. To describe these stabilization mechanisms in detail, interactions between the particles, the particle and the stabilizer as well as the interactions between the stabilizer and the solvent must be considered [22–25].

In the last years, nanoparticles with superior properties were obtained from the syntheses in hot organic media. Whilst, in many cases, surfactants are present and result in instant stabilization, their selection is arbitrary and empirical, and often large excess of organics is present in the final product. In other cases, only inert solvents are used and the particles consequently tend to agglomerate during the synthesis; however, they can be stabilized by the addition of surfactants. Generally, organic moieties from the synthesis are often present at the particle surface and it remains unclear whether these facilitate or hinder the stabilization as well as whether the stabilizer replaces these groups or adsorbs via additional binding sites at the particle surface. Additionally, in the case of nanoparticles less than 20 nm in size, stabilization can be achieved by the use of small molecules rather than polymer chains. Thereby, a decrease in the particle size leads to a smaller contribution of attractive particle interactions at a given distance, so that small molecules, such as surfactants, can prevent agglomeration [26–28, 33].

The influence of the organic layer thickness is often investigated by varying chain length of the stabilizer. For example, Bergström et al. [27] published the stabilization of Al_2O_3 particles with fatty acids of different chain lengths. Siffert et al. [29] stabilized TiO_2 nanoparticles with various n-alkylamines in nonpolar solvents. The results of these studies as well as the experiments from Sun et al. [30] and Marczak et al. [31] have shown that stabilization principally depends on the electrostatic and steric effects.

Furthermore, different models which describe the stabilization of nanoparticles in polar and nonpolar solvents were proposed in the literature. Segets et al. [32] modeled the colloidal stabilization of ZnO particles using dimensionless numbers as a function of the geometry as well as attractive and repulsive forces. In contrast to the DLVO theory, this allows for not only the calculation of energy barriers, but also the consideration of the whole stabilization process [32]. Still, the applicability of these models to nanoparticles prepared in hot organic media remains unclear.

Within this project, experimental results and theoretical models were combined to describe and predict the stabilization of metal oxide nanoparticles using small molecules. For the synthesis of well-defined highly crystalline metal oxide nanoparticles as model systems, the non-aqueous sol-gel synthesis was employed. This synthesis is an easily reproducible method that enables the control of the particle size as well as the morphology of the particles. To describe and model the stabilization with short molecules, such as amines or carboxylic acids, ITO and ZrO_2 nanoparticles were selected as model systems. To prevent influences of the in situ stabilization

on the particle formation and to obtain a more detailed understanding of the interrelation between the adsorption-desorption process on the particle surface and the deagglomeration of the nanoparticles, post-synthetic stabilization was selected.

The main focus of the project was the elucidation of particle-stabilizer-solvent interactions as a function of the binding strength, the chain length, the concentration of the stabilizers, the polarity of the solvents, and the surface configuration as well as the size and morphology of the metal oxide nanoparticles. Therefore, to characterize the stabilization kinetics, a number of analytical methods, such as thermogravimetric analysis, isothermal titration calorimetry, and spectroscopic methods, were combined.

To complement the experimental results, an empirical model was developed to predict particle-stabilizer-solvent interactions. The model allows for the consideration of different stabilizer properties, such as the chain length, the concentration and the binding strength of the stabilizer. Furthermore, the stabilization time and temperature as well as solvent and particle properties can be included in the model. Depending on these influences, the efficiency of the stabilization process for different particle system can be identified and used to optimize the combination of particle-stabilizer-solvent systems.

2 Experimental

ITO and ZrO_2 nanoparticles were synthesized via the non-aqueous sol-gel method using benzyl alcohol as the high boiling solvent [3, 14–16]. In accordance with Ba et al. [3], In(III) acetylacetonate (≥99.99 % trace metals basis, Aldrich) and Sn(IV) *tert*-butoxide (≥99.99 % trace metals basis, Aldrich) as molecular precursors were dissolved in the organic reaction medium to prepare highly crystalline ITO nanoparticles. In the case of ZrO_2, Zr(IV) *n*-propoxide in 1-propanol (70 wt%, Aldrich) was used as precursor [14–16]. The reaction solutions were transferred into Teflon-lined steel autoclaves (Parr Instr.) and heated to 200 °C for 24 h (ITO) and 220 °C for 96 h (ZrO_2).

To stabilize the nanoparticles after synthesis, the particles were separated from the reaction mixture by centrifugation and washed twice with chloroform (ITO) and ethanol (ZrO_2). For the post-synthetic stabilization, small organic molecules, such as n-alkylamines (ITO) and carboxylic acids (ZrO_2), with different chain lengths and in a variety of concentrations were added to the dispersed nanoparticles in chloroform. The reaction between the stabilizer and the particle surface is achieved through simple shaking for 24 h at room temperature. Typically, this results in instant disintegration of agglomerates. A fraction of the particles is stabilized at primary particle level (termed “stable particles”) whereas another fraction remains present as agglomerates in the µm range (termed “unstable particles”). To separate the stable and unstable particle fractions, the particle dispersion must be centrifuged at 8500 rpm for 15 min. After the separation of both fractions, the stable fraction was precipitated by adding an organic solvent. In the case of ITO nanoparticles, methanol (in a volume ratio of 1:1) and for ZrO_2, ethyl acetate

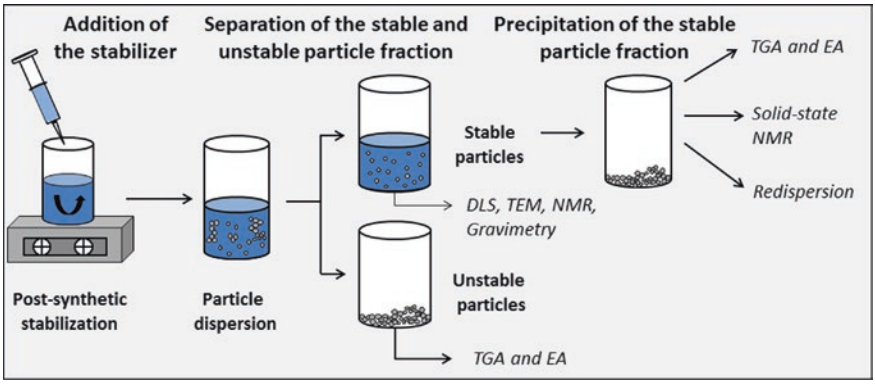

Fig. 1 Scheme of the stabilization process

(in a volume ratio of 5:1 ethyl acetate:dispersion) was used. The obtained precipitate was dried under vacuum at room temperature. The process scheme is plotted in Fig. 1.

To determine the particle size of the stable particle fraction of ITO and ZrO_2 nanoparticles, dynamic light scattering (Malvern Zetasizer Nano ZS) was used. The content of ITO and ZrO_2 nanoparticles in the dispersion was calculated using thermogravimetric analysis (TGA), which was performed on the dried powder samples and carried out on a Mettler Toledo TGA/SDTA 851 under oxygen flow in the range of 25–750 °C at 10 °C min^{-1}. To investigate the amount of the bound stabilizer in detail, elemental analysis (FlashEA 1112, ThermoQuest Italia S.p.A) was utilized. As spectroscopic methods, ^{13}C NMR spectroscopy (Bruker AV II-600) and solid-state-^{13}C-NMR (TU Paderborn, Tecmag, Apollo) were applied to verify the attachment of the stabilizer molecules. The quantification of the binding affinity was performed by isothermal reaction calorimetry (MPI Mainz, VP-ITC, Microcal. Inc., USA).

3 Results and Discussion

3.1 Particle Model Systems

ZrO_2 and ITO nanoparticles were prepared via the non-aqueous sol-gel synthesis. Thereby, highly crystalline and uniform nanoparticles were obtained; the synthesis is described in earlier works in detail [3, 14]. First, to show the differences between stable and unstable particle fractions, DLS measurements of the stable and unstable ITO particle fractions are exemplarily plotted in Fig. 2 left. After the particle synthesis, agglomerates with a particle size of approximately 1 µm for both particle systems were found; by using different stabilizers, particle sizes of approximately 10 nm for the ITO system (Fig. 2) and 5 nm for the ZrO_2 particle system (data not shown) were measured by DLS. This corresponds to the primary

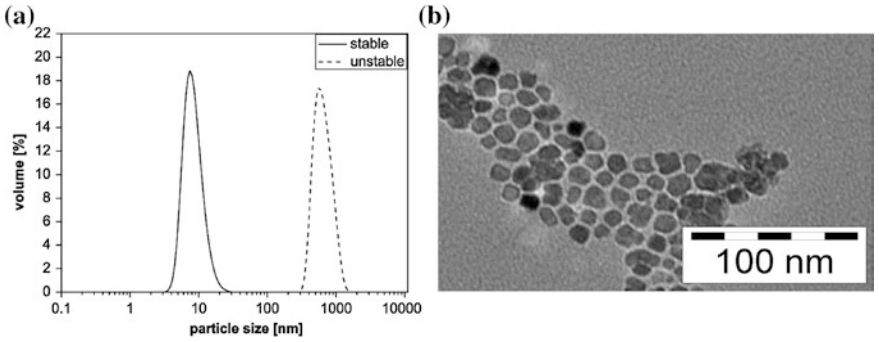

Fig. 2 DLS of a stable and unstable ITO nanoparticle fraction (*left*) and TEM image of ITO particles (*right*)

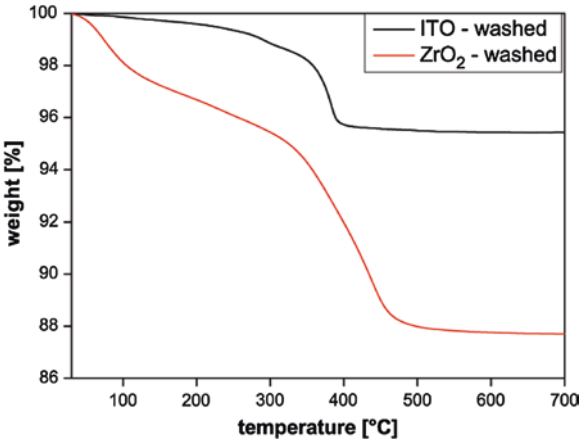

Fig. 3 TGA of ITO and ZrO_2 nanoparticles after washing

particle size of around 10 nm for ITO as shown by using TEM (Fig. 2, right) and 5 nm for ZrO_2 as presented in earlier works [17]. The TEM images also indicate similar particle morphologies, to be approximately spherical. For the further investigations, described in this work, DLS measurements were used to differentiate into stable and unstable particle fractions.

Gravimetric analyses of these synthesized ITO and ZrO_2 particles have shown that after a number of washing steps a constant amount of benzyl alcohol or alcohol derivatives are bound to the ITO and ZrO_2 particle surface. In the case of ITO around 5 wt% of benzyl alcohol is coupled to the particle surface; the TGA analysis of washed ZrO_2 nanoparticles shows an amount of around 10 wt% (Fig. 3). For both samples, washed ITO and ZrO_2 nanoparticles, the weight loss occurs in two steps. Thereby, the first step is attributed to weakly bound species such as volatile solvents; the second step at around 400 °C is assigned to chemisorbed benzyl alcohol and its side products. Based on the works of Zhou et al. [18] and Pinna et al. [19],

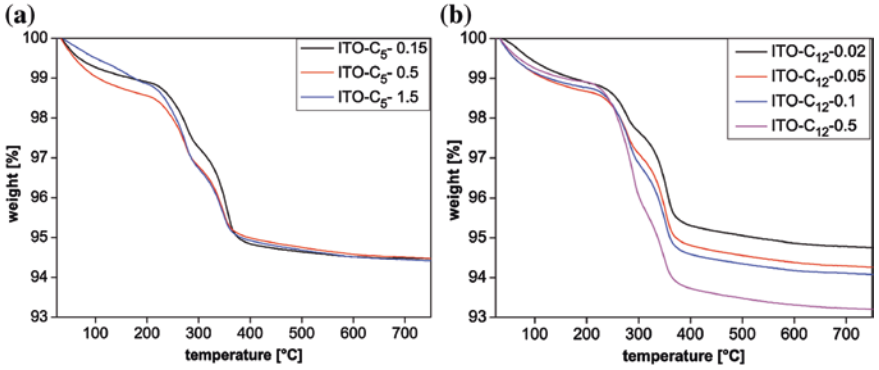

Fig. 4 TGA of ITO nanoparticles stabilized with the short-chain stabilizer amylamine (*left*) and the long-chain stabilizer dodecylamine (*right*)

we identified that in the case of ZrO_2 nanoparticles, benzoic acid was formed during the synthesis [16]. This change of the surface chemistry must be considered for further investigations and the elucidation of the stabilization of ZrO_2 particles.

3.2 Stabilization of Metal Oxide Nanoparticles

The absence of the stabilizer during the synthesis offers the possibility to investigate the dynamic and kinetic processes on the particle surface, both on a microscopic and macroscopic scale during the post-synthetic stabilization. The investigation of stabilization mechanisms furthermore involves the determination of particle, stabilizer and solvent influences.

First, to study the influence of stabilizer properties, such as the chain length, the amount of needed stabilizer and the binding strength, the other parameters, such as the temperature, the solvent as well as the stabilization time were kept constant. Therefore, depending on the affinity of the functional group of the stabilizer to the particle surface, ITO nanoparticles were stabilized with n-alkylamines of chain length between C_5 and C_{12} and the stabilization of ZrO_2 particles occurs upon the addition of carboxylic acids (C_6 to C_{12}).

3.3 Stabilization of ITO Nanoparticles with n-Alkylamines

For the stabilization of ITO nanoparticles, a variety of n-alkylamines with different chain length and added concentrations of the stabilizer in chloroform were applied. The TGA measurements plotted in Fig. 4 show strong differences between the short-chain stabilizer amylamine (left) and the long-chain stabilizer

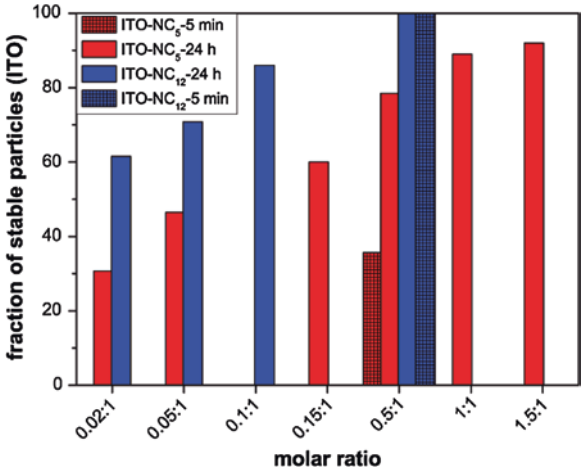

Fig. 5 Fraction of stabilized ITO nanoparticles as a function of different added stabilizer concentrations

dodecylamine (right). Thereby, the stable particle fractions were precipitated and dried prior to the measurements.

The addition of larger amounts of amylamine does not lead to an increase in the quantity of organics adsorbed to the particle surface. However, when higher amounts of dodecylamine were added to the dispersion, a continuous rise in the amount of bound stabilizer is observed. This points to a higher affinity of the long-chain stabilizer to the particle surface and results in different molar stabilizer-to-particle ratios required to stabilize 100 % of the particles in the system. In detail, the first weight-loss step is attributed to fragile bound volatile solvents; the second step is related to the bound stabilizer and the third step reflects the desorption of coupled benzyl alcohol from the particle surface [17].

To show the influence of the amount of added stabilizer on the stabilization, a range of concentrations were selected. In order to realize constant conditions, the amount of stable particles was measured after 24 h stirring in each experiment by separating the particle fractions. Figure 5 indicates the stable ITO content in % resulting from adding different molar ratios of the stabilizer.

As expected, an increase in the molar ratio leads to a higher amount of stable particles. In the case of dodecylamime, a value of 0.5:1 (stabilizer:ITO) is sufficient to stabilize 100 % of the particles in the experiment. Due to the strong influences of the chain length, higher amounts of amylamine are necessary for the stabilization. With the addition of 1.5:1 (stabilzer:ITO), around 90 % of the particles are stable [20].

Furthermore, to demonstrate the influence of the stabilization time, i.e. the period from the addition of the stabilizer until the investigation of the sample, the amount of stable particles after 5 min is additionally plotted for a molar ratio of 0.5:1 stabilizer to ITO nanoparticles. For the long chain stabilizer dodecylamine, 100 % of the particles were stabilized after 5 min stabilization time. In the case of the short chain stabilizer amylamine only 50 % of the particles, compared to the amount of stable particles after 24 h, could be stabilized [20].

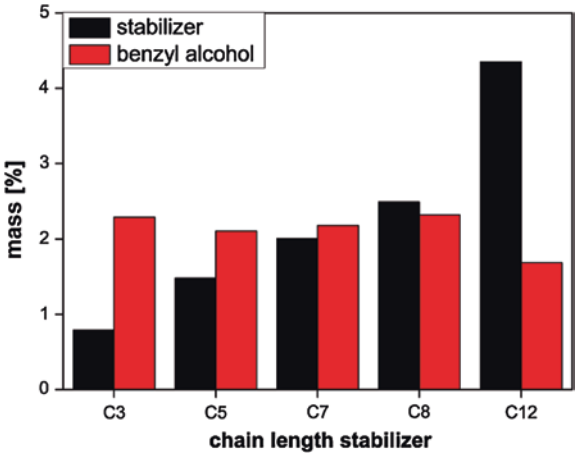

Fig. 6 Mass of the bound organics on the particle surface of stable ITO nanoparticles as determined by elemental analysis for stabilizers of different chain length

To show the stabilization mechanisms in detail, elemental analysis of the stable particle fractions was used to determine the amounts of benzyl alcohol and the stabilizer on the particle surface. Figure 6 indicates that, from the original 5 wt% benzyl alcohol adsorbed to the particle surface, about 2.5 wt% were desorbed with the adsorption of the stabilizer. Depending on the molecular weight of the stabilizer, the amount of bound stabilizer increases with the chain length; the amount of bound benzyl alcohol remains approximately constant.

To characterize the binding affinity of the n-alkylamines to the particle surface, isothermal titration calorimetry (MPI Mainz) combined with ^{13}C-NMR (TU Braunschweig) was applied. The attachment of the amines was analyzed with ^{13}C-NMR spectroscopy in order to show the selective interaction of the amine group with the particle surface. As an example, the spectrum of dodecylamine in deuterated chloroform (left) is compared to the spectrum of dodecylamine-stabilized ITO nanoparticles (right). The presence of the ITO nanoparticles results in changed intensity of the signal. The strong shift of the signals 1 and 2 which correspond to the two methyl groups next to the amine group, indicates an interaction of the amine with the ITO surface [20] (Fig. 7).

The binding strength between the stabilizer and the particle surface was determined using isothermal titration calorimetry (ITC). Therefore, the n-alkylamines of different chain lengths dissolved in chloroform were titrated with dispersions of ITO nanoparticles. Figure 8 shows the calculated enthalpy (ΔH) and entropy ($T\Delta S$) values for the titration process as well as the free energy (ΔG). Thereby, the binding enthalpy ΔH reflects the strength of the interactions between the n-alkylamines and the ITO surface relative to those existing with the solvent. In the case of the ITO/n-alkylamine systems, a change from enthalpically driven interactions to entropically driven interactions can be observed with an increase in the chain length. This is because the interactions between the stabilizer and the particle surface become more and more unspecific. Additionally, the increase in the chain

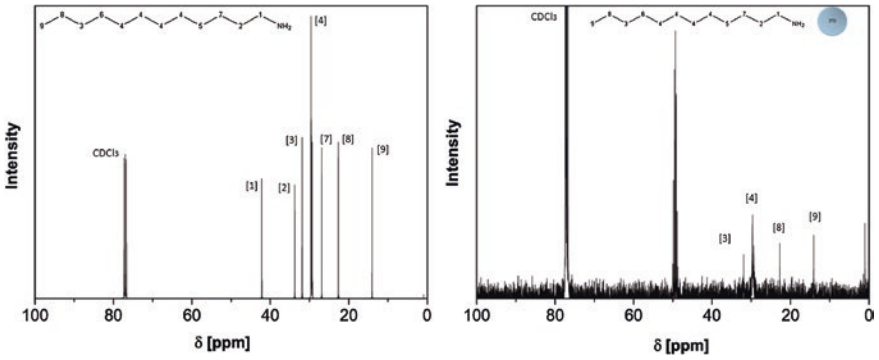

Fig. 7 ^{13}C-NMR spectra of docecylamine in $CDCl_3$ (*left*) and with dodecylamine stabilized ITO nanoparticles (*right*) [20]

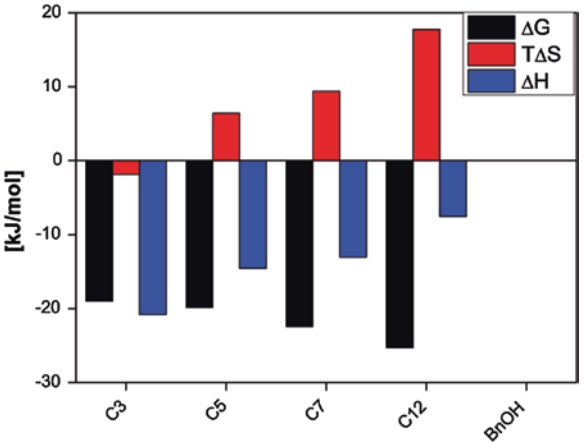

Fig. 8 Gibbs free energy, entropy and enthalpy values calculated with ITC for different chain length of n-alkylamines

length involves a decrease of the enthalpic contributions, so that the amine with the longest chain, dodecylamine, shows weak enthalpic interactions with the particle surface. Compared with the TiO_2 reference system, discussed in earlier works [21], the enthalpic contribution in the case of the ITO system is much lower, than for the TiO_2 reference system. Despite the weak interaction, the amino group of the stabilizer is still required to achieve the affinity to the particle surface. The addition of benzyl alcohol did not result in any detectable enthalpic effects. Details on these measurements and their evaluation can be found elsewhere [21].

Despite these weak interactions between stabilizer and particle surface, long-term stability of the particle system was observed [21]. Re-agglomeration of the ITO particles is possible by the addition of an anti-solvent to the particle dispersion. To investigate the re-agglomeration of the particles and the thereby incurred processes on their surface in detail, the amount of the stabilizer on the surface which was detected by solid-state ^{13}C-NMR is compared with TGA. ITO particles

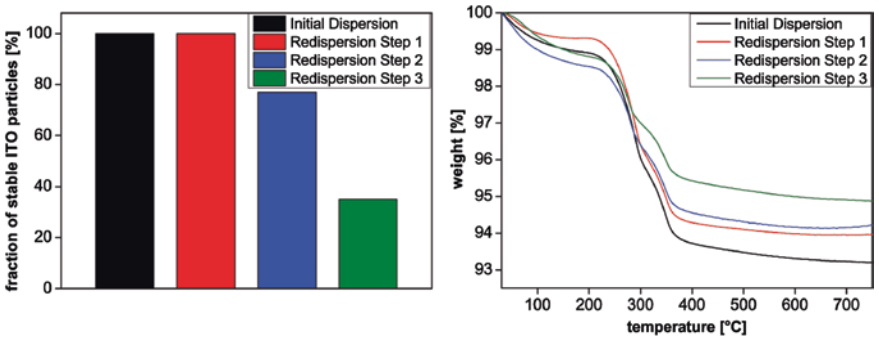

Fig. 9 Fraction of stable ITO particles (*left*) and TGA of ITO nanoparticles (*right*) before and after a number of precipitation-redispersion steps

stabilized with dodecylamine were precipitated by addition of an organic solvent (methanol) and redispersed three times. Figure 9 shows the results of TGA measurements (right) and the content of stable ITO particles before and after a number of precipitation-redispersion cycles (left).

The redispersion of the stabilized ITO nanoparticles leads to a decrease in stability of the nanoparticles, measured as decreased fraction of stable particles after the first redispersion cycle. This is due to the weak interactions between the stabilizer and the particle surface, as shown above by the ITC measurements. By precipitation and redispersion of the particles, some stabilizer molecules were detached from the surface because of the addition of the organic solvent. The detachment still small enough to achieve redispersion of the nanoparticles during the redispersion steps was verified by TGA and is plotted in Fig. 9 (right). In case of the first re-agglomeration step, the amount of bound stabilizer on the surface is still sufficient to achieve full redispersion of the nanoparticles. However, after three precipitation-redispersion cycles, the amount of coupled stabilizer molecules is so low that only 35 % of the particles are stable [20].

To investigate this process in detail, in cooperation Prof. Schmidt, University of Paderborn, solid-state ^{13}C-NMR spectroscopy was employed. Figure 10 shows the spectra of stabilized ITO nanoparticles after precipitation-redispersion cycles for 1, 2 and 3 times. The significant peaks are marked as peak 1, for the C-atoms of the alkyl chain, and peak 2, to assign benzyl alcohol. As already shown by TGA, an increase in the precipitation-redispersion steps leads to a decrease of the bound stabilizer on the particle surface. In contrast, the amount of benzyl alcohol remains constant over all steps.

In summary, the stabilization of ITO nanoparticles via n-alkylamines depends on the chain length and the amount of added stabilizer as well as on the stabilization time. The stabilization is based on the partial desorption of bound benzyl alcohol stemming from the synthesis and the concurrent adsorption of n-alkylamines, which only have a weak coordination to the surface. By addition of an anti-solvent, the precipitation and subsequent redispersion of the particles

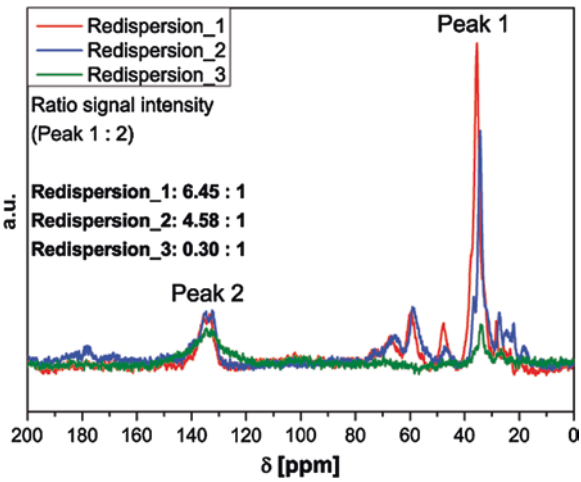

Fig. 10 Solid-state ^{13}C-NMR spectrum of redispersed ITO nanoparticles after different precipitation-redispersion steps

is possible, but the amount of stable particles decreases with every washing step. Nonetheless, the weak coordination between the stabilizer and the particle surface results in long-term stability of the ITO system.

3.4 Stabilization of ZrO_2 Nanoparticles with n-Carboxylic Acids

As a comparative model system, the stabilization of ZrO_2 with n-carboxylic acids of different chain lengths was investigated. Thereby, we have shown that the carboxylic acids bind to the particle surface via a selective interaction between the carboxylic acid group and the particle surface. Furthermore, a strong binding of the carboxylic acids to the ZrO_2 particle surface by the carboxylic group was determined by ^{13}C-NMR spectroscopy [17]. To show the influence of the strong interaction on the stabilization mechanism, a certain amount of the ZrO_2 nanoparticles were stabilized after synthesis under variation of the chain length and the added amount of stabilizer. The obtained solid content of stable ZrO_2 particles for carboxylic acids of different chain length is plotted in Fig. 11.

It should be noted, that due to the effect of the washing treatment, for the investigated system about 50 % of the ZrO_2 particles are stable without the addition of any stabilizer. As a result, only a small amount of the stabilizer is required to achieve full stability of the nanoparticles (stable fraction of 100 % of the used nanoparticles for the investigated setup). For low stabilizer-to-particle ratios, an increase in stable particles is registered for the stabilization with the short-chain stabilizer hexanoic acid (C_6). By using an amount higher than 0.05:1 (stabilizer: ZrO_2), almost 100 % of the particles are stable for all investigated carboxylic acids. The differences between the needed amounts of stabilizer to obtain

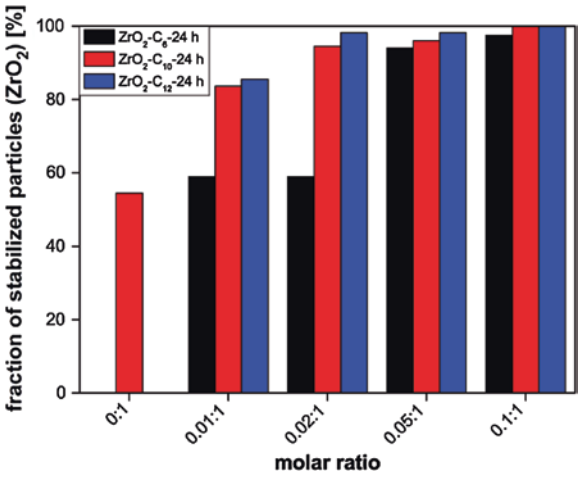

Fig. 11 Fraction of stabilized ZrO_2 nanoparticles depending on a variety of stabilizer concentration for carboxylic acids of different chain length; Reprinted with permission from [17]. Copyright 2012, American Chemical Society

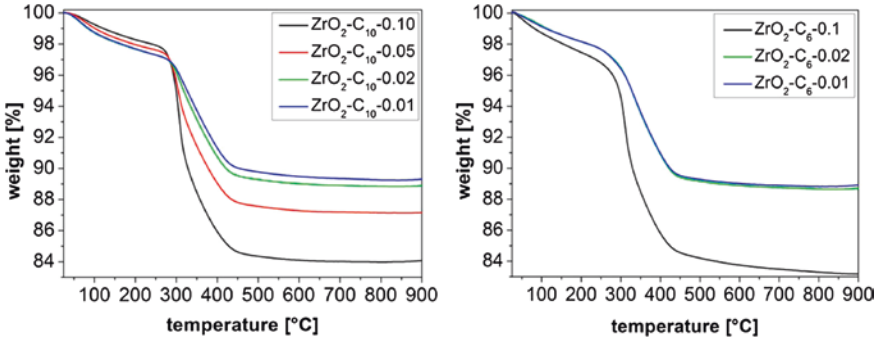

Fig. 12 TGA of ZrO_2 nanoparticles stabilized with the short-chain stabilizer hexanoic acid (*right*) and the long-chain stabilizer decanoic acid (*left*); Reprinted with permission from [17]. Copyright 2012, American Chemical Society

100 % stable particles of both particle systems can be attributed to the fact that, in the case of ZrO_2, a portion of benzyl alcohol is converted to benzoic acid, so that around 50 % of the particles are stable without any addition of the stabilizer. Furthermore, a stronger binding between the stabilizer and the particle surface leads to smaller amounts of needed stabilizer and less influences of the chain length on the stabilization process [17].

In order to investigate the adsorption and desorption processes on the particle surface in detail, TGA was carried out. Figure 12 shows the results of TGA measurements for the short-chain stabilizer hexanoic acid (right), and the long-chain stabilizer decanoic acid (left). For all measured samples, two main steps of weight

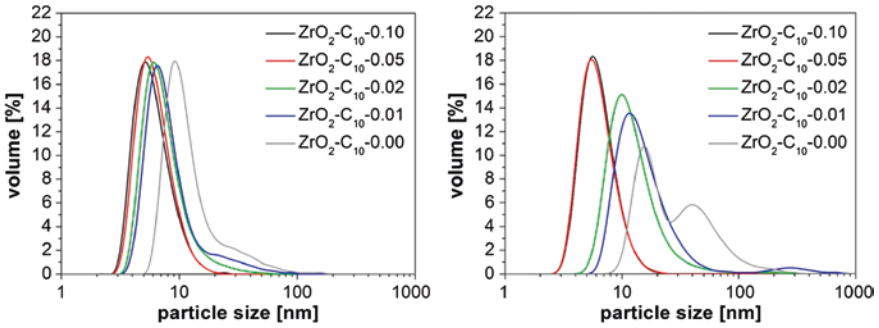

Fig. 13 Particle size distribution curves of stabilized ZrO_2 particles analyzed after 24 h (*left*) and after 1 month (*right*); Reprinted with permission from [17]. Copyright 2012, American Chemical Society

loss can be detected. The first step results from weakly-bound volatile solvents; the second step occurring at higher temperatures is attributed to the chemisorption of benzyl alcohol and its derivatives [17, 18]. Through the addition of the stabilizers with different chain lengths and in different amounts, an increase in the weight loss can be detected with TGA, which proves the presence of the stabilizer molecules on the particle surface. However, no significant differences are found for stabilizers with various chain lengths.

In order to show the influence of the chain length and the amount of added stabilizer on the long-term stability of ZrO_2 nanoparticles, we analyzed the produced dispersions via dynamic light scattering after 24 h and 1 month storage. The results of these experiments are plotted in Fig. 13 [17].

Above, a change in the particle size distribution after 1 month for a molar stabilizer-to-particle ratio lower than 0.05:1 is detected. Hence, for this system long-term stability is only achieved after the addition of higher amounts of stabilizer (i.e. molar ratio of 0.05:1 or higher) [17]. Furthermore, with the stabilization of ZrO_2 nanoparticles depending on the strong bindings, an unlimited number of precipitation-redispersion cycles are possible.

In conclusion, the long-term stability of ZrO_2 is achieved only after addition of a minimum concentration of a carboxylic acid as stabilizer. Thereby, no significant difference between stabilizers with different chain lengths could be identified. The peculiar surface chemistry of the ZrO_2 nanoparticles after the synthesis may explain the low amounts of needed stabilizer.

3.5 Modelling of Nanoparticle Stabilization

To predict the stabilization of nanoparticles by post-synthetic addition of stabilizers, an empirical model to describe the stabilization mechanisms on the

particle surface was developed. As shown in Figs. 5 and 11, the content of stable particles depends on the concentration of the stabilizer and reaches a saturation, which we postulate to be related to the saturation of stabilizer at the particle surface, to be mathematically expressed using the Langmuir equation. Following this equation, originally developed to describe the sorption of gas molecules on the surface of solid materials, but also being applicable to describe processes at solid-liquid interfaces, the ratio of stable particles as stability criterion was calculated. This is based on the assumptions that the stabilizer is chemically adsorbed as a molecular layer and that all binding sites are equal, so that only one molecule can be adsorbed to one binding site. The adsorption of the stabilizer moreover requires the desorption of benzyl alcohol and that there is no interaction between the molecules. Hence, the stability value (z) is a function of the maximum solid content (m_S) $\left[\frac{mass\ of\ the\ stable\ particle\ fraction}{total\ mass\ of\ all\ particles}\right]$ and the relative concentration (x) $\left[\frac{concentration\ stabilizer}{concentration\ particles}\right]$ of the used stabilizer. Thereby, the stability value can be described as the success of the stabilization, which reflects the maximum amount of particles which were stabilized to the primary particle size. Based on this function, the efficiency (E_S) of the respective stabilizer can be assessed and characterizes the potential of the particle-stabilizer system to achieve ideally 100 % stable particles by addition of a minimum stabilizer concentration. To be able to extend the model arbitrarily, the factor c as a function of the molecular weight, the time as well as the temperature was established.

$$stability\ value(z) = maximum\ solid\ content\ (m_S) \cdot \frac{concentration\ (x)^c}{concentration\ (x)^c + {}^{1}/_{efficiency\ (E_S)}}$$

Figure 14 shows the stability value, which is the solid content of the stable fraction, plotted over the concentration of the added n-alkylamines. To capture the influence of the chain length, the stability value was determined for different n-alkylamines. Furthermore, the maximum solid content as well as the efficiency are shown as functions of the molecular weight (chain-length) for a stabilization

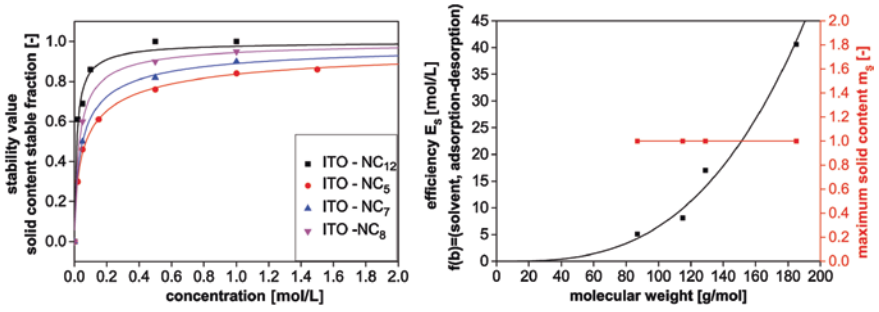

Fig. 14 Stability criterion for different stabilizers (*left*) and the efficiency of the systems depending on the molecular weight (*right*)

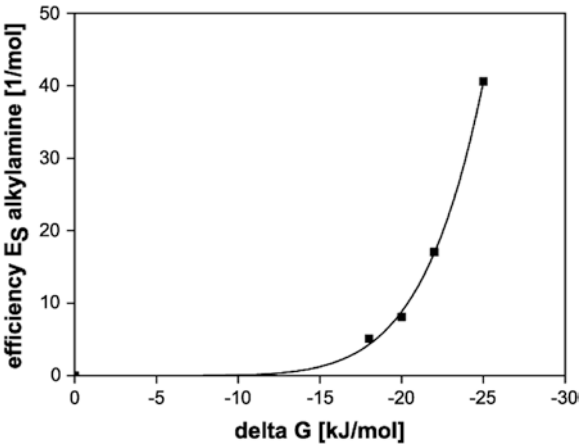

Fig. 15 Efficiency of the stabilization mechanism in relation to ΔG

time $t \rightarrow \infty$. Therefore, the maximum solid content is constant for all stabilizers and equals 1.

Due to the high number of free binding sites the solid content of the stable fraction increases almost linearly for low stabilizer concentrations. With an increase in the stabilizer concentration, the adsorption of the stabilizer and the desorption of the benzyl alcohol is hindered by conformational degrees and a decrease in free binding sites. This leads to a limitation of the diffusion and results in the formation of a plateau. As this plateau is reached, the stability criterion of 100 % stable particles is fulfilled. This is also shown in the efficiency of the different stabilizer systems (Fig. 14 right). Due to the strong influence of the chain length, the short-chain stabilizer amylamine shows a lower efficiency than the long-chain stabilizer dodecylamine. Combined with the results from ITC, the efficiency of the ITO/stabilizer systems is plotted over the free energy of stabilizer binding as shown in Fig. 15.

As already demonstrated in Fig. 8, the entropic effect and, thereby, the free energy ΔG of the whole system increases with longer chains. The correlation of the free energy to the efficiency of the system provides a comprehensive indication of the influences of dynamic and kinetic processes on the particle surface. The efficiency resembles the influences of the properties of the stabilizer molecules (chain-length, functional group, concentration); through ITC, influences of the binding strength could be coupled with the influence of solvent effects and the change of conformational degrees (entropic effects).

To compare both particle systems, the model was applied to the ZrO_2 system. In contrast to ITO, the stabilization of ZrO_2 is based on the addition of carboxylic acids. Furthermore, around 50 % of the particles are stable without adding stabilizer molecules; meaning that lower concentrations of the stabilizer are needed to achieve the stability value of 100 % stable particles. Figure 16 shows the implementation of the stabilization criterion on the stabilization process of ZrO_2 for carboxylic acids with different chain lengths.

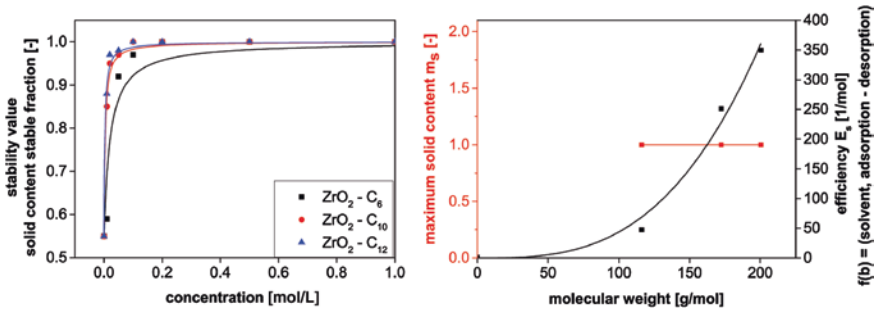

Fig. 16 Stability criterion for different carboxylic acids (*left*) and the efficiency of the systems depending on the molecular weight (*right*)

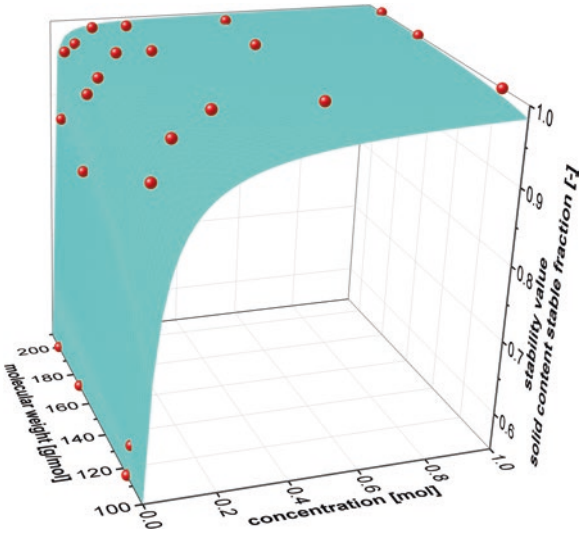

Fig. 17 3D plot of the stability value depending on the concentration and the molecular weight of the ZrO_2 system

Due to the strong interactions between the stabilizer and the particle surface, the stabilization is controlled by the amount of the stabilizer rather than the chain length of the stabilizer. Consequently, higher solid content and a sharper linear increase of the stability value for low stabilizer concentrations were achieved. This results in a higher efficiency with approximately 100 % stable particles in the ZrO_2 system and can be attributed to higher binding strength between the stabilizer and the particle surface in comparison to the ITO system.

To predict the stability value of different systems, a 3D plot based on the concentration, stability value and the molecular weight can be used and is shown in Fig. 17 for the ZrO_2 system.

The correlation of these parameters shows which factors are predominant for the stabilization. Furthermore, other parameters, such as the temperature, the

additional presence of different organics on the surface and the nature of the dispersion medium or different stabilization times, can be considered and extended via the empirical model.

4 Conclusion

The stabilization of metal oxide nanoparticles by addition of small-molecule stabilizers in a post-synthetic treatment was studied. By comparing two model systems, ZrO_2 and ITO, a number of differences between the stabilization mechanisms were elucidated. To stabilize ITO nanoparticles, weak interactions between the n-alkylamines and the particle surface were shown to be sufficient to achieve long-term stability of the system. Thereby, the stabilization depends on the concentration and the chain length of the stabilizer as well as on the stabilization time. Additionally, the stabilization of the particles is only achieved after some fractions of benzyl alcohol are desorbed. This interaction between the adsorption of stabilizer and the desorption of benzyl alcohol determines the stabilization mechanism.

In the case of ZrO_2 strong bonds between the stabilizer and the surface were detected and resulted in a higher efficiency of the system. In essence, the stabilization of ZrO_2 nanoparticles depends on the concentration of the added stabilizer to achieve long-term stability. Furthermore, due to the strong bonds a full redispersion of the particles is possible.

The differences between the stabilization mechanisms in the two systems may be explained by the formation of benzoic acid on the ZrO_2 surface as well as on the different binding strength, strong binding between the carboxylic acids and the ZrO_2 nanoparticle surface and weak interactions between the n-alkylamines and the ITO particles. Despite these differences, the developed empirical model can be used, to describe and predict surface processes and influences on the stabilization mechanism for different particle systems. Depending on the selected parameters, different influences, such as the temperature or the stabilization time, can be considered and implemented in the model. This allows arbitrary considerations of the model to predict particle-stabilizer-solvent interactions in a complex organic environment typical for nanoparticles prepared in hot organic media. In future the applicability of the model for different stabilization processes should investigate.

Acknowledgments The authors gratefully acknowledge the financial support provided by the German Research Foundation within SPP 1273 grants GA 1492/4-1 and 2. Furthermore, the authors acknowledge Dr. D. Vollmer and K. J. Chiad from the MPI Mainz for the isothermal titration calorimetry, Prof. Dr. C. Schmidt and M. Kube from the University Paderborn for the solid-state-^{13}C-NMR spectroscopy, Dr. K. Ibrom and P. Holba-Schulz from the TU Braunschweig for the NMR spectroscopy measurements, Dr. H.-O. Burmeister, S. Meyer and P. Reich for the elemental analysis as well as Dr.-Ing. D. Segets and Prof. Dr.-Ing. W. Peukert from the Institute of Particle Technology (LFG Erlangen) and Dr.-Ing. C. Schilde and Prof. Dr.-Ing. A. Kwade for discussions within the project.

References

1. Ginley DS, Bright C (2000) Transparent conducting oxides. MRS Bull 25:15–18
2. Minami T (2005) Transparent conducting oxide semiconductors for transparent electrodes. Semicond Sci Technol 20:S35–S44
3. Ba J et al (2006) Nonaqueous synthesis of uniform indium tin oxide nanocrystals and their electrical conductivity in dependence of the tin oxide concentration. Chem Mater 18:2848–2854
4. Tanabe K (1985) Surface and catalytic properties of ZrO_2. Mater Chem Phys 13:347–364
5. Garvie RC et al (1975) Ceramic steel?. Nature 258:703–704
6. Wilk GD et al (2001) High-k gate dielectrics: Current status and materials properties considerations. J Appl Phys 89:5243
7. Heuer AH, Hobbs LW (1981) Science and technology of zirconia, American Ceramic Society, vol. 3. Columbus and Ohio
8. Inoue M et al (1993) Novel synthetic method for the catalytic use of thermally stable zirconia: thermal decomposition of zirconium alkoxides in organic media. Appl Catal A 97:L25–L30
9. Joo J et al (2003) Multigram scale synthesis and characterization of monodisperse tetragonal zirconia nanocrystals. J Am Chem Soc 125:6553–6557
10. Buchanan RC, Pope S (1983) Optical and electrical properties of yttria stabilized zirconia (YSZ) crystals. J Electrochem Soc 130:962
11. Krell A et al (2009) Transparent compact ceramics: Inherent physical issues. Opt Mater 31:1144–1150
12. Robertson J (2006) High dielectric constant gate oxides for metal oxide si transistors. Rep Prog Phys 69:327–396
13. Taroata D et al (2012) High integration density capacitors directly integrated in single copper layer of printed circuit boards. IEEE Trans Dielectr Electr Insul 19:298–304
14. Garnweitner G (2007) Large-scale synthesis of organophilic zirconia nanoparticles and their application in organic-inorganic nanocomposites for efficient volume holography. Small 3(9):1626–1632
15. Tsedev N, Garnweitner G (2008) Surface modification of ZrO_2 nanoparticles as functional component in optical nanocomposite device. Mater Res Soc Symp Proc 1076:K05–03
16. Cheema TA, Garnweitner G (2014) Phase-controlled synthesis of ZrO_2 nanoparticles for highly transparent dielectric thin films. Cryst Eng Commun 16:3366
17. Grote C et al (2012) Comparative study of ligand binding during the postsynthetic stabilization of metal oxide nanoparticles. Langmuir 28:14395–14404
18. Zhou S et al (2007) Dispersion behavior of zirconia nanocrystals and their surface functionalization with vinyl group-containing ligands. Langmuir 23:9178–9187
19. Pinna N et al (2005) Synthesis of yttria-based crystalline and lamellar nanostructures and their formation mechanism. Small 1(1):112–121
20. Zellmer S, Garnweitner G (2013) Stabilization of metal oxide nanoparticles by binding of molecular ligands. In: PARTEC—international congress on particle technology, proceedings, Nuremberg, 23–25 April 2013
21. Grote C et al (2012) Unspecific ligand binding yielding stable colloidal ITO-nanoparticle dispersions. Chem Commun 48:1464–1466
22. Russel WB et al (1989) Colloidal dispersions. Cambridge University Press, Cambridge
23. Heller W, Pugh TL (1954) “Steric protection” of hydrophobic colloidal particles by adsorption of flexible macromolecules. J Chem Phys 22:1778
24. Tripathy SS, Raichur AM (2008) Dispersibility of barium titanate suspension in the presence of polyelectrolytes: A Review. J Dispersion Sci Technol 29:230–239
25. Overbeek JTG (1966) Colloid stability in aqueous and non-aqueous media. Discuss Faraday Soc 42:7–13

26. Boal AK et al (2002) Monolayer exchange chemistry of γ-Fe_2O_3 nanoparticles. Chem Mater 14:2628–2636
27. Bergström L et al (1992) Consolidation behavior of flocculated alumina suspensions. J Am Ceram Soc 75:3305–3314
28. Bell NS et al (2005) Rheological properties of nanopowder alumina coated with adsorbed fatty acids. J Colloid Interface Sci 287:94–106
29. Siffert B (1994) Location of the shear plane in the electric double layer in an organic medium. J Colloid Interface Sci 163:327–333
30. Sun D et al (2007) Purification and stabilization of colloidal ZnO nanoparticles in methanol. J Sol-Gel Sci Technol 43(2):237–243
31. Marczak R et al (2010) Optimum between purification and colloidal stability of ZnO nanoparticles. Adv Powder Technol 21(1):41–49
32. Segets D et al (2011) Experimental and theoretical studies of the colloidal stability of nanoparticles-a general interpretation based on stability maps. ACS Nano 5(6):4658–4669
33. Garnweitner G (2010) Small molecule stabilization. In: Segewitz L, Petrowsky M (eds) Polymer aging, Stabilizers and Amphipilic Block Copolymers

Liquid Distribution and Structural Changes During Convective Drying of Gels

Abdolreza Kharaghani, Christoph Kirsch, Thomas Metzger and Evangelos Tsotsas

Abstract Experimental and three-dimensional numerical simulation studies on convective drying of gels are presented in this chapter. As a physical model of a real gel, highly porous particle aggregates are produced by sintering of glass beads inside a graphite mold. A lab-scale X-ray microtomograph is used to perform a series of drying experiments with loose packings of sintered glass beads (mean diameter 700 μm) initially saturated with water. The reconstructed images (voxel size 16 μm) are analyzed to obtain the time evolution of the solid, liquid, and gas phase distributions during convective drying. A computational tool based on the volume-of-fluid approach is developed to simulate the liquid distribution over time at the microscopic scale in this model particle aggregate, which is subjected to convective drying. The simulated liquid phase distributions are found to be in good qualitative agreement with the experimental results. The major physical effect of capillary flow from large pores into small pores is easily recognized: large pores dry out first while small regions of the void space stay saturated with liquid. In addition to these pore-scale studies, resorcinol-formaldehyde (RF) hydrogels are synthesized by sol-gel polycondensation of resorcinol (R) with formaldehyde in the presence of sodium carbonate as a catalyst (C). The mechanical effects (cracks and shrinkage) in RF gels with three different R/C ratios and three different aging times are studied. The results show that the degree of shrinkage drastically increases with decreasing R/C ratio and also that the degree of shrinkage is slightly reduced by longer aging.

A. Kharaghani (✉) · E. Tsotsas
Thermal Process Engineering, Otto von Guericke University,
4120, 39016 Magdeburg, Germany
e-mail: abdolreza.kharaghani@ovgu.de

C. Kirsch
Institute of Computational Physics, Zurich University of Applied Sciences,
Wildbachstrasse 21, 8401 Winterthur, Switzerland

T. Metzger
BASF SE, GCP/TT-L540, 67056 Ludwigshafen, Germany

M. Kind et al. (eds.), *Colloid Process Engineering*,
DOI 10.1007/978-3-319-15129-8_5

Keywords Resorcinol-formaldehyde hydrogels · Mechanical deformation · Phase distribution · Volume-of-fluid method · X-ray microtomography

Nomenclature

F Force (N)
f Volume fraction (-)
h Mesh size (m)
n (unit) normal vector (-)

Greek letters

α, β Scaling parameters (-)
θ Contact angle (rad)
κ Curvature (1/m)
σ Surface tension (N/m)

Subscripts and superscripts

c Capillary
eq Equilibrium
g Gas
s Solid
w Liquid (water)

1 Introduction

Dry gels are nanoporous materials with outstanding physical properties, such as high porosity, large specific surface area, low thermal conductivity, low sound speed etc. The production of these gels with high quality is a great challenge that has led to an accumulation of both theoretical and practical knowledge by numerous research projects. In the research literature, various methods have been employed to produce dry gels (see Fig. 1): The supercritical drying technique is traditionally used to produce aerogels [1]. This drying route allows the liquid to be slowly dried off without causing the delicate solid matrix in the gel to collapse under capillary stress. While the solid structure of the gel sample stays intact during supercritical drying, the process needs to be performed at particular operating conditions and is thus rather slow, complex and expensive. Cryogels can be obtained by

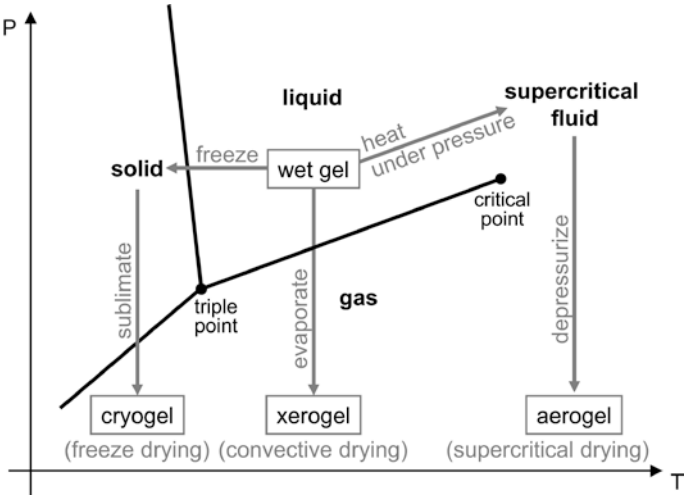

Fig. 1 Different routes for gel drying illustrated in the phase diagram. In freeze drying the liquid solvent is replaced by gas via freezing and subsequent sublimation. In convective drying the replacement occurs via direct evaporation, whereas in supercritical drying the liquid solvent is first brought to the supercritical state by heating under pressure and then to the gas state (taken from [23])

costly freeze-drying [19] during which, however, the gel structure may collapse, particularly in the freezing stage of the process. Besides these traditional gel drying methods, xerogels have been produced by vacuum drying [10]. Microwave drying has also been used to produce xerogels [32] and the measurement results have been compared with freeze-drying; the drying time is tremendously reduced for samples dried by the microwave technique, but freeze-drying yielded samples with better structural quality. Later, microwave drying has been combined with ultrasonic irradiation resulting in dry gels with improved porous properties [31].

Since the above-mentioned drying routes need to be conducted at specific temperature and pressure conditions, they are rather expensive and of limited use for large-scale production. Convective (evaporative) drying might be an alternative technique as it can be carried out under standard atmospheric conditions. However, convective drying is not yet suited to produce monolithic dry gels, because the receding liquid-gas interface in micron and sub-micron sized pores causes high stress in the solid network throughout the drying process, which results in shrinkage [25] and also damage [11] of the material. An extensive study done by Brinker and Scherer [3] on the convective drying of gels provides a good basis for understanding structural damage and for exploring possibilities to prevent it. Nevertheless, a better quantitative understanding of mechanical effects during convective drying may lead to an extended range of applications for this inexpensive and safe drying process.

Several attempts have been made so far in order to understand the drying characteristics of porous material, bringing forward various modeling approaches. Continuum models have been widely used to describe the drying of deformable

porous media. Generally in these models, the gel properties are expressed as a function of effective parameters, and partial differential equations representing mass, heat and momentum balances are solved by efficient numerical techniques. For example, Léonard et al. [21] developed a thermo-hygro-mechanical coupled model for the convective drying of resorcinol-formaldehyde gels where the liquid transport in the (fully saturated) gel is described by only the diffusion equation with a constant effective diffusion coefficient. Cáceres et al. [4] developed a more fundamental model based on volume averaging that provides a physically correct description of the fluid transfer. In these macroscopic models, however, local structural information is lumped into effective parameters, and the micro-scale transport phenomena are obscured in the model equations.

In order to retain this pore-level information, which may also be essential in the design of a production process for special materials, a modeling approach based on discrete pore and particle networks has been developed. In this approach, the void space of a particle aggregate is represented by a network of cylindrical pores, and all relevant fluid transport phenomena are directly modeled at the pore level [22]. The solid phase is represented by a network of spherical primary particles, which are bonded at the inter-particular contacts. The capillary forces are computed over time from the filling state of the pores and applied as loads on each particle, using the discrete element method [5], in a one-way coupling scheme (liquid $\rightarrow$ solid). First simulation results of the micro-mechanical behavior of compact particle aggregates during drying obtained by this approach have been shown in [12].

Pore network models, however, are not suited for the approximation of the void space of highly porous particle aggregates such as gels. The two main reasons for this are: (1) the assumption of purely axial liquid flow cannot be justified in large pores and (2) the pore network would need to be continuously updated to account for the motion of the solid phase.

In order to compute the dynamics of the liquid-gas phase boundary in spatially complex porous structures, other numerical techniques such as the volume-of-fluid (VOF) method should be used instead [7]. The VOF method relies on a description of the spatial distribution of the phases by time-dependent volume fractions defined in each cell of the computational grid. This method has already been utilized to simulate problems involving highly complicated free surface flow such as, capillary condensation [27], formation of gas cavities [28], and layering growth in wet granulation [29].

In this work, X-ray microtomography (μ-CT) is used as an experimental counterpart to the simulations. μ-CT is a powerful non-invasive and non-destructive imaging technique that is able to provide a 3D image of a scanned object from a series of X-ray projections. It is based on X-ray absorption, which can be quantified by an attenuation coefficient (or mass absorption coefficient). This coefficient depends on the material density, atomic number, and thickness (for more details on μ-CT principles, see [24]. Attenuation values are represented in 3D images as gray values in discrete volume elements (voxels). Discrimination of the individual phases within an image (i.e., solid, liquid, and gas) is achieved by thresholding, which denotes a process of converting a gray-scale image to a binary image by identifying populations in the image based on their intensity values.

μ-CT is popular across several disciplines related to drying and is used, e.g., in the analysis of cracks and shrinkage of soft materials [20], and in the investigation of the geometrical structure of liquid inside a particle aggregate made of spherical glass beads [26]. A review of the major applications of μ-CT in many different fields of research and, in particular, in the area of granular and porous materials can be found in [24].

In the present chapter, model particle aggregates made of glass beads were produced. In order to obtain highly porous structures, small assemblies of glass beads were first sintered and then packed into a cylindrical container. μ-CT was then used to study the phase distributions in these particle aggregates during drying. For the numerical simulation, the 3D pore-scale representation of highly porous aggregates including interactions between all three phases (solid *s*, liquid *l*, and gas *g*) is addressed. Phase distributions are represented by volume fractions in a Cartesian grid, and a volume-of-fluid technique is used to track the interfaces during drying. Local evaporation rates at the liquid-gas (*lg*) interface are obtained from a finite difference simulation of the vapor diffusion in the gas phase. The motion of the *lg* interface is governed by (volume-preserving) mean curvature flow, which has been implemented in an iterative numerical scheme: In a quasi-static approach which resolves only the (slow) evaporation time scale, liquid is removed according to the local evaporation rates computed from the solution of a vapor diffusion problem in the gas phase. The remaining liquid is subsequently allowed to relax to capillary equilibrium. This chapter ends with results from lab-scale drying experiments performed on resorcinol-formaldehyde (RF) hydrogel samples. The influence of aging (curing) on shrinkage and crack formation of gel samples is studied.

2 X-Ray Microtomography of Sintered Particle Aggregates During Drying

2.1 Materials and Experimental Set-up for Drying

Highly porous model particle aggregates were produced by sintering glass beads in a mold (Fig. 2a) made from graphite, which has a low thermal diffusivity and does not bond with the glass when heated. The sintering is done in an oven at 600 °C for 7 min. These conditions should be chosen depending on the type of glass used: the temperature must exceed the glass transition limit but remain below the crystallization point. The sintered particle structures (Fig. 2b) were used to create highly porous packings in a cylindrical tube made of PMMA with a diameter of 8 mm (Fig. 2c).

μ-CT measurements were taken with the cone beam X-ray tomography scanner CT-ALPHA (manufactured by ProCon, Germany). The X-ray source operates at voltages up to 160 kV with 15 W of power. The detector is a 2300 × 2300 pixel sensor with 16 bit grayscale resolution. The maximum spatial resolution

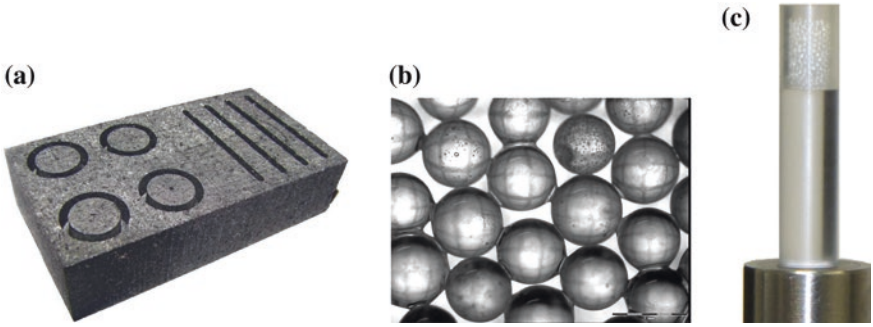

Fig. 2 **a** Graphite mold used for sintering, **b** resulting glass bead structures and **c** packed bed of particles with sample holder

of the device is <1 μm. For the measurement, the sample is placed on a rotating holder between the X-ray source and the detector. X-rays are attenuated as they pass through the sample; the extent of this attenuation is proportional to the local mass density, and this yields a gray-level transmission image on the detector side. Images obtained at different rotation angles are used to reconstruct a three-dimensional map of the attenuation coefficient within the sample, which then provides insight into its microstructure.

2.2 Image Acquisition and Data Processing

For the image acquisition by μ-CT, X-ray parameters such as voltage, filter settings and exposure time were adjusted with reference to the systems analyzed, in order to obtain the best possible image contrast. The images were acquired at 90 kV and 160 mA, and 800 different projections were considered in a full scan. The tube was covered by a layer of aluminum of 1 mm thickness in order to reduce beam hardening effects [24].

In addition to a suitable selection of parameters during image acquisition, extensive corrections were also necessary during image reconstruction in order to minimize a variety of artifacts, including misalignment of the sample rotation axis, beam hardening, motion and ring artifacts. A histogram of normalized gray values together with a slice of the reconstructed 3D grayscale image for a model glass bead aggregate is shown in Fig. 3.

The three phases (gas, liquid, and solid) can be discriminated from the contrast in the gray values: for the scan shown in Fig. 3, we assign voxels with gray values <0.05 to the gas phase, voxels with gray values >0.2 to the solid phase, and values in-between to the liquid phase. These thresholds can be determined automatically from the gray value histogram. The process yields a segmentation of the image into three regions corresponding to the three phases, so that the geometry of the sample can be analyzed.

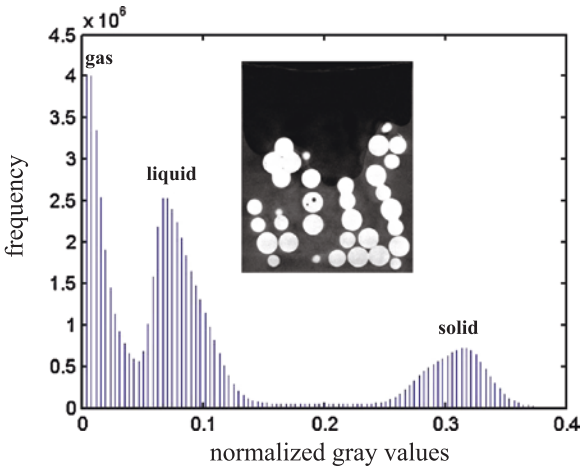

Fig. 3 A histogram of normalized gray values together with a slice of the reconstructed 3D grayscale image of a model glass bead aggregate. The peaks correspond to the gas, liquid and solid phases (from left to right)

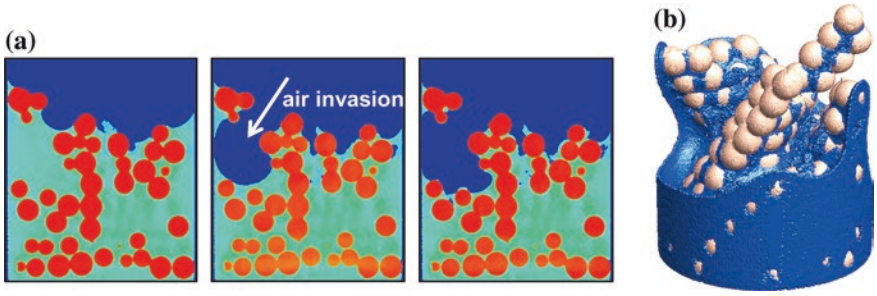

Fig. 4 **a** Cross section of 3D tomograms for a packing of sintered glass beads at various liquid saturations and **b** 3D visualization of a partially saturated sintered particle aggregate

After segmentation of the phases, median filtering and morphological operations were applied to eliminate artifacts. Air bubbles inside the particles were removed by a sequence of erosion and dilation operations. The center coordinates and radii of the particles were determined by the preflooded watershed algorithm. All image processing and analysis steps were performed using the MAVI software package developed at Fraunhofer ITWM [6].

Figure 4a shows phase distributions in a cross section of a drying glass bead structure. The microstructure geometry of the solid phase and the evolution of the liquid phase during drying are clearly visible. A corresponding 3D visualization is presented in Fig. 4b. The major physical effect of capillary flow from large pores into small pores is easily recognized: large pores dry out first whereas smaller regions of the void space stay saturated with liquid.

3 Liquid Distributions in a Drying Particle Aggregate Simulated by the Volume-of-Fluid Method

The solid phase of the gel is represented by an aggregate of spherical solid particles, which is initially saturated with liquid, and the major simulation goal is to compute the capillary forces on the particles during convective drying, as well as the effect of these forces on the aggregate structure. As a crucial first step, the time evolution of the liquid distribution in the drying particle aggregate has to be computed. For this purpose, the three-dimensional space is discretized into a fixed grid of voxels, which contain time-dependent volume fractions of the three phases (solid, liquid, and gas volume fractions f_s, f_w and f_g), as illustrated in Fig. 5.

Initially, the void space between the particles is completely filled with liquid ($f_g = 0$ for all voxels). Evaporation from the liquid-gas interface and liquid relaxation into capillary equilibrium are then computed in an alternating sequence. For this simulation we assume a scale separation in time, i.e., that the evaporation occurs on a much slower time scale than the liquid motion. We resolve only the evaporation time scale, which yields a quasi-static approach: in each evaporation step, liquid is removed according to the local evaporation rates computed from the solution of the vapor diffusion problem in the gas phase. Then the liquid is relaxed to the capillary equilibrium by volume-preserving mean curvature flow. This quasi-static approach is in contrast to a fully dynamic simulation (via computational fluid dynamics), but may come with considerably lower computational cost. Evaporation is modeled by vapor diffusion in the gas phase, with a no-flux condition at solid-gas interfaces and equilibrium vapor pressure imposed on liquid-gas interfaces (for more details, see [15]). The equilibrium liquid distribution

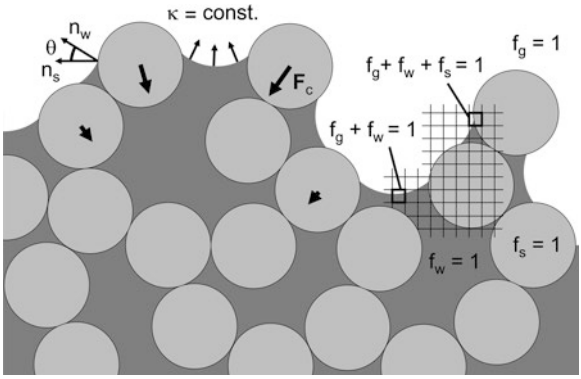

Fig. 5 Concept of the volume-of-fluid method for convective gel drying simulation. The figure shows a partially dried particle aggregate, a portion of the voxel grid as well as quantities used in the simulation: the phase volume fractions f_s (solid), f_w (liquid), f_g (gas), from which single-phase, two-phase and three-phase cells can be distinguished, the outward-pointing unit normal vectors of the solid and liquid phases ($\boldsymbol{n}_s$, $\boldsymbol{n}_w$), the contact angle θ, the mean curvature of the liquid-gas interface κ and the capillary forces $\boldsymbol{F}_c$ (taken from [23])

has to fulfill the contact angle condition $\boldsymbol{n}_w \cdot \boldsymbol{n}_s = cos\theta_{eq}$ at all three-phase boundaries and, in each liquid cluster, uniform mean curvature of the liquid-gas interface ($\nabla\kappa = 0$). The outward unit normal vectors $\boldsymbol{n}_i$ and the mean curvature of the liquid-gas interface κ are computed from the phase volume fractions as $\boldsymbol{n}_i = -\frac{\nabla f_i}{|\nabla f_i|}$ and $\kappa = \frac{1}{2}\nabla \cdot \boldsymbol{n}_w$, respectively, incorporating a Gaussian smoothing step [16].

The interface dynamics, i.e., the geometrical redistribution of the liquid to attain capillary equilibrium, is now described by the concept of *volume-preserving mean curvature flow* [2]: the normal velocity of the liquid-gas interface is given by the deviation of its local mean curvature from the cluster average $\bar{\kappa}$. This method has been shown to work successfully for two-phase problems: a liquid cube transforms into a liquid sphere of equal volume [15].

Since the condition of uniform curvature has to be satisfied in each liquid cluster separately, a cluster labeling routine based on the Hoshen-Kopelman algorithm [8] has been implemented. During the redistribution of liquid, clusters may split or merge, so that periodic re-labeling is necessary. In this way, topological changes in the liquid phase are conveniently handled.

For the interaction with the solid phase, new rules for the redistribution had to be developed. The equilibrium contact angle condition does not provide any insight into the dynamics of the contact line motion and, moreover, the microscale phenomena in the vicinity of a moving contact line are not well understood even from a physical point of view. Therefore, we made the heuristic argument that the liquid velocity at the three-phase boundary should be tangential to the solid surface, orthogonal to the contact line and proportional to the deviation from the equilibrium contact angle. The liquid velocity in the three-phase cells is thus proportional to $\left(cos\theta_{eq} - \boldsymbol{n}_w \cdot \boldsymbol{n}_s\right)(\boldsymbol{n}_w - (\boldsymbol{n}_w \cdot \boldsymbol{n}_s)\boldsymbol{n}_s)$. This vector points out of the liquid phase if the current contact angle, $\arccos(\boldsymbol{n}_w \cdot \boldsymbol{n}_s)$, is greater than the equilibrium contact angle, indicating that the velocity has the correct sign. Two weighting parameters $\alpha, \beta > 0$ have been introduced in the code to balance the two competing dynamics in the liquid-gas and three-phase cells, respectively:

$$f_w^{new} = f_w^{old} + \alpha(\kappa - \bar{\kappa}) \quad \text{in liquid-gas cells,} \tag{1}$$

$$f_w^{new} = f_w^{old} + \beta\left(\cos\theta_{eq} - n_w \cdot n_s\right) \quad \text{in three-phase cells.} \tag{2}$$

Additionally, volume conservation has to be assured, which is not trivial in the three-phase case (in liquid-gas problems without solid, Gauss's divergence theorem can be used). Since the sum of all "desired" volume fraction changes $f_w^{old} - f_w^{new}$ computed from (1), (2) is not zero in general, the individual changes are corrected for liquid volume conservation by a routine, which is designed to prevent sign changes of $f_w^{old} - f_w^{new}$ in three-phase cells.

This updating is applied iteratively, and the liquid normal vectors and mean curvatures are recomputed in each step, until the interface velocities are smaller than a prescribed threshold. A similar approach has been used by Štěpánek and Rajniak [30] to simulate the wetting of particles with a rough surface. Notice that

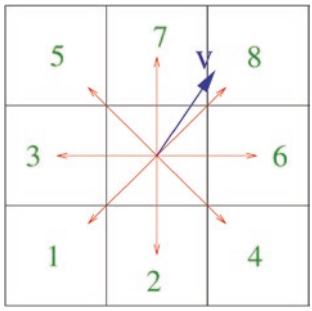

Fig. 6 Neighbor cell order for liquid redistribution (in 3D, every interior cell has 26 neighbors)

(1), (2) is not meant to yield a representation of the true fluid dynamics; instead, it is designed to reach the capillary equilibrium quickly.

The above changes leave the set of interface cells unchanged, which would only allow for very small liquid displacements. Larger changes are reflected in unphysical liquid fractions, $f_w > 1-f_s$ or $f_w < 0$, and require *passing liquid to neighboring cells* or taking it from them. This is done by a local redistribution routine [18], which is less computationally expensive than a global routine. The basic idea is to go through the neighbors of a particular cell in a certain order (described below) and to check for each of them whether they can accept/donate liquid. If yes, liquid is passed to/taken from this cell and the over-/underflow in the center cell is reduced accordingly. This procedure is repeated for other neighbor cells as long as necessary; remaining over-/underflow is discarded. We notice that this last step does not satisfy the volume conservation constraint, but the scaling parameters α, β allow us to bound the maximum over-/underflow and make liquid volume loss/gain in the redistribution step arbitrarily small.

The order in which neighbors of a given cell are considered for liquid distribution is obtained by sorting them according to the scalar product of the liquid velocity $\boldsymbol{v}$ with (normalized) vectors connecting the cell centers (see Fig. 6). From now on, we describe the situation for the case of overflow ($f_w > 1-f_s$) only, but the redistribution strategy is similar in the case of underflow, with just the signs reversed.

The idea is that for *liquid-gas cells*, liquid should be redistributed in such a way that the change in local mean curvature is minimal, because otherwise the redistribution would counteract the mean curvature flow, and convergence to equilibrium would deteriorate. In Fig. 7, we illustrate two different redistribution strategies for liquid-gas cells: at left-hand side, the liquid volume fractions for a cell (with an overflow 0.4 and liquid velocity $\boldsymbol{v}$ pointing upwards) and its neighbors are shown. In the upper right hand-side strategy the liquid is redistributed to the neighbor cells in the order from 1 to 8 (cf. Fig. 6), whereas the lower right-hand side strategy addresses the neighbors in the order from 8 to 1. Following the goal of minimal change in local mean curvature, we choose the upper strategy (green arrow), which also results in a smaller total variation of the liquid volume fractions.

For *three-phase cells*, however, it is advantageous to use the opposite strategy, i.e., to pass liquid to neighbors in the order from 8 to 1, since we would like the liquid to creep along the solid surface, so that the equilibrium contact angle is

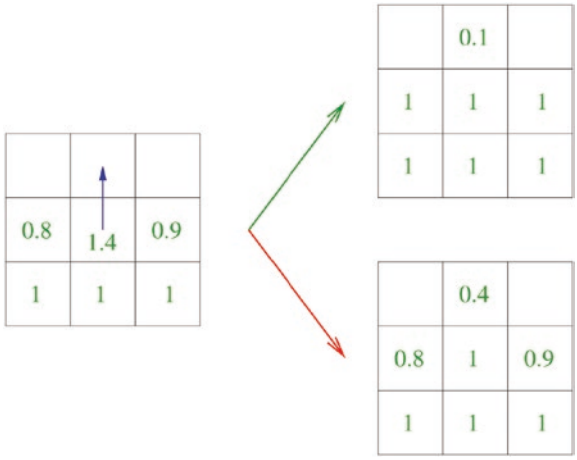

Fig. 7 Overflow redistribution illustration (in 2D): liquid-gas cell strategies (the upper one is chosen)

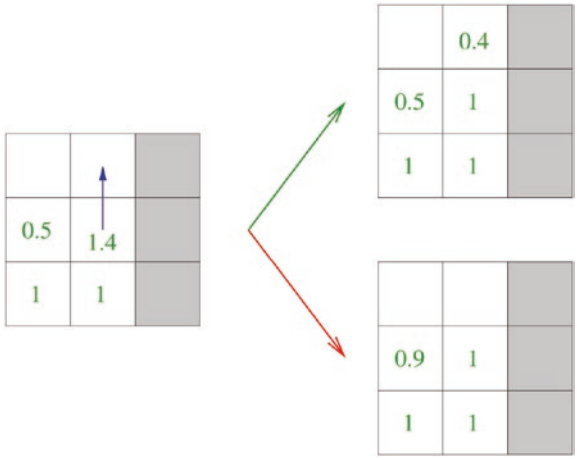

Fig. 8 Overflow redistribution illustration (in 2D): three-phase cell strategies (the upper one is chosen)

rapidly attained. This is illustrated in Fig. 8. (Notice that the redistribution strategies, illustrated here in 2D, are actually implemented in 3D.)

Several test problems have been solved numerically, in order to show that the algorithm can adequately describe the liquid relaxation into capillary equilibrium, e.g. the relaxation of a flat meniscus in a cylindrical solid tube containing a spherical solid particle (Fig. 9) and the relaxation of a cubic liquid block between two (immobile) solid spheres. In Fig. 10, binary liquid bridges of different liquid volume corresponding to the latter case are shown as smoothed surfaces. These tests verify the correctness of our simulation approach.

The following example simulation [14] is based on the μ-CT measurements described before. This measurement yields the initial configuration of the solid phase comprised of 192 glass-bead particles in a cylindrical container. The solid

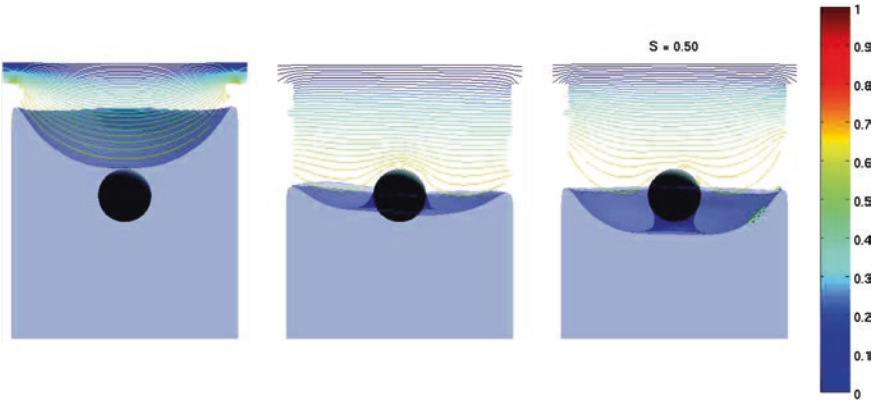

Fig. 9 Drying simulation of a circular cylinder containing a spherical solid particle. Shown is the liquid distribution for different saturations, as well as the vapor pressure isolines in the gas phase

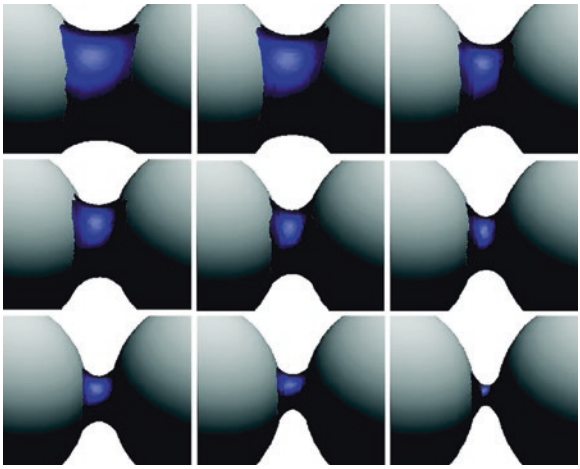

Fig. 10 Binary liquid bridges with different volume, $cos\theta_{eq} = 0.95$, 25 voxels per sphere radius (from [17])

phase was assumed to be static with an approximate porosity of ~0.83. The whole domain including the sintered primary particles and the cylindrical container is discretized with a voxel mesh of 90 × 90 × 94 cells. Initially, the particle aggregate is fully saturated with liquid, and evaporation starts from the top face.

The liquid phase distribution over time obtained from the numerical simulation is shown in Fig. 11: At the onset of evaporation, a curved meniscus develops inside the cylinder and recedes. Upon further evaporation, capillary effects become clearly visible: large pores dry out earlier, while small pores stay saturated for a longer time. In order to study the effect of wettability, another simulation with the same particle packing but with a different value of the equilibrium contact angle has been performed, see Fig. 12. By comparing these two figures, one can see that the capillary effects are clearly more pronounced for smaller equilibrium contact angle.

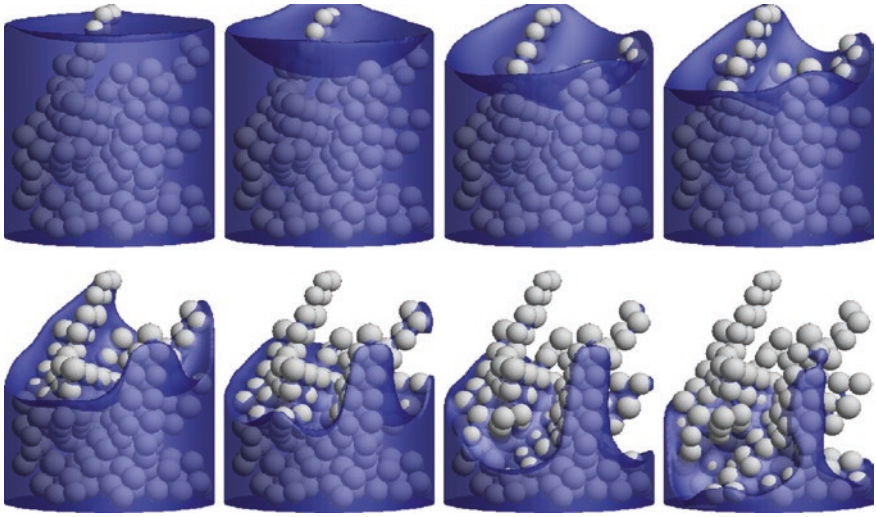

Fig. 11 The liquid distribution during drying in a sintered particle aggregate for a small equilibrium contact angle: $cos\theta_{eq} = 0.95$. The mesh resolution used for the computation is 10 cells per particle diameter. The aggregate liquid saturation decreases row-wise from left to right

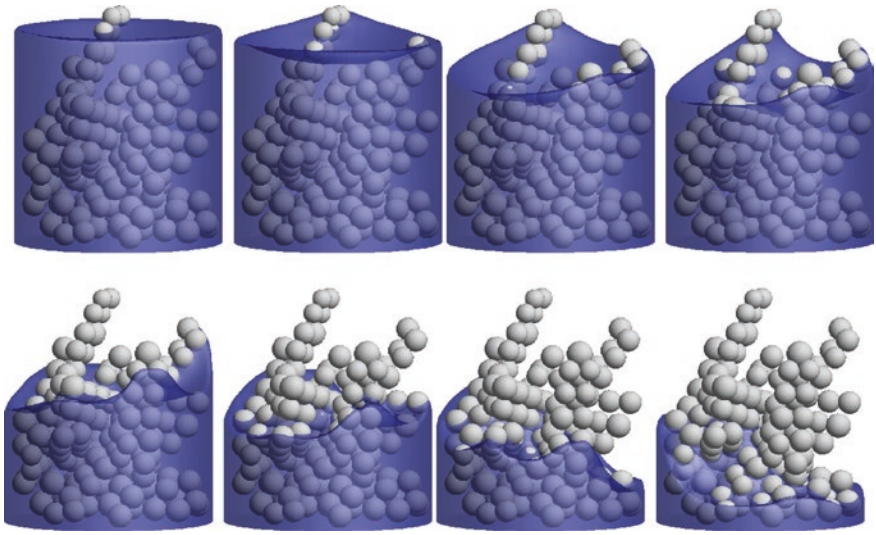

Fig. 12 The liquid distribution during drying in a sintered particle aggregate for a large equilibrium contact angle: $cos\theta_{eq} = 0.5$. The mesh resolution used for the computation is 10 cells per particle diameter. The aggregate liquid saturation decreases row-wise from left to right

3.1 Capillary Force Computation

After implementing the algorithm for liquid relaxation, the capillary forces were addressed. For every particle, there may be two contributions to the net force: on the one hand, the capillary pressure force that acts on the wet solid surface (solid-liquid (*sl*) interface) and is proportional to the mean curvature of the liquid cluster (via $p_g - p_w = 2\sigma\kappa$)

$$\mathbf{F}_{sl} = 2\sigma\kappa \cdot \iint \mathbf{n}_s \tag{3}$$

(note that several liquid clusters with different mean curvatures may be attached to one particle), and on the other hand the (direct) surface tension force along the three-phase contact line (solid-liquid-gas (*slg*) interface)

$$\mathbf{F}_{s\,\mathrm{lg}} = \frac{\sigma}{\sqrt{1 - \cos^2\theta_{eq}}} \cdot \int \left(\mathbf{n}_s - \mathbf{n}_w \cos\theta_{eq}\right) \tag{4}$$

The vector under the integral in Eq. (4) is tangential to the liquid-gas interface, orthogonal to the three-phase contact line, and it points out of the solid; it is normalized by the square root expression. (Again, different clusters attached to the same particle may contribute.)

In a first trial, we set the wet areas in all contributing liquid-solid and three-phase voxels to h^2 (where h denotes the edge length of the voxels)—corresponding to a SLIC (Simple line interface calculation) approximation—and the contact line lengths in all three-phase voxels to h. However, when the resulting capillary forces did not show the expected behavior (some were pointing out of the liquid, for example), a more refined strategy for *area and line approximation* was developed, which is described below [13].

First, by rotation and reflection, we bring the solid normal vector $\boldsymbol{n_s} = (n_x\ n_y\ n_z)$ into the cone $n_x \le n_y \le n_z$; then, it is approximated by one of the main directions [0 0 1], $1/\sqrt{2}$ [0 1 1], or $1/\sqrt{3}$ [1 1 1]. By this, we allow for 26 different directions in total. Next, an interface plane with surface normal in this main direction is placed into the cell at a position determined by the solid phase volume fraction f_s. For the three-phase cells, the liquid normal vector $\boldsymbol{n_w}$ is approximated by one of the six main directions (SLIC) and a corresponding liquid-gas interface plane is placed into the cell so that the liquid volume fraction f_w is correct. For this approximation, the wet area and contact line length are computed (this may require the solution of a quadratic or cubic equation). Figure 13 gives an example of one three-phase cell and shows the approximation of the wetted area of a solid sphere that is half immersed into the liquid, indicating a reasonable approximation. Depending on the orientation of the liquid half-space (both ϑ and φ have been varied in the range of 0°, 9°, 18°, 27°, 36° and 45°), the approximated wetted area was slightly too small (up to −4 %) and the approximated contact line length ranged between −15 % and +37 % of the true value. For a better approximation, more lattice directions should be allowed for the orientation of $\boldsymbol{n}_w$, which requires additional effort in code development.

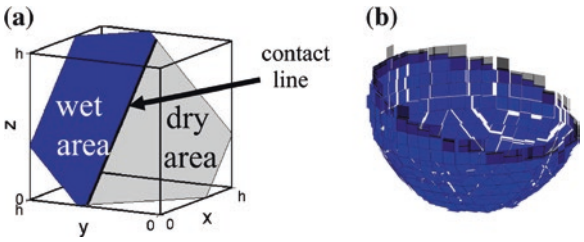

Fig. 13 Approximation of **a** a three-phase cell with $\boldsymbol{n}_w = 1/\sqrt{3}$ [−1−1 1] and $\boldsymbol{n}_s$ = [0−1 0] and **b** a half-wetted solid sphere, $\vartheta = 18°$ (wet area in *blue*, dry area in *gray*, contact line in *bold black*)

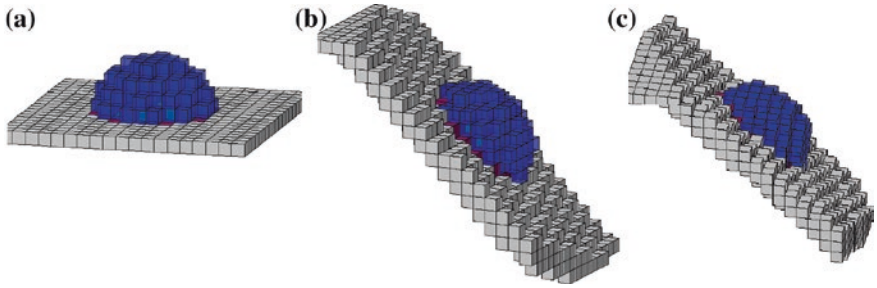

Fig. 14 Liquid droplet on a solid plane with varying orientation with respect to the spatial discretization **a** $\vartheta = 0°$, $\varphi = 0°$, **b** $\vartheta = 45°$, $\varphi = 18°$, **c** $\vartheta = 45°$, $\varphi = 27°$ (liquid cells in *blue*, solid-gas interface cells in *gray*, three-phase cells in *red*; $cos\theta_{eq} = 0.5$)

As another test problem, we simulated the relaxation of a liquid droplet on a solid plane with variable rotation with respect to the spatial discretization (again with angles ϑ and φ as above) as illustrated in Fig. 14. In this case, the capillary pressure force points into the solid plane and is compensated by the surface tension force, which points outward. Exact values for the mean curvature of the liquid-gas interface, wet area and contact line length can be calculated analytically in this case. The approximate area contribution to the force (Eq. 3) was within −26 % and +49 %, and the approximate contact line contribution (Eq. 4) within −26 % and +37 % of the exact values. (The maximum uncompensated force was 39 %.)

4 Structural Changes of RF Hydrogels During Convective Drying

The resorcinol-formaldehyde (RF) hydrogels are produced according to the following recipe: First, resorcinol (R) and formaldehyde are mixed at a molar ratio of 1:2 in the presence of a sodium carbonate catalyst (C), the amount of which is varied for different samples. The role of the sodium carbonate is to tune the pH value of the solution [9]. Then, the solution is heated up inside a closed container to

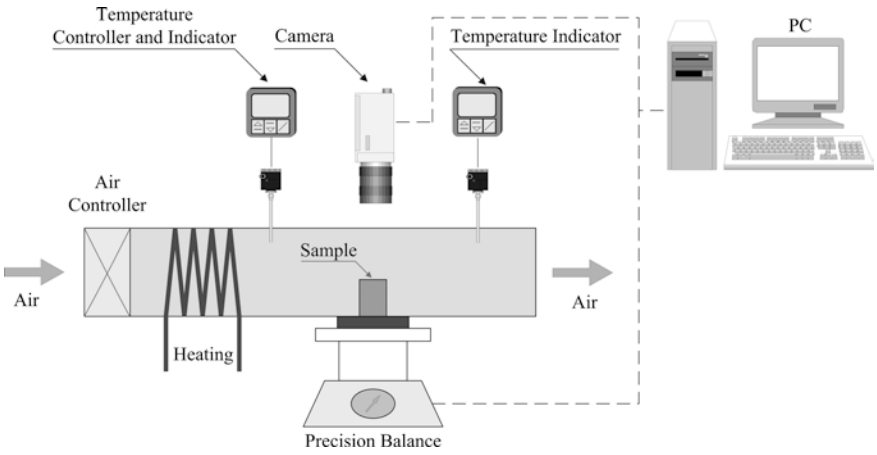

Fig. 15 Dryer setup for convective drying of RF gels

70 °C such that it forms a stable cross-linked gel. The necessary time for gelation is determined visually and varies with the R/C ratio. After gelation, the samples are aged in the mother liquor for a certain time. In this way, cylindrical gel samples have been prepared with a volume of approximately 1.5 ml (diameter 20 mm and height 12 mm) and a mass of approximately 2.5 g. The wet monolithic samples were dried under different air velocities and temperatures.

For this purpose, a dryer was designed specifically for the small individual samples (see Fig. 15). The drying air is fed from the laboratory compressed air network via a mass flow controller to adjust its flow rate (between 2.5 and 50 l/min); it is then heated to the desired temperature (between 25 and 80 °C) and directed to the drying tunnel. Through a hole, the gel is positioned inside this tunnel and supported by a holder, which itself is mounted on a precision balance (Sartorius-LC3201D; 0.1 mg accuracy, data acquired every minute). The sample surroundings are such that drying can occur on the whole external surface except the bottom surface; the drying air velocity was between 0.363 and 1.5 m/s. Besides the continuous recording of the sample weight, the shrinkage is monitored by a CCD camera installed above the sample taking a picture every minute. At the end of the convective drying process, the gel samples were dried in an oven at 105 °C for 24 h to determine their dry solid mass which is needed as a reference value for the evolution of the liquid mass or moisture content over time.

4.1 Shrinkage and Cracks: Influence of Aging Time

Figure 16 shows shrinkage curves for RF gels with three different R/C ratios, each of which have been aged for three different durations. The sample volume is normalized with the initial value (V_0) and plotted as a function of normalized

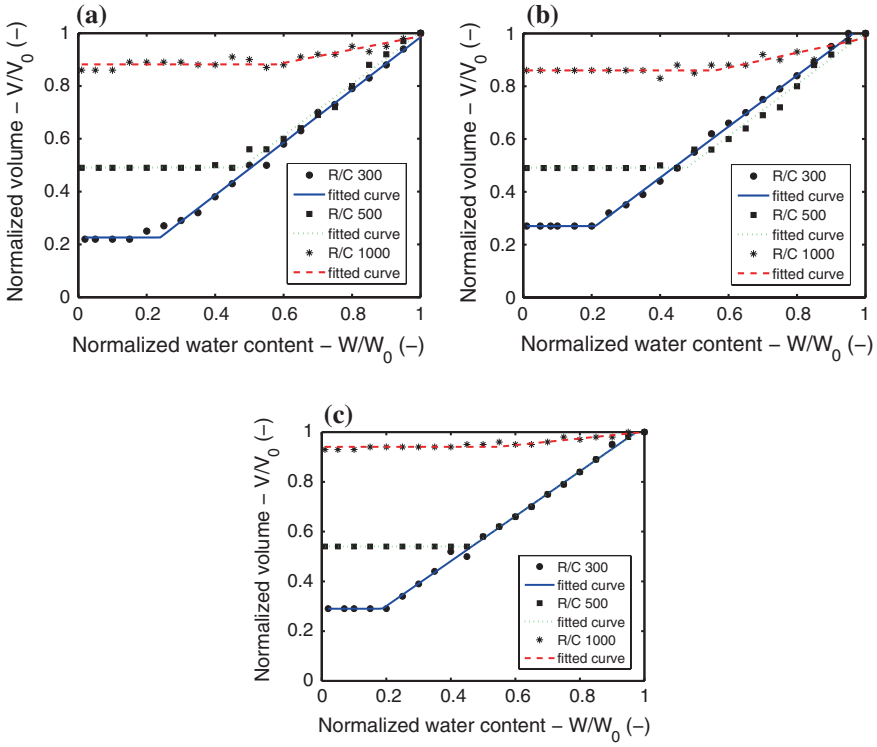

Fig. 16 Shrinkage curves for samples with R/C ratios 300, 500, and 1000 and aging times **a** 24 h, **b** 48 h, and **c** 72 h (for slow drying: air velocity 0.363 m/s and temperature 25 °C)

water content, W/W_0. All curves are obtained for identical (low-rate) drying conditions. It can be clearly seen that the degree of shrinkage drastically increases with decreasing R/C ratio. This is because a low R/C ratio produces a gel with smaller primary particles resulting in larger capillary forces. As a second result, we may state that by longer aging the degree of shrinkage can be slightly reduced. Since the solid bridges between primary particles may grow during aging, they are expected to withstand stronger capillary forces resulting in less shrinkage of the samples. This latter result complements an earlier publication about the influence of aging on microstructural properties [11].

Figure 17 shows photographs of gel samples dried at a high rate. The samples with R/C = 300 and aging time 24 and 48 h are completely fragmented after drying, whereas a monolithic dry sample could be obtained for 72 h of aging time. The samples with R/C = 500 remain monolithic for at least 48 h of aging time. The samples with R/C = 1000 stay monolithic regardless of the aging time.

The experience with this model gel shall later be used for X-ray microtomography measurements. A similar drying tunnel shall be mounted on top of the rotating cylindrical sample. In this way, online measurements of drying kinetics, internal

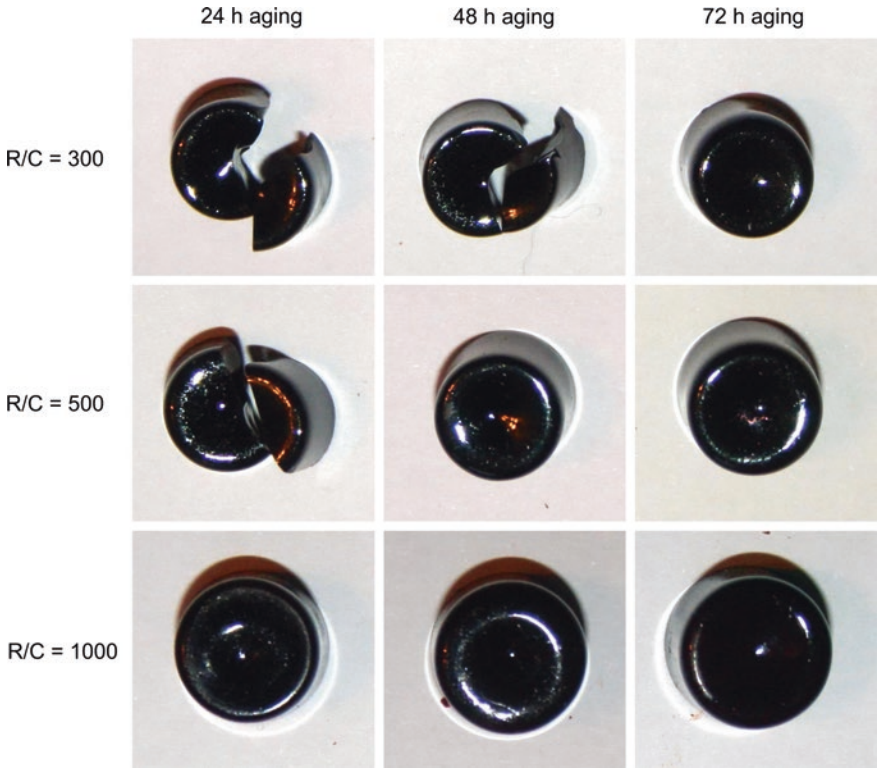

Fig. 17 Influence of aging time on sample breakage (for fast drying: air velocity 1.5 m/s and temperature 80 °C)

moisture profiles and micro-mechanical effects (cracks and shrinkage) in the samples shall be obtained from the high-resolution reconstructed X-ray images.

5 Conclusion

In this work, efforts have been taken to quantitatively understand the pore-scale phenomena which occur during the convective drying of gels and of highly porous particle aggregates, and which cause undesired damage and shrinkage.

The presented experimental results presented here were obtained by X-ray microtomography (μ-CT); they demonstrate pore-scale phenomena in highly porous model particle aggregates made of sintered glass beads. The micro-scale modeling approach is based on a discretization of the full space including all three phases. Thus the solid, liquid and gas phases are distinguishable and interfaces can be resolved. A scale separation in time is assumed (the liquid relaxation to capillary equilibrium is much faster than the evaporation), so that alternating computations

may be carried out in the liquid and gas phases. Simulation results performed for the corresponding solid phase data exhibit a similar qualitative behavior.

The effect of wettability on the liquid distribution in a particle aggregate over time has been shown qualitatively. A quantitative comparison of experimental and simulation results at the voxel level will evaluate the accuracy of our computational tool.

Future work on the simulation part will include the full integration of the capillary force computation into the simulation, as well as the coupling with a mechanical simulation in the solid phase. This should be sufficient for the simulation of the damage and shrinkage phenomena, which occur during the drying process. For very small pores the continuum assumption on the liquid may be violated, which requires the inclusion of additional effects, such as electrostatics. μ-CT measurements shall be carried out under various drying conditions and for different material properties of the primary particles, in order to assess the influence of these parameters on the drying behavior of highly porous particle aggregates.

Acknowledgments This project was funded by the German Research Foundation (DFG) within the Priority Program 1273 "Colloid Process Engineering". The X-ray tomography device used in this study was financed by the EFRD (European Fund for Regional Development) in project no. 121108002. We would like to thank Ms. Fahimeh Bahari for the synthesis of RF gels and for conducting the drying experiments described in Sect. 4.

References

1. Al Muhtaseb SA, Ritter JA (2003) Preparations and properties of resorcinol-formaldehyde organic and carbon gels. Adv Mater 15(2):101–114
2. Athanassenas M (1997) Volume-preserving mean curvature flow of rotationally symmetric surfaces. Commentarii Mathematici Helvetici 72:52–66
3. Brinker CJ, Scherer GW (1990) Sol-gel science. Academic Press, New York
4. Cáceres G, Bruneau D, Jomaa W (2007) Two-phase shrinking porous media drying: a modeling approach including liquid pressure gradient effects. Drying Technol 25:1927–1934
5. Cundall PA, Strack ODL (1979) A discrete numerical model for granular assemblies. Géotechnique 29:47–65
6. Fraunhofer ITWM (2005) MAVI—Modular algorithms for volume images
7. Hirt CW, Nichols BD (1981) Volume of fluid (VOF) method for the dynamics of free boundaries. J Comput Phys 39:201–225
8. Hoshen J, Kopelman R (1976) Percolation and cluster distribution. I. Cluster multiple labeling technique and critical concentration algorithm. Phys Rev B 14(8):3438–3445
9. Job N, Pirard R, Marien J, Pirard JP (2004) Porous carbon xerogels with texture tailored by PH control during sol-gel process. Carbon 42(3):619–628
10. Job N, Thery A, Pirard R, Marien J, Kocon L, Rouzard JN, Beguin F, Pirard JP (2005) Carbon aerogels, cryogels and xerogels: influence of the drying method on the textural properties of porous carbon materials. Carbon 43:2481–2494
11. Job N, Panariello F, Marien J, Crine M, Pirard JP, Léonard A (2006) Synthesis optimization of organic xerogels produced from convective air-drying of resorcinol-formaldehyde gels. J Non-Cryst Solids 352:24–34
12. Kharaghani A, Metzger T, Tsotsas E (2011) A proposal for discrete modeling of mechanical effects during drying, combining pore networks with DEM. AIChE J 57(4):872–885

13. Kharaghani A, Wang YJ, Kirsch C, Metzger T, Tsotsas E (2011b) Drying of highly porous particle aggregates: pore-scale simulation and X-ray microtomography. 7th Asia-Pacific drying conference (ADC2011), Tianjin
14. Kharaghani A, Kirsch C, Tsotsas E (2012) Influence of wetting properties on drying behavior of highly porous particle aggregates. Proceedings of 18th international drying symposium (IDS2012), Xiamen
15. Kharaghani A, Kirsch C, Metzger T, Tsotsas E (2013) Micro-scale fluid model for drying of highly porous particle aggregates. Comput Chem Eng 52:46–54
16. Kirsch C, Metzger T, Tsotsas E (2009) Towards a micro-scale simulation of convective gel drying. 12th polish drying symposium, Lodz, 223–234
17. Kirsch C, Metzger T, Tsotsas E (2010a) Micro-scale model for drying of highly porous particle aggregates. Proceedings of 17th international drying symposium (IDS2010), Magdeburg, vol A, pp 407–414
18. Kirsch C, Metzger T, Tsotsas E (2010b) Modeling and simulation of convective drying of gels. Proceeding (CD-ROM) of 3rd international conference on porous media and its applications in science, engineering, and industry, Montecatini
19. Kocklenberg R, Mathieu B, Blacher S, Pirard R, Pirard JP, Sobry R (1998) Texture control of freeze-dried resorcinol-formaldehyde gels. J Non-Cryst Solids 225(1):8–13
20. Léonard A, Blacher S, Marchot P, Pirard JP, Crine M (2004) Measurement of shrinkage and cracks associated to convective drying of soft materials by X-ray microtomography. Drying Technol 22:1695–1708
21. Léonard A, Crine M, Jomaa W (2006) Modelling of the convective drying of resorcinol-formaldehyde resins: influence of the drying conditions on the induced stress tensor. Proceedings of 15th international drying symposium (IDS2006), Budapest, vol A, pp 273–278
22. Metzger T, Irawan A, Tsotsas E (2007) Influence of pore structure on drying kinetics: a pore network study. AIChE J 53:3029–3041
23. Metzger T, Léonard A, Jomaa W, Tamon H (2011) Understanding and preventing structural changes during drying of gels. In: Tsotsas E, Mujumdar AS (eds) Modern drying technology. Product quality and formulation, vol 3. Wiley-VCH, Weinheim, pp 155–229
24. Moreno-Atanasio R, Williams RA, Jia X (2010) Combining X-ray microtomography with computer simulation for analysis of granular and porous materials. Particuology 8:81–99
25. Pakowski Z, Głębowski M, Adamski R (2006) Modeling of drying of highly shrinking materials using hydrogels as an example. Drying Technol 24:1075–1081
26. Scheel M, Seemann R, Brinkmann M, Di Michiel M, Sheppard A, Herminghaus S (2008) Liquid distribution and cohesion in wet granular assemblies beyond the capillary bridge regime. J Phys Condens Matter 20:494236
27. Štěpánek F, Marek M (1999) Modeling capillary condensation hysteresis cycles in reconstructed porous media. AIChE J 45(9):1901–1912
28. Štěpánek F, Marek M, Adler PM (2001) The effect of pore-space morphology on the performance of anaerobic granular sludge particles containing entrapped gas. Chem Eng Sci 56:467–474
29. Štěpánek F, Ansari MA (2005) Computer simulation of granular microstructure formation. Chem Eng Sci 60:4019–4029
30. Štěpánek F, Rajniak P (2006) Droplet morphologies on particles with macroscopic surface roughness. Langmuir 22:917–923
31. Tonanon N, Wareenin Y, Siyasukh A, Tanthapanichakoon W, Nishihara H, Mukai SR, Tamon H (2006) Preparation of resorcinol-formaldehyde (RF) carbon gels: use of ultrasonic irradiation followed by microwave drying. J Non-Cryst Solids 352:5683–5686
32. Yamamoto T, Nishimura T, Suzuki T, Tamon H (2001) Effect of drying method on mesoporosity of resorcinol-formaldehyde drygel and carbon gel. Drying Technol 19:1319–1333

Large Amplitude Oscillatory Shear Applications for the Characterization of Dispersed Systems

D. Merger, K. Reinheimer, M. Grosso, J.M. Brader, M. Ballauff, J. Kim, M.E. Helgeson and M. Wilhelm

Abstract The mechanical properties of dispersed systems, such as suspensions, emulsions and foams, have been studied for many years by oscillatory shear experiments in the linear regime using material functions as for example the frequency dependent storage and loss modulus. In the context of oscillatory shear tests, the linear regime is defined as the range of strain amplitudes where both excitation and response wave signals are sinusoidal and their amplitudes are proportional to each other. In this regime the connection between the material functions and the dispersed system's microstructure is well understood. However, dispersed systems are often processed or applied at conditions, where the linear regime is easily exceeded and the storage and loss moduli become insufficient to describe the material's mechanical properties. In addition, the nonlinear regime opens up enhanced characterization possibilities. Consequently, experimental protocols for *Large Amplitude Oscillatory Shear* (LAOS) have been developed to investigate and quantify this nonlinear behavior. In the following chapter we present basic theoretical descriptions of LAOS experiments, address technical aspects of the technique for systems with low viscosity and discuss three applications to

D. Merger · K. Reinheimer · M. Wilhelm (✉)
Institut für Technische Chemie und Polymerchemie, Karlsruhe Institute of Technology, 76128 Karlsruhe, Germany
e-mail: manfred.wilhelm@kit.edu

M. Grosso
Dipartimento di Ingegneria Meccanica, Chimica e dei Materiali, Università degli Studi di Cagliari, 09123 Cagliari, Italy

J.M. Brader
Department of Physics, University of Fribourg, 1700 Fribourg, Switzerland

M. Ballauff
Helmholtz Zentrum für Materialien und Energie, 14109 Berlin, Germany

J. Kim · M.E. Helgeson
Department of Chemical Engineering, University of California Santa Barbara, Santa Barbara, CA 93106, USA

M. Kind et al. (eds.), *Colloid Process Engineering*,
DOI 10.1007/978-3-319-15129-8_6

dispersed systems: First, LAOS experiments were used to modify the droplet morphology in a dilute polymer blend which gave information about the ratio of droplet radius to the interfacial tension in the system. Second, LAOS experiments were used to test the predictive capabilities of the schematic MCT model for dense colloidal suspensions under nonlinear deformation. Third, the yielding behavior of a colloidal nanoemulsion gel under oscillatory shear was investigated and the results were combined with a structural analysis using ultra-small angle neutron scattering. The two techniques allowed to propose a detailed microstructural mechanism for yielding of the gel and revealed that large scale inhomogeneities play a significant role for its mechanical properties.

Keywords Nonlinear rheology · Rheometry · Emulsions · Colloidal gels · Colloidal suspensions · Mode-coupling theory

1 Introduction

Dispersed systems, i.e. suspensions, emulsions and foams, are ubiquitous in industry and daily life. Their mechanical properties are often tested using oscillatory rheological experiments in the linear regime as a function of temperature and frequency [29]. The complex response function is described in terms of its real part (G') and imaginary part (G''). Physical properties like relaxation times or phase transitions of the non-perturbated samples can be evaluated. The linear rheology is characterized by the measurement of the viscoelastic moduli G' and G'' as a function of angular frequency ω at a small strain amplitude. The basics of linear rheology are described in detail in several textbooks [8, 29] and will not be repeated here. The relations between structure and linear viscoelastic properties of dispersed systems are well known [4, 7, 26].

However, most of the processing and application conditions for dispersed systems as they occur in pipe flows, squeeze flows and shear flows involve deformations that are well beyond the linear regime of these materials. Simple daily life processes that involve nonlinear oscillatory deformations for dispersions are for example applying paint to a wall or using a shaving foam. It is of great interest to extend the mechanical characterization of dispersed systems to the nonlinear regime to improve tailoring of their nonlinear mechanical behavior. Large amplitude oscillatory shear (LAOS) experiments represent a convenient way to impose deformations to a sample that are sufficiently large to generate a nonlinear stress response, that means the stress is not a simple sinusoidal wave. In contrast to steady shear, start-up of flow and creep experiments, LAOS experiments additionally provide information on the balance of elastic and viscous behavior beyond the linear regime.

When using oscillatory shear one can vary the strain amplitude γ_0 and angular frequency ω independently and therefore investigate different regions of a material's behaviour in the so called Pipkin space as shown in Fig. 1 (reproduced after [34]). At sufficiently low ω a viscoelastic material has enough time to relax and behaves

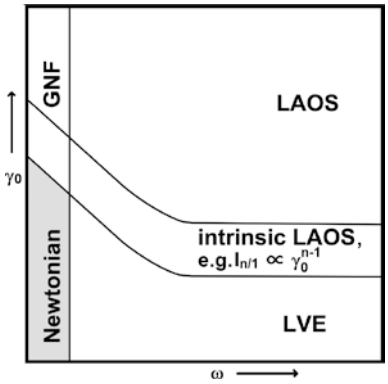

Fig. 1 Schematic two-dimensional map of nonlinear rheology as a function of angular frequency ω and strain amplitude γ_0, known as the Pipkin diagram (reproduced after [34]). Simple Newtonian and generalized Newtonian fluid behavior (GNF) are observed for small ω. For higher ω linear visco-elastic (LVE) properties are probed, which become nonlinear with increasing γ_0 (LAOS). For intermediate γ_0 an intrinsic LAOS regime can be defined. In this range scaling laws for the departure from linearity can be applied. They will be discussed in the Theory section

like a Newtonian liquid for small γ_0. Increasing γ_0 at constant ω leads to higher shear rates that result in shear thinning, which can be modelled by a generalized Newtonian fluid model [29]. If ω is varied at small γ_0 the experiment represents the common frequency sweep in the linear visco-elastic (LVE) region with G' and G'' being only dependent on the frequency. Increasing the strain amplitude γ_0 at higher (but constant) frequencies drives the material into the instrinsic LAOS region (where certain scaling laws for the departure from linearity apply, see Sect. 3) and finally even beyond.

Since dispersed systems are complex fluids whose macroscopic properties depend strongly on the microstructure [26, 43], LAOS is an interesting technique to probe these materials. With large deformations, structural changes can easily be induced, which in return modify the rheological response. A variety of nonlinear effects including shear thinning, shear thickening and the yielding behavior can be investigated. The information gained from LAOS tests is complimentary to results from other nonlinear rheological experiments as steady shear-, start-up of shear, and creep experiments and will provide a more complete description and understanding of these materials' mechanical properties. This understanding needs to be developed far enough, so that models and computer simulations can be used to predict nonlinear rheological behavior based on microstructural parameters.

2 Theory

Large amplitude oscillatory shear (LAOS) stress data in the time domain can be analyzed using the well established FT-rheology protocols [21, 44]. LAOS measurements impose a sinusoidal deformation of $\gamma(t) = \gamma_0 \sin(\omega_1 t)$, where

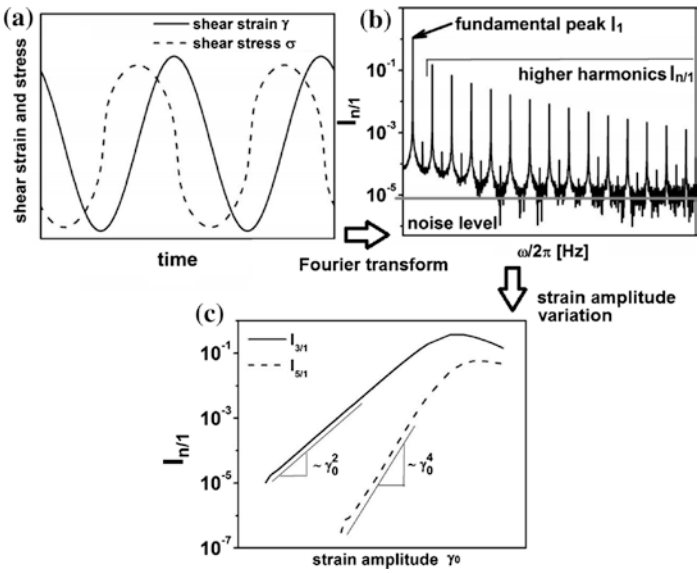

Fig. 2 Schematic depiction of the procedure for conducting LAOS experiments and analysis using FT-rheology. **a** Measurement of the oscillatory shear strain and shear stress response in the time domain. **b** Normalized frequency spectra after the Fourier transformation of the shear stress exhibit the fundamental peak at the angular frequency ω_1. Higher harmonics $I_{n/1}$ with n being a positive odd integer are detected for a periodic nonlinear shear stress. **c** By variation of γ_0 the transition from linear to nonlinear mechanical behavior can be observed in the increase of $I_{n/1}$

$\omega_1 = 2\pi\nu_1 = 2\pi/T$ is the characteristic angular frequency with T the oscillation period and γ_0 the strain amplitude that is selected to be within the nonlinear region [21]. As a result of the large amplitude deformation, the stress σ response is no longer simply sinusoidal as shown in Fig. 2a, but consists of a superposition of the excitation frequency ω_1 and its odd higher harmonics $n\omega_1$. The measured (or simulated) shear stress can be described by Eq. 1 using the intensities I_n and phases δ_n of the odd harmonics [10, 20, 44].

$$\sigma = \sum_{n=odd} I_n \sin(n\omega_1 t + \delta_n) \tag{1}$$

$$\sigma = \sum_{n=odd} I_n \cos\delta_n \sin n\omega_1 t + I_n \sin\delta_n \cos n\omega_1 t \tag{2}$$

$$\sigma = \sum_{n=odd} \gamma_0 G_n' \sin n\omega_1 t + \gamma_0 G_n'' \cos n\omega_1 t \tag{3}$$

$$I_{n/1} = \frac{I_n}{I_1} = \frac{\sqrt{G_n'^2 + G_n''^2}}{\sqrt{G_1'^2 + G_1''^2}} \tag{4}$$

Using trigonometric additional theorems Eq. 1 can be also expressed as in Eq. 2 with $I_n \cos \delta_n/\gamma_0 = G'_n$ and $I_n \sin \delta_n/\gamma_0 = G''_n$ giving the familiar storage and loss modulus for $n = 1$ (Eq. 3) and the higher order terms for $n > 1$ which take account for the deviation from linear oscillatory response. Usually for reasons of higher reproducibility, the intensities of the higher harmonics are normalized to the intensity of the base wave (Eq. 4).

Assuming a viscosity that is nonlinear in the shear rate, Wilhelm et al. [46] used a polynomial expansion and proposed that the absolute intensity of a higher harmonic I_n ought to scale with the nth power of the strain amplitude for small enough deviations from the linear regime. Therefore, a normalized intensity is expected to scale as $I_{n/1} \propto \gamma_0^{n-1}$ in the transition region between linear and nonlinear regime (Fig. 2c).

Subsequently Hyun and Wilhelm [20] and Reinheimer et al. [37] introduced the intrinsic nonlinear parameter ${}^nQ(\gamma_0, \omega)$ and, at low strain amplitude, ${}^nQ_0(\omega)$, the latter being only dependent on the angular frequency ω (Eq. 5):

$$ {}^nQ(\gamma_0, \omega) = \frac{I_{n/1}}{\gamma_0^{n-1}} \quad \text{with} \quad \lim_{\gamma_0 \to 0} {}^nQ(\omega) = {}^nQ_0(\omega) \tag{5} $$

These parameters can be used to infer the inherent nonlinear material properties of a sample as the trivial scaling for the relative intensities of the higher harmonics, $I_{n/1} \propto \gamma_0^{n-1}$, is eliminated. As an example of this, the intrinsic nonlinearity parameter ${}^3Q$, that is derived from the third harmonic, has been shown to be useful in evaluating the topology of polymer melts [20].

2.1 Sequence of Physical Processes (SPP)

A conceptually different approach to analyze temporal stress signals obtained from LAOS experiments that will be used for the yielding experiments performed on the colloidal gel (see Sect. 5.3), is the sequence of physical processes as it has been established by Rogers et al. [38]. Instead of describing the stress wave as a series of basis functions with their respective intensities and phases, here Lissajous figures, i.e. stress vs. strain or stress vs. strain rate curves, are analyzed as shown in Fig. 3. Specific parts of the Lissajous curve are associated with certain physical processes, that follow a sequence that is repeated twice per oscillation cycle. The SPP approach is especially useful to describe waveforms of yield stress fluids under LAOS, as for example glassy suspensions [38, 42] or colloidal gels [31]. In these cases the different physical processes are elastic straining, yielding and plastic flow. These processes can be quantified with the following parameters that are extracted from elastic Lissajous (stress vs. strain) plots, see Fig. 3:

- The cage modulus or residual modulus $G_R = \frac{d\sigma}{d\gamma}|_{\sigma=0}$ quantifies the strength of the residual elasticity in the linear region after reversal of flow direction that is

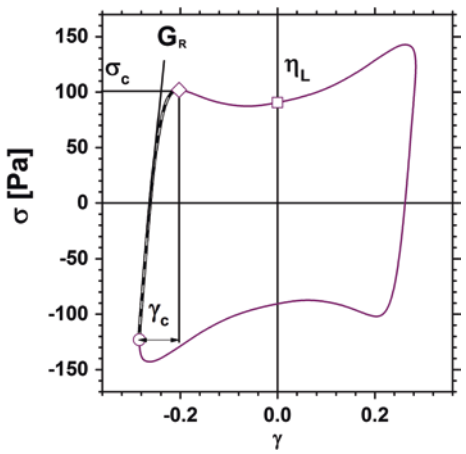

Fig. 3 Elastic Lissajous plot (stress vs. strain) for a colloidal gel (33 vol% PDMS droplets in an aqueous continuous phase containing 33 vol% of bridging polymer and 230 mM sodium dodecyl sulfate) at $\omega = 10\,\mathrm{rad/s}$ and $\gamma_0 = 0.284$, reprinted with permission from [23], copyright 2014, Society of Rheology. In the SPP framework the local waveform parameters G_c, γ_c and σ_c have been defined by Rogers et al. [38]

recovered in every cycle. For small deformations, that is in the linear regime, G_R is equal to the storage modulus G'.

- The yield stress σ_c measures the maximum stress that can be stored in the system before yielding (diamond symbol in Fig. 3).
- The yield strain γ_c measures the maximum strain that is accumulated from the point of flow reversal at $\gamma = -\gamma_0$ (circle symbol in Fig. 3) to the point of yielding designated by a local maximum in the stress after the linear region (diamond symbol).
- The instantaneous viscosity at maximum shear rate $\eta_L = \frac{\sigma(t)}{\dot{\gamma}(t)}$ (square symbol).

3 Advances in LAOS Rheometry

3.1 Improved Sensitivity of LAOS Measurements

The signal to noise ratio S/N is the parameter that defines the quality of an FT-spectrum and limits the lowest detectable nonlinear intensity. For a set of strain amplitudes at one excitation frequency, Eq. 5 shows, that within the concept of the ${}^nQ$ coefficient and the high sensitivity of FT-Rheology, the linear regime is defined by vanishing nonlinearities. Thus, the linear regime is, theoretically, achieved at only vanishing deformations and, therefore, a priori never occurs in any real experiment. Nevertheless, it is commonly accepted that the linear response can very accurately describe the mechanical response. The linear regime in oscillatory shear tests is assumed to be valid when the mechanical response contains approximately only 0.5 % nonlinearity, i.e. $I_{3/1} < 5 \times 10^{-3}$ [20]. However, the sensitivity, defined by the signal to noise ratio (S/N), limits the application of FT-rheology to detect nonlinearities $I_{n/1}$ with $n > 1$. In the following, experiments on dilute emulsions are described that have been performed to find the optimum measurement

conditions for achieving a maximum S/N. Hereby, the detection of $I_{3/1}$ was extended to lower strain amplitudes, which was necessary to be able to measure nonlinear properties of low viscosity beer foams [45].

Over the past 40 years important improvements in instrumentation and data processing have led to a strong increase in the sensitivity of FT-rheology [9, 12, 21, 45]. In the beginning, the shear stress response in the time domain was measured with an external recording device that was separated from the actual rheometer control. Analysis was done with a post-processing Fourier transform [9]. Today, the new generation of rheometers are equipped with software for LAOS measurements and Fourier transform. For example, the ARES G2 (TA Instruments) is a common rheometer which has a software that allows on one hand to use external post-processing of the raw shear stress in the time domain and, on the other hand, on-the-fly Fourier transform with direct output of the higher harmonic intensities $I_{n/1}$ can be performed. In order to improve S/N, different settings of the measuring protocol can be adjusted to reduce the influence of environmental disturbances, like mechanical noise and electrical noise. Furthermore the use of oversampling [10] also helps to increase S/N.

FT-rheological experiments for a a dilute polymer blend of PDMS (Rhodorsil 47 V 300,000, $M_n = 150$ kg/mol from C. H. Erbslöh) in PIB (Indopol H300, $M_n = 1.3$ kg/mol from Biesterfeld Spezialchemie GmbH) with a PDMS volume fraction of $\phi = 10\,\%$ were conducted on two different rheometers using the following four measuring protocols in order to compare and optimize S/N:

- **Method A** ARES G1 (1 k force rebalance transducer (FRT) for torques ranging from 2×10^{-4} to 10 mNm) with external recording of the shear stress in the time domain for post-analysis using a custom-written MATLAB routine. The external recording was performed as described in [44].
- **Method B** ARES G2 (FRT for torques ranging from 50 mNm to 200 mNm) with external recording of the shear stress in the time domain for post-analysis using the custom-written MATLAB routine.
- **Method C** ARES G2 with recording of the shear stress in the time domain using the TRIOS software from TA Instruments and post-analysis using the custom-written MATLAB routine.
- **Method D** ARES G2 with recording of the strain amplitude dependent nonlinearities $I_{n/1}$. The correlation mode applies an on-the-fly FT over an average of cycles.

Some representative spectra are displayed in Fig. 4. We have found that the ARES G2 rheometer is approximately 2.8 times more sensitive than the ARES G1 rheometer under optimized conditions using the identical detection method (external recording, Fig. 4a). Furthermore using the manufacturer's software TRIOS to record the time data (method C) resulted in a factor of 40 improvement in sensitivity compared to recording of the raw shear stress in the time domain (method B) as shown in Fig. 4b. With method C, a spectrum with S/N of $\approx 10^6$ could be achieved. It can be increased to $S/N \approx 10^7$ by averaging more cycles per amplitude (Fig. 4c) which of course prolongs the total measurement time

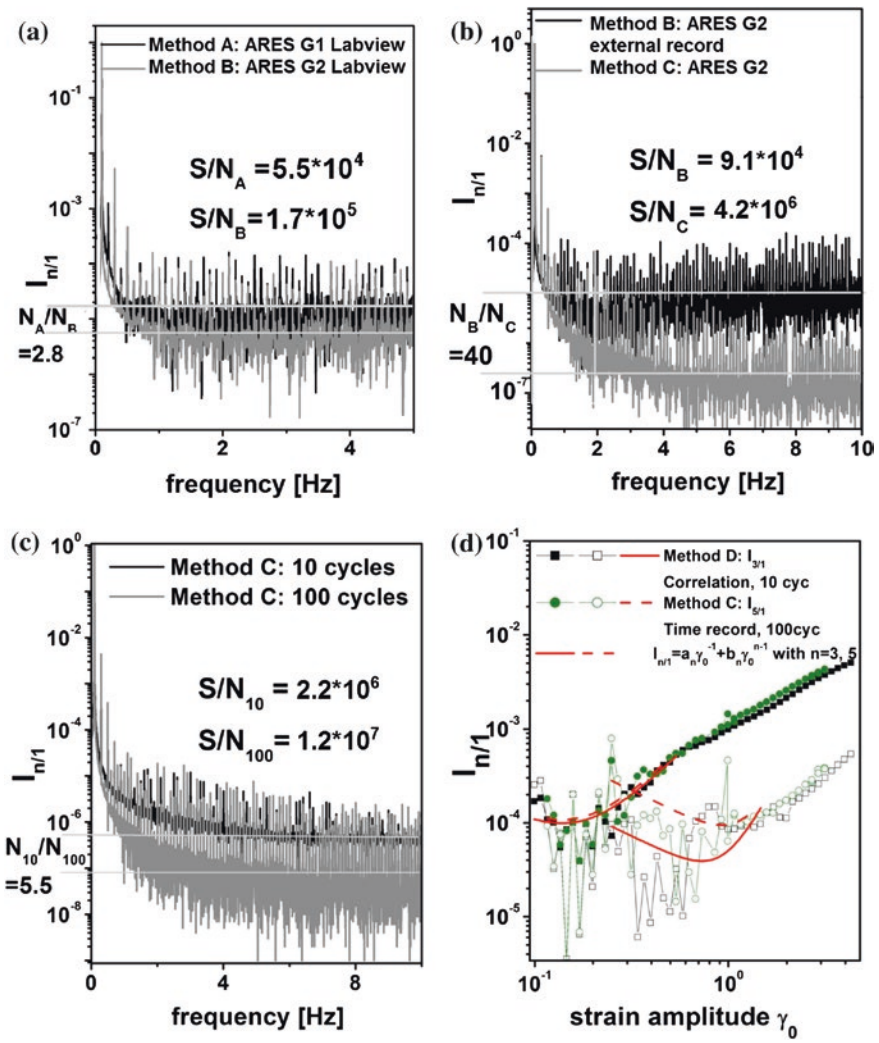

Fig. 4 Comparison of Fourier spectra and their respective signal-to-noise ratio. **a** Comparison of the methods A and B, **b** comparison of the methods B and C, **c** effect of increased sampling time per oscillation, **d** comparison of the methods C and D, reprinted from [45], copyright 2012, de Gruyter

and can be a disadvantage with systems where changes of the composition occur over longer time scales (e.g. solvent evaporation). The last panel of Fig. 4 shows a comparison between the methods C and D for an entire strain sweep. In this case the sensitivity is compared on the basis of fitting parameters to the Equation $I_{n/1} = a_n\gamma_0^{-1} + b_n\gamma_0^{n-1}$ and a lower a_3-value of 9.19×10^{-6} for the correlation method D versus 2.28×10^{-5} for the transient method C shows that the former

is more sensitive [45]. This improvement is even more pronounced for the fifth harmonic with $a_5 = 9.19 \times 10^{-6}$ and $a_5 = 7.00 \times 10^{-5}$ for the methods D and C, respectively.

Giacomin and Dealy [12] showed a typical spectrum of a nonlinear mechanical measurement from the mid-nineties with $S/N \approx 100$. Thus, the hardware and software developments of the rheometers with respect to minimum torque resolution have led to an overall improvement in sensitivity by a factor of 10^5 over the last 20 years [45].

3.2 Reproducibility of LAOS Measurements on Various Instruments

Currently, two general rotational rheometer types [29] are available commercially, that can be used for LAOS experiments: controlled strain rheometers (also known as separated motor-transducer, SMT) and controlled stress (or combined motor-transducer, CMT) rheometers. Apart from the rotational rheometers, custom built instruments, such as the sliding plate rheometer by Giacomin et al. [13] are also suitable, but will not be discussed here, as they are not available commercially.

However, the software of advanced stress controlled instruments allows for running an experiment at variable strain amplitudes. In this operation mode, several iterative cycles have to be measured before the actual measurement. In these iterations, the applied torque is adjusted to produce the desired strain amplitude [27]. In contrast to the classical way of amplitude adjustment, new operating modes of stress controlled rheometers (termed *Direct Strain Oscillation* or *Continuous Oscillation*) use a feedback control to compare the current strain signal $\gamma(t)$ at time t to the desired pure sinusoidal signal $\gamma_d(t) = \gamma_{d0} \sin(\omega_0 t)$. The control loop then adjusts the torque accordingly in order to minimize the difference $|\gamma_d(t + \Delta t) - \gamma(t + \Delta t)|$ for the next step at $t + \Delta t$. This deformation control enables a stress controlled rheometer to mimic a strain controlled experiment [27]. This holds true even beyond the linear regime where nonlinear contributions to the strain wave are compensated for and are then transferred into the stress wave, as the control loop tries to make the appropriate adjustments to the torque within minimum time.

For the strain controlled LAOS experiment (LAOStrain), a pure sinusoidal strain input is needed, which is why in the past it was necessary to use a SMT-rheometer. With the new developments in the deformation control of CMT-rheometers that enable them to perform strain controlled experiments [27], the question arises whether these instruments can be used in the same way as SMT-rheometers for LAOStrain experiments. It is of great interest to know if they can deliver quantitatively identical results or if the deformation control loop of the CMT-Rheometers influences the measured nonlinearities in the stress wave. Since CMT-rheometers are much more common due to the lower price and simpler design, it would be a great advantage if they could also be used for LAOStrain experiments, therefore

enabling more scientists in academia as well as in industry to work in this field. To explore this possibility, LAOStrain tests were made on two CMT-rheometers and the results were compared to measurements made on two SMT-rheometers. A recent study [1] was concerned with very similar questions but concentrated more on the validity of the stress-frequency superposition in LAOStress-experiments. Bae et al. [1] concluded from their experiments that LAOStrain results from CTM-instruments are identical to those gained on SMT-instruments, although they did not directly compare higher harmonic intensities for a complete strain sweep at different frequencies. Furthermore their experiments were restricted to one sample system and two rheometers. In contrast, in our work we concentrate on quantitative evaluations of LAOStrain data from various instruments [31].

LAOS measurements for two samples, a polyisoprene melt (abbreviated: PI-84k, $M_w = 84{,}000$ g/mol, PDI $= 1.04$) and a 10 wt% solution of polyisobutylene (abbreviated: PIB, $M_w = 1.1 \times 10^6$ g/mol) in oligoisobutylene, were conducted on four different rheometers. The first two were separated motor transducer(SMT)-rheometers, namely the ARES-G2 (TA Instruments) and the ARES-LS (TA Instruments) with a 1KFRTN1 transducer. The DHR-3 (TA Instruments) and the MCR501 (Anton Paar) are in principle stress controlled instruments, but can be used for strain controlled experiments when using the deformation control feedback option (called *continuous oscillation* for DHR-3 and *direct strain oscillation* for MCR501).

Frequency dependent measurements of ${}^3Q_0$ for both samples are displayed in Fig. 5. Since at T = 52.8 °C instruments using a Peltier plate (ARES-G2, DHR-3

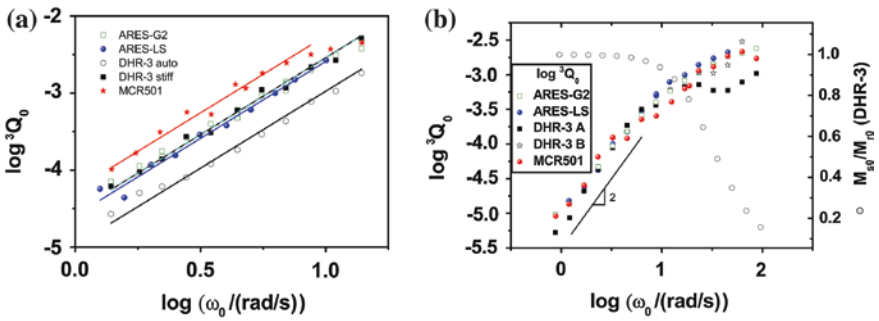

Fig. 5 **a** Frequency dependence of ${}^3Q_0$ for PI-84k, ${}^3Q_0$ is defined as the plateau value of ${}^3Q$ at small strain amplitudes (Eq. 5 with $n = 3$). The *lines* are linear regressions with a fixed slope of 2. The line for the ARES-G2 (*black*) and the DHR-3 (*light* and *dashed*) overlap. The DHR-3 data match, if the motor mode is set to *stiff*, a setting to *auto* instead caused severe deviations as shown by the open *circles*. **b** Frequency dependence of ${}^3Q_0$ for PIB. The DHR-3 A data was recorded using the correlation acquisition mode, whereas for the DHR-3 B-data, the transient acquisition mode was used. At low angular frequencies Q_0 is proportional to ω_0^2. Additionally, the ratio of the sample torque amplitude to the raw torque amplitude M_{s0}/M_{r0} for the DHR-3 A data is shown. When M_{s0}/M_{r0} reaches approx. 0.8, i.e. the inertia contribution makes up 20 % of the total torque, pronounced deviations in Q_0 are observed when no inertia correction is applied. Data reprinted from [31], copyright 2014, Springer

and MCR 501) had slightly different temperature settings in comparison to the ARES-LS, which used a forced convection oven, their data were shifted to higher frequencies using a factor of 1.39 for the PI-84k sample, see [31] for more details. No shift was necessary for the PIB sample at the measuring temperature of 25 °C.

To demonstrate the substantial effect of the motor control setting on the DHR-3 results, data from measurements using the *stiff* and the *auto* setting are shown. This motor setting has been created by the manufacturers to optimize the torque resolution and smoothness. The possible settings are *auto*, *soft*, *medium* or *stiff*. When performing LAOS experiments one would prefer to set the setting to *stiff*, since in that case the suppression of nonlinearities in the strain wave is most effective. The disadvantage is that a stiffer setting of the motor mode results in a lower torque sensitivity. The results obtained on the DHR-3 match remarkably well with the ones from the SMT instruments but only if the correct setting for the motor mode in the deformation control is used, which was the *stiff* setting for PI-84k. Other settings resulted in ${}^3Q_0$-values that are smaller by a factor of up to three as shown by the measurement using the *auto* setting.

With proper precautions the results for ARES-G2, ARES-LS and DHR-3 agreed well and the differences are only slightly larger than the reproducibility range of measurements on a single instrument, which was determined to be between 4 and 8 % (relative standard deviation of three independent measurements).

The MCR 501 delivers ${}^3Q_0$-values that were in general larger by a factor of 1.92 for PI-84 when compared to the ones from the SMT-rheometers. The reason for this deviation is assumed to be connected to the deformation control. The fact that the values were consistently larger relative to the other instruments suggests that the deformation control introduces additional nonlinearities into the stress signal. The ultimate source of this deviation remains unclear and might be sample dependent, but we can exclude several possible sources. First, the deviation cannot be caused by the use of the smaller diameter parallel plate geometry and therefore smaller sensitivity in terms of signal to noise ratio, as in an additional measurement with a 25 mm diameter plate with the MCR 501 identical deviations were obtained. Furthermore the result was confirmed on an additional measurement using a different MCR 501, suggesting that the deviation is not a technical problem of the specific instrument used so far. At last, the relatively large amount of nonlinear contribution that is still present in the strain wave (the ratio of $I_{3/1}$ in the strain to $I_{3/1}$ in the stress is roughly 1/10, see Merger and Wilhelm [31], Fig. 7), can not be responsible for the large deviations in ${}^3Q_0$ because these would transfer into the stress wave linearly and therefore would cause an error on the order of 10 % but not 192 % of the measured values. Note that changes of several percent in ${}^3Q_0$ seem to be of minor significance, since this parameter can vary over two to three decades of magnitude [21], but a factor of two might not be negligible.

The frequency dependence of Q_0 for the PIB sample is shown in Fig. 5b. In contrast to the PI-84k sample, in this case the results for the two SMT-rheometers and MCR 501 agreed reasonably well, as the relative standard deviation for

specific $Q_0(\omega)$ values from different instruments was below 25 % at most frequencies. At low frequencies Q_0 shows a quadratic dependence on the angular frequency ω_0. Therefore, a similar linear regression as shown for PI-84k was performed on the data in the range $-0.06 < \log(\omega_0/(\text{rad/s})) < 0.654$ in Fig. 5b. A comparison of the intercepts reveals that the average deviation between the instruments is below 12 % in this region.

For the DHR-3, an apparent maximum in the ${}^3Q_0$-curve was observed at 23 rad/s. This maximum is believed to be caused by instrument inertia effects. When using the DHR-3 in the correlation acquisition mode, the transient data that is Fourier-transformed by the software is the raw torque data. For a CMT-rheometer the raw torque M_r is the sum of the sample torque M_s and an additional contribution caused by instrument inertia M_I as shown in Eq. 6 [11].

$$M_r(t) = M_s(t) + M_I(t) \tag{6}$$

$$= \sigma(t)/K_\sigma + I\ddot{\theta}(t) \tag{7}$$

$$= \sigma(t)/K_\sigma - I\omega^2\theta_0 \sin(\omega t) \tag{8}$$

As M_I increases quadratically with the frequency due to the second time derivative of the deflection angle $\ddot{\theta}$, I represents the instrument inertia constant and is calibrated for every geometry, K_σ is the geometry constant for the torque-to-stress conversion. Due to the relationship $M_I \propto \omega^2$, M_I can dominate over the sample torque for low viscosity materials at high frequencies. Since the DHR-3 software gives the amplitudes for the raw torque M_{r0} and the sample torque M_{s0}, the ratio of M_{s0}/M_{r0} was calculated to monitor the frequency at which the inertia contribution starts to dominate the total torque. The decrease in ${}^3Q_0$ began at a frequency of around 23 rad/s and, at these conditions, the M_{s0}/M_{r0} ratio is roughly 0.8, meaning that the inertia contribution makes up 20 % of the total torque. If this inertia contribution is assumed to be free of nonlinearity, normalization leads to erroneous values for $I_{3/1}$ and, consequently, for ${}^3Q_0$. It can therefore be concluded that when conducting LAOS experiments at different frequencies using a CMT-rheometer, one has to ensure that the inertia effects are negligible by avoiding both high frequencies and low viscosities. Alternatively, it is possible to transform inertia corrected torque data, which is the sample torque $M_s(t)$, when using the transient acquisition mode. This was done for the frequencies above 23 rad/s and is shown by the data points named DHR-3 B in Fig. 5. These values agree better with the data from the other instruments. Although this acquisition mode is more tedious than the correlation acquisition because the Fourier transform step is no longer done automatically by the software, this procedure is necessary when working with low viscosities and high frequencies where inertia contributions become relevant. For MCR 501 the software applied an inertia correction, so the sample torque $T_s(t)$ could be analyzed directly and instrument inertia effects were corrected in the investigated frequency range.

4 Applications to Dispersed Systems

4.1 Dilute Emulsions

Emulsions are of strong interest, due to their ability of combining two immiscible liquids for example polar and nonpolar substances, as in the most common case using water and oil. They have a wide range of application in daily life, e.g. in body care products, wall paints and food products. The microstructural variables of an emulsion, i.e. the viscosities of the two phases, the interfacial tension, the volume fraction, the volume average droplet radius, R_{43}, and the droplet size polydispersity have an influence on the texture of such systems and their rheological behavior [26, 32]. Since LAOS can be used to induce nonequilibrium structures in complex materials and therefore nonlinear mechanical properties [21, 37], we apply this technique here to dilute emulsions to achieve a more complete mechanical characterization of these systems.

In order to identify the influence of microstructural parameters on the nonlinear behavior of dilute emulsions, specifically on the intensities of the higher harmonics and their strain amplitude dependence, we have employed modelling approaches [36, 37]. For dilute emulsions the individual droplets can be regarded as independent of each other, therefore, the measured shear stress can be obtained from a linear superposition of the matrix contribution and the contributions originating from each droplet and their interface [5, 16], as predicted by Batchelor [2]:

$$\underline{\underline{\sigma}}(t) = \underbrace{-p\underline{\underline{\mathbf{I}}}}_{\text{isotropic term}} + \underbrace{\eta_m(\nabla\underline{\mathbf{v}} + \nabla\underline{\mathbf{v}}^T)}_{\text{matrix contribution}} \underbrace{- \underbrace{\frac{\eta_m}{V}\int_A (\underline{\mathbf{n}}\underline{\mathbf{u}} + \underline{\mathbf{u}}\underline{\mathbf{n}})\mathrm{d}A}_{\text{viscous contribution}} - \underbrace{\frac{\Gamma}{V}\int_A (\underline{\mathbf{n}}\underline{\mathbf{n}} - \frac{1}{3}\underline{\underline{\mathbf{I}}})\mathrm{d}A}_{\text{elastic contribution}}}_{\text{interfacial contribution}} \tag{9}$$

In Eq. 9, Γ is the interfacial tension, p the pressure, $\nabla\underline{\mathbf{v}}$ the undisturbed velocity gradient tensor and $\nabla\underline{\mathbf{v}}^T$ its transpose, η_m is the viscosity of the continuous phase, V is the total volume of the system, $\underline{\mathbf{n}}$ is the unit vector orthogonal to the interface between the two phases, $\underline{\mathbf{u}}$ is the velocity at the interface, $\mathrm{d}A$ is the area of an interfacial element and the integrals are evaluated over the whole interfacial area of the system, A. Since the constituents are assumed to be Newtonian all nonlinear contributions to the stress $\underline{\underline{\boldsymbol{\sigma}}}(t)$ are caused entirely by the deformation of the droplet interface. The unit vectors $\underline{\mathbf{n}}$ and $\underline{\mathbf{u}}$ describe this deformation and can be computed using the Maffettone-Minale (MM) model for different frequencies and amplitudes. The MM model uses a second rank, symmetric and positive definite

tensor $\underline{\underline{\mathbf{S}}}$ to describe the time dependent shape behavior of an ellipsoid under nonlinear oscillatory shear, Eq. 10 [17, 30]:

$$\frac{\mathrm{d}\underline{\underline{\mathbf{S}}}}{dt} = -f_1(\lambda)\underline{\underline{\mathbf{S}}} - \frac{3}{II}\underline{\underline{\mathbf{I}}} + f_2(\lambda, Ca) \cdot (\underline{\underline{\mathbf{D}}} \cdot \underline{\underline{\mathbf{S}}} + \underline{\underline{\mathbf{S}}} \cdot \underline{\underline{\mathbf{D}}}) + (\underline{\underline{\Omega}} \cdot \underline{\underline{\mathbf{S}}} + \underline{\underline{\mathbf{S}}} \cdot \underline{\underline{\Omega}}) \quad (10)$$

$$f_1(\lambda) = \frac{40(\lambda + 1)}{(2\lambda + 3)(19\lambda + 16)}$$

$$f_2(\lambda, Ca) = \frac{5}{2\lambda + 3} + \frac{3Ca^2}{2 + 6Ca^2} \quad (11)$$

With the use of the emulsion time $\tau = \eta_m R/\Gamma$, where R is the radius, Eq. 10 is made dimensionless. In Eq. 10, $\underline{\underline{\mathbf{I}}}$ is the second rank unit tensor, $\underline{\underline{\mathbf{D}}}$ and $\underline{\underline{\Omega}}$ are the deformation rate and the vorticity tensors, respectively, II is the second scalar invariant of tensor $\underline{\underline{\mathbf{S}}}$ and the capillary number is $Ca = \gamma_0 \omega \eta_m R/\Gamma$, see also [30]. At rest, the droplet is spherical with $\underline{\underline{\mathbf{S}}} = \underline{\underline{\mathbf{I}}}$. Please note that droplet break-up will not occur under oscillatory shear flow as long as the ratio of the viscosities is greater than or equal to 2.5, i.e. that $\lambda = \eta_m/\eta_d \geq 2.5$ [15].

We used the Batchelor theory in combination with the MM-Model to calculate the interfacial stress waves for a number of varying emulsion parameters and frequencies as a function of strain amplitude γ_0 resembling a strain sweep experiment. Initially monodisperse emulsions were considered, characterized by a single droplet radius R, the interfacial tension Γ and the viscosities of the constituents η_d and η_m. The two functions f_1 and f_2 depend on the viscosity ratio λ and the capillary number Ca (Eq. 11). The modelled stress oscillatory signals were Fourier transformed and the relative intensities of the third and fifth harmonic were extracted from the spectra to obtain their ratio, $I_{5/3} = I_{5/1}/I_{3/1}$ as a function of strain amplitude γ_0.

The LAOS behavior of dilute emulsions is ruled by three dimensionless numbers: the capillary number Ca, the viscosity ratio λ and the ratio of the harmonics $I_{5/3}$. Therefore a relationship among them is in principle available. In particular, the following equality was found:

$$\frac{I_{5/3}}{(Ca\lambda^m)^2} = E_0 \quad (12)$$

The unknown constants m and E_0 in Eq. 12 were estimated by investigating the model (Eqs. 9 and 10) for a wide range of parameter values. It was finally found that a reasonable estimation of the constants is $E_0 \approx 0.64$ and $m \approx 0.823$ (for further details one can refer to [37]).

Therefore plotting $I_{5/3}/(Ca^2\lambda^{1.63})$ versus $Ca\lambda^{0.82}$ yielded the universal nonlinear master curve for dilute emulsions shown in Fig. 6. In the plateau region this curve gives a quantitative relation between the droplet parameters and the measured nonlinear rheological parameter ${}^{5/3}Q_0 = I_{5/3}/\gamma_0^2$ according to Eq. 13 for small deviations from the linear regime. This relation can be used to extract the

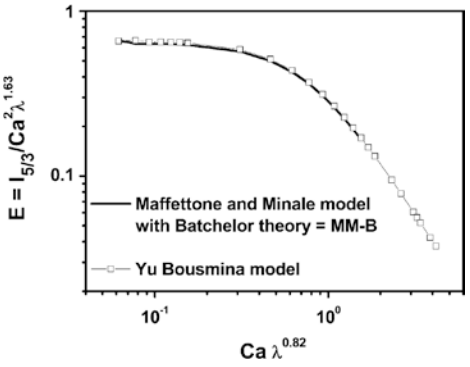

Fig. 6 Nonlinear mastercurve for emulsions as obtained from the Batchelor theory with the MM-model model (*line*) in comparison a curve obtained from the Yu and Bousmina model (*symbol*), reprinted from [37]

droplet radius R of an emulsion from nonlinear measurements if the interfacial tension is known or vice versa.

$$\frac{^{5/3}Q_0}{\omega_1^2} = E_0\lambda^{2m}\frac{\eta_m^2 R^2}{\Gamma^2} \tag{13}$$

The concept introduced here uses ubiquitous quantities, which are not specific to any given model. Therefore, other approaches can also be compared with the results obtained here. For example, the model of Yu et al. [47] uses the Maffettone and Minale model to describe the droplet shape behavior, but calculates the shear stress with the following equation instead of using the Batchelor theory.

$$\underline{\underline{\sigma}}_I = \frac{2f_2K}{II}(I\underline{\underline{\mathbf{S}}} - \underline{\underline{\mathbf{S}}}\cdot\underline{\underline{\mathbf{S}}} - \frac{2}{3}II\underline{\underline{\mathbf{I}}}) \tag{14}$$

where $\underline{\underline{\mathbf{S}}}$ is the non-dimensional droplet shape tensor, $\underline{\underline{\mathbf{I}}}$ the unit tensor, I is the trace and II is the second invariant of $\underline{\underline{\mathbf{S}}}$, respectively, and $K = \frac{6\Gamma}{5R}\frac{(\lambda+1)(2\lambda+3)\phi}{5(\lambda+1)-(5\lambda+2)\phi}$. The dependency of E as a function of Ca with these two different models shows quantitative agreement with the curve obtained by the MM-B model, as shown in Fig. 6. Furthermore, it should be noted that this result supports the assumption made in the calculation of the interfacial shear stress that only the elastic contribution of the interfacial stress needs to be considered, see Eq. 9, and that any viscous contribution to the interfacial contribution can be neglected in the first approximation using the MM-B model.

The nonlinear master curve for dilute emulsions has furthermore been extended to take polydisperse droplet distributions into account. Modelling procedures analogous to the ones presented above were used for a variety of distributions [36], finding that the same universal curve can be used for polydisperse systems if the volume averaged droplet radius is used in Eq. 13.

The relation in Eq. 13 has been validated by LAOS experiments on two systems of immiscible polymer blends. Strain sweeps as shown in Fig. 7 were made for blends of PDMS/PIB and PDMS/PI with blending ratio in the dilute regime of

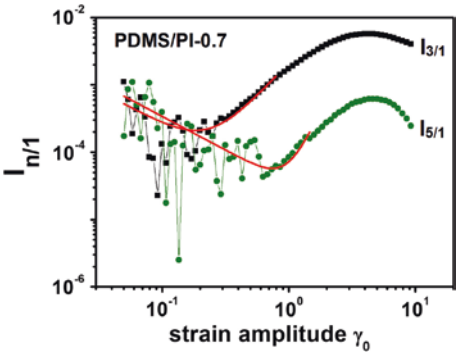

Fig. 7 Measurements of the relative intensity of third and fifth harmonic for a PDMS/PIB blend with 0.7 block-copolymer content at $\omega/2\pi = 0.1$ Hz. *Lines* are fits to equation $I_{n/1} = a_n\gamma_0^{-1} + {}^nQ_0\gamma_0^{n-1}$ with $n = 3$ and 5

10:1. From the strain sweeps ${}^{5/3}Q_0$ was extracted in order to calculate R_{43} for the PDMS/PIB system [36], as Γ was known here. In addition the volume averaged droplet radius has been determined from microscopic pictures by analyzing at least 500 droplets. The radii from the microscopic analysis and the ones obtained from LAOS-measurements using the emulsion curve relation were compared and good agreement was found, see Table 1. In the case of the PDMS/PI blend ${}^{5/3}Q_0$ was used to calculate Γ using $R_{43,M}$ from the microscopic analysis and Γ was found to decrease with increasing amount of block-copolymer which acted as a surface active agent.

Table 1 **a** Results of a droplet size determination for the PDMS/PIB system $R_{43,E}$, using LAOS measurements and the relation according to Eq. 13 compared to radii from a microscopic analysis $R_{43,M}$. In the first series of blends, PDMS/PIB was prepared using manual mixing with a spatula, PDMS/PIB-100 and PDMS/PIB-300 rpm with an electrical stirrer at the designated rotation speed. In the second series the blends differed in their block-copolymer content, as stated in wt% of block-copolymer in the PDMS phase. **b** Estimation of the interfacial tension Γ using Eq. 13 based on additional information about the radius from microscopic droplet size determination

(a) Blend	$R_{43,M}$ [μm]	$R_{43,E}$ [μm]
PDMS/PIB	5.10	5.14
PDMS/PIB-100 rpm	9.30	8.00
PDMS/PIB-300 rpm	7.90	6.50
PDMS/PIB-0.5	3.30	3.44
PDMS/PIB-0.7	4.10	3.29
PDMS/PIB-1	2.25	2.52
(b) Blend	$R_{43,M}$ [μm]	Γ [mN/m]
PDMS/PI-0.5	5.04	3.00
PDMS/PI-0.7	2.65	2.42
PDMS/PI-1	6.22	2.76

4.2 High Volume Fraction Suspensions

With increasing volume fraction a hard sphere suspension undergoes a transition from a fluid to a predominantly elastic solid due the particles being increasingly trapped in persistent cages of neighbor particles ('cage'-effect). Some characteristics of the glass transition, either induced by temperature or volume fraction variation, are listed in the following [24]:

- disorder and/or frustration in the structure or in the interactions
- no long range order
- non-ergodic phase transition
- time dependent correlation function shows a stretched exponential α-relaxation at long times and a β process with a power law behavior which merges into a plateau related to the cage effect.

LAOS measurements on glassy systems can be used to investigate their yielding behaviour, that is the transition from a solid to a liquid, under oscillatory and therefore quasistatic conditions. Simultaneously they can be used to test the predictive capabilities of constitutive models, as it was done by Brader et al. [3] for the schematic F_{12} model. The F_{12} model is a simplified, wave vector invariant version of the full microscopic mode coupling theory (MCT), that can be solved numerically under oscillatory shear conditions.

Within the F_{12} model the essential quantity that describes the structure of the suspension system and its evolution with time is the time dependent density correlator $\Phi(t)$. It can be determined by solving the following integro-differential equation which contains the initial decay rate Γ as model parameter and a memory function $m(t)$ to account for the influence of the shear forces on the microstructure.

$$\dot{\Phi}(t) + \Gamma(\Phi(t) + \int_0^t dt' m(t-t')\dot{\Phi}(t')) = 0 \tag{15}$$

The memory function is approximated with a second order polynomial of the correlator Φ as shown in Eq. 16.

$$m(t) = \frac{\nu_1 \Phi(t) + \nu_2 \Phi^2(t)}{1 + (\gamma_0 \omega t)^2} \tag{16}$$

with $\nu_1 = 2(\sqrt{2}-1) + \varepsilon/(\sqrt{2}-1)$ and $\nu_2 = 2$, that represent the role of the static structure factor in the microscopic theory. The crucial parameter that describes the state of the system is the distance from the glass transition $\varepsilon = (\phi - \phi_g)/\phi_g$. It is positive for a glassy suspension and negative for a flowing suspension. Under shear the model describes two competitive phenomena: increasing particle interactions leading to the non-ergodicity transition and the opposed shear-induced decorrelation. It is worth to mention that flow-induced ordering is assumed to be negligible in the range of applied Peclet numbers $Pe_0 \ll 1$. The Peclet number

defines the ratio of shear forces to particle dynamics determined by Brownian motion: $Pe_0 = \dot{\gamma} R_h^2 / D_0$ where D_0 is the diffusion coefficient of particles with hydrodynamic radius R_h. Under nonlinear deformation advection enforces the decorrelation processes against the mechanism of the cage effect.

Solving Eq. 15 for the correlator under shear $\Phi(t)$ allows to calculate the time-dependent modulus $G(t)$ according to Eq. 17 with v_σ as a model parameter that measures the strength of the stress fluctuations. Subsequently $G(t)$ can be used to obtain the shear stress as a function of time using Eq. 18.

$$G(t, t') = v_\sigma \Phi^2(t, t') \tag{17}$$

$$\sigma(t) = \int_{-\infty}^{t} dt' \dot{\gamma} G(t, t') \tag{18}$$

The theoretical predictions based on the MCT model that have been calculated in the group of Prof. Fuchs are compared with our LAOS experiments on a well characterized, thermoresponsive colloidal suspension synthesized by the Ballauff group [40]. As the suspension changes its hydrodynamic radius and consequently the volume fraction with temperature, measurements at three different temperatures were used to probe different volume fractions from a nearly fluid to a glassy system. Two experiments in the linear regime, the measurement of the flow curve and the linear moduli G′ and G″ as a function of frequency (Figs. 12 and 13 from Ref. [3]), were used to determine the model parameters needed for the nonlinear prediction with the schematic F_{12} model. The most important parameter, the separation parameter was determined as $\varepsilon = -2.45 \times 10^{-3}, -2.2 \times 10^{-4}$ and 5×10^{-5} for 20.0, 18.0 and 15.0 °C, respectively, thus describing two fluid and one glassy sample. This means the schematic model parameters were determined in advance in order to predict LAOS data based on the linear properties of the suspensions.

In Fig. 8, a direct comparison of theoretical prediction and experiment for the glassy sample at 15 °C at $\omega/2\pi = 1$ Hz is shown. Besides the shear stress in the time domain, Lissajous figures are added to demonstrate the increasing dissipated energy at each oscillation cycle, visualized by an increasing area. For small strain amplitudes a linear response is measured, expressed by a nearly perfect sinusoidal behavior, which becomes increasingly distorted with increasing deformation. The full black lines are the MCT predictions, they show good agreement but do not correctly predict the dip or overshoot of the measured data (broken black lines), at the top of the asymmetric peak for intermediate strain amplitudes. For higher strain amplitudes the agreement between experiment and prediction is better.

In addition to a comparison of the wave forms, a quantitative comparison of the nonlinearity, as measured by the normalized intensities of the higher harmonics $I_{n/1}$ with $n = 3$ and 5, is shown in Fig. 9. Our experimental results are presented as symbols, the predictions of the schematic MCT model are represented by solid lines. This comparison confirms the previous observation that the agreement at higher amplitudes ($\gamma_0 > 0$) is better than for intermediate amplitudes, where too

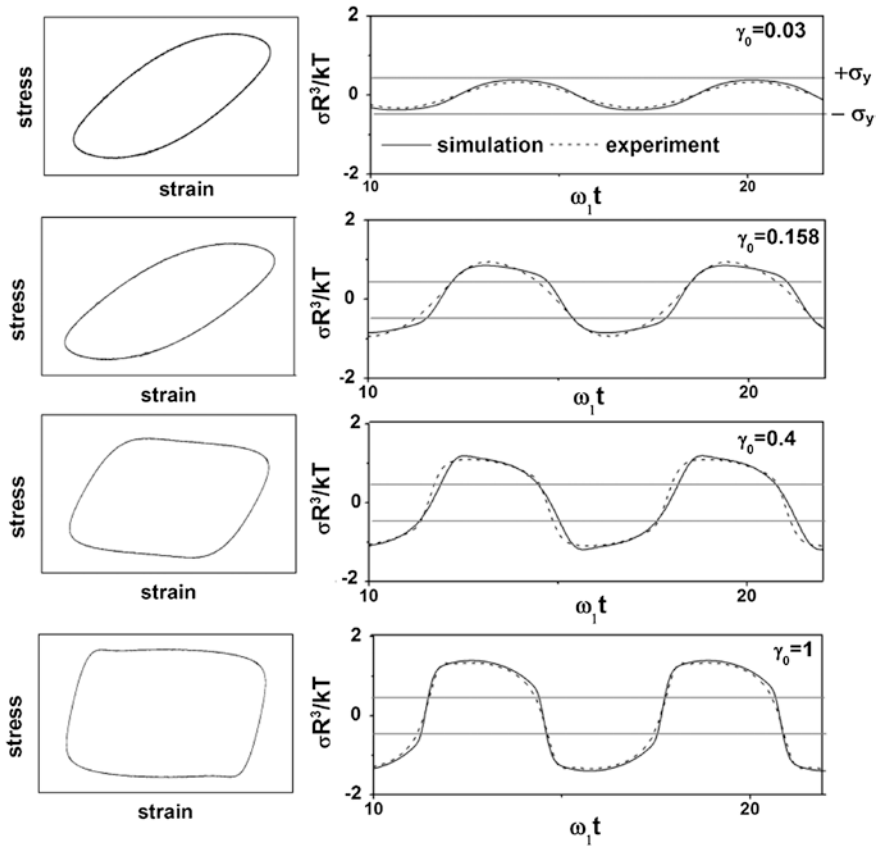

Fig. 8 *Dotted lines* are the shear stress in the time domain measured at an excitation frequency of 1 Hz for different strain amplitudes ranging from 0.03 to 1. The temperature was set to T = 15.1 °C to measure a glassy system. With increasing strain amplitude an increasing dissipative energy is measured, associated with an increasing area of the closed *Lissajous curves*. After exceeding the yield stress σ_y, that is indicated by the *grey lines*, the shear stress shows a distorted shape, which reflects the onset of nonlinearity. The MCT based predictions are depicted with *full lines* and show an overall good agreement with the experimental data, reprinted from Brader et al. [3], copyright 2010, American Physical Society

high nonlinearities are predicted by the MCT model. The source of the deviations at intermediate amplitudes is assumed to be connected to the excessively slow decay of the correlator to its plateau value, which is an inherent feature of any model based on the original schematic F_{12} model [3]. Nevertheless the overall agreement is remarkable when considering that the nonlinear data is actually predicted based on linear rheological parameters and not fitted directly. This shows that the schematic MCT is capable to successfully describe LAOS results.

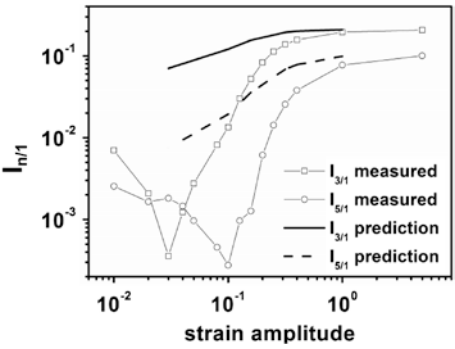

Fig. 9 Strain amplitude dependent higher harmonics $I_{n/1}$ with $n = 3$ and 5 at 15.1 °C from theoretical predictions by the schematic F_{12} model (*lines*) and measurements (*symbols*) at an excitation frequency of 1 Hz, reproduced after Brader et al. [3], copyright 2010, American Physical Society

4.3 Yielding of a Nanoemulsion Colloidal Gel

Recently, LAOS has been used to make detailed measurements of yielding in attractive suspensions at moderate volume fractions. In many cases, a broadened or so-called "two-step" yielding process is observed, in which the transition from a nonlinear material response to flow occurs over an order of magnitude or more in strain amplitude [6, 25, 28, 39]. This is in contrast to more dilute gels, which typically exhibit a distinct, unique yield point defined by a simultaneous maximum in the linear viscous modulus, G'', and crossover of G'' and the linear elastic modulus, G' [14, 33]. The two-step process is signified by two local maxima in either the viscous modulus, $G''(\gamma_0)$, or average elastic stress, $\sigma' = \gamma_0 G'(\gamma_0)$, with increasing strain amplitude, γ_0. Detailed measurements have shown that the locations of the local maxima are relatively insensitive to the applied frequency of oscillation, although the corresponding values of the stress and moduli can be either frequency dependent or independent, depending on the details of the material system [25, 39]. In some cases, two separate maxima are not distinctly evident, although a broadened yielding transition is still observed [19, 35]. It was also shown that a transition between one-step and two-step yielding could be induced by screening interparticle repulsions in a jammed suspension [39].

Rheo-USANS allows direct measurement of the microstructural processes that underlie yielding at length scales ranging from one to thousands of primary particles [31]. In this work, we hope to test whether large-scale heterogeneity in colloidal gels is the fundamental cause for broadened yielding, as suggested by our previous experiments [18].

As a model colloidal gel, we employ a well-characterized material system comprised of oil-in-water (O/W) nanoemulsions with low polydispersity [18, 22]. A temperature-responsive bridging polymer in the continuous phase allows for careful control over interparticle attractions, including the process of gelation, such that we are able to prepare gels with reproducible microstructure [18] without the need for shear rejuvenation that is required in many systems.

Figure 10 shows results of nonlinear oscillatory experiments on a nanoemulsion gel containing $\phi = 0.33$ PDMS droplets in an aqueous continuous phase with

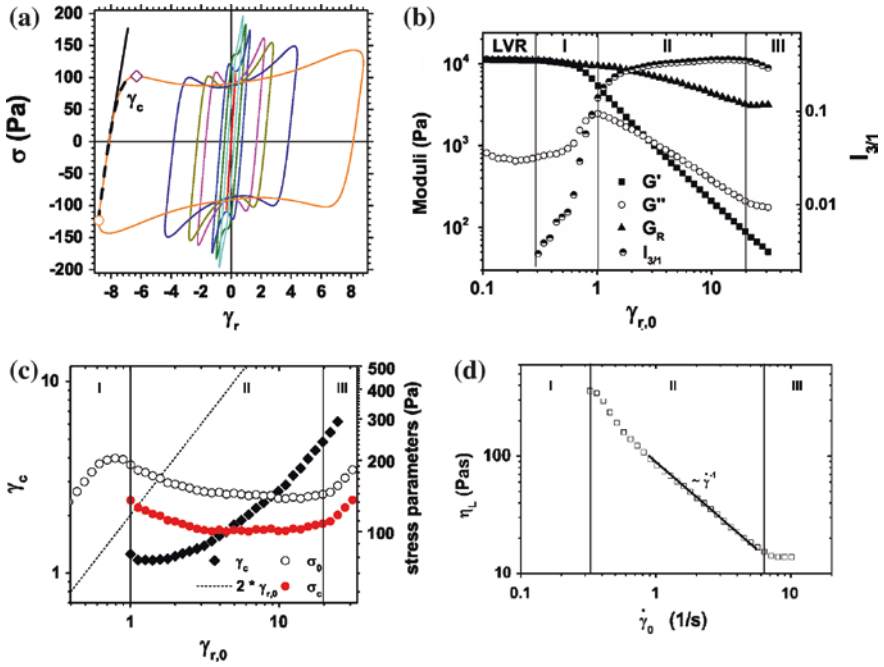

Fig. 10 **a** selected elastic Lissajous plots of a LAOS experiment on a nanoemulsion sample containing $\phi = 0.33$ PDMS droplets in an aqueous continuous phase with 33 vol% PEGDA and $C_s = 230$ mM SDS at $\omega = 10$ rad/s. The *circle* and *diamond* symbols show the points at flow reversal ($\gamma_r = -\gamma_{r,0}$ and $\dot{\gamma} = 0$) and the following local stress maximum, respectively. The broken *black line* illustrates the accumulated strain γ_c that is necessary to yield the material. The *black* tangent represents the residual modulus after yielding G_R ($d\sigma/d\gamma$ at $\sigma = 0$). **b** Residual modulus G_R together with the storage and loss modulus at $\omega = 10$ rad/s and the relative intensity of the 3rd harmonic $I_{3/1}$. **c** Nonlinear yielding parameters extracted from the waveform data of the LAOS measurements: γ_c represents the strain that has been accumulated between the point of flow reversal (*circle symbol*) and the local stress maximum (*diamond*) in (**a**), σ_c is the corresponding stress value which is plotted with the stress amplitude σ_0 as reported by the rheometer software. **d** Instantaneous viscosity at the point of zero strain and maximum shear rate as a function of increasing shear rate amplitude, reprinted from Kim et al. [23]

33 vol% PEGDA and $C_s = 230$ mM SDS. In Fig. 10a the stress response is plotted as a function of strain. Note that all strain axes have been normalized by the value of the strain amplitude where G″ is at its maximum ($\gamma_r = \gamma/0.0322$), in order to be able to correlate this data to the data of the SANS sample (for details see [31]). The distinct non-ellipsoidal waveforms can be interpreted using the sequence of physical processes approach following [38]: Starting at the point where the flow direction is reversed ($\gamma/\gamma_0 = \pm 1$, circle symbol in Fig. 10a) the gel network of agglomerated droplets is strained, the material initially behaves elastically and therefore the stress increases linearly with the accumulated strain. After the initial linear region, the stress continues to increase until a strain equal to γ_c has been accumulated (broken gray line), where it shows a local maximum σ_c (diamond

symbol in Fig. 10a). This overshoot in the stress curve is due to yielding of the gel network, and afterwards the sample begins to flow. The stress subsequently decreases with further increasing shear rate until a minimum is reached. With further increasing strain, the stress begins to increase again, suggesting thixotropic behavior where the structure is gradually rebuilt as the shear rate is decreasing. This continues until the end of the half-cycle ($\gamma = +\gamma_0, \dot{\gamma} = 0$), and subsequently the sequence is repeated in the opposite direction.

The extracted waveform parameters include the residual modulus G_R, yield strain γ_c and yield stress σ_c, as well as the instantaneous viscosity η_L at peak shear rate, that were introduced in Sect. 3. These parameters show strain amplitude dependencies which are displayed in Fig. 10b–d and have been used to define four different regions throughout the strain amplitude sweep experiment. These regions will aid the correlation of the nonlinear rheological parameters with the structural parameters from the neutron scattering experiments. In order to extract structural information from the SANS/USANS spectra (Fig. 11a) a model combining three primary contributions to the structure (Eq. 19) was fitted to the data (details see [31]): (1) a low-q contribution to capture the Porod scattering, (2) a model for off-critical phase separation at moderate q-values to capture the local maximum due to bicontinuous structure, and (3) a high-q contribution due to the fractal cluster microstructure (note that we have chosen not to include the higher-q scattering due to individual droplets). Figure 11b and c show the strain amplitude dependencies of the three relevant parameters: specific surface of the voids Σ (which is derived from a model-independent asymptotic analysis in the Porod limit [41]), characteristic length scale of the microphase separation $2\pi/\beta_{\max}$ and the peak sharpness $\xi_{c2}\beta_{\max}$.

$$I(q) - I_b = \frac{K_1 \xi_{c1}^3}{(1 + (q\xi_{c1})^2)^2} + \frac{K_2 \left[\frac{\xi_{c2}}{1+(q-\beta_{\max})^2 \xi_{c2}^2} - \frac{\xi_{c2}}{1+(q+\beta_{\max})^2 \xi_{c2}^2} \right]}{\beta_{\max} q} + \frac{K_3 \sin[(d_m - d_s + 2)\arctan(\xi_s q)]}{(\xi_s q)[1 + (\xi_s q)^2]^{\frac{d_m - d_s + 2}{2}}} + \frac{K_4 \sin[(d_m - 1)\arctan(\xi_m q)]}{(d_m - 1)(\xi_m q)[1 + (\xi_m q)^2]^{\frac{d_m - 1}{2}}} \tag{19}$$

The combined rheo-SANS/USANS measurements (Figs. 10 and 11) suggest that, as the intracycle mechanical response becomes progressively more dominated by the yielded and flowing states, the microstructure of the gel evolves at progressively smaller length scales (Fig. 12). We note that, due to the time-averaged nature of the SANS/USANS measurements, the changes in microstructure observed with increasing strain amplitude represent a moving average over the various dynamic stages of nonlinear behavior. As such, the amount of time per cycle spent in the yielded state will increase with increasing strain amplitude, and thus the measured time-average microstructure will evolve toward the fully flowing state. Therefore, in what follows, we will assume that the contribution of each of the instantaneous microstructural processes to the overall, time-averaged scattering is proportional to the time per cycle spent in a particular stage of nonlinear behavior.

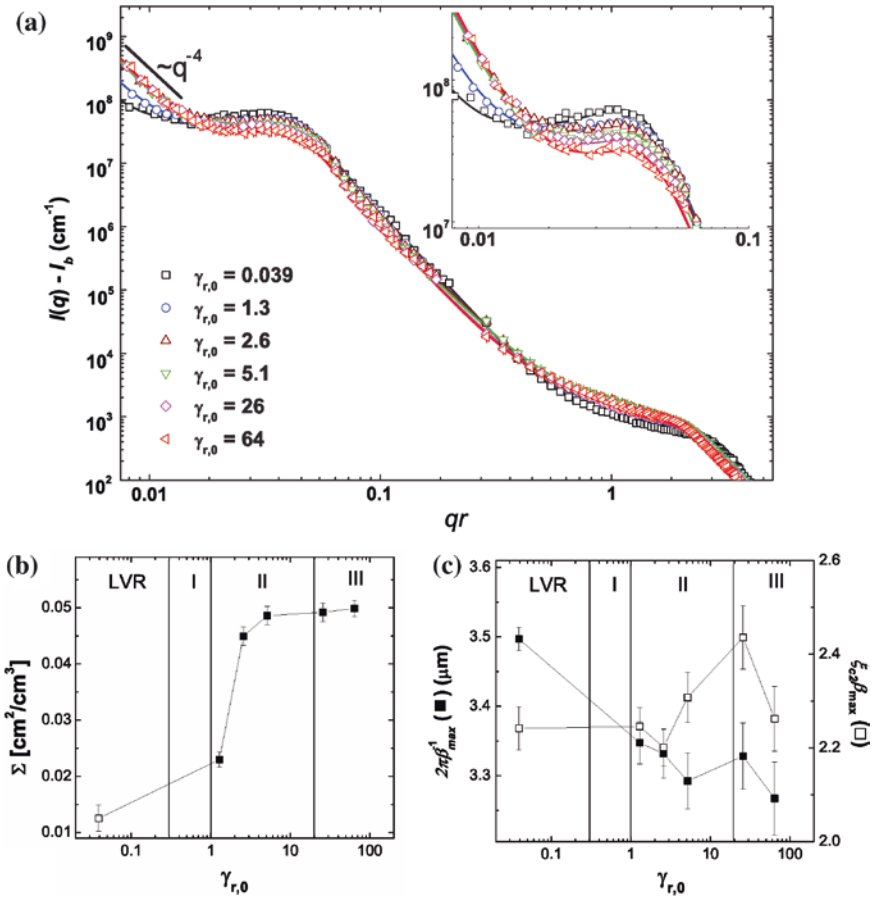

Fig. 11 **a** Combined rheo-USANS and SANS spectra of a nanoemulsion sample containing $\phi = 0.33$ PDMS droplets with P = 0.33 PEGDA and $C_s = 230$ mM SDS in 50/50 (v/v) H_2O/D_2O at the normalized strain amplitudes indicated. Lines are fits to Eq. 19. Inset magnification of low-q portion of USANS data with model fitting. **b** Specific surface area from the Porod-regime at very low-q. **c** Characteristic length scale of the microphase separation (*closed squares*) and the peak sharpness (*open squares*) from the model, reprinted from Kim et al. [23], copyright 2014, Society of Rheology

In the linear regime, the quiescent microstructure is comprised of a bicontinuous network of droplet-lean "pores" and droplet-rich network strands (middle panel), the latter of which are comprised of fractal clusters of droplets (bottom panel). The bicontinuous structure exhibits a domain size proportional to $1/\beta_{\max}$. Upon increasing the strain into the nonlinear regime, nonlinear deformation causes compression of the network due to compressibility of the droplet-rich domains. This results in the formation of voids, quantified by their specific surface Σ, at length scales significantly larger than the domain size (top panel), as evident by the significant Porod scattering that develops in Region I, which then saturates

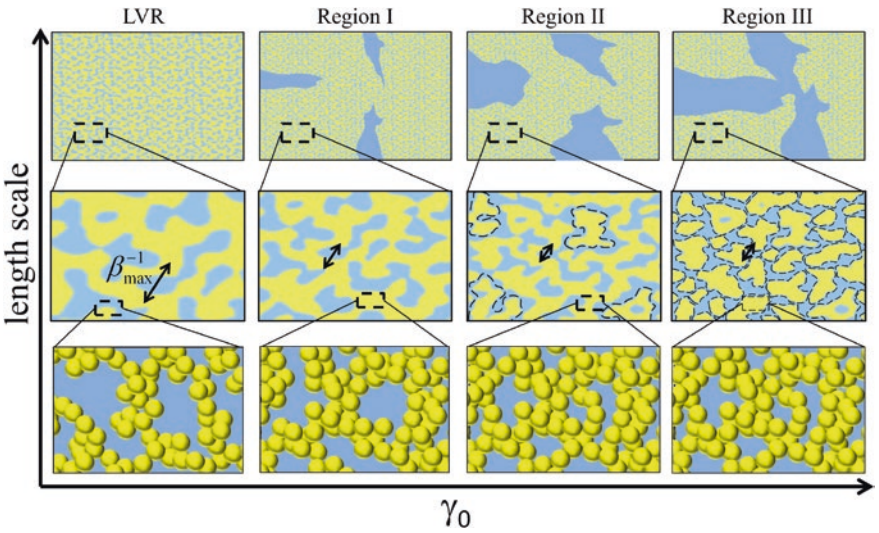

Fig. 12 Schematic of gel microstructure through the yielding transition. *Bottom* fractal clusters of droplets (*yellow*) with diameter D. *Middle* bicontinuous network structure consisting of droplet-lean (*blue*) and droplet-rich (*yellow*) domains on the length scale of 10–100 D. *Top* macroscopic structure at a length scale of 100–1000 D, reprinted from Kim et al. [23], copyright 2014, Society of Rheology

in Region II. Such voids are reminiscent of those observed in other gelling systems after yielding under startup of steady shear [35], and could be a pre-cursor for the shear-induced macroscopic heterogeneities that subsequently develop at large strains. In order to conserve the overall density of droplets, these voids must form at the expense of the bicontinuous structure, resulting in compression of the network and a decrease in $1/\beta_{\max}$ (middle panel). As previously discussed, this requires significant compression of the fractal droplet-rich domains relative to the droplet-lean domains (Fig. 11c), which in turn requires yielding of the dense phase. As the strain amplitude is increased further, the compression of the dense network becomes increasingly difficult, resulting in eventual saturation of both the voids and the domain size in Region II. Once the void structures saturate, additional strain input becomes sufficient to rupture the effective "bonds" between network strands, producing discrete agglomerates of fractal clusters (middle panel, dotted lines in Fig. 12). The primary signature of this process is the observed increase in the sharpness of the distribution of domain sizes, given by the product $\xi_{c2}\beta_{\max}$. This occurs because the most likely size of an agglomerate formed by rupturing of the bicontinuous network will have a characteristic size given by the characteristic domain size. As such, any irregular network strands will be annealed into smaller, disconnected domains with an average size given by $1/\beta_{\max}$. This concept could be viewed as similar to that put forth by Hsiao et al. [19], who proposed that the yielding of shear-rejuvenated colloidal gels under step strain was dominated by the rupture of weak network contacts with a small average contact number. However,

it should be noted that in our material it is rupture of contacts between network strands, rather than individual particles, that is responsible for yielding.

Eventually, at a critically high strain amplitude, enough bonds between domains will be ruptured in order to compromise the integrity of the network, resulting in (on average) a suspension of disconnected domains with a relatively narrow size distribution around $1/\beta_{\max}$, similar to what has been observed on colloidal gels at much larger strains after yielding is complete [35]. It is notable that the peak sharpness $\xi_{c2}\beta_{\max}$ exhibits a maximum precisely at the onset of Region III, suggesting that the distribution of domain sizes is most homogeneous at the final transition to flow. Previously, we observed a similar maximum during the incipient gelation of bicontinuous nanoemulsion gels that corresponded precisely with the critical gel point measured by rheology [18]. We hypothesized that such a maximum in homogeneity is a distinct signature of percolation of heterogeneous gels, and similar observations have been made in other gelling colloidal systems exhibiting phase separated microstructure [28]. It is thus tempting to consider that the final stage of yielding in the present study arises from "de-percolation" of the bicontinous gel network into a suspension of disconnected clusters. However, we do not discount the possibility that this common signature, i.e., of a maximum in homogeneity of the network at both the critical gel point and the critical yield point, is merely a coincidence.

We stress that the preceding is a time-averaged description of the gel microstructure, which is averaged over the sequence of processes (elastic straining, yielding, flow and recovery) comprising one LAOS cycle. In reality, it is reasonable to expect that the intracycle structure will exhibit a continuous transition between the various average microstructures depicted in Regions I–III. Indeed, we will explicitly consider this to be true in order to rationalize the observed time-dependent nonlinear mechanical response with the observed time-averaged microstructure in what follows.

4.4 Relation Between Microstructure and Nonlinear Mechanical Response

Our LAOS measurements have identified three distinct regimes of yielding in heterogeneous colloidal gels, where three qualitatively different intracycle responses are observed. We now present a comprehensive scenario by which the time-averaged microstructures observed for each of these regions can be reconciled with the nonlinear mechanical signatures observed during LAOS. We stress again that this scenario implicitly assumes that the time-averaged microstructure can be seen as a convolution of the instantaneous microstructures during the various intracycle processes (the elastic strain softening, viscoplastic behavior, yielding and flow). As such, in Region I the observed microstructure is dominated the elastic response, in Region II it evolves from primarily structures dominated by elastoplastic behavior to structures dominated by flow, and finally in Region III it is dominated by flow.

- Linear viscoelastic region ($\gamma_{r,0} < 0.16$)

At sufficiently small strain amplitudes the network structure of the material is only slightly perturbed by the shear forces, such that the gel network remains intact and the imposed strain produces a linear, predominantly elastic stress response, as can be seen by the storage modulus being over an order of magnitude higher than the loss modulus.

- Region I: onset of nonlinearity and pre-yielding ($0.3 < \gamma_{r,0} < 1$)

In this regime, we hypothesize that internal rupture and reconfiguration of bonds between clusters within the dense domains (ultimately resulting in compression of the gel network) weakens the elastic network due to nonlinear plastic deformation, resulting in intracycle strain softening. This is evidenced by a moderate decrease in G_R from its plateau value. Furthermore, G'' and $I_{3/1}$ increase strongly with increasing strain amplitude in this regime, signaling the onset of nonlinear behavior, as visible distortions of the waveform from its elliptical shape appear. Moreover, the compression of the dense domains requires the expulsion and drainage of interstitial fluid within the fractal microstructure in order to create additional large voids. This fluid motion causes a strong increase in the dissipated energy, which is evident in both the significant increase in G'' as well as the development of significant viscous behavior in the nonlinear waveform. The structural changes which are responsible for the nonlinear mechanical behavior of the gel mark this part of the strain sweep as a transition region to the highly nonlinear region II.

- Region II: broad yielding transition ($1 < \gamma_{r,0} < 20$)

In this region the most important yielding process occurs: the large-scale, dense domains of fractal agglomerates are compressed even stronger than in Region I (Fig. 11c). As the network structure is gradually disintegrated by the breakup of large dense domains during flow, the number of elastic junctions in the percolated structure that can be reformed at the end of a half-cycle is decreasing. This has severe consequences for the rheological properties. Due to the decreasing number of elastic junctions, the amount of elastic strain that the material can accumulate within the oscillation cycle is increasing slower than the applied strain amplitude. This is reflected in a sublinear increase of the yield strain (Fig. 10c). In addition the residual modulus G_R decreases markedly, proving a drastic weakening of the reversible network. In the flowing portion of the cycle, we observe a shear rate amplitude thinning behavior that is caused by the breakage of larger dense domains into smaller ones, resulting in the thixotropic behavior observed during the flowing portion of the intracycle response as a non-monotonicity in the waveform (Fig. 10a). This process homogenizes the domain size distribution and leads to an increase in the peak sharpness $\xi_{c2}\beta_{\max}$. As G' and G'' measure only the average elastic and viscous contributions to the stress, they obscure the fact that both elastic straining and viscous flow exist well before and after their crossover point. It is important to note that the flowing portion of the response occurs well before

the crossover in G' and G'', even though this is often used to define the yield point of the gel. This highlights the need for intracycle interpretations of LAOS in order to better characterize the yielding process.

- Region III: post-yielding flow ($\gamma_{r,0} > 20$)

For even higher strain amplitudes, the process of domain rearrangement and breakdown that is predominant in Region II is completed. From this point on, all of the intracycle measures including the transitions between various intracycle process as well as the residual modulus G_R become independent of strain-amplitude, and the intracycle yield strain and stress show a linear increase with strain amplitude. Thus, in every half-cycle only a small fraction of the applied strain is recovered by the elasticity of the network, and the mechanical response in this region is dominated by the yielded structure. The remaining strain is acquired through flowing of the now-suspended agglomerated domains. With the number of recoverable bonds between the dense domains minimized, the increasing strain amplitude results in further breaking of cluster-cluster bonds, but now within the suspended domains, and therefore some of the domains decrease in size even further. Thus the domain size distribution is broadened it this region, which is evident from a decrease of $\xi_{c2}\beta_{\max}$.

5 Conclusion

In this chapter we report several applications of large amplitude oscillatory shear (LAOS) to colloidal systems. LAOS is a technique that can induce structural changes in soft matter systems and was used here to characterize dilute emulsions, glassy suspensions and a colloidal nanoemulsion gel beyond the linear viscoelastic regime.

First we present some fundamental theoretical relationships needed for the quantitative analysis of LAOS data. Subsequently, we deal with technical aspects of the technique as we address sensitivity as well as reproducibility of LAOS experiments across various commercially available instruments. The main part concerns the application of LAOS to colloidal systems.

In the case of dilute emulsions constitutive modelling of a LAOS experiment based on the Batchelor theory and the Maffettone-Minale Model gave a relation between the nonlinear parameter ${}^{5/3}Q_0$ and structural properties of the emulsion, like the volume averaged droplet radius and the interfacial tension. This relationship was applied to a series of polymer blends to determine their average droplet radius or the interfacial tension.

A schematic model based on the Mode Coupling Theory was employed to model the nonlinear oscillatory shear stress of suspensions near the glass transition using model parameters that were determined from the linear viscoelastic moduli and the flow curve. The modeled stress waves were Fourier transformed and the intensities were compared to our experimental results from LAOS measurements

on a thermo-responsive core-shell latex. Qualitative agreement was found for the intensities of higher harmonics which became quantitative for high strain amplitudes.

The yielding of a colloidal nanoemulsion gel under LAOS flow was examined and full wave form analysis was performed. The extracted nonlinear waveform parameters G_R and γ_c and their strain amplitude dependencies were correlated to structural parameters obtained from simultaneous time-averaged SANS/USANS experiments. The combination of the two techniques revealed a broad yielding transition spanning almost a decade in strain amplitude and a hypothesis on the structural degradation of the material under LAOS could be proposed. Large-scale microstructure, on the order of hundreds or even thousands of particles, has been identified to be critical in determining the important processes governing the transition from solid-like to liquid-like behavior in heterogeneous colloidal gels.

References

1. Bae J-E, Lee M, Cho KS, Seo KH, Kang D-G (2013) Comparison of stress-controlled and strain-controlled rheometers for large amplitude oscillatory shear. Rheol Acta 52:841–857
2. Batchelor G (1970) The stress system in a suspension of force-free particles. J Fluid Mech 41:545–570
3. Brader JM, Siebenbürger M, Ballauff M, Reinheimer K, Wilhelm M, Frey SJ, Weysser F, Fuchs M (2010) Nonlinear response of dense colloidal suspensions under oscillatory shear: mode-coupling theory and fourier transform rheology experiments. Phys Rev E 82:061401
4. Brummer R (2006) Rheology essentials of cosmetic and food emulsions. Springer, New York
5. Carotenuto C, Grosso M, Maffettone PL (2008) Fourier transform rheology of dilute immiscible polymer blends: a novel procedure to probe blend morphology. Macromolecules 41:4492–4500
6. Chan HK, Mohraz A (2012) Two-step yielding and directional strain-induced strengthening in dilute colloidal gels. Phys Rev E 85:041403
7. Coussot P (2005) Rheometry of pastes, suspensions, and granular materials. Wiley, London
8. Dealy JM, Larson RG (2006) Structure and rheology of molten polymers. Hanser, München
9. Dodge JS, Krieger IM (1971) Oscillatory shear of nonlinear fluids I. Preliminary investigation. Trans Soc Rheol 15:589–601
10. van Dusschoten D, Wilhelm M (2001) Increased torque transducer sensitivity via oversampling. Rheol Acta 40:295–299
11. Franck A (2003) Measuring structure of low viscosity fluids in oscillation using rheometers with and without a separate torque transducer. Ann Trans Nord Rheol Soc 11, RH090
12. Giacomin AJ, Dealy JM (1998) Rheological measurement. In: Collyer AA, Clegg D (eds) Using large-amplitude oscillatory shear. Chapman Hall, London, pp 327–353
13. Giacomin AJ, Samurkas T, Dealy JM (1989) A novel sliding plate rheometer for molten plastics. Polym Eng Sci 29:499–504
14. Gibaud T, Frelat D, Manneville S (2010) Heterogeneous yielding dynamics in a colloidal gel. Soft Matter 6:3482–3488
15. Grace HP (1982) Dispersion phenomena in high viscosity immiscible fluid systems and and application of static mixers as dispersion devices in such systems. Chem Eng Commun 14:225–277
16. Grosso M, Maffettone PL (2007) A new methodology for the estimation of drop size distributions of dilute polymer blends based on LAOS flows. J Non-Newton Fluid 143:48–58

17. Guido S, Minale M, Maffettone PL (2000) Drop shape dynamics under shear-flow reversal. J Rheol 44:1385–1399
18. Helgeson ME, Moran SE, An HZ, Doyle PS (2012) Mesoporous organohydrogels from thermogelling photocrosslinkable nanoemulsions. Nat Mater 11:344–352
19. Hsiao LC, Newman RS, Glotzer SC, Solomon MJ (2012) Role of isostaticity and load-bearing microstructure in the elasticity of yielded colloidal gels. Proc Natl Acad Sci USA 109:16029–16034
20. Hyun K, Wilhelm M (2009) Establishing a new mechanical nonlinear coefficient Q from FT-rheology: first investigation of entangled linear and comb polymer model systems. Macromolecules 42:411–422
21. Hyun K, Wilhelm M, Klein CO, Cho KS, Nam JG, Ahn KH, Lee SJ, Ewoldt RH, McKinley GH (2011) A review of nonlinear oscillatory shear tests: analysis and application of large amplitude oscillatory shear (LAOS). Prog Polym Sci 36:1697–1753
22. Kim J, Gao Y, Hebebrand C, Peirtsegaele E, Helgeson ME (2013) Polymer-surfactant complexation as a generic route to responsive viscoelastic nanoemulsions. Soft Matter 9:6897–6910
23. Kim J, Merger D, Wilhelm M, Helgeson ME (2014) Microstructure and nonlinear signatures of yielding in a heterogeneous colloidal gel under large amplitude oscillatory shear. J Rheol 58(5):1359–1390
24. Kob W (2002) Supercooled liquids, the glass transition, and computer simulations. Les Houches 2002 Summer School—Session LXXVII
25. Koumakis N, Petekidis G (2011) Two step yielding in attractive colloids: transition from gels to attractive glasses. Soft Matter 7:2456–2470
26. Larson RG (1999) The structure and rheology of complex fluids. Oxford University Press, Oxford
27. Läuger J, Wollny K, Huck S (2002) Direct strain oscillation: a new oscillatory method enabling measurements at very small shear stresses and strains. Rheol Acta 41:356–361
28. Laurati M, Egelhaaf SU, Petekidis G (2011) Nonlinear rheology of colloidal gels with intermediate volume fraction. J Rheol 55:673–706
29. Macosko CW (1994) Rheology principles, measurements, and applications. Wiley-VCH, Weinheim
30. Maffettone P, Minale P (1998) Equation of change for ellipsoidal drops in viscous flow. J Non-Newton Fluid 78:227–241
31. Merger D, Wilhelm M (2014) Intrinsic nonlinearity from LAOStrain—experiments on various strain and stress-controlled rheometers: a quantitative comparison. Rheol Acta 53(8):621–634
32. Pal R (2006) Rheology of particulate dispersions and composites. CRC Press, Boca Raton
33. Pignon F, Magnin A, Piau J-M, Cabane B, Lindner P, Diat O (1997) Yield stress thixotropic clay suspension: Investigations of structure by light, neutron, and X-ray scattering. Phys Rev E 56:3281–3289
34. Pipkin AC (1972) Lectures in viscoelastic theory. Springer, New York
35. Rajaram B, Mohraz A (2011) Dynamics of shear-induced yielding and flow in dilute colloidal gels. Phys Rev E 84:011405
36. Reinheimer K, Grosso M, Hetzel F, Kübel J, Wilhelm M (2012) Fourier transform rheology as an innovative morphological characterization technique for the emulsion volume average radius and its distribution. J Colloid Interface Sci 380:201–212
37. Reinheimer K, Grosso M, Wilhelm M (2011) Fourier transform rheology as a universal non-linear mechanical characterization of droplet size and interfacial tension of dilute monodisperse emulsions. J Colloid Interface Sci 360:818–825
38. Rogers SA, Erwin BM, Vlassopoulos D, Cloitre M (2011) A sequence of physical processes determined and quantified in LAOS: application to a yield stress fluid. J Rheol 55:435
39. Shao Z, Negi AS, Osuji CO (2013) Role of interparticle attraction in the yielding response of microgel suspensions. Soft Matter 9:5492–5500

40. Siebenbürger M, Fuchs M, Winter H, Ballauff M (2009) Viscoelasticity and shear flow of concentrated, noncrystallizing colloidal suspensions: comparison with mode-coupling theory. J Rheol 53:707–726
41. Spalla O, Lyonnard S, Testard F (2003) Analysis of the small-angle intensity scattered by a porous and granular medium. J Appl Crystallogr 36:338–347
42. van der Vaart K, Rahmani Y, Zargar R, Hu Z, Bonn D, Schall P (2013) Rheology of concentrated soft and hard-sphere suspensions. J Rheol 57:1195–1209
43. Vermant J, Solomon MJ (2005) Flow—induced structure in colloidal suspensions. J Phys Condens Matter 17:187–216
44. Wilhelm M (2002) Fourier-transform rheology. Macromol Mater Eng 287:83–105
45. Wilhelm M, Reinheimer K, Kübel J (2012) Optimizing the sensitivity of FT-rheology to quantify and differentiate for the first time the nonlinear mechanical response of dispersed beer foams of light and dark beer. Z Phys Chem 226:547–567
46. Wilhelm M, Reinheimer P, Ortseiferer M, Neidhöfer T, Spiess HW (2000) The crossover between linear and non-linear mechanical behavior in polymer solutions as detected by fouriertransform rheology. Rheol Acta 39:241–246
47. Yu W, Bousmina M, Grmela M, Zhou C (2002) Modeling of oscillatory shear flow of emulsions under small and large deformation fields. J Rheol 46:1401–1418

Part II
Colloidal Systems with Solid Disperse Phase

Simulating the Restructuring of Colloidal Aggregates

Vincent Bürger, Eva Schlauch, Volker Becker, Ryohei Seto, Marek Behr and Heiko Briesen

Abstract Controlling the structural properties of colloidal aggregates is an active research topic for solid-liquid separation in the food, mining, and wastewater industry, is important for colloidal crystal synthesis, and has attracted attention progressively in the pharmaceutical industry for drug delivery vehicles. For such colloidal processing, the investigation of the restructuring behavior of colloidal aggregates by means of numerical methods has been the research subject for many years, utilizing diverse models for interparticle as well as hydrodynamic interactions. First, proper interparticle force models are required to explain the stability in the simulation of restructuring aggregates. External experimental observations of tangential forces between bonded colloidal particles and the capability of these bonds to support bending moments are

V. Bürger · H. Briesen (✉)
Chair for Process Systems Engineering, Technische Universität München, Freising, Germany
e-mail: heiko.briesen@tum.de

V. Bürger
e-mail: vincent.buerger@tum.de

V. Becker
Institute for Theoretical Physics, Otto von Guericke University Magdeburg, Madgeburg, Germany
e-mail: volker.becker@ovgu.de

R. Seto
Mathematical Soft Matter Unit, Okinawa Institute of Science and Technology, Okinawa, Japan
e-mail: setoryohei@me.com

E. Schlauch · M. Behr
Chair for Computational Analysis of Technical Systems, RWTH Aachen University, Aachen, Germany
e-mail: schlauch@cats.rwth-aachen.de

M. Behr
e-mail: behr@cats.rwth-aachen.de

M. Kind et al. (eds.), *Colloid Process Engineering*,
DOI 10.1007/978-3-319-15129-8_7

included in the proposed model. The resulting two particle contact model is set up with resistances against normal, sliding, and torsional displacement, as well as the newly introduced bending resistance. Second, we investigate two methods for the hydrodynamic interaction of a colloidal particle system in the zero-Reynolds-number regime, Stokesian dynamics and the finite element method. Calculating the long-ranged and many-body nature of hydrodynamic interactions in Stokes flow, Stokesian dynamics is very efficient, while the finite element method provides satisfactory precision of hydrodynamic forces on particles as well as the exact solution of a flow field in and around an aggregate. As the two methods complement each other for a comparison of particle dynamics, their application to restructuring aggregates is described, including numerical setup, origins of calculated particle drag forces, as well as applicability. Through coupling the models for hydrodynamic interactions and the particle contact, the restructuring of colloidal aggregates was finally investigated with the discrete element method. By means of simulating fractal aggregates suspended in shear flows, restructuring rates were studied by tracking mean structural parameters, i.e. the radius of gyration, now with the ability of investigating the full set of contact parameters to restructuring rates. Aggregate restructuring rates from simulations can be transferred to multi-scale formulations, such as involving population balance models, in order to improve the design and processing of colloidal systems.

Keywords · Colloidal aggregates · Stokesian dynamics · Discrete element method · Finite element method · Shear rate dependent structure · Tangential forces

1 Restructuring Aggregates in Flows: The Call for Simulations

Destabilizing a colloidal suspension to form aggregates has been investigated extensively [1, 2], while the next stage, restructuring and breakup mechanisms of these formed aggregates in flows, has been poorly understood [3]. This combined process has been investigated through experiments and early models, but the complexity of the hydrodynamics as well as the interaction forces has not been implemented to a satisfactory extend, with the major models either accompanied with some heavy limitation or set with an unfit approximation. Understanding this interplay between interaction and hydrodynamic forces is important, as controlling the microscopic aggregate structures influences macroscopic parameters such as sedimentation velocity, the diffusion constant, suspension viscosity, to name a few [4]. While the goal of modeling these aggregate mechanisms, with aggregates containing thousands of primary particles, is currently still an active research topic, we would like to present some findings and approaches that complement the research activities in this field.

Any approach to investigate colloidal aggregates in a fluid needs to take into account the cohesive forces between primary particles making up the aggregate as well as detailed structure. Early experiments attempted to represent aggregates

with a single dimensional parameters and then set up correlations of floc size and deformation rate of aggregates strained in flows [5, 6], or returning power-law relations between size of broken fragments and intensity of flow fields [3]. But these simple correlations were not satisfactory, and aggregates thus needed a more detailed structural look.

Some of the experiments looking at internal structure in restructuring aggregates is given by the work of Selomulya et al. [7, 8]. Here, small-angle static light scattering followed the temporal evolution of aggregate size and structure in shear flows. Although the researchers investigated both the aggregation and restructuring regimes, their investigation of the latter part is of primary interest here. They could link the inner structure to critical shear rates and proposed that these critical shear rates are dividing regions for which aggregates withstood the shear forces and regions where restructuring occurred. For more findings on studying aggregates restructuring or breaking due to flow, multiple experiments and approaches are available [9–15]. In an attempt to adapt such experimental findings and address this problem through modeling formulations, one actually needs to split up this problem into two parts—particle interaction models and hydrodynamics. A contact model needs to take into account the cohesive forces as well as breakage rates. An acceptable calculation of hydrodynamic forces is also required.

Determining the particle interactions within fully formed aggregates with complex structure is an intricate task and difficult to measure, yet is required for the setup of contact models. One can make use of small colloidal aggregates cohesively formed into simple shapes and study particle interactions made visible due to applied stress. Two experimental techniques come to mind: atomic force microscopy (AFM) and laser tweezer measurements. First, by experiments of Heim [16], the experiments they performed were taking silica spheres on the μm scale in simple chains, and compressing these chains under AFM tips. Surprisingly, their images show not just a simple sliding between particles; in fact their chains showed signs of rolling and bending motion.

These experimental findings are also evident from another group (Pantina and Furst [17]), making use of laser tweezing experiments. Their experimental setup is enabling them to hold single particles within chain aggregates in place, and applied forces orthogonal to the chain's alignment axis cause a deformation. The deformed chain did not, as expected, form a triangular shape, but for small deformations, the shape of a thin elastic rod. This indicates that the contact interactions between particles involves a rolling moment, a motion quite different from the sliding friction typically included in contact models. These experimental findings leave the following challenge: formulating a proper contact model describing these particle interactions.

For the hydrodynamic calculations required to describe restructuring events, models and simulations go hand in hand. Actually, tackling the restructuring of colloidal aggregates through simulations has plenty of history, though some of these are still to the dissatisfaction of the authors. Most notably were investigators [3, 18] who have simulated time evolutions of aggregates suspended in shear flows, though their contact models used facile restructuring of aggregates, with

the detailed aggregate structure not able to be linked to hydrodynamic properties. Indeed the modeling of particulate suspensions containing a large number of particles necessitates some degree of simplification due to high computational costs. An early approach was to model aggregates as porous spheres, with the Brinkman's equation extended from the Darcy's law of flow through porous media [5, 19, 20]. This aggregate is considered with a continuous porosity, which is perhaps valid for large and dense aggregates, but cannot be used for smaller, fractal aggregates where detailed structure explanation is very important.

Thus a trade off must be set, as perhaps the degree of simplification cannot be too high in order to quantify correct hydrodynamics. There exist several computational approaches to estimate the rheological behavior of particulate suspensions. Some approaches work with statistical factors written from a macroscopic point of view, others use micro-scale descriptions to parametrize their models. In population balance modeling, the particle number density is monitored over time and expressions are found for aggregate mass distributions before and after rate processes such as aggregation and fragmentation. There are many investigations on aggregates, such as flocculation in laminar and turbulent flows [21], or aggregation of particles under fluid motion [22]. A comparison with experiments has been undertaken by Soos et al. [11]. Other methods applied in the field of colloidal aggregates are molecular dynamics [23], as well as the method of reflections [24]. In a paper by Brasil et al. [25], for example, even a simple algorithm is given for the restructuring of aggregates.

If the detailed hydrodynamic phenomenona within an aggregate are then of interest, the Navier-Stokes equation with correct boundary conditions on particle surfaces needs to be applied. The application of the Stokes flow is quite established [26], yet the most complete approach is the use of the finite-element method (FEM), with only the size of aggregates being the restrictive part. An alternate source for an cost-effective calculation comes from Stokesian Dynamics (SD). In fact Bossis et al. [27] used their newly developed SD method for calculations of stress acting on aggregates. We would like to introduce both SD and FEM and compare/assess these two methods to the application of colloidal aggregates.

This work then attempts to highlight the theory and approaches going into both the contact model and the hydrodynamics and finally combines these to setup detailed simulations for the restructuring of colloidal aggregates. The organization is given as follows: Sect. 2 introduces particle interaction models, while Sect. 3 tackles the hydrodynamic calculations. Both of these are then joined in Sect. 4 and some insights into the simulation of the restructuring of colloidal aggregates can be provided. Finally, Sect. 5 gives some conclusions and outlook on the presented work.

2 Requirements of a Particle Interaction Model

The first part in understanding the restructuring process is the development of an interaction model between particles. We would like to propose a list of requirements of a two particle interaction model specifically for suitable simulation approaches:

- Attractive normal forces for long distances, repulsive force for short distances (or contact)
- Tangential forces able to support a bond bending moment
- A maximal supported bending moment and supported normal force per bond
- Experimental accessibility of parameters

Let us briefly revisit each. From the classical DLVO theory [28, 29] the first requirement is quite obvious and will not further be discussed for the sake of brevity. However, the investigation here is to understand aggregates restructuring, not initial formation, thus as long as particles are cohesively in contact, long range forces no longer play a role. Particles in contact can be seen as having a stable equilibrium distance.

The second requirement is actually worth to be discussed in detail, as the existence of tangential forces as well as associated moments are a necessary requirement for the stability of aggregates [30]. While tangential forces between particles were introduced by the pioneers of the discrete element method (DEM), Cundall and Strack [31], none of the interaction modes were able to explain moments. Tangential forces will be modeled as simple springs, with a maximum tangential force, or moment, that a bond can withstand. Each of these so-called interaction modes needs a critical force or moment where the bond may break; this is the third requirement. Experiments measuring the pull off force of two colloidal particles, until bond breakage, support this statement. Finally, the parameters require an accessibility from experiments, as the vigorous treatment of the bending resistance parameters will show us in the following section.

Few models have already tackled the contact dynamics. A short summary of these can be found in [30]. Most of the time, the approach is based on simple models, where, for example, sticking particles may roll, with bond breakage included. Further, Higahshitani et al. [3] took values from the classical DLVO theory, and for contact forces the model of Cundall and Strack was used. The model involves sticking and sliding friction but is not qualitatively able to describe bonding behavior of colloidal particles observed in experiments. Botet and Cabane [32] used a random distribution of springs on the surface of particles; this model is able to support both normal and tangential forces. While all of these models have their advantages, none of them is able to complete the set of all four requirements listed above. Yet experimental evidence by Pantina and Furst [17] shows that single bonds between bonded colloidal particles can take up bending moments, and none of the models except from Botet and Cabane can show this behavior within discrete element simulations. Thus we will summarize the phenomena seen in the experiments by Pantina and Furst and show the determination of contact model parameters from these experiments.

2.1 Experimental Observations

In the laser tweezing experiments by Pantina and Furst [17], a linear chain of polymethylmethacrylate (PMMA) particles were immersed in an aqueous salt solution. Aided by optical tweezers, terminal particles of the chain were held and a central

particle in the chain was pulled perpendicular to the chain direction. With only classic central forces acting between particles, a triangular equilibrium structure was expected. Yet the resulting chain structure was similar to that of a thin elastic rod:

$$\frac{y(x)}{F_{Bend}} = -\frac{1}{EI}\left(\frac{L}{4}x^2 - \frac{|x|^3}{6}\right) \tag{1}$$

where $y(x)$ is the deflection as a function of the position x, L is the length of the chain, and EI represents the product of the Young's modulus and the second moment of area. This phenomenon is clear evidence that supporting bending moments exist between colloidal particles.

The researchers further measured the bending rigidity κ defined as the constant of proportionality between the deflection δ of the chain aggregate and the applied force, $F_{Bend} = \kappa\delta$. It was found that $\kappa \propto L^{-3}$, as expected from Eq. (1). The bending rigidity is given as $\kappa = \kappa_0\left(\frac{a}{L}\right)^3$ with a being the particle radius and κ_0 the bending rigidity per bond. Experiments also provided a critical bending moment M_c. Forces applied above this value caused particle sliding and rearrangements. For possible explanations of the tangential forces in terms of Johnson-Kendall-Roberts theory for adhesive surfaces [33], Pantina and Furst [17] related single bond rigidity κ_0 related to the work of adhesion W_{sl} and the Young's modulus of the particles.

2.2 Tangential Force Model

The need for an improved tangential force model is justified from the above described experimental findings. For our approach we would like to propose a model similar to that by Cundall and Strack, which models a spring $\boldsymbol{\xi}_{ij}$ with rigidity k_t, initialized when two particles, i and j, get into contact [34]. In the original model by Cundall and Strack, the time evolution of the spring grows proportional to the relative tangential velocity from the contact point:

$$\boldsymbol{\xi}(t) = \int_{t_0}^{t} \mathrm{d}t' \mathbf{v}_t\left(t'\right) \Rightarrow \dot{\boldsymbol{\xi}} = \mathbf{v}_f \tag{2}$$

with t_0 being the time when two particles contact. The relative tangential velocity can be expressed from translational $\mathbf{v}$ and angular $\boldsymbol{\omega}$ components:

$$\mathbf{v}_t = \left(\mathbf{v}_j - \mathbf{v}_i\right)_t + a\left(\boldsymbol{\omega}_j + \boldsymbol{\omega}_i\right) \times \mathbf{n}_{ij} \tag{3}$$

$$\mathbf{n}_{ij} = \frac{\left(\mathbf{r}_j - \mathbf{r}_i\right)}{|\mathbf{r}_j - \mathbf{r}_i|}. \tag{4}$$

The projection of the relative velocity onto the tangential plane is denoted through t. If the tangential force component exceeds a critical value, which by Cundall and Strack is the Coulombic friction μF_n, the spring will be set to

$$\boldsymbol{\xi} = \mu \frac{F_n \boldsymbol{\xi}}{k_t |\boldsymbol{\xi}|} \tag{5}$$

where μ is the friction coefficient. This spring has to be mapped to the tangential plane perpendicular to $\mathbf{n}_{ij}$ for each time step. Tangential forces and torques for the ith and jth particle are:

$$\mathcal{F}_{i,t} = k_t \boldsymbol{\xi},\ \mathcal{T}_{i,t} = R_i \mathcal{F}_{i,t} \times \mathbf{n}_{ij}, \tag{6}$$

$$\mathcal{F}_{j,t} = -k_t \boldsymbol{\xi},\ \mathcal{T}_{j,t} = -R_j \mathcal{F}_{j,t} \times \mathbf{n}_{ij}. \tag{7}$$

With these equations, it can be seen that the model captures sliding and sticking friction, yet no bending moment between two bonded particles can be supported. The response to this challenge is a simple contact model able to support bending moments, still based on springs. When two particles contact, two thought rods are rigidly connected to one of the particle's center while reaching to the center of the second particle. A spring is now initialized between the end point of the rod and the center of the other particle, growing proportionally to the relative tangential velocity between the rods end points and the particle center. The evolution for the springs are given as:

$$\dot{\boldsymbol{\xi}}_{ij} = \left(\mathbf{v}_j - \mathbf{v}_i\right)_t - \left(\boldsymbol{\omega}_i \times \mathbf{n}_{ij}\right) 2a, \tag{8}$$

$$\dot{\boldsymbol{\xi}}_{ji} = \left(\mathbf{v}_i - \mathbf{v}_j\right)_t - \left(\boldsymbol{\omega}_j \times \mathbf{n}_{ij}\right) 2a, \tag{9}$$

with $\boldsymbol{\xi}_{ij}, \boldsymbol{\xi}_{ji}$ as the springs for the imaginary rods. This leaves the forces and moments acting on particles i and j as

$$\mathcal{F}_i = k_t\left(\boldsymbol{\xi}_{ij} - \boldsymbol{\xi}_{ji}\right), \quad \mathcal{T}_i = 2ak_t \mathbf{n}_{ij} \times \boldsymbol{\xi}_{ij}, \tag{10}$$

$$\mathcal{F}_j = k_t\left(\boldsymbol{\xi}_{ji} - \boldsymbol{\xi}_{ij}\right), \quad \mathcal{T}_j = -2ak_t \mathbf{n}_{ij} \times \boldsymbol{\xi}_{ji}. \tag{11}$$

Similarly to the Cundall-Strack model, both of these springs are mapped to the perpendicular plane to $\mathbf{n}_{ij}$ after each time step. As supported by experiments, the springs can reach a maximum elongation through the definition of a critical moment.

2.3 Parameter Determination

A major improvement of the above proposed simple contact model is the accessibility of the parameters for various colloidal systems. Here, we have two parameters: the spring stiffness k_t and the maximum spring length ξ_{max}. These parameters

can be determined by the laser tweezing experiments from the previous section, starting from the static shape of a linear chain of particles under bending stress:

$$\frac{y(x)}{F_{Bend}} = -\frac{1}{8a^3k_t}\left(\frac{L}{4}x^2 - \frac{|x|^3}{6}\right), \tag{12}$$

where L is the center-center distance of the first and the last particle in the chain. Comparing with Eq. (1), one sees that $EI = 8a^3k_t$. From the deflection of the chain, one can get $\kappa = 192(a/L)^3k_t$, and also $k_t = \frac{\kappa_0}{192}$. Also the model parameter for the tangential stiffness k_t is obtained from the measured value κ_0, while the value of ξ_{max} is required from specific measurements measuring the critical bending moment M_c. The bending torque acting on each particle is given by Eq. (11), and from the perpendicular $\mathbf{n}_{ij}$ and $\dot{\boldsymbol{\xi}}_{ij}$, ξ_{max} is expressed as

$$\xi_{max} = \frac{M_c}{2ak_t}. \tag{13}$$

Thus all parameters of the force model can be determined directly from experimental data. Again, while the model of Botet and Cabane [32] is also able to capture the same effects observed by Pantina and Furst [17], their model parameters seem to be more difficult to determine and their model eventually consumes much more computational resources to handle their multiple pins and springs on the particles' surfaces.

2.4 Method of Validation

As a validation step for the proposed tangential force model and its implication for restructuring aggregates, DEM simulations were set up incorporating the new model. DLVO forces between primary particles an aggregate were calculated from the experimental conditions of the laser tweezing experiments, including the particle radius of 0.735 μm and surface potentials of 40 mV. Drag forces and torques were taken from the Stokes formulas, and tangential contact parameters were chosen that correspond to different salt concentrations. An aggregate consisting of 200 primary particles suspended in a resting fluid was tracked temporally.

The indicative parameter for restructuring events was the mean number of neighbors for the aggregate. Using classical DLVO forces, without some sort of bending resistance, the aggregate structure started to collapse even in the resting fluid (see Fig. 1). This is due to the long range van der Waals forces, with bonded particles having the freedom to orient. However, it is known that aggregates even in moderate shear flows are often stable [7]: a resisting bending moment for fractal aggregates needs to be part of the contact model. Without the appropriate tangential force model, the number of neighbors grows continuously; on the other hand the aggregate compaction is negligible when the tangential force model is used.

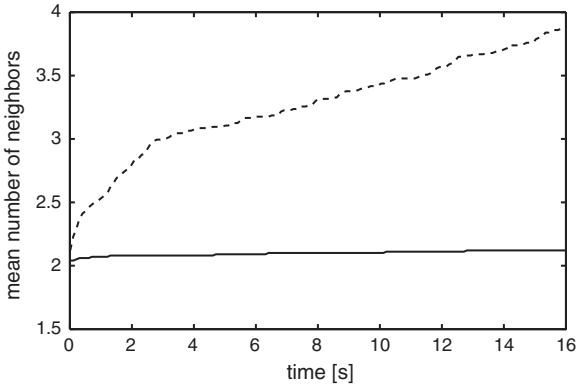

Fig. 1 Time evolution of the average number of neighbors of a given aggregate in a resting fluid. When considering DLVO forces only (*dashed line*) the number of neighbors increased without applying shear flow. Using the tangential-force model (*solid line*) keeps the structure stable

At this point we used an experiment using a deformation of only simple structures and determined parameters for a contact model required to describe colloidal interactions within much more complex structures. We would like to point to the original paper by Becker and Briesen [30] for more details on the contact model derivation, but some extensive modeling was performed with the new contact model approach [34, 35]. These works also incorporated a torsional element to account for all degrees of freedom for two particles in 3-D space. More importantly, the effects of the hydrodynamics were checked and it became quite clear that using the Stokes formulas, valid for colloids in the dilute limit, was a big limitation when considering the close nature of colloidal particles within aggregates. A proper hydrodynamic method is thus required.

3 Modeling Hydrodynamic Interactions

Besides the choice for a proper contact model, a major part when investigating the behavior of restructuring aggregates is a valid hydrodynamic method. Two simulation methods frequently used for hydrodynamic forces and torques on particles within aggregates, namely Stokesian dynamics and the finite element method, are compared and assessed [36]. The Lattice Boltzmann method was also included in the original comparison, yet details are left out here due to its many similarities to FEM. To our knowledge, this comparison is the most comprehensive study on comparing simulation strategies for colloidal aggregates. Although this comparison still considers rigid aggregates, it should be useful for the selection method of appropriate simulation scheme, with its inherent limitations.

As a first step toward a model of mutual interaction of fluids and aggregates, the steady-state condition, with aggregates fixed in space, is used, where forces and torques now can be determined with satisfactory accuracy. For aggregate shapes to be compared, two different samples were chosen. In their work, Harshe et al. [37] investigated four different sorts of aggregates characterized by their

fractal dimension and compared these to equivalent ellipsoids with the same principal moments of inertia. As we consider only aggregates with few primary particles, the determination of fractal properties such as fractal dimension is not straightforward. Thus, we consider two types of aggregates, openly structured and compact, with varying primary particle number.

3.1 Methods

To quickly summarize the different approaches valid for particles immersed in flow conditions: SD obtains the drag forces directly from particle positions and general flow information while FEM calculates the complete flow field and its effect on the particles.

The behavior of continuum fluid flow is governed by the well-known Navier-Stokes equations. In the low-Reynolds-number regime, where the kinematic fluid viscosity ν is large compared with the characteristic velocity of the flow u and inertia terms can safely be neglected, the Stokes equations can be deduced from the Navier-Stokes equations. The particle Reynolds number is defined for the particle radius a as:

$$Re_{\mathrm{p}} = \frac{ua}{\nu}, \tag{14}$$

and approaches zero for this investigation. Therefore, the Stokes equations can be summarized as follows: On a bounded domain Ω, obtain a velocity $\boldsymbol{u}$ and a stress $\boldsymbol{\sigma}$ such that:

$$-\nabla \cdot \boldsymbol{\sigma} = 0 \ \text{ in } \Omega \tag{15}$$

$$\nabla \cdot \boldsymbol{u} = 0 \text{ in } \Omega \tag{16}$$

$$\boldsymbol{u} = \boldsymbol{u}_{\mathrm{D}} \ \text{ on } \partial\Omega_{\mathrm{D}} \tag{17}$$

$$\boldsymbol{n} \cdot \boldsymbol{\sigma} = 0 \ \text{ on } \partial\Omega_{\mathrm{N}}, \tag{18}$$

with boundary values of $\mathbf{u}_{\mathrm{D}}$ given for the Dirichlet portion of the boundary ($\partial\Omega_{\mathrm{D}}$), and normal stresses given for the Neumann portion ($\partial\Omega_{\mathrm{N}}$), where $\partial\Omega = \partial\Omega_{\mathrm{N}} \cup \partial\Omega_{\mathrm{D}}$. Dirichlet boundaries for the fluid flow will be considered for the colloidal particles. The kinematic viscosity is related to the dynamic viscosity by the fluid density: $\nu = \eta / \rho$.

Finally, the system of equations is closed by the choice for the stress tensor $\boldsymbol{\sigma}$ for a Newtonian fluid:

$$\boldsymbol{\sigma} = -p\boldsymbol{I} + \eta\left(\nabla \boldsymbol{u} + \nabla \boldsymbol{u}^{\mathrm{T}}\right), \tag{19}$$

with $\boldsymbol{I}$ denoting the identity matrix in R^3. With the Stokes equations at hand, we now introduce the computational methods to solve the governing equations. FEM

uses a discretization of the spatially bounded domain, while the SD method is based on the solution for particle drag and torque within an infinite fluid domain.

3.1.1 Stokesian Dynamics

Calculating hydrodynamic interactions is approached by using SD, providing relationships between motion and hydrodynamic stress acting on particles in the Stokes regime. The SD method has been suggested in the 1980s [38, 39] and adopted, adapted and improved by many others since [27, 40–44]. SD is a popular method for problems concerning colloidal aggregates, e.g., hydrodynamic properties of rigid clusters [4, 37, 45] and restructuring/breakage [15, 46]. It itself is based on the solution of the Stokes equations for a point force given by the Oseen tensor. The flow disturbance caused by the particles can be formulated as a superposition of point forces positioned on the particle surfaces. This superposition is given in an integral form making use of the linearity of the Stokes equations and with the assumption that the particles are rigid spheres. A multipole expansion is applied to the obtained integrals such that linear relations between the force moments and the velocity moments are obtained [43], typically truncated at first order. Since only integrals over particle surfaces are evaluated, the method is fast and efficient.

At the heart of Stokesian dynamics lies the information of the applied flow field, be it uniform or shear, and expressing the flow field at any point in space $\mathbf{u}^\infty(\mathbf{r})$:

$$\mathbf{u}^\infty(\mathbf{r}) = \boldsymbol{U}^\infty + \boldsymbol{\Omega}^\infty \times \mathbf{r} + \boldsymbol{E}^\infty \mathbf{r}. \tag{20}$$

with $\mathbf{U}^\infty$ being the translational velocity, $\boldsymbol{\Omega}^\infty$ vorticity, and $\boldsymbol{E}^\infty\mathbf{r}$ the rate of strain. In order to evaluate the hydrodynamic interaction in shear flows, the force-torque-stresslet (FTS) version of SD has been applied [46].

For shear flows with shear rate $\dot{\gamma}$, the nonzero elements of the matrices are $\Omega_y^\infty = \dot{\gamma}/2$, and $E_{xz}^\infty = E_{zx}^\infty = \dot{\gamma}/2$. This, in return, evaluates to three hydrodynamic components acting on one particle i as the drag force $\mathcal{F}_H^{(i)}$, torque $\mathcal{T}_H^{(i)}$, and the stresslet $\mathcal{S}_H^{(i)}$. The force and torque come from translational and rotational flow fields, while the stresslet is the symmetric part of the first-order moment of force exerted by the fluid on the particle (sphere). Hydrodynamic interactions (the drag forces $\mathcal{F}^{(n)}$, torques $\mathcal{T}^{(n)}$ and stresslets $\mathcal{S}^{(n)}$ acting on a particle n) are then given as a linear combination of the translational velocities $\boldsymbol{U}^{(n)}$ and rotational velocities $\boldsymbol{\Omega}^{(n)}$ from the background flow $\boldsymbol{U}^\infty(r)$, of all particles $n = 1, \ldots, N$ and the rate-of-strain $\boldsymbol{E}$. These linear combinations for all particles are given in matrix form:

$$\begin{pmatrix} \mathcal{F} \\ \mathcal{T} \\ \mathcal{S} \end{pmatrix} = \mathrm{R} \begin{pmatrix} \boldsymbol{U} - \boldsymbol{U}^\infty \\ \boldsymbol{\Omega} - \boldsymbol{\Omega}^\infty \\ -\boldsymbol{E}^\infty \end{pmatrix}, \tag{21}$$

with each of the vectors consisting of $11N$ elements with $\mathcal{F} = (\mathcal{F}^{(1)}, \ldots, \mathcal{F}^{(N)})$ and analogously for the other quantities. Since the stresslet $\mathcal{S}^{(n)}$ has 5 independent

elements, the size of the grand resistance matrix R is $11N \times 11N$. Thus only particle positions and rotations together with the fluid information need to be defined and with SD the forces, torques, and the stresslet can be evaluated. A second option is the inverse version, where the so-called mobility matrix $\mathcal{M}$ requires the forces and torques on particles, and will give both the translational and rotational motion:

$$\begin{pmatrix} \boldsymbol{U} - \boldsymbol{U}^{\infty} \\ \boldsymbol{\Omega} - \boldsymbol{\Omega}^{\infty} \\ -\boldsymbol{E}^{\infty} \end{pmatrix} = \mathcal{M} \begin{pmatrix} \mathcal{F} \\ \mathcal{T} \\ \mathcal{S} \end{pmatrix} \tag{22}$$

Except for the doublet case ($N = 2$), the lubrication correction [27] is not used because relative velocities are zero in rigid clusters, yet this correction in the case of the doublet gives the exact solutions [47, 48]. For this work, we have used a numerical library developed by Ichiki [49] with a conjugate-gradient iterative method used to improve computational performance [43].

3.1.2 Finite Element Method

FEM, a discretization method to solve partial differential equations such as those governing the fluid as a continuum, can be applied with the assumption that particles of sizes above several microns are immersed in a fluid [50]. More importantly, the Navier-Stokes equations may be replaced by the Stokes equations as a particle Reynolds number smaller than 0.1 is considered. So, FEM provides a way to investigate full flow fields of fluid around a static or moving aggregate for steady or temporally changing flow. Typically, the domain volume is discretized by using a computational mesh on which the solution is obtained in form of nodal vectors. In contrast to SD, particles of arbitrary shapes can be simulated.

With Eqs. (15–18) solved in a discrete form, a discretization was chosen based on the stabilized Galerkin/Least-Squares variational formulation, using an equal-order interpolation for the velocity and the pressure [51, 52]. The solver is parallelized, allowing for efficient simulations on highly resolved unstructured meshes [53], and the solution of the discretized weak form is known to converge to the solution of the original Stokes equations with finer and finer discretizations of the domain.

As the forces $\mathcal{F}^{(n)}$ and torques $\mathcal{T}^{(n)}$ acting on the nth particle immersed in the Stokes flow are the parameters of interest, surface integrals of the stress tensor have to be evaluated in the following form:

$$\mathcal{F}^{(n)} = \int \left(\boldsymbol{\sigma} \cdot \widehat{\boldsymbol{n}}\right) \mathrm{d}\Gamma^{(n)} \tag{23}$$

$$\mathcal{T}^{(n)} = \int \boldsymbol{r}^{(n)} \times \left(\boldsymbol{\sigma} \cdot \widehat{\boldsymbol{n}}\right) \mathrm{d}\Gamma^{(n)}, \tag{24}$$

where $\Gamma^{(n)} \subset \partial\Omega_D$ is the surface of the nth particle with the unit outer normal vector $\widehat{\boldsymbol{n}}$ and $\boldsymbol{r}^{(n)}$ denotes the distance vector to the particle center of mass.

3.2 Simulation Cases

We now would like to set up a proper comparison between these two different methods. Several aspects have to be predefined to reduce the number of parameters. For this reason we introduce a set of aggregate samples, dimensionless units for drag and torque values, and domain and boundary descriptions.

3.2.1 Samples of Colloidal Aggregates

Although computational fluid dynamics (CFD) methods like FEM are in principle capable of dealing with arbitrarily shaped particles, the inherent limitation of SD necessitates the choice of spherical particles for a comparative study. Particles have small gaps between surfaces (gap-to-radius ratio of 0.0003), allowing for an easier mesh generation. Our method validation includes simple structures also chosen by Binder et al. [54]—a doublet of two spherical particles and a 7-particle star.

The small aggregates considered in our studies of not more than 50 primary particles, formed by the classical mechanisms (diffusion-limited, reaction-limited), are rendered indistinguishable. Instead diffusion-limited and Eden-type clusters [4] have been chosen. A diffusion-limited mechanism results in openly structured clusters while Eden-type clusters are randomly built and highly compact. Eden-type clusters are only compact as single particles diffuse into the inner core, and a high number of primary particles making up a very compact cluster is required, too high for accurate FEM simulations. Very large Eden-type clusters were thus created and only the innermost particles were extracted, appropriately named "core-Eden" clusters. Aggregate sizes were chosen as $N = 8, 20, 50$, and each of these six choices, set by aggregate type and number of primary particles, consisted of ten samples.

3.2.2 Computational Domains

The computational domain for the SD simulations differs from FEM in the fact that for SD, particles are immersed in an infinite fluid volume. Clusters are positioned at the origin and the fluid extends equally far into all three spatial directions. For the discrete cases, the computational domain has to be truncated as discretizing an infinite domain with a finite number of elements is not possible.

A 3-dimensional simplex (tetrahedral) mesh, generated by a Voronoi/Delaunay algorithm, was used for discretization of the domain for FEM calculations. First, inserted nodes with a given distribution inside the computational domain helped

generate the FEM mesh, then elements were created by a Delaunay triangulation algorithm. For both parts, the meshes are locally refined to accurately resolve complex aggregates. This also means that complex aggregates have a coarser grid in regions with lower velocity gradients.

Prior to the full simulations, the influence of the domain discretization was checked. A simple test case of a single sphere immersed in a uniform fluid flow was designed, and the drag force on the surface was calculated as a function of refinement of the mesh size. The mesh refinement is accepted if the change in drag force induced by the refinement is smaller than 1 %. The ratio of domain edge length to sphere diameter was 15.

3.2.3 Boundary Conditions

Finally, boundary conditions need to be set. Commonly used conditions are as follows: on each particle's surface the fluid velocity is set to zero, indicating a no-slip boundary condition. FEM uses finite domains for the computations and hence adequate boundary conditions have to be chosen for artificial walls. Although, in principle, the finite domain has an influence on the boundary conditions, their disturbance in the flow field can be neglected if one assumes that the walls are located far enough from particles. Then the values of the imposed flow at the position of the artificial walls can be chosen as the boundary flow velocities.

From a relative viewpoint of the aggregate, the walls will introduce a flow field disturbance. Unfortunately, this disturbance drops slowly with the reciprocal of distance and cannot be neglected for smaller domain sizes. The choice for domain size and the influence of flow boundary values on particle drag and force has been investigated in detail in previous work [34], yet the following approach is taken: For a ratio of domain to particle size of 60, the flow solution calculated by FEM and the background flow velocity were subtracted, showing deviations caused by walls and aggregates. This shows that in the uniform flow case, the flow is affected rather drastically and requires artificial enhancement, while in the shear-flow case, the flow profile is disturbed only in the vicinity of the aggregate.

3.3 Comparison

The need for introducing both SD and FEM stems from the fact that the interaction between fluid and particles have to be considered as a two-way interaction (see our previous work on aggregates [34]). On one hand, the fluid flow is influenced by the presence of particles while on the other hand the particles experience forces and torques due to the surrounding flow. Although FEM allows us to observe the flow field, both methods can evaluate the hydrodynamic interactions on aggregates.

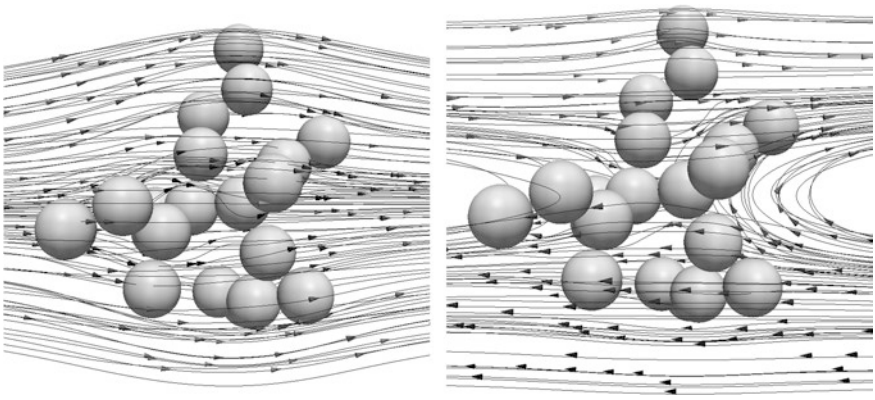

Fig. 2 Streamlines in the neighborhood of a 20-particle aggregate (open structure) for (*left*) uniform flow and (*right*) shear flow; arrows point in the direction of the flow. Data taken from the FEM results. Reprinted from [36] with kind permission from Elsevier

3.3.1 Particle Influence on Flow Field

Though from SD one can qualitatively derive flow strength from particle forces and torques, with FEM one solves the flow field directly and with a very high precision. In case of an aggregate immersed in an fluid, the flow is deflected by the particles and velocity and pressure fields adapt to the new geometry. Regions with high vorticity are of interest, as for these the drag on primary particles is increased. For a back flow region near the center of the aggregate immersed in a shear flow, the flow velocity as well as the pressure are negligibly small that no drag is expected for primary particles.

Primary variables of the fluid equations are fluid velocity and pressure. For uniform flow, high pressure values appear upstream of the aggregate, while behind the aggregate a pressure drop is actually observed (Fig. 2). For the shear flow, a more complicated pattern emerges, reminding of a quadrupole field: high pressure values are where the flow attacks the aggregate surface, and low pressure values are found in flow shadows. From the pressure distributions one can then make a clear distinction between the two flow fields: in the uniform flow field the dominant entity is the fluid drag force, while in the shear flow the fluid torque is the dominant entity.

3.3.2 Fluid Drag and Torque Acting on Particles in Flow Fields

At this point we are able to compare the drag forces for the different simulation methods. First, we would like to show the difference between the two methods for a small particle ensemble, namely two doublets and a 7-particle star. Results are given in Tables 1 and 2 for both uniform and shear flow, respectively. For two particles the resistance matrix is known exactly and the solution as calculated by SD

Table 1 Total drag values on three different shapes in a uniform flow

	SD	FEM	FEM/SD
Doublet (para)	$1.29e+00$	$1.26e+00$	0.98
Doublet (ortho)	$1.45e+00$	$1.41e+00$	0.97
7-particle star	$2.70e+00$	$2.34e+00$	0.87

Units are normalized. Partially reprinted from [36] with kind permission from Elsevier

Table 2 Total torque values on three different shapes in a shear flow

	SD	FEM	FEM/SD
Doublet (para)	$1.01e+00$	$0.98e+00$	0.97
Doublet (ortho)	$3.97e+00$	$3.86e+00$	0.97
7-particle star	$1.24e+01$	$1.18e+01$	0.95

Units are normalized. Partially reprinted from [36] with kind permission from Elsevier

can be considered as exact. It shows that the FEM results agree very well for the doublets in both types of flows, while the deviation becomes slightly more significant for the 7-particle stars.

Having established the comparison for small structures also presented in the works of Binder et al. [54], we extend our comparison to actual aggregates. For particles within aggregates, average drag values for SD and FEM for a uniform flow environment are calculated by:

$$\langle \mathcal{F}_x \rangle = \left\langle \sum_{n=1}^{N} \mathcal{F}_x^{(n)} \right\rangle, \quad N \in \{8, 20, 50\}, \tag{25}$$

where averaging (denoted by the brackets) was performed for the ten samples for each type of aggregate. Similarly to average force values, total torque values obtained by the methods for compact and open aggregates were calculated by:

$$\langle \mathcal{T}_y \rangle = \left\langle \sum_{n=1}^{N} \left(\mathcal{T}_y^{(n)} + z^{(n)} \mathcal{F}_x^{(n)} - r_x^{(n)} \mathcal{F}_z^{(n)} \right) \right\rangle, \quad N \in \{8, 20, 50\}. \tag{26}$$

$\langle \cdot \rangle$ denotes again the average over the 10 aggregate samples.
Results for drag forces between open and denser structures as a function of aggregate size are given in Fig. 3. For smaller aggregates with $N = 8, 20$, we see a very good agreement between SD and FEM, while for $N = 50$, slight deviations can be seen for mean drag forces. Detailed torque comparisons in shear flows as well as drag force distributions within the aggregates can be found in the original paper [36] but these tend to agree with the trend of increasing deviations for larger aggregates. For our simulations using non-rigid aggregates, we use $N = 64$ primary particles for SD, which is still in a reasonable range to make sure calculated hydrodynamics can be validated by FEM.

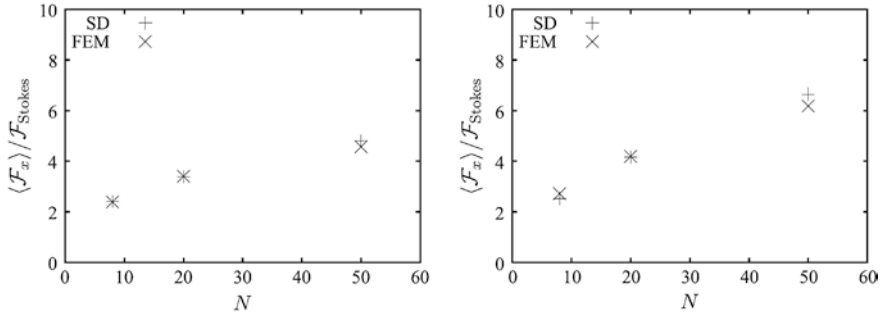

Fig. 3 Comparison of the mean aggregate drag values in uniform flow for compact (*left*) and open (*right*) aggregates. Reprinted from [36] with kind permission from Elsevier

While the torque is the representative parameter to investigate for shear flows, the drag force distribution inside the aggregates can give an overview of strain within aggregates [55]. Since we are in the Stokes regime, higher forces appear in regions with higher flow velocities, and the force and velocity distributions almost follow linearly throughout the structure. While this effect is most pronounced for small aggregates ($N = 8$), for the 20- and 50-particle aggregates, deviations can be seen in the center of the aggregates, with the force-velocity scaling no longer following a linear relationship. Particles are shielded by the outer particles from the fluid flow through a flow-shielding effect. Both methods show good agreement of this behavior, but rougher approximations for the estimation of hydrodynamics, namely the free-draining-approximation, are not detailed enough to explain this effect.

A few words should be mentioned about the computational costs. The bottle neck calculation of SD is the creation of the resistance or mobility matrix. For discrete simulations (in terms of the grid), a criterion for convergence of the iterative processes needs to be set. Typically incorporated in the FEM software, a solver applies a set algorithm to achieve this. Here, the solver uses the generalized minimal residual method (GMRES) and one nonlinear iteration corresponds to one convergence step. Usually FEM simulations are not performed on single cores and require approximately a magnitude of time more effort for particle drag forces and torques: however a quantitative comparison is misleading due to the serial (SD) versus parallel (FEM) architecture. The applicant has to make the decision whether a fully resolved fluid flow or an efficient method for the drag forces on particles is wanted.

With a good agreement of the forces and torques on the aggregates established, one has to keep in mind that these calculations were done with rigid aggregates. These types of aggregates are not allowed to restructure as limitations exist with the FEM method to solve the equations for movable boundary parts. The currently only effective way to investigate movable primary particles within large ($N \geq 50$) aggregates is with SD. We will thus combine a properly chosen contact model and hydrodynamic calculations done with SD with the following investigation on the simulation of restructuring of colloidal aggregates.

4 Restructuring of Colloidal Aggregates

Now that two methods for the calculation of hydrodynamic interactions are available, simulations using DEM for the restructuring of colloidal aggregates will be presented. As we will be focusing on the restructuring of aggregates, the formation and theory behind various types of aggregates will not be discussed here, but can be found in the literature available for details of fractal nature [4, 56]. Fractal clusters generated by the reaction limited hierarchical cluster-cluster aggregation were used as an initial configuration. The fractal dimension is $d_f \approx 2$. Small clusters with N = 64 were investigated, and since the aggregates are random, 50 independent clusters were prepared and simulated using the same conditions. The given simulations study aggregates in shear flows. Although theoretical and not often the cause for primary aggregate restructuring, the shear flow brings in the rotational motion that aggregates undergo.

At the heart of the DEM simulation lies the relationship of hydrodynamic forces and moments $\mathcal{F}_H, \mathcal{T}_H$ on particles in an interplay with particle contact forces and moments $\mathcal{F}_P, \mathcal{T}_P$, both incorporated in Newton's equations of motion:

$$m\frac{d\boldsymbol{U}}{dt} = \mathcal{F}_P + \mathcal{F}_H,\ I\frac{d\boldsymbol{\Omega}}{dt} = \mathcal{T}_P + \mathcal{T}_H \tag{27}$$

where m and I are the mass and moment of inertia. Since inertia terms diminish for particles with diameters on the $1\mu m$ scale and smaller, the equations reduce to the overdamped equations of motion:

$$\mathcal{F}_P + \mathcal{F}_H \approx 0,\ \mathcal{T}_P + \mathcal{T}_H \approx 0. \tag{28}$$

The hydrodynamic parts are solved using SD as presented in the earlier section, but for the contact model, we would like to introduce a slightly different approach.

4.1 Extension of the Contact Model

While the earlier proposed tangential force model provides a framework for the discrete element simulations for colloidal restructuring (see Becker and Briesen [35]), a similar yet slightly adapted contact model was used. This model is based on the same logic as the previous tangential force model, and features the following qualifications: Tangential forces and bending moments, with bond rigidity and bond-breakage effects, while the parameters should be easily accessible from experiments, and incorporation into simulations should not be limiting.

For two particles interacting cohesively, we set up four types of degrees of freedom: normal, sliding, bending, and torsional displacements [46, 57]. To keep the model simple, force-displacement relationships are used for hindering motion for these degrees of freedom, with a spring constant associated with each of them. The model further assumes monodisperse hard sphere particles. These can be modeled

for the four modes for particles with radius a in a three dimensional space in terms of forces as well as moments. Each particle i and j has the orientation $\mathbf{r}^{(i)}$ and $\mathbf{r}^{(j)}$, and $\mathbf{n}^{(i,j)} \equiv \left(\mathbf{r}^{(j)} - \mathbf{r}^{(i)}\right) / r^{(i,j)}$, with $r^{(i,j)}$ being the center to center distance. We obtain

$$\mathcal{F}_N^{(i,j)} = k_N \left(r^{(i,j)} - 2a\right) \mathbf{n}^{(i,j)}, \tag{29}$$

for the normal force and

$$\mathcal{F}_S^{(i,j)} = k_S \mathbf{d}^{(i,j)}, \tag{30}$$

for the sliding force, where $\mathbf{d}^{(i,j)}$ represents a sliding displacement vector a projection of the deviation of so-called contact point indicators ($\xi^{(i,j)}$, see Fig. 4), introduced as soon as particles get into contact, onto the perpendicular bisector between two particles.

The bending mode involving a rolling-type rotation, quantified with an angle between the contact-point indicators, is modeled as:

$$\mathcal{T}_B^{(i,j)} = k_B a^2 \phi^{(i,j)}, \tag{31}$$

with $\phi^{(i,j)}$ describing the bending angle vector. Finally, the torsion is given as a rotational displacement around the normal direction between the two particle centers. For this description, we use torsion indicators $\eta^{(i,j)}$ standing perpendicular to the center-to-center direction. We can relate these to torsional angle vectors $\theta^{(i,j)}$. The torsional moment is described as

$$\mathcal{T}_T^{(i,j)} = k_T a^2 \theta^{(i,j)}. \tag{32}$$

So for each degree of freedom of motion, we have spring constants describing the stiffness of each mode for slight displacement or rotation relative to each other. To sum up forces and moments between particle i and j, we write:

$$\mathcal{F}_P^{(i)} = \sum_j \left(\mathcal{F}_N^{(i,j)} + \mathcal{F}_S^{(i,j)}\right), \tag{33}$$

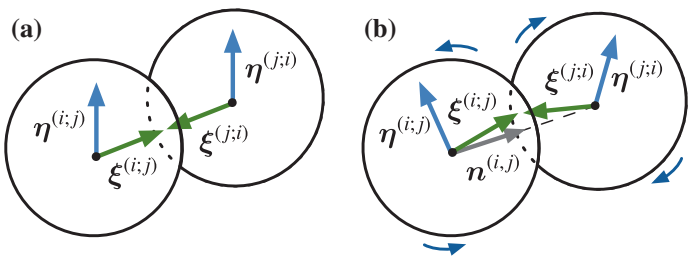

Fig. 4 Contact model used: Contact point indicators ξ, torsion indicators η, and normal vector indicating the center-to-center direction $\mathbf{n}$, for the stress-free state (**a**) and stressed state (**b**). Reprinted from [46] with kind permission from Springer

$$\mathcal{T}_P^{(i)} = \sum_j \left(a\mathbf{n}^{(i,j)} \times \mathcal{F}_S^{(i,j)} + \mathcal{T}_B^{(i,j)} + \mathcal{T}_T^{(i,j)} \right). \tag{34}$$

Interactions are set pairwise, so for a two particle system, the forces and moments are equal and opposite. As well as for the prior contact model, each mode can break and dissipate the energy held up in bonds. The corresponding parameters are two critical forces and critical moments, F_{Nc}, F_{Sc} and M_{Bc}, M_{Tc} respectively. If particles remain in contact, a new bond is created. For a complete description of a particle system of hard sphere particles in contact, a set of only two parameters per contact mode must be found. Resistances associated with all degrees of freedom between two particles are then given through eight contact model parameters and invites comparison to other particle contact formulations (see Tomas [57]). The parameters should be available from experiments where networks of particles in contact are strained, namely from confocal laser scanning microscopy methods [58].

While the exact parameters for this four-modal contact model are not known, some estimates can be taken from the literature. For example, Dominik and Tielens [59] show that the critical normal and tangential forces, F_{Nc} and F_{Sc} respectively, are typically much greater than the scaled critical bending and torsional moments, M_{Bc}/a and M_{Tc}/a. As the normal and sliding resistances are on the order of 10^2 greater, the primary restructuring phenomena actually involve bending and torsional modes. Input parameters of simulations are then only the associated spring constants and the critical moments. For our specific simulation setup, we set spring constants as the same value for bending and torsional resistances, and tenfold this value for normal and sliding modes: $k_N = k_B$; $k_N = k_S = 10k_B$. Values for the critical bending and torsional moments M_c are set to 1 % of the particle's radius.

4.2 Simulation Setup

For the hydrodynamic aspect, a slightly different concept is used as compared to simulation studies available (c.f. [60]). Typically, a very abrupt shear rate is applied to aggregates, causing three distinct behaviors: rotation without restructuring, onset of restructuring, and breakage. In this study we would like to investigate the first two behaviors: restructuring and consolidation behavior. To be able to see this effect, the shear rate is applied in a stepwise manner, holding a shear rate for a predetermined number of steps before increasing it. Inputs for such a setup are given in Table 3. The advantage is that when working such a shear rate program, at first we expect rigid aggregate rotation (of course only for proper contact model parameters), at some point the onset of restructuring, a consolidation behavior, and finally the fast rotation of very consolidated structures.

Lubrication corrections are typically an important point to consider when using SD. While the far field interactions are satisfactory, the near field approximation

Table 3 Parameters of imposed flow

	Units	FDA	SD
Initial shear rate	$6\pi\eta_0 a^2\dot{\gamma}/F_0$	0.003	0.001
Final shear rate	$6\pi\eta_0 a^2\dot{\gamma}/F_0$	15.9	10
Number of steps	–	28	30
Time interval factor	–	20	20

Number of steps dictates the stepwise increase of shear rate and the time interval factor represents the amount of time a single shear rate is applied. F_0 is the critical force for bending and torsional breakage

is often taken as the exact solution of forces between two spheres. However for rigid aggregates it is possible to omit these lubrication corrections as particles do not have relative motion to each other. While this assumption does not strictly hold true for the study of restructuring, the corrections will have negligible effects if the relative motion of two particles is small enough. We omit lubrication corrections for these reasons, and the SD method seems to correctly calculate drag forces on particles, as validated with FEM. A more detailed discussion on lubrication corrections can be found in the literature [4, 27, 37].

In order to speed up the simulations, the concept of reusing of the mobility matrix is introduced. The construction of this matrix, linking particle motion and hydrodynamics, is a bottle neck of the simulation. This operation, however, is based on particle positions, and as long as the particle positions remain identical for each iterative step [46]. Also the accuracy of the numerical method has no primary importance for the overdamped motions (see Sect. 3.1.1), therefore the explicit Euler method scheme was used to integrate the differential equations with a fixed discretized time step. To compare the SD calculations with a method that can handle non-rigid aggregates, the free-draining approximation (FDA) is shown as a reference, although this approximation is known to overestimate drag forces [34].

4.3 Compaction

A simple indication of compaction due to flow strength is required. For this matter the radius of gyration is used, given by

$$R_G^2 \equiv \frac{1}{N}\sum_{i=1}^{N}(\mathbf{r}^{(i)} - \mathbf{r}_0)^2 \tag{35}$$

around $\mathbf{r}_0$, the center of mass of the cluster. The radius of gyration is often related to the hydrodynamic radius of fractal clusters and, although often used for evaluating structural information of aggregates, is not the best descriptor for the compaction of clusters due to its averaging nature. The detailed orientation of aggregates, at least the shape of aggregates, should rather be linked to restructuring phenomena.

4.3.1 Compaction Regimes

Again, simulations were set up so that aggregates first start to rotate and no restructuring will occur. The step-wise increased shear rate segregates the temporal evolution of aggregates into three different regimes (Fig. 5).

Rigid body rotation: at very low shear rates the aggregates will under go no restructuring. The bonds between all particles are able to withstand the hydrodynamic stresses, and the aggregate simply rotates in the flow.

Restructuring: at intermediate shear rates the aggregates will show first as an onset of restructuring. The hydrodynamic forces causes rotating and relative motion within the aggregate. However, an important effect is now visible. Due to modeling simply adhesive contact forces, the aggregate compromises its structure upon the creation of new bonds within the aggregate; either branches or single particles find new neighbors. This compromises the entire structure, causing it to become denser.

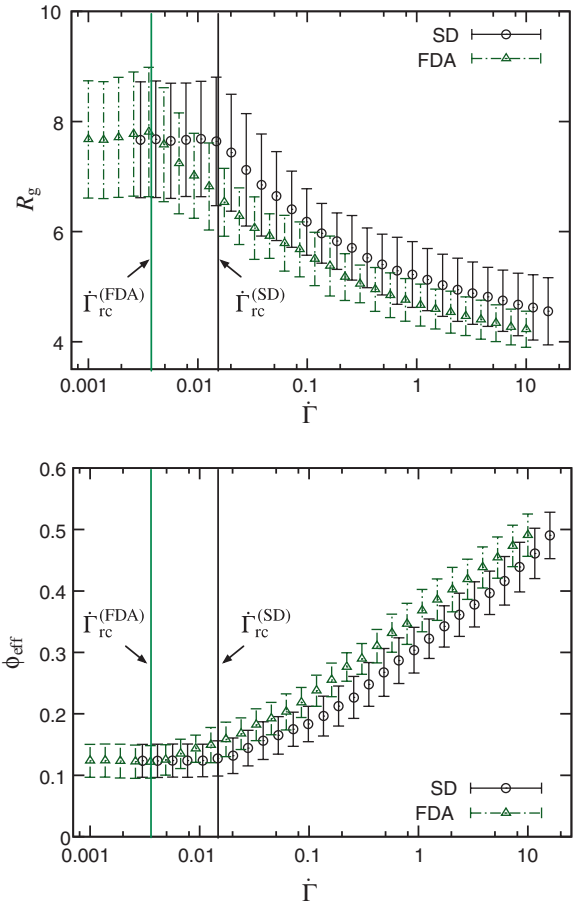

Fig. 5 Radius of gyration (**a**) and effective volume fraction (**b**) averaged over 50 aggregates as a function of dimensionless shear rate. Note the FDA overestimating the drag forces, thus the onset of restructuring (indicated by $\dot{\Gamma}_{rc}$) occurs much earlier. Reprinted from [46] with kind permission from Springer

Dense Compaction: at high shear rates the aggregate tend rotate very quickly around the axis of shear. Little restructuring is seen from already very compromised structures, but internal rearrangement occurs. Care has to be taken whether assumptions about the Stokes flow still hold valid.

The simulations of our restructuring and compaction are actually quite different from the regimes found by an abrupt application of shear rate, with expected breakage. For our simulations, no breakage is encountered.

The compaction behavior is also indicated by the effective volume fraction of an aggregate ϕ_{eff} (Fig. 5), calculated from the aspect ratio of an equivalent ellipsoid. The shear-rate dependence on effective volume fraction was small so that a maximum compaction was not observed even at high shear rates. Again, higher shear rates required for higher compaction may violate model assumptions, such as Stokes regime for the hydrodynamics and the conditions for the overdamped motion.

To obtain a more visual idea of the initial and final states of aggregates, a sample of 20 are presented in Fig. 6, and to overcome the 3-D visualization, for each aggregate views onto the $z-x$ and $z-y$ plane are given. The initial states show the very fractal character of cluster-cluster-type aggregates. Of course typical aggregates consist of a much higher number of primary particles, up to the order of many thousands [61], but for $N = 64$ we have a good size for the presentation of the open shape and can see a considerable change in shape due to restructuring.

One big surprise effect was actually the way the aggregates then compacted throughout the simulations: an emergence of round as well as rod-shaped clusters were identified (see bottom part of 6). Predictions can probably be made about the restructuring mechanisms if one follows every particle's position and distance to other neighbors, but already for multiple aggregates this provides to be a tedious task. Some thoughts about a broader quantification are required, given in the following section.

4.3.2 Shape and Orientation

Following the visual analysis, an intriguing question remains to be asked. How can the final aggregate shape (spherical or elongated) be traced back to their original shape?

One parameter describing the relative orientation is calculated from the aspect ratio of the equivalent ellipsoid (giving cluster slenderness) and aggregate tilt angle, with the latter calculated between the y-axis (axis of shear) and the principal axis of the least principal moment of inertia with the smallest value. Plotting the aspect ratio versus the tilt angle, one can track the aggregates orientation throughout the simulations. For initially random structures, the scattering on this plot is uniform. At some point during the simulation, one can start to distinct between round and rod-shaped structures: rod-shaped structures have aligned relative to the direction of the shear flow [46] and the tilt angle is decreased. The more spherical clusters have tilt angles uniformly distributed over all angles from 0 to 2π . Interestingly, the aggregates tend to keep in their orientation throughout further consolidation, however, the prediction of newly forming bonds have not been able to be traced back to certain restructuring events.

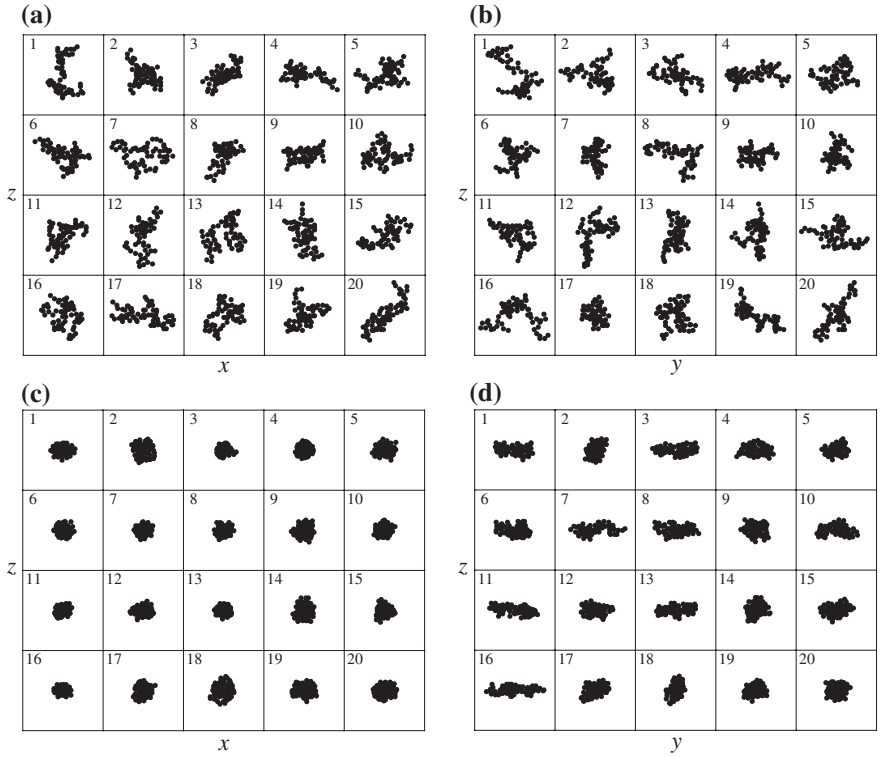

Fig. 6 Snapshots of aggregates prior to (**a**, **b**) and after (**c**, **d**) the simulation. Two side views are given to indicate the fractal character. To note is the inability to match initial structure to rod-like and spherical final shapes. Reprinted from [46] with kind permission from Springer

Nonetheless, the few rod-shaped clusters that have oriented to the rotational axis, indicated in Fig. 6, show a unique behavior. Their orientation hints at the pioneer works by Jeffery on spheroids in shear flow, where for the dilute limit, these spheroids tend to have periodic orbits. This period scales with the inverse of the shear rate and becomes longer with an increasing deviation from sphericity [62]. Since aggregates tend to retain their orientation, we would like to propose that if the orientation of clusters is variable, a more uniform compaction can be expected. Yet these elongated shapes then only form by keeping the rotational axis constant throughout the simulation, thus giving an anisotropic compaction.

Having done a detailed comparison between methods for calculating hydrodynamics, some words should be mentioned about the need for expensive calculations. While FEM was not considered in this study due to applicability, the FDA was compared with the results from SD (see Fig. 5). Hydrodynamic differences are clearly seen through the critical shear rate defined by the onset of restructuring. In low Reynolds number flows, the disturbance decays proportional to r^{-1}, resulting in drag force reduction of particles within isolated clusters. Also, the

shape and orientation of final aggregate shape shows differences between the two methods. The spatial distribution of drag forces within clusters has the same symmetry, however the tendency of aggregates to form spherical or elongated shapes was not as pronounced for the FDA.

5 Conclusions and Outlook

Improving the simulation approaches and capabilities for the restructuring of colloidal aggregates was the main objective within this work. The interplay of interparticle and hydrodynamic forces was investigated, starting from existing work and inherent limitations, proposing new approaches, and combining all of these in simulations in our final formulation.

First, we showed that experimental findings dictate a need for a formulation of bending resistances within colloidal bonds. A set of requirements is proposed for any colloidal contact model, and significance is put upon the experimental accessibility of these parameters. For one contact mode between bonded colloidal particles, namely the bending resistance, a vigorous attempt was shown to quantify these parameters. We introduced an extension of our first contact model, yet this extension is still based on force-distance relationships with spring constants and critical forces/moments upon which a bond breaks. These springs resist motion for all degrees of freedom between two particles.

The next step was to investigate how the hydrodynamics can be formulated correctly and efficiently. Two methods, FEM and SD, were introduced and tested on rigid aggregates. Although these methods approach the calculation of particle forces and torques in totally different ways, results have shown satisfactory agreement. If one considers a few restrictions, spherical particles immersed in low-Reynolds number fluids, the SD is an extremely efficient method for the investigation of colloidal aggregates. Luckily on colloidal time and length scales, these assumptions often hold true. FEM provides a detailed look into the full fluid-particle interaction including the influence of the particles on the fluid flow behavior, but at a high computational cost and for a restricted number of particles. Between the two methods, some drag force and torque deviations were seen for the larger aggregates with primary particle size of $N = 50$, while the agreement is better for smaller aggregates and simple shapes. Future work dealing with hydrodynamics may include comparing drag force differences for even larger aggregates to investigate the origin of the deviations.

We hope to have shown that the SD implementation can be used for hydrodynamics for any appropriate DEM simulation, be it restructuring aggregates or aggregate sedimentation behavior, but the fully-resolved CFD methods are always required for validating the simulations. The free-draining approximation should not be considered as a valid comparison for colloidal aggregates in shear flow as it neglects many-particle effects [35].

The restructuring of colloidal aggregates in shear flows has been investigated by coupling an interparticle contact models with Stokesian dynamics. A special type of applied shear flow, i.e. the stepwise increase of shear rate, was considered. This actually lead to the reinforcement of aggregate structures due to irreversible compaction. The structure evolution was tracked by shape and orientation in order to explain the two types of compaction behaviors of aggregates: rod- and round-shaped clusters. Therefore, simulations incorporating a valid contact model as well as detailed hydrodynamics show the characteristic behaviors of colloidal aggregates under flow conditions.

One inherent limitation that the restructuring simulations have is the ability of simulating only one aggregate at a time. For full investigation of any colloidal system, simulation techniques on other length and time scales have to be adopted. A choice would be population balance equations, mass balances for the entire population of aggregates able to quantify the temporal evolution of distributions. This technique requires so-called aggregation and breakage kernels: rate constants explaining how specific distributions break or further aggregate. Kernels are typically a function of cluster size, number of primary particles, applied shear rate, and interparticle interactions, and Harshe and Lattuada [63] give an approach utilizing SD as well as an implementation similar to our proposed bending resistances [30]. Compared to our restructuring simulations, however, they do not apply shear rate in a step-wise manner: their aggregates are exposed to a full flow field and are allowed to break. Although this population balance approach cannot simulate the restructuring of each aggregate, the two methods depend on each other for the simulation of entire colloidal systems.

Some work has to be done to relax the restrictions of simulations handling only monodisperse primary particles in aggregates. All of the simulation studies utilizing the efficiency and accuracy of SD for aggregates consider primary particles of the same size, yet handling polydispersity remains an open question for aggregates. Eggersdorfer and Pratsinis [64] show effects of polydisperse primary particles on aggregation mechanisms, but neither restructuring nor breakup are well known topics for such aggregates in the literature. DEM simulations can incorporate arbitrary size, but this becomes quite challenging when incorporating proper polydisperse particle contact models. SD can handle polydisperse particles by extending the resistance or mobility functions to include particle radii [65], so if one extends these contact models for arbitrary size, the effects of polydispersity within restructuring aggregates is something that remains to be investigated.

Current research interest of applying simulations in order to understand the realm of colloidal process engineering is evident through the emergence of a recent review on colloidal suspension dynamics simulations [66]. Efficiency of hydrodynamic methods, e.g. SD, as well as the need for tangential particle interaction models were highlighted. Indeed from an applications perspective, the authors pushed to goal of studying colloidal suspension in order to understand, predict and control suspension rheological properties and particle microstructure. Research on restructuring of colloidal aggregates involves all of the above goals for the same kind of colloidal interactions and hydrodynamics for engineering purposes:

understand and predict how aggregates restructure, and, as the ultimate goal, control how aggregates restructure.

References

1. Witten T, Sander L (1983) Diffusion-limited aggregation. Phys Rev B 27(9):5686
2. Meakin P (1999) A historical introduction to computer models for fractal aggregates. J Sol-Gel Sci Technol 14:97
3. Higashitani K, Iimura K, Sanda H (2001) Simulation of deformation and breakup of large aggregates in flows of viscous fluids. Chem Eng Sci 56:2927
4. Seto R, Botet R, Briesen H (2011) Hydrodynamic stress on small colloidal aggregates in shear flow using Stokesian dynamics. Phys Rev E 84:041405
5. Sonntag RC, Russel WB (1986) Structure and breakup of flocs subjected to fluid stresses: I. Shear experiments. J Colloid Interface Sci 113(2):399
6. Sonntag RC, Russel WB (1987) Elastic properities of flocculated networks. J Colloid Interface Sci 116(2):485
7. Selomulya C, Amal R, Bushell G, Waite TD (2001) Evidence of shear rate dependence on restructuring and breakup of latex aggregates. J Colloid Interface Sci 236:67
8. Selomulya C, Bushell G, Amal R, Waite TD (2002) Aggregation mechanisms of latex of different particle sizes in a controlled shear environment. Langmuir 18:1974
9. Serra T, Casamitjana X (1998) Effect of the shear and volume fraction on the aggregation and breakup of particles. AIChE J 44(8):1724
10. Tolpekin VA, Duits MHG, van den Ende D, Mellema J (2004) Aggregation and breakup of colloidal particle aggregates in shear flow, studied with video microscopy. Langmuir 20:2614
11. Soos M, Sefcik J, Morbidelli M (2006) Investigation of aggregation, breakage and restructuring kinetics of colloidal dispersions in turbulent flows by population balance modeling and static light scattering. Chem Eng Sci 61(8):2349
12. Soos M, Moussa AS, Ehrl L, Sefcik J, Wu H, Morbidelli M (2008) Effect of shear rate on aggregates size and morphology investigated under turbulent conditions in stirred tank. J Colloid Interface Sci 319:577
13. Ehrl L, Soos M, Morbidelli M (2008) Dependence of aggregate strength, structure, and light scattering properties on primary particle size under turbulent conditions in stirred tank. Langmuir 24:3070
14. Zaccone A, Soos M, Lattuada M, Wu H, Bäbler M, Morbidelli M (2009) Breakup of dense colloidal aggregates under hydrodynamic stresses. Phys Rev E 79:061401
15. Harshe YM, Lattuada M, Soos M (2011) Experimental and modeling study of breakage and restructuring of open and dense colloidal aggregates. Langmuir 27:5739
16. Heim LO, Blum J, Preuss M, Butt HJ (1999) Adhesion and friction forces between spherical micrometer-sized particles. Phys Rev Lett 83(16):3328
17. Pantina JP, Furst EM (2005) Elasticity and critical bending moment of model colloidal aggregates. Phys Rev Lett 94:138301
18. Harada S, Tanaka R, Nogami H, Sawada M (2006) Dependence of fragmentation behavior of colloidal aggregates on their fractal structure. J Colloid Interface Sci 301:123
19. Bagster DF, Tomi D (1974) The stresses within a sphere in simple flow fields. Chem Eng Sci 29:1773
20. Adler P (1979) A study of disaggregation effects in sedimentation. AIChE J 25:487
21. Flesch JC, Spicer PT, Pratsinis SE (1999) Laminar and turbulent shear-induced flocculation of fractal aggregates. AIChE J 45(5):1114
22. Melis S, Verduyn M, Storti G, Morbidelli M, Bałdyga J (1999) Effect of fluid motion on the aggregation of small particles subject to interaction forces. AIChE J 45(7):1383
23. Dzwinel W, Yuen D, Boryczko K (2002) Mesoscopic dynamics of colloids simulated with dissipative particle dynamics and fluid particle model. J Mol Model 8(1):33

24. Gastaldi A, Vanni M (2011) The distribution of stresses in rigid fractal-like aggregates in a uniform flow field. J Colloid Interface Sci 357:18
25. Brasil AM, Farias TL, Carvalho MG, Koylu UO (2001) Numerical characterization of the morphology of aggregated particles. J Aerosol Sci 32:489
26. Kim AS, Yuan R (2005) Hydrodynamics of an ideal aggregate with quadratically increasing permeability. J Colloid Interface Sci 285(2):627
27. Bossis G, Meunier A, Brady JF (1991) Hydrodynamic stress on fractal aggregates of spheres. J Chem Phys 94(7):5064
28. Derjaguin B, Landau L (1993) Theory of the stability of strongly charged lyophobic sols and of the adhesion of strongly charged particles in solutions of electrolytes. Prog Surf Sci 43(14), 30
29. Verwey E (1947) Theory of the stability of lyophobic colloids. J Phys Colloid Chem 51:631
30. Becker V, Briesen H (2008) Tangential-force model for interactions between bonded colloidal particles. Phys Rev E 78:061404
31. Cundall PA, Stack ODL (1979) A discrete numerical model for granular assemblies. Geotechnique 29(1):47
32. Botet R, Cabane B (2004) Scaling behaviors of colloidal aggregates under uniform pressure. Phys Rev E 70:031403
33. Johnson KL, Kendal K, Roberts AD (1971) Surface energy and the contact of elastic solids. Proc R Soc Lond A 324:301
34. Becker V, Schlauch E, Behr M, Briesen H (2009) Restructuring of colloidal aggregates in shear flows and limitations of the free-draining approximation. J Colloid Interface Sci 339:362
35. Becker V, Briesen H (2010) A master curve for the onset of shear induced restructuring of fractal colloidal aggregates. J Colloid Interface Sci 346:32
36. Schlauch E, Ernst M, Seto R, Briesen H, Sommerfeld M, Behr M (2013) Comparison of three simulation methods for colloidal aggregates in Stokes flow: Finite elements, lattice Boltzmann and Stokesian dynamics. Comp Fluids 86:199
37. Harshe YM, Ehrl L, Lattuada M (2010) Hydrodynamic properties of rigid fractal aggregates of arbitrary morphology. J Colloid Interface Sci 352:87
38. Brady JF, Bossis G (1988) Stokesian dynamics. Ann Rev Fluid Mech 20:111
39. Durlofsky L, Brady JF, Bossis G (1987) Dynamic simulation of hydrodynamically interacting particles. J Fluid Mech 180:21
40. Phillips RJ, Brady JF, Bossis G (1988) Hydrodynamic transport properties of hard-sphere dispersions. I. Suspensions of freely mobile particles. Phys Fluids 31(12):3462
41. Phillips R, Brady J, Bossis G (1988) Hydrodynamic transport properties of hard-sphere dispersions. II. Porous media. Phys Fluids 31:3473
42. Sierou A, Brady JF (2001) Accelerated Stokesian Dynamics simulations. J Fluid Mech 448:115
43. Ichiki K (2002) Improvement of the Stokesian dynamics method for systems with finite number of particles. J Fluid Mech 452:231
44. Wagner N, Brady J (2009) Shear thickening in colloidal dispersions. Phys Today 62:27
45. Fellay LS, Vanni M (2012) The effect of flow configuration on hydrodynamic stresses and dispersion of low density rigid aggregates. J Colloid Interf Sci
46. Seto R, Botet R, Auernhammer G, Briesen H (2012) Restructuring of colloidal aggregates in shear flow. Eur Phy J E 35(12):128
47. Jeffrey DJ, Onishi Y (1984) Calculation of the resistance and mobility functions for two unequal rigid spheres in low-Reynolds-number flow. J Fluid Mech 139:261–290
48. Jeffrey D (1992) The calculation of the low Reynolds number resistance functions for two unequal spheres. Phys Fluids A 4(January):16
49. Ichiki K (2011) Ryuon—simulation library for Stokesian dynamics. URL http://ryuon.sourceforge.net
50. Happel J, Brenner H (1983) Low Reynolds number hydrodynamics, 2nd edn. Kluwer, London

51. Behr M, Tezduyar T (1994) Finite element solution strategies for large-scale flow simulations. Comput Method Appl Mech 112:3
52. Donea J, Huerta A (2003) Finite element methods for flow problems. Wiley, London
53. Wylie B, Geimer M, Nicolai M, Probst M (2007) Recent advances in parallel virtual machine and message passing interface. In: Cappello F, Herault T, Dongarra J (eds) Springer, Berlin, pp 107–116
54. Binder C, Feichtinger C, Schmid HJ, Thürey N, Peukert W, Rüde U (2006) Simulation of the hydrodynamics drag of aggregated particles. J Colloid Interface Sci 301:155
55. Vanni M, Gastaldi A (2011) Hydrodynamic forces and critical stresses in low-density aggregates under shear flow. Langmuir 27(21):12822
56. Jullien R, Botet R (1987) Aggregation and fractal aggregates. World Scientific Publishing, Singapore
57. Tomas J (2007) Adhesion of ultrafine particles---A micromechanical approach. Chem Eng Sci 62(7):1997
58. Roth M, Schilde C, Lellig P, Kwade A, Auernhammer GK (2012) Colloidal aggregates tested via nanoindentation and quasi-simultaneous 3D imaging. Eur Phy J E 35(11):124
59. Dominik C, Tielens AGGM (1997) The physics of dust coagulation and the structure of dust aggregates in space. Astrophys J 480:647
60. Potanin AA (1993) On the computer simulation of the deformation and breakup of colloidal aggregates in shear flow. J Colloid Interface Sci 157:399
61. Weitz D, Oliveria M (1984) Fractal structures formed by kinetic aggregation of aqueous gold colloids. Phys Rev Lett 52(16):1433
62. Kim S, Karrila SJ (2005) Microhydrodynamics. Dover, New York
63. Harshe YM, Lattuada M (2012) Breakage rate of colloidal aggregates in shear flow through Stokesian Dynamics. Langmuir 28(1):283
64. Eggersdorfer ML, Pratsinis SE (2012) The structure of agglomerates consisting of polydisperse particles. Aerosol Sci Tech 46(3):347
65. Jeffrey DJ, Corless RM (1988) Forces and stresslets for the axisymmetric motion of nearly touching unequal spheres. Physicochem Hydrodyn 10(4):461
66. Bolintineanu D, Grest G, Lechman J, Pierce F, Plimpton S, Schunk R (2014) Particle dynamics modeling methods for colloid suspensions. Comput Part Mech pp 1–36

Gelation, Fragmentation and Reorganization of Precipitated Silica

Sebastian Wilhelm and Matthias Kind

Abstract The polymerization process of silica involves gelation, fragmentation and reorganization. Each of these processes depends on the process parameters and strongly influences the solid formation as well as the particle properties (particle size distribution, structure or firmness). Process parameters like temperature, pH and ionic strength of solution as well as chemical composition and energy dissipation are crucial for the production of silica powder with particular specifications. Characteristic parameters for gelation, fragmentation and reorganization are, among others, the gelation time, gel firmness and fragment sizes in the case of stirred experiments. They depend in different degrees on the process parameters. Different orders of magnitude for gelation time (from a few seconds up to several hours) and gel firmness are obtained by varying the pH and chemical composition of the solution. Modifications in the solid structure appear during the reorganization process, resulting in volume decrease. Thus, the process of reorganization offers the possibility to modify the particle properties even after they have formed. A new method is suggested to reduce the time requirement for the process of reorganization that allows for a faster identification of relevant process parameters. An empirical model is proposed that correlates the data of slow and accelerated process of reorganization. This model predicts the reorganization of a model silica gel for various temperatures.

Keywords Precipitation · Colloidal gels · Fragmentation · Restructuring · Syneresis · Gel firmness · Silica

S. Wilhelm (✉) · M. Kind
Institute of Thermal Process Engineering,
Karlsruhe Institute of Technology (KIT), Karlsruhe, Germany
e-mail: Sebastian.Wilhelm@kit.edu

M. Kind
e-mail: Matthias.Kind@kit.edu

M. Kind et al. (eds.), *Colloid Process Engineering*,
DOI 10.1007/978-3-319-15129-8_8

List of symbols

c	mass concentration (mg/l)
$\tilde{c}$	molar concentration (mmol/l, mol/l)
$\tilde{c}^{\star}$	molar concentration, equilibrium (mmol/l, mol/l)
d	fragment size (μm)
d_c	cone diameter of rheometer (mm)
d_f	fractal dimension
e	elementary electric charge (1.602×10^{-19} C)
G'	storage modulus (Pa)
G''	loss modulus (Pa)
I	ionic strength of solution (mol/l)
k_B	Boltzmann constant (1.380×10^{-23} J/K)
$\dot{m}$	mass flow rate (g/min)
m_{fill}	mass of filling substance (deionized water) (g)
m_{gel}	mass of gel (g)
N_A	Avogadro constant (6.022×10^{23} mol^{-1})
N_c	number of ion species
n	exponent
n_s	stirring speed (min^{-1})
Δp	pressure difference (bar)
pH	value of pH
pH_{iso}	pH of isoelectric point
q_3	volume density (μm^{-1})
s_{gap}	gap width of rheometer (μm)
S	supersaturation
t	time (min)
t_g	gelation time (min)
t_{norm}	normalised time
T	absolute temperature (K)
V_{fill}	filling volume (pycnometer) (ml)
$V_{\text{fill, max}}$	maximum filling volume (pycnometer) (ml)
V_{gel}	volume of gel (ml)
ΔV	volume decrease of gel (ml)
V_0	starting volume of gel (ml)
$(\Delta V/V_0)\text{max}$	maximum relative volume decrease of gel
x	mass fraction (kg/kg$_{\text{Sol}}$)
X	mass load (kg/kg)
z_i	electrical valence
α_c	cone angle of rheometer (°)
ε	dissipated energy (W/kg)
ε_r	relative permittivity
ε_0	electrical field constant (8.854×10^{-12}As/Vm)
$1/\kappa$	Debye length (nm)

ρ_{fill}	density of filling substance (g/ml)
ϑ	temperature (°C)
τ	characteristic time constant (h)

1 Introduction

Precipitated silica has a wide field of industrial applications. On the one hand, its physical properties (specific surface area, particle size) are used for adsorption of liquids and gases or colour pigments in paintings. On the other hand, it is added to polymeric and pharmaceutical products as an inexpensive and inert filling material. The industrial production of precipitated silica is usually performed in a stirred semi-batch process by mixing sulphuric acid and aqueous sodium silicate. The resulting monomeric silicic acid polymerises to solid silica particles, which eventually agglomerate and link together into a porous solid skeleton that immobilises all liquid contained [1]. This state is known as a gel. It is destroyed due to the stirrer, resulting in gel fragments. It will be shown that the agglomeration and the fragment sizes can be controlled by varying the process parameters.

Furthermore, polymerization continues beyond the formation of the gel. As a direct consequence, the fragments can reorganise and polymerise internally to a more compact state. The gel fragments shrink, leading to an expulsion of liquid enclosed. This process is known as syneresis [1]. The gel volume decreases about 15–18 % after five days [2]. According to [3], syneresis can be accelerated by applying an external mechanical force to the gel, leading to an accelerated drainage of enclosed liquid. Thus, it is appropriate to define this process as ‘enforced syneresis’ in contrast to the previously described, slow ‘natural syneresis’. An extrapolation method based upon measurement of enforced syneresis is proposed that allows for a correlation between natural and enforced syneresis.

The process of particle formation, aggregation and gelation as well as reorganization of silica depends on temperature, pH, ionic strength, and composition of the reactants. Although these process parameters are not fully independent of each other, the influence of each parameter on the precipitation process is reviewed theoretically. In particular, their impact on polymerization reaction and kinetics are considered.

The progress of polymerization can be monitored with rheometric and light scattering analysis, respectively, the gel fragments are characterized. An adapted pycnometer and a specially designed pressure cell are proposed for measuring both natural and enforced syneresis.

In the following section, the relation between the systematically varied process parameters and the phenomenology of gelation is given. The gelation time, gel firmness, fragment size distribution, and the reorganization process of the silica formed are particularly investigated.

2 State of the Art

Firstly, the process of silica precipitation with its different mechanisms—growth, gelation, fragmentation, and reorganization—is reviewed. Special attention is paid to the catalytic polymerization reaction of monomeric silicic acid to oligomers, aggregates and eventually to a gel. Secondly, the processes of fragmentation and reorganization are presented. All these steps are influenced by the process parameters temperature ϑ, pH and ionic strength I. In order to understand their influences on the precipitation of silica, the theoretical backgrounds of the process parameters are illustrated.

2.1 Precipitation of Silica

2.1.1 Theory of Gelation and Fragmentation

Liquid routes of producing silica exist in addition to a gaseous reaction of silicon tetrachloride. One of the routes is shown in Fig. 1. It comprises the mixing of sulphuric acid with aqueous sodium silicate.

At typical process conditions, see Sect. 3.1, monomeric silicic acid $Si(OH)_4$ has a concentration of about $c_{Si(OH)_4} = 10^5$ mg/l. By comparison, its solubility is low ($c^{\star}_{Si(OH)_4} = 192$ mg/l corresponding to $\tilde{c}^{\star}_{Si(OH)_4} = 2$ mmol/l at $\vartheta = 25\,^{\circ}$C [4]). Hence, a high supersaturation $S = \frac{c_{Si(OH)_4}}{c^{\star}_{Si(OH)_4}} \approx 500$ occurs. In the course of the precipitation process, see Fig. 1, the supersaturation S is depleted by polymerization of silanol groups (Si–OH) to siloxane bonds (Si–O–Si) with water as a byproduct. Depending on the pH of the mixture, catalysts are either H^+ ions or OH^- ions [4, 5] (also refer to Sect. 2.1.2).

$$\equiv \mathrm{Si{-}OH} + \mathrm{HO{-}Si} \equiv \xrightarrow{\text{cat.}} \equiv \mathrm{Si{-}O{-}Si} \equiv + \mathrm{H_2O}$$

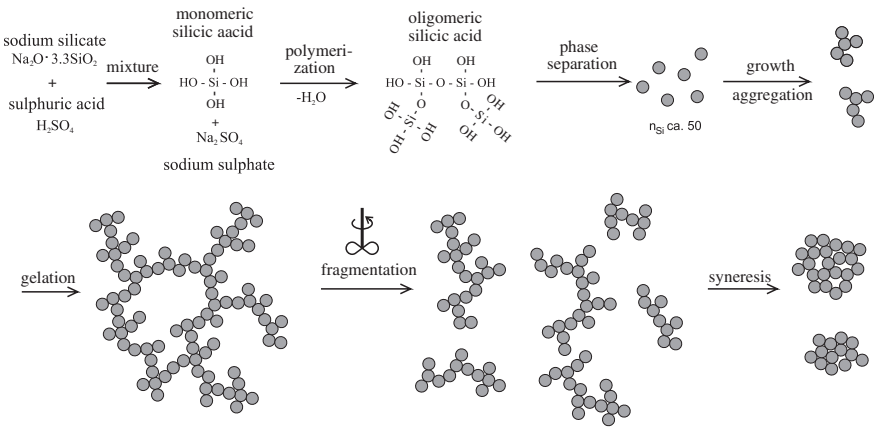

Fig. 1 Precipitation process of silica, taken from [6, 21]

Monomeric silicic ac1id builds di-, tri- and larger oligomers that are assumed to be stabilised by solvation [6]. Further polymerization leads to colloidal, solid primary particles (indicated by the filled rings in Fig. 1). Seeding is not necessary for the particle formation. Both growth and aggregation of these primary particles contribute to gelation. It is appropriate to define a gelation time t_g as the time elapsed after the reactants have been mixed. The gel structure itself consists of a solid, porous skeleton of silica and immobilised liquid in the pores [7]. The gel is destroyed, for example, by means of a stirrer, whereby gel fragments occur. Fragmentation is a secondary effect in industrial production, but the proper mixing of further added reactants cannot be guaranteed without stirring. For the application of silica in form of a fine powder it is a crucial process step since fragmentation strongly affects the particle size. As the process continues, the fragments shrink while expelling enclosed liquid. Typically, the solid particles are separated from the liquid and are dried to obtain the silica powder.

2.1.2 Theory of Reorganization

Reorganization of agglomerates in shear flows can be observed for a variety of colloidal systems [8, 9]. The agglomerates shrink and compact resulting in an increasing fractal dimension d_f. Two different types of reorganization can be identified depending on the size of the primary particles. Agglomerates composed of small primary particles tend to restructure and to compact, while agglomerates made of larger primary particles break and reagglomerate. For more detailed information, see [6, 9–12].

However, even without external mechanical stress imposed by shear flow, reorganization of the agglomerates occurs. In dairy science, the separation of milk into curd and whey and the conversion of amorphous starch into a crystalline state with expulsion of physically bonded water are known examples. Silica, aluminum oxide and latex represent industrially produced compounds that show reorganization. The reason for reorganization of silica is the same polymerization reaction which is responsible for gelation. After the gel network has formed, there are still uncondensed silanol groups. A zoom of two solid silica particles is shown in Fig. 2.

Due to thermal vibrations of the initially flexibly bonded silica particles (indicated by the shaded areas), silanol groups on the particle surface can get into

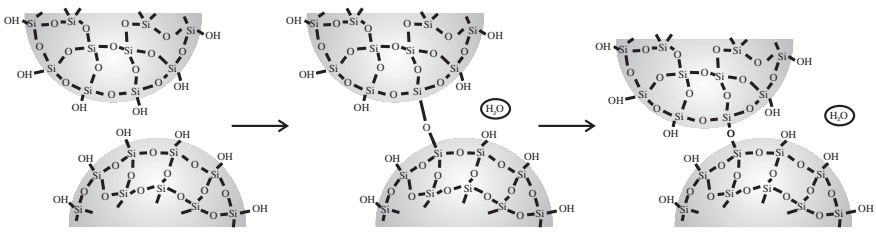

Fig. 2 Schematic illustration of syneresis

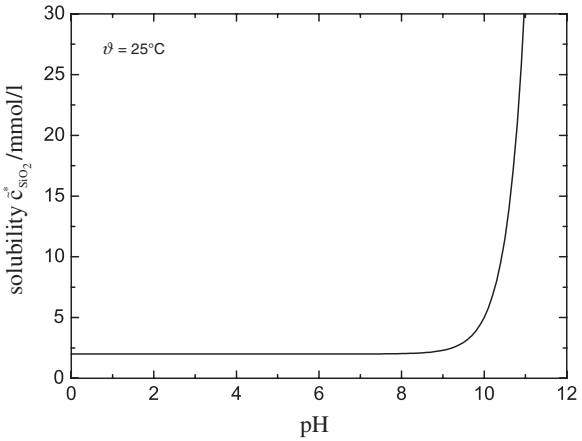

Fig. 3 Calculated solubility $\tilde{c}^{\star}_{SiO_2}$ of silica as a function of pH, according to [4]

contact and form siloxane bonds. Two neighbouring silanol groups require more space than one siloxane bond. Thus, as a new siloxane bond is formed, stress is put on the solid skeleton [1]. This stress is relaxed by contraction as long as the skeleton remains flexible. As a direct consequence of the contraction, the liquid enclosed is poured out. These two mechanisms are known as syneresis. With further formation of stiffening siloxane bonds, the silica skeleton becomes less flexible and the rate of syneresis decreases. Finally, syneresis stops because the skeleton can no longer deform [1].

2.2 Influence of PH

The influence of the pH is threefold. Firstly, the total solubility of silica, including monomeric silicic acid and its ionic form, depends strongly on the pH of the solution. It is calculated by Eq. (1). Hereby, $\tilde{c}_{SiO_2,1} = 2\,\text{mmol/l}$ and $\tilde{c}_{SiO_2,2} = 2.3\,\text{mmol/l}$ for $\text{pH}_2 = 9$ are found [6].

$$\log\left(\frac{\tilde{c}^{\star}_{SiO_2} - \tilde{c}^{\star}_{SiO_2,1}}{\tilde{c}^{\star}_{SiO_2,2} - \tilde{c}^{\star}_{SiO_2,1}}\right) = \text{pH} - \text{pH}_2 \tag{1}$$

Figure 3 shows the course of the total solubility. For $\text{pH} < 8$ and $\vartheta = 25\,°\text{C}$, the solubility is constant ($\tilde{c}^{\star}_{SiO_2} = 2\,\text{mmol/l}$) and it increases for $\text{pH} > 8$. An equilibrium exists between the monomeric silicic acid and its deprotonated anion. At high pH, the equilibrium is shifted to the anionic form, leading to the increased solubility. The anion can be stabilised by water molecules [4, 6].

Secondly, the pH directly affects the polymerization reaction. The polymerization reaction involves an ionic mechanism that depends on pH. Two different regions can be identified that are separated by the isoelectric point, i.e.

$pH_{iso} \approx 1.7-2$ in the case of sulphuric acid [1, 5, 10]. For $pH < pH_{iso}$, the polymerization is acid-catalysed (proportional to the concentration of H^+ ions), whereas for $pH > pH_{iso}$, it is proportional to the concentration of OH^- ions (base-catalysed) [4].

In the case of acid-catalysed polymerization, an equilibrium condition between temporarily positively charged and neutral species of monomeric silicic acid is proposed [13]. This equilibrium is shifted greatly to the right. The cationic monomeric silicic acid is formed due to the addition of an H^+ ion [5].

$$\equiv Si\text{–}OH + H^+ \longrightarrow \equiv Si\text{–}OH_2^+$$

$$\equiv Si\text{–}OH_2^+ + OH\text{–}Si\equiv \rightleftharpoons \equiv Si\text{–}\overset{H^+}{O}\text{–}Si\equiv + H_2O$$

The additional proton of the intermediate silica is removed either by water or another silanol group so that the overall reaction scheme corresponds to the one shown above. The cationic monomeric silicic acid attacks silanol groups of least acidic silicon atoms [5]. In general, the acidity of a silicon atom in silica increases with the greater number of siloxane bonds and fewer number of silanol groups [4]. Thus, the cationic silicic acid reacts preferentially with the least condensed end groups. Therefore, formation of linear chains or weakly branched structures with a low degree of internal polymerization predominates initially. With proceeding polymerization, the silanol groups that are attached to the branched structures polymerise internally or bind together with other polymeric units, resulting in dense, but among each other loosely connected agglomerates [10].

Above $pH_{iso} \approx 1.7-2$, the polymerization proceeds by an OH^- ions catalysed mechanism. The OH^- ion deprotonates a neutral monomeric silicic acid. Subsequently, it polymerizes. In the case of a very high pH, the equilibrium between the anion and the siloxane is shifted backwards to the left side, resulting in dissolution of the siloxane (if ever formed). The anionic silicic acid attacks silanol groups of the most acidic silicon atoms, i.e. the silicon atoms with the fewest number of attached OH-groups and the greatest number of siloxane bonds. They are rather middle than end groups. Therefore, formation of highly condensed and branched clusters is promoted [5, 10].

$$\equiv Si\text{–}OH + OH^- \longrightarrow \equiv Si\text{–}O^- + H_2O$$

$$\equiv Si\text{–}O^- + OH\text{–}Si\equiv \rightleftharpoons \equiv Si\text{–}O\text{–}Si\equiv + OH^-$$

Thirdly, the pH affects the rate of polymerization and thus, directly the gelation time t_g and the reorganization, respectively, syneresis. These dependencies are illustrated in Fig. 4. Since the polymerization reaction requires the cationic, respectively, anionic monomeric silicic acid, the gelation time t_g decreases with an increasing concentration of these ionic intermediates. For $pH = pH_{iso}$, their concentrations are at a minimum, resulting in maximum gelation times t_g. The gelation times t_g drop sharply due to a small change in pH. The same effect is

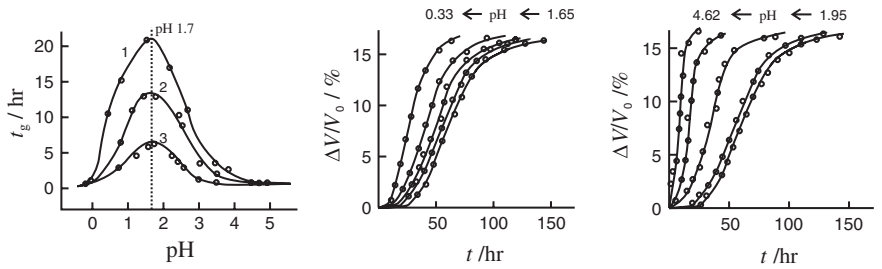

Fig. 4 Gelation time t_g depending on pH of solution and SiO_2 concentrations $\tilde{c}_{SiO_2} = 1.09$ (*1*), 1.33 (*2*) and 1.78 mol/l (*3*) (*left*); volume decrease as a function of time t and pH for acid-catalysed (*middle*) and base-catalysed (*right*) polymerization [2]

observed for the rate of syneresis. The closer the pH of the solution approaches pH_{iso}, the slower syneresis is.

2.3 Influence of Temperature

The solubility of silica increases with temperature ϑ. It is calculated by Eq. (2) [4].

$$\log\left(\frac{c^{\star}_{SiO_2}}{\text{mg/l}}\right) = \frac{-731}{\vartheta + 273.15\,^{\circ}\text{C}} + 4.52 \tag{2}$$

In Fig. 5, its course is plotted for $pH < 8$. Note that the molar solubility $\tilde{c}^{\star}_{SiO_2}$ is plotted. The solubility in that range of the pH is independent of pH according to Fig. 3, and one curve describes the solubility. For $pH > 8$, the pH-dependency of the solubility $\tilde{c}^{\star}_{SiO_2}$ must also be taken into account [4].

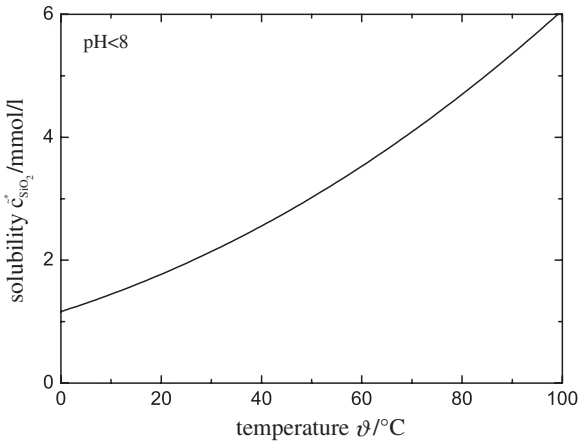

Fig. 5 Calculated solubility $\tilde{c}^{\star}_{SiO_2}$ of silica as a function of temperature ϑ, according to [4]

Beside its impact on the solubility $\tilde{c}^{\star}_{SiO_2}$, the temperature ϑ directly affects the polymerization reaction rate [1]. This might be expected because polymerization involves a kinetic phenomenon. However, the influence of temperature ϑ cannot be discussed without considering the two different pH regions [4].

For acid-catalysed polymerization, a strong acceleration of both gelation and syneresis is detected with increasing temperature ϑ [10, 14]. This is due to a higher mobility of the molecules promoting the agglomeration and condensation of polymeric clusters. By contrast, the maximum amount of shrinkage decreases [14]. To obtain shrinkage, the stress induced by newly forming siloxane bonds must be relaxed, therefore, the compliance of the solid silica skeleton is of great importance. During the shrinkage process, pore liquid must move through the skeleton of solid silica to be squeezed out. The viscosity of the pore liquid decreases with increasing temperature ϑ, but the reaction rate increases disproportionately. The squeezing out of the pore liquid becomes the limiting process. It is assumed that the stress produced by the formation of siloxane bonds is lowered by shear deformation [1]. The shear deformation does not contribute to a volume decrease. Thus, for a given number of siloxane bonds, the shrinkage is lower at higher temperatures.

By contrast, an unrestricted acceleration of gelation for the base-catalysed polymerization with increasing temperature ϑ cannot be stated [4, 10]. It is reported that the gelation time t_g increases for temperatures from $\vartheta = 15\,^{\circ}\mathrm{C}$ to $\vartheta = 35\,^{\circ}\mathrm{C}$, but decreases again with higher temperatures. It is assumed that this peculiar behaviour is due to a preequilibrium step involving an induction period. During this period, small polymeric units are formed initially with which monomeric silicic acid reacts preferentially [4].

2.4 Influence of Ionic Strength

The ionic strength I is a property of a liquid which contains dissociated salts. The concentrations $\tilde{c}_i$ of ions i that dissociate from the salt with their electrical valences z_i are summed up for all ions N_c, that is

$$I = \frac{1}{2} \sum_{i=1}^{N_c} \tilde{c}_i \cdot z_i^2. \tag{3}$$

By means of the ionic strength I, the Debye length $1/\kappa$ of the electrostatic interaction forces between particles can be influenced:

$$\frac{1}{\kappa} = \sqrt{\frac{\varepsilon_r \cdot \varepsilon_0 \cdot k_B \cdot T}{2 \cdot e^2 \cdot N_A \cdot I}} \tag{4}$$

Here, ε_r and ε_0 represent the relative permittivity, respectively, the electrical field constant. k_B is the Boltzmann constant, T the absolute temperature, e the

elementary electric charge, and N_A the Avogadro constant. Because of addition of salts to a solution, the ionic strength I increases, respectively, the Debye length $1/\kappa$ decreases. The electrical double layer surrounding each particle is compressed, resulting in a reduced range of electrostatic forces [10]. As a direct consequence, the particles do not repel each other and can agglomerate.

The influence of the pH, temperature ϑ and ionic strength I on the polymerization of silica involving gelation, fragmentation and reorganization are reviewed. Different experimental set-ups are suggested for proving, transferring and extending these influences to the resulting fragment size distribution and the macroscopically determinable volume decrease. They are explained in detail in the next section.

3 Experimental Set-up

In the following, a simple, but powerful experimental set-up is proposed which allows one to determine the influence of the process parameters pH, temperature and ionic strength on the formation of the solid and the resulting gel network. For that purpose, unstirred batch experiments are appropriate. A syringe pump in combination with a Y-mixing nozzle ensures rapid and complete mixing of both reactants. The gel samples prepared are investigated with a cone/plate rheometer with respect to their gelation time and gel firmness. An adapted pycnometer device is proposed for characterization of the reorganization process and the principle of measuring natural syneresis is explained. The equipment for the measurement of enforced syneresis consists of a pressure cell and a uni-axial testing machine. Finally, the set-up for stirred batch precipitation in a stirred tank and a Taylor-Couette reactor is explained with which the influence of fluid mechanic stress on the fragment size distributions can be determined.

3.1 Batch Precipitation, Unstirred

Gel samples are produced via a batch precipitation apparatus for analysis of the gelation kinetics. The apparatus consists of a Y-mixing nozzle, described in [15], and a manually operated or electrically driven syringe pump, *Nexus 6000, Chemyx*. The scheme and actual arrangement of the manually operated pump are shown in Fig. 6. The Y-mixing nozzle allows for rapid and homogeneous mixing of the reactants that are pumped with a constant volumetric ratio of 1:1. Sulphuric acid (96 % H_2SO_4 by weight, *Roth GmbH*) and sodium water glass (35.5 % $Na_2O \cdot 30.3\ SiO_2$ (sodium silicate) by weight, *Roth GmbH*) with different dilutions are used as reactants. Both reactans and the mixed solution are thermostated at $\vartheta = 20\,°C$. Thus, an adiabatic temperature rise due to the released heat of mixing is eliminated.

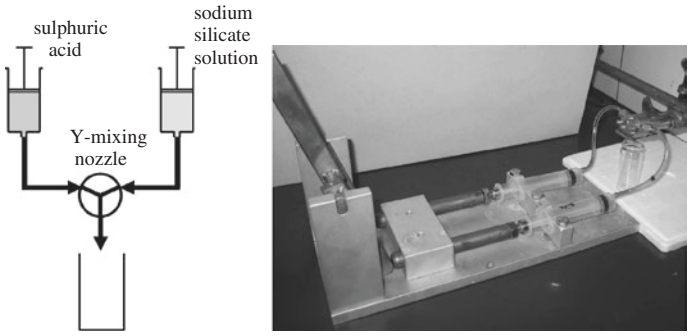

Fig. 6 Scheme and actual arrangement of batch precipitation apparatus

A suitable method for the determination of gelation time t_g and gel firmness proved to be oscillating rheometry. We used a cone/plate rheometer (*Bohlin CVO 100NF*, cone diameter $d_c = 40\,\text{mm}$, cone angle $\alpha_c = 4°$ and gap width $s_{\text{gap}} = 150\ \mu\text{m}$). The gel sample has to be placed on the plate immediately after mixing. Due to the very small oscillating amplitude A_ω, the forming gel network is not destroyed [10]. During the measurement, the time-dependent storage and loss modulus (G' and G'') are recorded. The sample is gelled if both moduli G' and G'' increase parallely with varying frequency f. In the case of a continuously polymerizing gel network the polymerization state of the gel changes constantly and, thus, this method is only applicable to gels that have a very slow or stoppable polymerization. However, for precipitated silica, the intersection point of G' and G'' at a constant frequency $f = 1$ Hz coincides with the visual determinable gelation, i.e. the time elapsed since mixing the reactants corresponds to the gelation time t_g [10].

3.2 Measurement of Syneresis

Several studies exist on natural syneresis of silica produced by mixing sulphuric acid and sodium silicate solutions [2]. The shrinkage can be measured with a cathetometer that records vertical changes in position. However, due to the assumption of an isotropic shrinkage, the change in the vertical dimension must be converted into a corresponding volume decrease [2]. In order to measure the changes in all geometrical dimensions and their impact on the volume decrease, here a different approach based on the principle of displacement and pycnometry is adapted, see Fig. 7 (left).

The pipette tip with a small opening at its top will guarantee that the same volume is always filled in the pycnometer device. Firstly, the maximum filling volume $V_{\text{fill,max}}$ of the pycnometer without the gel sample is determined. Afterwards, the gel sample with its volume V_{gel} is put into the pycnometer flask and its mass m_{gel} is noted. The measurement liquid is poured in through the filling

hole and its mass m_{fill} is weighed. Due to its known density ρ_{fill}, the volume V_{fill} can be calculated. Knowing the maximum filling volume $V_{\text{fill,max}}$, the volume of the gel sample V_{gel} is computed by simple subtraction. During the syneresis, liquid enclosed in the gel is drained and must be removed from the flask before the measurement liquid (deionized water) is poured in. Because the gel gets into contact with deionized water, its chemical composition may change, and thus, it cannot be used for further analysis. Therefore, a series of gel samples (here 36 samples) must be prepared to record the time-dependent volume changes. Three samples are analysed to obtain one measurement point (see Sect. 4.3.1) and their volume changes $\Delta V/V_0$ are averaged in order to compensate for inaccuracies. Hence, 12 measuring points can be taken with 36 samples. At every single measuring point, the temperature ϑ_{fill} of the filled measurement liquid is noted and accounted for [16]. All pycnometer flasks are immersed in a thermostated water-bath for investigating the influence of different measuring temperatures ϑ.

The concept of enforced syneresis is an acceleration of natural syneresis by applying an external force F to the gel sample. Consequently, a pressure difference Δp between the gel sample and the environment is induced in order to drain out the liquid enclosed. For that purpose, a uni-axial testing machine in combination with a pressure cell is proposed [3]. The testing machine (*ProLine Z010, Zwick/Roell*) applies a specified force F to the gel sample and records the resulting change in sample height Δs which can be converted to a corresponding volume decrease $\Delta V/V_0$. The gel sample investigated is itself poured directly into in the measuring cell, see Fig. 7 (right). Head plate, cylinder and base plate are made of stainless steel. Porous sintered filter plates (*Tridelta Siperm R*) are employed to support the nanofiltration membranes (*Dow Filmtec NF270*) that are necessary for retention of the gel. The force F is applied to the gel sample by means of the plunger. Liquid contained in the gel sample may pass through the membranes and is picked up by a lower collecting device or pushed upwards through the head plate. As with the pycnometer flasks, the measuring cell is immersed in a thermostated water-bath for assuring a constant temperature ϑ during the experiment.

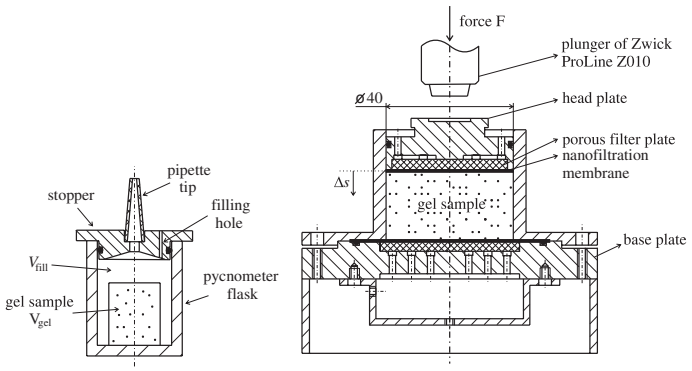

Fig. 7 Measurement equipment for natural (*left*) and enforced (*right*) syneresis [19]

3.3 Batch Precipitation, Stirred

Stirred batch precipitation experiments have to be carried out to account for the impact of fluid mechanic stress on the resulting fragment size distribution. Instead of the apparatus described in the previous Sect. 3.1, an experimental set-up is suggested that produces gel volumina of about $V_{gel} = 1-2.5\,\mathrm{l}$. These volumina are not solely prepared by the simple syringe pump but by a continuous process, see Fig. 8. Different solutions of sodium silicate, respectively, sulphuric acid are filled into the thermostated tanks B-1 and B-2. These solutions are pumped by P-1 and P-2 to the Y-mixing nozzle where they are mixed. Afterwards, the mixed solution flows either into a stirred tank reactor ($V_{STR} \approx 5\,\mathrm{l}$, $h_{STR} = 300\,\mathrm{mm}$, $d_{STR} = 150\,\mathrm{mm}$ with a double-stage intermig stirrer, $d_s = 119\,\mathrm{mm}$ [11]) or into a taylor-couette reactor ($h_{TCR} = 390\,\mathrm{mm}$, $d_{a,TCR} = 100\,\mathrm{mm}$, $d_{i,TCR} = 75.8\,\mathrm{mm}$ [17, 22]) where it is stirred before and beyond gelation. Equal mass flow rates $\dot{m}$ of the reactants are assured by means of magneto-inductive flow meters. Water is used for their calibration and for the cleaning of the mixing nozzle. Multi-pass valves switch between them. Due to the different densities ρ_i of reactants and water, a correction for the mass flow rates $\dot{m}$ is necessary [11].

Typical initial parameters for two standard experiments are listed in Table 1. The masses m of sodium silicate, respectively, sulphuric acid are referred to the total mass of water in the mixed solution. On the basis of these parameters, the temperature ϑ, ionic strength I (addition of NaCl and Na_2SO_4) and the energy dissipation ε due to the stirrer speed n_s may be varied systematically. After gelation, i.e. $t > t_g$, samples of the reactor content are taken with a syringe and the fragment size distribution is determined with laser light diffraction (*Mastersizer S, Malvern Instruments*).

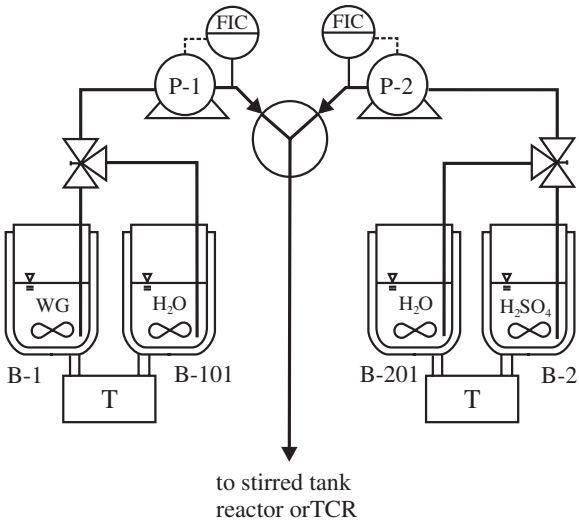

Fig. 8 Scheme of batch plant and outlet to stirred tank reactor or TCR (Taylor-Couette reactor) [11]

Table 1 Initial parameters for stirred batch process [11]

	Composition ($X_i / \frac{g}{g_{H_2O}}$)	Gelation time (t_g/min)	Temperature (ϑ/°C)	Stirrer speed (n_s/min^{-1})
Acid-catalysed	$X_{H_2SO_4} = 0.25$	80	20	400
	$X_{Na_2O \cdot 3.3SiO_2} = 0.084$			
Base-catalysed	$X_{H_2SO_4} = 0.019$	40	20	400
	$X_{Na_2O \cdot 3.3SiO_2} = 0.136$			

4 Phenomenology of Gel Formation

This section is structured as follows: firstly, the influence of systematically varied chemical composition of the reactants on the measured gelation time is presented. Then, a model is proposed that considers quantitatively the dependencies of the process parameters pH and ionic strength on the gelation time. The influences of pH, ionic strength and temperature on the gel firmness after gelation are discussed. Further on, the volume decrease of natural and enforced syneresis for unstirred gel samples is presented. Based upon these data, a predictive model is discussed which correlates both. In the last section, the influence of fluid mechanical stress on the resulting fragment size distributions is determined.

4.1 Gelation Time t_g

4.1.1 Experimental

Oscillatory rheometry is used to determine the gelation time t_g experimentally depending on the chemical composition of the reactants. For that purpose, silica is precipitated batch-wise via the manually operated syringe pump. The measured gelation time t_g is plotted as a function of different mass fractions x_i of the reactants in Fig. 9. There are two regions of fast gelation. One region can be identified for a mass fraction of sulphuric acid $x_{H_2SO_4} \approx 0.1$ and almost all mass fractions of water glass x_{WG}, while, for the second region greater mass fractions of sulphuric acid $x_{H_2SO_4}$ and water glass x_{WG} are necessary. Between these two regions, a maximum in gelation time t_g occurs. The division into two regions and the occurrence of the maximum is due to the pH of the mixed solution. The pH as well as the solubility $\tilde{c}^{\star}_{Si(OH)_4}$ and ionic strength I are calculated in the next section.

4.1.2 Model

For the calculation of the pH it is assumed that the sulphuric acid dissociated completely and an equivalence exists between sodium ions in the silicate solution and hydroxyl ions, i.e. Na_2O acts as 2NaOH [10]. The pH is calculated with

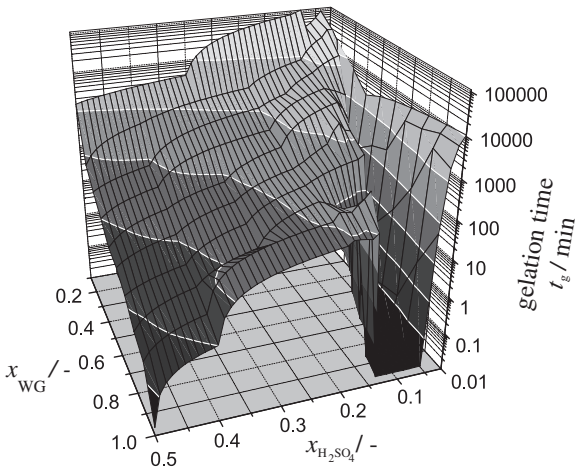

Fig. 9 Measured gelation time t_g as a function of different mass fractions x_i of reactants [10]

$$\mathrm{pH} = -\log(c(\mathrm{H}^+) - c(\mathrm{Na}^+)) \quad \text{for acid region} \tag{5}$$

$$\mathrm{pH} = -\log\left(\frac{10^{-14}}{c(\mathrm{Na}^+) - c(\mathrm{H}^+)}\right) \quad \text{for basic region} \tag{6}$$

The concentrations of inert Na^+ ions and the catalytic H^+ ions changes negligibly during the reaction. This is due to a changed liquid volume as a consequence of produced water and the transition of solved to solid silica. The calculated pH is shown in Fig. 10a. For $x_{H_2SO_4} \geq 0.15$, a $\mathrm{pH} < 2$ is calculated. According to [1, 5, 10], the polymerization reaction is acid-catalysed, resulting in shorter gelation times t_g with increasing mass fractions of sulphuric acid $x_{H_2SO_4}$ and sodium silicate solution x_{WG} of the reactants. The pH is in the basic region for low mass fractions of sulphuric acid ($x_{H_2SO_4} \leq 0.1$). Thus, the polymerization is base-catalysed. Between these two boundary values for $x_{H_2SO_4}$, the pH rises strongly, resulting in a transition from acid- to base-catalysed polymerization. That is the reason for the maximum in gelation time t_g.

In addition to the pH of the mixed solution, the sum of the solubility $\tilde{c}_i^\star$ of monomeric silicic acid $Si(OH)_4$ and the silicate anion $Si(OH)_3O^-$ as well as ionic strength I are relevant. For $\mathrm{pH} < 7$, the anion does not exist and the saturation concentration of monomeric silicic acid $\tilde{c}^\star_{Si(OH)_4}$ is calculated by Eq. (7) [4].

$$\log\left(\frac{\tilde{c}^\star_{Si(OH)_4}}{\mathrm{mol/l}}\right) = -2.44 - 0.053 \cdot \mathrm{pH} \tag{7}$$

Above $\mathrm{pH} = 9$, the saturation concentration of monomeric silicic acid is constant and about $\tilde{c}^\star_{Si(OH)_4} = 1.66 \times 10^{-3}\mathrm{mol/l}$. However, the equilibrium between the monomeric silicic acid and its anion must be considered. It is characterized by Eq. (8) [4].

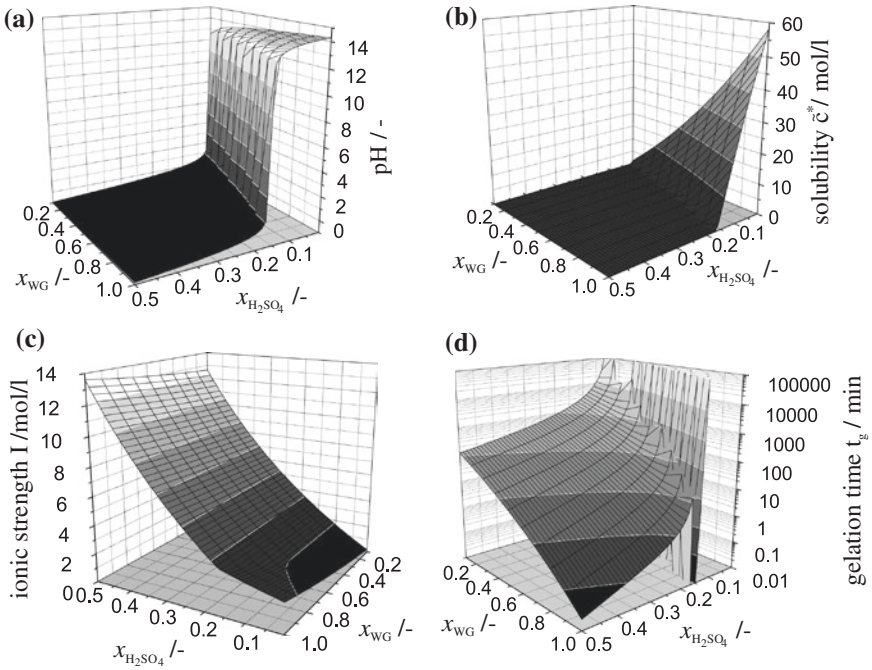

Fig. 10 pH (**a**), solubility $\tilde{c}^\star$ at $\vartheta = 25\,°C$ (**b**), ionic strength I (**c**) and calculated gelation time t_g (**d**) depending on mass fractions x_i of reactants [10]

$$\frac{\tilde{c}^\star_{Si(OH)_3O^-}}{mol/l} = 1.85 \times 10^4 \cdot \left(\frac{\tilde{c}^\star_{Si(OH)_4}}{mol/l}\right) \cdot \left(\frac{\tilde{c}_{OH^-}}{mol/l}\right) \tag{8}$$

The sodium and sulphate ions and pH are considered for the calculation of ionic strength I. Here, it should be mentioned that both pH and ionic strength I change slightly during the polymerization due to the produced water. According to Eq. (3), the ionic strength I is calculated by

$$I = \frac{1}{2} \cdot \left[10^{-pH} + 10^{-(14-pH)} + 4 \cdot \tilde{c}(SO_4^{2-}) + \tilde{c}(Na^+)\right]. \tag{9}$$

By combining these parameters in an empirical equation of the form

$$t_g = A \cdot I^{-0.5} \cdot 10^{-|pH_{iso}-pH|} \cdot 10^{-\left(\frac{\tilde{c}-\tilde{c}^\star(pH)}{mol/l}\right)} \tag{10}$$

the gelation time t_g can be calculated [10] (see Fig. 10d). The constant A is a fitting parameter that has been found to be $A = 6 \times 10^5\,\text{min}\,(\text{mol/l})^{0.5}$. Hereby, $\tilde{c}$ and $\tilde{c}^\star$ represent the concentration of silicate used, respectively, the pH dependent saturation concentration. For the latter, the calculated values of Eqs. (7) and (8) must be summed up. Their difference is the driving force for particle formulation. The absolute

difference between pH and pH_{iso} is used to account for the different pH-dependent catalytic mechanisms. For the dependency of ionic strength I, an exponent of -0.5 has been chosen due to the influence of the Debye-length $1/\kappa \propto I^{-0.5}$ [10]. With Eq. (10), the influence of the chemical composition of reactants and their subsequent changes in pH and ionic strength I can be regarded. In the following section, the influence of pH, ionic strength I and temperature ϑ on the gel firmness are discussed.

4.2 Gel Firmness

4.2.1 Influence of pH

The impact of pH without a changed sodium silicate concentration is analysed by mixing sulphuric acid solution with different mass fractions $x_{H_2SO_4}$ to a sodium silicate solution with a constant mass fraction $x_{WG} = 0.6$. The mass of sulphuric acid, and thus, its mass fraction $x_{H_2SO_4}$ of the reactant, is referred to the total mass of water in the mixed solution, i.e. the load of sulphuric acid $X_{H_2SO_4} = \frac{M_{H_2SO_4}}{M_{H_2O,mix}}$. Typical courses for the time-dependent storage G' and loss modulus G'' are shown in Fig. 11 (left). The circles indicate the intersection of both moduli, and thus, the gelation time t_g. The pH changes and different gelation times t_g are obtained by means of different loads $X_{H_2SO_4}$. To compensate for that, time t is normalised with the gelation time t_g, i.e. $t_{norm} = t/t_g$, see Fig. 11 (right). For reasons of simplicity, the loss modulus G'' is not shown. The sharp rise for $t_{norm} \leq 1$ is due to the gelation that leads to a fast increase in viscosity. Acid-catalysed ($0.204 \leq X_{H_2SO_4} \leq 0.427$) gels offer greater values for the storage modulus G' for $t_{norm} \to \infty$ resulting in stronger gels than base-catalysed ($0.019 \leq X_{H_2SO_4} \leq 0.021$).

It is remarkable that the curves of acid- and base-catalysed polymerization coincide to one master curve for each region of catalysis. This behaviour has been shown for polymeric lattices with the same fractal dimension, agglomeration

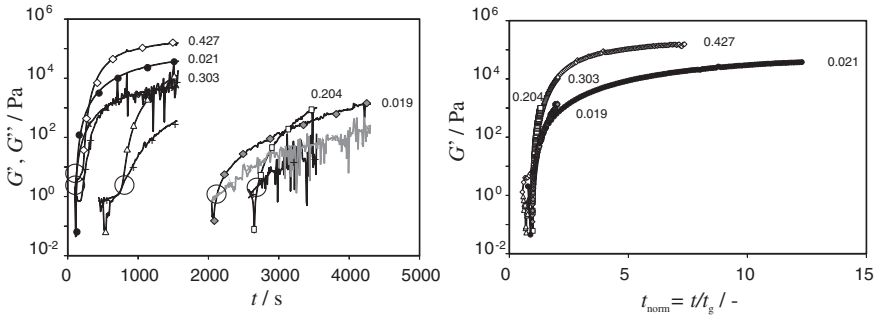

Fig. 11 Storage modulus G' (*filled* base-catalysed, *blank* acid-catalysed) and loss modulus G'' (x: base-catalysed, +: acid-catalysed) for different loads $X_{H_2SO_4}$ (*left*), G' as a function of normalised time t_{norm} (*right*) [10]

conditions and solid content [18]. Because of an equal solid content of the gels investigated, the differences in the maximum of G' indicate different fractal dimensions d_f and agglomeration mechanisms [10]. That can be determined even visually. Since acid-catalysed gels are translucent and tend to brittle fracture, base-catalysed gels are rather turbid or opaque. Because the primary particles of both gels are in the same order of magnitude (about 20 nm), a different agglomeration mechanism is responsible for the different appearance. This agrees with the theory for development of solid structures presented in Sect. 2.2. The primary particles are too small to scatter white light, but the secondary particles on a higher organization level are too distant to interfere constructively in the case of acid-catalysed gels. However, for base-catalysed gels, the secondary structure allows for interference with white light, resulting in the turbid appearance [10].

4.2.2 Influence of Ionic Strength

Due to addition of salts to the mixed solution the ionic strength I increases. According to Sect. 2.4, the electrostatic double layer is compressed, resulting in reduced repulsive interacting forces. An ionic strength of $I = 12$ mol/l is calculated for the acid-catalysed gel (pH $\approx 0 - 1$), which is large compared to that of the base-catalysed gel (pH $\approx 12 - 13$) of $I = 0.8$ mol/l. For that reason, the latter is much more sensitive to small amounts of added salts. This relation is shown in Fig. 12.

The more salt is added to the mixed solution, the earlier the sharp increase of the storage modulus occurs, i.e. a reduced gelation time t_g. There seems to exist a different effectiveness of NaCl and Na_2SO_4. For small concentrations, NaCl leads to a faster gelation, whereas it is vice versa for higher concentrations. A faster gelation is observed by exchange of Na^+ ions through H^+ ions. This is not due to a change in ionic strength I, but to a decrease in pH and thus, a shifting towards the global minimum of gelation time t_g. For $t_{norm} \to \infty$, the storage modulus G' has the same final value for both salts and concentrations, and all curves coincide. Thus, addition of salt only affects the rate of gelation, but not the final gel firmness [10].

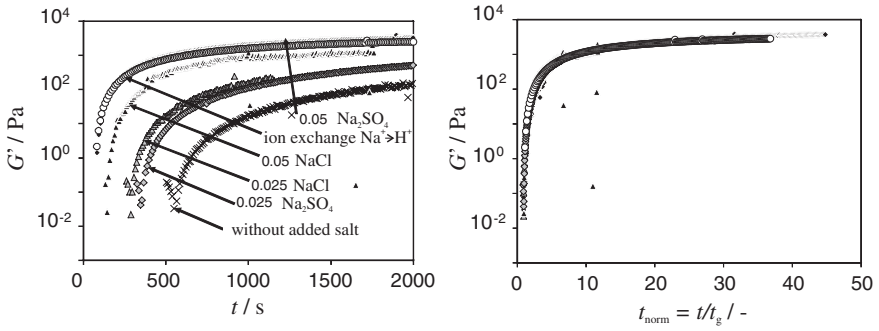

Fig. 12 Storage modulus G' for different salts and concentrations in mol/(kg H_2O of solution), base-catalysed gel with $X_{Na_2O \cdot 3.3SiO_2} = 0.084$ and $X_{H_2SO_4} = 0.017$ [10]

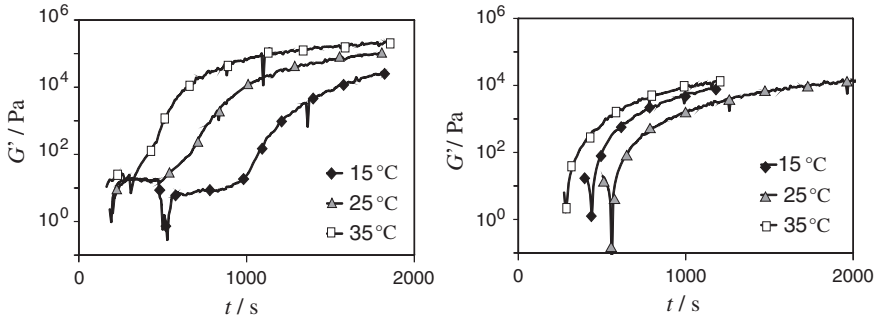

Fig. 13 Storage modulus G' for different temperatures ϑ, acid-catalysed ($X_{Na_2O \cdot 3.3SiO_2} = 0.099$ and $X_{H_2SO_4} = 0.42$) (*left*) and base-catalysed ($X_{Na_2O \cdot 3.3SiO_2} = 0.084$ and $X_{H_2SO_4} = 0.017$) (*right*) [10]

4.2.3 Influence of Temperature

Since a polymerization reaction is responsible for gelation, the temperature ϑ is another important process parameter. With rheological measurements at $\vartheta = 15, 25$ and $35\,°C$, its influence on both acid- and base-catalysed gels is investigated, see Fig. 13. In the case of an acid-catalysed gel, an increase in temperature ϑ results in a reduction of gelation time t_g. This is explained with a higher mobility of the reactants and a reduction in activation energy for polymerization. For base-catalysed gels, a monotonous decrease of gelation time t_g with temperature ϑ cannot be identified. A solution polymerizing at $\vartheta = 25\,°C$ needs more time for gelling than at $\vartheta = 15\,°C$ or $\vartheta = 35\,°C$. The explanation for this peculiar behaviour is a preequilibrium step involving an induction period. During this period, small polymeric clusters grow and monomeric silicic acid prefers to react with these (see Sect. 2.3).

In summary, the process parameters temperature ϑ, pH and ionic strength I influence the gelation process of silica. The transition from the mixed solution of the reactants to the gel is rather gradual than abrupt. The temperature ϑ and ionic strength I affect only the rate of polymerization. In general, with an increase of temperature ϑ, the rate is accelerated, resulting in shorter gelation times t_g (except for the phenomenon explained above). Addition of salts to the mixed solution weakens the electrostatic repulsive interaction forces and leads to faster agglomeration, resulting in shorter gelation times t_g as well. However, pH of the solution strongly affects the gelation time t_g as well as the resulting structures and properties of the gel. By varying the pH, the gelation time t_g comprises different orders of magnitude ranging from few seconds to several hours. For $\mathrm{pH} < 2$, the polymerization is acid-catalysed and less crosslinked solid particles form. The resulting gel has a high firmness, tends to brittle fracture and appears translucent. In the case of base-catalysed polymerization ($\mathrm{pH} > 2$), the silica particles form a netlike bonded, crosslinked gel with a lower firmness that appears opaque or turbid.

4.3 Syneresis

4.3.1 Unstirred, Natural Syneresis

We propose cylindrical gel samples with $d_{\text{sample}} = 20\,\text{mm}$ and $V_{\text{sample}} \approx 6\,\text{ml}$ that are prepared at $\vartheta = 20\,°\text{C}$ for measurement of natural syneresis. The relative volume decrease $\Delta V/V_0$ of an acid-catalysed model gel (reactants with mass fractions $x_{H_2SO_4} = 0.50$ and $x_{WG} = 0.40$) for three different temperatures ϑ is shown in Fig. 14. Independent of temperature ϑ, two regions of volume decrease can be identified. The first one is for $t \leq 50\,\text{h}$ in that the gel shrinks fast due to the initial flexible solid skeleton. With time the skeleton stiffens because uncondensed silanol groups polymerize, slowing down further volume decrease. An increase in temperature ϑ leads to faster shrinkage of the gel because of a higher movement of the pore liquid through the gel network and a higher polymerization rate. In the second region ($t > 50\,\text{h}$), the volume decrease $\Delta V/V_0$ asymptotically approaches a maximum value $(\Delta V/V_0)_{\max}$ and finally, shrinkage stops. It is remarkable that the total amount of shrinkage is independent of temperature ϑ. This is against the phenomenon of a slightly smaller volume decrease $\Delta V/V_0$ with increasing temperature ϑ, determined by [14]. When regarding the error bars, this statement can be neither proved nor disproved.

To describe the course of volume decrease $\Delta V/V_0$ with time t and its maximum value at $t \to \infty$ by means of a mathematical model, each curve may be fitted via an empirical model, see Eq. (11).

$$\frac{\Delta V}{V_0} = \left(\frac{\Delta V}{V_0}\right)_{\max} \cdot \left[1 - \exp\left(-\left(\frac{t}{\tau}\right)^n\right)\right] \tag{11}$$

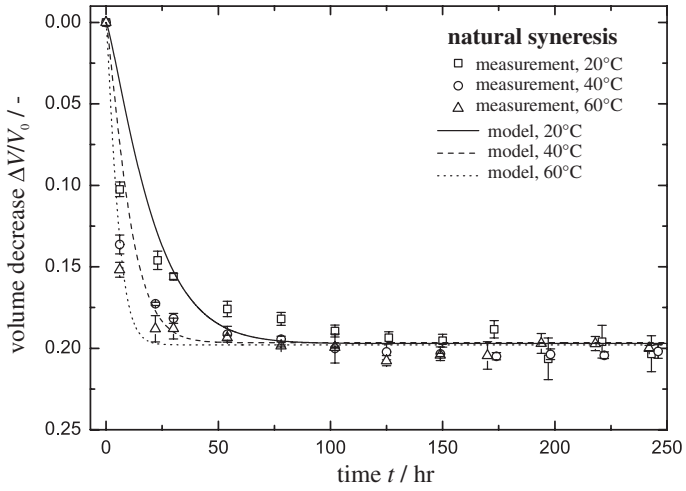

Fig. 14 Relative volume decrease $\Delta V/V_0$ for different temperatures ϑ, natural syneresis [19]

Table 2 Fitting parameters of empirical model Eq. (11) for natural syneresis [19]

Temperature	Max. volume decrease	Time constant	Exponent
ϑ/°C	$(\Delta V/V_0)_{max,nat}$/–	τ_{nat}/h	n/–
20	0.20	21.7	1.23
40	0.20	11.1	1.23
60	0.20	5.6	1.23

While the first fit parameter $(\Delta V/V_0)_{max}$ accounts for the maximum volume decrease, the second parameter τ represents a characteristic time constant affecting the rate of volume decrease. An exponent n is added to ensure a good agreement between the measured and modeled rates. The values of these fitting parameters are listed in Table 2.

The curves of the empirical model are shown in Fig. 14. A higher temperature ϑ leads to a reduced time constant τ. It turns out that the exponent n varies between 1.21 and 1.25 depending on the temperature ϑ. In order to minimize the number of fitting parameters, a constant value of 1.23 is chosen without changing the residuum sum of squares to any appreciable extent.

4.3.2 Unstirred, Enforced Syneresis

The idea behind enforced syneresis is an acceleration of natural syneresis in order to make investigations in significantly shorter time. Therefore, a pressure difference Δp is applied to the gel. In Fig. 15, the measured (solid line) volume decrease $\Delta V/V_0$ is plotted for a constant temperature of $\vartheta = 20\,°C$ as a function of time t and the pressure difference Δp. As expected, higher pressure differences Δp result in faster gel shrinkage and larger maximum volume decreases $(\Delta V/V_0)_{max}$. Each measured course may be fitted with Eq. (11) (dashed lines in Fig. 15) to determine their characteristics with respect to maximum volume decrease and rate. Only for $\Delta p = 0.8\,bar$ and $t < 12\,h$ there are small deviations caused by the model itself. Gel samples with increased measurement temperatures (i.e. $\vartheta = 40\,°C$ and $\vartheta = 60\,°C$) are investigated to account for the temperature dependency of enforced syneresis. Refer to [19] for their graphical representation. In comparison with $\vartheta = 20\,°C$, each curve is shifted to shorter times, but to negligibly different values for the maximum volume decrease $(\Delta V/V_0)_{max}$. A temperature change affects only the course, but not the maximum volume decrease. Thus, enforced syneresis behaves in exactly the same way as natural syneresis with respect to temperature dependency.

The maximum volume decrease $(\Delta V/V_0)_{max}$ and the characteristic time constant τ are modeled as a function of pressure difference Δp and temperature ϑ to correlate natural and enforced syneresis, and the predictive model equations for syneresis Eqs. (12) and (13) are proposed.

$$\ln\left(\frac{\Delta V}{V_0}\right)_{max} = A + \frac{B}{C + \Delta p} \tag{12}$$

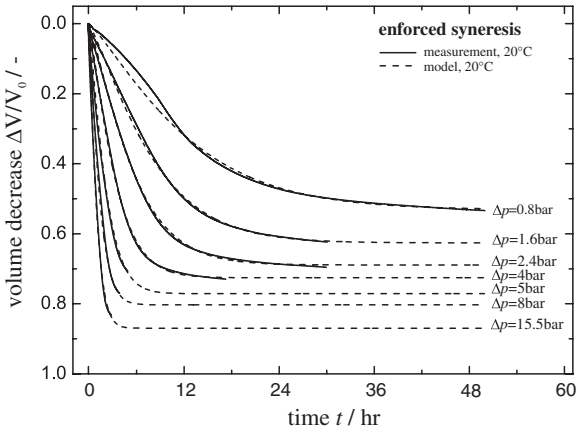

Fig. 15 Relative volume decrease $\Delta V/V_0$ for $\vartheta = 20\,°\mathrm{C}$, enforced syneresis [19]

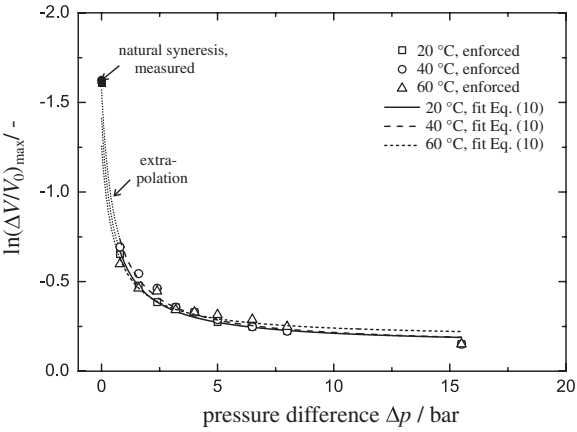

Fig. 16 Max. volume decrease $(\Delta V/V_0)_{\max}$ as a function of pressure difference Δp [19]

$$\log\tau = D - E \cdot \log(p^\star + \Delta p) \tag{13}$$

The symbols in Fig. 16 represent the values of maximum volume decrease $(\Delta V/V_0)_{\max}$ that are determined by the empirical model Eq. (11). Here, natural syneresis is in accordance with $\Delta p = 0\,\mathrm{bar}$ (the filled symbols).

In analogy, Fig. 17 shows the values of the characteristic time constant τ. An artificial pressure $p^\star = 1\,\mathrm{bar}$ is added for a correct logarithmic representation of the pressure difference Δp.

The values of the fitting parameters are given in Table 3. They sufficiently reflect the progression of enforced syneresis [19]. Besides that reflection, the predictive model equations allow for extrapolation to natural syneresis (dotted lines for $\Delta p < 0.8\,\mathrm{bar}$ shown in Figs. 16 and 17).

The extrapolated values for natural syneresis can be calculated from these fitting parameters by setting Δp to 0 bar and simple arithmetic operations. They are

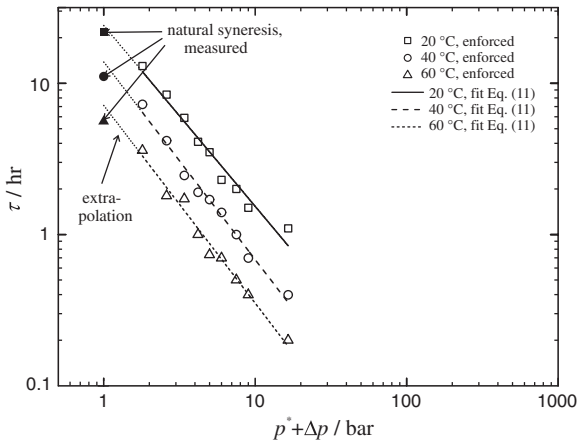

Fig. 17 Characteristic time constant τ as a function of pressure difference Δp [19]

Table 3 Values of fitting parameters A, B, C, D and E for three different temperatures [19]

Temperature (ϑ/°C)	A (–)	B (bar)	C (bar)	D (–)	E (–)
20	−0.14	−0.72	0.57	1.38	−1.20
40	−0.14	−0.81	0.57	1.14	−1.31
60	−0.18	−0.61	0.57	0.85	−1.31

listed in Table 4. For natural syneresis, we determined $(\Delta V/V_0)_{\mathrm{max,nat}} = 0.20$ independent of the temperature ϑ. Thus, we are able to predict the maximum volume change with a relative error of 25 % in the case of $\vartheta = 20\,^{\circ}\mathrm{C}$. For $\vartheta = 60\,^{\circ}\mathrm{C}$, the error is about 45 %. In the case of the second parameter, the characteristic time constants τ are overestimated by the predictive model, but their sequential arrangement is predicted correctly, i.e. $\tau_{\mathrm{extra}}(\vartheta = 20\,^{\circ}\mathrm{C}) > \tau_{\mathrm{extra}}(\vartheta = 40\,^{\circ}\mathrm{C}) > \tau_{\mathrm{extra}}(\vartheta = 60\,^{\circ}\mathrm{C})$. Here, the maximum relative error is 24 %. Through experimental results at even lower pressure differences than $\Delta p = 0.8$ bar, a minimization of the errors for maximum volume decrease $(\Delta V/V_0)_{\mathrm{max,nat}}$ as well as for the characteristic time constant τ is assumed.

To summarise, an extrapolation method based upon enforced syneresis is suggested that allows for prediction of natural syneresis of silica. The method depends on an empirical model with two fitting parameters. The first parameter accounts for the maximum volume decrease $(\Delta V/V_0)_{\mathrm{max}}$, while the second considers the rate of syneresis in form of a characteristic time constant τ. Both parameters depend on the temperature ϑ and the applied pressure difference Δp. In order to fit these parameters, the time-dependent shrinkage process of enforced syneresis with $0.8\,\mathrm{bar} < \Delta p < 15.5\,\mathrm{bar}$ is determined experimentally for three temperatures of $\vartheta = 20$, 40 and 60 °C. The greater the pressure difference Δp, the greater the total shrinkage of the gel, i.e. larger maximum volume decreases $(\Delta V/V_0)_{\mathrm{max}}$ are obtained. An increase in temperature ϑ leads to a faster shrinkage (lower characteristic time constants τ) but to almost unchanged maximum volume decreases.

Table 4 Comparison of extrapolated max. volume decrease $(\Delta V/V_0)_{max}$ and characteristic time constant τ with values determined by Eq. (11) [19]

Temperature (ϑ/°C)	Max. volume decrease ($(\Delta V/V_0)_{max,nat}$/–)	Max. volume decrease ($(\Delta V/V_0)_{max,extra}$/–)	Time constant (τ_{nat}/h)	Time constant (τ_{extra}/h/–)
20	0.25	0.20	24.0	21.7
40	0.21	0.20	13.8	11.1
60	0.29	0.20	7.1	5.6

As already shown in Sect. 4.3.1, the temperature ϑ affects only the rate. In addition, the process of natural syneresis can be calculated with this predictive model. For validation, natural syneresis is measured with an adapted pycnometer device that allows the recording of the rate of shrinkage and maximum volume decrease. A comparison between predicted and measured natural syneresis shows that the characteristic time constants τ are calculated with a maximum relative error of 24 %. However, the maximum volume decrease $(\Delta V/V_0)_{max}$ cannot be calculated correctly for all temperatures investigated. Maximum relative errors of about 45 % occur. To account for that, measurements of enforced syneresis at even lower pressure differences than $\Delta p < 0.8$ bar are suggested.

4.3.3 Stirred, Influence of Fluid Mechanical Stress

In the previous Sect. 4.1, the influences of temperature ϑ, pH and ionic strength I on the gelation process without stirring are shown. Due to mechanical work, the formation of a wide-reaching gel network is avoided and instead, gel fragments occur. Experiments of stirred batch precipitation are carried out to analyse the impact of the stirrer on the time-dependent fragment size distribution. Thereby, a stirred tank and a Taylor-Couette reactor are used in order to consider the homogeneity of the input of mechanical work. Typical fragment size distributions for the standard acid- and base-catalysed stirred batch precipitation (see Table 1 for parameters) are shown in Fig. 18.

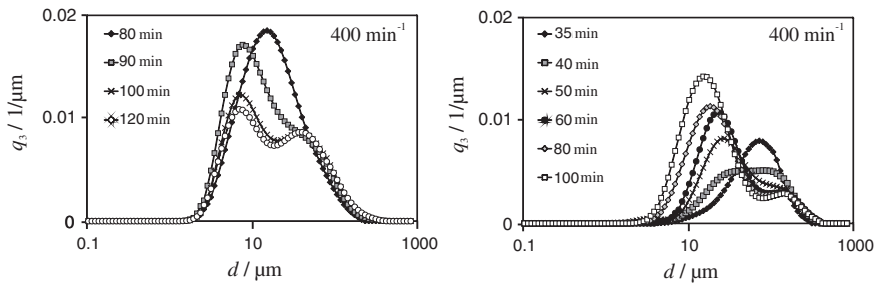

Fig. 18 Time-dependent fragment size distribution for standard batch experiments, acid-catalysed (*left*) and base-catalysed (*right*) [20]

The stirred tank reactor is used for both types of catalysis and bimodal distributions are determined. In the case of acid-catalysed polymerization, the peak at $d \approx 10\ \mu m$ splits up into one peak at $d \approx 8\ \mu m$ and a second at $d \approx 50\ \mu m$. With increasing time t, the first peak diminishes and develops towards the second. The fragment size distribution of the base-catalysed polymerization behaves vice versa. Two peaks at $d \approx 10\ \mu m$ and $d \approx 130\ \mu m$ develop from the initial peak of $d \approx 90\ \mu m$, but the first one grows and is shifted to smaller fragments with time t.

A Taylor-Couette reactor may be used instead of the stirred tank to ensure that the bimodal distributions are not caused by the inhomogeneous input of mechanical work. Figure 19 shows the resulting fragment size distributions. The Taylor-Couette reactor generates bimodal distributions as well, albeit less distinctive for the acid-catalysed gelation. Smaller gel fragments occur ($d_{max} \propto \varepsilon^{-0.25}$) [11] with increasing speed of the inner cylinder, and thus, increasing input of mechanical work. Due to the different viscosities, the dissipated energy of the acid-catalysed gel has a larger range ($3.6\,W/kg \leq \varepsilon \leq 70.2\,W/kg$) than the base-catalysed ($1.5\,W/kg \leq \varepsilon \leq 26.4\,W/kg$), but its impact on the fragment size distribution is less significant for acid-catalysed gels. However, the maximum fragment size x_{max} is stabilised directly after gelation [20]. This is expressed in the fact that the specified abscissa value of the second peak remains almost unchanged with time t.

Addition of salt in different concentrations changes the ionic strength I of the gel, and subsequently, the fragment sizes. Base-catalysed gels with a much higher sensitivity to a varying ionic strength I in comparison to acid-catalysed gels (see Sect. 4.2.2) are considered. By the addition of salts, i.e. NaCl and Na_2SO_4 (see Fig. 20), the gelation time t_g is reduced and the fragment sizes $d_{90,3}$ are increased. A reduction in gelation time t_g has already been shown in Sect. 4.2.2. Due to the dissociating salts, the electrical double layer is compressed, resulting in promotion of agglomeration, and thus, larger particles. It is remarkable that neither the concentration of Na^+ions nor the ionic strength I is responsible for the fragment sizes. For gels that are mixed with Na_2SO_4, the resulting fragment size $d_{90,3}$ is smaller than for gels mixed with NaCl. The reason is the equilibrium between sulphate ions (SO_4^{2-}), hydrogen ions (H^+) and the hydrogen sulphate (HSO_4^-). It is shifted towards the hydrogen sulphate by additional sulphate. As a result, hydrogen ions disappear, leading to a slightly increased pH (1.76 instead of 1.71) and reduced gel fragment sizes.

As determined in Sect. 4.2.3, the temperature ϑ affects the kinetic of gelation. Additionally, temperature ϑ also influences the size of the primary particles [20]. The usage of a thermostated tank reactor (see Fig. 8) with stirring speed $n_s = 400\,min^{-1}$ is appropriate to account for both effects under influence of stirring. See Table 1 for the composition of the reactants, heated up to experimental temperature.

It can be seen in Fig. 21 that ϑ an acceleration of gelation resulting in shorter gelation times t_g is achieved with increasing temperature. While the fragment sizes $d_{90,3}$ of the acid-catalysed gel hardly depend on the temperature ϑ, a strong dependency for base-catalysed gels exists. The fragment size raises $d_{90,3}$, but remains static at about 500 μm. An analysis of the median $d_{50,3}$ even provides

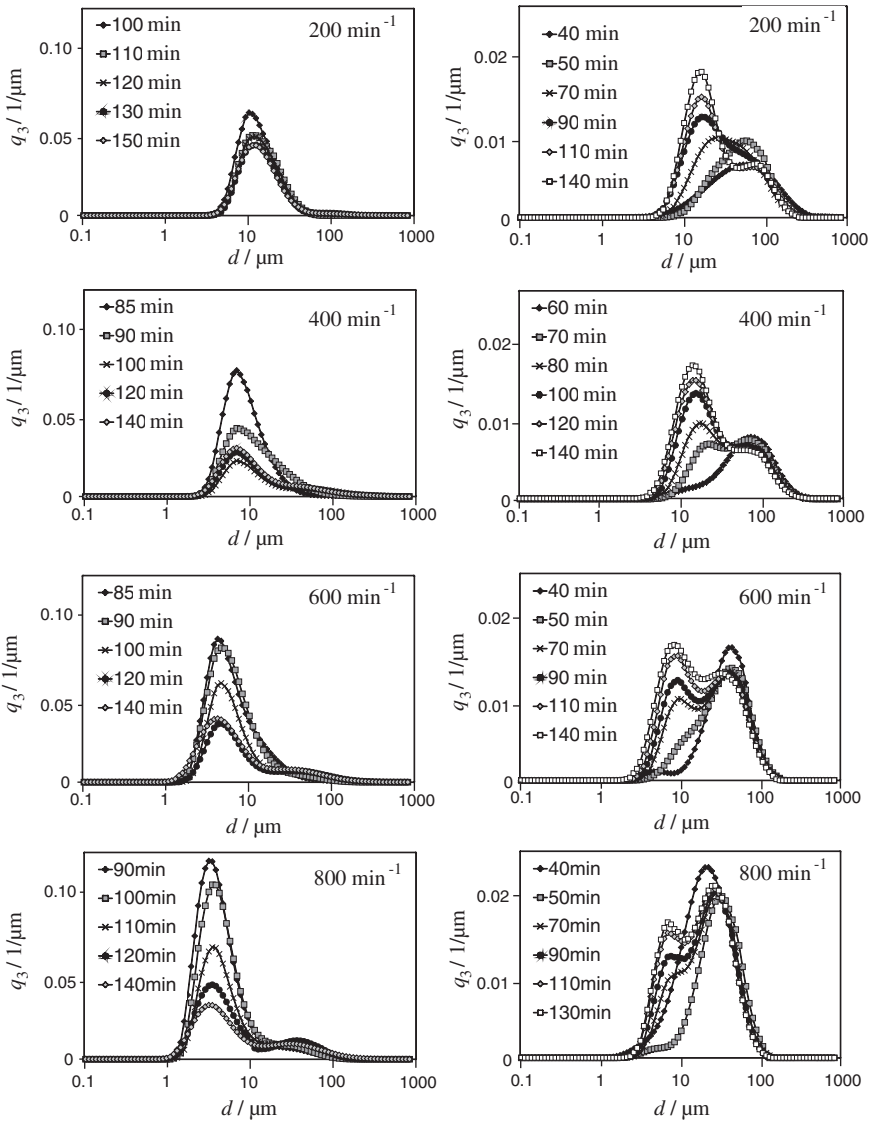

Fig. 19 Fragment size distributions for batch experiments with Taylor-Couette reactor, acid-catalysed (*left*) and base-catalysed (*right*) [11]

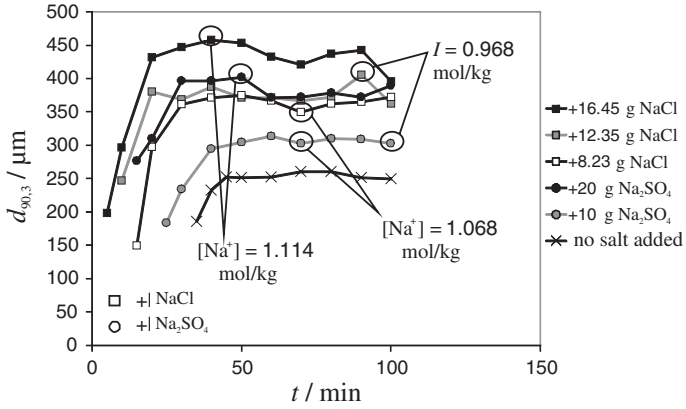

Fig. 20 Time-dependent fragment size $d_{90,3}$ as a function of added salts with different concentrations [20]

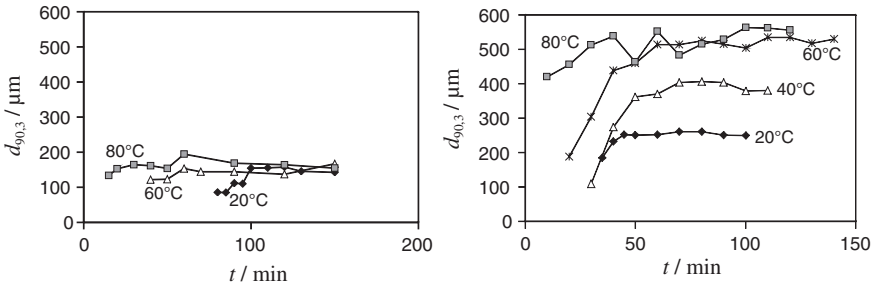

Fig. 21 Time-dependent fragment sizes $d_{90,3}$ for different temperatures ϑ, acid-catalysed (*left*) and base-catalysed (*right*), salts added to 3000 g H_2O [20]

a maximum for $\vartheta = 60\,°C$. This result is confirmed by BET measurements and SEM pictures [20].

Conclusions

The precipitation process of silica consisting of particle formulation, gelation and reorganization is reviewed. Process parameters, such as temperature ϑ, pH, ionic strength I and chemical composition x_i of the reactants used as well as stirring of the solution strongly affect that precipitation.

Precipitation of silica involves a catalytic polymerization reaction. The polymerization rate can be influenced depending on the pH. The pH of the mixed solution can be influenced by systematically varying the composition x_i of the

reactants (i.e. sulphuric acid and sodium silicate solution). The minimum polymerization rate is at pH $\approx$ 2, that is, the isoelectric point, and increases with changing pH. Thus, the resulting gelation time t_g takes values from a few seconds to several hours. In addition to an impact on the gelation time t_g, an altered pH changes the appearance and firmness of the gel. For pH $<$ 2 (acid-catalysed), translucent gels tending to brittle fracture are obtained. In the case of pH $>$ 2 (base-catalysed), they are rather opaque or turbid and offer a lower firmness.

The addition of salts (equivalent to an increased ionic strength I) to the mixed solution leads to a faster gelation, i.e. shorter gelation times t_g. Due to a low ionic strength ($I = 0.8$ mol/l) of the standard base-catalysed gel, small amounts of salts result in a considerable reduction of gelation time t_g (1 min instead of 10). That reduction cannot be identified for the acid-catalysed gel since it has a much higher ionic strength ($I = 12$ mol/l). However, the firmness of the gel is unaffected by added salts. Thus, an increased ionic strength I only affects the rate of polymerization. An increasing temperature ϑ has the same effect. It reduces the gelation time t_g of both acid- and base-catalysed gels, but less significantly than due to an increased ionic strength I.

The polymerization process that is responsible for the precipitation continues long beyond the gelation time t_g, leading to reorganization and syneresis. In the case of natural syneresis, the volume decreases of about 20 % after ca. 10 days independent of the measurement temperature ϑ. With increasing temperature ϑ, only the rate of syneresis is accelerated. In order to analyse this and other possible influences in less time t, natural syneresis may be accelerated by applying an external force F to the gel ('enforced syneresis'). Thereby, the maximum volume decrease $(\Delta V/V_0)_{\max}$ as well as the rate of syneresis strongly increases (maximum volume decreases $(\Delta V/V_0)_{\max}$ of 85 % in a few hours). To correlate enforced and natural syneresis, a predictive model based upon enforced syneresis is proposed. This method considers all results of enforced syneresis and allows for extrapolation to an external force $F = 0$, that is, the natural syneresis. In particular, the model predicts the maximum volume decrease $(\Delta V/V_0)_{\max}$ and the rate of syneresis. A comparison between extrapolated and measured values for natural syneresis yields maximum relative errors of 45 % for the maximum volume decrease $(\Delta V/V_0)_{\max}$ and 24 % for the rate. The extrapolation method is very sensitive to measurements at very low external forces F, but these measurements cannot be operated yet with the equipment presented. However, a qualitative prediction of natural syneresis is given.

Gel fragments occur instead of a continuous solid skeleton due to a stirrer. Small fragments of the acid-catalysed gel diminish and grow to larger fragments with time t. The exact opposite is the case with the base-catalysed gel. The initial larger particles shrink, and thus, the fragment size distribution is shifted to smaller particles. Due to larger energy dissipation, the fragments are smaller, but the fragment size itself is established before gelation time t_g. It cannot be changed after gelation by means of higher energy dissipation. Additionally, the fragment size distributions can be manipulated by the same process parameters as described above. Different gels (acid- and base-catalysed) can be realised by changing the

composition x_i of the reactants. Due to addition of salts, agglomeration of particles is promoted, leading to faster gelation and larger fragment sizes (almost a doubling from 250 to 450 μm). As explained previously, this phenomenon is observed only for the base-catalysed gel because of its greater sensitivity to small amounts of salts. Increasing temperature ϑ accelerates the gelation for both gels. While the fragment sizes of acid-catalysed gels are almost unaffected, greater fragments form in the base-catalysed gel.

Acknowledgments We thank Deutsche Forschungsgemeinschaft (DFG) for the financial support within the research project SPP1273—colloid process engineering. We want to acknowledge Kerstin Quarch who did her PhD in the field of gelation and fragmentation and Hussein Sahabi who developed the experimental setup for measurement of enforced syneresis.

References

1. Brinker CJ, Scherer GW (1990) Sol-gel science—the physics and chemistry of sol-gel processing. Academic Press Inc., San Diego
2. Vysotskii ZZ, Strazhesko DN (1973) Isoelectric state of disperse silicas and ion exchange in acid solutions, adsorption and adsorbents, 1st edn. Wiley, New York, pp 55–71
3. Sahabi H, Kind M (2011) Consolidation of inorganic precipitated silica gel. Polymers 3:1423–1432. doi:10.3390/poly3031423
4. Iler RK (1978) The chemistry of silica—solubility, polymerization, colloid and surface properties, and biochemistry. Wiley, New York
5. Zerda TW, Artaki I, Jonas J (1986) Study of polymerization processes in acid and base catalyzed silica sol-gels. J Non-Cryst Solids 81:365–379
6. Schlomach J, Kind M (2004) Investigations on the semi-batch precipitation of silica. J Colloid Interface Sci 277:316–326
7. Bergna HE (1994) The colloid chemistry of silica. American Chemical Society, Washington, DC
8. Aubert C, Cannell DS (1986) Restructuring of colloidal silica aggregates. Phys Rev Lett 56(7):738–741
9. Oles V (1992) Shear-induced aggregation and breakup of polystyrene latex particles. J Colloid Interface Sci 154(2):351–358
10. Quarch K, Kind M (2010) Inorganic precipitated silica gel. Part 1: gelation kinetics and gel properties. Chem Eng Technol 33(6):1034–1039
11. Quarch K, Kind M (2010) Inorganic precipitated silica gel. Part 2: fragmentation by mechanical energy. Chem Eng Technol 33(7):1208–1212
12. Selomulya C, Bushell G, Amal R, Waite TD (2002) Aggregation mechanisms of latex of different particle size in controlled shear environment. Langmuir 18:1974–1984
13. Okkerse C (1970) In: Linsen BG, Fortuin JMH, Okkerse C, Steggerda JJ (eds) Physical and chemical aspects of adsorbents and catalysts. Academic Press, New York
14. Ponomareva TP, Kontorovich SI, Chekanov MI, Shchukin ED (1984) Sov J Colloids 46(1):118–120 (Eng trans)
15. Haselhuhn F, Kind M (2003) Pseudo-polymorphic behavior of precipitated calcium oxalate. Chem Eng Technol. doi:10.1002/ceat.200390053
16. Stephan P, Kabelac S, Kind M, Martin H, Mewes D, Schaber K (eds) (2010) VDI-heat atlas. Springer, Berlin
17. Racina A, Kind M (2006) Specific power input and local micromixing times in turbulent Taylor-Couette flow. Exp Fluids 41:513–522
18. Sefcik J, Grass R, Sandkühler P, Morbidelli M (2005) Kinetics of aggregation and gelation in colloidal dispersions. Chem Eng Res Des 83(A7):926–932

19. Wilhelm S, Kind M (2014) Prediction model for natural and enforced syneresis of acidic precipitated silica. Polymers 6(12):2896–2911. doi: 10.3390/polym6122896
20. Quarch K (2010) Produktgestaltung an kolloidalen Agglomeraten und Gelen - Gelierung und Fragmentierung anorganisch gefällten Siliciumdioxids. KIT Scientific Publishing, Karlsruhe
21. Schlomach J (2006) Feststoffbildung bei technischen Fällprozessen - Untersuchungen zur industriellen Fällung von Siliziumdioxid und Calciumcarbonat. Universitätsverlag Karlsruhe, Karlsruhe
22. Racina A (2009) Vermischung in Taylor-Couette Strömung. Universitätsverlag Karlsruhe, Karlsruhe

Synthesis, Structure and Mechanics of Nano-Particulate Aggregates

Carsten Schilde and Arno Kwade

Abstract In the most industrial processes nano-sized particles aggregate during their synthesis and the subsequent drying step forming aggregates with sizes in the order of several micrometers. The properties of these aggregates for application or further processing are specified by particle characteristics such as morphology, size, size distribution, bonding mechanism and structure of primary and secondary particles. In this study, the effect of the process parameters during particle synthesis and the following drying step on the structure formation and the resultant product and processing characteristics of precipitated nano-structured silica aggregates were investigated. For this purpose, the educts concentrations, stabilizing additives, mechanical energy input, pH-value and precipitation temperatures were varied during the precipitation process. In addition to the structure formation during precipitation, the resultant micromechanical aggregate properties of spherical silica model aggregates with a well-defined aggregate structure were characterized via nanoindentation and related to the aggregate structure and the interparticulate interaction forces. The micromechanical properties of these model aggregates were modelled depending on their structure using a modified form of the elementary breaking stress model of Rumpf. Since the characterization of particle-particle interactions in the nanometer size range is hardly possible, this effect on the aggregate fracture and deformation behavior was investigated by simulating the nanoindentation measurement of single aggregates using the "discrete element method".

Keywords Aggregates · Micromechanical properties · Nanoindentation · DEM · Silica · Precipitation

C. Schilde (✉) · A. Kwade
Institute for Particle Technology, TU Braunschweig,
Volkmaroder Str. 5, 38104 Braunschweig, Germany
e-mail: c.schilde@tu-bs.de

M. Kind et al. (eds.), *Colloid Process Engineering*,
DOI 10.1007/978-3-319-15129-8_9

1 Introduction

In the last years, the industrial mass production of nano-particulate products via pyrolysis or precipitation processes which are commonly used in the chemical, pharmaceutical, food and dye industry increases continuously. For these processes, the nano-sized particles typically aggregate during their synthesis and the subsequent drying step to aggregates with sizes on the order of several micrometers. The application of nanoparticle-based products is specified by the characteristics of the nanoparticle's resulting primary and secondary particles (Fig. 1). Thus, morphology, size, size distribution, bonding mechanism, and structure of primary and secondary particles are crucial factors, for determining possible applications [4]. These characteristics depend on the physicochemical properties of the particles as well as on the process parameters during synthesis and the subsequent drying step. Typically, a redispersion is necessary to obtain separately dispersed primary particles or defined aggregate sizes. The influential factors for such a dispersion process can be classified into the formulation of the homogenous phase, the stress mechanisms, intensity and frequency of the dispersing device, and the mechanical aggregate properties generated during particle synthesis [31, 41].

In order to obtain an optimized and economical dispersion process as well as the desired product properties, extensive knowledge of the structure formation during particle synthesis and its effect on the mechanical aggregate properties is necessary. This includes the surface modification, particle-particle interactions, the formation of solid bridges, the porosity, and the size distribution of the primary particles and aggregates. Currently, very little information is available regarding the relationship of the process and formulation parameters of the particle synthesis and the resulting aggregate structure properties on the one hand, and the micromechanical aggregate properties and the dispersion behavior on the other hand. This

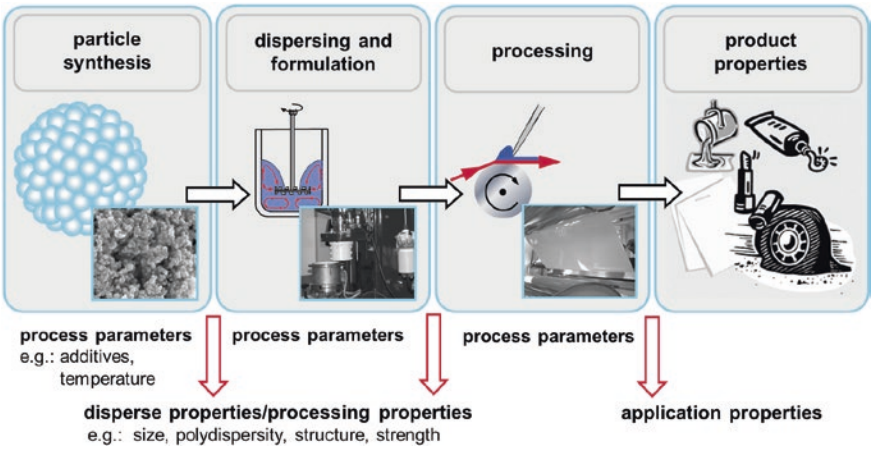

Fig. 1 Effect of process parameters on the processing and application properties

process-structure-property relationship is the main contribution within this study [6, 21, 25–27, 32, 34–39, 42]. Here, we discuss the following questions:

1. How do the process and formulation parameters during particle synthesis affect the primary particle formation, aggregate structure, and solid bridge formation?
2. What is the relationship between the micromechanical properties and the aggregate structure? How does one obtain/receive detailed information about particle interactions, solid bridges, and the behavior of deformation and fracture?
3. Can stress-strain relationships be derived from a series of indentation experiments, e.g. with the help of the discrete elements method?
4. Is it possible to relate micromechanical aggregate properties to application properties such as the dispersion process?

2 Structure Formation During Precipitation

In this project, a semi-batch silica precipitation process from inorganic solvents was investigated. Due to economic reasons and the well-known aspects of this silica synthesis, this process is established for mass production of silica in industrial processes. The precipitation process, especially those of water-soluble silicates are summarized extensively by Hinz [12], Iler [13], and Bergna [7]. By continuously adding sulphuric acid and sodium silicate to a buffer solution of water and sodium silicate, simultaneous primary processes take place. These process include the primary processes such as mixing, reaction and condensation of monomers, phase separation and primary particle growth, as well as the secondary processes such as aggregation, fragmentation, reorganization and aging [15] (see Fig. 2). These physicochemical processes and

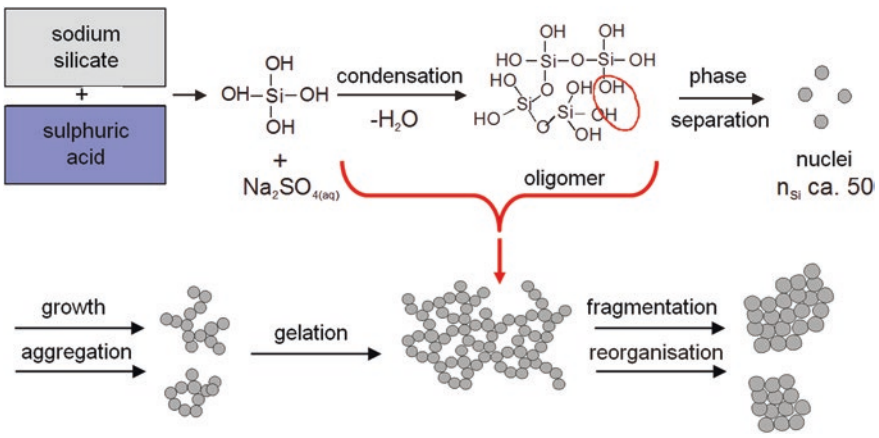

Fig. 2 Primary and secondary processes during silica precipitation process according to Schlomach and Kind [43, 44] (condensation, phase separation, growth and aggregation, gelation, fragmentation and reorganization)

the resultant processing and application properties of the finished product, e.g. the depressibility in further processing, are related to the various formulation and process parameters in a complex way [36]. An extensive investigation of process and formulation parameters of the specific set-up used in this work is given by Schlomach, Kind and Quarch [24, 43, 44]. However, the effect of these parameters on further processing and the micromechanical product characteristics has not been sufficiently investigated until now. Hence, in this project, the effect of formulation parameters, e.g. ion concentration, supersaturation, additives, and process parameters, e.g. precipitation temperature, pH-value, precipitation time, stirrer tip speed, supply of mechanical energy for fragmentation, and flow rate was investigated [30, 36, 37].

Figure 3 illustrates an example of the effect of mechanical energy input by different process units on the precipitated product. The stress mechanism, the stress intensity and stress frequency of the processing unit influence the primary (e.g. mixing

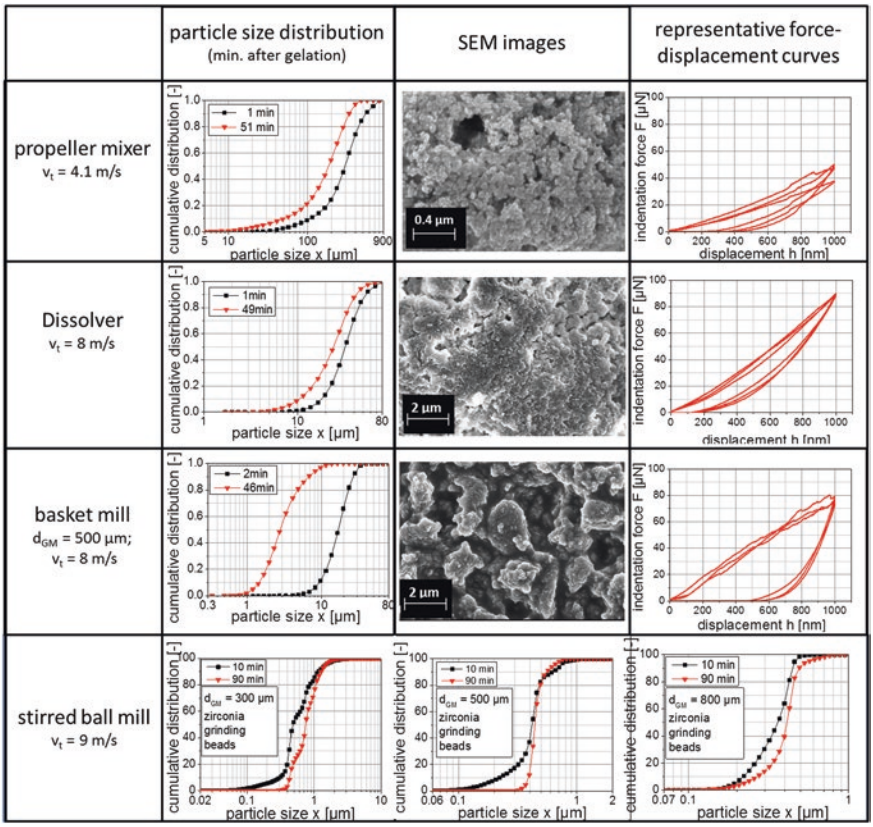

Fig. 3 Effect of mechanical energy input during silica precipitation on the resulting particle size distribution, aggregate structure and mechanical properties (particle size distribution measured via static and dynamic light scattering immediately after the point of gelation and at the end of the precipitation experiment; SEM images of the aggregate structure; representative force-displacement curves measured via nanoindentation)

and reaction of educts, phase separation and primary particle growth) and especially secondary growth and structure formation (e.g. aggregation, fragmentation, reorganization and aging). Typically, precipitation processes are investigated with respect to the mechanical energy input using a stirrer of varying stirrer type or tip speed or T-mixers and ultrasonic homogenizers during various precipitation processes [11, 17, 29, 47, 49]. In this study, the effect of mechanical energy input was investigated for turbulent shear flow using a stirred 4 L tank, equipped with a propeller mixer (Eurostar Euro-ST P CV, company IKA Labortechnik) and a dissolver, which has a process chamber volume of 1 l (toothed lock washer, company Getzmann). Moreover, the compression and shear stress between the surfaces was investigated by integrating a basket mill, which was based on the dissolver set-up (company Getzmann) inside the precipitation reactor, or by using a stirred media mill as precipitation unit (PM1, company Bühler) [30]. Consequently, by using various stirrer and mill types during precipitation, the primary particles and aggregated structures are stressed by different stress mechanisms, stress intensities, and frequencies. For example, in basket mills or stirred media, the stress intensity acting on the aggregates is inversely proportional to the third power of the particle size. Thus, the stress intensity increases strongly with increasing product fineness [18–20, 40]. In contrast, by using stirred precipitation units, the stress intensity is independent of the aggregate size or even decreases with decreasing aggregate size [16].

In case of the semi batch precipitated silica, the concentration and the solubility of monomeric sodium silicate are the crucial factors for the nuclei formation and growth, and not the mechanical energy input. Aggregation, fragmentation and reorganization processes are, however, significantly affected by different stress mechanisms, stress intensities and frequencies during the precipitation process (Fig. 3). Typically, when using a mechanical energy input by turbulent shear flow using stirrers or discs, the aggregate size distribution is shifted to smaller particle sizes and broader particle size distributions with increasing precipitation time after the point of gelation. The higher the mechanical energy input of the stirrer, the more decisive its effect on fragmentation and reorganization processes is. Quarch et al. derived a semi-empiric model for the minimum median aggregate size following the point of gelation [25]. Here, the maximum aggregate fineness is determined as a function of the fluid density and viscosity as well as the power input of the stirrer. Since various stress mechanisms as a function of aggregate size and the stirrer geometry are not considered, this semi-empiric model is not applicable for other dispersing units such as T-mixers, ultrasonic homogenizers, basket mills or stirred media mills. For basket mills and stirred media mills, the effect of the operating parameters on the maximum median aggregate size during precipitation can be described by the frequency of stress events between the grinding media. Thus, according to Schilde et al. [37], the equation for the stress frequency, which depends on the grinding media diameter, grinding media density, tip speed and filling ratio, is applicable for the calculation of the resulting aggregate sizes.

Generally, the higher the mechanical power input the higher the product fineness at the end of the precipitation process. Due to high stress intensities and frequencies between the grinding media, a high product fineness and narrow particle

size distributions are obtained using a stirred media mill as the dispersing unit. The effect of grinding media on aggregate formation and mechanical aggregate properties (see nanoindentation results in Fig. 3) is discussed in more detail by Schilde et al. [37]. In summary, the aggregate size and structure at the end of the silica precipitation process depends on:

- Properties of the fluid phase: Additives, temperature, pH-value, ion concentration, and concentration of precursors
- Properties of the generated gel structure at the point of gelation: Structure, primary, coordination number, porosity, strength of solid bonds or type of particle-particle interactions
- The dispersing unit: Operating parameters, geometry, stress mechanism.

3 Effect of the Aggregate Structure on the Mechanical Properties

In addition to the structure formation during the precipitation process, the relationship between the resultant deformation and fracture behavior, the aggregate structure, and the interparticulate interaction forces was investigated. The effect of the process temperature, the mechanical energy input, various additives to the aggregate structure, and solid bridges formation during the precipitation process as well as the resultant aggregate deformation behavior is described by Schilde [30]. However, since the precipitated silica aggregates are broadly distributed and inhomogeneous in structure, a relationship between specific aggregate structure properties and the deformation and fracture behavior is hardly possible. For this reason, silica model aggregates with different monomodal primary particle sizes between 50 and 400 nm produced from Stöber synthesis (ISC, Würzburg, Germany) were investigated using Tetraalkoxysilane and water as precursors [10, 48]. A narrow aggregate size distribution of homogeneous, spherical aggregates between 5 and 50 µm was obtained by a spray drying process; the classification of aggregates less than 5 µm was acquired using a cyclone (spray dryer, company Büchi). The aggregate structure for a primary particle size of 50 nm is shown in Fig. 4. Due to the spray drying process, a small amount of aggregates contains undesirable void volumes in the aggregate center [51].

The micromechanical properties of the silica aggregates were measured via a displacement controlled deep-sensitive normal force measurement, which used a complete automated nano-mechanical testing system (TriboIndenter® TI 900, company Hysitron Inc.). The silica model aggregates were stressed at a constant loading rate of 100 nm per second (loading and unloading) using a Flat Punch specimen. To guarantee an indentation displacement less than 10 % of the aggregate size which is equivalent to a minimized influence of the substrate, a maximum indentation displacement of 500 nm was chosen. Moreover, the confidence level was increased and the measurement artifacts due to different aggregate sizes were avoided by stressing aggregates in a size range between 10 and 15 micrometers [38, 39]. Further specifications as well as a detailed description

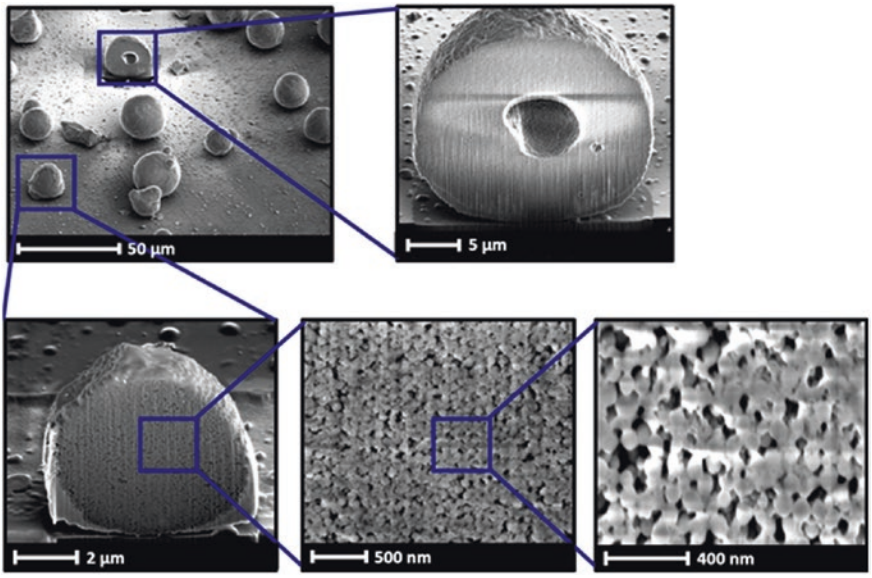

Fig. 4 Combined SEM-FIB images of silica model aggregates with a primary particle size of 50 nm (*top right* aggregate with void volume; *bottom* without void volume)

on the working principle of the nanoindentation device and the sample preparation (precise calibration regarding parallelism between sample and indenter tip and sample preparation via the dry dispersing device RODOS, company Sympatec) are summarized by Schilde [30] and Arfsten [3]. Since the model of Oliver and Pharr (calculation of Young's modulus or hardness) is not applicable for materials with high viscoplastic deformation behavior, the maximum indentation force as well as plastic and elastic deformation energies were determined as characteristics for the micromechanical aggregate properties [36, 39, 42]. Typically, the measurement of these micromechanical properties approached a constant median value as well as a constant standard deviation of approximately 40 single measurements [42].

Figure 5 shows the maximum indentation force and standard deviation as a function of the number of measured silica model aggregates. A constant standard deviation is determined by the inherent distribution of the micromechanical properties of the aggregated system [42]. In contrast to the distribution of the micromechanical properties of individual particles or single crystals, which can be described by Weibull statistics [14, 50], the distributions of aggregates can be described by a log-normal distribution [42]. Consequently, the specification of the log-normal fit can be used for the characterization of the measured system.

In accordance with Schönert and Rumpf [28, 45], an increase in the strength of aggregates and their resistance against fragmentation into smaller sized aggregates was observed with decreasing primary particle size [30]. This effect is due to a reduction of defects within the particulate structure and a smaller decrease in the bonding forces compared to other forces [33]. Figure 6 shows the logarithmic

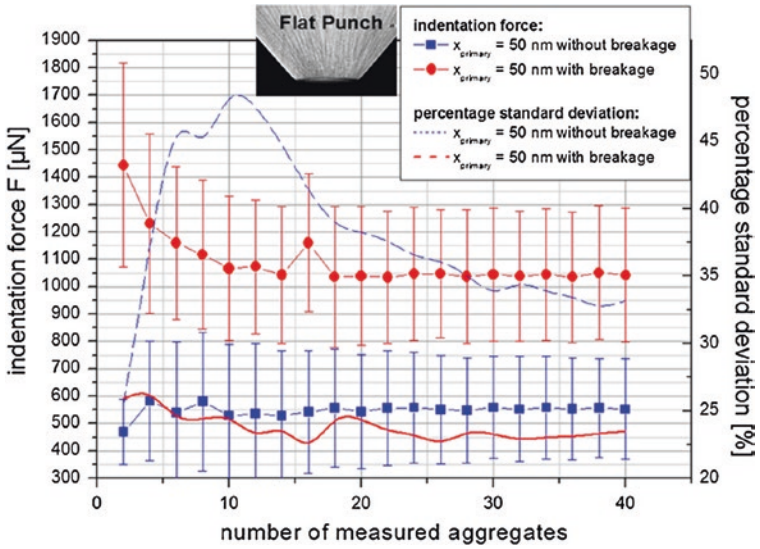

Fig. 5 Maximum indentation force and standard deviation as a function of the number of measured silica model aggregates ($x_{primary} = 50$ nm) using a flat punch indenter geometry [39]

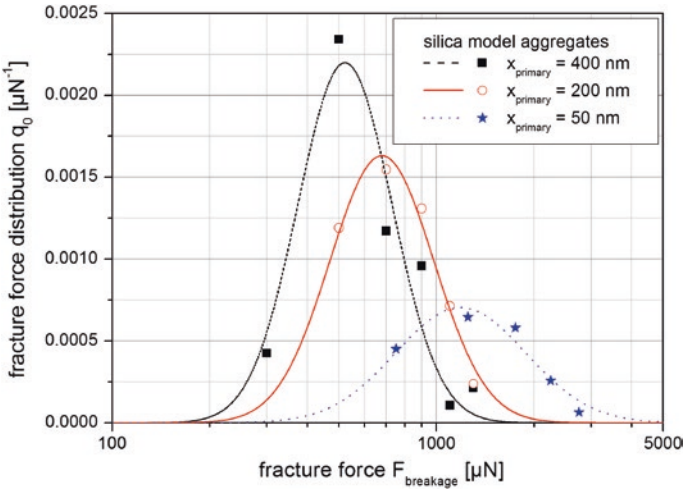

Fig. 6 Logarithmic breakage force distributions of the silica model aggregates with various primary particle sizes [30]

breakage force distributions of the silica model aggregates with various primary particle sizes. At a constant aggregate size, the fracture force increases with decreasing primary particle size. This characteristic micromechanical properties obtained from the load-displacement curves of fractured aggregates can be

Table 1 Aggregate structure properties [39]

Primary particle size $x_{primary}$ (nm)	Porosity ε (−)	Coordination number k(ε) (−)	Solid bridge diameter d_{sb} (nm)
50	0.396	6	30.36
200	0.255	12	84.94
400	0.242	12	163.45

used for the correlation of process properties, e.g. the stress energy distribution obtained from DEM-CFD simulations with dispersion kinetics. First correlation between the fracture force distribution, the stress conditions during stirred media milling and the dispersion results is presented by Schilde et al. [32] and Beinert et al. [5, 6]. Based on the stress energy distribution of the mill, $Q_{0,m}(SE)$, the number of grinding bead contacts per unit time, N_c/t, and the fracture energy distribution of the aggregated system, G3(FE), an effective dispersion fraction, Deff, can be calculated:

$$D_{eff} = \frac{N_c}{t} \cdot \int_{FE_{min}}^{SE_{max}} \left(1 - Q_{0,m}(SE)\right) \cdot G_3(FE) dE \tag{1}$$

Generally, the micromechanical aggregate properties depend on structure characteristics such as primary particle surface, porosity, strength and radius of solid bridges, and coordination number. Based on the structure characteristics in Table 1 (porosity and coordination number determined via mercury porosity, primary particle and solid bridge radius via SEM) and the assumption of isotropic aggregate deformation behavior, the fracture forces for spherical primary and secondary particles can be represented by the concept of the elementary breaking stress according to Rumpf [39]:

$$\sigma_{\text{Rumpf}} = \frac{(1-\varepsilon)}{\Pi} \cdot k(\varepsilon) \cdot \frac{F}{x_{\text{primary}}^2} \tag{2}$$

where ε is the specific void volume of the aggregate, k the average coordination number, π is the mathematical constant Pi, $x_{primary}$ is the primary particle size and F the particle-particle interaction force acting in the particle contacts. Under the assumption of cylindrical solid bridges, the particle-particle interaction force (for tensile, compression or shear stress) can be described as a function of the strength of the solid bridge, σ_{sb}, and the narrowest portion, or neck, of the bridge, r_{sb}, according to the model of Bika et al. [8]:

$$F = \Pi \cdot r_{sb}^2 \cdot \sigma_{sb} \tag{3}$$

For constant strength of the solid bridges, Fig. 7 shows the ratio of the median fracture force and the cross-section area of the aggregates as a function of the structure characteristics according to the Rumpf formula (Eqs. 2 and 3). As

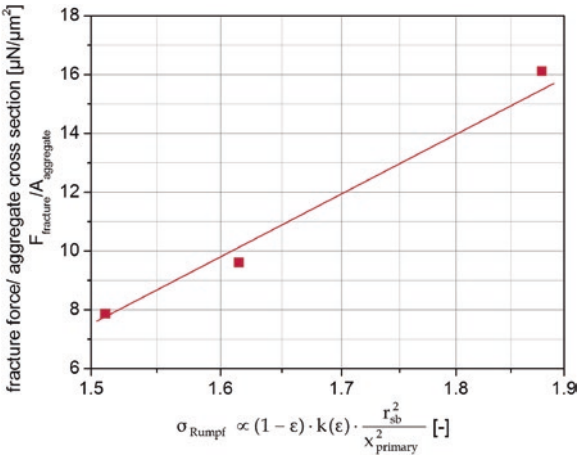

Fig. 7 Median fracture force of the silica model aggregates with various primary particle sizes as function of the elementary breaking stress according to Rumpf (simplified; strength of the solid bridge, σ_{sb}, is assumed constant)

expected, a linear correlation can be obtained. Therefore, the slope of this correlation is a value of the strength of the solid bridges. This relation is valid for the same particle material and, thus, a nearly constant deformation behavior [39].

Since the aggregate structure characteristics such as porosity and coordination number depend strongly on the primary particle morphology, the generalized form of the theory of Rumpf has to be adopted for variations in the primary particle morphology. Thereby, the porosity and coordination number can be characterized as function of the aspect ratio of the primary particles, f_0, which is already described for bulk solids by various authors [9, 52]. An example for the adaption of the generalized model of Rumpf for agglomerates containing primary particles with different morphologies is discussed by Schilde et al. [42]:

$$\sigma_{Rumpf} = (1-\varepsilon) \cdot k \cdot \frac{F_A}{S_p} = c \cdot \phi(f_0) \cdot k(f_0) \cdot \frac{F}{S_p} \tag{4}$$

where φ ($\varphi = 1 - \varepsilon$) is the volume fraction and S_p is the specific particle surface. In principle, the model of Rumpf is applicable in describing the micromechanical aggregate properties for spherical aggregates or agglomerates, constant aggregate diameter, similar deformation behavior and particle-particle interactions, and constant load function during the nanoindentation measurement.

4 DEM Simulation of the Mechanical Aggregate Properties

For application and further aggregate processing, the particle-particle interactions between primary particles are of substantial interest. A characterization of these particle-particle interactions in the nanometer size range and their effect

on the micromechanical aggregate properties is possible only with an increased measurement effort. More detailed information can be obtained by simulating the nanoindentation measurement with the help of the discrete elements method (DEM). The used contact model for the DEM simulation (EDEM 2.3™, company DEM Solutions) during this project was based on a standard Hertz-Mindlin [23] model, a contact model for solid bonds, and an additional attractive van der Waals interaction force. A detailed description of the contact models, dimensioning and aggregate built up is given by Schilde et al. [35]. Depending on the aggregate structure, normal stresses and tensile stresses, fracture may occur during the nanoindentation process. Figure 8 shows force-displacement curves of measured and simulated aggregate compression tests via nanoindentation with and without aggregate fracture (xprimary = 400 nm). As expected for high solid bridge strengths, no fracture occurs and the characteristic values of the deformation energies, relative amount of broken solid bonds, and the maximum indentation force remain constant [35]. The deformation behavior without aggregate fracture obtained from simulation is in qualitatively good agreement to the measured force-displacement curve (without regard to absolute values). Although slight differences can be observed, the used DEM contact model is suitable for the characterization of the stress-strain relationship and particle-particle interaction forces. Since the local structure (defects, coordination number, solid bridge strength and diameter) of the measured aggregates in the simulation differ, the force-displacement curves for fractured aggregates cannot match. To achieve similar force-displacement curves, the 3D-structure of the aggregated system has to be taken into account which is shown for micro sized particles by Roth et al. [26, 27] (via confocal microscopy).

The effect of various contact model parameters on the resultant values of deformation energies, the quotient of plastic and elastic deformation energy, the relative amount of broken solid bonds, as well as the breakage force are given by Schilde

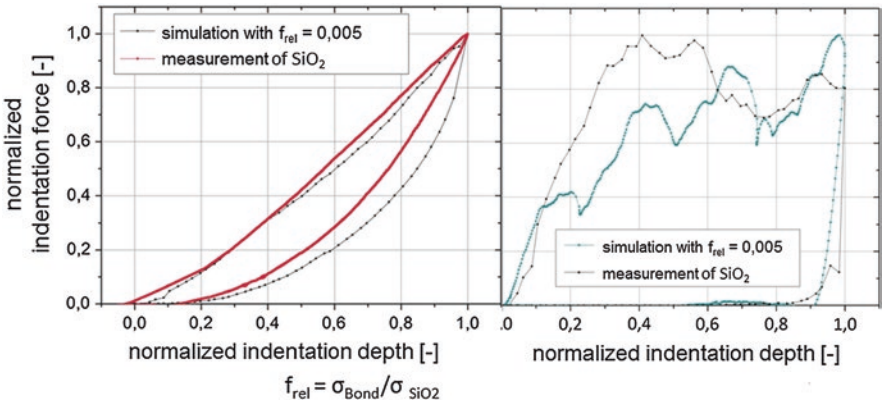

Fig. 8 Force-displacement curves of measured and simulated aggregate compression tests via nanoindentation with (*right*) and without (*left*) aggregate fracture

et al. [35]. Additionally, the load distribution in horizontal direction, which is vertical to the force direction of the indenter, was calculated [35] and compared to the theoretical considerations of Antonyuk et al. [2]. The load distribution provides information on the stresses within the aggregate as well as the deformation behavior [22, 27].

Depending on the particle interactions and the structure, gliding or cleavage cracks occur during the fracture of aggregates (cleavage) or agglomerates (gliding) [1]. Schönert [46] assumed that the highest stress level during impact or compression stress is presented in the area of contact. In the case of aggregates (including solid bridges), these stresses initiate perpendicular to cleavage cracks in the outer radius of the contact region. The cracks are substantially affected by radial stresses between the primary particles. The calculation of the radial stresses based on geometrical aggregate dimensions and forces acting within the solid bridges are described by Schilde et al. [35]. In order to increase the confidential level, the radial forces were averaged over the entire height of the aggregate. Figure 9 illustrates the progression of the absolute values of the radial

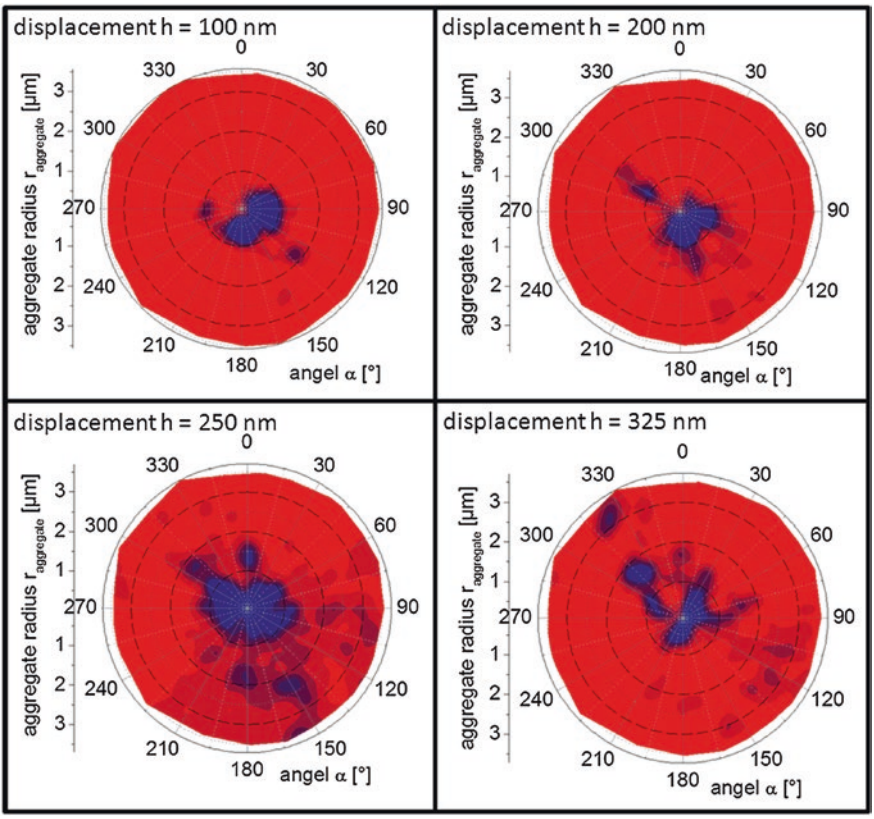

Fig. 9 Distribution of the radial stresses vertical to the force direction of the indenter (x-y section) at different time steps (*dark colors* indicate high radial stresses) [21, 30, 35]

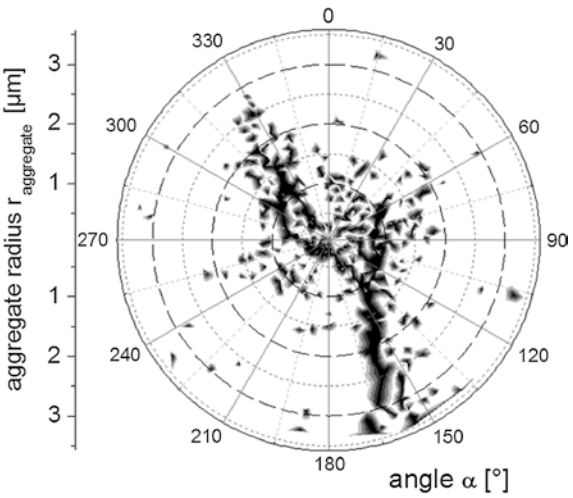

Fig. 10 Solid bonds in case of aggregate fracture (x-y section) (*dark colors* indicate broken solid bonds with acting Van der Waals and Hertz-Mindlin particle-particle interaction forces) [30, 35]; figure by Kwade et al. [21]

stresses at different indentation displacements. As expected, the maximum stresses are located in the area of contact. At a displacement between 200 and 250 nm, the maximum radial stresses are located in the direction of 150° where a first cleavage crack propagates through the entire aggregate (see Fig. 10). At a displacement of 325 nm, a second cleavage crack is induced in the direction of 330° (see Figs. 9 and 10). This is in accordance with the Schönert's conclusions that the radial stresses are responsible for the initiation and propagation of cleavage cracks [46].

5 Conclusion

In summary, it can be stated that the product and processing characteristics of precipitated aggregates are determined by the material itself as well as its structure formation during the particle synthesis. Due to a variation of significant process and formulation parameters, the resulting aggregate structure as well as the micromechanical properties are affected. In the case of particulate systems with plastic or viscoplastic deformation behavior, non-intrinsic characteristics for the characterization of the deformation behavior have to be adopted. In the case of the investigated silica precipitation process, the micromechanical aggregate properties (deformation energies, maximum indentation forces, etc.) can be described by log-normal distributions. With the help of these distributions, the effect of various process and formulation parameters, e.g. additives, educts concentrations, mechanical energy input, pH-value and precipitation temperature, on the structure and solid bridge formation can be described qualitatively. However, the aggregate structure is related to process and formulation parameters of the particle synthesis in a complex way. For this reason, spherical silica

model aggregates with a well-defined aggregate structure were investigated to characterize the effect of the primary particle size, aggregate size, and solid bond strength and stiffness on the micromechanical characteristics. The micromechanical properties of these model aggregates were modelled depending on their structure using a modified form of the elementary breaking stress model of Rumpf. For an isotropic deformation behavior, stresses calculated from the maximum indentation forces and fracture forces can be described by this enhanced model. However, since a characterization of particle-particle interactions between nanoparticles and their effect on the micromechanical aggregate properties is possible only with an increased measurement effort, discrete element simulations were carried out. A combination of a Hertz-Mindlin contact model, a solid bridge model and a model for Van der Waals attraction is suitable to describe the stress-strain-relationship and particle-particle interactions, of nanostructured aggregates. Moreover, the radial stresses acting between primary particles can be correlated to the formation and propagation of cleavage cracks according to Schönert's theoretical considerations.

Generally, the aggregate structure and its effect on their micromechanical properties was investigated and combined with the stress conditions during the dispersion process. Certainly, the process-structure-property-relationship cannot be determined completely and was only represented exemplarily in this project.

Acknowledgements The authors gratefully acknowledge the financial support by the DFG within the SPP 1273 "colloid technology". The FIB-SEM pictures were kindly taken by Michael Kappl (MPI, Mainz). Many thanks for the support in the surface functionalization of model silica aggregates and addition of additives during precipitation to Sabrina Zellmer (Institute for Particle Technology, Braunschweig).

References

1. Antonyuk S (2006) Deformations-und Bruchverhalten von kugelförmigen Granulaten bei Druck- und Stoßbeanspruchung. Otto-von-Guericke-Universität Magdeburg, Magdeburg
2. Antonyuk S, Tomas J, Heinrich S, Mörl L (2005) Breakage behaviour of spherical granulates by compression. Chem Eng Sci 60:4031–4044
3. Arfsten J (2009) Mikromechanische Charakterisierung von Saccharomyces cerevisiae. TU Braunschweig, Braunschweig
4. Barth N, Schilde C, Kwade A (2014) Influence of electrostatic particle interactions on the properties of particulate coatings of titanium dioxide. J Colloid Interface Sci 420:80–87
5. Beinert S, Schilde C, Gronau G, Kwade A (2014) CFD-discrete element method simulations combined with compression experiments to characterize stirred-media mills. Chem Eng Technol 37:770–778
6. Beinert S, Schilde C, Kwade A (2012) Simulation of stress energy and grinding media movement within a wet operated annular gap mill using the discrete element method. Chem Eng Technol 35:1899–2059
7. BERGNA HE (1994) The colloid chemistry of silica. American Chemical Society, Washington, DC
8. Bika D, Tardos GI, Panmai S, Farber L, Michaels J (2005) Strength and morphology of solid bridges in dry granules of pharmaceutical powders. Powder Technol 150:104–116

9. Donev A, Cisse I, Sachs D, Variano EA, Stillinger FH, Connelly R, Torquato S, Chaikin PM (2004) Improving the density of jammed disordered packings using ellipsoids. Science 303:990–993
10. Gellermann C, Ballweg T, Wolter H (2007) Herstellung von funktionalisierten oxidischen nano-und mikropartikeln und deren verwendung. Chem Ing Tech 79:233–240
11. Gradl J, Schwarzer H-C, Schwertfirm F, Manhart M, Peukert W (2006) Precipitation of nanoparticles in a T-mixer: coupling the particle population dynamics with hydrodynamics through direct numerical simulation. Chem Eng Process 45:908–916
12. Hinz W (1971) Grundlagen der Silikatwissenschaft und Silikattechnik. Verlag Bauwesen, Berlin
13. Iler RK (1979) The chemestry of silica. Wiley, New York
14. Kendall K (1988) Agglomerate strength. Powder Metall 31:28–31
15. Kind M (2002) Colloidal aspects of precipitation processes. Chem Eng Sci 57:4287–4293
16. Kolmogorov AN (1958) Die lokale Struktur der Turbulenz in einer inkompressiblen zähen Flüssigkeit bei sehr großen Reynoldsschen Zahlen. Sammelband zur statistischen Theorie der Turbulenz, Akademie Verlag Berlin
17. Kucher M, Babic D, Kind M (2006) Precipitation of barium sulfate: experimental investigation about the influence of supersaturation and free lattice ion ratio on particle formation. Chem Eng Process 45:900–907
18. Kwade A (2001) Physical model to describe and select comminution and dispersion processes. Chem Ing Tech 73:703
19. Kwade A (2003) A stressing model for the description and optimization of grinding processes. Chem Eng Technol 26:199–205
20. Kwade A, Kampen I, Breitung-Faes S, Schilde C (2009) Basic course—grinding and dispersing with stirred media mills. Arno Kwade, Braunschweig
21. Kwade A, Schilde C, Burmeister CF, Roth M, Lellig P, Auerhammer GK (2013) Micromechanical properties of colloidal structures. Powders and Grains 1542:939–942
22. Malzbender J, de Witt G (2002) Indentation load-displacement curve, plastic deformation, and energy. J Mater Res 17:502–511
23. Mindlin RD (1949) Compliance of elastic bodies in contact. J Appl Mech 16:259–268
24. Quarch K (2010) Produktgestaltung an kolloidalen agglomeraten und gelen. Karlsruher Institute of Technology, Karlsruhe
25. Quarch K, Durand E, Schilde C, Kwade A, Kind M (2010) Mechanical fragmentation of precipitated silica aggregates. Chem Eng Res Des 88:1639–1647
26. Roth M, Schilde C, Lellig P, Kwade A, Auerhammer GK (2012) Colloidal aggregates tested via nanoindentation and quasi-simultaneous 3D imaging. The Eur Phys J E 35:1–12
27. Roth M, Schilde C, Lellig P, Kwade A, Auerhammer GK (2012) Simultaneous nanoindentation and 3D imaging on semi-crystalline colloidal films. Chem Lett 41:1110–1112
28. Rumpf H (1958) Grundlagen und methoden des granulierens. Chem Ing Tech 30:144–158
29. Saeki T, Ishida M (2011) Production of acid silica sols and gels by using a Y-shaped reactor and dilution technique. Int J Chem Reactor Eng 9:1–11
30. Schilde C (2013) Structure, mechanics and fracture of nanoparticulate aggregates. TU Braunschweig, Braunschweig
31. Schilde C, Arlt C, Kwade A (2009) Einfluss des dispergierprozesses bei der herstellung nanopartikelverstärkter verbundwerkstoffe. Chem Ing Tech 81:775–783
32. Schilde C, Beinert S, Kwade A (2011) Comparison of the micromechanical aggregate properties of nanostructured aggregates with the stress conditions during stirred media milling. Chem Eng Sci 66:4943–4952
33. Schilde C, Breitung-Faes S, Kwade A (2007) Dispersing and grinding of alumina nano particles by different stress mechanisms. Ceram Forum Int 84:12–17
34. Schilde C, Breitung-Faes S, Kwade A (2013) Grinding kinetics of nano-sized particles for different electrostatical stabilizing acids in a stirred media mill. Powder Technol 235:1008–1016

35. Schilde C, Burmeister CF, Kwade A (2014) Measurement and simulation of micromechanical properties of nanostructured aggregates via nanoindentation and DEM-simulation. Powder Technol 259:1–13
36. Schilde C, Gothsch T, Quarch K, Kind M, Kwade A (2009) Effect of important process parameters on the redispersion process and the micromechanical properties of precipitated silica. Chem Eng Technol 32:1078–1087
37. Schilde C, Hanisch C, Naumann D, Beierle T, Kwade A (2013) A novel way to vary the structure of precipitated silica and calcium carbonate aggregates in a wide range by using grinding media during the precipitation process. Chem Eng Sci 94:127–137
38. Schilde C, Kampen I, Kwade A (2010) Dispersion kinetics of nano-sized particles for different dispersing machines. Chem Eng Sci 65:3518–3527
39. Schilde C, Kwade A (2012) Measurement of the micromechanical properties of nanostructured aggregates via nanoindentation. J Mater Res 27:672–684
40. Schilde C, Mages-Sauter C, Kwade A, Schuchman HP (2011) Efficiency of different dispersing devices for dispersing nanosized silica and alumina. Powder Technol 207:353–361
41. Schilde C, Nolte H, Arlt C, Kwade A (2010) Effect of fluid-particle-interactions on dispersing nano-particles in epoxy resins using stirred-media-mills and three-roll-mills. Compos Sci Technol 70:657–663
42. Schilde C, Westphal B, Kwade A (2012) Effect of primary particle morphology on the micromechanical properties of nanostructured alumina agglomerates. J Nanopart Res 14:1–11
43. Schlomach J (2005) Feststoffbildung bei technischen Fällprozessen. Universität Karlsruhe, Karlsruhe
44. Schlomach J, Kind M (2004) Investigations on the semi-batch precipitation of silica. J Colloid Interface Sci 277:316–326
45. Schönert K (1991) Advances of communication fundamentals and impacts on technology. Aufbereitungstechnik 32:487–494
46. Schönert K (2004) Breakage of spheres and circular discs. Powder Technol 143–144:2–18
47. Schwarzer H-C, Peukert W (2004) Combined experimental/numerical study on the precipitation of nanoparticles. AIChE J 50:3234–3247
48. Stöber W, Fink A, Bohn E (1968) Controlled growth of monodisperse silica spheres in the micron size range. J Colloid Interface Sci 26:62–69
49. Tung H-H, Wang L, Panmai S, Riebe M (2009) Nanoparticle formation via rapid precipitation. Patent US20110053927 A1, EP2273978A1, WO2009131930A1
50. Vogel L, Peukert W (2005) From single particle impact behaviour to modelling of impact mills. Chem Eng Sci 60:5164–5176
51. Walker WJ Jr, Reed JS (1999) Influence of slurry parameters on the characteristics of spray-dried granules. J Am Ceram Soc 82:1711–1719
52. Williams SR, Philipse A (2003) Random packing of spheres and spherocylinders simulated by mechanical contraction. Phys Rev E 67:1–9

Aggregation and Deformation Induced Reorganisation of Colloidal Suspension

Günter K. Auernhammer, Doris Vollmer, Miao Wang, Marcel Roth and Maria D'Acunzi

Abstract Various mechanisms can lead to colloidal aggregation. Attractive interactions being the most prominent amongst them. In this chapter we describe the synthesis of well defined colloids with a smooth or rough surface, their mechanical characterization, controlled aggregation and the study of the mechanical and structural properties of the colloids and the formed aggregates. Depending on the interplay between the properties of the single colloids, the interactions between the colloids and the structure formed by the colloids, the macroscopic response of the system can greatly change.

Keywords Aggregation · Deformation induced reorganisation · Colloidal suspension · Mechanical and structural properties · Scanning transmission X-ray microscopy · Atomic force microscopy · Elasticity

1 Introduction

The aggregation and reorganization behavior of colloids depends on the hydrophobicity, roughness and density difference between the colloids and the solvent. Model colloids include polystyrene, polymethylmethacrylate and silica colloids [1–5]. Most colloids are spherical however lately different strategies have been developed to synthesize colloids with asymmetric shapes or patterned surfaces, resulting in interactions that depend on orientation [6–10].

For the macroscopic mechanical characterisation of colloidal and granular systems a wealth of methods is available that is described in various textbooks (see, e.g., [11]).

G.K. Auernhammer (✉) · D. Vollmer (✉) · M. Wang · M. Roth · M. D'Acunzi
Max Planck Institute for Polymer Research, Ackermannweg 10, 55128 Mainz, Germany
e-mail: auhammer@mpip-mainz.mpg.de

D. Vollmer
e-mail: vollmerd@mpip-mainz.mpg.de

M. Kind et al. (eds.), *Colloid Process Engineering*,
DOI 10.1007/978-3-319-15129-8_10

Getting a detailed insight into the microscopic origin of the macroscopic mechanical properties of a colloidal system is more complex, because it requires a combination of microscopically resolved structural analysis and macroscopic mechanical stimulation and testing of the system. For the 3D imaging of colloidal systems, laser scanning confocal microscopy (short "confocal microscopy") is a widely used method [12–15]. Alternative methods include light sheet illumination [16], optical coherence tomography [17, 18], and X-ray tomography [19, 20]. A recent overview of the methods can be found in [21]. In the field of micrometer sized colloidal particles, these alternative methods have however the draw back of a limited temporal and spatial resolution. For this reason we concentrate in the present chapter mainly on results optioned by confocal microscopy in combination with mechanical testing methods.

Automatized analysis of the 3D images is essential to get statistically meaningful results out of the data sets. An efficient analysis strategy is based on algorithms originally developed by Crocker and Grier [22] and further established by Weeks and coworkers [23]. This way of analysing 3D data sets has gained considerable attention in colloidal physics. There are also voxel based algorithms (see, e.g., [24, 25]) that use watershed-type methods. The major difference is that the algorithms by Crocker and Grier used the knowledge (or assumption) of a spherical shape of the colloids to improve the positioning accuracy. If this assumption is justified, the colloid positions can be found with an uncertainty well below the optical resolution of the 3D data set, even for polydisperse samples [26]. Since the focus of the present chapter is on model systems with simple geometries, we will concentrate on spherical colloids and the corresponding automatic analysis of the 3D data based on algorithms developed by Crocker, Grier, and Weeks.

2 Beyond Optical Resolution: X-Ray Microscopy

All optical techniques for the structural analysis of colloidal systems rely on good optical properties of the sample. More specifically the refractive index must be as homogeneous as possible inside the sample. This implies that the refractive index of the colloids must be matched by the surrounding medium. Obviously this excludes the possibility of using gas or vacuum as a surrounding medium. For many base material of colloids a liquid to index-match the continuous phase is available. With a suitable modification of the colloidal surfaces, the interactions between the colloidal particles can be tuned to be similar to interaction known from colloids surrounded by gas or vacuum. This limitation does not hold for X-ray tomography studies. For all relevant materials the index of refraction at the wavelength of the X-rays used for tomography is very close to unity. For this reason, index-matching condition is automatically fulfilled.

An alternative approach to obtain high-resolution images of non-index matched samples are X-ray microscopes, especially scanning transmission X-ray microscopes (STMXs). With the use of Fresnel lenses soft X-ray beams (energy typically 1 keV) can be focussed to spots with a cross section below 50 nm [27]. This allows for imaging thin samples with a resolution that is well below the resolution

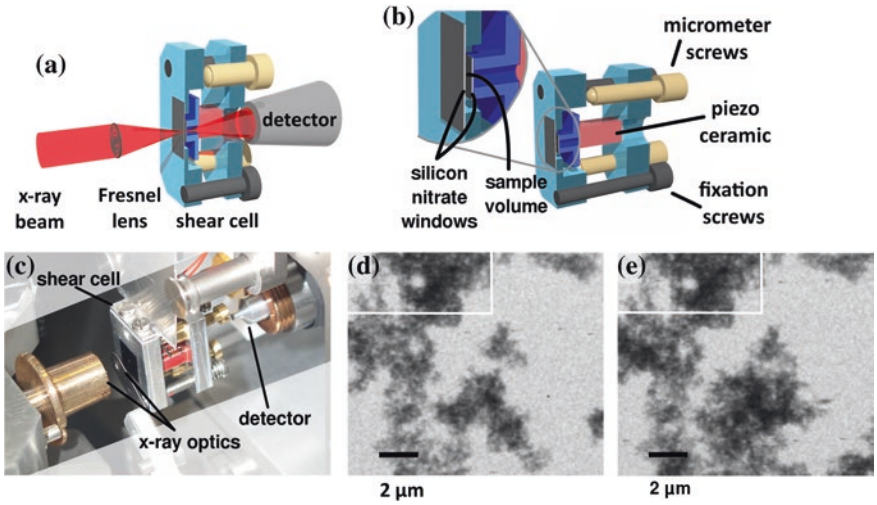

Fig. 1 **a** Illustrates how the shear cell was introduced into the beam path of the STXM. The detector-sided windows were mounted on peizo ceramics, allowing the application of shear to the sample. **b** and **c** give to snap shots of the shear induced restructuring of the aggregates. Inside the marked area, the sample was crosslinked to fix the structure. Reorganization took only place in the non-crosslinked region (adapted and reprinted with permission from Auernhammer et al. [29])

of standard laser scanning confocal microscopes [28]. Different to electron microscopes, with STXMs the sample can be imaged in solution. With a newly designed measurement cell we explored the possibility of using the STXM to study shear induced reorganisation in aggregated colloidal systems [29].

For this we have chosen magnetic nano colloids that were dispersed in a melt of polydimethylsiloxane (PDMS). The colloids are known to give a loose aggregated structure at low volume fractions [30]. A good absorption contrast was achieved in the STXM images due to the high iron content of the magnetic colloids (Fig. 1b, c). An important question in the STXM measurements is the possibility of beam damage to the sample. With the help of a miniaturised shear cell (Fig. 1a), it was possible to observe shear-induced structural rearrangements in the sample. This also showed that a possible beam damage did not alter the response of the system significantly, when the X-ray dose on the sample was kept low.

3 Synthesis and Characterization of Colloids with Tunable Hydrophobicity and Roughness

STXM permits to investigate the rearrangement of nanometer sized colloids. These measurements turned out to be quiet time-consuming and we did not achieve quantitative information on the reorganisation dynamics of single colloids. This is possible by laser scanning confocal microscopy. However, therefore micrometer-sized

colloids were required. We synthesized micrometer sized core shell colloids with different roughness [31, 32]. The hybrid colloids possessed a polystyrene core and rough silica shell that completely covered the polystyrene surface. This has the advantage that the polystyrene core has a density close to water, greatly increasing the sedimentation time. To tune the surface hydrophobicity we coated the polystyrene colloids with a silica shell of tunable roughness. The silica surface of the colloids was hard, chemically inert and could be easily modified.

3.1 Synthesis and Characterization of Polystyrene Colloids

Polystyrene colloids (PS) were synthesized by soap-less emulsion polymerization [5, 33, 34]. This prevents desorption of surfactant from the surface with time, resulting in better defined surface properties. The colloids were synthesized in presence of acrylic acid as co-monomer and the anionic radical initiator ammonium persulfate was used to start the reaction. Above a certain size the colloids are electrostatically stabilized. Since acrylic acid is a weak acid, its negative charge is pH dependent. Emulsion co-polymerization of styrene with small amounts of acrylic acid results in poly(styrene-co-acrylic acid) polymer chains provides a steric stabilization as the chains are partially situated at the water-colloid interface [35, 36].

Dependent on the reaction parameters, colloids with a diameter between 200 and 700 nm were obtained. The size of the colloids increased with the amount of styrene. The size of the colloids also depends on the initiator concentration and temperature. Increasing the initiator concentration [37] led to a reduction of the size of the colloids because the larger number of stabilizing groups coming from the initiator (i.e. sulphate groups) favorites the formation of more nuclei. Increase in temperature results in a decreased size of the colloids. At higher temperature [5] the reaction is faster. The yield of the reaction was in the range of 60–70 %.

To get detailed information on the growth process, we followed the reaction with time focusing on the morphology of the colloids. Every 15 min a small aliquot was taken from the reaction mixture. The aliquots were diluted and imaged by scanning electron microscopy without purification (Fig. 2). During the first hour no colloids could be identified within the background of unreacted polystyrene. After 1.75 h almost monodisperse colloids embedded in the polymer melt were visible, (Fig. 2a). With increasing reaction time the colloids grew further, but still remained soft and contained significant amount of unreacted styrene. During evacuation the styrene evaporates, leading to a collapse of the colloids resulting in a donut-like shape, (Fig. 2b). After another 2.5 h not only the size of the colloids but also their hardness increased. The colloids appeared much more spherical (Fig. 2c) although still evaporation of styrene caused formation of small dimples in the surface of the colloids. Only after another couple of hours the colloids appeared smooth in SEM, (Fig. 2d). From the SEM images the diameter of the polystyrene was measured. Figure 2e illustrates the increase of the diameter of the

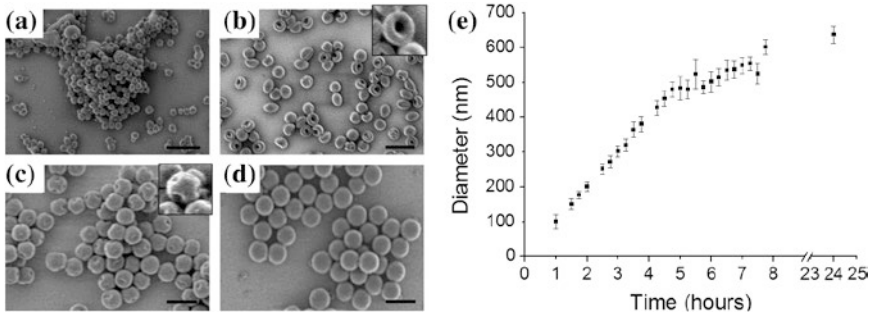

Fig. 2 Scanning electron microscopy images of polystyrene colloids obtained by soap-free emulsion polymerization, taken after **a** 1.75 h, **b** 4.5 h, **c** 7 h, **d** and after 24 h. *Scale bar* 1 μm. *Insets* Images at higher magnification. **e** Growth of polystyrene colloids during emulsion polymerization. Experimental conditions: ammonium persulfate: 0.11 g; acrylic acid: 0.15 g; sodium chloride: 0.2 g; milli-Q water: 300 ml; styrene: 25 g; divinylbenzene: 0.25 g. [34]

colloids with time. Within the first 5 h, they grew linearly with time. Thereafter, the growth rate was slowed down, until after about 8 h the diameter almost remained constant. However, still the surface of the colloids changed according to scanning electron microscopy images.

If larger colloids were needed, the size of the colloids was increased by seeded emulsion polymerization [38]. It consists in performing emulsion polymerization in presence of pre-formed colloids. The preformed polystyrene colloids were swollen with styrene. When the polymerization starts, they were the main locus of polymerization. By seeded emulsion polymerization the size of the colloids could be increased up to about 1.5 μm.

In order to characterize the effective surface charge, the amount of sulphate and carboxylic groups on the colloids was determined by polyelectrolyte titration [39]. At pH 7 the Z-potential of the polystyrene colloids was about -55 ± 5 mV in water.

3.2 Synthesis of Core-Shell Polystyrene-Silica Colloids

The synthesis of the core-shell colloids was performed according to the scheme in Fig. 3 [34]. To coat negatively charged polystyrene colloids with a smooth silica shell, the surface charge needs to be reversed, Fig. 3a [40]. Therefore, the colloids were dispersed in a solution of poly (allylamine hydrochloride) (PAH) and sodium chloride. Silica was grown making use of the Stöber method [41, 42]. This implies that ammonia and different amounts of tetraethoxysilane (TES) were added. The shell thickness increased with the amount of tetraethoxysilane and varied between 15 and 70 nm. To obtain a rough shell acrylic acid needed to be added to the synthesis of the polystyrene colloids. Silica particles grew at the surface of

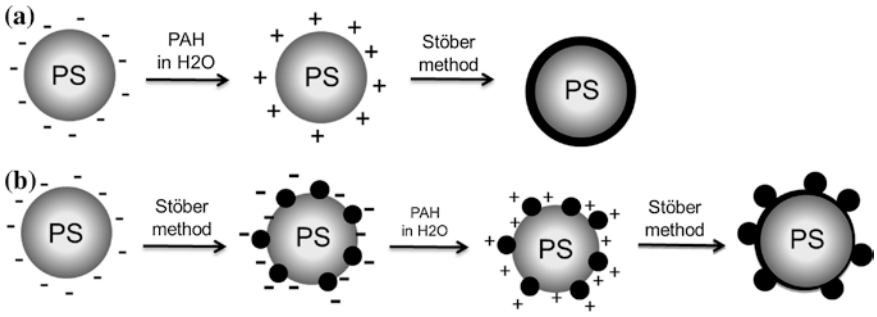

Fig. 3 Scheme of the preparation of hybrid polystyrene-silica colloids with a (**a**) smooth or (**b**) rough shell [31, 34]

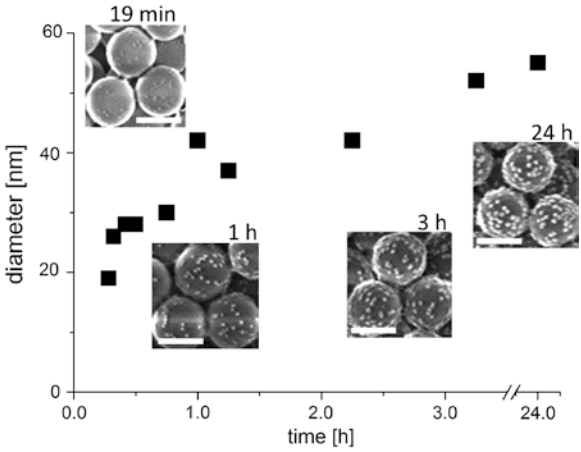

Fig. 4 Dependence of the size of the silica particles on reaction time. The PS colloids were synthesized as follow: 0.11 g ammonium persulfate, 0.2 sodium chloride, 1.6 wt/wt acrylic acid, and 13.6 g styrene. For the Stöber synthesis the following components were mixed: 0.05 g PS colloids, 0.66 ml ammonia and 0.5 g tetraethoxysilane in 1.5 ml ethanol. *Scale bar* 0.5 μm. Reproduced by permission of The Royal Society of Chemistry [31]

PS colloids at all acrylic acid concentrations tested. However, at low acrylic acid concentrations the particles detached easily from the surface. Only at concentrations above ≈1 % wt/wt the silica particles were sufficiently strongly bonded to the surface that they remained attached even after several centrifugation steps. The size of the silica particles did not depend on the size of the PS colloids but is determined by the amount of tetraethoxysilane.

To investigate the growth process in more detail we imaged aliquots of the reaction mixture after different reaction times, Fig. 4. Already after 20 min, 30 nm sized silica particles appeared on the surface of the PS colloids. After this initial fast growth, the silica grain size steadily increased until it approached 55 ± 5 nm after 3 h. Thereafter, the size remained almost constant. The growth process is limited by lack of reaction material. To prevent detachment of the silica particles, the rough colloids were coated with a silica shell. Therefore, they were immersed in a water solution of poly (allylamine hydrochloride) and a Stöber synthesis was

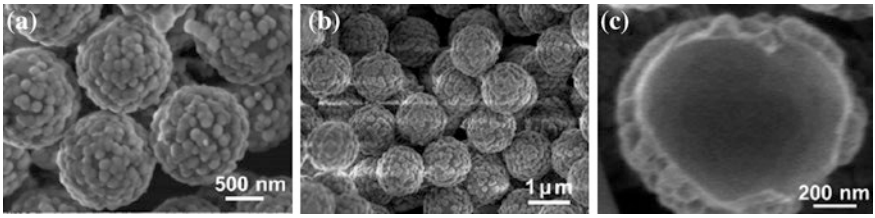

Fig. 5 Scanning electron microscopy images of colloids with a rough shell. Colloids **a** before thermal treatment, **b** hollow colloids after thermal treatment at 500 °C, and **c** a broken empty shell. Reproduced by permission of The Royal Society of Chemistry [31]

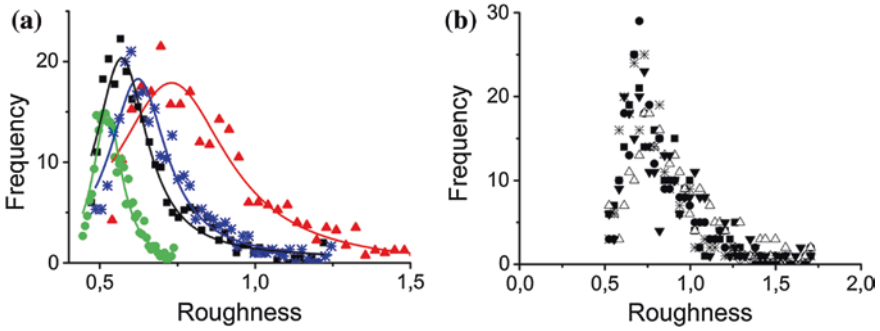

Fig. 6 **a** Dependence of the surface roughness on the drying temperature. To minimize large scale inhomogenities or sample tilt the imaged areas of 800 × 800 μm^2 were divided in 256 small squares of 50 × 50 μm^2 each and the roughness was determined for each of these squares. The solid lines serve as guides to the eye. Evaporation temperature: *circles* 20 °C, *squares* 50 °C, *stars* 70 °C, *triangles* 90 °C. **b** Reproducibility of roughness measurements of a film dried at 70 °C. The different *symbols* denote different samples and positions while the temperature was kept at 70 °C. Reproduced by permission of The Royal Society of Chemistry [31]

performed again, Fig. 3b. The resulting colloids had a polystyrene core and a completely closed rough silica shell, Fig. 5a. The thickness of the shell can be tuned via the amount of tetraethoxysilane. To ensure that the colloids were fully covered with a silica shell, small amounts of sample were heated to 500 °C for 4 h in order to remove the polystyrene core. SEM images taken after the thermal treatment show that the silica shelly were complete and the shape of the colloids hardly changed, Fig. 5b, c [31].

The colloids with a rough silica shell were hydrophilic and could be dispersed in water. Multi-layers were prepared by evaporation of water [31]. The roughness of the films, given by the arrangement of colloids during drying, was influenced by the temperature at which the water was evaporated, Fig. 6. At room temperature sedimentation time was short compared to the water evaporation time. With increasing drying temperature the evaporation time decreased until it determined

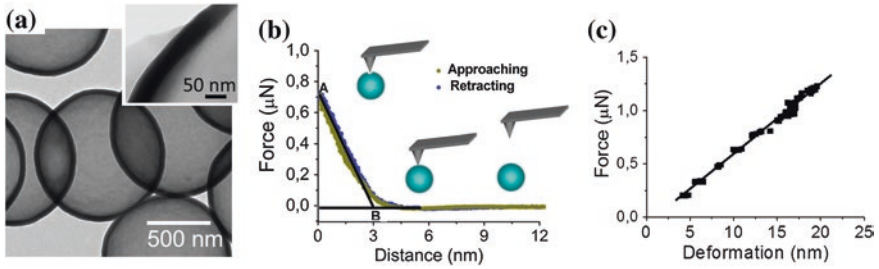

Fig. 7 **a** Transmission electron microscopy images of core-shell polystyrene-silica colloids after the polystyrene core was removed by heating the samples at 500 °C for 3.5 h. *Inset* TEM image of a shell at high magnification. The *dark area* representing the shell shows uniform thickness. **b** A typical force curve of a hollow silica sphere with a shell of 50 nm and a diameter of 1.9 μm. The open spheres denote the approach, and the filled spheres denote the retract part of the curve. Hardly any hysteresis is visible, i.e., the deformation is elastic. **c** Deformation of hollow silica spheres as a function of applied load. The *straight line* shows a linear fit to the data

the time scales. Then, evaporation induced convection interacted with sedimentation of colloids, causing that the colloids sedimented in homogeneously. The surface consisted of irregularly distributed "hills and valleys".

3.3 Young's Modulus

The mechanical properties of the colloids are determined by the mechanical properties of the silica shell. To calculate the Young's modulus of the silica shell, the shell thickness needs to be known. Therefore, the mechanical characterization was performed on hollow silica colloids with smooth surface, [32, 43]. The size of the colloids was adjusted by using polystyrene templates of different diameter and the shell thickness was tuned by the amount of tetraethoxysilane added to the reaction mixture. The polystyrene core was removed by calcination. The shell thickness of the hollow colloids was measured from transmission electron microscopy images (Fig. 7a).

The elastic moduli of the hollow silica spheres were determined by applying a point load on a single hollow sphere using an atomic force microscope (AFM) tip with a radius of 20 nm [32, 44, 45]. To prevent the colloids from shifting or rolling on the substrate during measurements, they were partially embedded in a thin PS film. For the analysis of the force measurements, the thickness of the PS film underneath the colloids was determined so ensure that the deformation originates only from deformation of the shells. Only a 2–5 nm thick PS film remained between the sphere and the substrate. As soon as the tip contacts the sphere, the sphere started to deform. To obtain a force-deformation curve, the deformation at maximum applied force F_{max} was determined for each force-distance curve. F_{max} is given by the intersection of the linear extrapolation of the force versus distance

curve with the force axis (a in Fig. 7b). The corresponding deformation was determined from the intersection of the linear fit with the linear extrapolation of the zero deformation line (b in Fig. 7b). From each such force distance curve a single data point (b, a) was obtained for the corresponding force versus deformation curve (Fig. 7c).

From taking force curves at different defined maximum forces, we obtained the dependence of the deformation on the applied force (Fig. 7c). For deformations smaller than the shell thickness, the approaching and retracting curves were almost congruent and linear, indicating a fully reversible behavior. Plastic deformations could be excluded. In this case, the Young's modulus E is given by the thin shell model [46].

$$E = \frac{\sqrt{3(1-\nu^2)}}{4}\frac{FR}{dh_s^2} \tag{1}$$

where d is half the measured deformation, h_s is the shell thickness, R is the radius of sphere, F is the loading force, and ν is the Poisson ratio, with $\nu = 0.17$. Under these assumptions, the Young's modulus of the hollow spheres was found to be about 35 ± 6 GPa, irrespective of shell thickness and the size of the colloids. The measured value for the elastic modulus is half of that for fused silica, $E = 76$ GPa [47].

In order to investigate the dependence of the mechanical properties of the hollow silica colloids on annealing temperatures the deformations of hollow silica colloids were measured by AFM at room temperature and after annealing at different temperatures [43]. For annealing temperatures below 800 °C, the Young's modulus slowly increased to 40 GPa. Annealing at temperatures above 1000 °C caused a strong increase of the Young's modulus which becomes close to the value of fused silica, 72–76 GPa [47].

In order to relate the changes in the mechanical properties to changes in the chemical structure during the annealing process, ^{29}Si solid state NMR measurements were performed at different stages of the annealing treatment [42, 48, 49]. Upon annealing the number of silanol groups decreased [43]. After annealing the hollow colloids at 500 °C only a minor contribution of silanol sites was observed. The curing of the silica network was almost completed at an annealing temperature of $T \approx 800$ °C. No structural changes in the silica network upon annealing at temperatures above 850 °C was observed. The change of the local chemical bond structure causes only a moderate increase of the Young's modulus with annealing temperature. At even higher temperatures, a strong increase of the Young's modulus accompanied by a smoothening of the surface of the hollow silica colloids and increase in density was observed. Remarkably, the silica shell retained their perfect spherical shape although the diameter and shell thickness decreased by 20 %. Thus, high temperature annealing provides a method to obtain hollow silica colloids with a completely closed shell with a thickness as thin as a few tens of nm and a Young's modulus comparable to that of fused silica. Furthermore, characterizing the dependence of the Young's modulus on temperature and on

changes in bond structure and surface morphology offers the possibility to tune the mechanical properties of silica capsules [50, 51].

4 Soft Colloids: Influence of Single Colloid Mechanics

Aggregation in colloidal systems can be introduced by various mechanism. Attractive interactions between the colloids is the most prominent example. Another possibility is to confine the colloids in one phase of a phase separating mixture, e.g., in the isotropic phase of a liquid crystalline fluid that is undergoing the isotropic-to-nematic transition [52, 53]. This unusual soft solid consists of a foam like structure, where the bubbles are filled with liquid crystal in the nematic phase and the colloids are confined in the walls separating the bubbles [54].

We investigated a system that consisted of sterically stabilised polymethylmethacrylate (PMMA) colloids [55] dispersed in the isotropic phase of the liquid crystalline compound 4-n-pentyl-4′- cyanobiphenyl (5CB). When cooling the dispersion below the isotropic-to-nematic transition of 5CB, first nematic bubbles formed. Including the colloids in the nematic phase would create defects in the nematic order that are energetically very unfavourable [56, 57]. For this reason the colloids were expelled from the nematic bubbles and concentrated in the isotropic areas between the bubbles. At a high enough volume fraction of the colloids, this generated a strong increase in the mechanical modulus [53, 54, 58] that was correlated with the phase transition (see also Fig. 8a).

Mechanical disturbances of the sample due to the mechanical measurement were discussed to be an origin of poorly reproducible mechanical data in these systems [53]. To circumvent these problems, we used piezo rheology [59–62] as the suitable mechanical testing method. The used piezo rheometer works as a

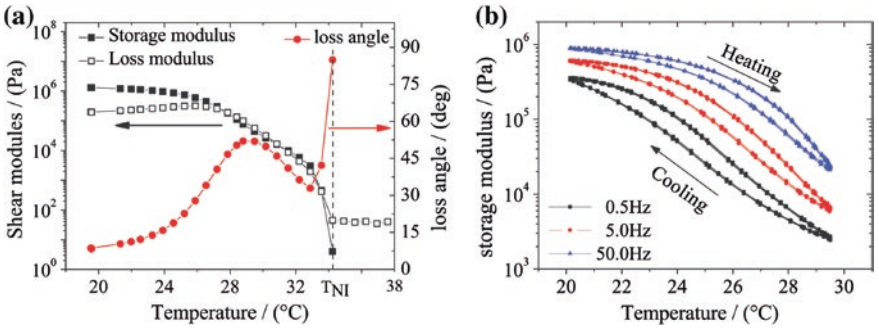

Fig. 8 **a** Measured at 50 Hz, the storage and loss modulus (G' and G'') of the sample strongly increased when entering the nematic phase of 5CB. The modulus kept on growing even well below the phase transition temperature. **b** Cyclic ramping the temperature up and down illustrated the reproducibility of the piezo rheological measurements. No influence of the measurement technique on the evolution could be detected. Reprinted with permission from Roth et al. [62]

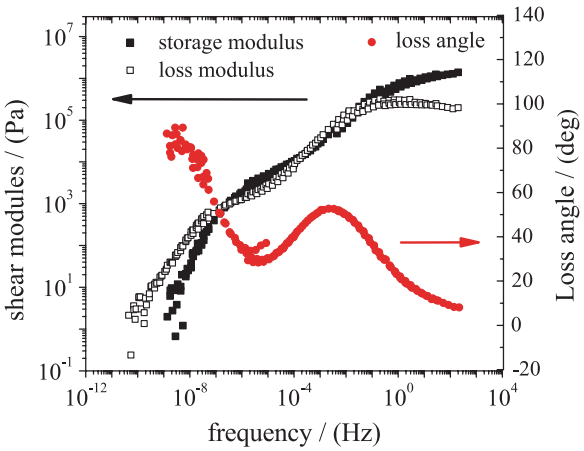

Fig. 9 The frequency dependent mechanical spectra could be superimposed to a master curve using time-temperature superposition. Reprinted with permission from Roth et al. [62]

plate-plate rheometer with oscillatory simple shear at very low relative deformation γ_0 $\left(\gamma_0 < 10^{-3}\right)$ in a broad frequency range ($0.1\,\text{Hz} \leq f \leq 1\,\text{kHz}$). This small deformation guaranteed that the evolution of the sample was not altered due to the applied shear (Fig. 8b).

From imaging the sample at different temperatures, we showed that the structure of the sample changed strongly in the temperature region close to the isotropic to nematic transition. However below approximately 28 °C, no significant structural changes were observed [63]. However, the mechanical data clearly showed a strong change in the storage and loss modulus. Also the loss angle decreased significantly towards lower temperatures, indicating a change towards a less viscous and a more elastic behaviour. To get deeper insight in this behaviour, it was instructive to apply time-temperature superposition to the frequency dependent mechanical spectra that were taken at different temperatures during the cooling of the sample. In this way we could generate a mechanical master curve of the sample (Fig. 9).

The superposition suggested that the system followed a phase separation dynamics know from polymer dispersed liquid crystals [64–66]. Experiments performed with linear PMMA chains dissolved in 5CB at comparable concentrations confirmed this assumption. The isotropic phase of 5CB is a solvent to PMMA. Under cooling the system phase separated and the mechanical properties followed a very similar behaviour to the one shown in Fig. 9 [63].

5 Structural Properties: Local Rearrangement Versus Plastic Deformation

As mentioned in Sect. 1, particle tracking in time series of 3D images obtained using confocal microscopy is widely used in the studies of colloidal systems. The examples from fundamental research include colloids as model atoms [12, 67, 68],

visualising capillary waves at the interface between a colloidal liquid and a colloidal gas [14], dislocation dynamics in weak colloidal crystals [68], and the colloidal glass transition [15, 23]. These experimental studies go along with detailed theoretical analysis, e.g., for the colloidal glass transition [69, 70]. From the processing side the studies include influences of the structural properties [71], the grinding and dispersion processes [72, 73], energy dissipation on the nano scale [74]. In this section we focus on studies combining mechanical testing with nano indentation and simultaneous 3D structural analysis.

5.1 Measuring the Strain Tensor in Colloidal Systems

To measure the deformation inside the sample simultaneous to a nano-indention experiment (Fig. 10), we used fluorescently labelled PMMA colloids (1.6 μm diameter). The colloids were first dried from a stable dispersion to form a densely packed, disordered, and amorphous colloidal film. For a good matching of the refractive index, the colloidal film was thereafter infiltrated with an index-matching non-solvent for the colloids. From 3D images that were taken while indenting the sample with a sphere (25 μm diameter), the trajectories of all colloids in the observed volume could be determined [75].

With the data of the trajectories available, a detailed analysis of the motion and deformation was possible. The simplest example is the averaged displacement (Fig. 10b). Also deeper insight into the internal deformation was deduced from the trajectories. The central question hereby was whether the deformation was dominated by single-colloids processes or alternatively an averaged quasi-macroscopic displacement could be assumed. The quantity that had to be compared to macroscopic models was the strain tensor ε. The strain tensor is related to the changes in the relative colloid positions ($\delta\mathbf{d}$, see Fig. 10a) by the relation

$$\delta\mathbf{d} = \varepsilon \cdot \mathbf{d}, \tag{2}$$

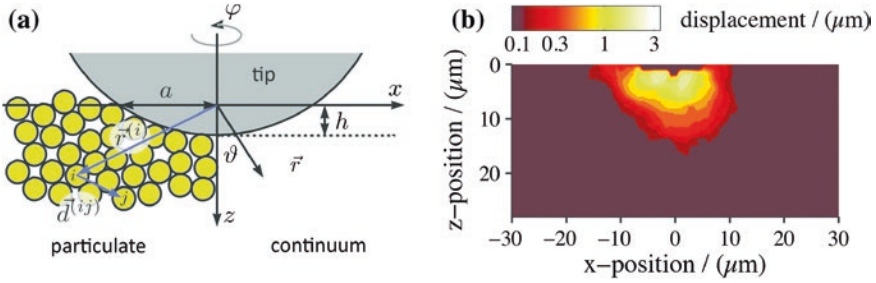

Fig. 10 **a** Scheme of the indentation experiment. The indenter is larger but not very large compared to the colloids in the sample. $\mathbf{r}^{(i)}$ is the position of the colloid i, $\mathbf{d}^{(ij)}$ the distances between colloids i and j. The absolute averaged displacement is shown in panel (**b**) for an indentation depth $h = 3$ μm. With kind permission from Springer Science + Business Media: Roth et al. [75]

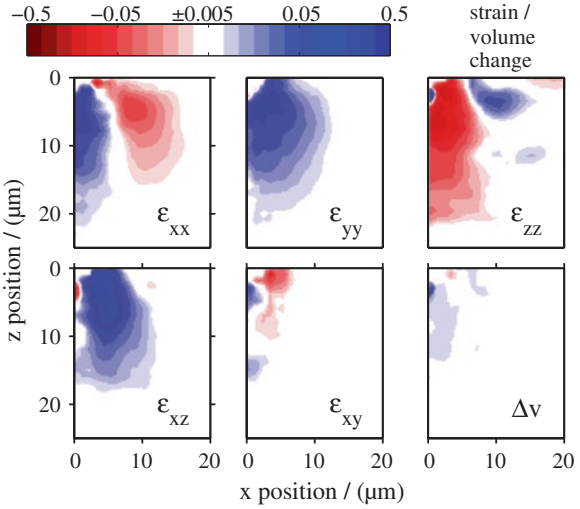

Fig. 11 The components of the strain tensor as calculated from the colloid trajectories using Eq. (3). The *lower right panel* depicts the trace of the strain tensor that is a measure of the volume conservation in the system. With kind permission from Springer Science + Business Media: Roth et al. [75]

where the quantities are now continuous in space (averaged) and no longer discrete (on a colloid basis). It has been shown [68, 76] that a good representation of ε can be obtained by minimising the functional

$$\mathscr{F}^{(i)} = \sum_{j=1}^{N} \left| \delta \mathbf{d}^{(ij)} - \varepsilon^{(i)} \cdot \mathbf{d}^{(ij)} \right|, \tag{3}$$

where all quantities are calculated on a single colloid basis and the sum goes over all nearest neighbours of colloid i. After averaging over a radial distance of 3 μm and using the rotational symmetry over the angle φ all components of the strain tensor (Fig. 11) were obtained.

A more quantitative analysis and comparison of the strain tensor to macroscopic modelling was possible, but beyond the scope of this chapter. More details can be found in [63, 75]. The averaging to obtain Fig. 11 included a relatively small number of colloids (<100) per data point but generated a pattern that showed the same features than expected form continuum mechanics calculations [63, 75]. From these experiments we could conclude that a quasi-macroscopic description of the deformation of a colloidal system was possible, when averaging over enough colloidal particles. In present case the largest microscopic length scale was the colloidal diameter. Under these conditions a good quasi-macroscopic description was obtained with averaging over less than 100 colloids.

Furthermore, the almost complete vanishing of the trace of the strain tensor (Fig. 11, lower right panel) showed that most of the irreversible part of the quasi-macroscopic deformation was due to colloidal rearrangements. Within the resolution of the confocal method, only close to the indenting sphere a contribution due to the deformation of individual colloid could not be excluded.

5.2 Influence of Colloidal Crystals

The above picture of an easy mapping of the averaged trajectories of the colloids on a quasi-macroscopic description only held for amorphous structures, i.e., when the largest microscopic length scale was the colloidal diameter. In case the colloids formed some kind of structure, e.g., colloidal crystals or fractal structures, the situation was different. These internal structures brought in a different length scale that interfered with the averaging. We illustrate this in the case of a polycrystalline colloidal film [77].

From a given arrangement we calculated the degree of order of the nearest neighbor shell of colloids [63, 77–79]. In brief, a crystal is then defined as a region where all particles have a high degree of order in their surrounding. The yellow line in Fig. 12 indicated the border between a region of high (I) and low order (II).

The displacement field depicted in Fig. 12 illustrates such a situation. Two different regions were observable. In region (I) a colloidal crystalline structure was present, whereas region (II) was amorphous. The spherical indenter entered the sample at the boundary between region (I) and (II). The maximum of the displacement visible region (I) indicated the orientation of the colloidal crystal in this region [77]. The crystal structure broke the rotational symmetry of the experiment and limited further data analysis. Although the displacement field was still smooth and suitable for a comparison to quasi-macroscopic models, calculating the strain tensor was not possible, because the number of colloids for averaging was too low. Similar observations were made with fractal-like aggregates. The combination of denser and looser structures in the system also led to strong heterogeneities in the colloidal displacements.

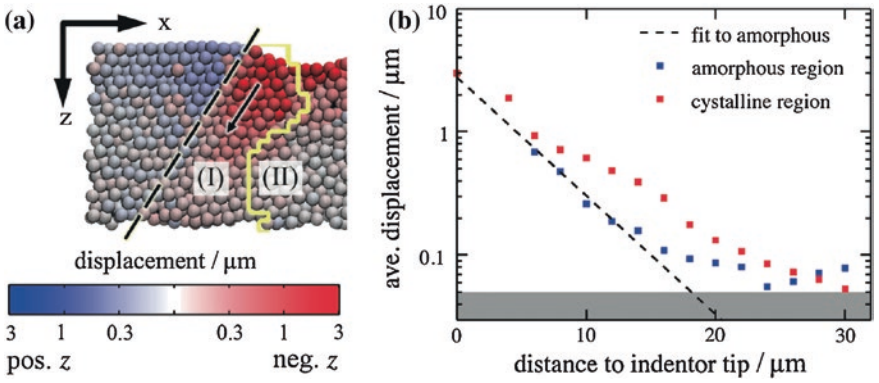

Fig. 12 **a** Visualisation of an indentation experiment on a polycrystalline colloidal film. The region labeled with (I) was crystalline, the region labeled (II) was amorphous. The displacement in the crystalline region followed the crystal axes and **b** was longer ranged than in the amorphous region. Reproduced from Roth et al. [77], used with permission

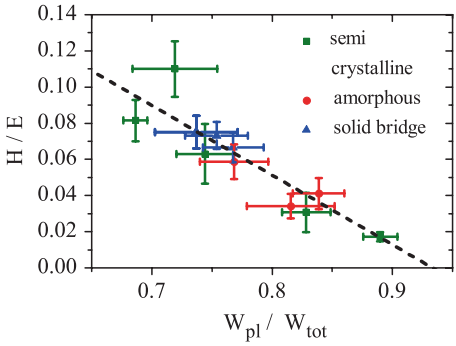

Fig. 13 The ratios between the hardness and the elastic modulus *H/E* and between the plastic and the total work of deformation W_{pl}/W_{tot} followed a linear relation. With kind permission from Springer Science + Business Media: Roth et al. [75]

5.3 Correlation with the Mechanical Properties

The mentioned heterogeneities were also visible in the mechanical analysis of the nano indentation experiments [63, 75, 77]. We calculated the hardness H and the elastic modulus E from the indentation curves following the model by Oliver and Pharr [80, 81]. In the case of the dense amorphous structure, the mechanical modulus of the sample was homogeneous over the tested area. In contrast, strong scattering of the data was observed in the case of the polycrystalline sample. The latter result reflects the intrinsic structural heterogeneity of the sample.

Despite the structural differences, all investigated samples followed a scaling law between the ratio H/E and the ratio of the plastic to the total work of deformation W_{pl}/W_{tot}. A linear relation between both ratios was previously found for a broad range of materials [82–84], including amorphous films. As shown in Fig. 13 the linear relation holds also in our case of colloidal films over a broad range of preparation procedures.

6 Reactive Colloids: Bonds with Finite Lifetime

Colloids that still undergo a chemical reaction have attracted attention of scientists for a long time. The colloidal gel transition has been investigated from the fundamental side [85–89] and the application side (as can be seen from many other chapters of this book). The aggregation is induced by an attractive interaction of the colloids. Depending on the strength or reversibility of the bond between the colloids one distinguishes between physical (reversible) and chemical (irreversible) gels. During the sol-gel transition (gelation) physical and chemical gels show similarities in the rheological behavior. At the gel point the ratio between the real (G') and imaginary part (G'') of the shear modulus (i.e., the loss tangent) is independent of frequency [90–93]. Additionally, similarities between the physical gelation and the glass transition were discussed [94–96]. Recently however, chemical gelation has been shown to have a pronounced difference in the rheological signature compared to the glass transition [97].

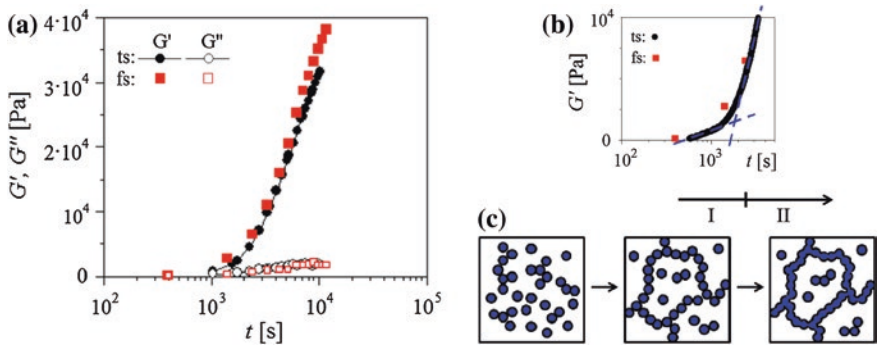

Fig. 14 **a** The temporal evolution of the shear (G') and loss modulus (G'') of precipitated silica gels as measured at a given frequency of 10 rad/s (*black circles*) or extracted from repeated frequency sweeps (*red squares*). **b** The zoom-in at small G' revealed two distinct growth regimes. **c** Schematic for the evolution of the gel, composed of an aggregation and a stiffening process. Reprinted from publication Wang et al. [104]. Copyright (2014), with permission from Elsevier

6.1 Temporal Evolution

As a model system, we used precipitated silica that is widely used as filler particles and intensely studied [74, 98–103]. After mixing the components, the modulus of the gel increased with time. Plotting G' and G'' against the logarithm of time, a two step process became obvious (Fig. 14). We interpreted this as an aggregation followed by a stiffening of the bonds [104]. In order to focus on the sol-gel transition, we started with sodium silicate at high pH and slightly lowered the pH by adding diluted sulphuric acid. Throughout the experiment, the pH of the sample stayed around 11. All concentrations were chosen to prepare the system close to the percolation threshold, i.e., the system was very close to the limit of not forming a gel. Diluting the sample only slightly (adding 20 % more water), increased significantly the time needed to form the gel (Fig. 15a).

6.2 Internal Relaxation and Frequency Dependence

Our precipitated silica gel differed from other (non-reactive) silica gels [105] by the fact that a low-frequency relaxation was evident in the mechanical spectra (Fig. 15b). This structural relaxation was a hint for the finite life time of the bond between the silica nano colloids in the gel. To quantify this structural relaxation mode different models were applied to fit the mechanical spectra, e.g., a modified Cole-Cole model [106] and the Baumgaertel-Schausberger-Winter (BSW) model [107]. The characteristic time scales extracted from both models were similar, though not identical, and showed

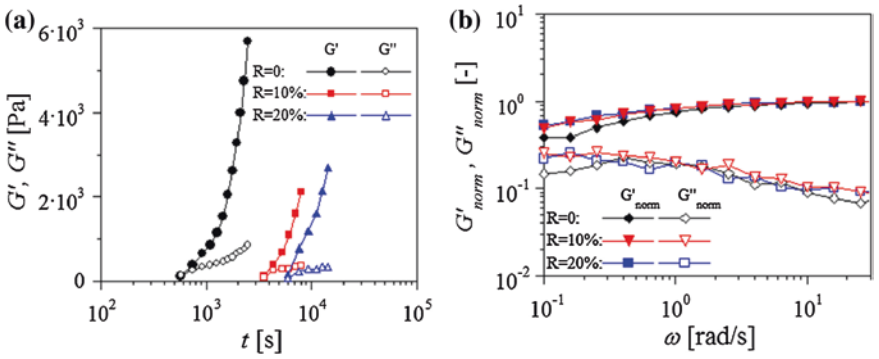

Fig. 15 **a** Increasing the water content of the sample by 10 or 20 % strongly increased the time scale of the gel formation. **b** Frequency dependent measurements revealed a low-frequency relaxation mode in the system. Details of this relaxation mode depended in the system parameters (here the dilution). Reprinted from publication Wang et al. [104]. Copyright (2014), with permission from Elsevier

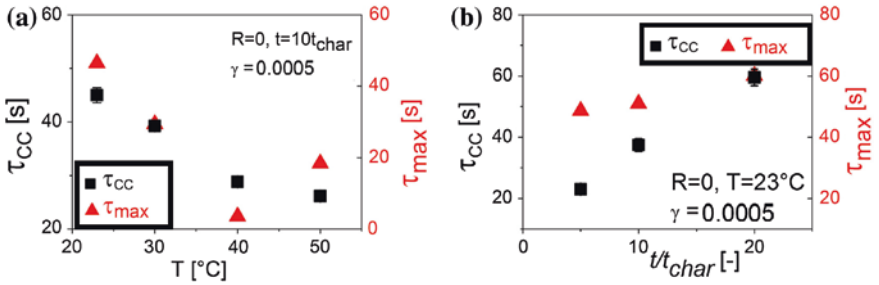

Fig. 16 The characteristic relaxation time of the low-frequency structural relaxation in the precipitated silica gel, as fitted with a modified Cole-Cole model (τ_{CC}) [106] or the BSW model (τ_{max}) [107], for **a** varying temperature and **b** different ages of the gel. Reprinted from publication Wang et al. [104]. Copyright (2014), with permission from Elsevier

the same dependency on the system parameters like temperature and age of the gel (Fig. 16b) [104]. The origin of the finite life time of the bonds between the colloids in this case seemed to lie in the finite solubility of silica at the pH (about 11) of the sample [108].

In summary, this finite solubility gave our presented silica gel features of physical gels, like the logarithmic growths of the modulus with time [93, 96] and the structural relaxation at low frequencies [109]. Despite the fact of having a chemical reaction, the bonds between the colloids were apparently not of infinite life time and gave the system a physical gel-like behaviour.

References

1. Lekkerkerker H, Poon W, Pusey P, Stroobants A, Warren P (1992) Phase behaviour of colloid + polymer mixtures. Europhys Lett 20:559
2. Gasser U, Weeks ER, Schofield A, Pusey PN, Weitz DA (2001) Real-space imaging of nucleation and growth in colloidal crystallization. Science 292:258
3. Pham KN, Egelhaaf SU, Pusey PN, Poon WCK (2004) Glasses in hard spheres with short-range attraction. Phys Rev E 69(1): 011503
4. Verhaegh NAM, Blaaderen Av (1994) Dispersions of rhodamine-labeled silica spheres: synthesis, characterization, and fluorescence confocal scanning laser microscopy. Langmuir 10(5):1427
5. Goodwin JW, Hearn J, Ho CC, Ottewill RH (1974) Studies on the preparation and characterisation of monodisperse polystyrene laticee. Colloid Polym Sci 252(6):464
6. Kim JW, Larsen RJ, Weitz DA (2006) Synthesis of nonspherical colloidal particles with anisotropic properties. J Am Chem Soc 128(44):14374
7. Nie Z, Li W, Seo M, Xu S, Kumacheva E (2006) Janus and ternary particles generated by microfluidic synthesis: design, synthesis, and self-assembly. J Am Chem Soc 128(29):9408
8. Walther A, Mueller AHE (2008) Janus particles. Soft Matter 4(4):663
9. Pawar AB, Kretzschmar I (2010) Fabrication, assembly, and application of patchy particles. Macromol Rapid Commun 31(2):150
10. Dendukuri D, Pregibon DC, Collins J, Hatton TA, Doyle PS (2006) Continuous-flow lithography for high-throughput microparticle synthesis. Nat Mater 5(5):365
11. Schwedes J (2003) Review on testers for measuring flow properties of bulk solids. Granular Matter 5(1):1
12. van Blaaderen A (2003) Colloidal molecules and beyond. Science 301(5632):470
13. Schall P, Cohen I, Weitz DA, Spaepen F (2004) Visualization of dislocation dynamics in colloidal crystals. Science 305(5692):1944
14. Aarts DGAL, Schmidt M, Lekkerkerker HNW (2004) Direct visual observation of thermal capillary waves. Science 304:847
15. Besseling R, Weeks ER, Schofield AB, Poon WCK (2007) Three-dimensional imaging of colloidal glasses under steady shear. Phys Rev Lett 99(2):028301
16. Tsai JC, Voth GA, Gollub JP (2003) Internal granular dynamics, shear-induced crystallization, and compaction steps. Phys Rev Lett 91(6):064301
17. Gao Y, Haavisto S, Tang CY, Salmela J, Li W (2013) Characterization of fluid dynamics in spacer-filled channels for membrane filtration using doppler optical coherence tomography. J Membr Sci 448:198
18. Saarinen T, Haavisto S, Sorvari A, Salmela J, Seppälä J (2014) The effect of wall depletion on the rheology of microfibrillated cellulose water suspensions by optical coherence tomography. Cellulose 21:1261
19. Scheel M, Seemann R, Brinkmann M, Di Michiel M, Sheppard A, Breidenbach B, Herminghaus S (2008) Morphological clues to wet granular pile stability. Nat Mater 7(3):189
20. Weon BM, Lee JS, Kim JT, Pyo J, Je JH (2012) Colloidal wettability probed with X-ray microscopy. Curr Opin Colloid Interface Sci 17(6):388
21. Cierpka C, Kähler CJ (2012) Particle imaging techniques for volumetric three-component (3D3C) velocity measurements in microfluidics. J Vis 15(1):1
22. Crocker JC, Grier DG (1996) Methods of digital video microscopy for colloidal studies. J Colloid Interface Sci 179:298
23. Weeks ER, Crocker JC, Levitt AC, Schofield A, Weitz DA (2000) Three-dimensional direct imaging of structural relaxation near the colloidal glass transition. Science 287:627
24. Videla A, Lin CL, Miller JD (2006) Watershed functions applied to a 3D image segmentation problem for the analysis of packed particle beds. Part Syst Charact 23(3–4):237

25. Al-Raoush R (2007) Microstructure characterization of granular materials. Physica A 377(2):545
26. Wenzl J, Seto R, Roth M, Butt HJ, Auernhammer G (2013) Measurement of rotation of individual spherical particles in cohesive granulates. Granular Matter 15(4):391
27. Chao WL, Harteneck BD, Liddle JA, Anderson EH, Attwood DT (2005) Soft X-ray microscopy at a spatial resolution better than 15 nm. Nature 435:12100
28. Araki T, Ade H, Stubbs JM, Sundberg DC, Mitchell GE (2006) Resonant soft x-ray scattering from structured polymer nanoparticles. App Phys Lett 89:124106
29. Auernhammer GK, Fauth K, Ullrich B, Zhao J, Weigand M, Vollmer D (2009) Time-resolved X-ray microscopy of nanoparticle aggregates under oscillatory shear. J Synchrot Radiat 16:308. doi:10.1107/S0909049509000314
30. Auernhammer GK, Collin D, Martinoty P (2006) Viscoelasticity of suspensions of magnetic particles in a polymer: effect of confinement and external field. J Chem Phys 124:204907
31. D'Acunzi M, Mammen L, Singh M, Deng X, Roth M, Auernhammer GK, Butt HJ, Vollmer D (2010) Superhydrophobic surfaces by hybrid raspberry-like particles. Faraday Discuss 146:35
32. Zhang L, D'Acunzi M, Kappl M, Auernhammer GK, Vollmer D, van Kats CM, van Blaaderen A (2009) Hollow silica spheres: synthesis and mechanical properties. Langmuir 25(5):2711
33. Furusawa K, Norde W, Lyklema J (1972) Method for preparing surfactant-free polystyrene latices of high surface charge. Kolloid-Z u Z Polymere 250(9):908
34. D'Acunzi M (2010) Core-shell particles and their application for superhydrophobic surfaces. Ph.D. thesis, University Mainz
35. Reynhout XEE, Hoekstra L, Meuldijk J, Drinkenburg AAH (2003) Contribution of steric and electrostatic repulsion forces to the stability of styrene latices copolymerized with acrylic acid. J Polymer Sci Part Polymer Chem 41(19):2985
36. Reynhout XEE, Beckers M, Meuldijk A, Drinkenburg BAH (2005) Electrosteric stability of styrene/acrylic acid copolymer latices under emulsion polymerization reaction conditions. J Polymer Sci Part Polymer Chem 43(4):726
37. Shouldice GTD, Vandezande GA, Rudin A (1994) Practical aspects of the emulsifier-free emulsion polymerization of styrene. Eur Polymer J 30(2):179
38. Ottewill RH, Shaw JN (1967) Studies on the preparation and characterization of monodisperse polystyrene latices. Kolloid-Z u Z Polymere 215(2):161
39. Musyanovych A, Rossmanith R, Tontsch C, Landfester K (2007) Effect of hydrophilic comonomer and surfactant type on the colloidal stability and size distribution of carboxyl- and amino-functionalized polystyrene particles prepared by miniemulsion polymerization. Langmuir 23(10):5367
40. Graf C, Vossen DLJ, Imhof A, van Blaaderen A (2009) A general method to coat colloidal particles with silica. Langmuir 19:6693
41. Stöber W, Fink A, Bohn E (1968) Controlled growth of monodisperse silica spheres in the micron size range. J Colloid Interface Sci 26(1):62
42. van Blaaderen A, Kentgens APM (1992) Controlled growth of monodisperse silica spheres in the micron size range. J Non-Cryst Solids 149(3):161
43. Zhang L, D'Acunzi M, Kappl M, Imhof A, van Blaaderen A, Butt HJ, Graf R, Vollmer D (2010) Tuning the mechanical properties of silica microcapsules. Phys Chem Chem Phys 12(47):15392
44. Butt H, Graf K, Kappl M (2006) Physics and chemistry of interfaces. Wiley, Weinheim
45. Butt HJ, Cappella B, Kappl M (2005) Force measurements with the atomic force microscope: technique, interpretation and applications. Surf Sci Rep 59(1–6):1
46. Fery A, Weinkamer R (2007) Mechanical properties of micro- and nanocapsules: single-capsule measurements. Polymer 48(25):7221
47. Adachi T, Sakka S (1990) Dependence of the elastic moduli of porous silica gel prepared by the sol-gel method on heat-treatment. J Mat Sci 25(11):4732

48. Engelhardt DMG (1987) High-resolution solid-state NMR of silicates and zeolites. Wiley, Chinchester
49. Marsmann HC, Raml W, Hengge E (1980) ^{29}Si NMR Measurements on polysilanes. 2. Isotetrasilanes. Z. Naturforsch B 35(12):1541
50. Deng X, Mammen L, Zhao Y, Lellig P, Muellen K, Li C, Butt HJ, Vollmer D (2011) Transparent, thermally stable and mechanically robust superhydrophobic surfaces made from porous silica capsules. Adv Mater 23(26):2962
51. Nagao D, van Kats CM, Hayasaka K, Sugimoto M, Konno M, Imhof A, van Blaaderen A (2010) Synthesis of hollow asymmetrical silica dumbbells with a movable inner core. Langmuir 26(7):5208
52. Meeker SP, Poon WCK, Crain J, Terentjev EM (2000) Colloid-liquid-crystal composites: an unusual soft solid. Phys Rev E 61(6):R6083
53. Vollmer D, Hinze G, Ullrich B, Poon WCK, Cates ME, Schofield AB (2005) Formation of self-supporting reversible cellular networks in suspensions of colloids and liquid crystals. Langmuir 21:4921
54. Anderson VJ, Terentjev EM, Meeker SP, Crain J, Poon WCK (2001) Cellular solid behaviour of liquid crystal colloids 1. phase separation and morphology. Eur Phys J E 4:11
55. Bosma G, Pathmamanoharan C, de Hoog EHA, Kegel WK, van Blaaderen A, Lekkerkerker HNW (2002) Preparation of monodisperse, fluorescent PMMA-latex colloids by dispersion polymerization. J Colloid Interface Sci 245(2):292
56. Stark H (2001) Physics of colloidal dispersions in nematic liquid crystals. Phys Rep 351(6):387
57. Terentjev EM (1995) Disclination loops, standing alone and around solid particles, in nematic liquid crystals. Phys Rev E 51(2):1330
58. Anderson VJ, Terentjev EM (2001) Cellular solid behaviour of liquid crystal colloids 2. mechanical properties. Eur Phys J E 4(1):21
59. Bartolino R, Durand G (1977) Plasticity in smectic-A liquid crystal. Phys Rev Lett 39(21):1346
60. Yamamoto Y, Nakamura H, Okano K (1986) Apparatus for measurement of complex shear modulus of liquid crystaks at low frequencies. Jap J Appl Phys 26–1:29
61. Martinoty P, Gallani J, Collin D (1998) Hydrodynamic and nonhydrodynamic behavior of layer-compression modulus B at the nematic-smectic- A phase transition in 8OCB. Phys Rev Lett 81:144
62. Roth M, D'Acunzi M, Vollmer D, Auernhammer GK (2010) Viscoelastic rheology of colloid-liquid crystal composites. J Chem Phys 132:124702
63. Roth M (2012) Rheology of arrested colloids: a parameter study using novel experimental methods. PhD thesis, Universität Mainz. http://ubm.opus.hbz-nrw.de/volltexte/2012/3009/
64. West JL (1988) Phase separation of liquid crystals in polymers. Mol Cryst Liq Cryst Inc Nonlin Opt 157:427
65. West JL (1990) Polymer-dispersed liquid crystals. Liquid-Crystalline Polymers 435:475–495
66. Coates D (1995) Polymer-dispersed liquid crystals. J Mater Chem 5(12):2063
67. Frenkel D (2002) Playing tricks with designer "atoms". Science 296:65
68. Schall P, Cohen I, Weitz DA, Spaepen F (2006) Visualizing dislocation nucleation by indenting colloidal crystals. Nature 440:319
69. Brader JM, Voigtmann T, Fuchs M, Larson RG, Cates ME (2009) Glass rheology: from mode-coupling theory to a dynamical yield criterion. Proc Natl Acad Sci 106(36):15186
70. Brader JM, Siebenbürger M, Ballauff M, Reinheimer K, Wilhelm M, Frey SJ, Weysser F, Fuchs M (2010) Nonlinear response of dense colloidal suspensions under oscillatory shear: mode-coupling theory and fourier transform rheology experiments. Phys Rev E 82(6):061401
71. Zaccone A, Soos M, Lattuada M, Wu H, Babler MU, Morbidelli M (2009) Breakup of dense colloidal aggregates under hydrodynamic stresses. Phys Rev E 79(6):061401

72. Schilde C, Kampen I, Kwade A (2010) Dispersion kinetics of nano-sized particles for different dispersing machines. Chem Eng Sci 65(11):3518
73. Schilde C, Breitung-Faes S, Kampen I, Kwade A (2013) Grinding kinetics of nano-sized particles for different electrostatic stabilizing acids in a stirred media mill. Powder Technol 235:1008
74. Schilde C, Gothsch T, Quarch K, Kind M, Kwade A (2009) Effect of important precipitation process parameters on the redispersion process and the micromechanical properties of precipitated silica. Chem Eng Techn 32(7):1078
75. Roth M, Schilde C, Lellig P, Kwade A, Auernhammer GK (2012) Colloidal aggregates tested via nanoindentation and simultaneous 3D imaging. Eur Phys J E 35:124
76. Chen D, Semwogerere D, Sato J, Breedveld V, Weeks ER (2010) Microscopic structural relaxation in a sheared supercooled colloidal liquid. Phys Rev E 81(1):011403
77. Roth M, Schilde C, Lellig P, Kwade A, Auernhammer GK (2012) Simultaneous nanoindentation and 3D imaging on semicrystalline colloidal films. Chem Lett 41(10):1110
78. Steinhardt PJ, Nelson DR, Ronchetti M (1983) Bond-orientational order in liquids and glasses. Phys Rev B 28:784
79. Lechner W, Dellago C (2008) Accurate determination of crystal structures based on averaged local bond order parameters.. J Chem Phys 129
80. Oliver WC, Pharr GM (1992) An improved method for determining hardness and elastic modulus using load and displacement sensing indentation experiments. J Mater Res 7:1564
81. Oliver WC, Pharr GM (2004) Measurement of hardness and elastic modulus by instrumented indentation: Advances in understanding and refinements to methodolgy. J Mater Res 19:3
82. Cheng YT, Cheng CM (1998) Relationships between hardness, elastic modulus, and the work of indentation. Appl Phys Lett 73:614
83. Malzbender J, de With G (2000) Energy dissipation, fracture toughness and the indentation load–displacement curve of coated materials. Surf Coat Technol 135:60
84. Bartali R, Michelia V, Gottardia G, Vaccaria A, Laidania N (2010) Nanoindentation: unload-to-load work ratio analysis in amorphous carbon films for mechanical properties. Surf Coat Technol 204:2073
85. Zaccarelli E (2007) Colloidal gels: equilibrium and non-equilibrium routes. J Phys Cond Matt 19:323101
86. Dawson KA (2002) The glass paradigm for colloidal glasses, gels, and other arrested states driven by attractive interactions. Curr Opin Colloid Interface Sci 7:218
87. Sciortino F, Zaccarelli E (2011) Reversible gels of patchy particles. Curr Opin Solid State Mat Sci 15:246
88. Smith PA, Petekidis G, Egelhaaf SU, Poon WCK (2007) Yielding and crystallization of colloidal gels under oscillatory shear. Phys Rev E 76(4):041402
89. Lindström SB, Kodger TE, Sprakel J, Weitz DA (2012) Structures, stresses, and fluctuations in the delayed failure of colloidal gels. Soft Matter 8:3657
90. Chambon F, Winter HH (1987) Linear viscoelasticity at the gel point of a crosslinking PDMS with imbalanced stoichiometry. J Rheol 31(8):683
91. Matricardi P, Dentini M, Crescenzi V, Ross-Murphy SB (1995) Gelation of chemically cross-linked polygalacturonic acid derivatives. Carbohydr Polym 27(3):215
92. Hodgson DF, Amis EJ, Non-Cryst J (1991) Dynamic viscoelasticity during sol-gel reactions. Dynamic viscoelasticity during sol-gel reactions. J Non-Cryst Solids 131–133:913
93. te Nijenhuis K, Winter HH (1989) Mechanical properties at the gel point of a crystallizing poly(vinyl chloride) solution. Macromolecules 22:411
94. Tanaka H, Jabbari-Farouji S, Meunier J, Bonn D (2005) Kinetics of ergodic-to-nonergodic transitions in charged colloidal suspensions: aging and gelation. Phys Rev E 71(2):021402
95. Parker A, Normand V (2010) Glassy dynamics of gelatin gels. Soft Matter 6(19):4916
96. Ronsin O, Caroli C, Baumberger T (2009) Interplay between shear loading and structural aging in a physical gelatin gel. Phys Rev Lett 103(13):138302

97. Winter HH (2013) Glass transition as the rheological inverse of gelation. Macromolecules 46(6):2425
98. Iler RK (1979) The chemistry of silica: solubility, polymerization, colloid and surface properties, and biochemistry. Wiley, New York
99. Quarch K, Kind M (2010) Inorganic precipitated silica gel. Part 1: Gelation kinetics and gel properties. Chem Eng Technol 33:1034
100. Quarch K, Durand E, Kind M (2010) Inorganic precipitated silica gel. Part 2: Fragmentation by mechanical energy. Chem Eng Technol 33
101. Schlomach J, Kind M (2004) Investigations on the semi-batch precipitation of silica. J Colloid Interface Sci 277(2):316
102. Sahabi H, Kind M (2011) Experimentally justified model-like description of consolidation of precipitated silica Polymers 3(4):2156
103. Sahabi H, Kind M (2011) Consolidation of inorganic precipitated silica gel. Polymers 3(3):1423
104. Wang M, Winter HH, Auernhammer GK (2013) Time and frequency dependent rheology of reactive silica gels. J Coll Int Sci 413:159
105. Manley S, Davidovitch B, Davies NR, Cipelletti L, Bailey AE, Christianson RJ, Gasser U, Prasad V, Segre PN, Doherty MP, Sankaran S, Jankovsky AL, Shiley B, Bowen J, Eggers J, Kurta C, Lorik T, Weitz DA (2005) Time-dependent strength of colloidal gels. Phys Rev Lett 95(4):048302
106. Friedrich C, Braun H (1992) Generaized cole-cole behavior and its rheological relevance. Rheol Acta 31:309
107. Baumgaertel M, Schausberger A, Winter HH (1990) The relaxation of polymers with linear flexible chains of uniform length. Rheol Acta 29:400
108. Prasad M, Mehta SM, Desai JB (1931) Viscosity of the silicic acid gel-forming mixtures. J Phys Chem 36(5):1384
109. Laurati M, Petekidis G, Koumakis N, Cardinaux F, Schofield AB, Brader JM, Fuchs M, Egelhaaf SU (2009) Structure, dynamics, and rheology of colloid-polymer mixtures: from liquids to gels. J Chem Phys 130(13):134907

Fluidization of Highly Concentrated Colloidal Dispersions by Tailoring of Attractive Interactions

E. Bartsch, D. Burger, S. Burger, J. Gisin, R. Schneider, O. Thorwarth, J. Vesaratchanon, C. Weis, M. Wiemann and N. Willenbacher

Abstract Mode coupling theory (MCT) predicts fluid states of colloidal dispersions at particle volume fractions ϕ well above the hard sphere (HS) colloidal glass transition due to weak attractive interactions among particles. This opens a versatile, new route to manufacture highly concentrated, freely flowing dispersions with narrow particle size distribution. Our investigations are based on two model systems: polystyrene (PS)-microgel particles suspended in an isorefractive organic solvent and an aqueous polymer dispersion based on a well-stabilized, commercial polymer latex. Both systems exhibit hard sphere type flow behavior with a divergence of zero-shear viscosity at $\phi = 0.58$. Suspensions were fluidized via addition of non-adsorbing polymers to the continuous phase, thus introducing weak depletion attraction among particles. The index-matched microgel system was used to study phase behavior as a function of particle and polymer concentration as well as polymer to particle size ratio and particle rigidity. A tight correlation between structural relaxation times from dynamic light scattering (DSL) experiments and rheological data was found. Fluid states were observed at particle loadings close to $\phi = 0.7$ and a minimum viscosity has been achieved at polymer concentrations below the overlap concentration c*. Low viscosity values at particle loadings beyond $\phi = 0.58$ could so far only be obtained for dispersions with bi- or multimodal particle size distribution. Flow curves obtained here for monomodal dispersions fluidized due to weak attractive interactions are similar to those of commercial dispersions with broad

E. Bartsch (✉) · D. Burger · S. Burger · J. Gisin · R. Schneider · O. Thorwarth · M. Wiemann
Institut für Physikalische Chemie, Albert-Ludwigs-Universität Freiburg,
Albertstr. 21, 79104 Freiburg, Germany
e-mail: eckhard.bartsch@physchem.uni-freiburg.de

E. Bartsch · D. Burger · S. Burger · J. Gisin · R. Schneider · O. Thorwarth · M. Wiemann
Institut für Makromolekulare Chemie, Albert-Ludwigs-Universität Freiburg,
Stefan-Meier-Str. 31, 79104 Freiburg, Germany

J. Vesaratchanon · C. Weis · N. Willenbacher (✉)
Bereich Angewandte Mechanik, KIT, Institut für Mechanische Verfahrenstechnik
und Mechanik, Gotthard-Franz-Straße 3, 76131 Karlsruhe, Germany
e-mail: Norbert.Willenbacher@kit.edu

M. Kind et al. (eds.), *Colloid Process Engineering*,
DOI 10.1007/978-3-319-15129-8_11

particle size distribution, demonstrating the competitive strength of the new concept. Sharply monodisperse aqueous polymer dispersions were used to demonstrate that beyond the predictions of MCT, also densely packed, crystalline suspensions can be fluidized upon adding small amounts of non-adsorbing polymer. A microfluidic flow channel attached to an inverted fluorescence microscope was used to study the true flow profiles of suspensions doped with size-matched fluorescent tracer particles. Reducing the range of weak depletion attraction by reducing the size of free, non-adsorbing polymer extended the fluidized region to even higher particle loadings of about $\phi = 0.72$—in qualitative agreement with MCT predictions. However, an increase of the microgel crosslink density from 1:50 to 1:10 reduced the fluidized region significantly to about the effect observed with hard sphere-like PMMA dispersions. Particle softness and osmotic deswelling are discussed as possible origins of the exceptionally effective depletion fluidization in case of 1:50 crosslinked microgels. To enable similar studies combining DLS and rheology on model systems which are closer to aqueous, technical dispersions, perfluoroacrylate particles sterically stabilized with polyethylene-glycol (PEG) chains have been synthesized and characterized. A first study indicates that such dispersions can be refractive index matched in aqueous media and undergo a glass transition, thereby exposing dynamics in DLS which are quite analogous to that seen in so far studied model systems. The potential of fluidizing such dispersions at high particle loading by addition of free PEG or other depletants will be systematically explored in future work.

Keywords Microgels · Colloids · Colloid polymer mixtures · Re-entrant melting · Glass transition dynamics · Rheology · Microchannel flow · Atom transfer radical polymerization (ATRP) · Core–shell structures · Sterical stabilization · Fluoro-acrylates

1 Introduction

Colloidal dispersions are encountered in many traditional applications, including paints, inks, cosmetics, pharmaceuticals or foods [1]. Nowadays, colloid science and technology also play a key role in emerging technologies such as tissue engineering scaffolding [2], photonic crystals [3], 3D ink-jet technology [4], advanced ceramics processing [5] or microfluidics [6]. A key technological challenge in designing such materials is to control their flow properties in order to meet the manifold requirements during processing and application. This topic is especially relevant when dealing with nanoparticle formulations on a technical scale were high particle loadings are required. Making highly concentrated dispersions is a persistent challenge since it allows for higher time-space yield during manufacturing, reduced transport costs and drying energy, particularly in large scale industrial coating applications, and also provides additional degrees of freedom in formulation of complex fluids.

The classical route to achieve high particle loading at low viscosity level in suspensions is to provide a bimodal or broad particle size distribution [7, 8]. This is not always technically or economically feasible and large particles may disturb

final product properties. In colloidal systems viscosity reduction is limited due to interactions among particles, which get increasingly relevant as particle size decreases. For bimodal dispersions including particles with short range repulsive interactions typical for commercial systems a minimum viscosity is reached at a fraction of small particles of about 30 % and a size ratio $\sigma \approx 4$–5 [9, 10] (or $\Gamma = R_S/R_L = \sigma^{-1} = 0.2 - 0.25$). Here we present an alternative concept to make highly concentrated, freely flowing dispersions, based on the so-called re-entry glass transition in colloidal dispersions which has been predicted theoretically and confirmed experimentally for various model dispersions. Weak attractive interactions are supposed to lead to reversible particle clustering, which opens up space and melts the glassy state by allowing for long-range particle motion and macroscopic flow. We demonstrate that mono-modal dispersions with particle loadings up to $\phi \approx 0.7$ can be fluidized and that viscosity can be reduced to the level of commercial dispersions with broad particle size distribution in a wide shear rate range representing essential manufacturing and processing conditions.

Phase behavior [11], dynamics and flow of colloidal dispersions are strongly controlled by particle volume fraction ϕ [12]. Progressive crowding eventually leads to a vitrification when particles are trapped within a virtual cage provided by nearest neighbors. Long range particle motion slows down and the low shear viscosity diverges when a critical concentration ϕ_g, the glass transition, is approached [13], a finite zero-frequency modulus G_0 is observed beyond ϕ_g. Mode coupling theory (MCT) has been successfully employed to describe this phenomenon [14]. Barrat et al. [15] have predicted a critical scaling exponent for the divergence of the zero-shear viscosity. Nägele and Bergenholtz [16] have developed a general method to describe the linear viscoelastic properties. Fuchs and Cates [17, 18] have generalized MCT to treat the non-linear dynamics of colloidal suspensions in shear flow and careful experiments on well-characterized model systems have confirmed that flow curves are predicted very well by MCT in a wide shear rate range [19, 20].

MCT also predicts that two different glassy states exist in dispersions of particles with weak short-range attraction, one due to particle caging (repulsive glass), the other due to particle bonding (attractive glass) and the glass transition is shifted to higher ϕ [21, 22]. This has been confirmed experimentally for different colloidal dispersions, namely polymethylmethacrylate (PMMA) particles [23, 24] and PS-microgel particles [25–27] suspended in isorefractive organic solvents. In both cases attractive depletion interactions were introduced by addition of non-adsorbing polystyrene (PS) molecules to the continuous phase of the dispersion. Phase diagrams were obtained from DLS experiments and the transition from the ergodic to the non-ergodic, glassy state is identified by the non-vanishing dynamic structure factor $f(q,\tau\rightarrow\infty) > 0$. The phase diagrams show a significant curvature of the fluid-glass transition line and at fixed particle loading a transition from the glassy to the fluid state and then again from the fluid to the attractive glassy state is observed when polymer concentration and hence the strength of attractive interaction is increased (re-entry glass transition or re-entry phenomenon). Fluid states were observed up to $\phi \approx 0.61$ for the PMMA system and $\phi \approx 0.68$ for the PS-microgel system.

Up to now little is known about the consequences of the re-entry phenomenon for the macroscopic flow behavior. The effect of depletion attraction on the

rheology and the viscoelasticity of nearly hard sphere silica particles suspended in decalin or toluene has been investigated carefully [28, 29] and a minimum of the low shear viscosity as a function of polymer concentration has been observed [30, 31]. The zero shear viscosity is reduced by a factor of three at $\phi = 0.49$ and a polymer concentration $c_P/c^* = 0.03$ well below the overlap concentration c^*. This clearly demonstrates that weak attractive particle interactions can lead to a significant decrease of the viscosity compared to hard sphere systems. However, it should be noted that in this case the particle volume fraction is still below the hard sphere glass transition. Another example has been reported by Pham et al. [32], who observed a reduction of the storage modulus G' by a factor of three for a system of sterically stabilized PMMA particles suspended in decalin at $\phi = 0.6$ and a polymer concentration of $c_P/c^* = 0.15$. This shows that weak attractions among colloidal particles in suspension can alter macroscopic rheological quantities even in the particle concentration range above the hard sphere glass transition. On the other hand, the rheological effects observed so far may be too small to be of significant technical relevance. Moreover, the re-entry phenomenon has not been investigated so far for aqueous suspensions, which are of paramount importance from a technical point of view.

Therefore, we embarked onto a systematic study of the applicability of the polymer-induced re-entry phenomenon for the formulation of freely flowing, yet highly concentrated dispersions. Starting from the observation of an extraordinary large re-entry region with fluid volume fractions up to $\phi \approx 0.68$ on the addition of free, i.e. non-adsorbing, polystyrene (PS) chains to a PS microgel system in a good, isorefractive organic solvent (2-ethylnaphthalene, 2EN) [27], we addressed the following questions. (i) Is the huge re-entry region in the PS microgel system which has so far only been observed by dynamic light scattering (DLS) indicative of a corresponding behavior in rheology, i.e. of a fluidization, and if so, how do the re-entry regions seen with both methods compare? (ii) The re-entry phenomenon has so far only been observed for model colloids dispersed in organic media. Can this fluidization effect also be induced by introduction of short-ranged attractions via free polymer in aqueous dispersions and could this then be used to formulate technical dispersions with high particle loadings which are still freely flowing? If a proof-of principle can be achieved, how does this effect influence the rheological behavior in other rheological experiments which mimic shear scenarios typically encountered during processing or application of technical dispersions, e.g. levelling, sagging, mixing, screen printing, dispersion blade coating or stirring? (iii) How is the re-entry effect influenced by the variation of system parameters like particle interactions (particle hardness), size or number ratio of particles (variation of particle size distribution) and polymer size (range of depletion attractions)? Can these parameters be used to further enhance the re-entry phenomenon? (iv) While the questions raised in (iii) were to be studied in the well-characterized model system of PS microgel dispersions, it seemed of high interest to have at hand a similarly well characterized model dispersion for aqueous (i.e. technical dispersions) which allows to study the re-entry effect and its variations also with the complementary techniques DLS and rheology. As DLS requires (near) isorefractivity of

particles and dispersion medium, the low refractive index of water implies use of monomer with a high fluorine content as fluoropolymer dispersions are known to have refractive indices almost as low as the value for water [33–36].

2 Comparative Study of Particle Dynamics and Flow Behavior in Well-Defined PS Microgel Model Dispersions

In a first step we wanted to apply two complementary methods to monitor dispersion dynamics in the same carefully chosen and well-studied model system—dynamic light scattering (DLS) which probes particle dynamics on a microscopic scale and rheology which measures macroscopic flow. Here the aim was to verify that both methods do indeed "see" the same dynamics as predicted by MCT [14]. This is by no means a trivial question as there is an ongoing controversy whether the zero shear viscosity η measured by rheology and the structural or α-relaxation time τ_α determined via DLS diverge at the same volume fraction ϕ_g, thus identifying the glass transition, and whether this divergence occurs for hard sphere (HS)-like colloids at $\phi_g = \phi_{c,MCT} = 0.58$ as seen in DLS experiments or at $\phi_g = \phi_{rcp} = 0.64$ as suggested from several rheology experiments [37, 38]. Here, a major drawback has been that DLS and rheology have—besides rare exceptions like the work of Segre et al. [39] which did not extend into the glass transition regime—not been applied to identical systems. Given that different model systems may differ in their approximation of a true HS system, in their degree of polydispersity and in the accuracy of the volume fraction determination [40, 41], a comparative study of particle dynamics with DLS and macroscopic flow on the same systems appears to be essential for data interpretation close to (repulsive or attractive) glass transitions.

For this purpose we re-designed the previously studied PS microgel system [27]—here addressed as the reference system—as closely as possible. As before we employed a binary mixture of nearly monodisperse 1:50 crosslinked[1] PS microgel particles (polydispersity $\sigma_R = (\langle R^2\rangle - \langle R\rangle^2)^{1/2}/\langle R\rangle \approx 0.04 - 0.05$ as estimated from TEM and static light scattering). This allowed slowing down or even suppressing crystallization such that metastable super compressed and glassy states were experimentally accessible. At the same time the study of the fluid-solid coexistence region of the individual components (which crystallized easily) enabled us to determine the swelling ratio of the particles and, thus, the volume fractions of the binary mixture (including a mapping to the hard sphere (HS) system) with high precision (for details of samples and sample preparation see Ref. [42]). The effective HS radii were $R_S = 144 \pm 2$ nm and $R_L = 199 \pm 4$ nm, respectively

[1] A crosslinking of 1:50 implies one crosslink per 50 monomer units.

(the subscripts S and L indicate small and large particles in the following), yielding a size ratio of $\Gamma = 0.722 \pm 0.022$. It should be noted that the "error margin" here does not reflect the inaccuracy of the particle size determination, but rather the slight differences in two batches of S and L particles (S1, L1 and S2, L2, respectively) which needed to be synthesized to provide sufficient sample material for both DLS and rheology experiments. To assess how close the microgel particles can be expected to mimic HS behavior we determined the volume fraction dependence of the plateau modulus G_P which according to Paulin and Ackerson [43] as well as to Senff and Richtering [44] allows to extract the hardness exponent n of an assumed inverse power pair interaction potential $u(r) \propto r^{-n}$. For the S1 and L1 particles we find $n = 66 \pm 5$ whereas the S2 and L2 particles yield significantly lower values of $n = 39 \pm 5$. These differences in particle softness are possibly due to a variation of the amount of crosslinker within the microgel particles and its spatial distribution which depends on subtle details of the synthesis protocol which are difficult to identify and to control. These values have to be compared with the value $n = 197$ obtained for the currently best HS model colloids, sterically stabilized PMMA, by Koumakis et al. [45] in an analogous analysis. However, it has been shown for inverse power potentials with $n > 18$ that structure and dynamics of particles are identical to the HS case irrespective of the n-value, if the systems are compared at the same relative distance to the freezing point [46], i.e. at the same value of $(\phi - \phi_f)/\phi_f$. This implies that slightly soft spheres like the PS microgels can be treated as effective hard spheres as long as an appropriate adjustment of volume fractions is performed.

With these particles two binary mixtures, M1 (S1, L1) and M2 (S2, L2) were prepared with number ratios $N_1 = N_{S1}/N_{L1} = 11$ and $N_2 = 2.5$, respectively, in the good, isorefractive solvent 2-ethylnaphthalene. These values have to be compared with those of the reference system with $\Gamma = 0.83 \pm 0.3$, $N = 2.5 \pm 0.3$, $n_S = 35$ and $n_L = 55$. While the second number ratio is identical to that of the reference system, the first one has been chosen to check up on the effect of the particle size distribution on the re-entry region. Due to the small amount of large particles this mixture is closely approximating a nearly monodisperse system while reducing the crystallization velocity reasonably well to allow for the measurement of glassy dynamics.

First we compared the glassy dynamics of binary mixture M1 as seen by DLS and rheology, thereby checking up on HS behavior of the PS microgels and comparing the power law divergence of the zero shear viscosity $\eta(\phi)$ with that of the structural relaxation time $\tau_\alpha(\phi)$. The results are summarized in Fig. 1. One clearly observes qualitatively identical behavior in DLS (Fig. 1a) and in steady shear experiments (Fig. 1b). Fluid samples, characterized by a dynamic structure factor that decays to zero ($f(q,\tau\to\infty) = 0$) are found up to $\phi = 0.57$ followed by a glass transition region up to $\phi = 0.586$ which is followed by glassy behavior indicated by a well-expressed infinite time plateau $f(q,\infty)$ in the correlation function ($f(q,\tau\to\infty) = f(q,\infty)$). This behavior is also expressed in the steady shear curves. Here, fluid behavior is indicated by the existence of a Newtonian plateau for $\eta(\dot{\gamma} \to 0)$ up to $\phi = 0.56$ and glassy states are identified by a power law form

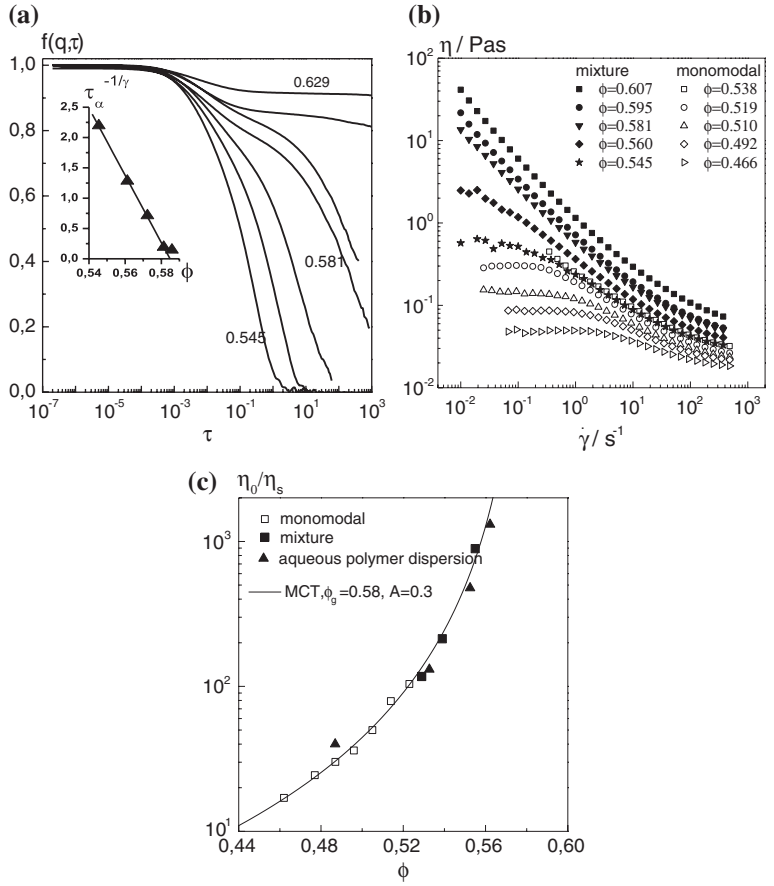

Fig. 1 **a** Time evolution of the density autocorrelation function $f(q,\tau)$ for the HS microgel mixture M1 ($R_S = 144$ nm and $R_L = 199$ nm, $\Gamma = 0.722$ and $N_1 = 11$) in the good, isorefractive solvent 2-ethyl-naphthalene (2-EN) at volume fractions $\phi = 0.545$, 0.561, 0.572, 0.581, 0.586, 0.594 and 0.629 (from *left* to *right*). Measurements were taken at a scattering vector $qR_S = 3.96$ close to the main peak of the static structure factor. The inset shows the rectification plot of the MCT power law (Eq. 2) for the structural relaxation times τ_α used to determine the glass transition volume fraction of the mixture M1 as $\phi_g = 0.585$. τ_α was determined by the condition $f(q,\tau_\alpha) = 0.5$. **b** Steady shear viscosity as a function of shear rate for the monomodal microgel ($R_S = 144$ nm, *open symbols*) and for the mixture M1 (*closed symbols*). **c** Relative zero shear viscosity η_0 against volume fraction for PS microgels (monomodal = *open squares*, bimodal (M1) = *solid squares*) and the aqueous dispersions (*solid triangles*). Prediction by the mode coupling theory (MCT) (Eq. 1) is shown as a solid line. η_s is the viscosity of the dispersion medium. Reproduced from Ref. [42] with permission

of the low shear viscosity for higher volume fractions. The sample at $\phi = 0.581$ again shows transition behavior. Figure 1b also demonstrates that the shear curves for a monomodal dispersion ($R_S = 144$ nm) at lower ϕ smoothly matches with the data for the binary mixture at higher ϕ. This is also visible in Fig. 1c where the

zero shear viscosity η_0 [taken as $\eta(0.01\ s^{-1})$] normalized to the medium viscosity η_s is depicted in dependence on the volume fraction. The divergence of the normalized zero shear viscosity follows the power law predicted by MCT [14],

$$\eta_0/\eta_s = A\left(1 - \phi/\phi_g\right)^{-\gamma} \tag{1}$$

with $\phi_g = 0.58$, $\gamma = 2.55$ and $A = 0.3$ corresponding to the known HS values [14, 15]. A similar divergence is found for the structural relaxation time τ_α, determined as $f(q,\tau_\alpha = 0.5)$, in accordance with the MCT prediction [14]

$$\tau_\alpha = \tau_0\left(1 - \phi/\phi_g\right)^{-\gamma} \tag{2}$$

where τ_0 is a microscopic relaxation time reflecting the short-time dynamics which is determined by hydrodynamic interactions.

This power law behavior is verified in a rectification plot in Fig. 1a (inset). The power law yields in this description a straight line which intersects the abscissa at ϕ_g. Using the HS value $\gamma = 2.55$ the linear fit returns $\phi_g = 0.585 \pm 0.008$, a value fully in agreement with both the HS value and the result from the zero shear viscosity power law. The corresponding analysis for the mixture M2 yields $\phi_g = 0.584 \pm 0.008$, again consistent with theory and with the results for M1. In addition we performed small amplitude oscillatory shear (SAOS) experiments on the binary mixture M1. The obtained storage and loss moduli, $G'(\omega)$ and $G''(\omega)$, could be well fitted with relations derived by MCT (cf. Fig. 2 in Ref. [42]) and the resulting longest relaxation time λ_{max} again follows a power law predicted by MCT with $\phi_g = 0.58$ (cf. Fig. 3 in Ref. [42]). As a corollary, our DLS results also indicate that the glass transition dynamics for the studied binary mixture does not depend on the number ratio N within experimental resolution. This is in qualitative agreement with MCT results for HS binary mixtures by Götze and Voigtmann [47]. Ignoring the error bars for the obtained ϕ_g values even the small shift of the glass transition to higher volume fractions as compared to the value of 0.58 for the monomodal system would be qualitatively consistent with the MCT for binary hard spheres [47], where such an effect has been predicted for $\Gamma = 0.7$ and $N = 11$ (corresponding to $\phi_S/\phi_L = 0.8$ in Fig. 1 of Ref. [47]).

From these results we conclude that (i) the studied PS microgel dispersions can be considered as very good approximations of the ideal HS system, (ii) that the glass transition dynamics for a size ratio of $\Gamma \approx 0.7$ does not depend significantly on the number ratio, i.e. on the details of the particle size distribution, that (iii) the relative zero shear viscosity η_0/η_S, the longest relaxation time λ_{max} from SAOS and the structural relaxation time τ_α from DLS diverge at the same HS glass transition value $\phi_g = 0.58$ with identical power laws, and that iv), thus, our findings are fully consistent with MCT predictions for HS glass transition dynamics.

After verifying that rheology and dynamic light scattering yield consistent results for the glass transition dynamics of pure binary microgel mixtures we studied whether this analogy still holds when weak short-ranged attractions are introduced by the addition of free polymer. Here, the question of most interest was in

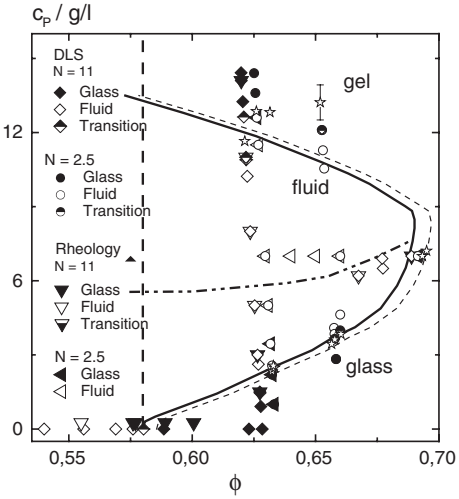

Fig. 2 Re-entry phase diagram for the mixed microgel systems with N = 11 (M1) and N = 2.5 (M2) as indicated. *Open symbols* denote the fluid state, *closed symbols* denote glass states, *half filled symbols* mark the transition region where the state could not be unambiguously defined. Stars are transition points estimated by an extrapolation from relaxation times τ_α similar to Fig. 1a, inset (cf. text). For clarity the volume fractions for M1 have been multiplied by 0.99 (thus making the glass transition of this sample coincident with $\phi_g = 0.58$, the value for the one-component HS system). The *solid line* and the *dash-dotted line* indicate the glass transition line and the line of minimal structural relaxation time determined previously for the reference microgel system for comparison. These lines were shifted along the ϕ-axis to account for the different $\phi_g = 0.595$ obtained in that study [27] and matched to the rescaled glass transition volume fraction of M1. The *thin dashed line* is the same glass transition line, only adjusted to match the glass transition of M2 ($\phi_g = 0.584$). The difference of these two lines also serves to visualize the effect of an inaccuracy in the volume fraction scale for M1. The vertical dashed line indicates the location of the glass transition of that binary microgel mixture. If not explicitly indicated, errors are smaller than the symbol size. Reproduced from Ref. [42] with permission

how far very strong re-entry effect that has been previously observed in an binary microgel mixture with short-ranged attractions [27]—the reference system—is expressed in an identical manner in the flow behavior. For this purpose non-adsorbing linear (free) PS with a molar mass $M_w = 133{,}000$ g mol^{-1}, $R_g = 13.1$ nm, $M_w/M_n = 1.07$, overlap concentration $c^* = 3M_w/(4\pi R_g^3) = 23.5$ g l^{-1} (in toluene) yielding an (average) attraction range $\delta = R_g/\langle R_{colloid}\rangle \approx 0.085$ was added to a number of binary mixtures and the dynamics was then studied with DLS and/or rheology. Figure 2 gives the location of the samples in the c_P-ϕ phase diagram with respect to the glass transition lines established for the reference system. We performed four cuts through the phase diagram three at constant volume fraction [$\phi \approx 0.62$ (M1), $\phi \approx 0.63$ (M2) and $\phi \approx 0.665$ (DLS only)] and one at constant polymer concentration ($c_P \approx 7$ g/l), the latter following the "path of highest mobility", i.e. where the structural relaxation times τ_α were found to be minimal in the reference system. Figure 3 compares the dependence of dynamics as seen by

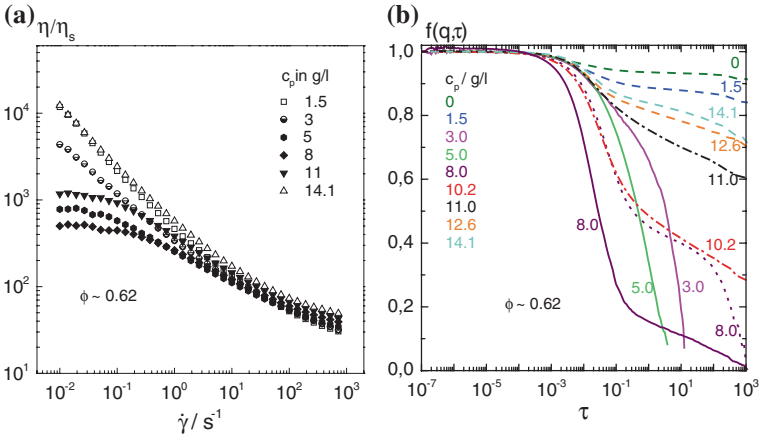

Fig. 3 Comparison of reduced viscosity η/η_s versus shear rate and density autocorrelation function $f(q,\tau)$ from DLS for a series of microgel dispersions (M1, N = 11) with similar particle volume fraction $\phi \approx 0.62$ but different polymer concentrations. **a** η/η_s versus shear rate: The *closed symbols* indicate the samples with fluid behavior and *open symbols* represent the glassy state. Reproduced from Ref. [42] with permission. **b** $f(q,\tau)$: *Solid lines* indicate fluid behavior, *dashed lines* glassy behavior. *Dash-dotted lines* identify samples which are in the glass transition regime and cannot be clearly assigned to fluid or glassy states. *Dotted line*: sample at 8 g/l after a waiting time of several weeks. The slow mode (second, long-time decay step) is attributed to formation of crystals

rheology and DLS at $\phi \approx 0.62$. Both methods see samples that are in a repulsive, i.e. packing driven, glass state at low polymer concentration c_P and in an attractive, i.e. bonding-driven, glass state at high c_P which are separated by fluid states at intermediate c_P. Some discrepancy appears to exist with samples at $c_P = 10.2$ and 11 g/l which should be still fluid as seen in the reduced viscosities, but where $f(q,\tau)$ does not decay to zero on experimental time scales. We attribute this to the formation of clusters which are precursors to formation of crystal nuclei and introduce a second, slow mode into the particle dynamics.

This can be clearly seen by the development from a small long-time tail to a well-expressed second decay for the sample $c_P = 8$ g/l in DLS. For this sample Bragg peaks could be observed in static light scattering after long waiting times. The similarity of the slope of the long-time decay of this sample and the samples at $c_P = 10.2$ and 11.0 g/l supports this interpretation. Obviously, binary mixture M1 with its number ratio N = 11 behaves rather like a narrowly distributed monomodal system where crystallization is somewhat slowed down, but not completely suppressed. These pre-crystalline clusters do, however, not affect the rheology data as the applied shear forces are sufficient to destroy these clusters during the usually applied preshear period.

Disregarding this complication, the comparison of steady shear and DLS experiments shows that on addition of a free polymer the re-entry effect can also be observed in the flow behavior. This is highlighted in Fig. 4 by comparing

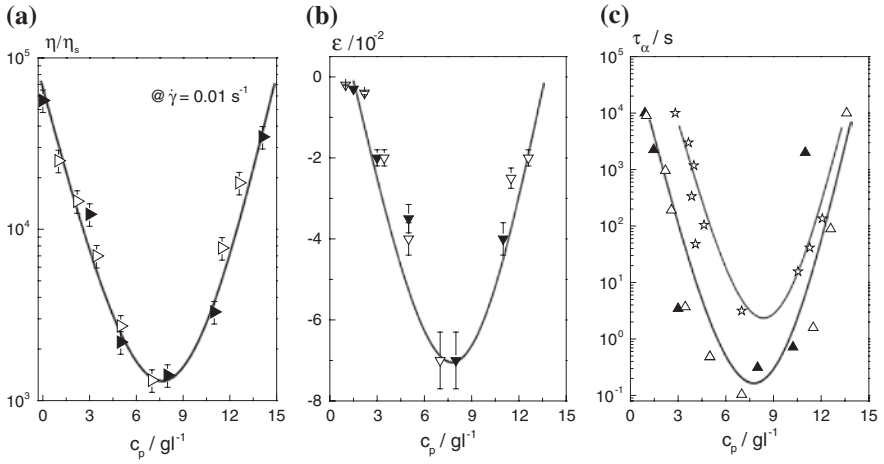

Fig. 4 **a** Low shear viscosity η determined at $\dot{\gamma} = 0.01\ s^{-1}$, **b** parameter ε from a fit of MCT equations to small amplitude oscillatory shear data and **c** structural relaxation time τ_α from DLS as a function of polymer concentration c_P for microgel suspensions M1 with N = 11 (*closed triangles*) and M2 with N = 2.5 (*open triangles*) at $\phi \approx 0.63$ as well as for M2 at $\phi \approx 0.66$ (*open stars*). *Lines* are for visual guidance. Reproduced from Ref. [42] with permission

the polymer concentration dependence of the zero shear viscosity (taken as the reduced viscosity at a shear rate of 0.01 s^{-1}) and of the separation parameter $\varepsilon = (\phi_g - \phi)/\phi_g$ determined from MCT fits of SAOS data (see Ref. [42] for details) with that of the structural relaxation time τ_α from DLS. A separation parameter $\varepsilon \geq 0$ implies a glassy state whereas fluid states are indicated by $\varepsilon < 0$. One clearly sees identical behavior with glassy states indicated by reduced viscosities around 10^5, a separation parameter close to zero and structural relaxation times $\geq 10^4$ s at both low and high polymer concentration. On increasing and on decreasing polymer concentration the systems enter fluid states with a maximum fluidity indicated identically around $c_P \approx 7.5$ g/l. The observation that the reduction of viscosity covers only 2 decades while the structural relaxation time decreases by about 5 orders of magnitude can be traced back to the differences in dynamical range of the two methods. While steady shear experiments are restricted to shear rates $\geq 10^{-2}\ s^{-1}$ the DLS data extend up to 10^4 s corresponding to $\dot{\gamma} \approx 10^{-4}\ s^{-1}$.

Figure 5 shows the comparison of the dynamics as obtained from steady shear rheology and DLS for a series of increasing particle volume fractions along the path of highest mobility of the reference system, i.e. at nearly constant polymer concentration $c_P \approx 7$ g/l, and probing identical samples. One sees that the samples show essentially the same behavior by both methods, indicating that at this polymer concentration fluid states up to $\phi = 0.692$ are accessible. Small deviations can be attributed to the significant crystallization tendency of binary mixture M1 (cf. sample at $\phi = 0.668$) which affects both methods differently.

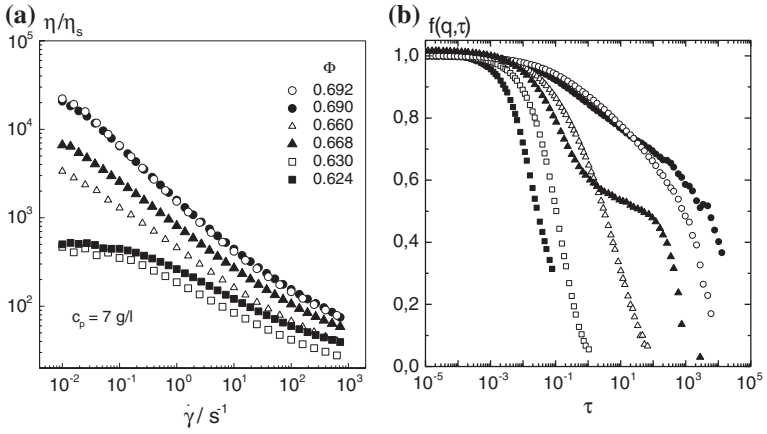

Fig. 5 Viscosity as a function of shear rate **a** and density autocorrelation function f(q,τ) **b** for different particle concentrations ϕ but constant polymer concentration $c_P \approx 7$ g l^{-1}, N = 11 (M1, *closed symbols*), N = 2.5 (M2, *open symbols*). **a** Reproduced from Ref. [42] with permission

Finally we verify the assignment of samples as glassy or fluid as indicated in Fig. 2 by determining glass transition points using the rectified MCT power law Eq. 2 for the DLS data in analogy to the inset of Fig. 1a. The location of the thus determined glass transition points are indicated by the stars in Fig. 2. This works quite nicely along the repulsive branch of the glass line where the location of the transition line of the reference system is quantitatively reproduced. The results are less consistent along the attractive branch due to the significant inaccuracies of the extrapolated glass transition points. This can partly be attributed to the fact that the extrapolation with the rectified power law requires samples which are already close to the glass transition. This was more difficult to achieve close to the attractive glass line where the polymer concentration is the control parameter instead of the volume fraction which controls the repulsive glass transition. Alternatively, the location of the attractive glass line may be more sensitive to subtle differences in the sample characteristics as size ratio and attraction range.

In summary these results show that the re-entry phenomenon is not only visible in the DLS method which monitors microscopic particle dynamics, but is as well expressed in the macroscopic flow behavior of dispersions with short-ranged attractions. This now leads to the question, whether and in how far this effect can be introduced in technical, i.e. aqueous, dispersions as well.

3 Aqueous Dispersion

The model system for aqueous dispersions was a polystyrene-butylacrylate (P-S/BA) latex which has been supplied by BASF SE. In order to provide short range electrosteric repulsion acrylic acid was used as a functional co-monomer at a

Fig. 6 Texture of aqueous dispersion ($\phi = 0.64$, R = 85 nm) without PEO (*left*) and with added PEO ($M_w = 4000$ g/mol) at concentrations of $c_p = 5$ g/l (*middle*) and $c_p = 10$ g/l (*right*). Reproduced from Ref. [42] with permission

concentration of 2 wt% relative to the total monomer concentration resulting in a thin hairy surface layer. More details of the system are found in [48].

The investigated particles had a radius of 85 and 133 nm, respectively. Linear polyethylene oxide (PEO) has been added as non-adsorbing polymer in order to introduce weak attractive interactions. To vary the strength of the attractions, different commercial grades of PEO with M_w between 4 and 400 kg/mol have been used. With the particular M_w values and the corresponding radius of gyration in water [49] the polymer-to-particle R_g/R size ratio was between $\delta = 0.03$–0.42. According to Aaskura and Oosawa [50] the depletion attraction among two particles in contact was estimated to be in the order of 1–10 kT [42].

Highly concentrated dispersions including polymer in the continuous phase were prepared via a two-step dialysis procedure. First, the dispersion was dialyzed against 10 mM NaCl in order to remove excess monomer and oligomer. After dissolving the desired amount of non-adsorbing polymer, the dispersion was filled in a dialysis membrane (Carl Roth, MWCO: 4–6 kg/mol) which was immersed in a dialysis bath filled with an aqueous solution of PEO ($M_w = 35$ kg/mol) at a concentration of 20 wt%. The high osmotic pressure of the PEO solution concentrates the dispersion to the desired particle volume fraction ϕ.

The dispersion with a particle radius of 85 nm behaves essentially like a hard sphere system [42]. The zero-shear viscosity diverges at a particle volume fraction of $\phi_g = 0.58 \pm 0.005$. Fluid states are observed in this case for PEO molecular weights between 4 and 35 kg/mol and a polymer concentration $c_P = 5$ g/l. For $M_w = 10$ and 20 kg/mol a viscosity reduction is also found for $c_P = 8$ g/l. No significant change in viscosity was observed upon addition of $M_w = 400$ kg/mol. The fluidization upon addition of PEO is directly visible as shown in Fig. 6. The fluidized sample at a volume fraction $\phi = 0.64$ with $c_P = 5$ g/l and $M_w = 4000$ g/mol, resulting in a $\delta = 0.03$, spreads easily on the surface whereas the glassy or gel-like suspensions ($c_P = 0$ and 10 g/l) retain their original shape.

The dependence of the flow curves on the concentration of added PEO ($M_w = 10$ kg/mol) is shown in Fig. 7a for $\phi = 0.644$. The introduction of weak attractive interactions leads to a sharp drop of the low shear viscosity by almost 2 orders of magnitude whereas the high shear viscosity remains essentially unchanged. The variation of the reduced viscosity at a fixed shear rate

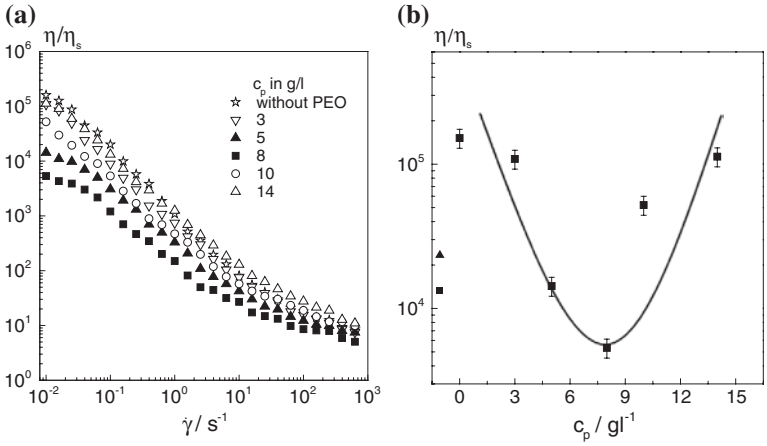

Fig. 7 **a** Reduced viscosity η/η_s versus shear rate for a series of aqueous glassy dispersions with similar volume fraction $\phi \approx 0.644$ ($R = 85$ nm) but different PEO ($M_w = 10$ kg/mol) concentrations as indicated in the legend. The *closed symbols* indicate the samples with fluid behavior whereas the *open symbols* represent the glassy state. **b** Reduced low shear viscosity η/η_s determined at $\dot{\gamma} = 0.01\ s^{-1}$ as a function of added PEO concentration c_p. η_s is the viscosity of the pure solvent. The line is a guide to the eye. Reproduced from Ref. [42] with permission

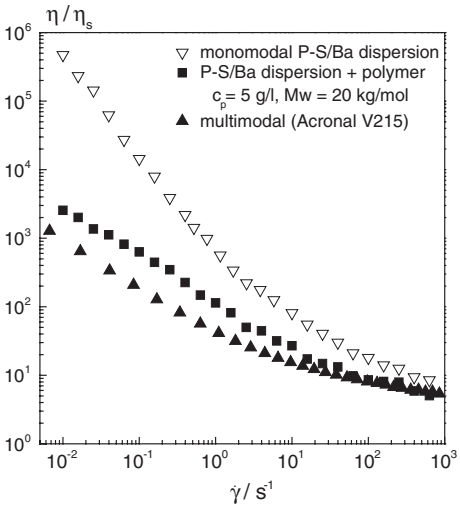

Fig. 8 Comparison of flow curves for a dispersion fluidized due to weak attractive depletion interactions and a dispersion with broad multimodal size distribution. Reproduced from Ref. [42] with permission

$\dot{\gamma} = 0.01\ s^{-1}$ is displayed in Fig. 7b. A pronounced minimum of the reduced viscosity is reached at a polymer concentration of 8 g/l.

A classical strategy to provide a viscosity reduction at these high volume fractions is to provide a broad particle size distribution. In Fig. 8 the viscosity reduction due to the introduction of weak attractive interactions is compared to a commercial polymer dispersion Acronal V215 (BASF SE) at the same particle

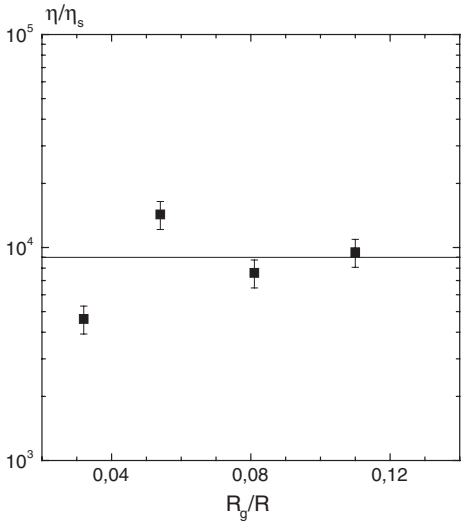

Fig. 9 Reduced low shear viscosity η/η_s determined at $\dot{\gamma} = 0.01\ s^{-1}$ and a volume fraction of $\phi = 0.644$ as a function of polymer-to-particle size ratio ($M_w = 4000$ g/mol, 10, 20 and 35 kg/mol) at $c_P = 5$ g/l. Reproduced from Ref. [42] with permission

volume fraction ϕ. The particle size distribution of the latter dispersion is very similar to that described in [51] and particle radii cover the range from 70 to 350 nm.

A comparison of the low shear viscosity taken at a constant shear rate $\dot{\gamma} = 0.01\ s^{-1}$ and particle loading $\phi = 0.644$ for different M_w between 4 and 35 kg/mol of the added PEO, expressed here in terms of R_g/R at constant polymer concentration $c_P = 5$ g/l, is shown in Fig. 9. The viscosity varies within a factor of three, but obviously no clear trend can be detected. This may be due to the fact that increasing M_w corresponds to an increase of the range of attraction but at the same time to a decrease of the interaction strength. The observed viscosity variation is also small compared to the drastic drop of viscosity relative to the pure dispersion.

Obviously, the viscosity reduction achieved through the addition of PEO ($M_w = 20$ kg/mol, $c_P = 5$ g/l) as non-adsorbing polymer is close to that resulting from a broad particle size distribution demonstrating that the new fluidization concept introduced here is technologically competitive to the state of the art.

The second aqueous polymer dispersion ($R = 133$ nm) had a narrow, monodisperse particle size distribution resulting in crystallization of the sample at appropriate particle loadings. Thus, it could be demonstrated here for the first time that beyond the predictions of MCT, fluidization can also be obtained in densely packed, crystalline dispersions due to the introduction of weak attractive interactions.

Reduced low shear viscosity could be obtained for PEO molecular weights of 20 and 35 kg/mol corresponding to a polymer-to-particle size ratio δ of 0.048 and 0.067 and polymer concentrations between 1 and 8 g/l, respectively. For $M_w = 10$ kg/mol ($\delta = 0.03$) particles formed clusters which could not be redispersed by adding water. Similar as for glass forming systems the introduction

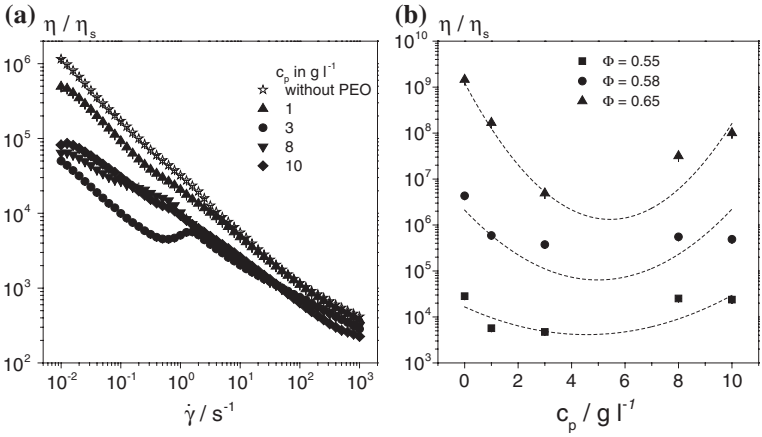

Fig. 10 **a** Reduced viscosity η/η_s versus shear rate for a series of aqueous crystalline dispersions ($R = 133$ nm) with volume fraction $\phi \approx 0.55$ but different PEO concentrations ($M_w = 20$ kg/mol) as indicated in the legend. **b** Reduced low shear viscosity η/η_s determined at $\dot{\gamma} = 0.1\ s^{-1}$ for different volume fractions as indicated in the legend as a function of added PEO ($M_w = 35$ kg/mol). The lines are guides to the eye. Reproduced from Ref. [52] with permission

of weak attractive interaction leads to a sharp drop of the low shear viscosity by almost two orders of magnitude, whereas the high shear viscosity ($\dot{\gamma} > 100\ s^{-1}$) is independent of the added polymer, see Fig. 10a. The hump observed in the viscosity curves at shear rates between 1 and 10 s^{-1} and polymer concentrations of 3 and 8 g/l indicates a characteristic structural change which may be related to a change of crystal size and orientation. Further details can be found in [52].

The c_P dependence of the low shear viscosity at a fixed shear rate of $\dot{\gamma} = 0.1\ s^{-1}$ and volume fractions $\phi = 0.55$, 0.58 and 0.65 is shown in Fig. 10b. At a polymer concentration between 1 and 8 g/l a pronounced minimum of the reduced viscosity η/η_s can be seen.

The dramatic drop of the reduced viscosity here can be rationalized in terms of the corresponding change of the phase diagram [53]. The addition of non-adsorbing polymer leads to a substantial broadening of the fluid-crystalline coexistence regime and at a given particle loading densely packed crystals coexist with dilute fluid like regions. The density of the crystallites increases and the particle loading in the fluid region decreases with increasing polymer concentration. This results in a reduction of the viscosity, but when a critical polymer concentration is exceeded the strong attractive interaction leads to the formation of a gel-like attractive glass. Accordingly, the viscosity increases again at a certain polymer concentration. For the system investigated here, the viscosity minimum occurs at a polymer concentration $c_P \approx 3$ g/l relative to the aqueous phase volume fraction, well below the overlap concentration c*.

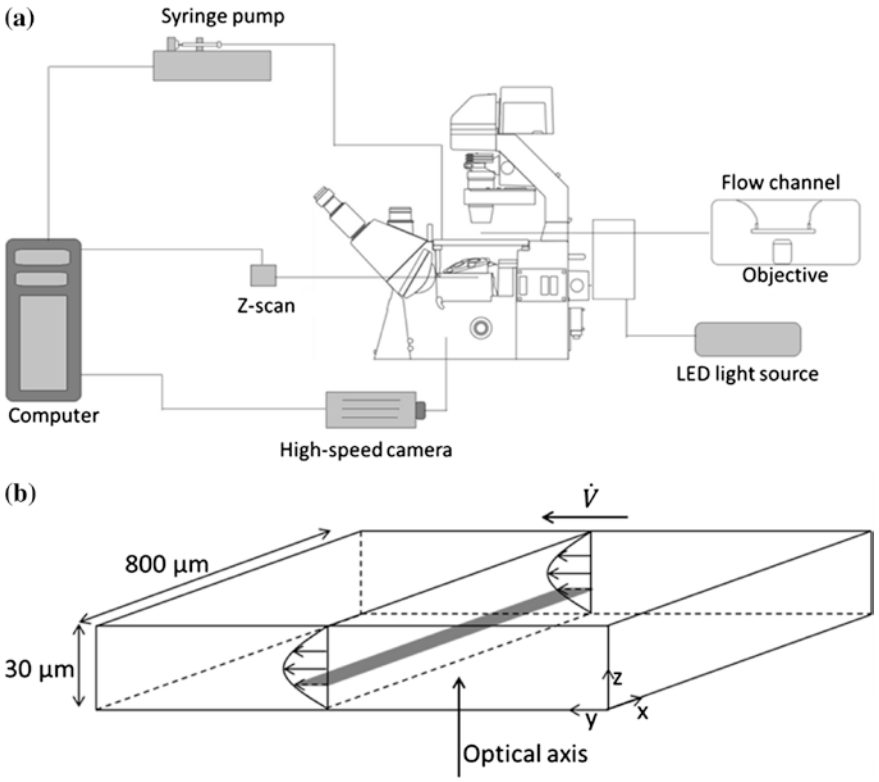

Fig. 11 **a** Schematic description of the flow cell including the syringe pump and the components of the optical fluorescent microscope setup. The flow channel with the necessary inlet and outlet connection as well as the objective underneath is shown separately on the *left*. **b** Close up of the microchannel and the orientation of the optical axis. Via the ocular of the microscope the x-y plane, marked as the *grey area*, can be observed. Reproduced from Ref. [52] with permission

4 Micro Flow Channel

In order to investigate the true flow profiles of the fluidized suspensions, samples were forced to flow through a micro flow channel attached to an inverted fluorescence microscope. In order to visualize the flow velocity size matched fluorescent tracer particles were added to the suspensions ($\phi = 0.1$). The setup of this channel is shown in Fig. 11.

The cross section of the microchannel was selected depending on the turbidity of the sample, 30 × 800 or 200 × 200 µm, respectively, and its length is 58 mm. A connected syringe pump with a 250 µL syringe provides flow rates between 2.5×10^{-4} and 1×10^{-3} µL/s corresponding to shear rates between 5 and 20 s^{-1}. A high-speed sCMOS camera with a frame rate of 100 fps is used to track particle velocities in the focal plane. A piezo actuator (z-Scan) is used to shift the focal

plane with a step width of 2 μm perpendicular to the flow direction (z-direction in Fig. 11b). The flow profile is then determined based on the spatially resolved particle velocity in different planes. Therefore, the center of mass of each particle in each frame is identified. From the displacement of each particle between a certain number of pictures and the corresponding time lag the velocity of each particle can be determined. The corresponding average value of all particle velocities is assigned as the velocity of this layer. The flow profile is then determined from the average particle velocity in each layer.

Additionally, the flow can be observed through the ocular of the microscope. Looking through the ocular allows an observation of the tracer particles moving in the focal plane, which is marked as the grey area in Fig. 11b.

For validation of the particle tracking protocol glycerin was used as a Newtonian test fluid. As expected, a parabolic flow profile could be retrieved and good agreement between theoretical and experimentally determined flow profiles was found in these preliminary experiments.

For determining the flow profiles of colloidal suspensions, the crystallizing dispersion was used. The particle volume fraction was set to $\phi = 0.52$. At higher particle loadings the viscosity was too high to push the sample through the channel with the given setup. PEO with molecular weight $M_w = 35$ kg/mol was selected to achieve a strong viscosity reduction and in addition to the polymer free suspension two samples with 3 and 6 g/l added PEO were investigated.

Without added polymer a typical plug flow formed with large crystalline regions in the center of the channel showing up in red and green and a thin disordered or molten layer next to the wall. At a nominal wall shear rate $\dot{\gamma} = 20\ s^{-1}$ a slip velocity of about 15 μm/s at the wall and a constant flow velocity $w \approx 60$ μm/s in the channel center was revealed. The corresponding flow profile is shown in Fig. 12. The thickness of the disordered layer decreased with decreasing

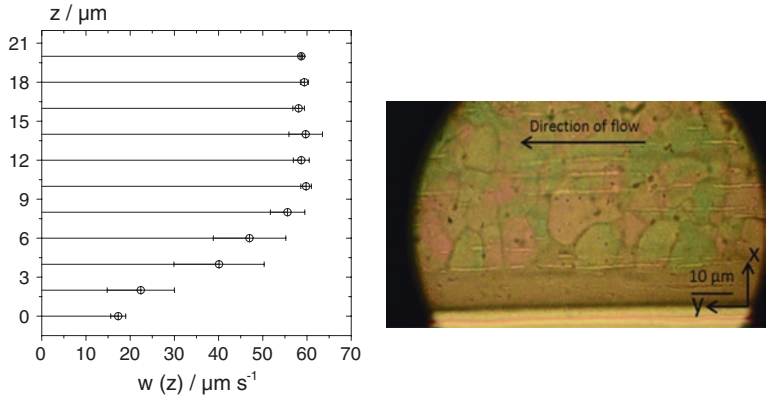

Fig. 12 *Left* Velocity profile in z-direction of a dispersion without added PEO, $\phi = 0.52$ and shear rate $\dot{\gamma} \approx 20\ s^{-1}$. *Right* View through the ocular (x-y plane). Reproduced from Ref. [52] with permission

shear rate and at a nominal wall shear rate $\dot{\gamma} \leq 5\ s^{-1}$ the shear melting zone vanished and accordingly the channel clogged.

No steady flow could be established with the given setup for the dispersions containing non-adsorbing polymer even though the bulk viscosity was significantly lower than for the polymer-free dispersion. In this cases wall crystallization dominated [54, 55] resulting in channel clogging.

Observing extensive wall crystallization in microchannel flow but a strong reduction of low shear viscosity in bulk rheometry clearly demonstrates that the introduction of weak attractive interaction among particles due to added polymer not just deswells the hairy surface layer of the particles thus reducing ϕ_{eff}. The observed fluidization is in fact a consequence of the modified interaction among particles.

5 Influence of Attraction Range and Particle Softness on the Re-Entry Phenomenon

Having established that the re-entry phenomenon, i.e. the fluidization of glassy (or even crystalline samples), which was first observed for colloids dispersed in organic solvent, can be also be employed for technical, aqueous dispersions, it is of considerable interest to see how this effect is influenced by system properties like range of attractive forces and particle softness. The latter is a property of the colloidal particle and can, in case of PS microgels, easily be varied via the cross-link density. The former is connected which the size of the polymer relative to the colloid size, i.e. $\delta = R_g/R$.

With respect to attraction range there exists the intriguing prediction by MCT that the re-entry region increases significantly when the attraction range is reduced [22]. Even though there exist quantitative MCT results for attraction ranges $\delta < 0.1$, only systems with $\delta \approx 0.08$ have been studied extensively in the glass transition range [23–27, 56]. Therefore we studied with DLS the re-entry phenomenon for a similar binary mixture as the reference system, but using a smaller polymer [57]. The size ratio was $\Gamma = R_S/R_L = 149.1 \pm 3\ nm/175.1 \pm 2\ nm = 0.855 \pm 0.027$ which compares well with $\Gamma = 0.83$ for the reference system [26]. While the hardness exponents have not been determined the swelling ratios $Q = (R_{2EN}/R_{H2O})^3$ obtained by mapping the determined freezing volume fraction onto the HS value $\phi_f = 0.494$ were within error identical to those of the reference system: $Q_{HS,S} = 5.9$ ($Q_{HS,S} = 6.2$ [56]) and $Q_{HS,L} = 4.5$ ($Q_{HS,S} = 5.2$ [56]). From this it can be assumed that the hardness exponents are also fairly close to those of the corresponding particles of the reference system. The polydispersity of the individual components was found to be $\langle\sigma_S\rangle = 4.3 \pm 0.5\ \%$ and $\langle\sigma_L\rangle = 5.7 \pm 0.5\ \%$, respectively, slightly smaller than the value for the reference system—($\sigma_R \approx 7\ \%$ [56]). To compensate for this and achieve a comparable overall polydispersity for the binary mixtures the number ratio was slightly increased to $N = 3.06$ as compared to

$N = 2.5$ for the reference system.[2] For this binary mixture the glass transition value has been determined to be $\phi_g = 0.577 \pm 0.002$ [57]

To introduce short-ranged attractive interactions, non-adsorbing linear polystyrene with $M_w = 79{,}600$ g/mol, $R_g = 9.18$ nm, $M_w/M_n = 1.08$, $c^* = 40.8$ g/l was added to this binary mixture, yielding an attraction range $\delta = 0.059$ with respect to the average particle size $\langle R \rangle = 156 \pm 4$ nm.

Four cuts through the ϕ, c_P-phase diagram were performed: three at constant volume fractions $\phi \approx 0.62$, 0.66 and 0.7 and one following the "path of maximum mobility", i.e. the extrapolated path of the minima of the τ_α values found for the $\phi \approx$ constant cuts, at $c_P \approx 15.9$ g/l. The results are summarized in Fig. 13. In contrast to the results obtained for binary mixtures with the larger attraction range $\delta = 0.08$ we found at higher polymer concentrations intermediate scattering functions (ISFS) $f(q,\tau)$ with a slow mode similar to the sample at $c_P = 8$ g/l in Fig. 3b. However, these slow modes appeared as low-lying $f(q,\tau)$ plateaus as exemplarily shown for a cut at $\phi \approx 0.62$ by the dotted line in Fig. 13a. This behavior was reminiscent of the observation of solidification in an eutectic mixture of attractive PS microgels closely approximating the reference system into pure S and L crystals closely below the ϕ_g of the purely repulsive corresponding binary mixture [58]. There, above the repulsive ϕ_g similar ISFs were observed without any clear appearance of Bragg peaks in static light scattering [59]. Thus, we interpret such ISFs as indicating the presence of colloidal clusters which may represent precursors to the formation of crystal nuclei and address the corresponding samples to be in cluster states. The typical evolution of line shapes of the ISFs along a cut at constant ϕ is shown in Fig. 13a. The characteristic line shapes were then used to identity the states of the samples as repulsive glass, fluid, cluster states or attractive glass as indicated in the figure. The resulting phase diagram and the prospective location of the glass transition lines for $\delta \approx 0.06$ are compared in Fig. 13b with the corresponding results for the reference system with $\delta \approx 0.08$. To allow for this comparison the phase diagrams are given in rescaled units, $\varepsilon = (\phi - \phi_g)/\phi_g$ and c_P^{free}/c^*, where c_P^{free} is the concentration of the polymer in the free volume not occupied by the particles which has been calculated within scaled particle theory and which is the relevant quantity for determining the strength of depletion attraction [53]. The rescaling thus eliminates differences of the glass transition volume fraction, of the free volume (which depends at constant ϕ on the number ratio N) and of the overlap concentration between the compared dispersions. The differences in the phase diagrams are obvious: while the repulsive glass line for the attractive dispersion with $\delta \approx 0.06$ is virtually identical to that for the reference system with $\delta \approx 0.08$ at volume fractions up 15 % above ϕ_g ($\varepsilon = 0.15$), it extends much further up to higher ϕ (up to $\varepsilon = 0.25$) before bending over and

[2]It should be noted that the polymer to size ratio δ and the size ratio N of the reference system have in Refs. [25–27] been reported as $\delta = 0.054$ and $N = 2.75$ on the basis of a size determination of S and L particles via DLS. A lateron refinement on the basis of a HS mapping of the fluid-crystal coexistence region yielded values of $\delta = 0.078$ and $N = 2.5$ instead [56].

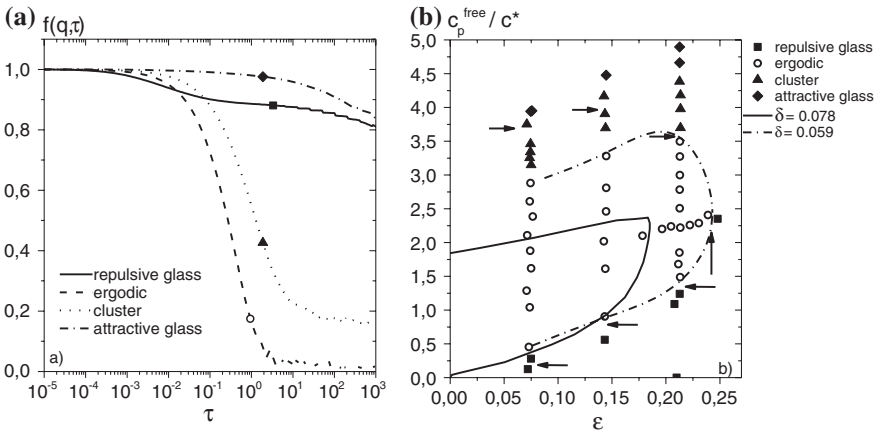

Fig. 13 **a** Typical development of intermediate scattering functions (ISFs) f(q,τ) along a cut through the ϕ, c_P-phase diagram at ε ≈ 0.075 (equal to ϕ ≈ 0.62) of an attractive colloidal binary mixture of PS microgel particles with Γ = $R_{HS,S}/R_{HS,L}$ = 0.85, an attraction range of δ = $R_g/\langle R\rangle$=0.059 and an overlap concentration of c* = 40.8 g/l. The line shapes indicate that the samples can be classified into four categories: *solid line* repulsive glass, ε = 0.072, $c_P^{free}/c^* = 0.12$; *dashed line* ergodic (fluid) sample, ε = 0.071, $c_P^{free}/c^* = 2.11$; *dotted line* cluster, ε = 0.071, $c_P^{free}/c^* = 3.75$; *dash-dotted line* attractive glass, ε = 0.075, $c_P^{free}/c^* = 3.94$. **b** Phase diagram of an attractive binary colloidal mixture of 1:50 crosslinked PS–microgel particles with an attraction range of δ = 0.059 (symbols). The samples are categorized according to the shape of their ISFs as indicated in **a**. To compare with previous results [27], data are given in rescaled units: c_P^{free}/c^* and ε = (ϕ − ϕ_g)/ϕ_g with c* = 40.8 g/l and ϕ_g = 0.577, respectively. c_P^{free} was calculated within the framework of scaled particle theory following [53]. The *dash-dotted line* symbolizes the location of the (repulsive and attractive) glass transition lines, here taken as identifying the transition from fluid (ergodic) to glassy, respectively, cluster states. The arrows indicate glass transitions as predicted by a MCT power law extrapolation with Eq. (2) using mean α—relaxation times obtained from KWW fits of the first relaxation step of the measured ISFs (cf. Ref. [57]). The *solid line* indicates the location of the glass transition lines of the reference system ϕ_g = 0.595, N = 2.5, Γ = 0.83) with an attraction length δ = 0.08 [27, 56, see footnote text 2]. Reproduced from Ref. [57] with permission

turning into the attractive glass line. The attractive glass line is clearly shifted to higher rescaled polymer concentrations at the shorter attraction range, even though the exact location is difficult to determine due to the appearance of cluster states at high polymer concentrations (solid triangles in Fig. 13b). Here we have chosen to define the attractive glass line by the transition from ergodic (fluid) to cluster states. An alternative definition is indicated by the arrows in the figure. Here the extrapolation of the rectified power law (Eq. 2) for the structural relaxation times τ_α of the ISFs has been used as in Figs. 1 and 2. One sees that the corresponding glass transition points agree nicely with the estimated location (dash-dotted line in Fig. 13b) along the repulsive branch of the glass line. The situation is less clear along the attractive branch where only for the highest ϕ cut the extrapolated attractive glass transition point coincides with the transition from cluster state to attractive glass state. At lower ϕ the extrapolation yields transitions within the region of

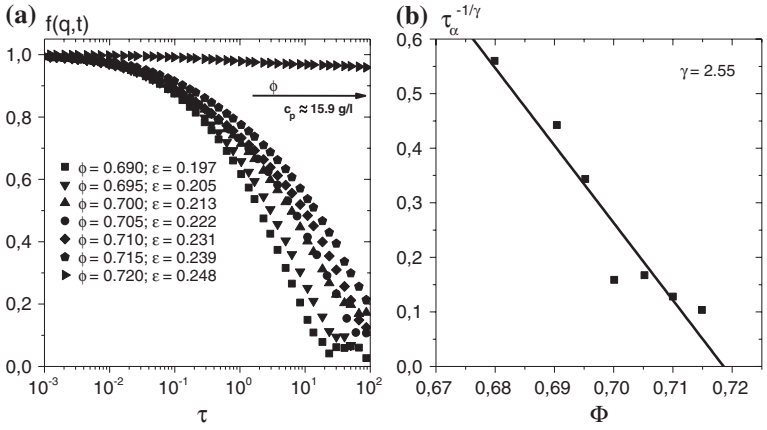

Fig. 14 **a** ISFs of samples with nearly constant polymer concentrations ($c_P \approx 15.9$ g/l) but increasing volume fractions. The systems' dynamics slow down monotonically without any indication of a two-step decay. The latter would be expected for a repulsive glass transition driven by the cage effect. The system shows a sharp nonergodicity transition from a fluid sample at $\varepsilon = 0.239$ and $c_P^{free}/c^* = 2.41$ to a frozen sample at $\varepsilon = 0.248$ and $c_P^{free}/c^* = 2.35$. Reproduced with permission from [57]. **b** Determination of the glass transition volume fraction at $c_P \approx 15.9$ g/l via the rectified power law for the structural relaxations times τ_α (Eq. 2) yields $\phi_g = 0.719$

cluster states. This discrepancy can be again traced back to the intrinsic difficulties of determining the attractive glass line discussed in the context of Fig. 2, but now aggravated by the emergence of the clusters states whose physics is not covered by mode coupling theory (MCT) [14]. Disregarding these difficulties the main result of Fig. 13b is that as predicted by MCT a decrease of the attractive range (by use of a smaller free polymer) allows to amplify the re-entry phenomenon, thus allowing to shift the occurrence of fluid states to even higher colloid volume fractions.

This finding is further supported by the evolution of the ISFs along the path of highest mobility which is depicted in Fig. 14a. As can be seen from the figure all samples except the one at the highest volume fraction show a monotonous decay of $f(q,\tau)$ to zero, indicating clearly fluid samples. The sample at $\phi = 0.72$ is, however, a non-ergodic glassy sample. It shows almost no decay within the experimental time window. Thus, one observes a very sharp glass transition from a fluid sample at $\phi = 0.715$ to a glassy sample at $\phi = 0.72$. This result is fully consistent with the determination of the glass transition volume fraction by extrapolation with the rectified MCT power law Eq. 2 which returns a value $\phi_g = 0.719$ as shown in Fig. 14b.

Our findings are in qualitative agreement with MCT predictions [22]: the repulsive glass transition lines for $\delta = 0.08$ and $\delta = 0.059$ coincide; the attractive line of the smaller δ is shifted to higher attraction strength and is almost parallel to the one at larger δ. However, there is a remarkable quantitative disagreement between theoretical and experimental values. The observed maximum shift of

the glass transition to higher volume fractions by ~25 % (from $\phi_{g,HS}^{exp} = 0.577$ to $\phi_{g,max}^{exp} = 0.719$) for $\delta = 0.059$ is dramatically larger than predicted by MCT (~2 % from $\phi_{g,HS}^{MCT} = 0.515$ to $\phi_{g,max}^{MCT} = 0.524$ for $\delta = 0.06$ [22]). In addition, even though the re-entry region of the previously studied attractive binary mixture of 1:50 crosslinked PS microgel particles already extends to a colloid volume fraction higher than random close packing ($\phi_{rcp} = 0.64$), i.e. to 0.70 [27] (a shift by 18 % from $\phi_{g,HS}^{exp} = 0.595$), this could be shifted to an even higher maximum volume fraction on decreasing the attraction range. It is well known [60, 61] that MCT calculations overestimate the freezing tendency of the HS system due to approximations introduced when using the equilibrium static structure factor S(q) of monodisperse HS below their freezing density. As a consequence MCT predicts the glass transition to occur at $\phi_g = 0.515$, whereas in experimental nearly monodisperse and HS colloidal systems $\phi_g \approx 0.58$ is observed.

Thus, in order to understand the physical origin of this enormous shift of ϕ_g on introducing short-ranged attraction in PS microgel dispersion it is more useful to compare these results with the re-entry behaviour observed for the HS like PMMA dispersion in [24] where linear PS has been used as free polymer as well. There fluid states were observed for $\delta = 0.09$ up to $\phi = 0.62$, corresponding to a shift of ~10 % with respect to the glass transition without any free polymer. Again, the re-entry effect is more pronounced in the real HS dispersion than predicted by theory. However, the effect was less pronounced than for the 1:50 crosslinked binary microgel mixture with a comparable attraction range ($\delta = 0.08$). Three major differences exist between the PMMA system and the studied microgel systems. Whereas the PMMA system is composed of one particle size with a polydispersity of about 7 %, the microgel systems consist of binary mixtures with polydispersities of 8–12 %. While the dispersion medium of the PMMA system (cis-decaline) is a marginal (i.e. near theta) solvent for the free polymer (PS), the same polymer in case of the microgel systems is dissolved in a good solvent (2EN). Thus, polymer non-ideality (excluded volume interactions) has to be taken into account in the latter case. Finally, whereas the PMMA particles are solid hard spheres, the microgel particles are highly swollen with solvent, imparting some softness to the latter which is reflected in the lower "hardness exponent" n = 35–70 as compared to the value n = 197 of PMMA particles [45].

The re-entry effect of PS microgels was found to be insensitive to the number ratio for $\delta = 0.08$ (cf. Fig. 2). Thus, polydispersity seems here not to play a prominent role. To study the effect of polymer non-ideality would require use of a solvent where the change of solvent quality from ideal to marginal (=theta solvent) could be easily induced by change of temperature. This appears to be impossible with the PS microgel system for two reasons: first, near isorefractivity is a boundary condition which limits the choice of solvents severely. It is required in order to achieve transparency of the dispersions even at high particle concentrations, which is a prerequisite for light scattering experiments and a precise determination of absolute volume fractions via study of the fluid-crystal coexistence. Second, even if a solvent were to be found which is close to marginal and at the same time isorefractive—a change of solvent quality would affect both the free polymer and the

particles as they are both composed of PS. The swelling degree of the PS microgels and, in turn, the "hardness", would change as well, making it impossible to disentangle the effect of changing of polymer ideality from the effect of changing particle interactions ("hardness exponent" n). However, it is possible to study the effect of particle softness alone by changing the crosslink density. For this purpose we used 1:10 crosslinked PS microgels which have a hardness exponent $n \approx 100$ [62] and thus take an intermediate position between 1:50 crosslinked PS microgels and PMMA particles.

The studied system consisted of a binary mixture of PS microgels which was nearly identical in the system parameters to the reference system with a size ratio $\Gamma = R_S/R_L = 0.82$ ($R_S = 150 \pm 2$ nm, $R_L = 184 \pm 2$ nm) and a number ratio $N = N_S/N_L = 2.7$ ($\sigma_{R,S} = \sigma_{R,L} = 0.06$), except for the crosslink density which was 1:10, thus yielding significantly smaller swelling ratios, $Q_{HS,S} = 2.2$ and $Q_{HS,L} = 2.4$, respectively [62]. The glass transition of this binary mixture was determined with the same procedure as for the other systems to be $\phi_g = 0.564 \pm 0.005$ [63], a value somewhat lower than for the so far studied 1:50 crosslinked microgel dispersions. To this binary mixture the same free polymer was added as for the reference system, yielding the identical attraction range $\delta \approx 0.08$. The ISFs were classified as fluid or glassy in a slightly different manner [63]. Interestingly, no cluster states could be identified for this system.

Figure 15 compares the location of the glass transition line and the width of the re-entry region for the attractive binary mixture of 1:10 crosslinked PS microgel colloids with those of the reference system, i.e. the 1:50 crosslinked system [27], and of the monomodal PMMA HS-like particles [24]. As can be seen from Fig. 14a, the large re-entry region of the 1:50 cross-linked particles could not be reproduced with the more strongly cross-linked particles. Whereas the glass transition and, thus, the fluid region is shifted up to about 18 % (corresponding to a maximum volume fraction of about 0.69 at a polymer concentration of $c_P \approx 8$ g/l) for the 1:50 microgels, the re-entry effect is much weaker for the 1:10 microgel colloids, amounting to a maximum shift of 8 % (corresponding to a volume fraction of 0.61 at a polymer concentration of $c_P \approx 1.8$ g/l. In addition the polymer concentration needed to induce the attractive glass transition is significantly reduced for the 1:10 microgels as compared to the 1:50 ones. Close to the glass transition the polymer concentrations at the attractive glass transition differ by a factor of 5, corresponding to a change from $c_P = 15$ g/l (1:50) to 3 g/l (1:10) with respect to total sample volume. It is noticeable that the attractive glass line is now located at a c_P^{free} much lower than the overlap concentration $c^* = 23.5$ g/l, in qualitative agreement with observations for the PMMA system. In contrast, the arrest of dynamics due to depletion attraction in the 1:50 crosslinked microgel mixture required polymer concentrations c_P^{free} twice as large as c^*.

Figure 15b shows that while the phase diagrams of the 1:10 crosslinked PS microgel mixture and of the monomodal PMMA dispersion appear to be qualitatively similar, there are differences in detail. For the PMMA particles dispersed in cis-decalin fluid states were observed up to volume fractions $\phi \approx 0.62$, i.e. up to slightly higher values than found for the 1:10 microgels. Whether this difference

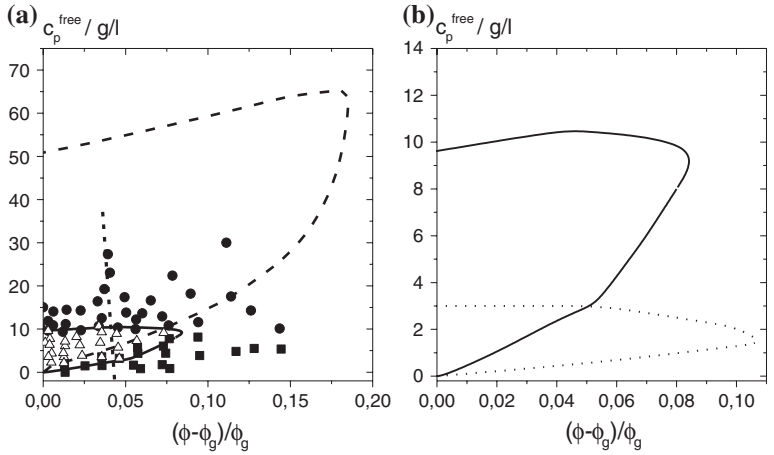

Fig. 15 Comparison of the phase diagram of the binary mixture of 1:10 cross-linked PS particles with the phase diagrams of **a** the binary mixture of 1:50 crosslinked PS particles [27] with nearly identical size and number ratios (see text), and with a monomodal dispersion of HS like PMMA spheres [24] **b**. In all cases linear PS has been used as free polymer to induce attractions yielding comparable attraction ranges of $\delta \approx 0.08$ (**a**) and $\delta \approx 0.09$ (**b**). Polymer concentrations in the free volume, c_P^{free}, were calculated within the framework of scaled particle theory (see Ilett et al. [53] for details). Overlap concentrations were $c^* = 23.5$ g/l for the microgel systems and $c^* = 26$ g/l for the PMMA system, respectively. The glass transition values were $\phi_g = 0.595$ [27], 0.564 [63] and 0.56 [24] for 1:50 crosslinked, 1:10 crosslinked and PMMA particles, respectively. **a** *Squares* denote samples in the repulsive glass, circles those in the attractive glass, *open triangles* indicate fluid states. Overlapping symbols of *solid* and *open symbols* indicate a sample in the transition region. The *straight dotted line* denotes the samples shown in Fig. 3 of [63]. The *solid line* indicates the glass transition lines of the 1:10 cross-linked particles, the *dashed line* indicates the same for 1:50 cross-linked particles. **b** *Solid line* glass transition line of 1:10 crosslinked particles; *dotted line* same for PMMA particles (adapted from [24]). Reproduced from [63] by permission

is significant is unclear given the uncertainties in the location of the respective glass transition lines and the differences in the methods of determination (in case of the PMMA particles the re-occurrence of crystallization was used to identify fluid samples). More pronounced is the difference in the location of the attractive branch of the glass transition line which is found in the 1:10 microgel systems at a three times higher polymer concentration than for the PMMA system.

The observation that the re-entry region for 1:10 crosslinked PS microgels is significantly smaller than that of the reference system indicates that particle softness and/or deformability may be indeed at the origin of the extended re-entry region of the (softer) 1:50 crosslinked microgel particles. However, the fact that these microgel particles consist of spheres that are swollen in a good solvent also raises the question whether the observed large re-entry region shown in Fig. 13b may be a consequence of osmotic deswelling. Osmotic deswelling would lead to volume fractions significantly lower than the nominal ones. Such deswelling has been observed for particles with a much smaller degree of crosslinking (1:200

[64]). To estimate the volume reduction induced by osmotic deswelling for the 1:50 crosslinked PS microgel particles, we used data on the osmotic deswelling of PS macrogels in solutions of linear PS chains [65]. Assuming osmotic deswelling of microgels being essentially identical to that of macrogels one can estimate that even at nominal volume fractions as high as 0.7 the reduction of ϕ by osmotic deswelling is on the order of a few percent. By an iterative procedure (deswelling decreases c_P^{free} due to more free volume for the polymer which then leads to less deswelling, etc.) using the data in Ref. [65] we obtain a deswelling of about 6 % at the highest fluid ϕ for $\delta \approx 0.06$. This leads to a reduction of the maximum fluid volume fraction to 0.673 instead of 0.715, a value that is still above the maximum value for random close packing found in simulation for HS of comparable poly dispersity (ranging between 0.638 and 0.658 depending on the compression rate with which the system is prepared [66]). Applying the same procedure for the previously studied system with $\delta \approx 0.08$ the maximum fluid volume fraction is decreased from $\phi = 0.692$ to an estimated value of 0.66, which is still significantly smaller than the corresponding value for $\delta \approx 0.06$. Thus, deswelling does not affect the qualitative agreement with the MCT prediction that reducing the attraction range leads to a larger re-entry region and larger fluid volume fractions.

Thus, it seems that osmotic deswelling alone cannot account for the observation of fluid states beyond random close packing in these PS–microgel–polymer mixtures and the dependence of the extent of the re-entry region on the crosslink density of the microgel particles. It appears plausible that other effects must come into play as well. Polymer non-ideality effects can be ruled out as possible cause. Polymer non-ideality leads to a reduced attraction range δ as compared to the ideal free polymer [67] and this in turn should lead to an enlarged re-entry region according to MCT predictions [22]. However, there is no reason to assume that the effect of polymer non-ideality depends on the degree of crosslinking of the microgel particles. Thus, it should affect both 1:10 and 1:50 crosslinked microgel systems in the same manner. Another possibility to access disordered fluid states beyond random close packing would be the generation of regions with crystalline order. As there the particles could be more densely packed than in disordered fluid regions, this could create sufficient free volume to allow for coexistence of fluid regions with much lower volume fraction and high particle mobility such that the sample as a whole appears as fluid. Such a situation has been observed for a similar binary mixture of 1:50 crosslinked microgel particles at a volume fraction very closely below the repulsive glass transition [58]. There the formation of highly packed ($\phi_{crystal} \approx 0.72$–$0.73$) crystals was observed which were composed of either only S or only L particles in a polymer concentration range slightly below the attractive glass line. The crystals were rather small, extending over less than 10 particle diameters. It is intriguing to speculate that this polymer-enforced crystallization is operative at higher volume fractions as well, leading to even smaller, but possibly more numerous nanocrystals with very high crystal packing fractions or to highly packed clusters that could be interpreted as precursors of crystal nuclei. The many samples with the presence of slow modes in the ISF which are denoted as cluster states for $\delta \approx 0.06$ in Fig. 13b and the infrequent

observation of such ISFs for $\delta \approx 0.08$ could be indicative of such a scenario. This leads to the question why such cluster states and the corresponding large re-entry region do not occur for 1:10 crosslinked microgels and not for the PMMA system. One possible explanation could be that such states are kinetically blocked in these systems. Whereas more packed states are kinetically not accessible due to jamming in case of hard spheres, this kinetic restriction could be relaxed in case of slightly soft spheres. Reaching a more packed state, e.g. with some regions of partial crystallinity, would require the passage of states with spheres partially overlapping or slightly deformed, but this is not possible for ideal hard spheres or for the 1:10 crosslinked spheres. In case of the 1:50 crosslinked system, the particles are slightly soft and the passage of such states might be possible, thus opening up routes to more densely packed states. Polydispersity may then additionally allow for more efficient packing of spheres. However, we are not aware of systematic studies of the influence of polydispersity on the jamming of soft spheres and on the corresponding volume fractions of maximum packing comparable to the work in Ref. [66], which could shed some light on this issue. While at present this line of argumentation is more or less speculative, it receives some support from the fact that with an aqueous, technical dispersion fluid states up to $\phi = 0.644$ were observed on addition of free polymer (cf. Fig. 8). Here some softness may have been imparted to these particles by the stabilizing hairy layer [48].

6 Synthesis of PEG-Stabilized Fluoroacrylate Particles and Their Glass Transition in Aqueous Dispersion

We have found that the extent of the re-entry phenomenon, i.e. the fluidization of kinetically arrested states by addition of free polymer, shows some pronounced dependence on the characteristics of the studied dispersions, with rather "hard" particles showing the weakest effect and rather "soft" particles the strongest. The so far only studied technical, aqueous dispersion showed an intermediate effect. However, this type of dispersion is not as well-defined as the studied model systems. This is an intrinsic problem with technical dispersions which are synthesized with rather complex industrial formulations. Therefore it would be highly interesting to have at hand a model dispersion which closely mimics such aqueous dispersion, but where a detailed characterization is accessible. For this purpose we have developed synthesis protocols which allow for the preparation of such a model system. The requirements were: (i) the particles should be sterically stabilized in water such that nearly HS interactions can be realized, but at the same time a controlled softening of the repulsive interactions is possible; (ii) the particles should be nearly isorefractive in water, so that characterization of interactions at moderate volume fraction as well as glass transition studies with light scattering methods are possible. We have made significant progress in this direction, but the final goal has not yet been achieved. Thus, we give a brief account of the state of the art. For more detailed information the reader is referred to Refs. [68–70].

To achieve the isorefractivity condition we chose perfluoro-n-butyl-methacrylate (FBMA) as monomer since corresponding charge-stabilized colloidal particles with a refractive index close to that of water have been described in the literature [34–36]. To prepare sterically stabilized particles from this monomer we adapted a synthesis strategy reported for the preparation of polyethylene glycol (PEG) stabilized polystyrene (PS) particles via a batch emulsion polymerization process [71] to FBMA. PEG has been chosen as stabilizing polymer as it is known to sterically stabilize colloids in aqueous media and that depletion attraction can be induced in such dispersions by addition of free PEG [72]. However, studies of such systems at higher volume fractions have been limited to rheological experiments due to the turbidity of the resulting dispersions. Only recently has the glass transition of PEG-stabilized PS particles become accessible due to the use of multiple scattering suppressing light scattering methods [73]. The effect of depletion attraction on the glass transition and the re-entry phenomenon have, however, not yet been addressed with these systems.

Following Ref. [71] we used the macromonomer poly(ethylene glycol) methyl ether methacrylate (PEGMA) with a degree of polymerization DP = 23 of the PEG chain as a surfmer, i.e. as polymerizable surfactant, in a batch emulsion polymerization process. With this recipe we were able to obtain stable, nearly monodisperse dispersions where the particle radius could be tuned by the molar ratio of macromonomer to monomer between 230 and 160 nm (cf. Fig. 3 of [69]). Colloidal stability was demonstrated by showing that the particles can be redispersed after compaction of a dilute dispersion by centrifugation and by freeze-thaw cycles. As shown in Fig. 16 by monitoring the angular dependence of the particle radii via DLS, the original particle radii (after synthesis) are recovered after these procedures. In addition, the absence of a strong increase of the hydrodynamic radius at small angles demonstrates that no particle aggregates have been formed.

Colloidal stability of the PEG stabilized poly(FBMA) (PFBMA-PEG) particles has also been demonstrated against addition of salt (cf. Fig. 5 of Ref. [69]). The refractive index $n_{633} = 1.380$ of these particles is not sufficiently close to the one for water $n_{625} = 1.332$ for preparing transparent dispersions. However, adding a small amount of DMSO (10.8 mol.%) to water, transparent aqueous dispersions can be achieved even at highest volume fractions. This is shown in Fig. 17 where it is also demonstrated that glassy states can be achieved for a binary mixture with a size ratio close to that of the studied PS microgel systems ($\Gamma = 0.805$, $N = 1.3$). This binary mixture showed qualitatively similar glass transition dynamics in DLS experiments as has been found for near HS dispersions, however with a much to low glass transition volume fraction of $\phi_g = 0.262$ (cf. Figs. 7 and 8 of Ref. [69]). This finding could be explained by a rather extended PEG shell of about 30 nm thickness, which resulted in an erroneous volume fraction determination. This layer can be thought to have formed via homopolymerization of the macromonomer and attachment of these homopolymers at a late stage of the batch polymerization. For these particles the standard procedure of fixing the volume fraction scale via a mapping of the fluid-crystal coexistence region onto that of the

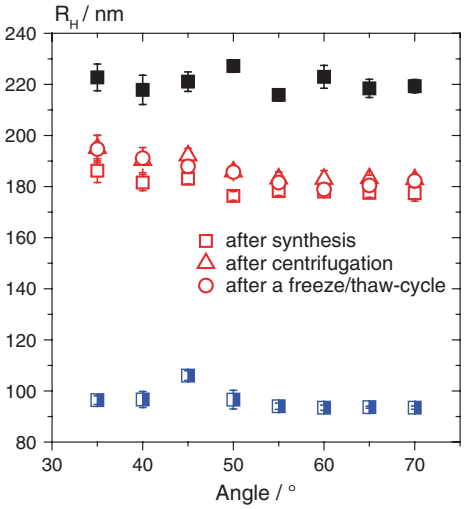

Fig. 16 Hydrodynamic radii versus the scattering angle measured directly after synthesis for two batches of copolymerizations with different molar ratios of PEG macromonomer to FBMA (*black*, *filled squares* $n_M/n_{FBMA} = 0.01$; *red open squares* $n_M/n_{FBMA} = 0.026$). *Blue half-filled squares* are electrostatically stabilized poly(FBMA) particles synthesized for reference (cf. [69]). The particle size remains constant after centrifugation and freeze-thaw processing as shown for one batch (*red triangles* and *circles*) which is indicative of sterically stabilized particles. Reproduced from [69] with permission

HS system could not be applied due to a failure of the individual components to properly crystallize. As an alternative, a stock dispersion was spun down by centrifugation and the sediment was assigned the value of $\phi_{rcp} = 0.64$. Dispersions in

Fig. 17 Preparation of transparent highly concentrated aqueous dispersions of PFBMA-PEO particles. From *left to right* (i) monomodal dispersion ($R_L = 190$ nm) at $\phi = 0.64$; (ii) binary mixture with $\Gamma = R_S/R_L = 153$ nm/190 nm $= 0.805$ at $\phi = 0.64$—both in an isorefractive water-DMSO mixture; (iii) monomodal dispersion ($R_L = 190$ nm) at $\phi = 0.02$ in pure water; (iv) same as (i) showing that the sample does not flow

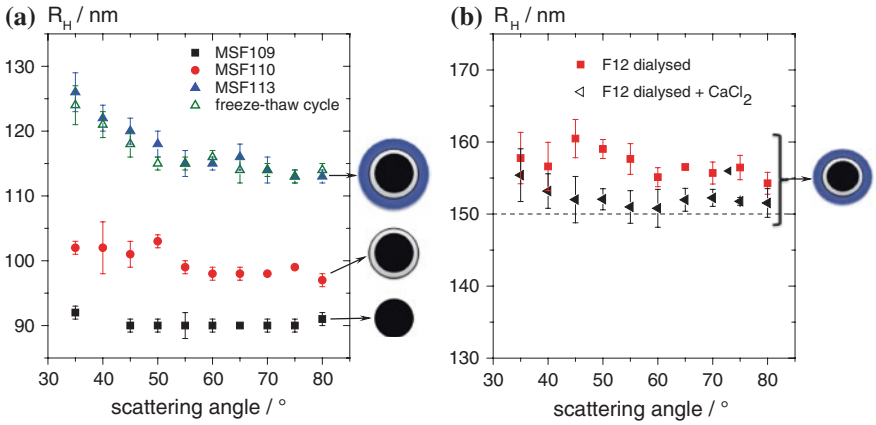

Fig. 18 Angular dependence of hydrodynamic radii (R_H) as determined by DLS for PFBMA-PEG particles prepared using atom transfer radical polymerization (ATRP) to couple a PEG macromonomer to PFBMA seed particles via **a** seeded growth and **b** semi-batch emulsion polymerization, respectively. Reproduced from Ref. [70] with permission. **a** Seed particles prepared by batch emulsion polymerization are covered in a second step by a shell containing the ATRP initiator BIEM which is then reacted with the PEG macromonomer in the final step. Shown are the results for each step of the three step synthesis without any prior purification of the dispersion (e.g. by dialysis). The angular averages yield $R_H = 91 \pm 3$ nm for the PFBMA cores (MSF109, *squares*), $R_H = 100 \pm 2$ nm for the seed-particles with a poly(FBMA-co-BIEM) shell (MSF110, *circles*) and $R_H = 117 \pm 4$ nm for the final PEG-stabilized PFBMA particles (MSF113, *solid triangles*). The absence of angular dependence of the particle size indicates absence of aggregates and suggests a rather narrow size distribution of MSF109 and MSF110. The increase of R_H at low angles for MSF113 is most likely due to a small number of larger particles or aggregates. To verify the sterical stabilization of the MSF113, data for this dispersion after freeze–thaw cycling are shown for comparison (*open triangles*). **b** PFBMA particles with a (FBMA-co-BIEM) shell are prepared by semibatch emulsion polymerization (cf. [70] and then reacted with PEG macromonomer in a second step. Shown are results for a purifed (via dialysis) PEG-stabilized PFBMA dispersion prepared via the semibatch/ATRP synthesis strategy (sample code F12) before (*squares*) and after (*triangles*) adding salt. The average radii of the dispersions were 157 ± 3 nm and 152 ± 2 nm, respectively. Hence, there is no aggregation and the dispersion is sterically stabilized. The radius of the FBMA-co-BIEM seed dispersion (F9; $R_H = 150 \pm 2$ nm) is indicated as a *dashed line*

the glass transition region were then obtained by dilution and the volume fractions calculated from the dilution ratio of the stock dispersion. However, in the centrifugation process water is squeezed out of the hairy PEG layer which then leads to a random close packing of the PFBMA cores in the sediment and, thus, to an large underestimation of the absolute volume fractions on dilution when the PEG layer is again swollen with water. Currently work is in progress to access the fluid-crystal coexistence region of such particles [74].

In addition to attempts to improve on the crystallization behaviour of PFBMA-PEG particles synthesized by batch polymerization we have also developed new synthesis strategies which allow to decouple the particle size from the n_M/n_{FBMA}

ratio and which lead to particles with a rather thin, about 6 nm thick PEG layer [71]. In a first approach we use standard emulsion polymerization for synthesis of a PFBMA seed dispersion. The seed particles are then functionalized in a seeded growth polymerization with a thin shell composed of the bromine carrying monomer 2-(2-bromoisobutyryloxy) ethyl methacrylate (BIEM) co-polymerized with FBMA. BIEM is an initiator for atom transfer radical polymerization (ATRP) which is used in the final step to graft the particle surfaces with PEG using the macromonomer poly(ethylene glycol) methacrylate (PEGMA, DP = 23). In a second approach we combine seed preparation and functionalization into one step with a semi-batch emulsion polymerization, generating a core–shell particle with PFBMA as core and a P(BIEM-co-FBMA) shell, again followed by ATRP to graft PEG onto the particles. Both strategies provide nearly monodisperse particles which are sterically stabilized in water as demonstrated by dynamic light scattering experiments in combination with colloidal stability tests. Typical results are depicted in Fig. 18.

One obtains PEG-stabilized PFBMA particles with a 17 nm thick shell via the three step synthesis (Fig. 18a) whereas the two-step process leads to a shell thickness of 6 nm which is compatible with a “monolayer” of nearly fully stretched PEG chains. The latter particles can be expected to interact nearly like hard spheres. Work is in progress to characterized these particles and to study their behaviour at higher volume fractions up to the colloidal glass transition [74].

7 Summary

Motivated by the observation that polymer-induced short-ranged depletion attraction shifts the colloidal glass transition to higher volume fractions we have studied the potential of this so-called re-entry phenomenon to achieve fluid dispersions at very high volume fractions and whether this effect can be employed for technical, aqueous dispersions as well. In a first step, we compared the microscopic dynamics monitored by dynamic light scattering to the—technically most relevant—macroscopic flow behavior measured by rheological methods. To avoid uncertainties due to the determination of volume fractions we studied both properties on the same model system a well-defined bimodal dispersion of 1:50 crosslinked polystyrene (PS) particles in the good, isorefractive solvent 2-ethyl-naphthaline, in some case even measuring identical samples. This is especially important as close to the glass transition small differences in the volume fraction lead to dramatic changes of the system dynamics. We could show that these particles behave as hard spheres to a good approximation and that the re-entry region is seen identically with both methods, especially the highest achievable fluid volume fraction was the same ($\phi = 0.69$) as well the polymer concentration where it occurred ($c_P = 7.5$ g/l). We also found that at the studied size ratio $\Gamma = R_S/R_L \approx 0.72$ the shape of the particle size distribution, determined by the number ratio $N = N_S/N_L$ did not play a prominent role. Essentially the same dynamics were observed for $N = 2.5$ and $N = 11$.

In the second step we demonstrated that the concept of preparing fluid dispersion by addition of a free, nonadsorbing polymer at volume fractions, where the system would be glassy without the polymer, could be applied to a technical, aqueous dispersion as well. Here fluid dispersions with volume fractions up to $\phi = 0.644$ could be generated by addition of linear polyethylene-glycol (PEG) to aqueous dispersions consisting of a polystyrene-butylacrylate (P-S/BA) latex which has been supplied by BASF SE. Here, a PEG concentration of 5 g/l was sufficient. Additionally, crystallizing dispersions also consisting of (P-S/BA) particles but having a very narrow particle size distribution have been investigated. In this case, a fluidization was visible for volume fractions up to $\phi = 0.65$ at PEG-concentrations $c_p = 3$–8 g/l. The flow properties of this effective hard-sphere system have been studied in steady shear using classical cone-plate and parallel plate rheometry as well as a rectangular microchannel (~30 μm width) flow cell.

In macroscopic flow the introduction of weak attractions among particles results in a drastic drop of the low shear viscosity which is attributed the corresponding change of the phase diagram. The addition of non-adsorbing polymer leads to a substantial broadening of the fluid-crystalline co-existence regime and at a given particle loading densely packed crystalline regions coexist with dilute fluid like areas. The density of the crystalline regions increases and the particle loading in the fluid regions decreases with increasing polymer concentration. This results in a reduction of the viscosity, but when a critical polymer concentration is exceeded the strong attractive interaction leads to the formation of a gel-like attractive glass. Accordingly, a viscosity minimum is observed. For the system investigated here this minimum occurs around a polymer concentration $c_p \approx 3$ g/l well below the overlap concentration c*. A minimum polymer to particle size ratio δ_{min} is required to induce the viscosity reduction. For the system investigated here $\delta_{min} = 0.03$ and above δ_{min} the viscosity reduction increases with increasing δ. A similar size ratio was reported for the fluidization of glass forming systems using non-adsorbing polymer. Finally, in the high shear regime the viscosity is not affected by attractive colloidal interactions since hydrodynamic forces are dominating.

A completely different scenario is observed in microfluidic flow. For the pure colloidal dispersion shear melting is observed close to the channel wall and this enables a plug-like flow of the fluid through the channel. Addition of the polymer slows down bulk crystallization and results in smaller crystals and crystal size decreases with increasing polymer concentration. But at the same time crystallization at the wall dramatically increases. This leads to a complete clogging of the channel and steady flow conditions cannot be achieved. Wall crystallization also shows up in classical rotational rheometry and results in a strong increase of the apparent viscosity if narrow gap fixtures (<0.5 mm) are used.

We then explored for the model system how the re-entry phenomenon depends on system parameters like attraction range ($\delta = R_{g,polymer}/R_{colloid}$) or particle softness (which can be tuned by the crosslink density). We found that decreasing the attraction range from $\delta \approx 0.08$ to $\delta \approx 0.06$ the fluid (re-entry) region is strongly extended and fluid volume fractions up to 0.715 could be achieved for a bimodal mixture of 1:50 crosslinked system similar to that studied in the first

step ($\Gamma \approx 0.85$, $N \approx 3.1$). This behaviour is qualitatively in agreement with predictions of mode coupling theory (MCT), even so the re-entry region in experiment is much larger than in theory. When reducing the crosslink density to 1:10, thus making the microgel particles "harder", i.e. closer to the HS case, we found for a binary mixture ($\Gamma = 0.82$, $N = 2.7$, $\delta \approx 0.08$) a severely reduced re-entry region with a maximum fluid volume fraction of only $\phi = 0.61$. The behaviour of this system is very similar to that for sterically stabilized PMMA particles which are considered as the currently best realization of a HS system by colloids. We rationalized these differences in behaviour by a combination of polymer induced deswelling of the less crosslinked microgels and their increased softness. The latter most likely allows for pathways to partially crystalline regions with crystal volume fractions up to 0.73 which generate less compact fluid regions in turn, which give rise to particle mobility and macroscopic flow. These pathways are blocked in the "harder" and less deformable PMMA and 1:10 crosslinked PS systems, thus leading to jammed stated at higher volume fractions even on addition of free polymer. To estimate to which extent deswelling is responsible for the nominally high fluid volume fraction we used results from macroscopic PS gels. The calculations indicate a deswelling of only a few percent in volume fractions for the highest observed fluid samples—thus reducing the values from 0.69 to 0.66 for $\delta = 0.08$ and from 0.715 to 0.673 for $\delta = 0.06$. This implies that the effect of softness is stronger than the effect of deswelling in producing high fluid volume fractions. This is further supported by the results obtained for the aqueous (P-S/BA) dispersion. These particles do not deswell upon addition of free water soluble polymer PEG, but they are deformable since the T_g ($\approx$10 °C) is slightly below room temperature and the shear modulus is in the order of 1 MPa. Accordingly, fluid states are observed up to $\phi = 0.644$.

In order to allow for similar systematic studies of the influence of system properties on the re-entry effect for technical, aqueous dispersions, we developed a new model system which is able to mimic such dispersions, but is accessible to light scattering studies. It consists of particles composed of a polymer core of perfluorinated n-butyl-methacrylate (PFBMA) and a shell of polyethylene glycol (PEG). Here, the high fluorine content reduces the refractive index of the particles, bringing it so close to the refractive index of water that isorefractivity with the dispersion medium is achieved by a small amount of a higher refractive index cosolvent like DMSO or glycerol. The PEG sterically stabilizes the particles in water and the softness of the particles can be tuned by varying the thickness of the stabilization layer. Using different synthesis strategies particle size could be varied between 160 and 230 nm (covering the size range needed to prepare binary mixtures similar to those of the studied microgel systems). Thickness of the PEG shell varied between 6 nm (close to HS behaviour expected) and 30 nm (soft sphere behaviour expected). In a first study we could demonstrate that binary mixtures prepared from such particles show a glass transition dynamics quite similar to that of the PMMA HS dispersions and the PS microgel dispersions. However, these systems need some further optimization and characterization before they are accessible for systematic studies of the re-entry effect in aqueous dispersions. Work along these lines is in progress.

References

1. Hiemenz PC, Rajagopalan R (1997) Principles of colloid and surface chemistry, 3rd edn. Dekker, New York
2. Irvine DJ, Stachowiak A, Jain S (2003) Engineering biomaterials for control of immune cell functions. Mat Sci Forum 426:3213–3218
3. Vlasov YA, Yao N, Norris DJ (1999) Synthesis of photonic crystals for optical wavelengths from semiconductor quantum dots. Adv Mat 11:165–169
4. Gratson GM, Mingjie X, Lewis JA (2004) Microperiodic structures: direct writing of threedimensional webs. Nature 428:386–389
5. Lewis JA (2000) Colloidal processing of ceramics. J Am Cer Soc 83:2341–2359
6. Terray A, Oakey J, Marr DWM (2002) Microfluidic control using colloidal devices. Science 296:1841–1844
7. Farris RJ (1968) Prediction of the viscosity of multimodal suspensions from unimodal viscosity data. Trans Soc Rheol 12:281–301
8. Wouterson ATJM, de Kruif CG (1991) The rheology of adhesive hard sphere dispersions. J Chem Phys 94:5739–5749
9. Dames B, Willenbacher N (2001) An empirical model predicting the viscosity of highly concentrated, bimodal dispersions with colloidal interactions. Rheol Acta 40:434–440
10. Willenbacher N, Börger L, Urban D (2003) Tailoring PSA-dispersion rheology for high-speed coating. Adhes Sealants 10(9):26–35
11. Pusey PN, van Megen W (1986) Phase behaviour of concentrated suspensions of nearly hard colloidal spheres. Nature 320:340–342
12. Liu AJ, Nagel SR (1998) Nonlinear dynamics: jamming is not just cool any more. Nature 6706:21–22
13. Meeker SP, Poon WCK, Pusey PN (1997) Concentration dependence of the low-shear viscosity of suspensions of hard-sphere colloids. Phys Rev E 55:5718
14. Götze W (1991) Aspects of structural glass transitions. In: Hansen J-P, Levesque D, Zinn-Justin J (Eds) Liquids, freezing and glass transition. North-Holland, Amsterdam, pp 287–504
15. Barrat JL, Götze W, Latz A (1989) The liquid-glass transition of the hard-sphere system. J Phys Condens Matter 1:7163–7170
16. Nägele G, Bergenholtz J (1998) Linear viscoelasticity of colloidal mixtures. J Chem Phys 108(23):9893–9904
17. Fuchs M, Cates ME (2002) Theory of nonlinear rheology and yielding of dense colloidal suspensions. Phys Rev E 89:248304-2
18. Fuchs M, Cates ME (2003) Schematic models for dynamic yielding of sheared colloidal glasses. Faraday Discuss 123:267
19. Fuchs M, Ballauff M (2005) Flow curves of dense colloidal dispersions: Schematic model analysis of the shear-dependent viscosity near the colloidal glass transition. J Chem Phys 122:094707
20. Siebenbürger M, Fuchs M, Winter H, Ballauff M (2009) Viscoelasticity and shear flow of concentrated, noncrystallizing colloidal suspensions: Comparison with mode-coupling theory. J Rheology 53:707
21. Bergenholtz J, Fuchs M (1999) Non-ergodicity transitions in colloidal suspensions with attractive interactions. Phys Rev E 59:5706–5715
22. Dawson K, Foffi G, Fuchs M, Götze W, Sciortino F, Sperl M, Tartaglia P, Voigtmann Th, Zaccarelli E (2001) Higher-order glass-transition singularities in colloidal systems with attractive interactions. Phys Rev E 63:011401
23. Pham KN, Puertas AM, Bergenholtz J, Egelhaaf SU, Moussaïd A, Pusey PN, Schofield AB, Cates ME, Fuchs M, Poon WCK (2002) Multiple glassy states in simple model system. Science 296:104–106
24. Pham KN, Egelhaaf SU, Pusey PN, Poon WCK (2004) Glasses in hard spheres with shortrange attraction.Phys Rev E 69:011503

25. Eckert T, Bartsch E (2002) Re-entrant glass transition in a colloid-polymer mixture with depletion attractions. Phys Rev Lett 89:125701
26. Eckert T, Bartsch E (2003) The effect of free polymer on the interactions and the glass transition dynamics of microgel colloids. Faraday Discuss 123:51
27. Eckert T, Bartsch E (2004) Glass transition dynamics of hard sphere like microgel colloids with short-ranged attractions. J Phys Condens Matter 16:S4937
28. Shah SA, Chen YL, Schweizer KS, Zukoski CF (2003) Phase behavior and concentration fluctuations in suspensions of hard spheres and nearly ideal polymers. J Chem Phys 118:3350
29. Shah SA, Chen YL, Schweizer KS, Zukoski CF (2003) Viscoelasticity and rheology of depletion flocculated gels and fluids. J Chem Phys 119:8747
30. Gopalakrishnan V, Zukoski CF (2004) Effect of attractions on shear thickening in dense suspensions. J Rheol 48(6):1321–1344
31. Krishnamurthy LN, Wagner NJ (2005) The influence of weak attractive forces on the microstructure and rheology of colloidal dispersions. J Rheol 49(3):475–499
32. Pham KN, Petekidis G, Vlassopoulos D, Egelhaaf SU, Poon WCK, Pusey PN (2008) Yielding behavior of repulsion-and attraction-dominated colloidal glasses. J Rheol 52(2):649–676
33. Degiorgio V, Piazza R, Bellini T et al (1994) Static and dynamic light scattering study of fluorinated polymer colloids with a crystalline internal structure. Adv Coll Interf Sci 48:61–69
34. Härtl W, Zhangheider X (1997) The synthesis of a new class of polymer colloids with a low index of refraction. J Coll Interf Sci 185:398–401
35. Koenderink GH, Philipse AP (2000) Rotational and translational self-diffusion in colloidal sphere suspensions and the applicability of generalized Stokes-Einstein relations. Langmuir 16:5631–5638
36. Koenderink GH, Sacanna S, Pathmamanoharan C, Raca M, Philipse AP (2001) Preparation and properties of optically transparent aqueous dispersions of monodisperse fluorinated colloids. Langmuir 17:6086–6093
37. Hunter GL, Weeks ER (2012) The physics of the colloidal glass transition. Rep Prog Phys 75:066501
38. Russel WB, Wagner NJ, Mewis J (2013) Divergence in the low shear viscosity for Brownian hard-sphere dispersions: at random close packing or the glass transition? J Rheol 57:1555–1567
39. Segre PN, Meeker SP, Pusey PN, Poon WCK (1995) Viscosity and structural relaxation in suspensions of hard-sphere colloids. Phys Rev Lett:958–961
40. Royall CP, Poon WCK, Weeks ER (2012) In search of colloidal hard spheres. Soft Matter 9:17–27
41. Poon WCK, Weeks ER, Royall CP (2012) On measuring colloidal volume fractions. Soft Matter 8:21–30
42. Willenbacher N, Vesaratchanon JS, Thorwarth O, Bartsch E (2011) An alternative route to highly concentrated, freely flowing colloidal dispersions. Soft Matter 7:5777–5788
43. Paulin SE, Ackerson BJ (1996) Equilibrium and shear induced nonequilibrium phase behavior of PMMA microgel spheres. J Colloid Interf Sci 178:251–262
44. Senff H, Richtering W (1999) Temperature sensitive microgel suspensions: colloidal phase behavior and rheology of soft spheres. J Chem Phys 111:1705–1711
45. Koumakis N, Pamvouxoglou A, Poulosa AS, Petekidis G (2012) Direct comparison of the rheology of model hard and soft particle glasses. Soft Matter 8:4271–4284
46. Lange E, Caballero JB, Puertas AM, Fuchs M (2009) Comparison of structure and transport properties of concentrated hard and soft sphere fluids. J Chem Phys 130:174903
47. Götze W, Voigtmann T (2003) Effect of composition changes on the structural relaxation of a binary mixture.Phys Rev E 67:021502
48. Vesaratchanon JS, Takamura K, Willenbacher N (2010) Surface characterization of functionalized latexes with different surface functionalities using rheometry and dynamic light scattering. J Colloid Interf Sci 345:214–221

49. Kawaguchi S et al (1997) Aqueous solution properties of oligo- and poly (ethylene oxide) by static light scattering and intrinsic viskosity. Polymer 38:2885–2891
50. Asakura S, Oosawa F (1958) Interaction between particles suspended in solutions of macromolecules. J Polym Sci XXXIII:183–192
51. Willenbacher N, Börger L, Urban D, Varela de la Rosa L (2003) Tailoring PSA-dispersion rheology for high-speed coating, ASI, Adhes Sealants 10(9):26–35
52. Weis C, Natalia I, Willenbacher N (2014) Effect of weak attractive interactions on flow behavior of highly concentrated crystalline suspensions. J Rheol 58:1583–1579 http://dx.doi.org/10.1122/1.4882955
53. Ilett SM et al (1995) Phase behavior of a model colloid-polymer mixture. Phys Rev E 51:1344–1352
54. Palberg T, Stipp A, Bartsch E (2009) Unusual crystallization Kinetics in a hard sphere colloid-polymer mixture. Phys Rev Lett 102:038302-1–038302-4
55. Beyer R et al (2012) Polymer induced changes of the crystallization scenario in suspensions of hard sphere like microgel particles. J Chem Phys 136:234906-1–234906-8
56. Eckert T (2004) Ph.D. thesis, Mainz
57. Burger S, Bartsch E (2014) Influence of the polymer size on depletion attraction—induced gel and glass transitions of microgel colloids. Coll Surf A 442:6–15
58. Kozina A, Sagawe D, Díaz-Leyva P, Bartsch E, Palberg T (2012) Polymer—enforced crystallization of a eutectic binary hard sphere mixture. Soft Matter 8:627–630
59. Kozina A (2009) Ph.D. thesis, Freiburg
60. Sciortino F, Tartaglia P (2005) Glassy colloidal systems. Adv Phys 54:471–524
61. Götze W (1999) Recent tests of the mode—coupling theory for glassy dynamics. J Phys Condens Matter 11:A1–A45
62. Wiemann M (2013) Ph.D. thesis, Freiburg
63. Wiemann M, Willenbacher N, Bartsch E (2012) Effect of cross-link density on re-entrant melting of microgel colloids. Coll Surf A 413:78–83
64. Saunders BR, Vincent B (1997) Osmotic de-swelling of polystyrene microgel particles. Colloid Polym Sci 275:9–17
65. Bastide J, Candau S, Leibler L (1981) Osmotic deswelling of gels by polymer solutions. Macromolecules 14:719–726
66. Hermes M, Dijkstra M (2010) Jamming of polydisperse hard spheres: the effect of kinetic arrest. Europhys Lett 89:38005-1–38005-6
67. Fleer GJ, Skvortsov AM, Tuinier R (2007) A simple relation for the concentration dependence of osmotic pressure and depletion thickness in polymer solutions. Macromol Theory Simul 16:531–540
68. Schneider R (2011) Ph.D. thesis, Freiburg
69. Wiemann M, Schneider R, Bartsch E (2012) Synthesis of PEG-stabilized fluoro-Acrylate particles and study of their glass transition in aqueous dispersion. Z Phys Chem 226:761–778
70. Burger D, Gisin J, Bartsch E (2014) Synthesis of sterically stabilized perfluorinated aqueous latices. Colloids Surf A 442:123–131
71. Brindley A, Davis SS, Davies MC, Watts JF (1995) Polystyrene colloids with surface-grafted polyethylene oxide as model systems for site-specific drug delivery: I. preparation and surface chemical characterization using SIMS and XPS. J Colloid Interface Sci 171:150–161
72. Tadros TF (1996) Correlation of viscoelastic properties of stable and flocculated suspensions with their interparticle interactions. Adv Colloid Interf Sci 68:97–200
73. Zackrisson M, Stradner A, Schurtenberger P, Bergenholtz J (2006) Structure, dynamics, and rheology of concentrated dispersions of poly(ethylene glycol)-grafted colloids. Phys Rev E 73:11408-1–11408-8
74. Werner M, M.Sc. thesis, work in progress

Process Engineering of Nanoparticles Below 20 nm—A Fundamental Discussion of Characterization, Particle Formation, Stability and Post Processing

Doris Segets and Wolfgang Peukert

Abstract In the following chapter fundamental aspects that have to be considered during the processing of small nanoparticles will be addressed. We investigated quantum confined manganese doped ZnS, ZnO, PbS and PbSe semiconductor nanoparticles, so-called quantum dots (QDs) and silver noble metal nanorods. All materials were chosen due to their technical relevance for future applications in the emerging fields of solar cells, sensors and diagnostics as well as due to the possibility of their *in situ* characterization by UV/Vis absorbance spectroscopy. After a brief introduction to the specific prospects and challenges of these materials we will focus on the important processing issues that need to be solved for producing these particles at high quality on a larger scale: (i) the modelling of particle formation including nucleation, growth and ripening based on a mechanistic understanding and on experimentally derived data on solubility and surface energies, (ii) the stabilization of nanoparticles not only against agglomeration but also against shape changes and (iii) classification. The latter is realized by size selective precipitation which allows surprisingly sharp separations ($\kappa = 0.75$) of particles with only a few nm in diameter. Although the extremely small particle sizes (feed PSD between 1.5 and 3 nm), classification results were successfully analyzed by well-known concepts from particle technology. Our results are seen to be an essential contribution to colloidal processing. They enable a future optimization of process parameters by a knowledge-based design strategy that can be applied within continuous as well as automatized batch reactor concepts.

Keywords Nanoparticle handling · Quantum dots · Optical properties · Particle formation mechanism · Ostwald ripening · Oriented attachment · Colloidal stability · Shape transformation · Classification

D. Segets · W. Peukert (✉)
Institute of Particle Technology, Friedrich-Alexander-Universität Erlangen-Nürnberg (FAU), Cauerstraße 4, 91058 Erlangen, Germany
e-mail: Wolfgang.Peukert@fau.de

D. Segets
e-mail: Doris.Segets@fau.de

M. Kind et al. (eds.), *Colloid Process Engineering*,
DOI 10.1007/978-3-319-15129-8_12

1 Introduction of the Process Chain Leading to Advanced Materials

Advanced materials always evolve from more or less complex processes. A key question is how to tailor the related and often multifunctional material properties by careful process design and control. In the field of nanotechnology a strong trend was observed towards smaller particles [2, 47] with more and more complex structures and shapes [9, 21] as well as hybrid materials [28]. Such well-defined products show outstanding properties in the emerging fields of solar cells [12], sensors [72], field effect transistors [19] but also diagnostics and therapy [38]. For these particle systems highly elaborated synthesis protocols were developed in the last 20 years whereas the transfer of these lab-scale approaches to scalable technical processes is largely missing.

To bridge the gap between academia and a future industrial production of larger quantities with well-defined product properties, fundamental questions need to be addressed:

- How to understand and to use the pronounced structure-property relationships of small nanoparticles during colloidal processing?
- How to model the particle formation in organic solvents, what is the role of oriented attachment and what are the differences to the mixing controlled model system $BaSO_4$?
- How to describe the stabilization mechanism of nanoparticles < 20 nm and how to tune the agglomeration of nanoparticles in a process?
- What are suitable strategies for the post-processing of colloids? Are they competitive with existing processes and can they be transferred to larger quantities?
- How can the previous findings be used to transfer lab synthesis protocols towards technically relevant applications?

These central questions must be answered at various stages throughout the process chain like it is shown in Fig. 1. It becomes clear that during all steps in situ characterization and the in-depth understanding of structure property relationships is of major importance.

Continuous synthesis concepts [32, 79] as well as automatized batch approaches [5] just began to be developed, strategies for a large scale post-processing in terms of the always mandatory purification or a final narrowing of an

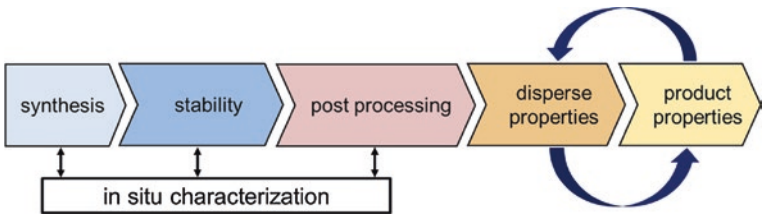

Fig. 1 Process chain during nanoparticle formation and application

as-synthesized particle size distribution (PSD) by classification are still missing. From a chemical engineering perspective knowledge on structure-property as well as process-structure functions is, however, a key requirement when promising materials on the lower nanometer scale shall be brought to the market.

Within the following sections we will discuss fundamental aspects of nanoparticle processing including the most important steps of characterization, particle formation, stabilization and post processing to end up with some general conclusions for a future process design. As model materials we use technically relevant semiconductor nanoparticles, so-called quantum dots (QDs) with direct band gap (ZnO, manganese doped ZnS and PbS(e)) and silver nanowires which have been proven to be excellent transparent electrodes for thin film solar cells [27].

For a detailed description of all experiments, chemicals, specifications of the measurement devices and characterization procedures the reader is referred to the cited literature. Additionally, two PhD-theses have been emanated from this project: in parts the thesis of Gradl [14] and the thesis of Segets [61] which provide detailed information on the topics that are discussed in the following.

2 Using Structure-Property Relationships for Characterization

2.1 Deconvolution of PSDs Using Literature Data

All QDs of the present work enable a unique possibility of characterization due to the size-dependent fundamental band gap energy of small and quantum confined semiconductor nanoparticles. As soon as the particle diameter of the material approaches the dimension of its specific Bohr radius, quantum confinement occurs in a way that the energy difference between the highest energy state in the valence band and the lowest energy state in the conduction band increases. Additionally, the non-forbidden energy levels discretize.

Figure 2 illustrates the basic principle that is used for the deconvolution of optical absorbance spectra of QDs [62]. It is based on assuming additive

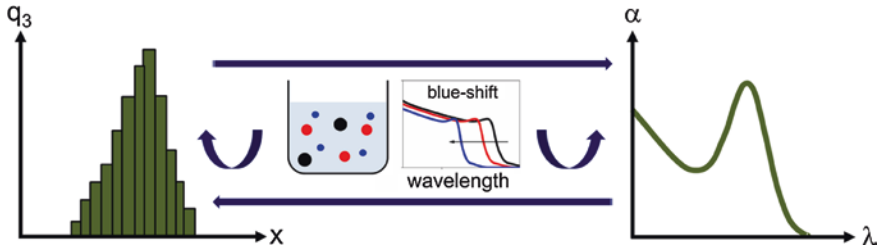

Fig. 2 Principle approach for using the deconvolution of optical absorbance spectra to derive the PSD of quantum confined semiconductor nanoparticles in solution [62]

contributions of the individual particle size fractions (like it is illustrated in Fig. 2 by large black, medium red and small blue particles) within a colloidal suspension to the final absorbance spectrum [65]. This assumption has not only been made by us but was already more than 20 years ago used by Mićić et al. [39], as well as ten years later by Pesika et al. [48] and Viswanatha and Sarma [76]. However, the method developed by us enables the derivation of full PSDs of arbitrary shape with the concomitant possibility to adapt improved optical properties used for the absorption data of small nanoparticles.

The deconvolution method applied by us starts with the largest wavelength with non-zero absorbance value. This value is normalized to the shifted absorption coefficient of the bulk spectrum and the contribution of the largest fraction is subtracted from the original measurement. This contribution is ascribed to the corresponding size in the PSD and the next smaller wavelength is analyzed. The correlation between wavelengths (or energies) and particle sizes is usually taken from literature. In case of ZnO we use the tight binding model (TBM) of Viswanatha et al. [77], in case of manganese doped ZnS we take the correlation found by Sapra and Sarma [56] and in case of PbS(e) we will use a correlation found by us [68]) as will be shown later.

After deconvolution the mass density distribution $q_3(x)$ is normalized to a value of 1

$$\int_{x\text{min}}^{x\text{max}} q_3 q(x) dx = 1. \tag{2.1}$$

Regarding the further boundary conditions of our method, it is applicable to Segets et al. [65, 66, 68]

(i) semiconductors with direct band gap (material property),
(ii) particles with diameters above ~1 nm to assure a monotone correlation between particle size and band gap energy (lower size limit),
(iii) particles that are small enough that confinement effects do occur (upper size limit)
(iv) particles with negligible scattering contribution to the overall extinction (particles need to be in the Rayleigh regime) and
(v) particles with known bulk absorption properties (literature data).

However, before its application to unknown samples, the method needs to be validated. Validation was first realized for ZnO QDs using a direct comparison between the calculated results with an expected PSD derived from transmission electron microscopy (TEM) [63, 65]. Additionally, bimodal size distributions were generated artificially by mixing a suspension of small nanoparticles with a suspension of large particles in different volume ratios. As it becomes clear from Fig. 3b, the bimodal PSDs derived directly from the bimodal absorbance spectrum show an excellent agreement with the expected PSDs artificially generated from the density distributions of the individual, un-mixed samples [63, 65].

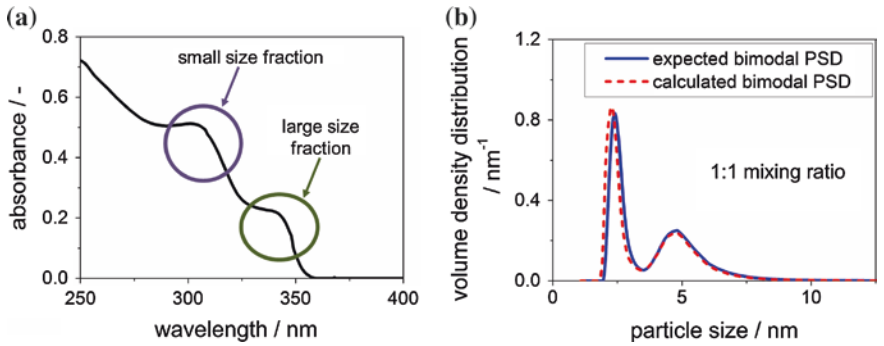

Fig. 3 Validation of the deconvolution technique by comparing the PSD obtained from the bimodal absorbance measurement (**a**) with the density distribution derived by artificial mixing the PSDs of the individual samples in a volume ratio of 1:1 (**b**) [62]

Thus, the method can be seen to be sufficiently validated as long as the aforementioned requirements are fulfilled and a relationship between band gap energy and particle size is established. The latter can be realized either experimentally by the evaluation of many differently sized samples in terms of their mean size and band gap shift or theoretically by quantum mechanical approaches such as tight binding or k·p models [46].

However, due to the fact that new multicomponent materials like $CuInS(e)_2$ are more and more in the focus of interest for which little knowledge in terms of their properties exists, methods for a fast derivation of optical properties are needed. This will be discussed as a further application of our concept in the next section.

2.2 Derivation of Spectral Properties

Based on the results of the previous section the question arises how to approach comparatively new QD materials for which little is known on their optical properties and especially the correlation between particle size and band gap is not yet established. The study was done in collaboration with the Alivisatos group (LBNL Berkeley, California, USA) on PbS(e). PbS(e) was chosen due to the fact that Pb-based QD-materials are investigated since decades and thus large sets of literature data on the size dependent band gap energy $E_g(x)$ are available for validation.

Figure 4 demonstrates the basic procedure. Whereas in case of ZnO the outcome of the calibration (PSD^{alg}) was validated by comparison to the expected distribution from TEM micrographs (PSD^{TEM}), the extended approach requires two PSDs of differently sized samples, a large and a small fraction. These are, for instance, directly analyzed by TEM. Then, a function of form

$$x_i = a \cdot \left(\frac{\Delta E_i}{eV} \right)^b + c, \tag{2.2}$$

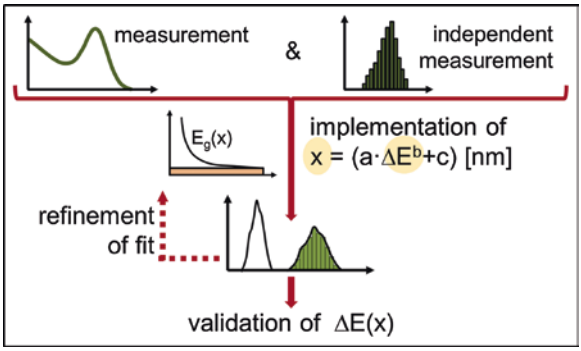

Fig. 4 Strategy applied for the determination of the size dependent band gap energy of unknown QD systems: PSDs derived from optical absorbance measurements are calibrated against the expected PSDs determined by an independent measurement technique; validation is done against the evolution of the fundamental band gap energy [62, 68]

that contains three empiric parameters a [nm], b [−] and c [nm] is implemented into the deconvolution algorithm to account for the size dependent band gap energy. The three parameters are adjusted until a best match between the expected PSD^{TEM} and the calculated PSD^{alg} is obtained. To cover a broad particle size range it turned out that a compromise of a, b and c derived for a smaller and a larger sized sample is recommended.

Finally, results for a, b and c have to be validated. This is realized by comparing the size dependent band gap energy $E_g(x)$ as it is calculated from the three fitting parameters

$$E_g(x) = E_{g0} + \left(\frac{x-c}{a}\right)^{\frac{1}{b}} \cdot eV, \tag{2.3}$$

to corresponding data from literature. Thus, in contrast to Sect. 2.1 validation is now done against the material property itself and not only against singular size distributions. For this purpose, we have chosen two of the most well-investigated QD materials that are currently available, PbS and PbSe, as model systems to ensure that enough data points of $E_g(x)$ are available for validation.

Regarding the specific study on PbS(e), smaller and larger sized samples were synthesized by Matt Lucas and Marcus Scheele (that time affiliated at University of California and LBNL Berkeley, details on the synthesis are found in the literature [68]). From them, underlying absorbance and aberration corrected TEM data was provided as well. For all samples, PSDs were determined from TEM micrographs using an automatized image analysis via the free Software ImageJ [1, 51]. The results of all mean volume weighted particle sizes $x_{1,3}$ are summarized in Table 1 (analysis of at least 124 particles per sample). THS_{min}, THS_{mean} and THS_{max} indicate the different threshold (THS) values that have been applied during image analysis [68].

In the next step, as shown in Fig. 4, the absorbance spectra were evaluated until a minimum deviation between the $PSDs^{alg}$ from the target $PSDs^{TEM}$ was obtained.

Table 1 Mean volume weighted particle sizes of the small and large sized sample of PbS and PbSe derived by application of different thresholds during image analysis (evaluation of a minimum of 124 particles) and summary of parameters a, b, and c showing the best match with the $PSDs^{TEM}$ in case of PbS(e) for THS_{min}, THS_{mean} and THS_{max} (bold values are recommended for future works [61, 68])

$x_{1,3}$/nm	THS_{min}	THS_{mean}	THS_{max}
PbS small	3.1	3.2	3.2
PbS large	4.1	4.2	4.4
PbSe small	5.7	5.7	5.9
PbSe large	8.5	8.6	8.7
Material	a (nm)	b (−)	c (nm)
PbS, THS_{min}	2.45	−0.9	0
PbS, THS_{mean}	**2.50**	**−0.9**	**0**
PbS, THS_{max}	2.60	−0.9	0
PbSe, THS_{min}	4.0	−0.6	−1.3
PbSe, THS_{mean}	**4.0**	**−0.6**	**−1.2**
PbSe, THS_{max}	4.0	−0.6	−1.1

The maximum deviation in $x_{1,3}$ for PbS(e) was found to be as small as 1.9 % (2.9 %). Details can be extracted from Table 1 together with the values of parameters *a*, *b* and *c*. For a direct comparison of PSDs and details of the image analysis procedure the reader is referred to the literature [61, 68]. For a future application the results obtained for THS_{mean} (Table 1, bold entries) are recommended as those are supposed to match best the expected particle edges during the TEM image analysis [66].

Figure 5 shows the results obtained for $E_{g,PbS(e)}(x)$ together with experimental and numerical literature data collected over the past 20 years [3, 4, 6, 7, 22, 26, 30, 31, 34, 41–43, 49, 57, 71]. It becomes clear that with our method the evolution of the size dependent band gap energy is described with high accuracy. However, this

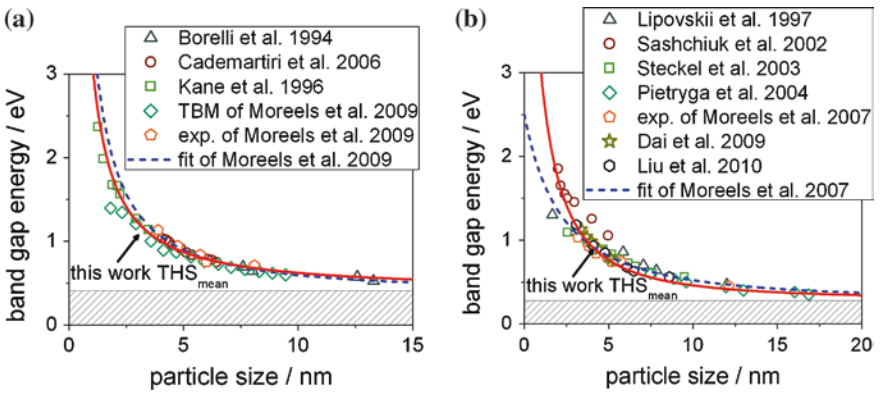

Fig. 5 Relationship between the fundamental band gap energy and particle size as derived for this project along with comparison to literature data for **a** PbS [3, 4, 22, 42, 43] and **b** PbSe [6, 7, 26, 30, 31, 34, 41, 49, 57, 71]. Reprinted with permission from Segets et al. [68]. Copyright 2012 American Chemical Society [61]

is realized by the evaluation of a limited quantity as small as two samples and thus at a minimum effort.

In conclusion, we see our analysis method sufficiently validated to investigate the QD particle formation mechanism. For kinetic studies ZnO will be used again as a model system due to the fact that it can be produced at moderate temperatures and without the application of Schlenck techniques [70]. ZnO precipitation will be analyzed with respect to the early stages of particle formation (nucleation and growth), but also with respect to long-term Ostwald ripening. Based on the experimental findings the particle formation process is modelled by population balance equations (PBE).

3 Analysis of Reaction Controlled Particle Formation

After having established a powerful measurement technique to determine PSDs between 1 nm and 10 nm, in the following chapter its application to the analysis of ZnO nucleation, growth and ripening will be demonstrated. All three regimes could be investigated in a first study by means of nonlinear optical spectroscopy using the incoherent Hyper-Rayleigh Scattering (HRS) [63, 74]. During this work two influencing factors on the HRS signal were discussed: the particle number density and the mean diameter of the nanoparticles. Both are in case of ZnO QDs leading to a signal increase and were used to evaluate the measurements shown in Fig. 6 with respect to nucleation, growth and ripening rates.

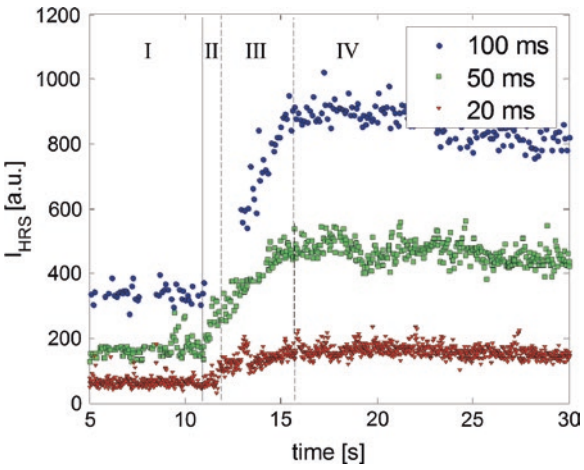

Fig. 6 HRS during nucleation (*II*), growth (*III*) and ripening (*IV*) of ZnO QDs monitored for three different time resolutions of 100 ms (*blue circles*), 50 ms (*green squares*) and 20 ms (*red triangles*). Note that the absence of data points (100 ms resolution) between 11 s and 13 s is due to a drop-out of the laser. Reprinted with permission from Segets et al. [63]. Copyright 2009 American Chemical Society [74]

Without the assumption of any nucleation mechanism we could already distinguish three characteristic regimes after the addition of alkaline LiOH an ethanolic zinc acetate precursor solution (vertical solid line between region (I) and region (II)):

- a nucleation regime where the signal increase is clearly ascribed to an increase in the particle number (region II),
- a growth regime in the still supersaturated solution that leads to a signal increase due to the increasing mean particle diameter (region III) and finally
- a coarsening regime where the signal decreases (region IV). This signal drop is explained by the decreasing particle number during Ostwald ripening due to the fact that larger particles grow at the expense of smaller ones. The effect of the particle number was shown to be superior to the positive contribution of the larger mean size to the total HRS [14, 63, 74].

However, we did not only want to analyze our data by experiments but to use them for a predictive modelling of particle formation. This was realized by population balance equations (PBE) which have been solved by using the commercially available program *PARSIVAL by CiT GmbH* [81]. For experimental details and specifications of the measurement devices the reader is again referred to the literature [14, 64, 65]. The most important findings will be summarized in the following.

3.1 Understanding ZnO Nucleation and Growth

Before we could start to model the nucleation and growth of the ZnO nanoparticles we needed to determine the reaction kinetics. This was realized by stopped-flow measurements with high time resolution (ms). The solid concentration was derived from PSDs determined by absorbance measurements. Thereby we used the effect that prior normalization the spectra provide information on the particle concentration [14, 68]. From the initial reaction rates in dependence of the zinc acetate precursor concentration $c\left(\mathrm{Zn}^{2+}\right)$ the reaction rate constant was determined for T = 20 °C to be $51.6 \pm 1.1\ \mathrm{m^6\ kmol^{-2}\ s^{-1}}$ ($R^2 = 0.997$). The overall reaction kinetics are described by

$$\frac{d(c_{\mathrm{ZnO}})}{dt} = (51.6 \pm 1.1)\frac{\mathrm{m^6}}{\mathrm{kmol^2 s}} c\left(\mathrm{Zn}^{2+}\right)^3. \tag{3.1}$$

No influence of the hydroxide concentration was observed. However, this is rather ascribed to the low solubility of LiOH in the applied solvent ethanol leading to an incomplete dissolution of the hydroxide source [14, 64].

With known reaction kinetics the ZnO concentration which is needed in the PBE to express the nucleation rate, is accessible

$$B_{hom} = \frac{3}{2} D(c_{\mathrm{ZnO}} \cdot N_A)^{\frac{7}{3}} \cdot \sqrt{\frac{\gamma}{k_B T}} \cdot V_M \cdot \exp\left(-\frac{16}{3}\pi \cdot \left(\frac{\gamma}{k_B T}\right)^3 \cdot \frac{V_M^2}{(\nu \ln S)^2}\right). \tag{3.2}$$

D is the diffusion coefficient, c_{ZnO} is the monomer concentration of ZnO molecules, N_A is the Avogadro number, k_B is the Boltzmann constant, T is the temperature, V_M is the molecular volume of ZnO, γ is the surface tension that was determined experimentally [65], S is the supersaturation and ν is a stoichiometric factor [14, 64].

However, the simulations revealed already after less than 5 s of reaction time a particle size of ~100 nm which is far away from the experimental observations ($x \ll 5$ nm). To reach the experimentally determined particle size of 2.5 nm an unrealistic low surface tension of 0.01 J m^{-2} would be necessary which is more than one order of magnitude below the experimentally derived value of 0.64 J m^{-2}. Applying the Kelvin equation and calculating the critical cluster size for such a small γ it turns out that already the precursor molecule (~0.32 nm) can be seen as stable nucleus. Thus, the model of classical homogeneous nucleation and growth is not applicable to the present case of ZnO QDs and needs to be revised. Based on considerations of other research groups from literature [69, 80], the chemical reaction of the precursor molecules towards ZnO was assumed to be the rate determining step. This is in agreement with the experimental finding that in case of ZnO mixing plays no role. Thus, two extrema need to be distinguished from each other whenever particle formation is analyzed: fast, mixing controlled nucleation with $BaSO_4$ being the most prominent example [16] and slow, reaction controlled nucleation like it is observed for ZnO QDs [14, 64].

Additionally, also the growth model was revised and adopted to the literature finding of oriented attachment. That means that growth due to transport by diffusion is reduced by an adhesion probability H_P. It takes into account that only "correct" collisions which are leading to so-called magic numbers are allowed [14, 64]. Here, magic numbers define the number of tetrahedral Zn_4OAc_6 structures which aggregate in an ordered way to build larger ZnO clusters [69]. Figure 7 reveals

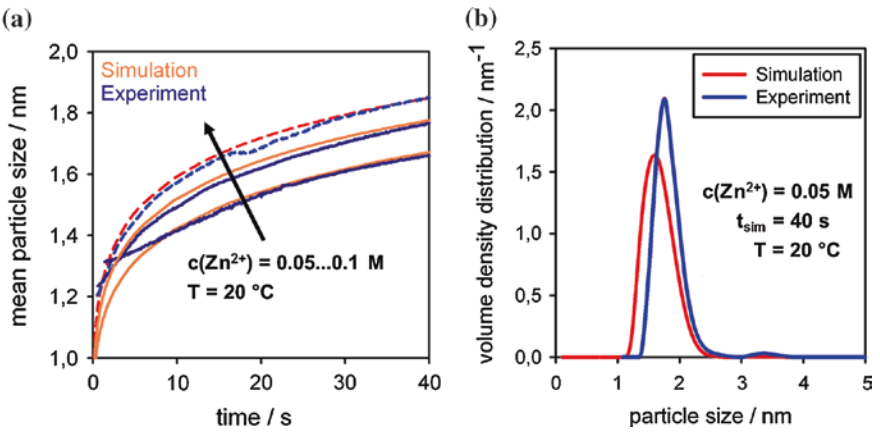

Fig. 7 **a** Measured (*dark blue* and *blue*) and simulated (*orange* and *red*) mean particle sizes $x_{1,3}$ with time for different zinc acetate precursor concentrations (0.05, 0.075 and 0.1 M, c(LiOH) = const. = 0.1 M) at T = 20 °C; **b** Exemplaric comparison between simulated (*red*) and measured (*blue*) PSDs, derived after 40 s of QD synthesis (c(Zn^{2+}) = 0.05 M, c(LiOH) = 0.1 M) (adopted from Segets et al. [64]) [14]

the good agreement between simulation and experiment when reaction controlled nucleation and growth by oriented attachment is considered [14, 64].

3.2 Understanding ZnO Ostwald Ripening

Regarding the finally obtained dispersity of the ZnO particles, nucleation and growth are usually of minor importance. Ostwald ripening which takes over at longer time scales and which is mostly determined by time and temperature was found to be the decisive process. It will be described in the following [36, 37, 65].

In general, ripening is driven by thermodynamics and strongly depends on the local solubility at the particle surface. It has to be clearly distinguished from the previously described nucleation and growth as it takes place at much longer time scales (h/months in contrast to seconds) and global supersaturations ($S_{ripening}$ ~1 in contrast to $S_{Nuc,\ Growth} > 1$). An excellent overview on Ostwald ripening is given by Iggland and Mazzotti [20]. In case of QDs, the most important influencing factors on the ripening rate are the surface tension γ which depends on the local curvature and thus on the particle size x and the temperature T.

Equation 3.3 is the finally derived expression for the ripening rate R that already contains the Gibbs-Thomson (or Kelvin) equation for the size dependent solubility. It is given in its original form where it includes an exponential term as well as in its approximated form by the first term of a Taylor series expansion [14, 64, 73]

$$\begin{aligned} R &= \frac{4 \cdot D \cdot Mc_L^{\infty}\left[\left(\frac{c_{bulk}}{c_L^{\infty}}\right) - \exp\left(\frac{4 \cdot \gamma \cdot V_M}{\nu \cdot x \cdot k_B T}\right)\right]}{\rho_s \cdot x} \\ &\approx \frac{4 \cdot D \cdot Mc_L^{\infty}\left[\left(\frac{c_{bulk}}{c_L^{\infty}}\right) - \left(1 + \frac{4 \cdot \gamma \cdot V_M}{\nu \cdot x \cdot k_B T}\right)\right]}{\rho_s \cdot x}. \end{aligned} \tag{3.3}$$

c_{bulk} is the bulk concentration and ρ_s is the density of the ZnO particles. The ratio between c_{bulk} and c_L^{∞} is the global supersaturation in the liquid which is put into relation to the local, curvature-dependent supersaturation at the particle surface [64].

Although the approximation underestimates the ripening kinetics of very small particles, the error must be taken into account when the ripening rate is solved explicitly like it is the case for the finite element method (FEM) used by *PARSIVAL*. To ensure numeric stability, an additional size-dependent diffusion term R_D needs to be introduced. It prevents the formation of too large gradients and smoothes out small oscillations. However, it is ensured that R_D does not affect the outcome of the final simulation result (less then ± 4 % with respect to $x_{1,3}$). A detailed discussion of all complications introduced by explicit solvers is found in the literature [17, 64]. Accordingly, the final PBE for the Ostwald ripening of ZnO QDs in ethanol is given by

$$\frac{\partial n(x)}{\partial t} = -\frac{\partial (R \cdot n(x))}{\partial x} + \frac{\partial^2 (R_D \cdot n(x))}{\partial x^2}. \tag{3.4}$$

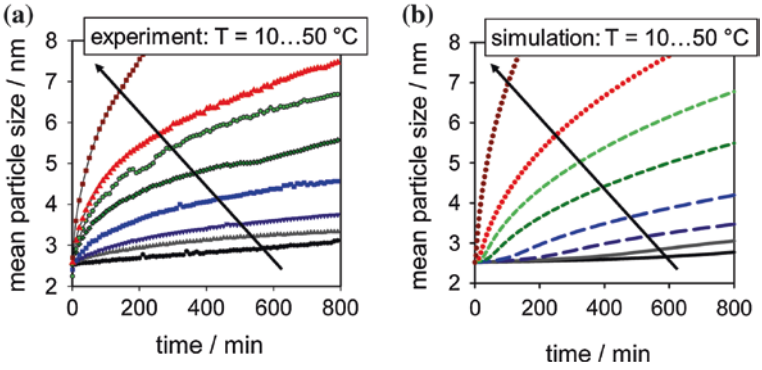

Fig. 8 Comparison between **a** experiment and **b** simulation of ZnO Ostwald ripening with different temperatures (from *bottom* to *top* 10 °C—*black*, 15 °C—*gray*, 20 °C—*dark blue*, 25 °C—*blue*, 30 °C—*dark green*, 35 °C—*green*, 40 °C—*red*, 50 °C—*brown*); all particles were aged from the same starting suspension with a concentration of 0.05 M with respect to Zn^{2+} (adopted from Segets et al. [64]) [14]

A comparison between simulation and experiment for ripening temperatures between 10 and 50 °C is illustrated in Fig. 8. It becomes clear that despite all simplifications that need to be introduced to maintain numeric stability, we could model the ageing of ZnO QDs for more than 12 h in good agreement with the experimental results [14, 64, 65]. Similar results were obtained when comparing the widths of the PSDs in terms of their standard deviations. Also bimodal distributions could be modelled that revealed the dissolution of the smaller particle size fraction with time.

However, for a successful QD processing not only the particle formation needs to be understood. After synthesis, usually a washing step is required to remove excess salts and ligands from the mother liquor. During washing colloidal stability against agglomeration as well as against shape changes needs to be ensured. This will be addressed in the next section.

4 Colloidal Stability Against Agglomeration

Colloidal stability against agglomeration was mainly investigated by means of ZnO QDs during washing. “Washing” in case of QDs means the repeated flocculation of the particles by a non-solvent (which is in case of a hydrophilic particle surface a nonpolar medium and vice versa). The larger flocs are separated from the solvent mixture by centrifugation and can be easily redispersed—in some cases even from the state of a dried powder—by the addition of a good solvent and short stirring or sonication. This finding is quite surprising as dispersion can be already quite challenging for particles below 1 μm [44]. The reason for this behaviour is

ascribed to the fact that the van der Waals attraction is effectively screened by already a monomolecular but complete layer of small molecules at the particle surface and in addition by the absence of any specific bonds between the particles. This effect will be discussed in the following section.

Typically, such a washing cycle is repeated several times. The ZnO QDs of this study are usually precipitated by heptane and analyzed with respect to their colloidal stability by means of extinction measurements. Due to the small particle diameter clearly situated in the Rayleigh regime the primary particles at the standard concentration of about 4 g l^{-1}, with sizes below 10 nm do not cause any measurable light scattering at larger wavelengths in the visible (400 nm). Superimposed absorbance is excluded due to the high ZnO bulk band gap of 3.37 eV (368 nm). However, during ongoing washing the particles become unstable with agglomerates causing remarkable turbidity.

Usually the stability of small particles is explained by DLVO theory where van der Waals attraction and electrostatic repulsion are balanced against each other [10, 75]. However, already the evaluation of ζ-potentials during washing reveals that the measured potentials are small, determined by specific ligand adsorption at the particle surface and not suitable for the explanation of colloidal stability. As it becomes clear from the ζ-potentials that were measured during washing of ZnO QDs and which are shown in Fig. 9a, the particles after synthesis are stable for several hours. In contrast, the particles after three washing cycles with more or less the same magnitude of ζ-potentials are highly unstable. They agglomerate within a few minutes. Thus, only the consideration of electrostatics is not sufficient to explain colloidal stability [35].

However, as it was shown by Reindl and Peukert, in case of particles in the lower nm-range, even a small ligand shell at the particle surface can have a remarkable influence on the overall stabilization. This is due to the fact that the shell significantly screens attractive van der Waals interactions [52, 53]. As it becomes clear from Fig. 9b acetate which is present from particle synthesis and which is coordinated to the particle surface [55] is removed with each washing

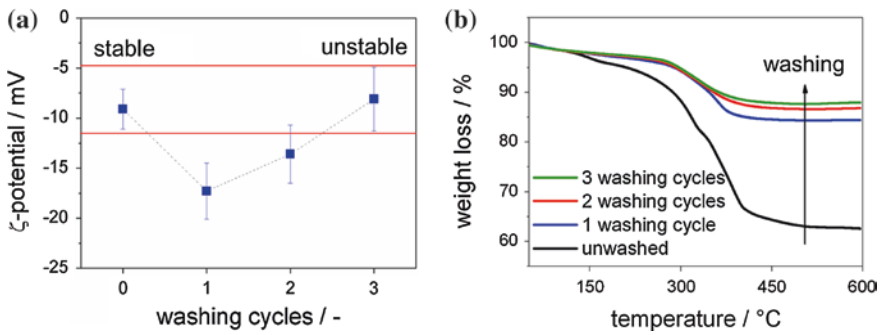

Fig. 9 **a** Evolution of ζ-potentials of ZnO QDs in ethanol during washing; **b** Corresponding thermograms evidencing the ongoing removal of coordinated acetate from the particle surface during purification of the QDs (adopted from Marczak et al. [35]) [61]

step. This was confirmed by ^{13}C NMR (nuclear magnetic resonance) spectroscopy in collaboration with the group of Prof. Schmidt (University of Paderborn).

Hence, two influencing factors need to be balanced: the electrostatic contribution that is accessible via the ζ-potential and the surface coverage that can be determined from thermogravimetric data. The latter needs to be normalized to the surface area of the particles. In case of the three times washed sample the remaining acetate ligand of less than 60 % of a monolayer is unable to maintain stabilization of the ZnO QDs [35, 66, 67].

Therefore the question arises if it is also possible to predict colloidal stability based on standard measurement techniques like it is shown in Fig. 9. Calculations based on DLVO theory using a core-shell model to address the influence of the ligand were performed. They revealed that the total interaction potentials of stable colloids are generally small in the order of ~1 k_BT with neither a large energy barrier nor with a pronounced primary minimum. Thus, the particles behave similar to hard spheres. When "removing" the stabilizing shell, a primary minimum of several k_BT is observed. This minimum is seen to be the explanation for the pronounced instability [35, 61].

However, such calculations are far away from being predictive and thus not applicable to quantify colloidal stability. To balance the two influencing factors, electrostatics and shell thickness, we performed a subsequent study. Thereby we applied the well-known concept of dimensional analysis on the stabilization of ZnO QDs [54]. From a set of nine dimensionless numbers we identified five to be relevant for ZnO QDs:

(i) dimensionless repulsion R including the ζ-potential,
(ii) dimensionless attraction F_A including the Hamaker constant,
(iii) dimensionless concentration C which is represented by the volume fraction c_v,
(iv) the Schmidt number Sc taking into account the ratio of mass transfer by viscous transport and molecular diffusion and
(v) the thickness of the ligand shell related to the mean particle size $x_{1,3}$, which will be denoted as geometry parameter G in the following.

Finally, (i)–(iv) are summarized by a stability parameter

$$S = \frac{R}{F_A} \times \frac{Sc}{C}. \tag{4.1}$$

The Reynolds as well as the Peclet number is zero due to the fact that no external flow field is applied. The distance between the particles related to the thickness of the double layer is similar for all experimental conditions and the dimensionless process time which would be related to the time needed to form the first doublet is not accessible. However, especially the latter would be the target quantity of all studies.

Therefore the dimensional factor "time" needs to be included. We investigated various synthesis conditions in terms of reactant ratios, temperatures, mean particle size and washing history and evaluated each datapoint with respect to G and S.

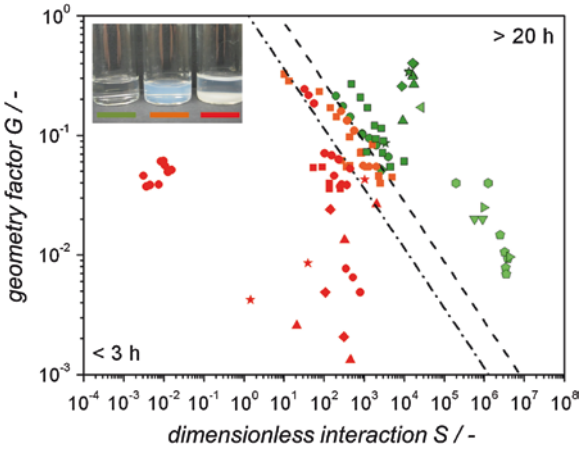

Fig. 10 Geometry factor G against dimensionless interaction S of ZnO QDs for different reactant ratios synthesized at 20 °C (*squares*) and 35 °C (*circles*). Additionally, the dimensionless numbers for quantum dots stabilized with the cationic dendrons CAMOBE (*triangles up*), CADIBE (*diamonds*), and MOMECA (*stars*) [13], as well as larger ZnO nanoparticles (*triangles down*) and other material systems like Si (*hexagons*), Au (*pentagons* and *triangles right*), and ZrO2 (*triangles left*) are shown [23, 24, 33, 53]. *Red color* indicates unstable suspensions, *orange color* represents metastable regions, and *dark* as well as *light green color* indicates suspensions which are stable for more than 20 h. Reprinted with permission from Segets et al. [67]. Copyright 2011 American Chemical Society [61]

Based on the experimental observation if the particles were stable (no scattering) for more than 3 h or more than 20 h we established a stability map. Every process condition that was stable for less than 3 h was colored red (unstable), every operating point stable for more than 3 h but less than 20 h was colored orange (metastable) and every operating point stable for more than 20 h was colored green (stable). Additionally data on Si, Au and ZrO_2 nanoparticles was extracted from the literature, however, usually only information on stable working points is provided (light green). The results are summarized in Fig. 10 [61, 67].

The stability map clearly reveals three regions with high, medium and low stability and is thus suitable for the prediction of colloidal stability from only a few measurements. As expected, with increasing charge of the nanoparticle surface or increasing shell thickness the operating points are shifted more to the stable region. The exact functional relationship between the original target quantity, the dimensionless doublet formation time τ_P and the influencing factors is still unknown. However, the following relation is assumed

$$\tau_P = f\left(\frac{R}{F_A} G^2 \times Sc \times C^{-1}\right) = f(interactions, transport, concentration) \quad (4.2)$$

Though the stability map might change for different material systems due to the fact that the interaction between the ligand and the surrounding medium needs

to be addressed in more detail, this kind of data representation gives important insights into the main contributions on colloidal stability [61, 67].

For a successful processing of small nanoparticles not only colloidal stability against agglomeration needs to be considered. Also the stability against any kind of shape transformation needs to be taken into account. This will be addressed in the following section.

5 Colloidal Stability Against Shape Transformation

Regarding noble metals like e.g. silver or gold, they belong to the most prominent examples for the synthesis of anisotropic shapes found in the literature [50, 82]. They are frequently used material systems regarding the overall research done on shape directing particle synthesis. However, for bringing materials to the market, the as-synthesized particle shapes have to be long-term stable within a certain temperature and concentration range in solution but also after drying [61].

Therefore, in the following silver nanorods will be investigated in more detail due to the fact that silver is identified within all noble metals as the particle system with the strongest tendency to change the shape [61]. To address the important aspect of colloidal stability against shape transformation, a study on the ageing of silver nanorods was performed [8]. CTAB stabilized Ag nanorods with lengths of 250 nm $\pm$ 60 nm and an average aspect ratio of 14 $\pm$ 5 were synthesized in water. Then, their spontaneous decay at room temperature (samples were stored in the dark, no external energy input) was monitored [8, 61].

Figure 11 exemplarily shows scanning electron micrographs (SEM) after synthesis (A), after 2 h of ageing (B), after 24 h of ageing (C) and after 17 d of ageing (D) at 25 °C. It becomes clear that most of the nanorods decay in a comparatively short time. Especially after 2 h a certain thickening of dedicated parts of the nanorods is observed that could be ascribed to a reorganization of material (arrows in Fig. 11b). After 24 h, shorter nanorods are identified that give the impression that a decay of formerly ~200 nm long nanorods occurred during drying (highlighted regions in Fig. 11c). Finally, mostly spherical structures and so-called "nanobuns" with an aspect ratio around 2 (highlighted in Fig. 11d) are found after 17 d of ageing [8, 61].

In addition to SEM that is only applicable to particles deposited onto e.g. Si/SiO_2 wafers, extinction measurements can be used to follow the shape transformation in situ. The results are summarized in Fig. 12a. For monitoring the ageing process with time, the characteristic longitudinal surface plasmon resonance band (SPR) of the silver nanorods at 500 nm is used.

During ageing at 25 °C, the SPR decreases continuously and approaches the transverse SPR at 415 nm. After 17 d only one peak around 420 nm is identified that results from a superposition of the SPR of spherical silver nanoparticles (40 $\pm$ 10 nm) formed during ageing and the SPR of the nanobuns with different, but generally small aspect rations (<5). Extinction measurements and aspect ratio distributions derived from SEM data are summarized in Fig. 12b [8, 61].

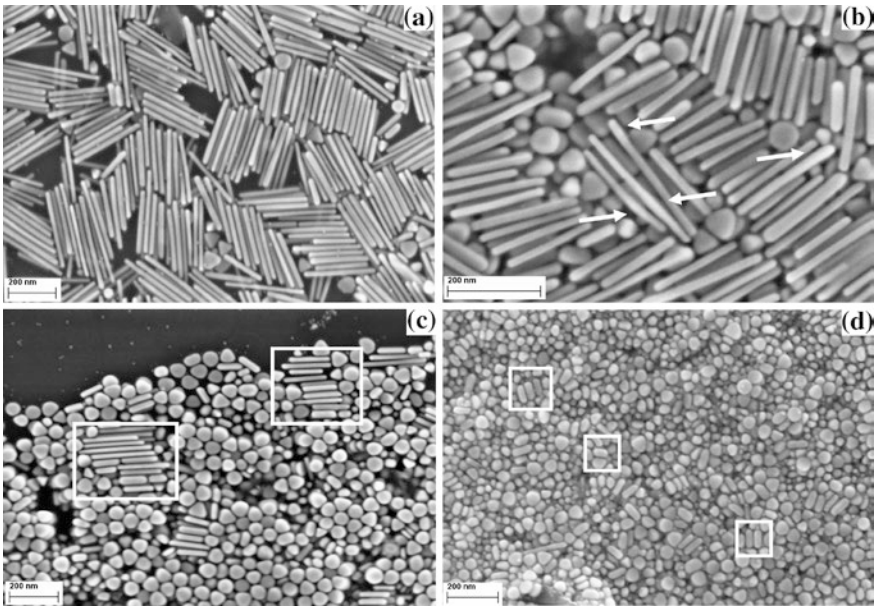

Fig. 11 SEM images of silver nanorods **a** immediately after synthesis; **b** after ageing at 25 °C for 2 h, *arrows* highlight thicker regions within the nanorods; **c** after ageing at 25 °C for 24 h, *squares* highlight separated nanorods; **d** after ageing for 17 d at 25 °C, *squares* highlight nanobuns (adopted from Damm et al. [8]) [61]

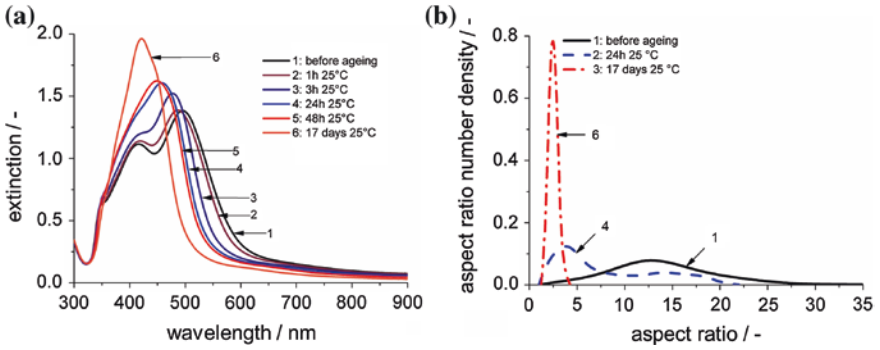

Fig. 12 **a** Extinction spectra of aqueous suspensions of rodlike silver particles as a function of ageing time at 25 °C; **b** density functions of the aspect ratio distribution for freshly prepared silver nanorods (*black solid line*) and for rodlike silver particles aged for 24 h (*blue dashed line*) and 17 d (*red dashed-dotted line*) at 25 °C (adopted from Damm et al. [8]) [61]

Additionally, experiments by anodic stripping voltammetry were performed that proved the absence of any significant amount of dissolved silver ions in the liquid phase (less than 0.006 % of the total amount of silver). Thus, it is assumed that all silver present in the suspension is situated in the solid phase and the following equation needs to be fulfilled

$$m^A_{solid} = V^A_{solid} \cdot \rho_{Ag=} V^B_{solid} \cdot \rho_{Ag} = m^B_{solid}, \tag{5.1}$$

where index A refers to the suspension before ageing and index B to the final suspension after 17 d of ageing. Canceling the density of silver ρ_{Ag} and replacing the overall volume by the number density distributions $q^A_0(x)$ and $q^B_0(x)$ multiplied by the absolute number of particles N^A and N^B and the volume of each particle size fraction $\frac{\pi}{6}x_i^3$, the following equation is derived [8, 61]

$$\sum_i \left(\frac{\pi}{6}x_i^3 \cdot q^A_0(x_i) \cdot \Delta x_i\right) \cdot N^A = M^A_{3,0} = M^B_{3,0} = \sum_i \left(\frac{\pi}{6}x_i^3 \cdot q^B_0(x_i) \cdot \Delta x_i\right) \cdot N^B. \tag{5.2}$$

Thus, the ratio between the particle number before and after ageing is reciprocal to the ratio of the third moment of their number density distributions

$$\frac{N^A}{N^B} = \frac{M^B_{3,0}}{M^A_{3,0}}, \tag{5.3}$$

which was determined for the present study to be around $1/3$ [8, 61].

Therefrom it is concluded that the absolute particle number increases with ageing time [8, 61]. To find a mechanistic explanation of the decay, high resolution TEM studies were performed in collaboration with the group of Prof. Spiecker (CENEM, FAU Erlangen-Nuremberg). From theoretic considerations of Ding et al. and Monk et al. a clear criterion for the critical rod length l_C in dependence of the cross sectional area A_{CS} of multiply twinned nanorods was found [11, 40]

$$l_C = 3.38 \times A_{CS}. \tag{5.4}$$

The proposed decay mechanism is illustrated in Fig. 13.

When the dissolution at shallow surface pits proceeds, the dissolved silver has to go somewhere. From the fact that no dissolved silver could be found in the liquid phase by anodic stripping voltammetry, we conclude that the silver ions must be transient. The released Ag ions have to be reduced back to Ag^0 and reintegrated immediately into the solid phase in such a way that all the different types of particles found by HRTEM—buns, defect-free spheres, and defective spheres—can be explained.

The expected mechanisms are summarized as follows [8, 66]:

(a) Heterogeneous nucleation of metal dissolved from a surface dimple can occur either at other places of the same rod or at the surface of neighboring rods.

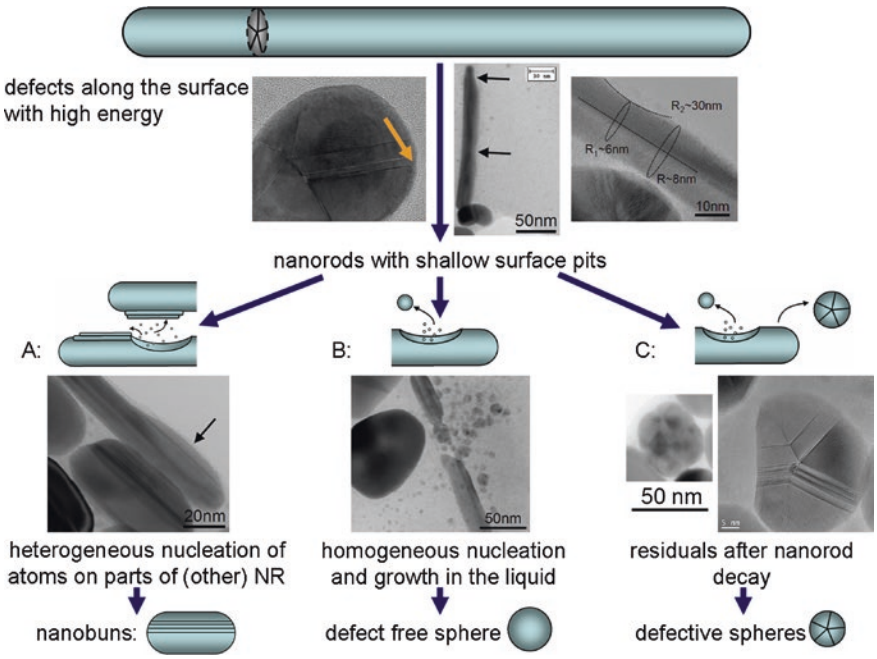

Fig. 13 Proposed model for the shape transformation from nanorods into nanobuns, defect-free spheres and defective spheres (adopted from Damm et al. [8]) [61]

Both pathways lead to the formation of nanobuns, which are remarkably shorter and thicker than the original nanorods.

(b) Homogeneous nucleation can occur directly in the liquid phase without the need of a foreign surface. The small nuclei grow and lead preferentially to defect-free spheres.

(c) As (a) and (b) cause ongoing necking of the particles, the nanorods will rapidly decay into two or more parts as soon as enough material has been dissolved. Therefore small residuals are continuously generated which are still characterized by the fivefold twin structure but are short enough to be stable against further fragmentation. Growth processes are expected to take place at the surface of these defective residuals leading to the formation of spherical particles with a fivefold twin structure.

Noteworthy, after 17 days of ageing only nanords that fulfill the stability criterion of Eq. 5.4 are found [8, 61]. The in-depth understanding of the decay mechanism of those structures also paves the way for an efficient shape stabilization of those nanorods. Due to the fact that the dissolution of material starts at the particle surface, a passivation by ligands like cetyltrimethylammoniumbromide (CTAB) or polyelectrolytes like PDADMAC that can be introduced during the washing procedure are able to significantly enhance the shape stability or even to prevent the decay of noble metal nanorods [18].

6 Classification of Manganese Doped ZnS Quantum Dots

Within the previous chapters we have addressed characterization, particle synthesis and colloidal stability. However, to cover the whole process chain from Fig. 1, post-processing needs to be considered. This will be realized by means of size selective precipitation (SSP) of manganese doped ZnS QDs (ZnS:Mn). The study was done together with the groups of Prof. Mori (Doshisha University, Kyoto) and Prof. Spiecker (CENEM, FAU Erlangen-Nuremberg). SSP was first reported by the groups of Murray and Weller [45, 78] and is often applied not only in the field of QDs but also for noble metal nanoparticles [58, 59]. It exploits the effect that after the gradual addition of a poor solvent into a suspension of QDs, larger particles flocculate first [25, 61, 66]. Nevertheless, the underlying mechanism is not well-understood and SSP was never characterized quantitatively with common methods usually applied in the field of particle technology. Here, we use well established approaches for the description of SSP and for analyzing if SSP could be used as a competitive, scaleable strategy during colloidal processing.

The overall classification procedure is illustrated in Fig. 14. Water is used as a good solvent, flocculation is induced by the gradual addition of 2-propanol. After centrifugation of the flocs the coarse fraction is dried and weighed whereas the supernatant is reused for a subsequent classification step. This is repeated three times leading to four samples #1 … #4 that can be analyzed with respect to their relative coarse fraction [61, 66]

$$g_i = \frac{m_{g,i}}{m_{tot}} = \frac{m_{g,i}}{\sum_i m_{g,i}}. \tag{6.1}$$

As already described in Sect. 2.1, PSDs $q_{g,\#i}$ are calculated from the redispersed coarse material and weighed by their mass fractions g_i. This is illustrated in Fig. 15. Obviously, the size of the fractionized ZnS:Mn QDs becomes smaller during the classification process. Additionally, the mass weighted PSDs were summed up (black dotted line in Fig. 15b).

It becomes clear that the overall error of the mass balance is as small as ±4.4 %. It could be ascribed to slight Ostwald ripening that occurred during

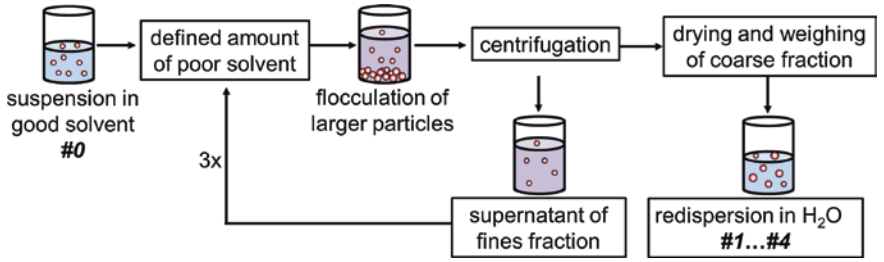

Fig. 14 Overview of the procedure used for classification of ZnS:Mn QDs (adopted from Segets et al. [66]) [61]

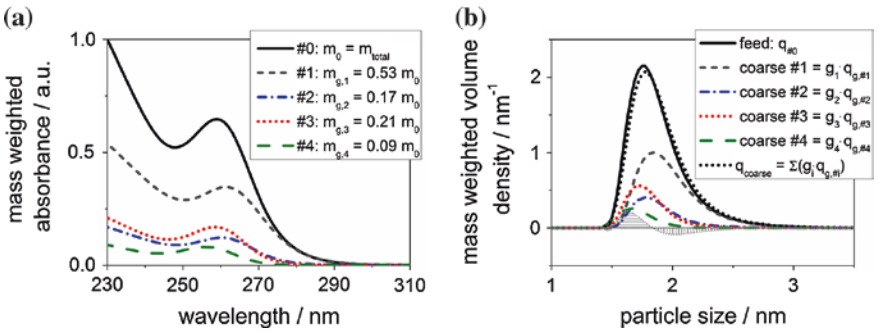

Fig. 15 **a** Absorbance spectra of ZnS:Mn QDs before (#0, *black solid line*), after the first (#1, *gray short dashed line*), the second (#2, *blue dashed-dotted line*), the third (#3, *red dotted line*) and the fourth (#4, *green dashed line*) classification step; all spectra are normalized to the measured value at 230 nm and subsequently scaled by their relative mass fraction g_i; **b** mass weighted PSDs calculated from the measured absorbance spectra of the ZnS:Mn QDs before and during the classification (color code is the same as in a) as well as the sum of the coarse fractions (*thick black dotted line*) in comparison to the feed distribution (*black solid line*); the difference between the two latter proves that negligible ripening occurs during the classification procedure (*light dotted line with horizontal or vertical shaded areas*) (adopted from Segets et al. [66]) [61]

the experiments, small weighing errors or a loss of material in the used glass ware. However, especially when taking the extremely small particle sizes between 1.5 and 3.1 nm into account, this is seen to be an excellent validation of the underlying UV/Vis-based size analysis presented in the previous section on characterization. Only the first classification step #1 turned out to be efficient. For the second #2 and third #3 step mainly a splitting of the feed was observed. Therefore only #1 will be analyzed further whereas for #2 and #3 the reader is referred to the literature [61, 66]. At this point it has to be mentioned that recent studies show that the position of the cut—being described by the cut size x_t—is adjustable along all sizes of the feed PSD by a proper choice of the used good solvent and poor solvent and their volume ratio.

Exemplarily, for the first classification step leading to sample #1, the volume density distribution of the initial sample $q_{\#0}$ is shown in Fig. 16a together with the mass weighted coarse and fines fraction. The classification is analyzed by distinguished parameters which are commonly used in the field of particle technology [61, 66]:

(i) The cut size x_t at the intersection between the mass weighted density distributions of the fines and the coarse to characterize the mean value of the classification.

(ii) The yield of fines η_f (or coarse η_g). It is a measure for the amount of particles with $x < x_t$ (or $x > x_t$) that went to the fines (or to the coarse) fraction referred to the area below the feed distribution with $x < x_t$ (or $x > x_t$,

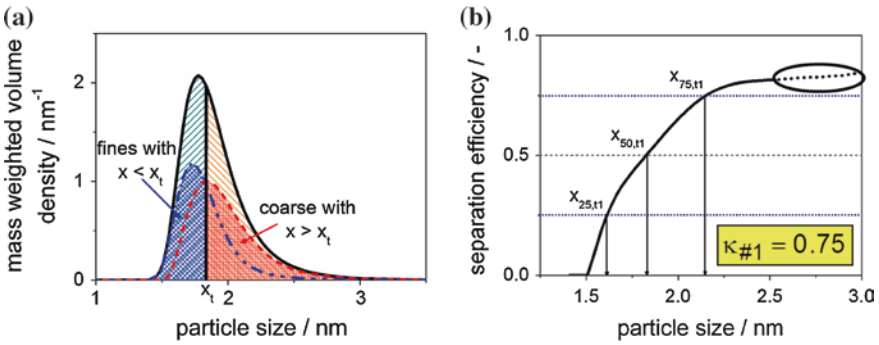

Fig. 16 **a** Volume PSD of the feed (*black solid line*) together with the mass weighted PSDs of the coarse (*red dashed line*) and the fines fraction (*blue dashed-dotted line*) obtained for the first classification step #1; the cut size at $x_{t,1} = 1.83$ nm is indicated by a *vertical line*; **b** separation efficiency $T_1(x)$ and characteristic sizes at $T_1(x) = 0.25$ and $T_1(x) = 0.75$ together with the cut size at $T_1(x) = 0.5$ for the first classification step (*black arrows*). (adopted from Segets et al. [66]) [61]

see Fig. 16a blue and red shaded areas) that are divided by the corresponding green and orange shaded areas of the feed distribution

$$\eta_{f,i+1} = \frac{\int_{x_{\min}}^{x_t} \left[f_{i+1} \cdot q_{f,\#1+1}(x) \cdot dx \right]}{\int_{x_{\min}}^{x_t} \left[q_{\#1}(x) \cdot dx \right]}, \tag{6.2}$$

and

$$\eta_{g,i+1} = \frac{\int_{x_t}^{x_{\max}} \left[g_{i+1} \cdot q_{g,\#1+1}(x) \cdot dx \right]}{\int_{x_t}^{x_{\max}} \left[q_{\#1}(x) \cdot dx \right]}. \tag{6.3}$$

(iii) The size-dependent separation efficiency $T(x)$ which relates the mass weighted density distribution of the coarse fraction to the density distribution of the feed material [29]

$$T_{i+1}(x) = g_{i+1} \cdot \frac{q_{g,\#i+1}}{q_{\#i}}. \tag{6.4}$$

In case of an ideal classification $T(x)$ is expected to be 0 for all $x < x_t$ and 1 for all $x > x_t$.

(iv) The separation sharpness κ which is used to characterize the sharpness of the cut [29]

$$\kappa_i = \frac{x_{25,t}}{x_{75,t}}, \tag{6.5}$$

with $x_{25,t}$ being defined as the particle size for which $T(x) = 0.25$ and $x_{75,t}$ being defined as the particle size for which $T(x) = 0.75$. Thus, κ is a measure

for the deviation of a technical classification from the ideal case that fulfills $\kappa = 1$.

From Fig. 16 it becomes clear that SSP is a highly efficient process to further narrow a feed distribution after synthesis on a size scale of only a few nm. The feed distribution is cut at 1.83 nm close to the modal value. The yields for both, the fines and the coarse fraction, are high with values of 0.64 and 0.67, and the separation sharpness κ_1 indicates a remarkably sharp separation with a value as high as 0.75 [61, 66]. This study clearly revealed, how concepts from particle technology, originally developed for structures larger than 1 µm, are successfully applied to QDs situated clearly below 10 nm. Moreover, SSP is seen to be a comparatively simple process that has a high potential to be successfully scaled up.

7 Summary

In conclusion, these results are an excellent platform for the further development of processing tools for small nanoparticles below 20 nm. We investigated highly relevant aspects of the process chain that needs to be considered. After having established a comparatively easy and in situ applicable characterization technique for quantum confined semiconductor nanoparticles, we analyzed the particle formation mechanism and different aspects of colloidal stability. The latter included agglomeration phenomena but also shape transformations and shape stability. Finally, post-processing was addressed via classification by size selective precipitation (SSP) (Scheme 1).

Based on the findings described in the previous sections a technical process scheme is proposed. The first step of mixing the reactants is of minor importance in case of reaction controlled systems like ZnO and of major importance in case of mixing controlled systems like $BaSO_4$. For the former, static mixers are sufficient whereas for the latter T-mixers operated at high energy inputs are required [15, 60]. After the mixer, the product is transferred to a reactor unit. In case of continuous processes this could be a laminar flow reactor, in case of a batch or semi-batch process a stirred tank could be used. After a defined growth and/or ripening time, primary particles are flocculated by the addition of a defined relative amount of poor solvent. The large flocculates (µm to mm) are isolated by a solid/liquid separation step, using e.g. a filtration setup or a hydrocyclone. Redispersion in a good solvent is performed for smaller quantities below 1 L by sonication or high-shear mixers. In case of larger quantities exceeding ~1 L rotor-stator devices could be an option. The flocculation-redispersion procedure is repeated several times depending on the required purity of the product and the stability of the particles during washing. At this point it has to be mentioned that the only difference between purification and classification is the relative amount of poor solvent which is added. Hence, directly after synthesis all primary particles will be flocculated (purification mode), later—if it is necessary with respect to the target dispersity—the amount of poor solvent

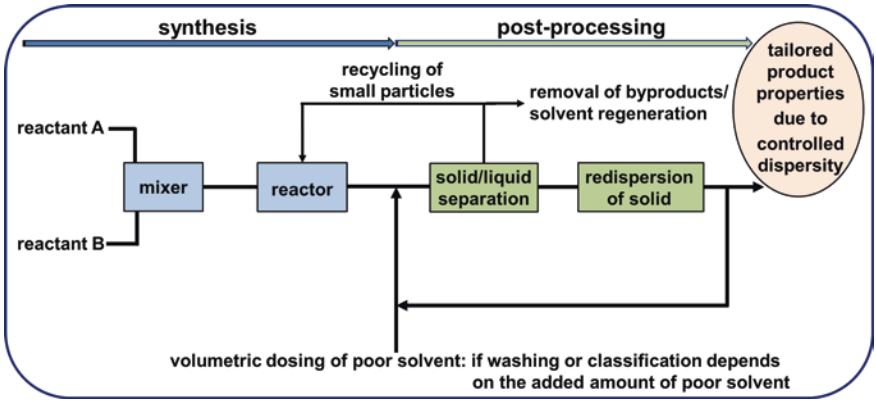

Scheme 1 Sketch of a technical process for the production of stable dispersions of functionalized nanoparticles based on the findings described in the previous sections

is reduced and classification by SSP is performed. Due to continuous monitoring and quality control by in situ characterization based on the formerly established structure-property relationships, a high-quality product with defined electro-optical characteristics is obtained.

Acknowledgments We want to acknowledge the DFG for funding of this project over the past six years (PE 427-18/1-3) and to thank our collaboration partners within SPP 1273 (groups of Prof. Garnweitner, Prof. Schmidt, Prof. Schmid and Prof. Peuker), our collaboration partners at Friedrich-Alexander-Universität Erlangen-Nürnberg (FAU) (groups of Prof. Hirsch, Prof. Spiecker and Prof. Leugering) and our international collaboration partners (groups of Prof. Alivisatos and Prof. Mori). Finally, we want to acknowledge the Cluster of Excellence 'Engineering of Advanced Materials' and the Bavaria California Technology Center 'BaCaTec'.

References

1. Abràmoff MD, Magalhaes PJ, Ram SJ (2004) Image processing with imageJ. Biophotonics Int 11:36–41
2. Alivisatos AP (1996) Semiconductor clusters, nanocrystals, and quantum dots. Science 271:933–937
3. Borrelli NF, Smith DW (1994) Quantum confinement of PbS microcrystals in glass. J Non-Cryst Solids 180:25–31
4. Cademartiri L et al (2006) Size-dependent extinction coefficient of PbS quantum dots. J Am Chem Soc 128:10337–10346
5. Chan EM et al (2010) Reproducible, high troughput synthesis of colloidal nanocrystals for optimization in multidimensional parameter space. Nano Lett 10:1874–1885
6. Dai Q et al (2009) Size-dependent composition and molar extinction coefficient of PbSe semiconductor nanocrystals. ACS Nano 3:1518–1524
7. Dai Q et al (2009) Reply to "comment on 'size-dependent composition and molar extinction coefficient of PbSe semiconductor nanocrystals' ". ACS Nano 3:2054

8. Damm C et al (2011) Shape transformation mechanism of silver nanorods in aqueous solution. Small 7:147–156
9. De Mello Donegá C, Liljeroth P, Vanmaekelbergh D (2005) Physicochemical evaluation of the hot-injection method, a synthesis route for monodisperse nanocrystals. Small 1:1152–1162
10. Derjaguin BV, Landau L (1941) Theory of the stability of strongly charged lyophobic sols and of the adhesion of strongly charged particles in solutions of electrolytes. Acta Phys Chim URSS 14:633–662
11. Ding F et al (2002) Elastic deformation and stability in pentagonal nanorods with multiple twin boundaries. J Phys Condens Matter 14:113–122
12. Emin S et al (2011) Colloidal quantum dot solar cells. Sol Energy 85:1264–1282
13. Gnichwitz J-F et al (2010) Efficient synthetic access to cationic dendrons and their application for ZnO nanoparticles surface functionalization: new building blocks for dye-sensitized solar cells. J Am Chem Soc 132:17910–17920
14. Gradl J (2010) 'Experimentelle und theoretische Untersuchungen der Bildungskinetik diffusions- sowie reaktionslimitierter Systeme am Beispiel der Nanopartikelfällung von Bariumsulfat und Zinkoxid', Doktorarbeit (FAU Erlangen-Nuremberg)
15. Gradl J, Peukert W (2009) Simultaneous 3D observation of different kinetic subprocesses for precipation in a T-mixer. Chem Eng Sci 64:709–720
16. Gradl J et al (2006) Precipitation of nanoparticles in a T-mixer: coupling the particle population dynamics with hydrodynamics through direct numerical simulation. Chem Eng Proc Process Intensification 45:908–916
17. Gröschel M (2013) Optimization of particle synthesis—new mathematical concepts for a controlled production of functional nanoparticles, Doktorarbeit (FAU Erlangen-Nuremberg)
18. Hanisch M (2014) Synthesis and characterizatiof of anisotropic noble metal nanostructures for applications in nanotechnology, Doktorarbeit (in preparation)
19. Hirschmann J, Faber H, Halik M (2012) Concept of a thin film memory transistor based on ZnO nanoparticles insulated by a ligand shell. Nanoscale 4:444–447
20. Iggland M, Mazzotti M (2012) Population balance modeling with size-dependent solubility: Ostwald ripening. Cryst Growth Des 12:1489–1500
21. Kamat PV (2008) Quantum dot solar cells, semiconductor nanocrystals as light harvesters. J Phys Chem C 112:18737–18753
22. Kane RS, Cohen RE, Silbey R (1996) Theoretical study of the electronic structure of PbS nanoclusters. J Phys Chem 100:7928–7932
23. Kim T et al (2005) Control of gold nanoparticle aggregates by manipulation of interparticle interaction. Langmuir 21:9524–9528
24. Kim T et al (2008) Kinetics of gold nanoparticle aggregation: experiments and modeling. J Colloid Interface Sci 318:238–243
25. Komada S et al (2012) Optical properties of manganese-doped zinc sulfide nanoparticles classified by size using poor solvent. Adv Powder Technol 23:872–877
26. Koole R et al (2008) Optical investigation of quantum confinement in PbSe nanocrystals at different points in the brillouin zone. Small 4:127–133
27. Krantz J et al (2011) Solution-processed metallic nanowire electrode as indium tin oxide replacement for thin-film solar cells. Adv Funct Mater 21:4784–4787
28. Landfester K (2009) Miniemulsion polymerization and the structure of polymer and hybrid nanoparticles. Angew Chem Int Ed 48:4488–4507
29. Leschonski K (1977) Das Klassieren disperser Feststoffe in gasförmigen Medien. Chem Ing Tech 49:708–719
30. Lipovskii A et al (1997) Synthesis and characterization of PbSe quantum dots in phosphate glass. Appl Phys Lett 71:3406–3408
31. Liu Y et al (2010) Dependence of carrier mobility on nanocrystal size and ligand length in PbSe nanocrystal solids. Nano Lett 10:1960–1969

32. Lohse SE et al (2013) A simple millifluidid benchtop reactor system for the high-throughput synthesis and functionalization of gold nanoparticles with different sizes and shapes. ACS Nano 7:4135–4150
33. Luo K et al (2008) Dispersion and functionalization of nonaqueous synthesized zirconia nanocrystals via attachment of silane coupling agents. Langmuir 24:11497–11505
34. Ma W et al (2011) Photovoltaic performance of ultrasmall PbSe quantum dots. ACS Nano 5:8140–8147
35. Marczak R et al (2010) Optimum between purification and colloidal stability of ZnO nanoparticles. Adv Powder Technol 21:41–49
36. Meulenkamp EA (1998) Size dependence of the dissolution of ZnO nanoparticles. J Phys Chem B 102:5566–5572
37. Meulenkamp EA (1998) Synthesis and growth of ZnO nanoparticles. J Phys Chem B 102:5566–5572
38. Michalat X et al (2005) Quantum dots for live cells, in vivo imaging, and diagnostics. Science 307:538–544
39. Mićić OI et al (1994) Synthesis and characterization of InP quantum dots. J Phys Chem 98:4966–4969
40. Monk J, Hoyt JJ, Farkas D (2008) Metastability of multitwinned Ag nanorods: molecular dynamics study. Phys Rev B 78:024112
41. Moreels I et al (2007) Composition and size-dependent extinction coefficient of colloidal PbSe quantum dots. Chem Mater 19:6101–6106
42. Moreels I et al (2009) Comment on "Size-dependent composition and molar extinction coefficient of PbSe semiconductor nanocrystals". ACS Nano 3:2053
43. Moreels I et al (2009) Size-dependent optical properties of colloidal PbS quantum dots. ACS Nano 3:3023–3030
44. Müller F et al (2004) Dispersing nanoparticles in liquids. Int J Miner Process 74:31–41
45. Murray CB, Norris DJ, Bawendi MG (1993) Synthesis and characterization of nearly monodisperse CdE (E = S, Se, Te) semiconductor nanocrystallites. J Am Chem Soc 115:8706–8715
46. O'Reilly EP et al (2002) Tight-binding and k.p models for the electronic structure of Ga(In)NAs and related alloys. Semicond Sci Tech 17:870–879
47. Park J et al (2007) Synthesis of monodisperse spherical nanocrystals. Angew Chem Int Ed 46:4630–4660
48. Pesika NS, Stebe KJ, Searson PC (2003) Relationship between absorbance spectra and particle size distributions for quantum-sized nanocrystals. J Phys Chem B 107:10412–10415
49. Pietryga JM et al (2004) Pushing the band gap envelope: mid-infrared emitting colloidal PbSe quantum dots. J Am Chem Soc 126:11752–11753
50. Rai M, Yadav A, Gade A (2009) Silver nanoparticles as a new generation of antimicrobials. Biotechnol Adv 27:76–83
51. Rasband WS (1997–2011) ImageJ [online text], US National Institutes of Health. http://imagej.nih.gov/ij/
52. Reindl A (2009) 'Dispersing and stabilizing semiconducting nanoparticles for application in printable electronics', Doktorarbeit (FAU Erlangen-Nuremberg)
53. Reindl A, Peukert W (2008) Intrinsically stable dispesions of silicon nanoparticles. J Coll Int Sci 325:173–178
54. Russel WB, Saville DA, Schowalter WR (1989) Colloidal dispersions. Cambridge University Press, Cambridge
55. Sakohara S, Ishida M, Anderson MA (1998) Visible luminescence and surface properties of nanosized ZnO colloids prepared by hydrolyzing zinc acetate. J Phys Chem B 102:10169–10175
56. Sapra S, Sarma DD (2004) Evolution of the electronic structure with size in II-IV semiconductor nanocrystals. Phys Rev B 69:125304
57. Sashchiuk A et al (2001) Synthesis and characterization of PbSe and PbSe/PbS core-shell colloidal nanocrystals. J Cryst Growth 240:431–438

58. Saunders SR, Roberts CB (2011) Tuning the precipitation and fractionation of nanoparticles in gas-expanded liquid mixtures. J Phys Chem C 115:9984–9992
59. Saunders SR, Eden MR, Roberts CB (2011) Modeling the precipitation of polydisperse nanoparticles using a total interaction energy model. J Phys Chem C 115:4603–4610
60. Schwarzer HC, Peukert W (2004) Tailoring particle size through nanoparticle precipitation. Chem Eng Commun 191:580–606
61. Segets D (2013) Fundamental aspects during the processing of semiconductor nanoparticles, Doktorarbeit (FAU Erlangen-Nuremberg)
62. Segets D, Peukert W (2014) UV/Vis-Spektroskopie zur in-situ-Teilchengrößenanalyse, Laborpraxis
63. Segets D et al (2009) Real-time monitoring of the nucleation and growth of ZnO nanoparticles using an optical hyper-Rayleigh scattering method. J Phys Chem C 113:11995–12001
64. Segets D et al (2012) A population balance model of quantum dot formation: oriented growth and ripening of ZnO. Chem Eng Sci 70:4–13
65. Segets D et al (2009) Analysis of optical absorbance spectra for the determination of ZnO nanoparticle size distribution, solubility and surface energy. ACS Nano 3:1703–1710
66. Segets D et al (2013) Quantitative evaluation of the size selective precipitation of Mn-doped ZnS quantum dots by size distributions calculated from UV/Vis absorbance spectra. J Nanopart Res 15:1486
67. Segets D et al (2011) Experimental and theoretical studies of the colloidal stability of nanoparticles—a general interpretation based on stability maps. ACS Nano 5:4658–4669
68. Segets D et al (2012) Determination of the quantum dot bandgap dependence on particle size from optical absorbance and transmission electron microscopical measurements. ACS Nano 6:9021–9032
69. Spanhel L (2006) Colloidal ZnO nanostructures and functional coatings: a survey. J Sol-Gel Sci Technol 39:7–24
70. Spanhel L, Anderson MA (1991) Semiconductor clusters in the sol-gel process: quantized aggregation, gelation and, and crystal growth in concentrated zinc oxide colloids. J Am Chem Soc 113(8):2826–2833
71. Steckel JS et al (2003) 1.3 μm to 1.55 μm tunable electroluminescence from PbSe quantum dots embedded within an organic device. Adv Mater 15:1862–1866
72. Su S et al (2012) Nanomaterials-based sensors for applications in environmental monitoring. J Mater Chem 22:18101–18110
73. Talapin DV et al (2001) Evolution of an ensemble of nanoparticles in a colloidal solution: theoretical study. J Phys Chem B 105:12278–12285
74. Tomalino L-OM (2009) Anwendung der optischen Frequenzverdopplung in der Partikelmesstechnik, Doktorarbeit (FAU Erlangen-Nuremberg)
75. Verwey EJW, Overbeek JThG (1948) Theory of the stability of lyophobic colloids. Elsevier, Amsterdam
76. Viswanatha R, Sarma DD (2006) Study of the growth of capped ZnO nanocrystals: a route to rational synthesis. Chem Eur J 12:180–186
77. Viswanatha R et al (2004) Understanding the quantum size effects in ZnO nanocrystals. J Mater Chem 14:661–668
78. Vossmeyer T et al (1994) CdS nanoclusters: synthesis, characterization, size dependent oscillator strength, temperatureshift of the excitonic transition energy, and reversible absorbance shift. J Phys Chem 98:7665–7673
79. Watanabe K et al (2012) Microreactor combinatorial system for nanoparticle synthesis with multiple reactors. Chem Eng Sci 75:292–297
80. Wood A et al (2003) Size effects in ZnO: the cluster to quantum dot transition. Aust J Chem 56:1051–1057
81. Wulkow M, Gerstlauer A, Nieken U (2001) Modeling and simulation of crystallization processes using parsival. Chem Eng Sci 56:2575–2588
82. Xia Y et al (2009) Shape-controlled synthesis of metal nanocrystals: simple chemistry meets complex physics? Angew Chem Int Ed 48:60–103

Part III
Colloidal Systems with Liquid Disperse Phase

Thermodynamic Models for the Adsorption of Alkyl Trimethyl Ammonium Bromides at the Water/Hexane Interface

N. Mucic, A. Javadi, J. Krägel, M. Karbaschi, E.V. Aksenenko, V.B. Fainerman and R. Miller

Abstract Based on surface/interfacial tension isotherms measured for the homologous series of alkyl trimethyl ammonium bromides (C_nTAB) using the drop profile analysis tensiometry the adsorption behavior at three different liquid-fluid interfaces is discussed: solution/air, solution/hexane vapor and solution/hexane bulk liquid. The adsorption behavior can be described by different models. In the presence of hexane molecules (as a bulk liquid or as vapor in the air phase) the adsorption of the C_nTAB molecules can be best described by a competitive adsorption with hexane molecules. This competitive thermodynamic model can be applied successfully to all three interfaces.

Keywords Thermodynamics of adsorption · Liquid/liquid interfacial tension · Drop profile analysis tensiometry · Cationic surfactant · Interaction between surfactant and hexane · Competitive adsorption

1 Introduction

Surfactants adsorb at interfaces and thereby modify the interfacial properties. The base line for understanding the efficiency of surfactants is the thermodynamics of their adsorption at respective interfaces. For a tailored application the main

N. Mucic · A. Javadi · J. Krägel · M. Karbaschi · R. Miller (✉)
Max-Planck Institute of Colloids and Interfaces, Potsdam/Golm, Germany
e-mail: miller@mpikg.mpg.de

A. Javadi
Chemical Engineering Department, University of Tehran, Tehran, Iran

E.V. Aksenenko
Institute of Colloid Chemistry and Chemistry of Water, UNAS, Kiev 03680, Ukraine

V.B. Fainerman
Donetsk Medical University, 16 Ilych Avenue, Donetsk 83003, Ukraine

M. Kind et al. (eds.), *Colloid Process Engineering*,
DOI 10.1007/978-3-319-15129-8_13

adsorption characteristics of the surfactants have to be investigated. For liquid-fluid interfaces, most easily measurable quantities are the surface and interfacial tension, respectively.

The adsorption of surfactants at liquid interfaces and their applications were described in many publications. Also books have been dedicated to this subject. For example in [1] not only the general classification of surfactants and the synthesis and application of the main types of surfactants were discussed but also the adsorption characteristics for a large number of homologous series of surfactants were summarized. In various technologies the action of surfactants is essential, such as in the formation for foams and emulsions [2].

Some specific properties are to be considered when working on the adsorption of surfactants at interfaces between two immiscible liquids. The main complication for non-ionic surfactants is their solubility not only in water but in most organic solvent. Hence, a quantitative description of the adsorption process requires knowledge on the partition coefficients [3]. In contrast, ionic surfactants are essentially insoluble in organic solvents so that any transfer across the interface can be ignored. However, the electric charge of the surfactants changes the corresponding kinetics of adsorption as the surface active ions have to diffuse through an electric double layer before adsorbing at the interface [4].

In addition to the thermodynamic characteristics of the adsorption equilibrium the dynamic dilational visco-elasticity of the surfactant interfacial layers is a very important quantity [5]. This frequency dependent property of a liquid interface is a significant quantity in the stabilization of foams and emulsions. Of course, in many practical situations mixtures of surfactants with particles, polymers or proteins are used, however, these rather complex systems are not the subject of this work.

Before the proposal of Fainerman et al. was published [6], the adsorption of surfactants at water/oil interfaces has been described only by theories developed for the water/air interface. Such a simply adaptation, of course, does not allow considering precisely the effect of the oil molecules. Hence, the interaction between the surfactant and oil molecules could only be specified indirectly summarizing different effects in so-called interaction parameters, such as when using in the Frumkin model [7–9]. In [6] a new thermodynamic picture was proposed which assumes that the oil molecules are part of the adsorption layer and compete with the adsorbing surfactant molecules.

This manuscript provides an overview of a new thermodynamic platform. It can be applied to describe the adsorption of surfactants at water/air, water/alkane vapor and water/liquid alkane interfaces in a quantitative way. The capacity of this new thermodynamic approach is demonstrated here for members of the homologous series of the cationic alkyltrimethylammonium bromides C_nTAB. This homologous series was intensively investigated at different interfaces in various ways and with different experimental methods, for example in [7, 10–12] by tensiometry or in [13–16] by neutron reflection. Studies at aqueous surfactant solution/alkane vapor interfaces with respect to a competitive adsorption of alkane and surfactant molecules were made only very recently and only rather few papers exist

on this subject [17, 18]. However, we are able to show here that the competitive adsorption model is well suited for the description of the adsorption of C_nTABs at all the three mentioned water/fluid interfaces.

2 Thermodynamic Adsorption Models

A theoretical overview on the modelling of adsorption of ionic surfactants at liquid interfaces was recently given by Fainerman and Lucassen-Reynders [19]. The theories are mainly based on the chemical potential of each component in the bulk and at the interface. The interrelation between the chemical potentials and the surface pressure was established first by Butler [20]. Most of the modern theoretical approaches are starting from these relationships. As a peculiarity for ionic surfactants the distribution of ions and counterions in the solution bulk has to be taken into account.

2.1 Theory Based on the Frumkin Adsorption Model

The most frequently used equations of state of ionic surfactant adsorption layers were discussed in [19, 21]. Among these the Frumkin adsorption model describes the adsorption behaviour of ionic surfactants very well

$$\Pi = -\frac{2RT}{\omega_0}\left[\ln(1-\theta) + a\theta^2\right] \tag{1}$$

$$b[c(c+c_2)]^{1/2} f = \frac{\theta}{1-\theta}\exp(-2a\theta) \tag{2}$$

where Π is the interfacial pressure ($\Pi = \gamma_0 - \gamma$), γ and γ_0 are the interfacial tensions in presence and absence of the surfactant, respectively, ω_0 is the partial molar area of the ionic surfactant at $\Pi = 0$, f is the average activity coefficient of ions in the solution bulk, c is the ionic surfactant concentration, c_2 is the (1:1) concentration of inorganic salt, a is the intermolecular interaction constant, and b is the adsorption equilibrium constant, and the average activity coefficient f is given by the Debye-Hückel theory

$$\log f = -\frac{0.5115\sqrt{I}}{1+1.316\sqrt{I}} + 0.055\,I \tag{3}$$

with $I = c + c_2$ as the ionic strength expressed in mol/l. The numerical constants given in this relationship correspond to a temperature of 25 °C.

In [22] it was assumed that the molar area ω of adsorbed surfactant molecules depends linearly on both, the surface pressure Π and surface coverage θ:

$$\omega = \omega_0(1 - \varepsilon \Pi \theta) \tag{4}$$

The coefficient ε is called two-dimensional relative surface layer compressibility coefficient while ω_0 is the molar area of a surfactant molecule at a surface pressure $\Pi = 0$. Values for ε were obtained from measurements for insoluble monolayers as presented in [23]. In later work it was shown that the consideration of a certain compressibility of adsorbed surfactant molecules improves the agreement between the experimental data and theoretical calculations of the surface dilational viscoelasticity [22, 24]. The theoretical analysis presented here for experimental data from literature is based on the set of Eqs. (1)–(4) which is named the Frumkin Ionic Compressibility model (FIC model) [24].

It was also shown that at sufficiently high ionic strength ($c_2 \gg c$ with c_2 as the concentration of added electrolyte) the classical Frumkin model can be applied [1], given by the simplified equations

$$\Pi = -\frac{RT}{\omega_0}\left[\ln(1-\theta) + a\theta^2\right] \tag{5}$$

$$bc = \frac{\theta}{1-\theta}\exp(-2a\theta) \tag{6}$$

Together with Eq. (4) we get the so-called Frumkin Compressibility model (FC model) which can also be used for data analysis supposed the condition $c_2 \gg c$ is fulfilled. As it becomes clear from the set of equations discussed above, no specific consideration of the oil phase was made. Any particular interaction of the oil molecules are somehow hidden in the model parameters and a quantitative understanding is impossible.

2.2 *Co-adsorption of Surfactants with Oil Molecules from the Vapor Phase*

Let us now consider the co-adsorption of surfactant molecules with alkane molecules at the solution/alkane vapor interface. This situation can be described by a two-component system in which component 1 corresponds to the alkane molecules adsorbed from the gas phase, while component 2 is the surfactant adsorbing from the aqueous solution bulk. We can assume that a mixed liquid adsorption layer is formed without any phase transitions. Using some simplifications discussed in [25], most of all the assumption $\omega_{10} \cong \omega_{20}$, we obtain an equation of state for the mixed surface layer:

$$-\frac{\Pi\omega_0^*}{RT} = \ln(1-\theta_1-\theta_2) + a_1\theta_1^2 + a_2\theta_2^2 + 2a_{12}\theta_1\theta_2 \tag{7}$$

The equation contains the average molar area $\omega_0^* = \frac{\omega_{10}\theta_1 + \omega_{20}\theta_2}{\theta_1 + \theta_2}$, and the surface coverages $\theta_i = \omega_i \cdot \Gamma_i$($\Gamma_i$ is the adsorption) of the two components *i*. In [25] it was demonstrated how the respective adsorption isotherm has to be modified in order to use the vapor pressure P of the alkane molecules instead of a bulk concentration. This adsorption isotherm then reads:

$$d_1 P_1 + k_1\theta_2 = \frac{\theta_1}{(1-\theta_1-\theta_2)} \exp\left[-2a_1\theta_1 - 2a_{12}\theta_2\right] \tag{8}$$

where d_1 is the adsorption activity coefficient of the alkane. The second term on the left hand side of Eq. (8) with the coefficient k_1 accounts for the interaction of the hydrocarbon chain of surfactant on the adsorption of alkane molecules from the vapor phase. For water-soluble surfactants (component 2) the adsorption isotherm reads:

$$b_2 c_2 = \frac{\theta_2}{(1-\theta_1-\theta_2)} \exp\left[-2a_2\theta_2 - 2a_{12}\theta_1\right] \tag{9}$$

The intermolecular interaction coefficient a_{12} influences the co-adsorption of surfactant and alkane molecules, and the coefficient ε in Eq. (4) takes into account the surface layer compressibility.

2.3 Co-adsorption of Surfactants with Oil Molecules from the Oil Bulk Phase

The set of equations proposed for the water/alkane vapor system is also suitable for the description of the co-adsorption at the aqueous solution/liquid alkane interface. In traditional adsorption models, for instance in [26], the decrease in surface tension is explained exclusively by the adsorption of surfactant molecules and the interaction between surfactant and alkane molecules is not considered specifically. The physical picture of the new approach is a competitive adsorption of surfactant and alkane molecules at the water/alkane interface [6]. Hence, the alkyl chains of the surfactants do not only find a hydrophobic environment at the interface, but the alkane molecules also adsorb and compete for the space in the interfacial layer. Due to the very high molar concentration of alkane molecules in the alkane bulk their adsorption is very fast. The characteristic adsorption time of the alkane molecules is surely less than 10^{-4} s.

In contrast to the water/alkane vapor interface, for the alkane adsorption at the aqueous solution/liquid alkane interface we have to use the adsorption equation from the liquid alkane phase as discussed in [6]:

$$b_1 c_1 = \frac{\theta_1}{(1-\theta_1-\theta_2)} \exp\left[-2a_1\theta_1 - 2a_{12}\theta_2\right] \tag{10}$$

The parameter b_1 refers to the surface activity and c_1 the concentration of the alkane molecules.

To summarise the results obtained for the theoretical background, it was shown that essentially the same model can be used to describe the adsorption of ionic surfactants at the water/air, water/alkane vapor and water/liquid alkane interfaces. For the water/air interface we use the set of Eqs. (1)–(4), for the water/vapor interface Eqs. (7)–(9), and for the water/bulk oil interface Eqs. (7), (9) and (10). In the following sections the theoretical models are used to fit experimental surface and interfacial tension data obtained in studies of C_nTABs at the three mentioned different water/fluid interfaces.

2.4 Comparison of Experimental Data with the Theoretical Adsorption Models

Using surface and interfacial tension data for some members of the homologous series of cationic surfactants we want to demonstrate to suitability of the thermodynamic approach of competitive adsorption for the formation of adsorption layers at different water/fluid interfaces, including those to alkane vapor and liquid alkane. We will restrict ourselves here to hexane as the oil or vapor phase. The particular effects of the alkane chain length have been discussed for example in [9]. For oils different from alkanes less systematic data exist, however, a specific impact of the molecular structure can be expected and the molecular characteristics might be rather different from those we obtained for alkanes.

2.5 Surface Tension Isotherms of C_nTABs at the Water/Air Interface

The most advanced studies on the adsorption of the cationic alkyl trimethyl ammonium bromides C_nTAB at the water/air interface are summarized in Fig. 1 in form of the equilibrium surface tension isotherms. Data are given for four alkyl trimethyl ammonium bromides C_nTAB with n = 10, 12, 14 and 16, respectively, plotted as a function of the surfactant mean ionic activity c*. In case no salt is added, $c^* = fc$, with f being the activity coefficient calculated from Eq. (3). The data in Fig. 1 correspond to measurements at room temperature (around 21 °C) and are taken from literature [7, 24, 27]. The agreement between the different references is very good. Figure 1 presents calculated isotherms (solid lines) using the FIC model given by the set of Eqs. (1)–(4).

As discussed first in [24] and later summarized in a review [21] the optimum value for the surface compressibility does not much effect the equilibrium surface tension isotherm but leads to a much better agreement with adsorption data for

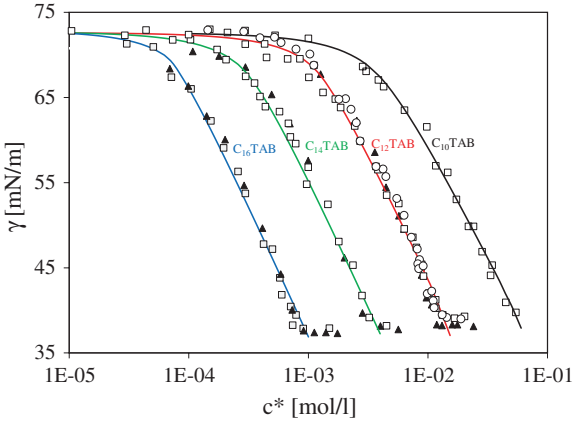

Fig. 1 Equilibrium surface tension of C_nTAB solutions as a function of the mean ion activity c* measured at a temperature of 20–22 °C: *square box*—data taken from [7]; *circle*—data taken from [27]; *black triangle*—data taken from [24]; the *solid curves* are calculated with the FIC model using the parameters summarized in Table 1

Table 1 Best fit parameters of the FIC model, Eqs. (1)–(4) with $\varepsilon = 0.007$ m/mN, used to calculate the dependencies for the C_nTAB solutions shown in Fig. 1

n	ω_0 [10^5 m^2/mol]	a [-]	b [l/mol]
10	3.68	1.05	7.97×10^1
12	3.60	1.30	2.14×10^2
14	3.66	1.45	8.19×10^2
16	3.54	1.56	2.84×10^3

Data taken from [21]

example directly determined by neutron scattering [13–15] and with surface dilational rheology [21]. From the best fit of the experimental data given in Fig. 1a value of $\varepsilon = 0.010$–0.012 m/mN was obtained in [22], which leads to an overestimation of the molar areas. In [22] for C_nTAB a value of $\varepsilon = 0.007$ m/mN was obtained which led to lower ω_0 values. The values of the other model parameters are given in Table 1.

The values for the molar area ω_0 for all C_nTAB discussed here are essentially the same and slightly lower than those presented in [24] which is caused by the consideration of the intrinsic compressibility here. A more detailed discussion of all model parameters and their dependence on the alkyl chain length and effect of added electrolyte was given in [21].

2.6 Co-adsorption of Hexane and C_nTAB Molecules at the Water/Hexane Vapor Interface

The adsorption of hexane from the vapor phase on $C_{12}TAB$ solution drops was studied in [17, 18] using the drop profile analysis tensiometer PAT-1. In these experiments a solution drop was formed in a closed cuvette and after a time of about 300 s 1 ml of hexane was injected into the cuvette. When the cell is

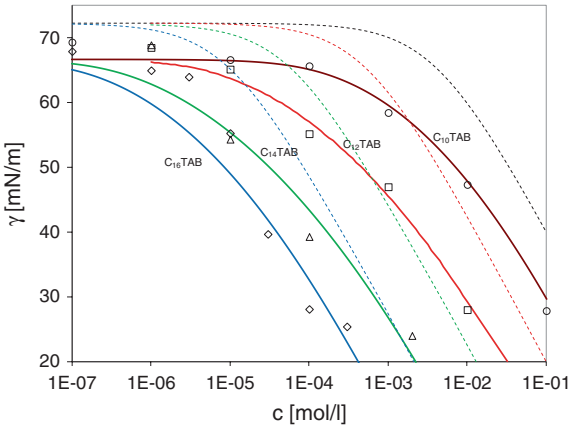

Fig. 2 Interfacial tension isotherms for aqueous solutions of C_nTAB in 10 mM phosphate buffer (pH 7) at the solution/hexane vapor interface: symbols are experimental data taken from [18]; *bold curves*, values calculated from Eqs. (7)–(9) using the parameters summarized in Table 2; *dashed curves* are adsorption data at the solution/air interface re-plotted from Fig. 1

Table 2 Parameter values obtained for the FC model from best fit of C_nTAB solutions in 10 mM $NaH_2PO_4/NaHPO_4$ phosphate buffer at the solution/air (dashed lines calculated using the values for the parameter b) and solution/hexane vapor interface (solid lines calculated using the parameter b_2)

n	*b* [l/mol]	a_{12}	b_2 [l/mol]
10	2.49×10^2	1.6	7.5×10^2
12	1.95×10^3	2.4	7.0×10^3
14	1.8×10^4	2.4	1.0×10^5
16	1.1×10^5	1.8	7.0×10^5

Data taken from [21]

sufficiently well closed after about two minutes a saturated hexane vapor atmosphere is established. In a second series of experiments, the saturated hexane atmosphere was first established and then the solution drop was formed. In both ways, isotherms of various surfactants with co-adsorbed hexane molecules from the vapor phase were obtained.

The surface tension isotherms measured after 300 s adsorption time of C_nTAB solutions at the solution/hexane vapor (symbols) and solution/air (dashed lines) interfaces are shown in Fig. 2.

From Fig. 2 the significant decrease of interfacial tension due to the co-adsorption of hexane molecules from the vapor phase at the drop surface is easily visible. At the experimental temperature of 25 °C the partial pressure of saturated hexane vapor is about 2.000 Pa. The solid lines in Fig. 2 were calculated using the parameter values required for Eqs. (7) and (8) were given in Table 2. Note, for very low surfactant concentrations, the obtained parameter values describe the adsorption effect of only the hexane molecules. The values $d_1 = 6 \times 10^{-5}$ 1/Pa and $\omega_{10} = 3.5 \times 10^5$ m^2/mol provide the best fit for the experimental data [17]. From

the data summarized in Table 2 we see that the b_2 values, referring to solution/hexane vapor interface, are essentially higher than the b values obtained for the solution/air interface. The fact that the mutual interaction parameter a_{12} has high and positive values supports the idea about the co-adsorption of surfactant and hexane. We can conclude that at low C_nTAB concentrations the adsorption of hexane adsorption is supported while at higher C_nTAB concentrations the hexane molecules are more and more replaced by increasingly adsorbing C_nTAB molecules.

2.7 Adsorption Characteristics of Selected CnTABs at the Water/Hexane Interface

Tin literature there are many studies on the adsorption of ionic surfactants at aqueous solution/alkane interface, such as [11, 26, 28–31]. A direct comparison of the adsorption behaviour of C_nTAB with alkyl chain lengths 10, 12, 14 and 16 at the water/air and water/hexane interfaces was presented in [8] and it was shown that the FIC model described the experimental data for both interfaces quite well. The new model proposed in [6], leading to the set of Eqs. (7), (9) and (10), has shown to be superior over the FIC model as it allows to assume that the oil molecules provide not only a hydrophobic environment for the adsorbing surfactant molecules but the adsorb themselves at the interface. The equilibrium interfacial tension isotherms presented in Fig. 3 for four C_nTABs (n = 10, 12, 14 and 16) adsorbed at the aqueous phosphate buffer solution/hexane interfaces allow to demonstrate the feasibility of the given physical picture of a co-adsorption of surfactant and alkane molecules.

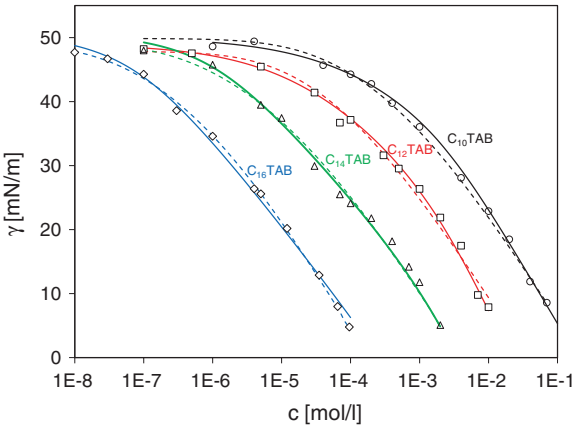

Fig. 3 Interfacial tension isotherms of C_nTAB at the interface between the aqueous solution and a hexane bulk phase in presence of 10 mM phosphate buffer (pH 7); *symbols* are experimental data taken from [8]; *dashed lines* are calculated with the FIC model; *solid lines* are calculated from Eqs. (7), (9) and (10) with the parameters summarized in Table 3

Table 3 Parameters for Eqs. (7), (9) and (10) used to best fit the data for aqueous C_nTAB solutions (component 2) at the water/hexane interface

n	b_2 [l/mol]	ω_{20} [10^5 m^2/mol]	a_2	a_{12}
10	4.3×10^4	3.45	0.8	1.1
12	2.0×10^5	3.5	1.3	1.4
14	1.2×10^6	3.4	1.4	1.6
16	1.2×10^7	3.2	1.6	1.7

$\varepsilon_2 = 0.005$ m/mN; data taken from [9] and [21]

The value of the hexane concentration c_1 can be calculated from its molecular mass and density. For 100 % hexane we get $c_1 = 7.58$ mol/l. The b_1 value can then be calculated via the decrease of the surface tension from the water/air at the water/hexane interface, i.e. from 72 to 51 mN/m, without any C_nTAB adsorption. For $\omega_1 = 3.3 \times 10^5$ m^2/mol and $\varepsilon_1 = 0$ this condition yields $b_1 = 2.6$ l/mol.

The dashed theoretical curves in Fig. 3 were calculated in [8] by using the FC or FIC models, while the solid curves were obtained using Eqs. (7), (9) and (10) and the C_nTAB parameters in Table 3. The b_2 values presented in Table 3 are about two orders of magnitude higher than those obtained for the FC model and more than one order of magnitude higher for the FIC model. For example, for $C_{14}TAB$ we obtain a value of $b = 9.3 \times 10^4$ l/mol for the FIC model while for the co-adsorption model we obtain $b_2 = 1.2 \times 10^6$ l/mol (see Table 3). The b_2 values in Table 3 fulfil the rules for a homological series of surfactant as expected from the Traube rule [32]. The rather large values of the interaction coefficient a_{12} indicate a significant increase of the adsorption activity of the C_nTAB molecules at the water/alkane interface.

2.8 *Effect of Alkane Chain Length on the Adsorption of C_nTABs at Water/Liquid Alkane Interfaces*

As mentioned further above, the chain length of the oil molecules can influence the adsorption properties of surfactants at the water/oil interface. It can be expected that for systems with matching alkyl chain length the adsorption properties could be special. This question was discussed recently in [9] for the two members of the homologous series $C_{10}TAB$ and $C_{12}TAB$ at seven different water/alkane interfaces (hexane to tetradecane). In these studies, however, no clear dependences of model parameters on the chain length of the alkane phase or of the surfactant were detected.

The composition of the adsorption layer by hexane and C_nTAB molecules at the hexane/solution interface is shown in Fig. 4. At very low surfactant concentration the adsorption layer contains essentially hexane and water molecules. With increasing surfactant concentration the adsorption layer contains more and more C_nTAB molecules. The interfacial activities of the C_nTAB and of hexane are mainly determined by the products b_ic_i, respectively.

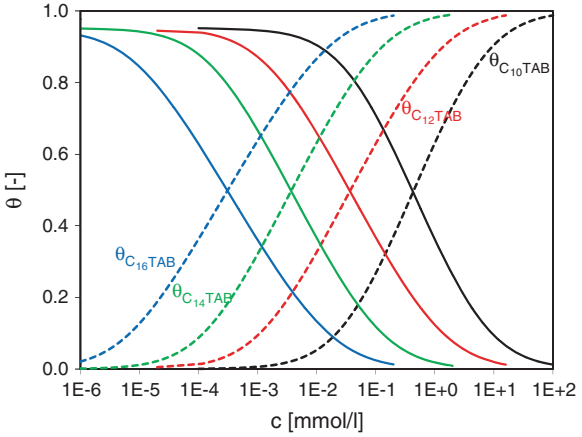

Fig. 4 Dependencies of partial surface coverages on the surfactant concentration c in the aqueous solution phase at the water/hexane interface for CnTAB (n = 10, 12, 14, 16, respectively); *solid lines*—coverage by hexane molecules; *dashed lines*—coverage by surfactant molecules

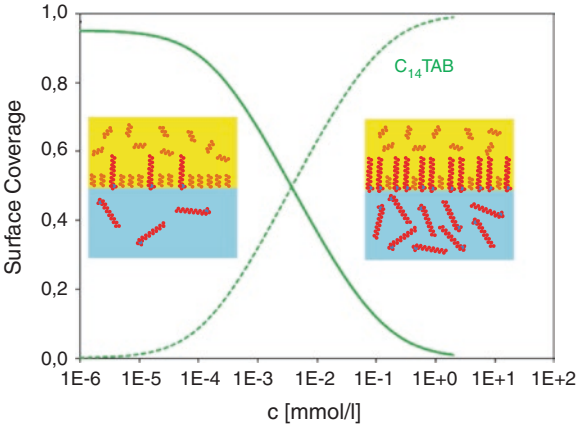

Fig. 5 Schematic of the molecular composition of interfacial layers at the interface between a surfactant solution and an oil bulk phase

For a more detailed analysis of the effect of different alkane phases on the adsorption characteristics of C_nTABs and other surfactants at water/alkane interfaces, more quantitative experiments are required.

3 Summary and Outlook

In the presented work different ways of describing the adsorption layers of the ionic surfactants are considered, assuming an electro-neutral double layer. Additionally, the definition of the dividing surface was used as proposed by Lucassen-Reynders [33] a specific compressibility of the adsorption layer was taken into account [23]. The new theoretical model based on a competitive

adsorption of surfactant and alkane molecules at the interface appears to be superior over versions of the classical Frumkin model. Its applicability is demonstrated by a very good agreement with the experimental results obtained in [21] for the homologous series of C_nTAB (n = 10, 12, 14 and 16) at the aqueous solution/hexane vapor and water/hexane bulk interface. The results obtained so far allow drawing the following picture shown in Fig. 5. It demonstrates the competition of oil and surfactant molecules at the interface, depending on the surfactant concentration in the solution bulk.

Additional experiments with C_nTAB solutions at the water/alkane (as vapor as well as bulk phase) interface are necessary to further approve and refine the new theoretical models. An extension of the model to non-ionic surfactants or to mixtures of surfactants would be favourable for this target. Most efficient in this direction are obviously studies of the interfacial dynamics, such as adsorption kinetics or dilational rheology experiments. As the result of such dynamic studies we cannot expect a quantification of the alkane (or in general of the oil) molecules' dynamic in the adsorption layer but their impact on the dynamics of the adsorbed surfactant molecules. Their characteristic times of adsorption or of diffusional transport should be changed due to the co-adsorbed oil molecules. Depending on the number of oil molecules in the adsorption layer and the corresponding strength of interaction the characteristics of the surfactants will change.

Acknowledgements The work was supported by projects of the DFG (Mi418/18-2), the DLR (50WM1129), and the COST actions CM1101 and MP1106.

References

1. Fainerman VB, Möbius D, Miller R (eds.) (2001) Surfactants—chemistry, interfacial properties and application. In: Studies in interface science, vol 13. Elsevier, Amsterdam
2. Maldonado-Valderrama J, Martin-Rodriguez A, Galvez-Ruiz MJ, Miller R, Langevin D, Cabrerizo-Vilchez MA (2008) Colloids Surf A 323:116–122
3. Ravera F, Ferrari M, Liggieri L (2000) Adv Colloid Interface Sci 88:129–177
4. Kalinin VV, Radke CJ (1996) Colloids Surf A 114:337–350
5. Monroy F, Ortega F, Rubio RG, Ritacco H, Langevin D (2005) Phys Rev Lett. **95**, Article Nr. 056103
6. Fainerman VB, Mucic N, Pradines V, Aksenenko EV, Miller R (2013) Langmuir 29:13783–13789
7. Bergeron V (1997) Langmuir 13:3474–3482
8. Pradines V, Fainerman VB, Aksenenko EV, Krägel J, Mucic N, Miller R (2010) Colloids Surf A 371:22–28
9. Mucic N, Kovalchuk NM, Aksenenko EV, Fainerman VB, Miller R (2013) J Colloid Interface Sci 410:181–187
10. Medrzycka K, Zwierzykowski W (2000) J Colloid Interface Sci 2000(230):67–72
11. Haydon DA, Taylor EH (1962) Trans Faraday Soc 58:1233–1250
12. Mucic N, Kovalchuk NM, Pradines V, Javadi A, Aksenenko EV, Miller R (2014) Colloids Surf A 441:825–830
13. Simister EA, Thomas RK, Penfold J, Aveyard R, Binks BP, Cooper P, Fletcher PDI, Lu JR, Sokolowski A (1992) J Phys Chem 96:1383–1388

14. Lyttle DJ, Lu JR, Su TJ, Thomas RK (1995) Langmuir 11:1001–1008
15. Purcell IP, Lu JR, Thomas RK, Howe AM, Penfold J (1998) Langmuir 14:1637–1645
16. Binks BP, Crichton D, Fletcher PDI, MacNab JR, Li ZX, Thomas RK, Penfold J (1999) Colloids Surf A 146:299–313
17. Javadi A, Moradi N, Karbaschi M, Fainerman VB, Möhwald H, Miller R (2011) Colloids Surf A 391:19–24
18. Mucic N, Moradi N, Javadi A, Aksenenko EV, Fainerman VB, Miller R (2014) Colloids Surf A 442:50–55
19. Fainerman VB, Lucassen-Reynders EH (2002) Adv Colloid Interface Sci 96:295
20. Butler JAV (1932) Proc Roy Soc Ser A 135:348–375
21. Fainerman VB, Aksenenko EV, Mucic N, Javadi A, Miller R (2014) Soft Matter 10:6873–6887
22. Fainerman VB, Miller R, Kovalchuk VI (2003) J Phys Chem B 107:6119–6121
23. Fainerman VB, Vollhardt D (2003) J Phys Chem B 107:3098–3100
24. Stubenrauch C, Fainerman VB, Aksenenko EV, Miller R (2005) J Phys Chem 109:1505–1509
25. Fainerman VB, Aksenenko EV, Kovalchuk VI, Javadi A, Miller R (2011) Soft Matter 7:7860–7865
26. Danov KD, Kralchevsky PA (2012) Colloid J 74:172–185
27. Asnacios A, Langevin D, Argillier J-F (1996) Macromolecules 29:7412–7417
28. Fang H, Shah DO (1998) J Colloid Interface Sci 205:531–534
29. Azizian S, Kashimoto K, Matsuda T, Matsubara H, Takiue T, Aratono M (2007) J Colloid Interface Sci 316:25–30
30. Schlossmann ML, Tikhonov AM (2008) Annu Rev Phys Chem 59:153–177
31. Takiue T, Tottori T, Tatsuta K, Matsubara H, Tanida H, Nitta K, Uruga T, Aratono M (2012) J Phys Chem B 116:13739–13748
32. Traube J (1891) J Liebigs Ann Chem 265:27–55
33. Lucassen-Reynders EH (1966) J Phys Chem 70:1777–1785

Filled Vesicles Formed by Phase Transfer of Emulsions or Microemulsions

Christian Strötges, Evelin Schmitte and Heinz Rehage

Abstract Vesicles or liposomes are of great interest as drug delivery system or simple model for cell membranes. In biological environments vesicles are capable of transporting messenger molecules in high concentrations within a cell. For industrial applications, it is necessary to produce vesicles which are unilamellar, monodisperse, easy to adjust in size, and which can be filled with various types of active compounds. Particularly the defined filling of these tiny compartments has not yet been brought to a large scale. Our research project within the DFG-priority program 1273 (Colloid Process Engineering) was focused on a new method, which can easily be used for the continuous production of such colloidal particles. Moreover, the novel approach allows us to use a large variety of incorporated ingredients. The high encapsulation efficiency in addition with the flexible synthesis facilitates the utilization as a drug carrier system. On grounds of the interesting structure, consisting of an unilamellar surfactant shell, which is swollen with oil, and an enclosed aqueous reservoir (core), the produced colloidal particles may alternatively be denoted as a special case of water-in-water-emulsions. The synthesis of these particles occurred in three steps. First, a water phase was covered by an oil phase containing surfactants or lipids. A water-in-oil emulsion or microemulsion was then added to the oil phase. In the third step the phase transfer of aqueous droplets from the oil phase into the underlying water phase was stimulated by sedimentation, flow, electric forces or centrifugation processes. During this phase transition a small amount of the organic solvent was entrapped in the ultra-thin membranes and influenced the properties of the filled, vesicular structures. The thin layer of organic solvents

C. Strötges (✉) · E. Schmitte · H. Rehage
Physikalische Chemie II, TU Dortmund, Otto-Hahn-Straße 6, 44221 Dortmund, Germany
e-mail: christian.stroetges@tu-dortmund.de

E. Schmitte
e-mail: evelin.kubatta@tu-dortmund.de

H. Rehage
e-mail: heinz.rehage@tu-dortmund.de

M. Kind et al. (eds.), *Colloid Process Engineering*,
DOI 10.1007/978-3-319-15129-8_14

reduced the diffusion processes from the core of the vesicles into the surrounding water phase. This might be of special advantage for the encapsulation of water soluble ingredients as drugs or other interesting compounds. It also offers the opportunity, to store oil soluble substances in the swollen membranes of the vesicles. On the other hand the thin oil layers surrounding the vesicles induced creaming processes and influenced the stability of these aggregates. For all applied experimental techniques we systematically measured the encapsulation capacity, the size of the filled vesicles, the amount of entrapped oil within the membranes and the stability of these aggregates. It turned out, that the jet-stream and the electrospray technique provided the best results concerning long-term stability, vesicle production and encapsulation efficiency. Due to the broad spectrum of different applications, we could use the phase-transfer process for the production of tailor-made, filled and swollen vesicles, which showed interesting properties.

Keywords Filled vesicles · Encapsulation method · Phase transfer across fluid interfaces · Multiple emulsions · Water-in-water emulsions

List of Symbols

A	surface area (nm²)
c_f	carboxyfluorescein concentration with intact vesicles (mmol/l)
c_v	carboxyfluorescein concentration after destroying vesicles (mmol/l)
d	diameter (nm, µm)
d_m	mean diameter (nm, µm)
d_i	inner diameter (nm, µm)
EE	encapsulation efficiency (%)
Q	flow rate (ml/min)
P	pressure (Pa)
PDI	polydispersity index (-)
T	time (s, min)
γ	interfacial tension (mN/m)
ε'	interfacial dilational storage modulus (mN/m)
ε''	interfacial dilational loss modulus (mN/m)
λ	wavelength (nm)

1 Introduction

In a series of experiments, we produced giant vesicles with dimension of several microns up to several millimeters by phase transfer processes [1, 2]. Giant vesicles are often used as model membranes for biological cells. Due to their size, it is possible to investigate typical effects like budding, fission or membrane fusion by

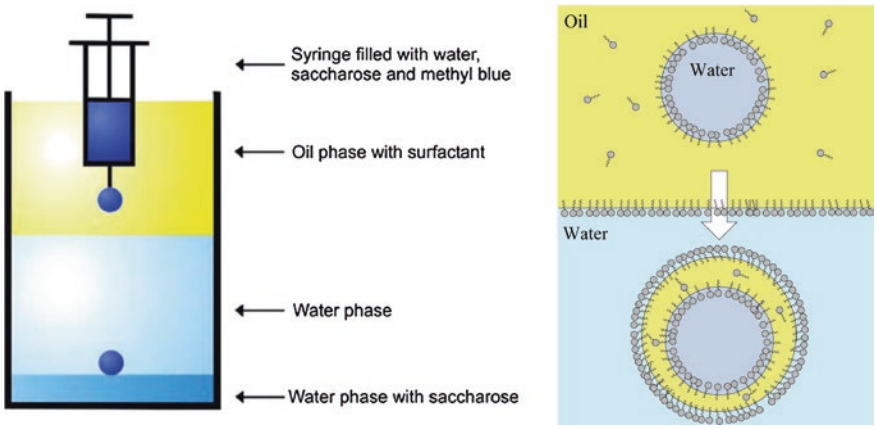

Fig. 1 Schematic drawing of the single droplet formation using a syringe with a cannula (*left*) [1]. The *right hand drawing* shows the simplified mechanism of vesicle formation

means of optical microscopy [3–5]. The principle of our new approach was based on the formation of water droplets in an organic phase which contained surfactants or other types of emulsifying compounds. After surrounding the aqueous droplets with a stabilizing surfactant film, these particles were transported through the fluid oil-water interface (Fig. 1) [6]. The first studies of such phenomena were based on experiments, which were recently performed by Pautot et al. [7].

We used extensively studied amphiphiles for the emulsion formation in the first step. The oil soluble surfactants Span® 80 and Brij® 72 are well-known to stabilize emulsions, and they can also form niosomes [8–10]. Furthermore we utilized the natural product lecithine, which is also oil-soluble, and an important component of biological membranes [11]. The emulsions were generated with established methods like sonication with ultrasound, applying electrosprays or using micro-emulsion formations [12–14]. In addition, we constructed different microfluidic devices to produce small aqueous droplets in oil. Similar techniques were often used for the production of double emulsions [15, 16]. During droplet formation in the organic phase, a single layer of surfactants adsorbed at the surface of these particles. This thin film of surface-active compounds stabilized the emulsion droplets and lowered the surface tension [17]. A second surfactant film was also formed at the plane oil-water interface of the reaction vessel (Fig. 1).

In the presence of a distinct density difference between oil and water or other external driving forces like centrifugal or flow fields, the water droplets passed the plane interface and vesicle-like structures were thereby formed [18, 19]. Based on this phase-transfer process, we produced a large variety of different types of vesicle-like structures. The main advantage of this new technique was the formation of defined, filled vesicles with complete control of the inner phase [20].

2 Experimental Section

2.1 Materials

The following compounds were used without further purification: Sorbitan Monooleate (Span® 80, Fluka), Bis(2-ethylhexyl) Sulfosuccinate Sodium Salt (AOT, Fluka, >96 %), Sodium Dodecylsulfate (SDS, Sigma, >99 %), L-Alpha-Phosphatidylcholine (Lecithine, AppliChem, >90 %), Polyoxyethylene-2-stearylether (Brij® 72, Sigma), 2,2,4-Trimethylpentane (Isooctane, Alpha Aesar >99 %), Dodecane (Alpha Aesar, 99 %), Olive Oil (Fluka), Methyl Blue (Sigma, >60 % Dye content), Sodium Chloride (NaCl, Sigma, >99,8 %), Sucrose (Sigma, >99 %), Triton X-100 (Fluka), Ammoniumheptamolybdate Tetrahydrate (Merck, p.a.). Water was deionized using a Millipore system.

2.2 Methods

2.2.1 Images

Images of the large vesicles were taken with a Canon Powershot S5 IS camera equipped with a 36–432 mm F2.7-3.5 zoom lens.

2.2.2 Optical Density

The optical density was analyzed with a Cary 1E UV-Visible Spectrophotometer (Varian, Palo Alto, USA) and Hellma Analytics QX 10 mm quartz cuvettes.

2.2.3 Drop Shape Analysis

For measurements of the interfacial tension we used a pendant-drop tensiometer (OCA 20, *Dataphysics*). A single drop of the denser aqueous phase was formed in the organic phase. The video image was recorded by a CCD camera and analyzed using the Laplace-Young equation (Dataphysics SCA20 software version 3.61.6). In addition, the interfacial tension and the dilation surface rheology was investigated using a spinning drop tensiometer (SVT 20, *Dataphysics*). In these experiments a droplet of the organic phase was prepared in the aqueous phase (Fig. 2). In order to measure the interfacial tension the droplet contour was, in both cases, analyzed using an "Axisymmetric Drop Shape Analysis" (ADSA) with the SVT software version 2.2.3. In these applications the Gauss-Laplace equation was used to calculate the interfacial tension.

The stationary values of the interfacial tension γ were determined for different surfactant concentrations over a time period of at least one hour. We measured

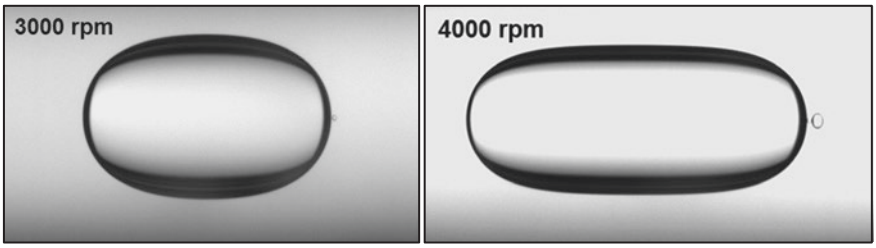

Fig. 2 Schematic illustration of a spinning drop at two different angular velocities in the rotating capillary. The interfacial tension was calculated from the droplet deformation

the surface dilation rheology by applying a harmonic sinusoidal amplitude to the rotational speed of the spinning drop tensiometer. In these experiments, the rheological data could be calculated by analyzing the changes of the interfacial tension $\gamma(t)$ as a function of the varying surface area A (Fig. 2). The angular frequency in our experiments was set to 0.05 Hz, and the deformation was measured at different amplitudes between 5 and 10 %. The oscillations were fitted by a Fourier transformation algorithm to obtain the rheological parameters like the surface dilation storage modulus (ε') and the surface dilatation loss modulus (ε'').

2.2.4 Dynamic Light Scattering

Dynamic light scattering experiments were performed using the Zetasizer Nano ZS (*Malvern*) with the Dispersion Technology Software (DTS, version 6.12). This instrument measures the velocity distribution of particles by analyzing the dynamic fluctuation of light scattering intensity caused by the Brownian motion. The monochromatic light is produced by a 4 mW He-Ne Laser (633 nm wavelength) and detected at a detector angle of 173°. From the intensity fluctuations the hydrodynamic diameter can be calculated via the Stokes-Einstein equation. The samples were investigated at a temperature of 25 °C and each measurement was repeated 5 times.

2.2.5 Preparation of Giant Vesicles

The oil-soluble surfactants were dissolved in the organic phase at a concentration of 10 mmol/l (unless indicated otherwise). A glass vessel was partly filled with a aqueous buffer solution usually Tris-buffer (5 mmol/l Tris, 100 mmol/l NaCl) or PBS-buffer (137 mmol/l NaCl, 2.7 mmol/l KCl, 8 mmol/l Na_2HPO_4, 1.5 mmol/l KH_2PO_4) and covered with a layer of the organic phase. In some cases, e.g. for the formation of floating vesicles, we added a second aqueous buffer solution with a higher density containing 30 wt% sucrose with a syringe to the bottom of our vessel. For the inner drop phase, a buffer solution was stained with Methylene

Blue at a concentration of 2 mmol/l. Emulsion droplets were then produced in the organic phase with a syringe. The inner diameter of the needles (Nordson EFD, Pforzheim, Germany) was varied from 100 μm to 1.5 mm. For water soluble substances we used a similar procedure, but we applied higher surfactant concentrations between 1 and 10 wt%.

2.2.6 Transmission Electron Microscopy (TEM)

Negative staining transmission electron microscopy was performed on a hydrophilic, carbon coated 300-mesh TEM grid. In these experiments a drop of the vesicle suspension was transferred on the grid and the bulk of the solution was separated with a filter paper after 30 s. The grid was then covered with an aqueous solution 2 % Ammoniumheptamolybdate for 60 s. After drying, the grid was observed in a transmission electron microscope (Philips CM 200, Germany).

2.2.7 Emulsification

We used ultrasonic sound to reduce the size of emulsion droplets. For this purpose 10 μl of an aqueous solution was added to each ml of the organic solution. Sonication was executed using an Elmasonic S30H (Elma, Germany) sound source for 15 min at a temperature of 25 °C.

For the preparation of microemulsions 264 μl water was emulsified in 6 ml Isoctane containing 140 mmol/l AOT.

2.2.8 Centrifugation

An aqueous buffer solution was covered with an organic emulsion (2 ml) in a 50 ml centrifugation tube and transferred into the centrifuge (Eppendorf 5702R, Germany). The solution was then executed to centrifugal forces (3,000 g) for 15 min. To avoid contamination with the organic phase, the aqueous vesicle solution was separated from the bottom of the tube.

2.2.9 Fluorescence Intensity Measurements

A part of the vesicle solution (0.1 ml) from centrifugation was diluted 1:10 and the fluorescence from 450 to 650 nm was measured with a Cary 1E UV-Visible Spectrophotometer (Varian, Palo Alto, USA). Further dilution steps were performed in order to calculate the Carboxyfluorescein concentration. After the addition of 50 μl Triton X 100 to the higher concentrated solution, we measured the fluorescence and calculated the difference in concentration.

3 Results

3.1 Properties of the Surfactants and Interfaces

We investigated the properties of the interface between the organic and the aqueous phase in order to evaluate the best conditions for the phase transfer process of the emulsion droplets.

3.1.1 Interfacial Tension (IFT)

The interfacial tension γ is an important parameter describing the work needed to expand the interface. As one would imagine, a high interfacial tension impedes the transfer of the droplets across the oil-water interface and therefore raises the energy required to pass the interface. In addition, a surfactant film is needed to stabilize the droplets and to reduce exchange and diffusion processes between both phases (Fig. 1). An increased surface concentration of surfactants after adsorption generally tends to lower interfacial tension (Fig. 3).

The kinetics of surfactant adsorption mainly depend on two factors; the diffusion coefficient and the concentration of the surfactant or lipid. It is worth mentioning, that the interfacial tension was already significantly lowered at the starting point of the measurement. The interfacial tension experiments began 10 s after drop formation (Fig. 3). Compared to 53 mN/m, which represents the interfacial tension of the pure isooctane/water interface, the adsorption for the Span® 80 concentrations of 1 and 10 mmol/l was almost complete. These results demonstrated that it was necessary to work at high surfactant concentrations in order to form stable monolayers at short time scales. The interfacial tension of Brij® 72, for example, decreased much slower. This might be the main reason for the lower stability of

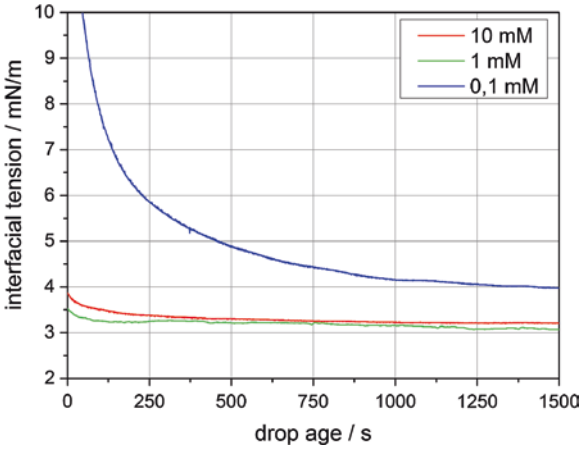

Fig. 3 Time dependent interfacial tension of a pendant water drop containing PBS buffer. The surrounding oil phase Isooctane contained different concentrations of the surfactant Span® 80

Table 1 Typical values of the interfacial tension of different surfactants at a concentration of 10 mmol/l

Amphiphile	Interfacial tension γ (Dodecane)/mN/m	Interfacial tension γ (Isooctane)/mN/m
Lecithine	2.2 ± 0.5	2.7 ± 0.5
Span® 80	2.3 ± 0.5	3.1 ± 0.3
Brij® 72	4.3 ± 1.1	5.7 ± 1.2
AOT	1.2 ± 0.6	1.9 ± 1.0

The experiments were performed in the spinning-drop tensiometer. In a series of experiments, we systematically investigated the Dodecane/water and the Isooctane/water interface

the produced Brij® 72 vesicles, and confirms our observation, that high surfactant concentration are needed to form stable vesicular structures (Fig. 5).

The absolute values of the interfacial tensions varied between different amphiphiles and solvents (Table 1). AOT, which is well known in the literature for the formation of microemulsions, showed the lowest surface tension at the interface of both solvents. The other nonionic surfactants mentioned here, Span® 80 and Brij® 72 showed slightly higher values. This was also observed for Lecithine, but this lipid precipitated partly during the spinning-drop measurements. Due to this phenomenon, it was not possible to measure accurate data for this emulsifying compound. The interfacial tension had also some influence on the mean size of the emulsion droplets and on the stability of the vesicles (Table 3). In addition to the stationary values of the surface tension, dynamic processes as the surfactant diffusion represented another important factor for the process of stimulated vesicle formation. If an aqueous droplet passed across the fluid interface it carried-over a thin layer of emulsifiers and thereby lowered the local surfactant concentration in the vicinity of the oil-water interface. In the short time span, before the next water droplet approached the interface, the surfactant films should entirely reform; and this only occurred, if the surfactant diffusion was fast enough.

3.1.2 Oscillating Spinning-Drop Experiments

We performed oscillating spinning-drop measurement in order to gain insight into the rheological properties of the surrounding surfactant films. In these measurements, we induced oscillating interfacial tensions with different amplitudes, and we observed the periodic increase of the drop surface. From the time difference and the amplitudes of these two parameters we could measure the interfacial dilatation storage modulus ε' and the interfacial dilatation loss modulus ε''. Typical results of these measurements are represented in Fig. 4.

The two-dimensional rheological properties of the surfactant films were observed by superimposing a sinusoidal oscillation onto the constant rotational speed of the glass tube of the spinning-drop tensiometer. This led to periodic oscillations of the surface tension and the drop surface. In general, the viscoelastic film response can be described by Gibbs- and Marangoni-effects [21]. Both properties

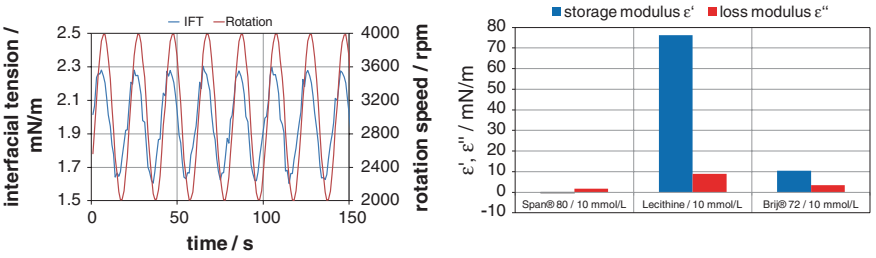

Fig. 4 Typical oscillating spinning-drop experiment at varying rotation speeds of an Isooctane droplet containing 10 mmol/l Span® 80 which was suspended in an aqueous PBS-buffer solution (*left*). The resulting storage (ε')—and loss (ε'') moduli for different amphiphiles are summarized on the *right-hand scale*

are influenced by diffusion processes of the surfactants in the bulk phase and in the plane of the oil-water interface. A large elastic film response points to the presence of low diffusion processes or to the presence of temporarily cross-linked, network-like film structures. Figure 4 shows the impact from the tested amphiphiles at a concentration of 10 mmol/l. Span® 80, which allowed the production of rather stable vesicles, exhibited the lowest elasticity. This surfactant can, therefore, compensate concentration differences very fast. In contrast, the surface storage modulus of Lecithine reached large values of about 80 mN/m. In this case, the diffusion and film reformation was significantly slower compared to Span® 80. The surfactant Brij® 72 only showed small elastic properties, and the vesicles, formed from this emulsifying compound, were found to be fairly stable.

3.1.3 Torsion Pendulum

A torsion pendulum apparatus was used to get information about the shear rheological properties of the surfactants at the interface. This sensitive instrument was not capable of detecting significant elastic or viscous properties except for Lecithine. The analysis provided data that indicated a low viscous resistance for Lecithine with an interfacial shear loss modulus of about 0.03 mN/m. Hence, we can conclude, that no network-like superstructures were formed, and that the large dilatational elastic response was mainly caused by Gibbs- and Marangoni-effects.

3.2 Vesicle Formation

3.2.1 Phase Transfer of Single Droplets

The phase transfer of a single droplet is visualized in the video images of Fig. 5. We used a syringe in order to form water droplets which were colored by the dye

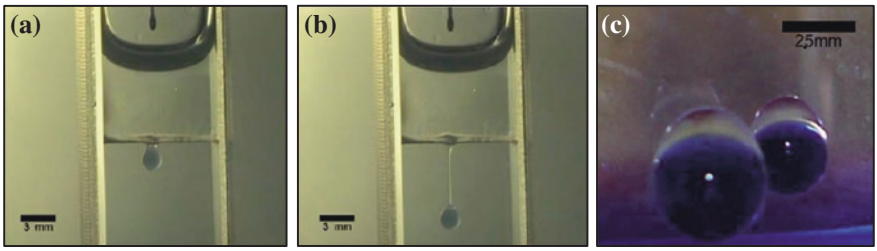

Fig. 5 Typical video images of the phase transfer of a single droplet (**a**, **b**) and floating droplets containing oil in their membrane (**c**). In this experiment, we used Dodecane as the organic phase which contained the surfactant Lecithine at a concentration of 10 mmol/l [1]

Methyl Blue. After transporting the aqueous droplet across the oil-water interface, a small thread of the organic phase was pulled, together with the vesicle, into the water phase (Fig. 5b). This transfer process led to the incorporation of oil into the vesicle membrane (Figs. 1 and 5b). The aqueous droplet contained 15 wt% sucrose to gain a sufficient density difference for the phase transfer and to counteract the buoyancy from the incorporated oil. Due to this density difference, the formed vesicles were slightly sedimenting in the subjacent buffer solution.

In several experiments we were able to achieve similar results using different types of organic phases and amphiphiles. It was even possible to use water soluble surfactants such as SDS to induce the formation of filled vesicles. Depending on the conditions and the size of the syringe capillary, we could vary the size, oil content and stability of the produced vesicles. However, in all experiments, the concentration of the surfactants had to be adjusted above the critical micelle concentration (cmc) in order to form stable vesicular structures.

3.2.2 Extrusion of Droplets

In a different approach we used thin brass plates with conical holes to generate emulsion droplets (Fig. 6). These plates were developed and manufactured in cooperation with Temicon GmbH (Dortmund, Germany). Their small pores with an average diameter of 3 μm allowed the pressure driven production

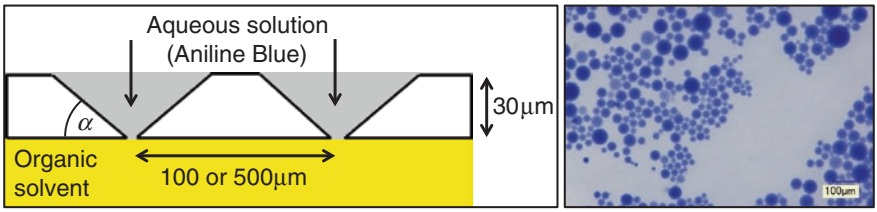

Fig. 6 Schematic view of the emulsion droplet production using a thin brass disk (*left*) and image of generated droplets from optical microscopy in Isooctane (*right*)

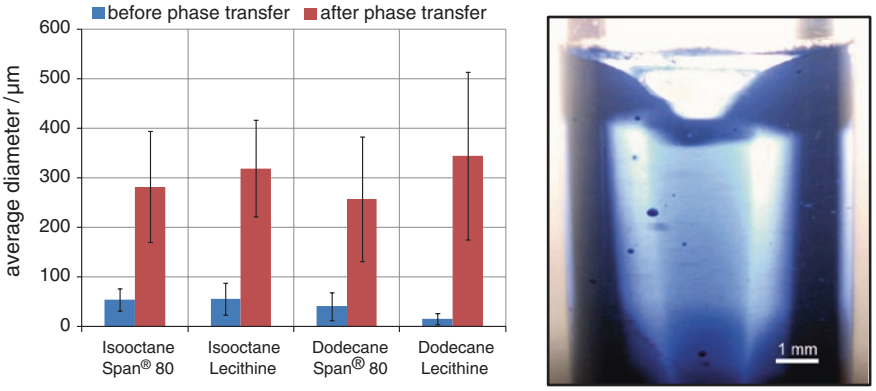

Fig. 7 Aqueous droplets generated in an Isooctane solution containing 10 mmol/l Span® 80 compared to the produced vesicles after the phase transfer. The image on the *right hand* side shows vesicles in a circular flow in the aqueous phase

($\Delta p = 1.0 \times 10^5$ Pa) of water in oil emulsions. The objective of these experiments was to generate a large number of droplets simultaneously and to push them through the oil-water interface. In theory this should prevent coalescence at the interface and a continuous formation of vesicular structures.

As demonstrated in Fig. 6 the brass plates had a thickness of 30 µm and average distance between the conical pores of 100 or 500 µm. A syringe pump delivered the pressure at constant flow rates and we reduced the flow resistance using a polysiloxane coating at the surface of the brass plates. The obtained droplets showed average diameters between 15 and 35 µm (Fig. 7). The emulsion droplet size depended on several parameters like the surfactant type, the amphiphile concentration and the flow rate. With Dodecane as organic solvent and Lecithine as emulsifier the mean droplet diameter reached a minimum of 15 µm.

Independent of the conditions, it was not easy to stimulate the phase transfer across the plane oil-water interface. If we applied, however, shear forces by vigorously stirring the water solution underneath the plane oil-water interface, the phase transition occurred without problems. In this context, it is interesting to note, that the generated vesicular structures exceeded the size of the emulsion droplets by the factor of about 10. This can be explained by droplet coalescence which occurred during flow. Due to the conical shapes of the pores and the presence of shear forces, the small water droplets got in contact with each other and formed larger droplets before the phase transition took place. The average diameter of the vesicles was 250–350 µm, but the efficiency of the phase-transfer across the fluid interface did not exceed 15 %. Compared to the single droplet phase transfer described in Sect. 3.2.1, the vesicles contained in their membranes a small amount of the organic phase. Due to the coalescence processes during stirring, the size distribution was broad. A large number of emulsion droplets were destroyed at the interface, and their dye content was then released into the lower aqueous phase.

3.2.3 Continuous Phase Transition

According to the requirements of industrial technologies, a continuous production of vesicular structures with high encapsulation efficiency is mandatory. In order to meet these demands, we tried to overcome the problems of drop-wise phase transitions. In an improved apparatus, we therefore used a jet stream containing an aqueous buffer solution which was formed in the oil phase. The continuous water jet was oriented perpendicular to the oil-water interface (Fig. 8). During the phase transfer process, a thin film of the organic phase was drawn into the aqueous solvent just covering the surface of the jet in the water phase (Fig. 8, left image). The separation into small droplets in the aqueous phase was driven by turbulences in the underlying aqueous phase [22].

The flow rate in this case with an inner capillary diameter of 500 μm was adjusted between 75 and 150 ml/min reaching three decades higher values than the brass disk method. In a series of experiments, we received similar results using different capillary sizes and flow rates. At all investigated conditions, the described, new method offered a flexible way to produce filled, vesicle-like structures with adjustable droplet sizes (Table 2). The smallest capillary with an inner diameter d_i of 80 μm allowed the production of vesicles with a mean diameter d_m of about 170 μm.

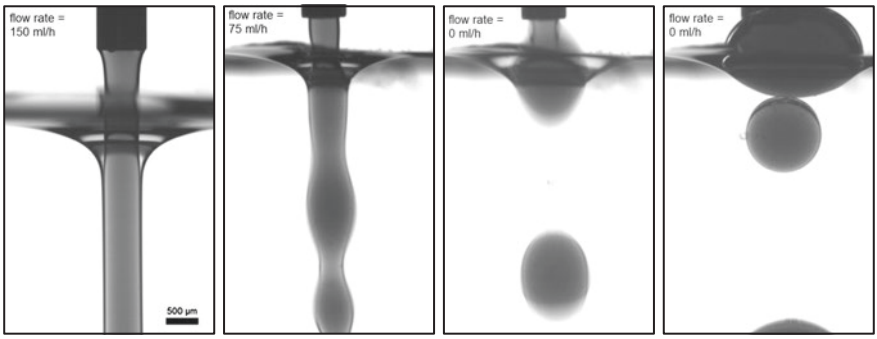

Fig. 8 Video image sequence showing the water jet passing the interface between isooctane (*top*) and an aqueous phase (*bottom*). After reducing the flow rate from 150 to 75 ml/h the jet becomes inhomogeneous. When the flow is stopped, the jet decomposed into single vesicles containing small amounts of Isooctane in their membranes (*right-hand image*)

Table 2 Comparison of different cannula sizes, the produced emulsion droplet sizes and the entrapment efficiencies

Capillary inner diameter (d_i/μm)	Flow rate (Q/ml/min)	Mean vesicle size (d_m/μm)	Entrapment efficiency (EE/%)
80	5	170	81
160	20	350	85
500	100	810	88

The biggest advantage of this flexible jet technique is the high entrapment efficiency of more than 80 %. We calculated these special features from UV-Vis measurements measuring the Aniline Blue concentration one hour after the vesicle production. The absorption of this blue dye after the destruction of the vesicles by adding Triton X 100 was taken as the reference and compared to the absorption before the destruction of the vesicular structures.

As it can be seen in Fig. 8 the organic phase is, similar to the transition of single droplets in Sect. 3.2.1, distributed within the vesicle membrane creating a diffusion barrier between inner and outer aqueous phase. On grounds of the density difference between oil and water, the vesicle-like particles rise in the aqueous phase and gather at the interface, forming densely packed, foam-like structures. The stability was influenced negatively by this process, but after hours most of the particles were still intact. The creaming process led to the formation of large, foam-like vesicle structures at the interface (Fig. 9).

The densely packed, foam-like structures, formed a continuous network of vesicle membranes, which allowed the organic phase to move upwards and join the bulk oil phase. This special draining process led to a considerable reduction of the organic solvent content within the vesicle membranes. A large portion of the formed vesicles (approximately 90 %) stayed intact and did not coalesce to form larger particles. After about 5 min we were able to break-up the foam-like structures by applying shear forces. After vigorously stirring, we found most of the vesicles isolated again. After this special treatment, they contained only a very thin film of the organic solvent.

The stability of Span® 80 stabilized vesicular structures was tested with UV-Vis spectroscopy measuring the release of Aniline Blue (Fig. 10). The samples were taken from a separated chamber excepting the vesicles from the measurements. Some of the vesicles (approximately 25 %) were destroyed in the initial process (single points in Fig. 10), but the rest was stable until the end of these measurements. We measured the concentration of these stable particles by destroying the vesicles after addition of the surfactant Triton X 100. After rupturing, they

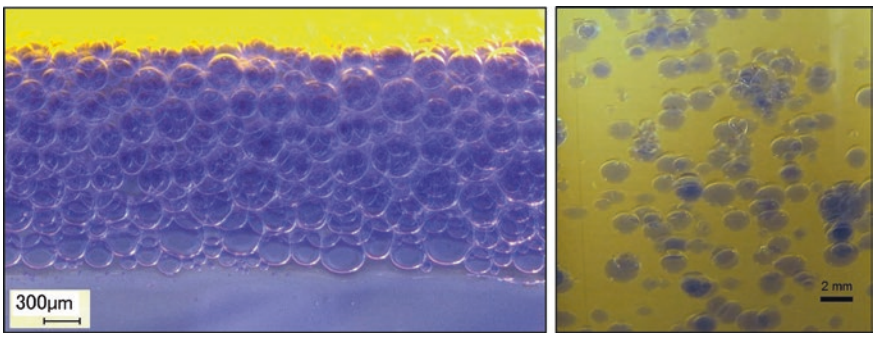

Fig. 9 Foam-like vesicle structures at the interface stained with *aniline blue* (*left*) and separated droplets after stirring the foam-like structures (*right*)

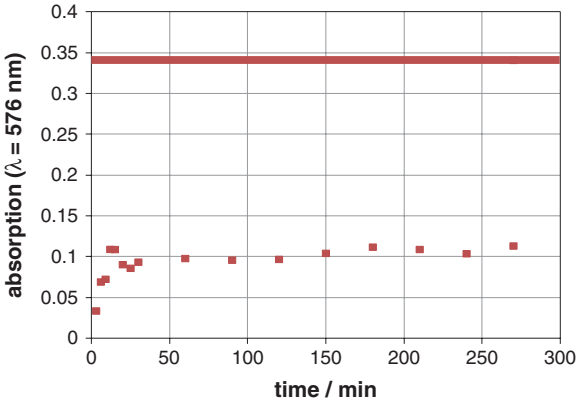

Fig. 10 Absorption of aniline blue at the wavelengths of 576 nm analyzed by UV-Vis spectroscopy. 2 ml of an aniline blue solution (2 mmol/l) in PBS buffer was transferred through the Isooctane-water interface. The *red line* indicates the absorption maximum after destroying of the vesicles with Triton X 100. *Single points* represent the fraction of vesicles, which ruptured during the formation process and afterwards releasing dye into the aqueous solution

released dye into the aqueous solutions and the concentration could be measured by means of UV-Vis spectroscopy. Similar results, describing the presence of stable vesicles, were achieved using Dodecane as organic solvent. However, other organic solvents like Olive Oil or different amphiphiles like Lecithine and Brij® 72 did not show this long-term stability.

3.2.4 Large Vesicles Formed from Emulsions and Microemulsions

In a series of experiments, we also used, besides shear forces, centrifugal fields in order to transfer small water droplets across the oil-water interface. In contrast to the method above, we used ultrasonic sound to generate emulsion droplets with a small diameter (Table 3). In analogy to larger water droplets for the formation of giant vesicles, the sole gravitational force appeared to be insufficient for the phase transfer.

It could be shown, that the mean diameter of those small droplets depended on the surface tension and the amount of energy brought into the system [23]. In our

Table 3 Mean diameter of small water in oil emulsion droplets which were formed in Dodecane containing different surfactants at a concentration of 10 mmol/l

Surfactant	Diameter (d/nm)	Polydispersity index (PDI)
Span® 80	108 ± 12	0.24
Brij® 72	192 ± 43	0.28
AOT	125 ± 18	0.26
Lecithine	124 ± 35	0.41

These dispersions were produced by sonication

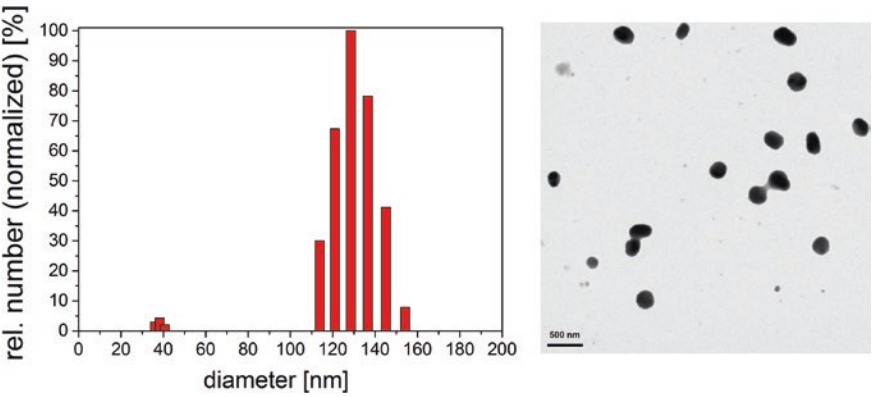

Fig. 11 Typical size distribution of vesicles containing PBS-buffer in Dodecane (*left*). Negative staining TEM-image of the vesicles (*right*). The organic phase contained the surfactant Span® 80 at a concentration of 10 mmol/l [2]

experiments the mean diameter varied between 10 and 500 nm. These droplets were dispersed by sonication of an aqueous phase in the organic phase. Span® 80 led to an average droplet size of 108 nm, which could not be resolved using optical microscopy. But light scattering measurements as well as electron microscopic images did show a large amount of these particles. We applied TEM (transmission electron microscopy) to visualize AOT stabilized emulsions showing smaller droplets with an average diameter of 130 nm (Fig. 11). In order to avoid coalescence processes, we only used relatively low water volume fractions. It turned out that a lower average distance between the droplets resulted in a reduced stability and a broader size-distribution. The effect of the phase transfer, which influenced the size and stability of the formed vesicles, can be observed in Fig. 14.

However, these images were not sufficient to quantify the stability of the vesicles after the phase transfer. The inner phase of these particles was analyzed by luminescence spectroscopy [2]. We used the fluorescent dye Carboxyfluorescein as our tracer agent because of its quenching effect at concentrations above 10 mmol/l [24]. The entrapment efficiency *EE* (Table 4) was calculated as follows:

$$EE = \frac{\left(c_f - c_v\right) \cdot 100}{c_v}$$

Table 4 Comparison of the encapsulation efficiency of vesicles produced by different phase transfer methods

Production method	Entrapment efficiency (*EE*/%)
Centrifugation of emulsions	13.1
Phase transfer of microemulsions	7.7
Phase transfer of giant vesicles	85

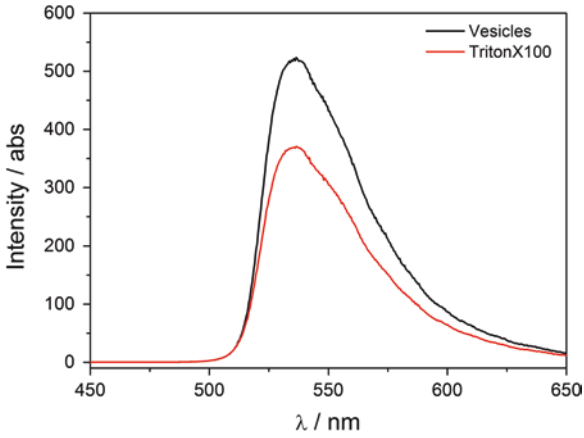

Fig. 12 Fluorescence emission spectrum of AOT-vesicles produced by centrifugation before (*black*) and after treating with Triton X 100 (*red*) [20]

The Carboxyfluorescein concentration of the vesicle suspension c_v and after destroying the vesicles with the surfactant Triton X 100 c_f were calculated from the fluorescence intensity of the diluted aqueous solutions. The turbidity of the vesicle solution declined within seconds after detergent addition (vesicle busting), and we obtained then a clear, aqueous solution. Typical results of these measurements are summarized in Fig. 12. Due to the self-quenching properties the destruction of the vesicles with a high inner Carboxyfluorescein concentration (0.05–0.2 mol/l) led to an increase of the Fluorophore concentration in the outer phase. This occurred if a large amount of emulsion droplets coalesced with the lower water phase, thus releasing their Carboxyfluorescein content.

The encapsulation efficiency varied depending on the method implied to generate the vesicles. Centrifugation of emulsions and microemulsions enabled the phase transfer with an efficiency of only 7–13 % [2]. Further measurements revealed that only a fraction of all microemulsion droplets were transferred into the water phase. Many emulsion droplets were still intact in the organic phase. In contrast to this, the efficiency of larger droplets was high regardless of the surfactants and their concentration. The gravitational force always depended on the size of the aqueous emulsion droplets.

3.2.5 Electrospray

The electrospray method represents another well-known technique to produce emulsions [13]. This process allowed the continuous formation of droplets. The apparatus consisted of a thin capillary and an annular counter electrode which were connected to a high voltage power supply (Fig. 13). The metal capillary containing the aqueous buffer solution was highly charged in respect to the annular ground electrode. We placed the circular ground electrode directly above the aqueous phase. Systematic measurements revealed, that the emulsion drop size mainly depended on the flow rate which was regulated with a syringe pump and the applied potential.

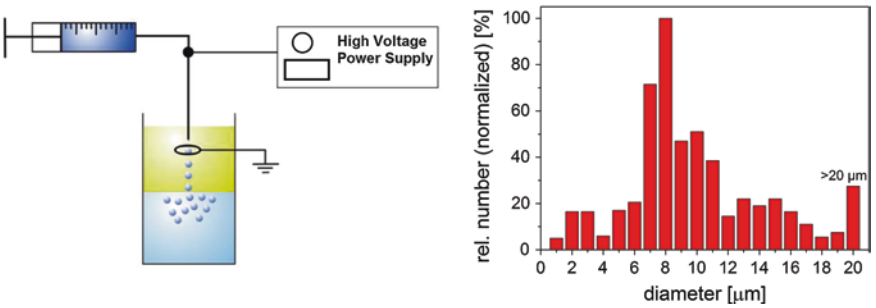

Fig. 13 Schematic illustration of the electrospray experimental setup (*left*). Size distribution of the emulsion droplets generated at 5 kV and a flow rate of 1 ml/h in olive oil with AOT as surfactant (*right*) [20]

The generated AOT stabilized emulsions showed an average droplet diameter of 11 µm at flow rates of 1 ml/h. Reducing the flow rate to 0.1 ml/h led to a considerable reduction of the droplet size with an average value of about 400 nm but the polydispersity increased. One important advance of the electrospray method concerned the proper adjustment of the droplet size which could be performed even within a single experiment.

At the present state, it is not clear, how the observed phase transfer occurs in the electrospray method. It is well known, that the high potential electric field can induce solvent flow. In addition to this, charged droplets are accelerated and guided towards the oil-water interface. The electric forces may also influence the structures of the surfactant films. Due to the high speed and the combination of several processes, we could not study these mechanisms in detail.

Figure 14 describes the influence of the flow rate on the average diameter of the vesicles. A flow rate of 1,000 µl/h led to larger droplets and a broader size distribution, while a lower flow rate limited the amount of droplets generated. In

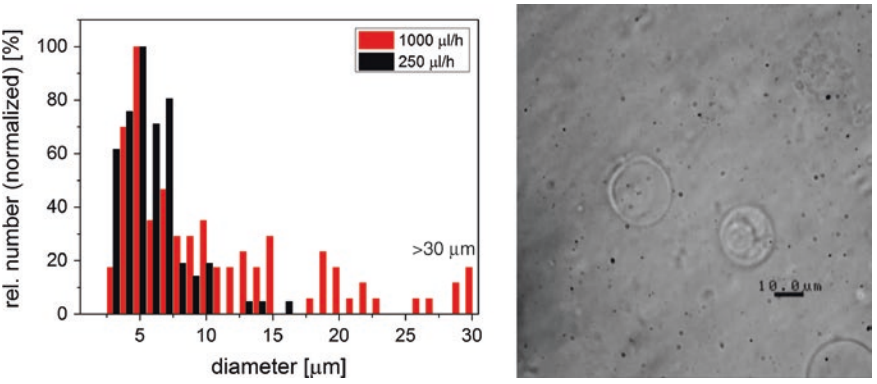

Fig. 14 Size distribution of the AOT stabilized vesicles after the phase transition at two different flow rates (*left*). Enhanced phase contrast microscopic image of AOT stabilized vesicles (*right*) [20]

addition, the electrical potential could be adjusted for further variation. In summary, we can state, that the electrospray method delivered a flexible way for the droplet and vesicle formation.

It is interesting to note that in the electrospray method the emulsion droplets survived the phase transfer without changing their shape and size. We were able to observe the vesicles using enhanced phase contrast microscopy (Fig. 14). Compared to the other phase transfer methods they did not show an incorporation of organic solvent into their membranes, and they were floating inside the lower aqueous phase. However, on grounds of the high speed, we were not able to resolve the phase transfer in detail. The low amount of generated vesicles, the entrapment efficiency of about 8 %, and the high applied electrical potential made it difficult to visualize this process.

4 Summary

The production of vesicles and especially the defined filling is a major task that has not yet been brought to a large scale. Our new approach utilized phase transfer processes of aqueous droplets from an organic solvent into the water phase to generate closed liquid volumes in the nanoliter to microliter scale. We found several surfactants and solvents being suitable for the production of filled, vesicle-like particles. Nonionic surfactants, as for example Span 80, showed favorable properties for the phase transfer process. At concentrations above the cmc the film formation at fluid interfaces was very fast and allowed concentration differences to be compensated within milliseconds. These special properties could be investigated in oscillating spinning-drop experiments.

Based on these results we investigated different methods for the formation of water droplets in the organic phase. The emulsions were generated by extrusion from syringes through capillaries or a thin brass disk with narrow pores in the low micrometer range. In addition, sonication with ultrasound, electrospray and a microemulsion system were analyzed in term of droplet size and stability for the phase transfer process. In all these experiments, we used different techniques to generate water droplets with various sizes and encapsulated compounds.

In order to optimize the transfer process across the oil-water interface we developed variable ways for the penetration of emulsion droplets into the aqueous phase and investigated the entrapment efficiency. These methods were based on sedimentation, centrifugal, electrostatic or flow fields, which forced the droplets to leave the oil phase and to enter into the underlying water phase. During this phase transition a significant amount of organic solvent was entrapped into the hydrophobic part of the membranes and influenced the properties of the filled, vesicular structures. On the one hand, this thin layer of organic solvents reduced the diffusion processes from the core of the vesicles into the surrounding water phase. This might be of special advantage for the encapsulation of water soluble ingredients as drugs or other interesting compounds. It also offers the opportunity

to store oil soluble substances in the membranes of the vesicles. On the other hand the density difference induced creaming processes and influenced the stability of the vesicular structures. In electrospray and water-jet experiments and we were able to lower the amount of the incorporated organic phase and keep the incorporated compounds inside. These techniques allowed the production of relatively stable, vesicle-like particles with the size of several to several hundred micrometers. On grounds of the very thin oil layer, which was still present in the membranes, these particles may also be described as multiple water-in-oil-in-water (w/o/w) emulsions. The special characteristic of these multiple emulsions lies in the fact, that the particle core only consist of one single droplet and is not divided into different cavities. Due to this special properties, the produced particles may simply be denoted as water-in-water emulsions. In appreciation of their interesting properties, the newly produced emulsions or vesicles exhibit a high potential for advanced methods of controlled drug storage, transport and release.

Acknowledgments Financial support by the "Deutsche Forschungsgemeinschaft" (DFG) within the Priority Program SPP 1273 (Colloid Process Engineering) is gratefully acknowledged (RE 681/17-1, /17-2 and /17-3).

References

1. Kubatta EA, Rehage H (2009) Characterization of giant vesicles formed by phase transfer processes. Colloid Polym Sci 287(9):1117–1122
2. Kubatta EA, Rehage H (2011) AOT-vesicles produced at the oil-water interface. Tenside Surf Deterg 48(3):221–227
3. Berndl K, Käs J, Lipowsky R, Sackmann E, Seifert U (1990) Shape transformations of giant vesicles: extreme sensitivity to bilayer asymmetry. Europhys Lett 13(7):659–664
4. Menger FM, Balachander N (1992) Chemically-induced aggregation, budding, and fusion in giant vesicles: direct observations by light microscopy. J Am Chem Soc 114(14):5862–5863
5. Moscho A, Orwar O, Chiu DT, Modi BP, Zare RN (1996) Rapid preparation of giant unilamellar vesicles. Proc Natl Acad Sci 93(21):11443–11447
6. Nishimura K, Suzuki H, Toyota T, Yomo T (2012) Size control of giant unilamellar vesicles prepared from inverted emulsion droplets. J Colloid Interface Sci 376(1):119–125
7. Pautot S, Frisken BJ, Cheng J-X, Xie S, Weitz DA (2003) Spontaneous formation of lipid structures at oil/water/lipid interfaces. Langmuir 19(7):10281–10287
8. Baillie AJ, Florence AT, Hume L, Muirhead GT, Rogerson A (1985) The preparation and properties of niosomes—non-ionic surfactant vesicles. J Pharm Pharmacol 37(12):863–868
9. Yoshioka T, Sternberg B, Florence AT (1994) Preparation and properties of vesicles (niosomes) of sorbitan monoesters (Span 20, 40, 60 and 80) and a sorbitan triester (Span85). Int J Pharm 105(1):1–6
10. Bayindir ZS, Yuksel N (2010) Characterization of niosomes prepared with various nonionic surfactants for paclitaxel oral delivery. J Pharm Sci 99(4):2049–2060
11. Enoch HG, Strittmatter P (1979) Formation and properties of 1000-Å-diameter, single bilayer phospholipid vesicles. Proc Natl Acad Sci 76(1):145–149
12. Maa YF, Hsu CC (1999) Performance of sonication and microfluidization for liquid-liquid emulsification. Pharm Dev Technol 4(2):233–240
13. Tang K, Gomez A (1996) Monodisperse Electrosprays of low electric conductivity liquids in the cone-jet mode. J Colloid Interface Sci 184(2):500–511

14. Lawrence MJ, Rees GD (2000) Microemulsion-based media as novel drug delivery system. Adv Drug Deliv Rev 45(1):89–121
15. Umbanhowar PB, Prasad V, Weitz DA (2000) Monodisperse emulsion generation via drop break off in a coflowing stream. Langmuir 16(2):347–351
16. Christopher GF, Anna SL (2007) Microfluidic methods for generating continuous droplet streams. J Phys D Appl Phys 40(19):319–336
17. Becher P (1965) Emulsions: theory and practice. Reinhold, New York
18. Okushima S, Nisisako T, Torii T, Higuchi T (2004) Controlled production of monodisperse double emulsions by two-step droplet breakup in microfluidic devices. Langmuir 20(23):9905–9908
19. Shum HC, Lee D, Yoon I, Kodger T, Weitz DA (2008) Double emulsion templated monodisperse phospholipid vesicles Langmuir 24(15):7651–7653
20. Schmitte EA (2011) Herstellung unilamellarer Vesikel durch Phasentransferprozesse. Dissertation, Technische Universität Dortmund
21. Lucassen-Reynders EH, Cagna A, Lucassen J (2001) Gibbs elasticity, surface dilational modulus and diffusional relaxation in nonionic surfactant monolayers. Colloid Surf A 186(1–2):63–72
22. Lin SP, Reitz RD (1998) Drop and spray formation from a liquid jet. Annu Rev Fluid Mech 30(4):85–105
23. Williams JM (1991) High internal phase water-in-oil emulsions: influence of surfactants and cosurfactants on emulsion stability and foam quality. Langmuir 7(7):1370–1377
24. Chen RF, Knutson JR (1988) Mechanism of fluorescence concentration quenching of carboxyfluorescein in liposomes: energy transfer to nonfluorescent dimers. Anal Biochem 172(1):61–77

Part IV
New Process Routes

Continuous Preparation of Polymer/ Inorganic Composite Nanoparticles via Miniemulsion Polymerization

Tobias Merkel, Lena L. Hecht, Alexander Schoth, Caroline Wagner, Rafael Muñoz-Espí, Katharina Landfester and Heike P. Schuchmann

Abstract Composite nanostructured particles can be produced by polymerization of monomer miniemulsion droplets loaded with inorganic nanoparticles. The article gives an overview on the development of a scalable continuous process for the production of such hybrid nanoparticles via miniemulsion polymerization. Different possibilities for the necessary surface modification of the inorganic material are discussed in detail. Furthermore, the influence of the surfactant concentration on the droplet size after emulsification as well as on the nucleation mechanisms during polymerization is highlighted. Possible process routes for the emulsification of the nanoparticle-loaded monomer phase are compared taking into account different process and material parameters, such as energy consumption, abrasion, dispersed phase viscosity, inorganic particle load and size, and morphology of the resulting hybrid particles. The possibility of an industrial implementation via an integrated high pressure homogenization process and a subsequent continuous polymerization are presented.

Keywords Miniemulsion polymerization · Continuous process · Structure control · Emulsification · Droplet breakup

1 Introduction

The incorporation of inorganic particles into polymers has a long history in academic and industrial research. The use of inorganic filler materials in a polymer matrix allows the combination of the properties of both material types. Industrial

T. Merkel (✉) · L.L. Hecht · H.P. Schuchmann
Institute of Process Engineering in Life Sciences, Section I: Food Process Engineering, Karlsruhe Institute of Technology (KIT), Karlsruhe, Germany
e-mail: tobias.merkel@kit.edu

H.P. Schuchmann
e-mail: heike.schuchmann@kit.edu

A. Schoth · C. Wagner · R. Muñoz-Espí · K. Landfester
Max Planck Institute for Polymer Research, Mainz, Germany

M. Kind et al. (eds.), *Colloid Process Engineering*,
DOI 10.1007/978-3-319-15129-8_15

relevant properties of polymers are, for example, flexibility, optical clarity or low weight. In the case of the inorganic filler material, mechanical strength, thermal stability, and optical, magnetic or electronic properties are important. Therefore, such composite materials are already used in a broad range of applications, such as paints, coatings, adhesives, functionalized plastic, and special applications, e.g. in biomedicine [1]. Recent research and developments in polymer science and engineering facilitate the tailoring of inorganic/polymer particles in the nanometer scale. Those particles do not only combine the properties of both materials but also show unique tunable features. The understanding and control of the resulting nanostructure of the composite particles is, thus, an ongoing challenge.

Heterophase methods for the production of inorganic/polymer composite nanoparticles include dispersion, suspension, seeded emulsion, and miniemulsion polymerization. In the case of the first three methods, the morphology control of the resulting composite particle is challenging. Due to diffusion processes during polymerization, the position of the inorganic material inside the polymer matrix is hard to predict. This problem can be overcome by using the miniemulsion polymerization technique. This technique allows the adjustment of the final particle structure in the emulsification step prior to polymerization [1, 2]. In general, miniemulsion droplets are kinetically stabilized. By adding an osmotic reagent, diffusion between the droplets and therefore a size shift due to Ostwald ripening can be suppressed. By adding a surfactant, droplets are stabilized against coalescence. Therefore, the droplet size ideally stays constant during the polymerization process, which leads to a narrow size distribution.

Inorganic/polymer composite nanoparticles can be produced applying a three-stage process (see Fig. 1) [3–7]. In a first step, the inorganic material being usually hydrophilic has to be functionalized to be compatible with the hydrophobic monomer. The functionalized particles can afterwards be dispersed in the oil phase. This nanoparticle-in-monomer suspension is then emulsified in a continuous aqueous-phase, resulting in particle-loaded submicron-sized monomer droplets. In a last

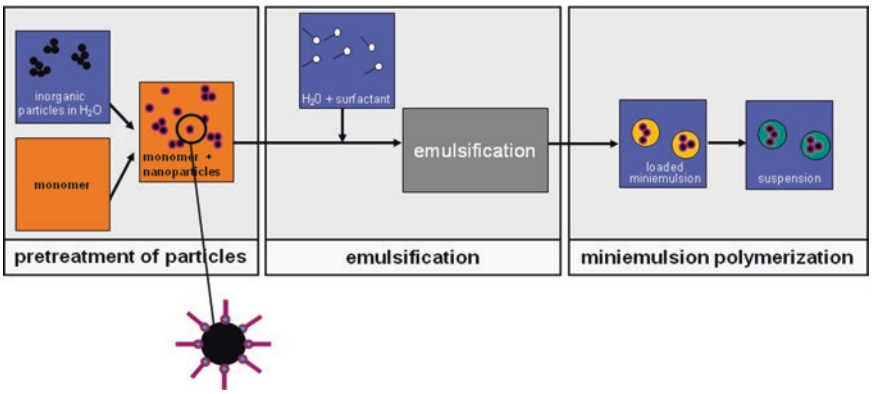

Fig. 1 Preparation of composite particles via miniemulsion polymerization

step, the polymerization is conducted inside these droplets, which act as nanoreactors. Therefore, not only the functionalization but also the emulsification step is essential, as the resulting filled monomer droplets are transformed directly into composite particles during the miniemulsion polymerization. By controlling process and material parameters, the droplets are copied 1:1 to particles. The droplets thus serve as templates for the resulting composite nanoparticles.

Technical processes to disrupt droplets include static mixers [8, 9], rotor-stator systems [9–11], ultrasound devices [9, 12, 13], and high pressure homogenizers [11, 13, 14]. Depending on the process, the resulting droplet size distribution is determined either by the type and concentration of the surfactant, which is needed to stabilize the monomer droplets, or by the energy input [13, 15]. At lab scale, ultrasonication is widely used to emulsify particle loaded droplets. For an industrial application a continuous process would be desirable. High pressure homogenization (HPH) is a suitable technique to produce submicron droplets at high throughput. High pressure homogenizers consist of a high pressure pump, which creates a pressure of 100–5000 bar, and a homogenization unit of variable design [16]. Most of the homogenization units have in common that the fluid is accelerated up to velocities of several hundreds of m/s in a narrow gap, and afterwards injected as a free jet in surrounding liquid. Simple shear, elongational shear, turbulent fluctuations, and cavitation produce stresses that are responsible for droplet breakup [17].

The aim of this chapter is to give an overview on the development of a scalable continuous process for the production of homogeneous inorganic/polymer composite nanoparticles of target size and morphology via miniemulsion preparation and polymerization. First, relevant process steps and parameters are addressed; these are the functionalization of the inorganic nanoparticles, the adjustment of the surfactant concentration, and the effect of particles inside the dispersed phase during emulsification. Subsequently, the possibility of an industrial implementation via an integrated HPH-process is presented.

2 Morphology Control by Surface Functionalization of the Inorganic Particles

The first challenge that has to be solved to synthesize polymer/inorganic hybrid nanoparticles is the difference in polarity between the two materials. Most of the inorganic components are hydrophilic, while a large number of polymers are lipophilic. To handle this difference, the surface of the inorganic material has to be hydrophobized by addition of organic molecules, which can be either low molecular entities or polymeric chains. In the following part, we will present three different ways to promote the interaction between inorganic material and polymer: the application of a surfactant to hydrophobize the inorganic surface, the covalent bonding of a copolymerizable functionalization agent, and the covalent attachment of an inert hydrophobization agent.

As the surfaces of most inorganic oxides (e.g., titania, magnetite or silica) are negatively charged, the positively charged head group of a *cationic surfactant* can be attached via ionic interaction [18]. Although this adsorption process offers a very simple and cheap route to hydrophobize inorganic nanoparticles, hydrophobization by surfactants has a significant disadvantage in the preparation of hybrid nanoparticles: the surfactant molecules are still able to desorb from the surface of the inorganic material, as ionic interaction is reversible. With regard to the application in focus, this reversibility leads to two effects critical for morphology control: the surface properties of the inorganic particles are no longer well-defined and the total amount of free surfactant in the system is not constant [19].

In a system consisting of poly(methyl methacrylate) (PMMA) and silica particles hydrophobized with cetyltrimethylammonium chloride (CTMA-Cl), desorption of the surfactant leads to a decrease of surface hydrophobicity, which prohibits the integration of the silica particles into the polymer matrix [19]. To overcome this problem, the interaction of polymer and silica has to be enhanced by using a *polar co-monomer* such as 4-vinylpyridin (4-VP) [19]. The increased interaction between polymer and silica results in an improved encapsulation of the silica [20].

To overcome desorption of the functionalization agent a second hydrophobization technique is proposed: the *covalent attachment of organic molecules* to the surface of the inorganic particles. In the above mentioned system, this can be carried out by silanization of silica with alkoxysilanes such as 3-methacryloxypropyltrimethoxysilane (MPS) [21–23]. The mechanism of the silanization was described by Philipse and Vrij [24] and consists of different equilibria. Under basic conditions, the alkoxysilane hydrolyzes to form a hydroxysilane. These hydroxyl groups are able to condensate and form siloxane oligomers. The chain length of these oligomers highly depends on the ambient conditions, especially temperature and pH [25, 26]. It is also possible to control the chain length of the polycondensates by the addition of a surfactant (e.g., sodium dodecyl sulfate), which limits their possible size in solution [23]. The oligomers formed can interact with the surface of silica nanoparticles in the next step by hydrogen bonding, leading to reversible adsorption [24]. Hence, the described process consists of three separate steps: hydrolysis, condensation, and adsorption. Each of these steps is sensitive towards variations in the reaction protocol and it can take up to several days to reach full equilibration [27]. Therefore, a precise control of the ambient conditions is mandatory to obtain a product with reproducible properties. After equilibration, the binding between the particles and the adsorbed functionalization agent can be fixed by thermal treatment. The free hydroxyl groups of the adsorbed siloxane oligomers condensate onto the silica surface and form covalent bonds [24].

Table 1 shows the effect of a stable connection between silica and functionalization agent. While desorption of a surfactant like CTMA-Cl leads to a decrease in particle size, the size remains constant for high amounts of MPS-functionalized silica particles [20]. A higher amount of free surfactant also supports secondary nucleation, which leads to a broader size distribution of the resulting hybrid particles [13].

Table 1 Particle sizes of hybrid nanoparticles with differently functionalized silica particles [20]

Functionalization agent	CTMA-Cl	MPS	ODTMS
Monomer	MMA-*co*-4-VP	MMA	MMA
Surfactant	Lutensol AT50	SDS	SDS
Amount of silica [wt%]	Diameter [nm]		
1	251 ± 25	122 ± 37	125 ± 45
5	212 ± 24	123 ± 38	126 ± 37
10	200 ± 41	124 ± 42	118 ± 47
20	186 ± 56	120 ± 38	120 ± 53
30	173 ± 58	133 ± 43	149 ± 50
40	145 ± 53	148 ± 58	158 ± 58

The next effect to be addressed is the connection between functionalization agent and polymer. Different functionalization agents offer the possibility to either hydrophobize the inorganic surface with inert end groups like alkyl chains [28, 18], or to add a polymerizable end group that can copolymerize with the surrounding monomer [29, 22]. Two examples offering these possibilities for the considered silica system are octadecyltrimethoxysilane (ODTMS) on the one hand, and MPS on the other hand. While the MPS-functionalized particles are homogeneously distributed inside the polymer particle, the ODTMS-functionalized particles form a Janus-like structure (see Fig. 2). This structure is caused by aggregation and segregation processes during polymerization [20].

A completely different strategy to synthesize polymer/inorganic hybrid nanoparticles in miniemulsion is the *solvent evaporation technique*. Instead of a monomer droplet that polymerizes after sonication, a pre-formed polymer is dissolved in an organic solvent such as chloroform or toluene [30]. This polymer solution forms the dispersed phase of the miniemulsion. Evaporation of the solvent from the miniemulsion droplets leads to precipitation of the polymer and the formation of nanoparticles. This technique could also allow for the synthesis of hybrid

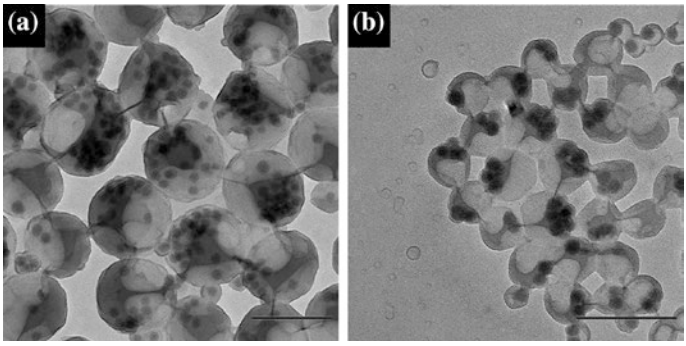

Fig. 2 Electron micrographs of PMMA/silica hybrid nanoparticles with **a** MPS-silica and **b** ODTMS-silica. Scale bars are 200 nm [20]

nanoparticles with different inorganic materials and varying polymers [31]. Due to the lack of copolymerization in this case, it should be possible to figure out the role of the compatibility between the polymer and the functionalization agent. The solvent evaporation technique is therefore a promising field for further investigations.

3 Influence of the Surfactant Concentration on Miniemulsion Polymerization

3.1 Determination of the Ideal Surfactant Concentration

In miniemulsion polymerization, droplets are transformed to polymer particles keeping constant particle size and composition during polymerization. However, instabilities in droplet structure may occur due to three main mechanisms:

1. Ostwald ripening leads to a growth of bigger droplets combined with a shrinkage of smaller ones due to differences in the Laplace pressures of the droplets. This can be controlled by adding an osmotic stabilizer (costabilizer, hydrophobe), which results in an osmotic pressure that counteracts the Laplace pressure.
2. Coalescence happens when the droplets are not sufficiently stabilized by surfactant.
3. Formation of new polymer particles in the continuous phase by droplet nucleation [32], micellar nucleation [33], and homogeneous nucleation [34]. Droplet nucleation should be the predominant nucleation mechanism in miniemulsion polymerization, as only here the composition of the droplet stays constant. Micellar nucleation and homogeneous nucleation lead to the unwanted formation of new polymer particles in the continuous phase and are therefore called secondary nucleation.

Before the polymerization starts, the initiator molecules can either be located in monomer-swollen micelles, in monomer droplets, or in the continuous aqueous phase [35]. The distribution depends on several factors, including first of all the hydrophilic properties of the initiator. But even when oil-soluble initiators are used, radicals are very likely to be present in the aqueous phase [35–37]. Those radicals in the aqueous phase either (re)enter a droplet and lead to droplet nucleation, enter a micelle and lead to micellar nucleation, or start polymerizing monomer molecules dissolved in the aqueous phase. Those oligomers can either enter a droplet or precipitate (homogeneous nucleation) [38].

To avoid changes of droplet size and morphology during polymerization, micellar nucleation and homogeneous nucleation, as well as coalescence, need to be suppressed. The surfactant concentration is essential to achieve that goal and, therefore, has to be adjusted according to formulation and droplet size.

Micellar nucleation can be eliminated by working below the critical micelle concentration (cmc). Homogeneous nucleation is more difficult to avoid. It depends not only on the surfactant concentration, but also on the solubility of the

monomer in water [39], the initiator concentration [40], its solubility in water, and the droplet size [40–42]. In this book chapter, we focus on the influence of the surfactant concentration. A low surfactant concentration leads to decreased polymer particle formation by homogeneous nucleation [40, 43], because less surfactant molecules are available to stabilize the generated oligomers. If the particles are not stabilized, they are either incorporated into a droplet or, as proposed by Ziegler et al. [39], they may aggregate with other particles.

In several investigations it was observed that below the cmc droplet nucleation is the dominating nucleation mechanism [15, 44, 45]. Therefore, the first step in calculating the maximum surfactant concentration $c_{max,}$ at which no secondary nucleation occurs, is the calculation of the cmc in the miniemulsion.

An approximation of the cmc in an emulsion $c_{cmc,emulsion}$ can be calculated using Eq. (1) [46, 47] based on the assumption that surfactant molecules build a monolayer at the oil/water (o/w) interface and that no micelles are formed before the interface is completely covered:

$$c_{\mathrm{cmc,emulsion}} = c_{\mathrm{cmc,water}} + \Gamma_{\mathrm{m}} \cdot \frac{6}{\mathrm{d}_{3,2}} \cdot \frac{\varphi}{1-\varphi} \tag{1}$$

Here, $c_{cmc,water}$ is the cmc of the surfactant in pure water, Γ_m is the total adsorption, $d_{3,2}$ is the Sauter mean diameter and φ is the dispersed phase content.

However, for monomer/water emulsions, due to the solubilization of monomer in micelles, micelles may be formed before the interface is completely covered [48–50]. Hence, the equilibrium between adsorbed surfactant molecules at the interface and free surfactant molecules in the bulk has to be regarded. This equilibrium can be described via the following mass balance [51].

$$c_{\mathrm{total}} \cdot V_{\mathrm{w}} = c_{\mathrm{b}} \cdot V_{\mathrm{w}} + \Gamma \cdot A_T \tag{2}$$

c_{total} is the total surfactant concentration in the emulsion, V_w is the volume of the continuous water phase, c_b the concentration of free surfactant molecules in the bulk phase, A_T the total interfacial area in the emulsion and Γ the adsorption (surfactant molecules per surface area). Combining Eq. (2) with the Langmuir adsorption isotherm Eq. (3) leads to Eq. (4) with b being the adsorption coefficient.

$$\Gamma = \Gamma_{\mathrm{m}} \frac{c}{c + 1/b} \tag{3}$$

$$c_{\mathrm{total}} \cdot V_{\mathrm{w}} = c_b \cdot V_{\mathrm{w}} + \Gamma_{\infty} \cdot \frac{c_b}{\frac{1}{b} + c_b} \cdot A_{\mathrm{T}} \tag{4}$$

c_{total} equals the cmc in the emulsion ($c_{cmc,emulsion}$) when c_b reaches the cmc in the water phase $c_{cmc,water}$. A new equation for the cmc in the emulsion is the result:

$$c_{\mathrm{cmc,emulsion}} = c_{\mathrm{cmc,water}} + \Gamma_m \cdot \frac{\mathrm{cmc}}{1/b + \mathrm{cmc}} \cdot \frac{6}{d_{3,2}} \cdot \frac{\varphi}{1-\varphi} \tag{5}$$

The cmc $c_{cmc,water}$, the total adsorption Γ_m as well as adsorption coefficient b can be determined via the adsorption isotherm measured at the water/monomer

Table 2 Results of fitting the interfacial tension measurements

Surfactant	cmc (measured at water/MMA interface) [mmol l^{-1}]	Model	Mean squared error of fit and experiment *MSE* [−]	Total adsorption Γ_{max} [mol m^{-2}]	Model constants a, α, ε^a	Adsorption coefficient b [m^3 mol^{-1}]
SDS	5.5	Reorientation [53]	0.07	1.62×10^{-6}	$\alpha = 2$; $\varepsilon = 0$	1.7
Lutensol AT50	2×10^{-3}	Frumkin	0.07	1.35×10^{-6}	$a = 2$; $\varepsilon = 0$	933.8

[a]α dependence of adsorption activity on molecular surfactant area [54]
ε two-dimensional relative surface layer compressibility coefficient [55]
a intermolecular interaction constant

interface. The adsorption isotherms of sodium dodecyl sulfate (SDS) and Lutensol AT50 at the water/MMA interface were measured and fitted with different adsorption models (see [52] for details). The best fit results are shown in Table 2.

To determine the ideal surfactant concentration experimentally, the stability of the droplets during polymerization was measured: it can be characterized via the change in Sauter mean diameter of the droplet or particle collective. The size distribution was measured via dynamic light scattering before and after polymerization. The change in Sauter mean diameter, corrected by the alteration of density during polymerization, is calculated via Eq. (6). At $\Delta d_{3,2} = 0$, a stable miniemulsion polymerization process took place. Values of $\Delta d_{3,2} < 0$ indicate the formation of new polymeric particles. In the case of the preparation of composite particles this would lead to the presence of unfilled polymer particles besides the target composite particles. Values of $\Delta d_{3,2} > 0$ indicate droplet-droplet coalescence during polymerization, and thus a loss of size control via the miniemulsification step. In this chapter, all surfactant concentrations are given in relation to the continuous phase.

$$\Delta d_{3,2} = d_{3,2\_after} - d_{3,2\_before} \cdot \sqrt[3]{\frac{\rho_{monomer}}{\rho_{polymer}}} \tag{6}$$

In Fig. 3 the change of Sauter mean diameter for different surfactant concentrations and droplet sizes is shown for two different surfactants. SDS is a small anionic surfactant ($M = 288.4$ g mol^{-1}), whereas Lutensol AT50 (a poly(ethylene oxide)-hexadecyl ether with an EO block length of about 50 units) is a nonionic surfactant with a molecular weight of $M = 2460$ g mol^{-1}. In Fig. 3a it can be seen that for Lutensol AT50 the surfactant concentration at which no change in $\Delta d_{3,2}$ occurs (stable miniemulsion polymerization) is nearly identical to the cmc in the emulsion $c_{cmc,\ emulsion}$. For SDS, however, a significant variation between the cmc in the emulsion and the ideal surfactant concentration can be seen. For all droplet sizes observed, the ideal surfactant concentration is significantly smaller than $c_{cmc,emulsion}$.

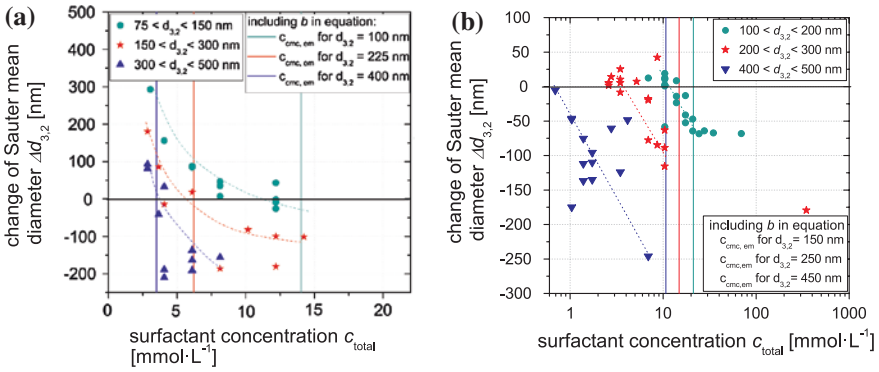

Fig. 3 Change of Sauter mean diameter for different surfactant concentrations **a** for Lutensol AT50 and **b** for SDS

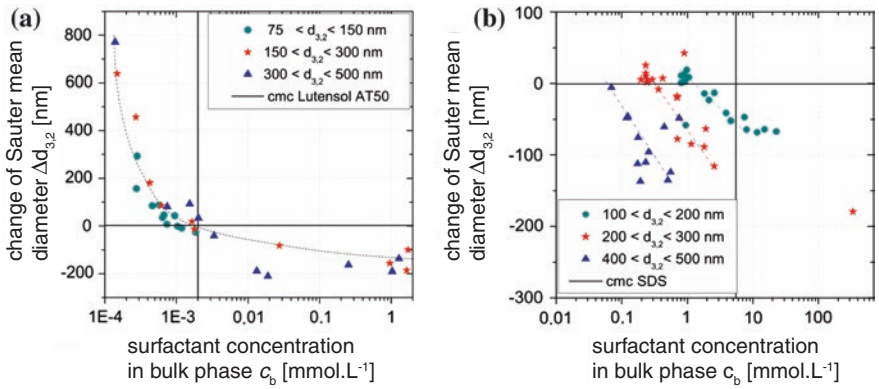

Fig. 4 Change of Sauter mean diameter depending on the surfactant concentration in the bulk phase for **a** Lutensol AT50 and **b** SDS. The dispersed phase content was $\varphi = 20$ %. The *solid line* corresponds to the cmc of the corresponding surfactant in water

In Fig. 4, the same experimental data is plotted versus the surfactant concentration in the bulk phase. It can be seen, that for SDS the concentration at which secondary nucleation occurs is changing with droplet size. Especially for bigger droplets, the bulk concentration c_b is significantly below the cmc (5.5 mmol L^{-1}) when secondary nucleation starts. This is a strong indication for homogeneous rather than micellar nucleation being the reason for the change in droplet/particle size during polymerization. Furthermore, for SDS the ratio r between surfactant molecules in the bulk phase and the number of droplets is nearly constant (see Table 3). The oligomers formed in the bulk phase can either be stabilized by surfactant molecules or incorporated in a droplet. According to the literature presented earlier [39–43], we propose that the probability for both events changes, depending on r. The higher the number of droplets is, the higher the surfactant

Table 3 Surfactant concentrations and number of droplets depending on the droplet size

Surfactant	Droplet size	Ideal surfactant concentration $c_{total,ideal}$ [mmol L^{-1}]	Surfactant concentration in bulk phase c_b at $c_{total,\ ideal}$ [mmol L^{-1}]	Number of surfactant molecules in bulk phase n [molecules L^{-1}]	Ratio r between number of surfactant molecules in bulk phase and droplets [molecules/droplet]
SDS	75	$(3.3 \pm 0.4) \times 10^{1}$	$(4.8 \pm 2.7) \times 10^{0}$	$(2.3 \pm 1.3) \times 10^{21}$	$(2.4 \pm 1.4) \times 10^{3}$
SDS	150	$(1.2 \pm 0.1) \times 10^{1}$	$(1.06 \pm 0.3) \times 10^{0}$	$(5.1 \pm 1.5) \times 10^{20}$	$(4.2 \pm 1.2) \times 10^{3}$
SDS	250	$(3.6 \pm 0.4) \times 10^{0}$	$(2.3 \pm 0.4) \times 10^{-1}$	$(1.1 \pm 0.2) \times 10^{20}$	$(4.3 \pm 0.7) \times 10^{3}$
SDS	350	$(1.2 \pm 0.1) \times 10^{0}$	$(8.4 \pm 1.1) \times 10^{-2}$	$(4.0 \pm 0.6) \times 10^{19}$	$(4.2 \pm 0.6) \times 10^{3}$
SDS	450	$(6.9 \pm 0.8) \times 10^{-1}$	$(5.7 \pm 0.8) \times 10^{-2}$	$(2.7 \pm 0.3) \times 10^{19}$	$(6.1 \pm 0.9) \times 10^{3}$
Lutensol AT50	100	$(1.0 \pm 0.1) \times 10^{1}$	$(1.0 \pm 0.2) \times 10^{-3}$	$(4.8 \pm 1.1) \times 10^{17}$	1.2 ± 0.3
Lutensol AT50	225	$(4.9 \pm 0.9) \times 10^{0}$	$(1.1 \pm 0.4) \times 10^{-3}$	$(5.4 \pm 2.3) \times 10^{17}$	15.1 ± 6.3
Lutensol AT50	400	$(2.6 \pm 0.7) \times 10^{0}$	$(1.0 \pm 0.7) \times 10^{-3}$	$(4.8 \pm 3.2) \times 10^{17}$	75.8 ± 51.1

concentration in the bulk phase can be, without secondary nucleation occurring. For Lutensol AT50 the ratio between number of surfactant molecules in the bulk phase and droplets is not constant, whereas c_b is constant and close to the cmc of Lutensol AT50.

For Lutensol AT50, secondary nucleation occurs at exactly the same surfactant concentration in the bulk phase for all droplet sizes (Table 3). This value is close to the cmc of Lutensol AT50 (2×10^{-3} mmol L^{-1}, measured at the MMA/water interface). The small deviation observed may be due to micelles or premicellar aggregates [56–58] that are already formed at this concentration and, thus, micellar nucleation takes place. Consequently, we conclude that for Lutensol AT50 micellar nucleation is the reason for the formation of new particles.

Possible explanations for the different nucleation mechanisms depending on the type of surfactant are the differences in dynamic adsorption behavior and equilibrium concentration in the bulk phase, as discussed in [52].

For Lutensol AT50, an example for a slow adsorbing surfactant with a low concentration of free molecules in the continuous phase (see Fig. 5), the ideal surfactant concentration correlates with the cmc in the miniemulsion [to be calculated with Eq. (5)]. Here, homogeneous nucleation is negligible. For SDS, a surfactant depicting fast adsorption kinetics and a high amount of free molecules in the continuous phase (see Fig. 5), homogeneous nucleation occurs and, consequently, new polymer particles are formed at concentrations smaller than the cmc in the emulsion. In this case, the ideal surfactant concentration in the bulk phase depends on various factors, e.g. the droplet size, the initiator concentration, and the dispersed phase content. That is why, for SDS the ideal surfactant concentration has to be determined experimentally. If a flexible process is needed, the application of Lutensol AT50 or other non-ionic polymeric surfactants with corresponding characteristics is recommended for the stabilization of miniemulsions.

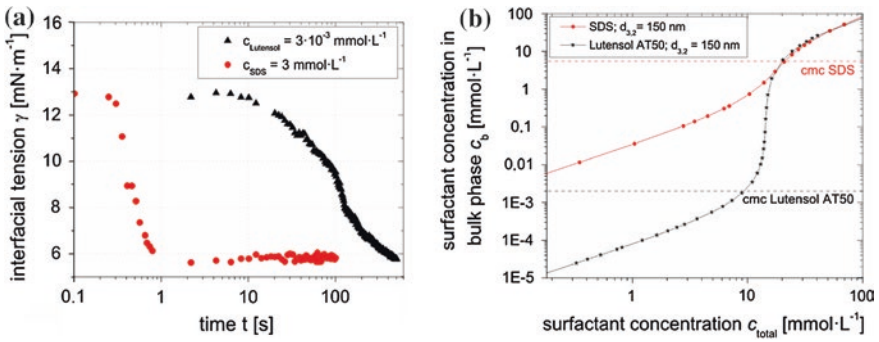

Fig. 5 **a** Dynamic adsorption behavior of SDS and Lutensol AT50 at the MMA/water interface (measured via drop profile and capillary pressure tensiometry) **b** equilibrium concentration of SDS and Lutensol AT50 in the bulk phase for a droplet size of 150 nm and different surfactant concentrations [calculated via Eq. (4)]

3.2 Influence of Inorganic Nanoparticles on the Ideal Surfactant Concentration

To show the influence of inorganic particles on the surfactant concentration, the parameter A_{surf}, the theoretical interfacial area per surfactant molecule is applied [13, 15, 59]. A_{surf} is calculated by dividing the total interfacial area in the miniemulsion by the number of surfactant molecules at the interface, which results in the following equation:

$$A_{\mathrm{surf}} = \frac{6 \cdot \varphi \cdot M_{\mathrm{surf}}}{d_{3,2} \cdot \rho_{\mathrm{monomer}} \cdot c_{\mathrm{surf}} \cdot N_A \cdot (1 - \frac{c_{\mathrm{b}}}{c_{\mathrm{total}}})} \tag{7}$$

Herein are φ the dispersed phase content, M_{surf} the molar mass of the surfactant, c_{surf} the concentration of surfactant, $d_{3,2}$ the Sauter mean diameter of the droplet collective, ρ_{monomer} the density of the monomer, N_A the Avogadro constant and $(1\text{-}c_{\mathrm{b}}/c_{\mathrm{total}})$ is a correction factor which accounts for the surfactant that does not adsorb at the interface but resides in the continuous bulk phase. A_{surf} shows the influence of the inorganic particles on the surfactant concentration needed to stabilize a certain amount of interface can be seen directly.

In Fig. 6, the influence of an inorganic particle load on the change of the Sauter mean diameter is shown. The intersection with the x-axis is the ideal value for A_{surf} as no change of droplet size is considered ideal in miniemulsion polymerization. It can be seen that $A_{\mathrm{surf,ideal}}$ increases significantly if CTMA-silica particles

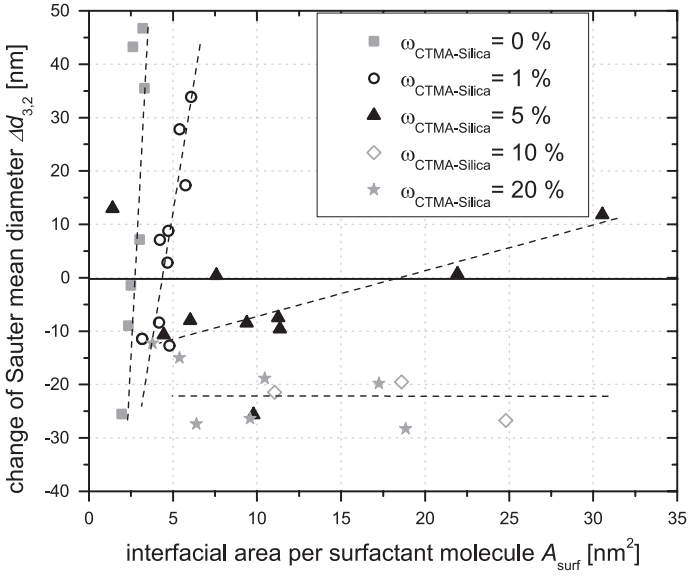

Fig. 6 Change in Sauter mean diameter versus interfacial area per Lutensol AT50 molecule A_{surf} for pure monomer droplets and droplets filled with CTMA-silica in different concentrations

are added to the dispersed phase. As A_{surf} is inversely proportional to the surfactant concentration this means that the ideal surfactant concentration decreased with the addition of the inorganic particles. The surfactant concentration can no longer be calculated with Eq. (5). At higher particle load, miniemulsions may even not be polymerized ed: With the chosen material system, only a maximum of 5 wt% silica particles could be homogeneously encapsulated. At 10 wt% silica particles or more, the change of droplet/particle size during polymerization indicates the presence of unfilled polymer particles alongside with the target hybrid ones.

In [19] it was shown that the mechanisms for the increase in $A_{surf,min}$ are: (1) The inorganic particles leave the droplet completely and falsify the measurement results. (2) The inorganic particles are localized in the interface, replacing the surfactant molecules there and forcing the latter to reside in the continuous phase. (3) The hydrophobizing agent CTMA-Cl desorbs from the silica particle surface and acts as additional surfactant.

The first mechanism can be avoided by the addition of 4-vinylpyridine to the dispersed phase (see Sect. 2). Mechanism 2 and 3 cannot be avoided when using a physical modification agent (see [19] for details), therefore a chemical modification of the particle surface is recommended. In order to achieve a chemical modification, particles were hydrophobized with MPS (see Sect. 2) and thoroughly washed to avoid the presence of additional, adsorbed MPS molecules on the particles. If these particles are added to the monomer phase even at a particle concentration of $\omega = 30$ %, no influence of the particle load on the ideal value for $A_{surf,}$ and therefore the surfactant concentration, could be measured (see Fig. 7). The

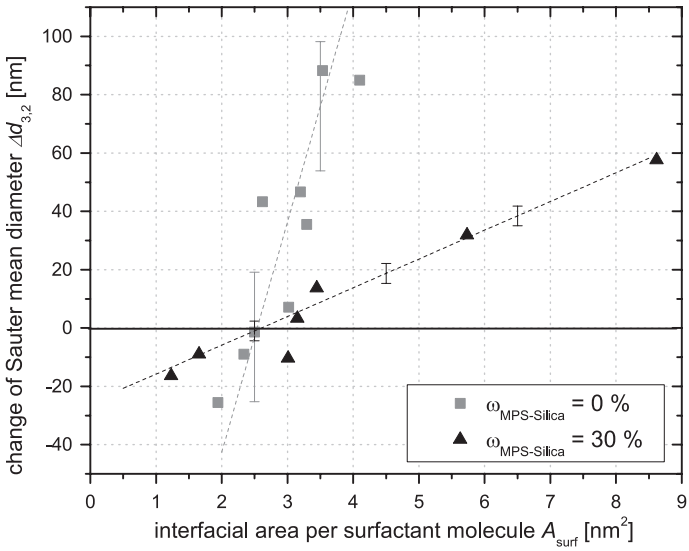

Fig. 7 Influence of MPS-silica particles on the ideal surfactant concentration (surfactant: Lutensol AT50, $\varphi = 20$ %, details for particle preparation as well as the fit can be found in [60])

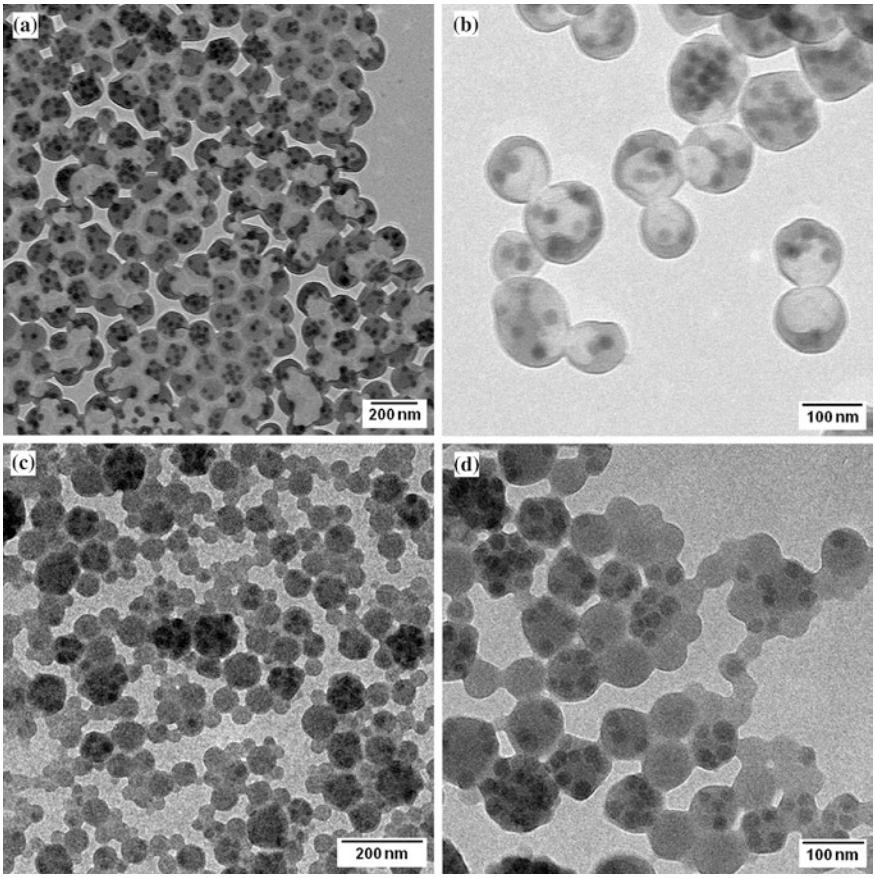

Fig. 8 TEM-pictures of 30 % MPS-silica encapsulated in PMMA. **a**, **b** Ideal surfactant concentration (Lutensol AT50, $A_{surf} = 3.0$ nm^2, $c_{total} = 4$ mmol L^{-1}). **c**, **d** surfactant concentration too high (Lutensol AT50, $A_{surf} = 1.2$ nm^2, $c_{total} = 12$ mmol L^{-1})

influence of the ideal surfactant concentration on the particle morphology is shown for MPS-Silica particles in Fig. 8.

For MPS-silica particles it is possible to produce hybrid nanoparticles with a high particle load without producing unfilled polymer particles by secondary nucleation. The surfactant concentration can be adjusted independently from the particle load. Only if the droplet size depends on the particle load (e.g., due to an increased viscosity), the surfactant concentration has to be adjusted.

4 Design of a Scalable Continuous Process Route

4.1 Utility of High Pressure Homogenization (HPH) in Regard to Miniemulsion Polymerization

For the production of inorganic/polymer composite nanoparticles via miniemulsion polymerization, the emulsification step prior to the polymerization of the particle loaded monomer droplets is of great importance. By adjusting the surfactant concentration (see Sect. 3), coalescence as well as secondary nucleation during polymerization resulting in additional unfilled polymer particles can be prevented, and the composite particle size distribution is determined directly in the emulsification step [13, 61].

In general, droplet deformation and breakup is governed by counteracting deforming viscous stresses and shape conserving interfacial and viscous stresses [62, 63]. In order to characterize different emulsification devices regarding their efficiency, a suitable method is to compare the respective applied energy density E_V. E_V is defined as the power input P divided by the flow rate of the emulsion $\dot{V}$ [64]. Therefore, E_V is a value characterizing the mean value of all stresses applied to the droplets in the emulsification step. When deforming and breaking particle loaded droplets, their rheological properties have to be taken into account. Typically, particle suspensions show an increase in viscosity and a shear thinning behavior with increasing particle load [65]. At lab scale, batchwise ultrasonication is widely used to emulsify particle loaded droplets [66–68], even when not being efficient in energy use. For an industrial application, a continuous, energy efficient process is required. HPH is a suitable technique to produce submicron droplets at a high throughput [17]. However, it has to be mentioned that HPH so far has been rarely used to prepare miniemulsions for polymerization [11, 14].

In Fig. 9, ultrasonication and HPH are compared regarding the droplet sizes for varied monomer viscosities [21]. The high pressure homogenizer was equipped with an orifice valve of spherical cross-section (diameter $d = 0.2$ mm, length $l = 0.4$ mm). As found in all emulsification processes, on the one hand the droplet size increases with increasing dispersed phase viscosity when emulsifying at a constant energy input. On the other hand, the droplet size decreases with increasing energy input for a constant dispersed phase viscosity [69]. When comparing HPH with ultrasonication for the emulsification of monomers of higher viscosities (here $\eta = 600$ mPa s), the resulting droplet size is smaller when using HPH despite the mean energy input being lower by a factor of 10. This can be explained by a broad and inhomogeneous distribution of shear rates and a very short residence time of droplets in the spatially confined breakup zone of ultrasonic devices [70]. This results in stresses that are mostly too low or applied for a period too short for deforming and breaking high viscous droplets.

This signifies that HPH is not only favorable regarding scalability and a continuous process design, but it is also better suited to break up high viscous droplets, as found in particle-loaded miniemulsions.

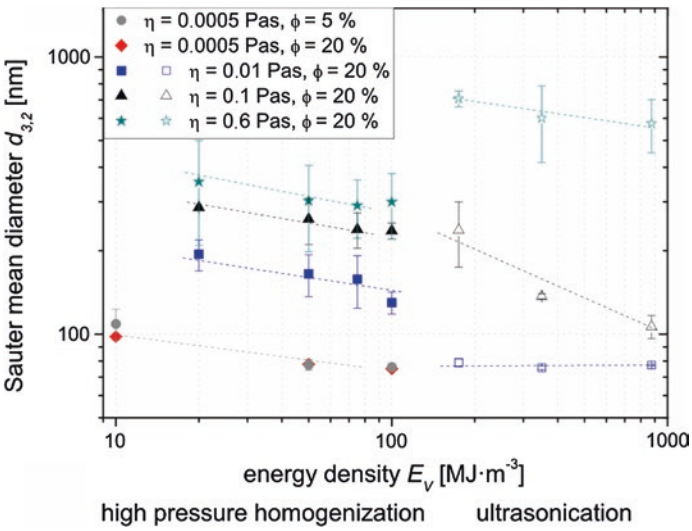

Fig. 9 Comparison of mean droplet sizes resulting from HPH or ultrasonication. The dispersed phase viscosity was adjusted by dissolving different amounts of PMMA in the monomer. The droplet size distribution was measured with dynamic light scattering (*DLS*); the surfactant concentration was 10 mmol L^{-1} SDS with respect to the continuous phase

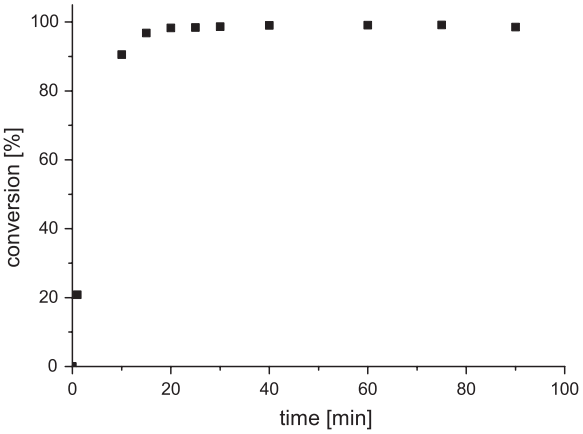

Fig. 10 Conversion versus time curve; $\varphi = 10$ %; without particles; $\vartheta = 80$ °C; volume flow = 0.4 ml s^{-1}, ω(SDS) = 0.3 %

For a feasibility test, a lab-scale continuous polymerization reactor was built. The continuous polymerization of a pure MMA miniemulsion was realized in a simple plug flow reactor (material polypropylene, tube length $l = 18$ m, tube diameter $d = 8$ mm) yielding a stationary conversion around 99 % (see Fig. 10).

4.2 *Influence of Inorganic Particles on Droplet Breakup in High Pressure Homogenizers*

The influence of silica nanoparticle load and agglomerate size on the droplet breakup was investigated [21]. For this, the silica nanoparticle agglomerates, formed in their functionalization step followed by phase transfer to the monomer, were deagglomerated. Different agglomerate sizes were achieved by applying different wetting times t_w of silica agglomerates in monomer (MMA) and additional deagglomeration by ultrasonication. Figure 11 shows the influence of agglomerate size on the breakup of droplets filled with this agglomerates in a high pressure homogenizer equipped with a simple orifice valve ($d = 0.2$ mm, $l = 0.4$ mm), and the corresponding viscosity of the respective dispersed phase.

If the silica nanoparticles are added to the monomer without prior wetting or deagglomeration ($t_w = 1$ h); a significantly increased droplet size in comparison to pure monomer droplets (shown in Fig. 9) can be observed. With increasing wetting time, the silica agglomerate size decreased and so does the resulting droplet size. However, no difference in viscosity could be observed for different wetting times of the suspension (see Fig. 11, right). Consequently, the differences in the resulting droplet size between $t_w = 1$ h and $t_w = 1$ d are probably due to agglomerates disturbing the droplet breakup. For low energy densities, however, the effect of wetting time was more pronounced than for higher energy densities. A possible explanation is that at higher energy densities not only droplets but also the agglomerates inside the droplets are reduced in size. At a short wetting time ($t_w = 1$ d) and a low energy input, the agglomerates may not break up and hence disturb the droplet breakup, resulting in bigger droplets. The positive effect of pre-wetting on the deagglomeration of several inorganic (nano) particles is described in literature [71, 72] and was affirmed for this suspension [21]. To investigate the influence of the agglomerate size on the emulsification the silica

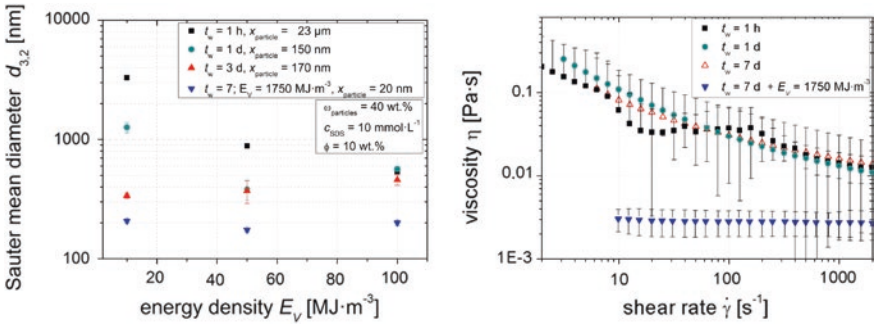

Fig. 11 *Left* Influence of the wetting time of the silica particles in MMA (and correspondingly the Sauter mean diameter of the particle agglomerates $x_{particle}$) on the Sauter mean diameter of the silica loaded MMA droplets. The droplet size distribution was measured with static light scattering (SLS). *Right* resulting shear viscosity functions

particles were deagglomerated to their primary particle size of about 25 nm by wetting them for seven days and subsequently exposing them to an energy density of $E_V = 1750$ MJ m^{-3}. If this suspension was emulsified via HPH, the size of the loaded droplets decreased significantly (e.g., from about 400 nm to less than 200 nm for a homogenization energy of $E_V = 50$ MJ m^{-3}). The resulting decrease in viscosity did surely help in reducing the droplet sizes. It has to be noted that even for well dispersed silica primary particles the resulting droplet size increases with increasing particle load (see Fig. 12). Droplets with a particle load of 40 and 50 wt% were broken up to a droplet size below 200 and 300 nm, respectively. By increasing the particle load up to 60 wt%, a massive increase in droplet size was observed, but still homogeneous composite particles were produced [21]. The increase in droplet size can only partially be explained by the increased viscosity of the dispersed phase (for details see [60]).

Similar results are found in literature for the emulsification of particle loaded droplets by ultrasound [22, 66, 68]. It is questionable if the bulk viscosity increase is the only reason for the hindered droplet breakup. The complex rheological behavior of suspensions and the possible interactions of the nanoparticles at the liquid-liquid-interface have to be taken into consideration in understanding these effects. Numerical simulation of the influence of nanoparticles on droplet deformation yielded a decreased deformation for an increased particle load due to viscous and interfacial effects [73]. Depending on particle-particle- and particle-fluid-interactions, suspensions show an increase in shear thinning or viscoelastic behavior with increasing particle load [65]. Investigations with non-Newtonian fluids without particles showed that droplet deformation and droplet disruption is reduced by

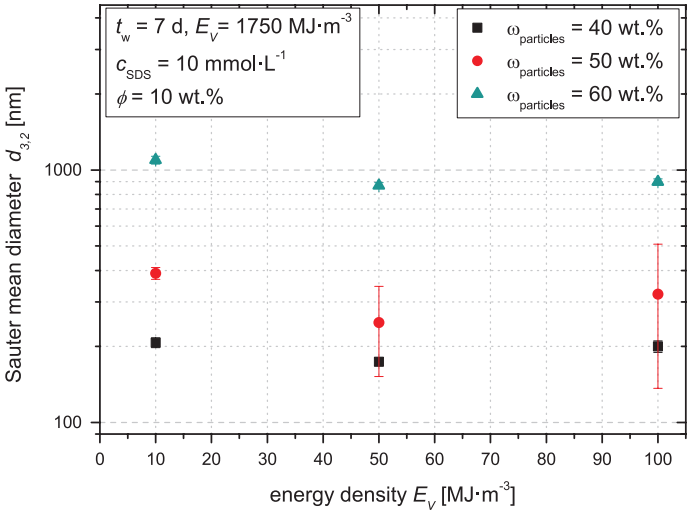

Fig. 12 Influence of the silica particle concentration on the size of the particle loaded droplets. The silica particles have been deagglomerated down to the primary particle size of $x = 25$ nm prior to homogenization. The droplet size was measured with SLS

visco-elastic effects [73, 74]. Regarding shear-thinning droplets, the deformation and breakup of these droplets is similar [75–77] or reduced [78, 79] compared to Newtonian droplets, if the shear rate dependent viscosity during droplet breakup is considered. Further investigations focusing on the effect of colloidal particles on the droplet deformation and breakup are therefore required.

For nearly all experiments, an increase of energy density from 50 to 100 MJ m^{-3} led to a larger droplet size. An increase of droplet size with increasing energy input is typically explained by insufficient stabilization of the droplets and fortified coalescence [46]. This, however, is astonishing, as smaller droplets without nanoparticles could be stabilized at $E_V = 100$ MJ m^{-3} using the same surfactant concentration (Fig. 9). A possible explanation is the increasing coalescence due to the so-called "pin-effect" of particles protruding into the continuous phase [80]. These particles form bridges between the surfaces of two droplets which leads to rapid film rapture and therefore increased coalescence.

4.3 HPPF Homogenization for Reduced Abrasion and Process Intensification

Particles in the monomer phase may influence equipment service life. Regarding an industrial implementation, this influences production costs. The service life of high pressure homogenizers is mainly limited by wear and abrasion in the pumps and the disruption unit. Wear also leads to an unwanted product contamination. Therefore, a method to quantitatively determine wear in HPH of particle loaded miniemulsions was developed [80]. The passage of 1 kg of silica particles through an orifice valve at $\Delta p = 900$ bar led to a significant increase of the volume flow through the orifice valve by more than 35 %. This change in volume flow can be cause by erosion of the inlet geometry and/or the orifice diameter. The same negative effect was observed when the silica particles were encapsulated in a monomer phase, making high pressure homogenization of particle-loaded miniemulsions a challenge.

Abrasion in the disruption unit of high pressure homogenizers can be avoided using the High Pressure Post Feeding (HPPF) valve setting, as proposed by [81]. Here, the fluid which contains the abrasive material is added into the jet forming directly after the orifice valve (see Fig. 13) [81, 82].

Emulsification in the HPPF geometry is possible due to the forced passage of the droplet containing phase through the turbulence field after the orifice valve [83, 84]. However, the droplets do not get elongated at the valve inlet, which is reported to be essential for the disruption of high-viscous droplets [47, 85, 86].

Figure 14 compares the resulting droplet size for a miniemulsion containing 50 wt% functionalized silica emulsified with a conventional orifice valve and a HPPF valve. For low homogenization pressure, HPPF homogenization yields significantly bigger droplets. This phenomenon is also known for Newtonian dispersed phases without particles [87]. A possible explanation is the above

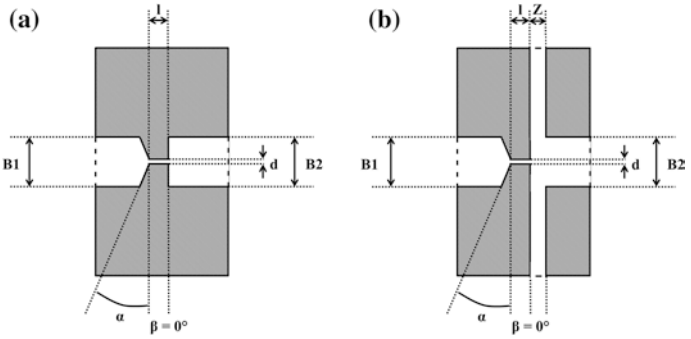

Fig. 13 Geometry details of **a** a conventional orifice valve and **b** a high pressure post feeding (HPPF) valve

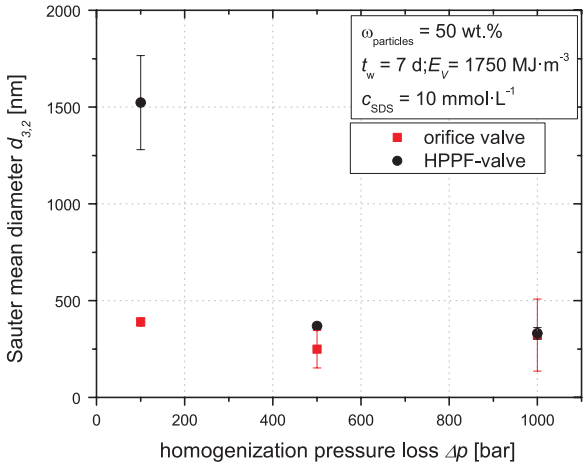

Fig. 14 Comparison of emulsification with a conventional orifice valve and a HPPF valve. The dispersed phase content was 10 wt% after emulsification. The droplet size was measured with SLS

mentioned missing elongation in the valve inlet. For higher homogenization pressures comparable droplet sizes can be achieved with both valves. Here, the disruptive stresses in the turbulent zone after the valve outlet are dominating and the highly viscous droplets can be broken up. TEM images of polymerized composite particles (see Fig. 15) which were emulsified with an HPPF valve do also not show a difference in the composite particle structure in comparison to particles produced with a conventional orifice valve. Additionally less energy density is required in the HPPF setup as only a part of the final emulsion phase passes the pump, making high-pressure homogenization with a HPPF setup a suitable technique for miniemulsion polymerization.

If the desired composite nanostructure can be achieved through a fast functionalization, the HPPF technique offers further possibilities for process intensification regarding the miniemulsion polymerization. The main idea is depicted in Fig. 16. Instead of time consuming batch-functionalization prior to the emulsification, the

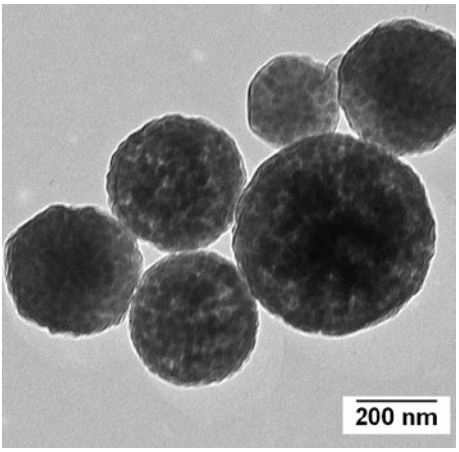

Fig. 15 TEM picture of hybrid particles with 50 wt% silica particles emulsified with an HPPF valve

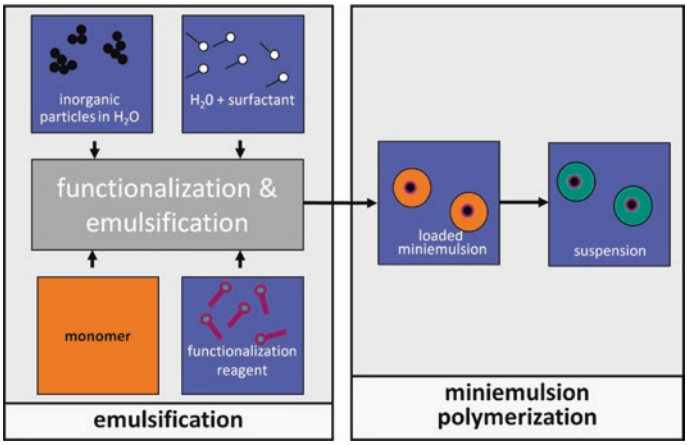

Fig. 16 Incorporation of the functionalization step into the emulsification step

functionalization is incorporated in the emulsification step. Several processes have to go on simultaneously. The inorganic particles have to be deagglomerated and brought into contact with the functionalization reagent. The functionalized particles have to collide with broken monomer droplets and pass the liquid-liquid-interface. The particle loaded droplets have to be stabilized by surfactant. Due to the high mixing efficiency and the high disruptive stresses in the turbulent zone behind the valve outlet, the HPPF device could be a suitable device for these tasks.

For a proof-of-concept, magnetite particles and ricinoleic acid as functionalization reagent were used in cooperation with Prof. Peuker (TU Bergakademie Freiberg) and Prof. Schmid (Universität Paderborn). The particle system was

chosen as simultaneous modification and phase transfer was already achieved at a planar interface. The functionalization of magnetite with ricinoleic acid is described in detail in [88, 89].

The high-pressure process implementation is depicted in Fig. 17. The pre-emulsion containing the monomer phase and the functionalization reagent was conveyed through the high pressure pump and the orifice. In a first mixing chamber of the HPPF valve, the magnetite-suspension was added. The surfactant was added in a second mixing chamber. In order not to disturb the interaction between ricinoleic acid, magnetite particles and the liquid-liquid interface between both mixing chamber a residence time of about 0.5 s was realized using a high pressure tube with a length of 1 m before adding surfactant.

Without additional surfactant, the emulsion could not be stabilized solely be the ricinoleic acid and phase separation occurred. The coalesced monomer phase was loaded with magnetite particles, showing that the phase transfer of magnetite was successful (see Fig. 18). With additional surfactant, a stable miniemulsion resulted. TEM images of the composite parties after polymerization however revealed that the magnetite particles were located at the polymer particle interface and inhomogeneously distributed (see Fig. 18). Presumably pickering emulsions

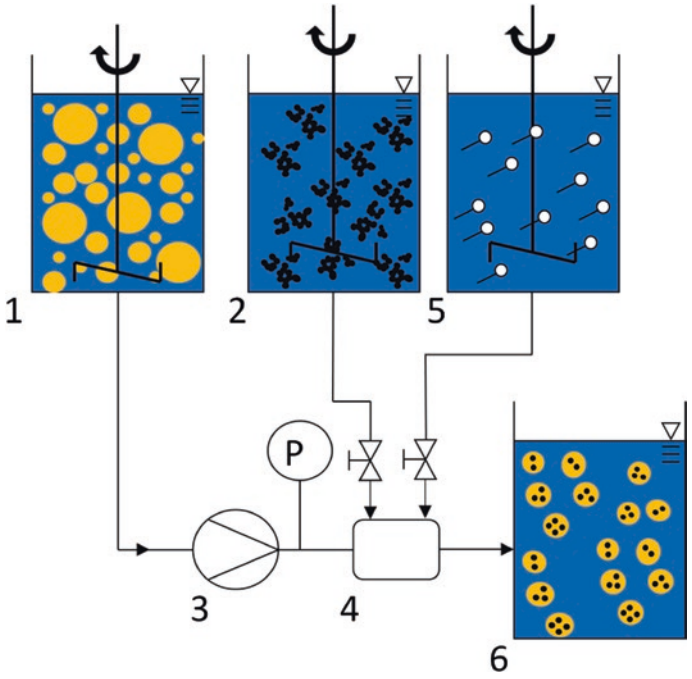

Fig. 17 HPPF process intensification set up; *1* pre-emulsion (ω(MMA) = 9.8 %, ω(hexadecane) = 0.4 %, ω(initator 59) = 0.2 %, ω(ricinoleic acid) = 0.3 %); *2* magnetite suspension (pH = 8, ω(magnetite) = 2.7 %); *3* high pressure pump (Δp = 1000 bar); *4* HPPF device (orifice diameter d = 0.2 mm, 2 mixing chambers); *5* surfactant solution (ω(Lutensol AT50) = 1.9 %; *6* fine emulsion (φ = 13.4 %); all mass fractions are based on the total mass of the fine emulsion

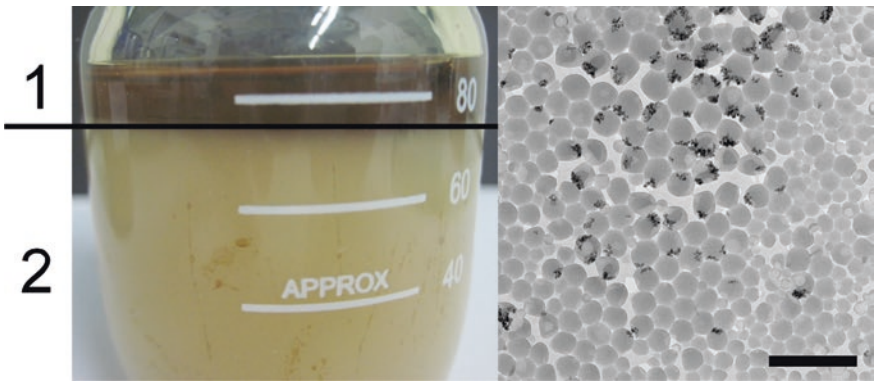

Fig. 18 *Left 1* magnetite loaded monomer phase, *2* unstable emulsion; *right* TEM image of hybrid particles with a magnetite load of 2.7 wt%. Scale bar is 500 nm

were formed during droplet breakup and the subsequent phase transfer of the magnetite particles during coalescence without the presence of an effective surfactant. The formation of pickering emulsions is often favourable due to the high energy of attachment of nanoparticles to a liquid-liquid-interfaces according to their hydrophobicity [90] making a phase transfer without coalescence procedures difficult. Another problem could be that the functionalization reagent chosen can not copolymerize with MMA. Even if the phase transfer was successful, an accumulation of the nanoparticles at the interface probably occurs during polymerization (see Sect. 2). This hypothesis was confirmed by conducting the phase transfer of the magnetite particles into the monomer phase in a stirred vessel prior to the emulsification step. All other parameters were kept constant. TEM images of the particles after polymerization showed that the magnetite accumulated at the interface. Therefore, it is still questionable whether a phase transfer can be realized in very short residence times in the HPPF device. Further research regarding suitable functionalization reagent-monomer combinations is recommended.

5 Concluding Remarks

Polymer/inorganic composite nanoparticles can be produced by miniemulsion polymerization. In order to achieve the desired morphology, the interactions between functionalization reagent, inorganic nanoparticle, monomer, and surfactant have to be controlled. High pressure homogenization proved to be most promising for the production of polymer/inorganic composite nanoparticles. Highly viscous dispersed phases and monomer phases of a high particle load can be broken up efficiently to droplet sizes required for miniemulsion polymerization. The process is well suited for an industrial application, it can be scaled up to throughputs of several thousand liters per hour. Abrasion on the disruption unit can be avoided by using a HPPF setup.

References

1. Landfester K (2009) Angewandte Chemie 48(25):4488–4507 (International Edition)
2. Asua JM (2002) Prog Polym Sci 27(7):1283–1346
3. Bechthold N, Tiarks F, Willert M, Landfester K, Antonietti M (2000) Macromol Symp 151(1):549–555
4. Erdem B, Sudol ED, Dimonie VL, El-Aasser MS (2000) J Polym Sci Part A Polym Chem 38(24):4431–4440
5. Hoffmann D, Landfester K, Antonietti M (2001) Magnetohydrodynamics 37:217–221
6. Zhang SW, Zhou SX, Weng YM, Wu LM (2005) Langmuir 21(6):2124–2128
7. Charoenmark L, Polpanich D, Thiramanas R, Tangboriboonrat P (2012) Macromol Res 20(6):590–596
8. Rahme R, Graillat C, Farzi G, Mckenna TFL, Hamaide T (2010) Macromol Chem Phys 211(21):2331–2338
9. Ouzineb K, Lord C, Lesauze N, Graillat C, Tanguy PA, McKenna T (2006) Chem Eng Sci 61(9):2994–3000
10. El-Jaby U, Mckenna TFL, Cunningham MF (2007) Macromol Symp 259:1–9
11. Lopez A, Chemtob A, Milton JL, Manea M, Paulis M, Barandiaran MJ, Theisinger S, Landfester K, Hergeth WD, Udagama R (2008) Ind Eng Chem Rese 47:6289–6297
12. Kentish S, Wooster J, Ashokkumar A, Balachandran S, Mawson R, Simons L (2008) Innovative Food Sci Emerg Technol 9(2):170–175
13. Hecht LL, Wagner C, Landfester K, Schuchmann HP (2011) Langmuir 27(6):2279–2285
14. Manea M, Chemtob A, Paulis M, de la Cal JC, Barandiaran MJ, Asua JM (2008) AIChE J 54(1):289–297
15. Landfester K, Bechthold N, Tiarks F, Antonietti M (1999) Macromolecules (USA) 32(16):5222–5228
16. Innings F, Fuchs L, Tragardh C (2011) J Food Eng 103(1):21–28
17. Schuchmann HP, Karbstein N, Hecht LL, Gedrat M, Köhler K In: Eggers R (ed) Industrial high pressure applications. Processes, equipment and safety. Wiley-VCH, Verlag, p 97–118, 22 Aug 2012
18. Tiarks F, Landfester K, Antonietti M (2001) Langmuir 17(19):5775–5780
19. Hecht LL, Wagner C, Özcan Ö, Eisenbart F, Köhler K, Landfester K, Schuchmann HP (2012) Macromol Chem Phys 213:2165–2173
20. Schoth A, Wagner C, Hecht LL, Winzen S, Muñoz-Espí R, Schuchmann HP, Landfester K (2014) Colloid Polym Sci 292:2427–2437
21. Hecht LL, Merkel T, Schoth A, Köhler K, Wagner C, Muñoz-Espí R, Landfester K, Schuchmann HP (2013) Chem Eng J 229:206–216
22. Bourgeat-Lami E, Lang J (1998) J Colloid Interface Sci 197(2):293–308
23. Bourgeat-Lami E, Herrera NN, Putaux JL, Reculusa SP, Perro A, Ravaine S, Mingotaud C, Duguet E (2005) Macromol Symp 229(1):32–46
24. Philipse AP, Vrij A (1989) J Colloid Interface Sci 128(1):121–136
25. Posthumus W, Magusin PCMM, Brokken-Zijp JCM, Tinnemans AHA, van der Linde R (2004) J Colloid Interface Sci 269(1):109–116
26. Paquet O, Brochier Salon MC, Zeno E, Belgacem MN (2012) Mater Sci Eng C 32(3):487–493
27. Nishiyama N, Horie K, Asakura T (1987) J Appl Polym Sci 34(4):1619–1630
28. Murray E, Born P, Weber A, Kraus T (2010) Adv Eng Mater 12(5):374–378
29. Ramirez LP, Landfester K (2003) Macromol Chem Phys 204(1):22–31
30. Staff RH, Rupper P, Lieberwirth I, Landfester K, Crespy D (2011) Soft Matter 7(21):10219–10226
31. Urban M, Musyanovych A, Landfester K (2009) Macromol Chem Phys 210(11):961–970
32. Hansen FK, Ugelstad J (1979) J Polym Sci Part A Poly Chem 17(10):3069–3082
33. Harkins WD (1947) J Am Chem Soc 69(6):1428
34. Priest WJ (1952) J Phys Chem 56(9):1077–1082

35. Nomura M, Suzuki K (2005) Ind Eng Chem Res 44(8):2561–2567
36. Autran C, de la Cal JC, Asua JM (2007) Macromolecules 40(17):6233–6238
37. Luo YW, Schork FJ (2002) J Polym Sci Part A Polym Chem 40(19):3200–3211
38. Capek I (2001) Adv Colloid Interface Sci 91(2):295–334
39. Ziegler A, Landfester K, Musyanovych A (2009) Colloid Polym Sci 287(11):1261–1271
40. Chern CS, Liou YC (1999) J Polym Sci Part A-Polym Chem 37(14):2537–2550
41. Alduncin JA, Forcada J, Asua JM (1994) Macromolecules 27(8):2256–2261
42. Rodriguez R, Barandiaran MJ, Asua JM (2007) Macromolecules 40(16):5735–5742
43. Saethre B, Mork PC, Ugelstad J (1995) J Polym Sci Part A-Polym Chem 33(17):2951–2959
44. Reimers J, Schork FJ (1996) J Appl Polym Sci 59(12):1833–1841
45. Huang H, Zhang HT, Li JZ, Cheng SY, Hu F, Tan B (1998) J Appl Polym Sci 68(12):2029–2039
46. Karbstein H (1994) Dissertation, Universität Karlsruhe (TH)
47. Tesch S (2002) Dissertation, Universität Karlsruhe (TH)
48. Piirma I, Chen SR (1980) J Colloid Interface Sci 74(1):90–102
49. Paxton TR (1969) J Colloid Interface Sci 31(1):19
50. Oehlke K, Garamus VA, Heins A, Stockmann H, Schwarz K (2008) J Colloid Interface Sci 322(1):294–303
51. Lin SY, Dong CD, Hsu TJ, Hsu CT (2002) Colloids Surf., A 196(2–3):189–198
52. Hecht LL, Schoth A, Muñoz-Espí R, Javadi A, Köhler K, Miller R, Landfester K, Schuchmann HP (2013) Macromol Chem Phys 214(7):812–823
53. Miller R, Aksenenko EV, Liggieri L, Ravera F, Ferrari M, Fainerman VB (1999) Langmuir 15(4):1328–1336
54. Fainerman VB, Miller R, Wüstneck R, Makievski AV (1996) J Phys Chem 100(18):7669–7675
55. Fainerman VB, Miller R (2008) Colloids Surf., A 319(1–3):8–12
56. Zettl H, Portnoy Y, Gottlieb M, Krausch G (2005) J Phys Chem B 109(27):13397–13401
57. Cui X, Mao S, Liu M, Yuan H, Du Y (2008) Langmuir 24(19):10771–10775
58. Hadgiivanova R, Diamant H (2007) J Phys Chem B 111(30):8854–8859
59. Okubo M, Yamada A, Matsumoto T (1980) J Polym Sci Part A Polym Chem 18(11):3219–3228
60. Hecht LL (2013) Dissertation, Karlsruher Institut für Technologie
61. Tcholakova S, Denkov ND, Danner T (2004) Langmuir 20(18):7444–7458
62. Taylor GI (1932) Proceedings of the royal society of london series a—containing papers of a mathematical and physical character, vol 138(41)
63. Taylor GI (1934) Proc Roy Soc 29:501–523
64. Karbstein H, Schubert H (1995) Chem Eng Proc 34:205–211
65. Pahl M, Gleißle W, Laun HM (1991) Praktische Rheologie der Kunststoffe und Elastomere, VDI-Verl
66. Diaconu G, Paulis M, Leiza JR (2008) Macromol React Eng 2(1):80–89
67. Bourgeat-Lami E, Farzi GA, David L, Putaux JL, Mckenna TFL (2012) Langmuir 28(14):6021–6031
68. Luo YD, Dai CA, Chiu WY (2009) J Appl Polym Sci 112(2):975–984
69. Walstra P (1993) Chem Eng Sci 48(2):333–349
70. Schuchmann HP, Freudig B, Behrend O (2012) In: Schuchmann HP, Köhler K (eds) Emulgiertechnik. Behr's Verlag
71. Pohl M (2005) Dissertation, Universität Karlsruhe (TH)
72. Mages-Sauter C (2010) Dissertation. Dr. Hut, München
73. Usta OB, Perchak D, Clarke A, Yeomans JM, Balazs AC (2009) J Chem Phys 130(23)
74. Guido S (2011) Curr Opin Colloid Interface Sci 16(1):61–70
75. Elmendorp JJ, Maalcke RJ (1985) Polym Eng Sci 25(16):1041–1047
76. Bruijn RAd (1989) Deformation and breakup of drops in simple shear flows
77. Delaby I, Ernst B, Froelich D, Muller R (1996) Polym Eng Sci 36(12):1627–1635
78. Boufarguine M, Renou F, Nicolai T, Benyahia L (2010) Rheol Acta 49(6):647–655
79. Favelukis M, Lavrenteva OM, Nir A (2005) J Nonnewton Fluid Mech 125(1):49–59
80. Tcholakova S, Denkov ND, Hristova D, Druelle M (2010) Proceeding 5th world congress on emulsions, Lyon

81. Kempa L, Schuchmann HP, Schubert H (2006) Chem Ing Tech 78(6):765–768
82. Köhler K, Santana AS, Braisch B, Preis R, Schuchmann HP (2010) Chem Eng Sci 65(10):2957–2964
83. Sauter C, Schuchmann HP (2008) Chem Ing Tech 80(3):365–372
84. Winkelmann M, Schuler T, Uzunogullari P, Winkler CA, Gerlinger W, Sachweh B, Schuchmann HP (2012) Chem Eng Sci 81:209–219
85. Kolb G (2001) Emulsionsherstellung in Blendensystemen. Shaker, Aachen
86. Freudig B (2004) Dissertation, Universität Karlsruhe (TH)
87. Köhler K (2010) Simultanes Emulgieren und Mischen. Logos Verlag, Berlin
88. Machunsky S, Grimm P, Schmid HJ, Peuker UA (2009) Colloids Surf., A 348(1–3):186–190
89. Erler J, Machunsky S, Grimm P, Schmid HJ, Peuker UA (2013) Powder Technol 247:265–269
90. Binks BP (2002) Current Opin Colloid Interface Sci 7(1–2):21–41

Process Development of a Liquid-Liquid Phase Transfer of Colloidal Particles for Production of High-Quality Organosols

Jacqueline V. Erler, Stefanie Machunsky, Steffen Franke, Philipp Grimm, Hans-Joachim Schmid and Urs A. Peuker

Abstract The emphasis of the study presented is on a new process of particle extraction to transfer magnetite nanoparticles from an aqueous into an immiscible organic phase directly through the liquid-liquid interface. For the production of high-quality organosols, stabilized colloidal and functionalized particles are required in a liquid organic phase. The mechanism of phase transfer is initiated by adsorption and chemical binding of surfactants (fatty acids) at the particle surface. The resulting physico-chemical dispersion of the hydrophobically modified particles leads to the formation of the stabilized organic colloid, or organosol. The aim here is to demonstrate the entire chain of the transfer process in a continuous miniplant, which comprises particle synthesis, conditioning, and transfer, and which uses a drop column for extraction and as a transfer device. Based on the investigation of the governing principles and the material parameters, the results obtained for the transfer kinetics in the individual contact devices (centrifuge, single-drop column, and drop column for different operations) are used for the dimensioning of the entire process chain.

Keywords Magnetite · Two-liquid-flotation · Fatty acid · Precipitation · Sedimentation · Iron reduction

J.V. Erler (✉) · S. Machunsky · U.A. Peuker
Institute of Mechanical Process Engineering and Mineral Processing,
Technical University Bergakademie Freiberg, Freiberg, Germany
e-mail: jacqueline.erler@mvtat.tu-freiberg.de

U.A. Peuker
e-mail: urs.peuker@mvtat.tu-freiberg.de

S. Franke · P. Grimm · H.-J. Schmid
Institute of Mechanical and Environmental Process Engineering,
University of Paderborn, Paderborn, Germany
e-mail: steffen.franke@upb.de

H.-J. Schmid
e-mail: hans-joachim.schmid@upb.de

M. Kind et al. (eds.), *Colloid Process Engineering*,
DOI 10.1007/978-3-319-15129-8_16

1 Introduction

1.1 Properties and Applications of Colloidal Organosols with Nanoscaled Magnetite Particles

Colloidal organosols with nanoscaled magnetite particles are one example of a ferrofluid, which is also termed a magnetic fluid. Such suspensions consist of a dispersed solid phase of magnetic particles (iron, nickel, cobalt, magnetite, or cobalt ferrite) with diameters in the range of ten nm, which are dispersed in an organic phase (oil or alkane). The problem, however, is that on an industrial scale, the nanoparticles are synthesized mainly in the aqueous phase, but the application takes place in the organic phase. The particle transfer is conventionally achieved by strategies based on filtration with subsequent drying and redispersion steps. For technical applications, the particles have to be stabilized against sedimentation, demixing by magnetic field gradients, and attractive van der Waals' forces between the particles. In principle, the method of electrostatic repulsion can be used, where the repulsion is created by particle surface charges of the same polarity. Furthermore, the method of steric stabilization can be applied, where long-chained amphiphile polymers are adsorbed on the particle surface, leading to higher distances between the particles. Moreover, the properties of the nanoparticles are restricted. Due to their increased surface area /volume ratio, they tend toward agglomeration and oxidation [1, 2]. Hence, the development of a continuous particle extraction process at the interface of two liquids is of great importance, and could be realized as an engineering concept in a miniplant using a drop column as the transfer device. The first experiments in this area of research took place in 1968 [3].

Due to the special magnetic properties of the magnetite nanoparticles used, especially in combination with polymers [4–6], the potential for further research is quite extensive. Therefore, research areas can be found in the field of functional materials and magnetic fluids applied in frictionless dynamic systems, e.g. for sealing of fast-rotating shafts, in the semiconductor industry, in vibration dampers, and in tweeters [7, 8]. In addition, possible areas of technical application are coatings and composite materials [9, 10] utilized in chemical reactors as magnetically separable catalyst materials [11], as well as in the biomedical field [12–14].

1.2 Process Steps for Continuous Production of a Magnetite Organosol

Figure 1 shows an overview of the process steps applied in the production of a magnetite organosol in an aqueous phase with downstream conditioning and the transfer of the particles into the organic phase. Furthermore, basic methods of the individual processes and devices used are described. In the 1960s, suitable

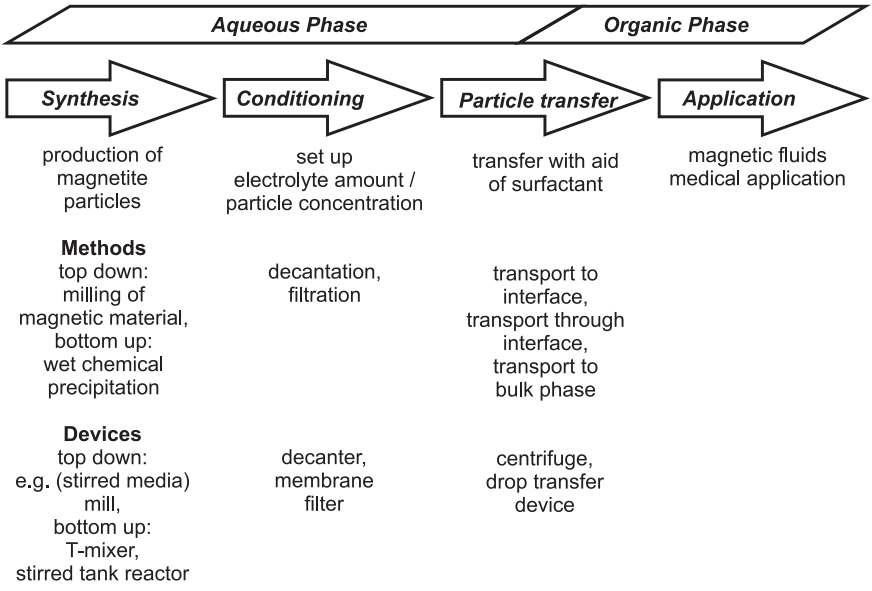

Fig. 1 Process steps, methods, and devices for continuous production of magnetite organosols

procedures were developed for the first time for the creation of magnetic fluids by "top-down" methods. Ball mills were used to obtain ferromagnetic nanoparticles with diameters in the range of 100 nm. Today, magnetic fluids are mostly produced by colloid chemical precipitation [1].

Typically, the nanoparticles are precipitated in the solvent in the presence of a surfactant [1]. One problem at this point is often the adsorption of the surfactant at the right time, such that, on the one hand, the particles do not agglomerate to larger complexes than required, and on the other hand, that the mechanism of growth is not too slow as a result of the thick surface coating of the surfactant [1]. Because of this problem, the synthesis process used in the present work was performed in a modified way. During synthesis, no surfactant was introduced into the system. Therefore, the synthesized nanoparticles initially formed agglomerates that were to be disintegrated by the surfactant into primary particles during the transfer process, or in the organic suspension after the transfer of the agglomerates [15]. The chemical reaction used for the precipitation of magnetite is given by Eq. (1).

$$Fe^{II}SO_4 + 2Fe^{III}Cl_3 + 8NH_4OH \leftrightarrow Fe_3O_4 + (NH_4)_2SO_4 + 6NH_4Cl + 4H_2O. \quad (1)$$

The water soluble salts ferrous sulfate and ferric chloride are used for the supply of iron atoms. The oxidizing agent ammonium hydroxide was introduced in a hyperstoichiometric quantity to achieve high nucleation rates, which are required for obtaining nanoscaled magnetite crystals. In this work, the reaction was performed in a T-mixer (University Paderborn) or in a stirred tank reactor (TU BAF).

Because of undesired ionic side products in the form of chlorides, sulfates, and ammonia which may disturb the transfer process, at least part of the aqueous carrier fluid has to be exchanged for purified water to reduce ion concentration in the suspension. Another reason for the reduction of ion concentration is that, at high concentrations, hardly any electrical repulsion between the particles can be achieved [16]. The process of exchanging the water can be carried out by, for example, decantation or filtration of the suspension. Both methods have as their aim the retention of particles while the carrier fluid is changed. For decantation, the magnetic particles can be fixed at the bottom of the vessel by a permanent magnet. With the filtration process, selective membranes are needed which separate a particle-free fluid permeated by ionic components from a retentate in which the magnetic particles are suspended.

Figure 2 outlines the transfer of magnetite particles, which can be divided into a number of fundamental steps [16].

First of all, the particles reach the interphase between the fluid phases. This is realized due to the destabilizing conditions within the magnetite suspension (aqueous phase). This means that the magnetite nanoparticles have surface charges in the aqueous phase, which lead to the formation of an interfacial potential between the solid and liquid aqueous phases. Thus, the particle surface is polar or, rather, hydrophilic as a result of the attachment of water molecules or hydroxyl ions to the iron ions of magnetite. Depending on the pH value of the aqueous phase, the dissociation of the hydroxyl groups takes place [17], as shown in Fig. 3.

Following the synthesis process, the aqueous phase has a pH value of approximately 8.5, which means that the magnetite nanoparticles have a negatively charged surface. The positively charged ammonium ions form a counter-ion layer around the particles, resulting in an electrochemical double layer. Thus, the stabilizing effect of the surface charge is compensated according to the DLVO theory. As a consequence, mutually attracted particles form agglomerates due to the

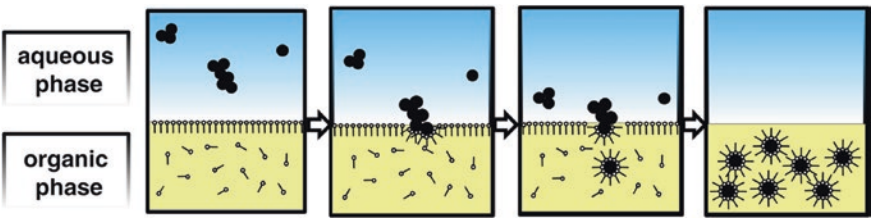

Fig. 2 Scheme of the fundamental steps in the process mechanism of phase transfer

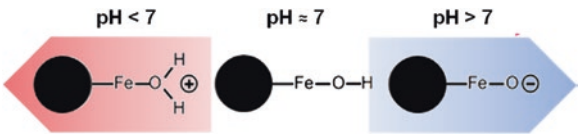

Fig. 3 Scheme of the dependency of the surface charge of magnetite on pH value in the aqueous phase

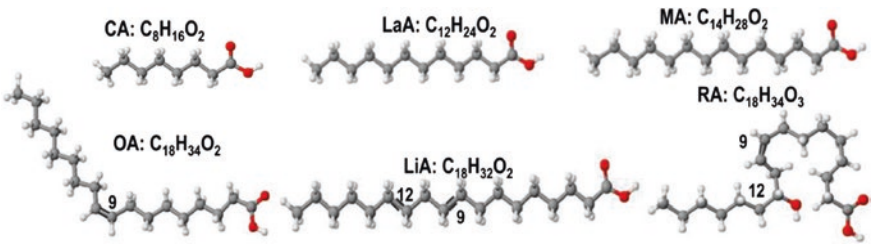

Fig. 4 Presentation of the saturated surfactant molecules (at the *top*) and the unsaturated C18 surfactants (at the *bottom*) used for the phase transfer process

dominant interaction forces—such as van der Waals' forces—and the particles can then be transported through sedimentation to the liquid-liquid interface.

At the interface, the surfactants from the organic phase interact with the hydrophilic particle surface, which leads to a chemical adsorption around a bidendate chelate complex [18]. Thus, the partially nonpolar magnetite surface formed implies the hydrophobization and functionalization of the particles, leading to the preferred wetting of the modified particle surface by the organic liquid. This allows the phase transition of the magnetite in the organic phase as the third step of the process mechanism. In the last step, stable organic colloids are formed by deagglomeration of the particles as well as physicochemical dispersion due to the strong repulsive potential of the adsorbed surfactant molecules [15].

Figure 4 outlines the variety of surfactants used. The surfactant molecules are fatty acids with different hydrophobic nonpolar carbon chain lengths and a hydrophilic polar carbon acid group (R-COOH). Caprylic acid (CA), lauric acid (LaA), and myristic acid (MA) are counted among the saturated fatty acids, with carbon chain lengths of C8 (CA), C12 (LaA), or C14 (MA). In contrast, oleic acid (OA), linoleic acid (LiA), and ricinoleic acid (RA) are C9-unsaturated C18 fatty acids. In addition, LiA has a second double bond at C12, while RA has a hydroxyl group at C12 that acts as an additional functional group.

Owing to the fact that a phase transfer in the absence of surfactant molecules is impossible, they have an extraordinarily important function in the process mechanism.

2 Synthesis and Conditioning of an Aqueous Magnetite Suspension

In this chapter, the first two preparatory steps of the production chain shown in Fig. 1 are discussed. The final target of demonstrating a continuous process for manufacturing nanoscale magnetite organosols is examined. The focus here lies on the devices found to be appropriate for the miniplant. In Sect. 2.1, the process of precipitation in a T-mixer is discussed, while in Sect. 2.2, the filtration process for conditioning of the suspension is specified.

2.1 Precipitation of Nanoscale Magnetite Particles in a T-Mixer

The first step was the wet chemical precipitation of the magnetite nanoparticles in an aqueous phase with a T-mixer. Figure 5 shows the chemical components involved as described in Sect. 1.2, including their amounts and volumetric flows. Dissolved in fully demineralized water from the left side, the iron supply media $Fe^{II}SO_4$ (a) and $Fe^{III}Cl_3$ (b) in their hydrated forms were conveyed by a diaphragm pump to the mixing zone. These chemicals were acquired from Merck in analytical quality (≥99.5 %) (a) and AppliChem in purest quality (≥98 %) (b). The ammonium hydroxide precipitant was typically introduced in a hyperstoichiometric manner at a factor of 1.5 (as shown in Eq. 1).

Figure 6 shows the relevant process steps for synthesizing magnetite in an aqueous phase. As a result of the chemical reaction, the initial supersaturation of iron ions occurred. As a result of supersaturation, the nucleation process started. According to the classical nucleation theory, the driving force of nucleation is an energy yield as a result of a reduction in Gibbs free energy, which is proportionate to the volume of the seed and, therefore, to the cube of the seed radius. For forming a new seed out of a homogenous phase, energy is required to bring out its new surface. This work is referred to as nucleation energy, and is proportionate to the surface tension and the size of the surface itself. As a result of competition between these two forces, a critical seed radius is necessary for creating new

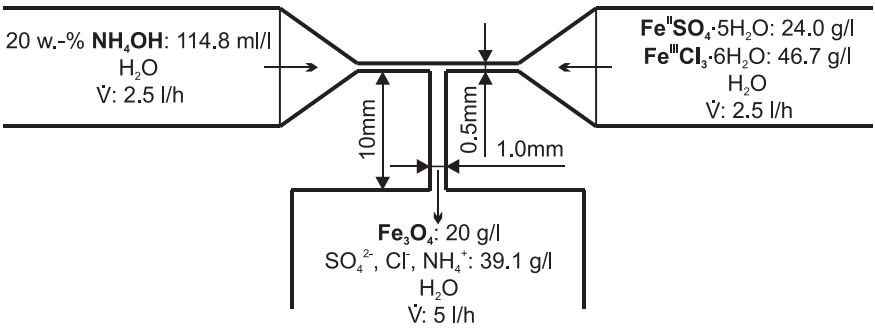

Fig. 5 Mixing zone of the T-mixer with geometric sizes, educts and products as well as their concentrations and flows

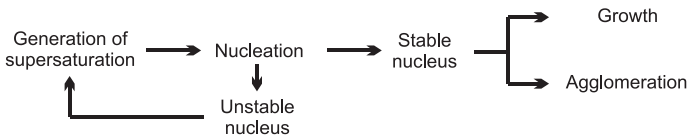

Fig. 6 Relevant process steps for the synthesis of magnetite

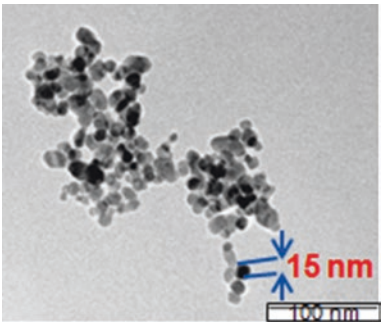

Fig. 7 TEM image of synthesized magnetite particles [20]

stable seeds. Seeds with a size under the critical radius decompose while seeds bigger than the critical radius are stable, grow, and can form agglomerates with other particles.

Experiments have shown that with an increase in the volumetric flow rate and, additionally, the energy input and temperature, smaller particles can be generated. Under the conditions shown in Fig. 5, production of sufficiently small particles can be ensured [19].

Figure 7 shows that the size of the precipitated primary particles was approximately 15 nm. The specific surface of the magnetite particles was nearly 65 m^2/g, which was determined using the BET-method [20]. After synthesis the particles were highly agglomerated, which was caused by the high concentration of ionic components that suppressed the particle stabilization described in Sect. 1.2. The resulting process of conditioning is explained in Sect. 2.2.

2.2 Conditioning of the Aqueous Magnetite Suspension by the Filtration Process

The main purpose of the conditioning process is the reduction of ionic components in the precipitated suspension without the loss of particles. To this end, membrane filters are regarded as suitable devices for separating particle-loaded retentate flows from particle-free permeate flows in which ionic components are dissolved. Figure 8 shows a simplified flow chart of the cross-flow filtration process used and the structure of a filter capillary with in- and outgoing flows.

Initial experiments have been realized for dimensioning of the filter process to be used in the miniplant. Therefore, a commercial membrane filter module MF 7 with hollow fibers made of polysulfone for the application of hemodialysis from the firm *Meditechlab* with a filter area of 1.6 m^2 was tested in batch mode. For measurement of the concentration of ions in the suspension, the electrical conductivity of the suspension was determined. Figure 9 shows the behavior of mass in the source tank of the suspension and the detected conductivity over the filtration process for a suspension with a volume of 2.7 l and a particle mass concentration of 2 m%.

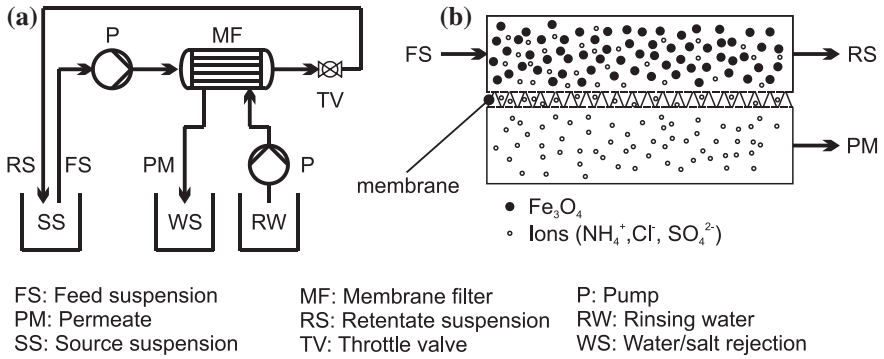

Fig. 8 Flow chart of filtration process (**a**), and functional principle of the filter module (**b**)

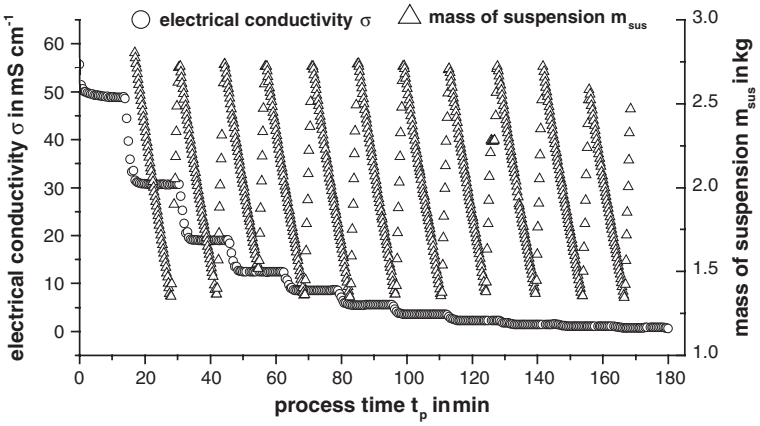

Fig. 9 Mass of suspension and electrical conductivity for the filtration process

In the first phase of the filtration process, the volume of the suspension was reduced to half of the initial volume. In this way, the reduction in volume was a direct result of the permeate flow. This flow was forced by the transmembrane pressure (TMP) from the inside of the capillaries to the housing of the filter module. The pressure in the housing in turn caused a convective flow over the selective membranes. The retentate was recycled to the surge suspension tank, and the ion concentration in this phase was nearly constant. After volume reduction in a second phase, fresh rinsing water was pumped from a tank into the filter module and was channeled through the retentate pipe to top up the suspension to its initial volume. By introducing rinsing water into the filter module, a very important site effect also occurred. Figure 10 shows pressures and the permeability [21] of the membranes during conditioning of the suspension. In the first phase of the filtration process, the permeability of the membranes decreased as a result of particle deposition on the inside of the hollow fibers. By purging at a pressure of more

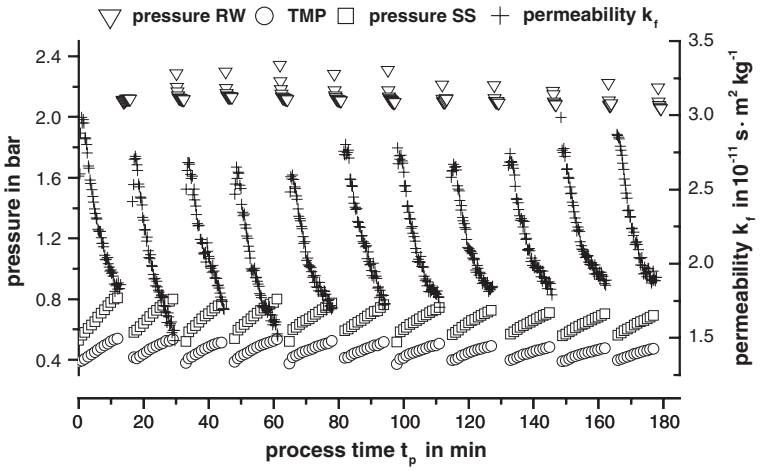

Fig. 10 Pressures and permeability of membrane filter

than two bar, the filter was effectively protected against irreversible blockage, while deposited particles were returned into suspension. The return to the initial situation—with regard to pressures, volume flows and, therefore, permeability after the completion of both phases of the batch process—confirmed the efficiency of the cleaning strategy. The process was repeated until the desired ion concentration was reached. For experiments in the single-drop device, a very low concentration in the area of 0.5 g/l had to be achieved to create stable individual drops, which corresponded to a conductivity of 0.987 ± 0.2 mS/cm as shown in Sect. 3. For transfer in other devices, ion concentrations can be significantly higher.

3 Particle Transfer Process

In this chapter, the transfer devices used for the production of organosols are described including their important parameters. With respect to the colloidal stability of organosols produced in the centrifuge and drop column transfer devices, the experimental results are compared with the theoretical model of Hansen [22].

3.1 Laboratory-Scale Centrifuge (Hettich Universal 30F) as Transfer Device

Using the laboratory centrifuge as a transfer device, the aqueous phase was placed on top of the organic phase, as shown in Fig. 11a Dichloromethane (DCM) was used as the organic solvent due to its having a higher density than water. The

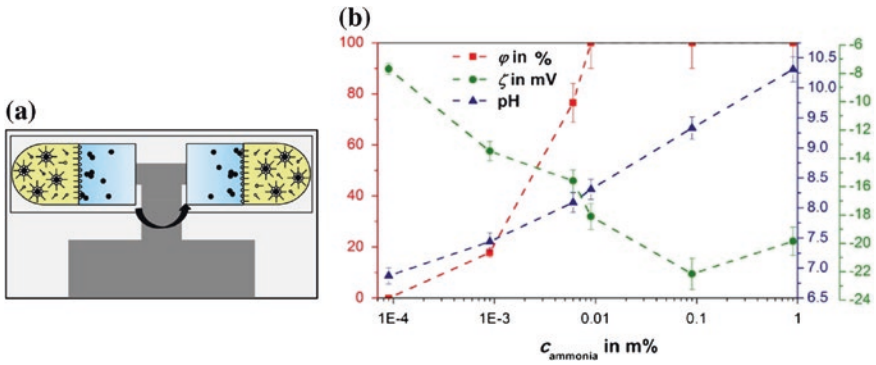

Fig. 11 Scheme of the laboratory-scale centrifuge for the application of the phase transfer in a centrifugal field (**a**), and quantification of the influence of ammonia on the phase transfer with ricinoleic acid as surfactant (**b**)

phase transfer itself was carried out at 1000 rpm (145 g) for 60 min. Figure 11b suggests that an ammonia concentration above 10^{-2} m% in the aqueous phase is necessary for a complete phase transfer of the used magnetite particles from the aqueous into the organic phase (transfer yield is approximately 100 %), which corresponds to a pH value in the range of between slightly less than 8.5–9 and a zeta potential ζ of approximately −20 mV. Subsequently, the transfer yield φ or, rather, the yield of transferred magnetite particles $\varphi_{\text{magn,trans}}$ was determined by measuring the iron content of the magnetite mass concentration using atomic emission spectroscopy (AES), as shown in Eq. (2).

$$\varphi_{\text{magn,trans}} = \frac{\beta_{\text{magn,trans}}}{\beta_{\text{magn,PT,theor}}} \tag{2}$$

The zeta potential and the particle sizes were measured in the diluted aqueous phase by photon correlation spectroscopy (PCS, Malvern Instruments Zetasizer Nano ZS) [2, 23]. Exclusively for the two saturated fatty acids myristic acid and lauric acid, a pH value of 8.0 is important to prevent bilayer formation and steric stabilization of the particles in the highly ionic aqueous phase [15].

By the identification and quantification of the material process parameters, including the surfactant ratio on magnetite particles $X_{\text{S/M}}$ as well as the surfactant concentration in the solvent x_{S}, the liquid-liquid phase transfer could be performed efficiently and with a high reproducibility, with a minimized use of surfactants and high transfer rates and yield. Typical values for $X_{\text{S/M}}$ and x_{S} were 0.2 g/g and 2 m% for monolayer coverage on the particles. This result was that secondary effects like emulsion and oleate formation as well as water entrapment could be excluded [2, 23].

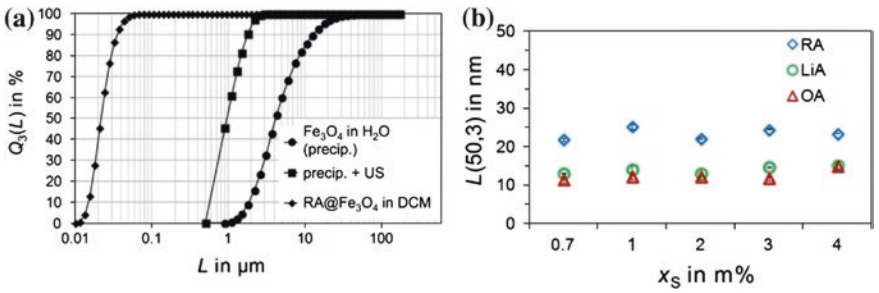

Fig. 12 Particle size volume distributions of the precipitated magnetite particles, the pretreated precipitation with ultrasound, and the functionalized particles (**a**). Median values of the coated magnetite nanoparticles with the unsaturated C18 fatty acids according to different surfactant concentrations in the solvent (**b**)

The ratio of specific surfactant amount to magnetite particles $X_{S/M}$ and the mass fraction of surfactant in the solvent x_S are defined by Eqs. (3) and (4).

$$X_{S/M} = \frac{m_{surfactant}}{m_{magnetite}} \tag{3}$$

$$x_S = \frac{m_{surfactant}}{m_{surfactant} + m_{solvent}} \tag{4}$$

That the agglomeration process of magnetite nanoparticles is reversible due to the unstable conditions in the aqueous phase is shown in Fig. 12. Examining the particle size volume distributions $Q_3(L)$[1] in (a), it becomes clear that the particle size of the agglomerates and aggregates formed in the aqueous phase could already be reduced by ultrasonic treatment of the precipitation and, further, through surfactant coverage of the particles, which resulted in production of the organosol (RA@Fe_3O_4). In addition, the median values of the functionalized magnetite particles in the organic phase using the unsaturated surfactants ricinoleic acid (RA), linoleic acid (LiA) and oleic acid (OA) with different surfactant concentrations in the solvent x_S (Fig. 12b) verified the disintegration of the agglomerates into particles with a primary particle size of approximately 15 nm.

However, the increase in primary particle size to nearly 20 nm with ricinoleic acid (RA) as the surfactant can be explained using the deagglomeration model based on the Alexander de Gennes theory (AdG), and is given by Eq. (5) [24].

$$P(D) = \frac{k_B \cdot T}{s^3} \cdot \left[\left(\frac{2 \cdot \delta}{D} \right)^{\frac{9}{4}} - \left(\frac{D}{2 \cdot \delta} \right)^{\frac{3}{4}} \right] \tag{5}$$

[1] The particle size is denoted by L to ensure a clear distinction to the mass fraction of surfactant in the solvent x_S.

The deagglomeration model is well established for the repulsive force demonstrated as pressure P between two surfaces at a distance D, covered by grafted polymers with a chain length δ, the distance between the chains on the particle surface s, the Boltzmann constant k_B, and the temperature T. Indeed, this theory can be applied for the deagglomeration and colloidal stability of magnetite particles in polymer solutions [15].

Furthermore, the solubility of the surfactant molecules in the solvent (*cf.* Sect. 3.2.1) influenced the conformation of the coverage on the particles (coils or brushes), which led to the increased median values of the magnetite particles covered with ricinoleic acid. Although the chain length δ of ricinoleic acid is the same as oleic acid at 1.64 nm and similar to linoleic acid (1.69 nm) [15], the ricinoleic acid is more soluble in the dichloromethane solvent as a result of the additional hydroxyl group in the molecule structure. This led to a more extended brush-like conformation towards the solvent for coverage on the particle surface, resulting in a higher layer thickness than oleic acid or linoleic acid.

A characteristic feature for the stabilization of primary particles in the organosol was the primary particle concentration w_{pp}, which can be described by the ratio in Eq. (6).

$$w_{pp} = \frac{m_{\text{centrifuged supernatant}}}{m_{\text{complete organosol}}} \tag{6}$$

Therefore, the complete organosol was centrifuged at 5000 rpm (2800 g) for 20 min in a 10 ml centrifugal cuvette. As a result, the particle size L in the supernatant was smaller than 26 nm, and was calculated according to Stokes law of settling particles in a centrifugal field using Eq. (7),

$$L = \left[\frac{t \cdot \left(\rho_{\text{nanoparticle}} - \rho_{\text{solvent}}\right) \cdot (2\pi \cdot n)^2}{18 \cdot \eta_{\text{solvent}} \cdot \ln\left(\frac{R_1+R_2}{R_2}\right)} \right]^{-\frac{1}{2}} \tag{7}$$

where $\rho_{\text{nanoparticle}}$ is the density of the nanoparticles (5.2 g/cm^3), ρ_{solvent} is the density of the solvent (1.33 g/cm^3), η_{solvent} is the dynamic viscosity of the solvent (0.41 mPas), R_1 is the distance below the surface of the dispersion (0.01 m), and R_2 is the rotation radius excluding the rotation axis (0.08 m) [25].

As can be seen in Fig. 13a, the primary particle concentration was plotted against the type of surfactant used with the ratio of the specific surfactant amount to magnetite particles $X_{S/M}$ of 0.2 g/g and the mass fraction of surfactant in the solvent x_S of 2 m%. The most efficient ability to disintegrate the agglomerates into primary particles for the production of stable colloidal functionalized magnetite nanoparticles is observed for ricinoleic acid, at nearly 65 %. Furthermore, the most effective deagglomeration for the phase transfer from water to dichloromethane can be seen for the C18 unsaturated fatty acids followed by the saturated fatty acids according to the decreased carbon chain length. This progression can be also observed in the pictures of the centrifuged supernatant for the surfactant used (Fig. 13b) due to the changes in color. The darker the color of the centrifuged

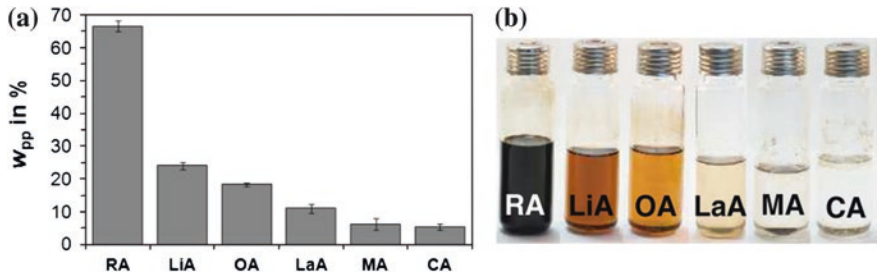

Fig. 13 Primary particle concentration in percent in the organosol (**a**) and demonstration of the resulting centrifuged supernatant (**b**) as a function of the surfactant used for $X_{S/M} = 0.2$ g/g and $x_S = 2$ m%

supernatant, the more colloidal particles could be stabilized. Due to the better solubility of ricinoleic acid in the solvent dichloromethane and the more extended brush-type conformation on the particle surface, the steric repulsion force as well as the pressure $P(D)$ for the repulsive force caused by the smaller distance between the surfactant molecules bonded to the particle surface s was considerably higher than for the other fatty acids used.

The thermogravimetric analysis (TGA) (Netzsch STA 449 F3 Jupiter, heating rate 20 K/min, flow rate of high-purity nitrogen 20 ml/min) of the produced organosols and the simultaneous FTIR investigations of the decomposition gases (Bruker Tensor 27 FTIR spectrometer) confirmed the assumptions. In general, for all organosols produced with different surfactants, three decomposition steps exemplified by the 1st derivation of the mass losses depending on temperature were obtained. In Fig. 14a, such a relationship is shown exemplarily for ricinoleic acid bonded to magnetite (RA@Fe_3O_4) with different surfactant concentrations in the solvent. In this process, the 1st decomposition step (between slightly less than 40 up to 300 °C) demonstrated the release of volatiles as a result of fatty acid autoxidation, while the 2nd decomposition step (between approximately 300 and 600 °C) illustrated the desorption of physisorbed fatty acid with dehydrogenation of chemisorbed fatty acid on the magnetite surface. Subsequently, the 3rd decomposition step (in the range of 600–900 °C) represented—due exclusively to CO- and CO_2-signals—, the reduction of magnetite by reaction with the residual carbon of chemisorbed fatty acid to wustite (FeO), hematite (α-Fe_2O_3), and elementary iron (α-Fe) as shown by the powder diffraction measurements (XRD) of the TGA residue in Fig. 14b [26]. At the same time, the last step verified the chemical adsorption of the surfactants onto the magnetite surface. Furthermore, the highest mass loss of nearly 35 m% in the 3rd decomposition step could be achieved with ricinoleic acid as the surfactant, in contrast to the other C18 unsaturated fatty acids, i.e. oleic acid and linoleic acid, with approximately 29 and 26 %, respectively. This indicates the impact of the small distance between the ricinoleic acid (RA) molecules bonded onto the magnetite surface s as previously mentioned, which led to a dense adsorption layer resulting in a higher mass loss as measured by the thermogravimetric analysis.

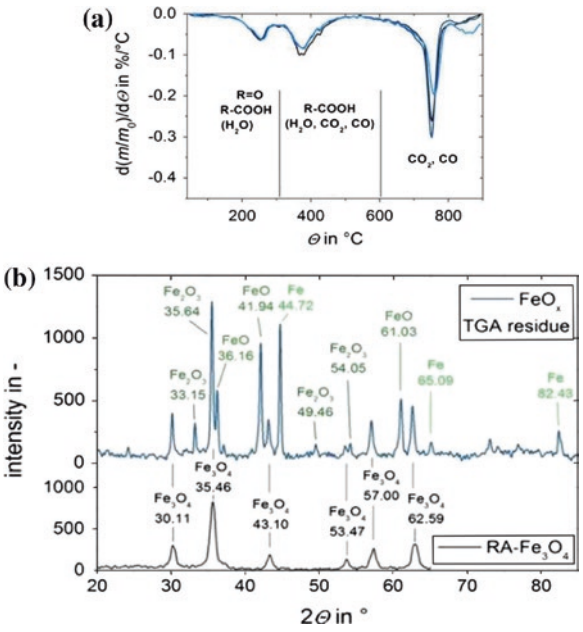

Fig. 14 DTG graph of the 1st derivative of the TG signal depending on temperature for the decomposition of RA@Fe_3O_4 for $X_{S/M} = 0.2$ g/g and $x_S = 1$, 2 and 3 m% (**a**), and XRD measurements of RA@Fe_3O_4 as well as the TGA residue (**b**)

The reason for the detailed investigations with surfactant concentrations in the solvent x_S of 2 m% for a monolayer coverage $X_{S/M}$ of 0.2 g/g [2, 23] is demonstrated in Fig. 15a. It can be recognized that from this surfactant concentration, the maximum primary particle concentration was reached. Further increase of the mass fraction of surfactant in the solvent did not lead to any significant changes in the resulting primary particle concentration. As a consequence, the diffusion of the fatty acid to the particle was optimal at this concentration, and all available space on the particle could be occupied. Furthermore, the primary particle concentration

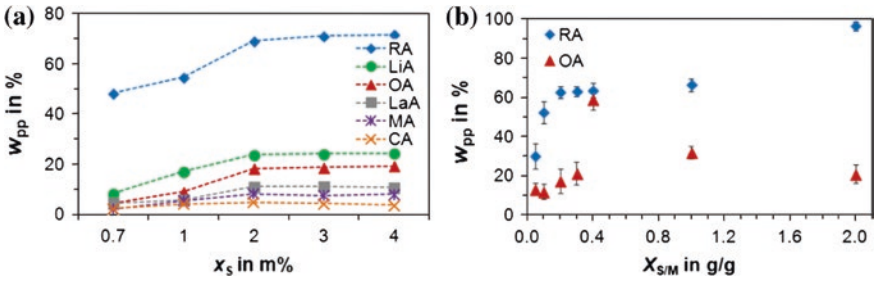

Fig. 15 Primary particle concentration depending on the surfactant concentration in the solvent x_S for $X_{S/M}$ of 0.2 g/g (**a**), and primary particle concentration depending on the surfactant ratio on magnetite particles $X_{S/M}$ for x_S of 2 m% (**b**)

was investigated with respect to different surfactant ratios on magnetite particles $X_{S/M}$ for x_S of 2 m% of ricinoleic acid and oleic acid as the surfactants, as shown in Fig. 15b. Using ricinoleic acid, a LANGMUIR adsorption isotherm from 0.2 g/g could be observed, which indicated monolayer coverage of the particles with a primary particle concentration of about 65 %. It only became apparent at a higher ratio between surfactant and magnetite of 2 g/g that the primary particle concentration reached nearly 100 %. As a result, a multilayer coverage of the particles took place, and up to this specific surfactant amount of magnetite, ricinoleic acid acted as a steric stabilizer particularly well. In contrast, a completely different plot was observed with oleic acid as the surfactant. It seems that the adsorption equilibrium was shifted to higher $X_{S/M}$. This means that the adsorption of oleic acid on the magnetite particle surface was weaker—caused by the poorer solubility in the solvent dichloromethane—whereas a higher $X_{S/M}$ was necessary for the monolayer coverage. This would have been reached at 0.4 g/g with an increase of the primary particle concentration to nearly 60 %. After that, the primary particle concentration decreased slowly as $X_{S/M}$ increased further. An explanation for this could be that the external layer of oleic acid was adsorbed to other occupied particles through, e.g. hydrogen bonding, caused by the poorer solubility in the solvent dichloromethane. As a result, destabilizing adsorbing or non-adsorbing phenomena can occur in terms of depletion or bridging flocculation [15].

3.2 Drop Column as Transfer Device

As mentioned for the development of a continuous particle extraction process, the miniplant—using a drop column as transfer device—was investigated in different modes of operation. The aims for the particle extraction process were high efficiency, meaning a high yield of magnetite, low transfer times/process times, and a stable product. Furthermore, a stable process was necessary, i.e. stable drop formation and movement, as well as a sufficient rate of coalescence, whereby particle transfer in the column could be achieved. Up to this point, ricinoleic acid and oleic acid had been used as surfactants in the experiments. Conditioning of the magnetite suspension was now necessary, however: Otherwise, secondary effects—like emulsion formation in the drop column—could have occurred. For ricinoleic acid, a quarter of the original salt concentration was used, while for oleic acid, the original salt concentration of 39.4 g/l was utilized. For both surfactants, the process pH (pH_p) was then adjusted to a value of 8.10 ± 0.05. Moreover, the necessary parameters for stable process behavior, which were the surfactant ratio on magnetite particles $X_{S/M}$ of 0.2 g/g and the surfactant concentration in the solvent x_S of 1.4 m%, were determined using the drop column in a discontinuous mode of operation. This meant that the aqueous phase was stationary and the organic phase was in circulation, as shown in Fig. 16a. The drop column had a length of 700 mm and an internal diameter of 25 mm. The magnetite suspension as a continuous phase with a volume of 300 ml—corresponding to a mass of 6 g magnetite

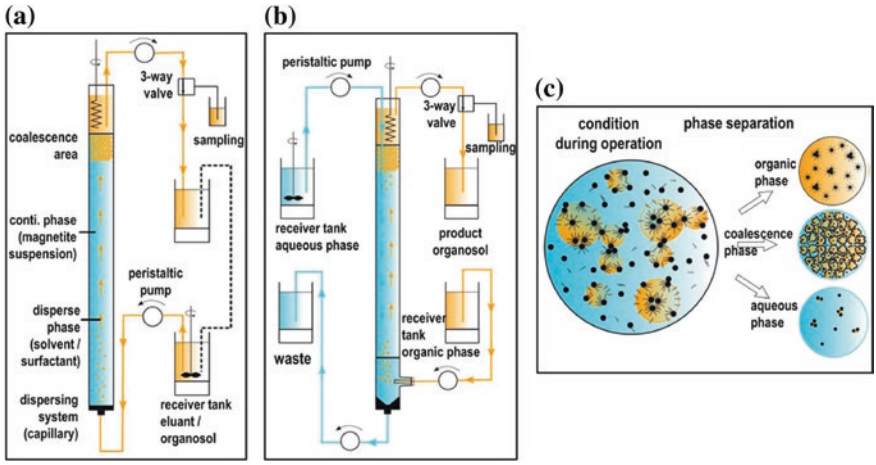

Fig. 16 Experimental setup of the miniplant in a discontinuous mode of operation (**a**) as well as in continuous circulation of both phases (**b**), and an illustration of the processes occurring during the particle extraction process (**c**) (schematics were created by Leistner, T)

nanoparticles—was already filled into the column. The organic phase acted as a dispersed phase, and was pumped from the receiver tank into the column through a dispersing system, which was a single metal capillary with an internal diameter of 3.2 mm centrally mounted in a perforated plate at the bottom of the transfer device. The drops so formed rose through the column and, in this way, the lower-density solvent iso-octane was applied. Due to the upwelling current of the organic phase, almost no sedimentation effects occurred in the column. Both the supply and removal systems consisted of a peristaltic pump (Ismatec Reglo Analog) and a Tygon tube with an internal diameter of 3.2 mm. In addition, the removal system had an automated sampling system (manufactured by Swagelok) with a pneumatic three-way valve, which was controlled by measurement software. The transferred magnetite concentration of the sample volume of 2.9 ml was determined with ICP-OES (inductively coupled plasma optical emission spectroscopy of Fe with the ICP spectrometer iCAP 6300 from Thermo Fischer Scientific). The samples were chemically digested with concentrated hydrochloric acid, resulting in a relative standard deviation of <1 %. To keep the volume of the dispersed phase constant, the volume was added to the receiver tank simultaneously with the organic phase. The volume flow rate was 29 ml/min. Figure 16b represents the miniplant in continuous circulation of both phases, which is discussed below. The length of the drop column was 920 mm as a result of additional glass components. For the implementation of the operating method, a volume flow rate of 14.5 ml/min was used to control the process. Figure 16c outlines the procedures in the drop column during the extraction process. Due to the collision of particles and rising drops in the column, a phase separation into an organic phase (containing the extracted

magnetite particles) and an almost particle-free aqueous phase took place in the column. Furthermore, a coalescence area was formed at the surface of the aqueous phase as an interface layer. The enrichment at the interface was a Pickering emulsion, consisting of droplets of the organic phase in water with only partially hydrophobized particles. If such coalescence is prevented due to the particle size, the particles cannot be extracted into the organic phase, resulting in a dispersion band [27].

For the characterization of the transfer kinetics the validation of the system was essential, because the amount of magnetite was reduced after each sample volume was removed. For the calculation of the time dependent corrected mass concentration of transferred particles in the receiver tank $\beta_{\mathrm{magn,rt}}(t)$, the temporal change of the mass concentration $d\beta_{\mathrm{magn,rt}}/dt$ is defined taking into consideration the input and output to the receiver tank in Eq. (8), where $\dot{V}_{\mathrm{disp}}$ is the volume flow of the dispersed phase, and V_{rt} is the volume in the receiver tank.

$$\frac{d\beta_{\mathrm{magn,rt}}}{dt} = \frac{\dot{V}_{\mathrm{disp}}}{V_{\mathrm{rt}}}\beta_{\mathrm{magn,in}}(t) - \frac{\dot{V}_{\mathrm{disp}}}{V_{\mathrm{rt}}}\beta_{\mathrm{magn,rt}} \tag{8}$$

Considering the dwell time distribution, the corrected mass concentration of transferred magnetite particles in the receiver tank can be determined by integration of the Eq. (8) in Eq. (9),

$$\beta_{\mathrm{magn,rt}}(t) = \beta_{\mathrm{magn,rt,0}} \cdot \mathrm{e}^{-\frac{\dot{V}_{\mathrm{disp}}}{V_{\mathrm{rt}}}t} + \int_{t'=0}^{t'=t} \frac{\dot{V}_{\mathrm{disp}}}{V_{\mathrm{rt}}}\beta_{\mathrm{magn,in}}(t) \cdot \mathrm{e}^{-\frac{\dot{V}_{\mathrm{disp}}}{V_{\mathrm{rt}}}(t-t')}dt \tag{9}$$

where $\beta_{\mathrm{magn,rt,0}}$ is the initial magnetite mass concentration of the system, and t' is the auxiliary variable, which describes the time of entry.

By linear interpolation and numeric integration, the Eq. (10) was applied for the evaluation,

$$\beta_{\mathrm{magn,rt}}(t) = \left(\beta_{\mathrm{magn,rt,0}} + \frac{a_{\mathrm{i}}V_{\mathrm{rt}}}{\dot{V}_{\mathrm{disp}}} - b_{\mathrm{i}}\right) \cdot e^{-\frac{V_{\mathrm{rt}}}{\dot{V}_{\mathrm{disp}}}t} + a_i t + b_i - \frac{a_{\mathrm{i}}V_{\mathrm{rt}}}{\dot{V}_{\mathrm{disp}}} \tag{10}$$

where a_{i} as well as b_{i} are formed by linear interpolation between the samples removed (28).

For the characterization of the process behavior within the drop column and depending on the surfactants used, the method of a particle-free phase transfer was applied.

When the dispersed phase rose in the column as drops in the aqueous phase and with ricinoleic acid as the surfactant, a multitude of very small droplets could be observed along with the development of a degree of turbidity. These were stabilized iso-octane droplets with a median value of 5–10 µm, as measured by laser diffraction spectroscopy (HELOS, manufactured by Sympatec). The formation of these iso-octane droplets was caused by the dissolution of ricinoleic acid in the

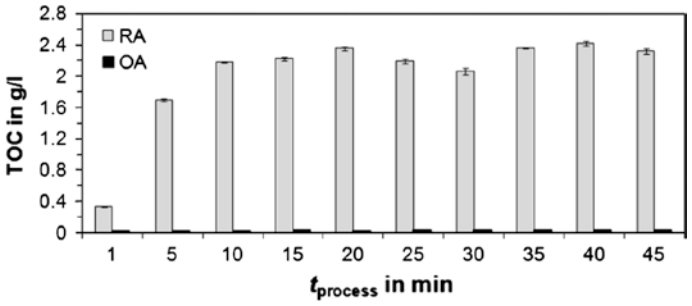

Fig. 17 Total organic carbon (TOC) content in the aqueous phase at defined sampling intervals using ricinoleic acid (RA) and oleic acid (OA) as surfactants

aqueous phase (which consisted of salts and ammonia), whereby an emulsion was formed spontaneously. Thus, ammonium ricinoleates could be formed at the interface, which led to an additional phase interface for the extraction process. In contrast, with oleic acid as the surfactant, larger and significantly fewer drops were formed, and no turbidity could be observed. Therefore, the phase interface available for phase transfer was smaller. This connection was also verified by the execution of the experiments using a bromothymol blue pH indicator in the continuous phase, whereby the formation of the surface-active ammonium ricinoleates was observed to result in color changes.

Measurement of the total organic carbon (TOC) content (by analytikjena multi N/C 2100 s) at defined sampling intervals in the aqueous phase confirmed these observations, as shown in Fig. 17. When using ricinoleic acid as the surfactant, a significant increase of the TOC content could be observed. Finally, after a process time of 5 min, the aqueous phase reached an average value of 2.0 g/l of dissolved ricinoleic acid. When oleic acid was used, however, its poor dissolution within the aqueous phase was clearly evident, as the TOC content was 0.02 g/l on average. Thus, it is evident that, in contrast to oleic acid, approximately 100 times more ricinoleic acid dissolved in the aqueous phase, irrespective of time.

Furthermore, the measurement of the interfacial tension γ on the magnetite particles using the pendant-drop method (Fig. 18a) demonstrates that ricinoleic acid—with its preferred dissolution in the aqueous phase—has a greater influence on interfacial tension than oleic acid. Thus, with ricinoleic acid as the surfactant, the interfacial tension is reduced from 31 to 8 mN/m, and a stable drop can only be formed for 2 min. After this time the drop disintegrates due to dissolution into the aqueous phase, resulting in a rapid mass transport through the phase boundary. With oleic acid in the system, an interfacial tension of 11 mN/m is achieved, while the dwell time of a stable drop—which is analogous to the equilibrium at the interface—amounts to 30–45 min. Due to reasons of comparability, a dimensionless representation of the time was chosen. For this, the measured times referred to the maximum possible dwell time t_{max} for a stable drop according to the surfactant used. As a result, the interaction of the processes at the phase boundary could be

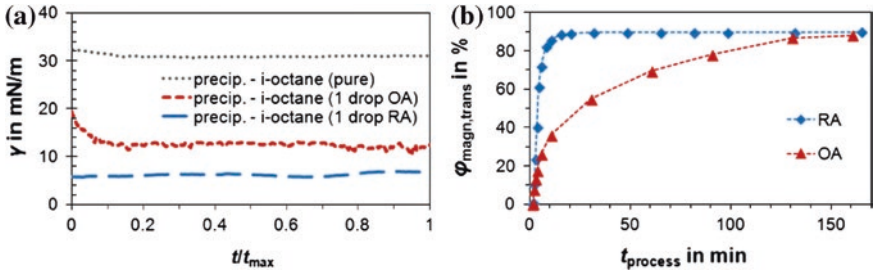

Fig. 18 Depiction of the interfacial tensions depending on the surfactant used with $t_{max,\,RA} = 2.32$ min and $t_{max,\,OA} = 31.03$ min (**a**) and the yield of transferred magnetite as a function of the process time for ricinoleic acid (RA) and oleic acid (OA) (**b**) using the pH_p of 8.10 ± 0.05

described. Thus, on the one hand, the mass transport of the surfactant from the organic phase into the aqueous phase took place and, determined the process time for the extraction, while on the other hand, the phase transfer of the magnetite occurred simultaneously. Therefore, the description of the yield of transferred magnetite $\varphi_{magn,trans}$, as described in Eq. (2), plotted against the process time (Fig. 18b) confirmed the prediction that shorter transfer times could be achieved with ricinoleic acid through dissolution in the aqueous phase. The increase of transferred magnetite to around 80 % after 10 min is nearly twice the amount compared to using oleic acid as the surfactant. After only 15 min, the maximum yield of transferred magnetite (nearly 90 %) with ricinoleic acid is reached, and is kept constant over the process time of up to 165 min, whereas with oleic acid, this amount is reached after a much longer 130 min processing time.

Consequently, both surfactants used exhibited different process behaviors with varying consequences for the particle extraction process. This is also reflected in the area of transfer kinetics. Here, a 1st order reaction is assumed. The theoretical mass concentration can be calculated by determination of the rate constant. As outlined by Fig. 19a, b, the comparison of the experimental and theoretical calculated relative changes in mass concentration $\Delta\beta_A/\beta_A$ for both surfactants as a function of the process time could only be confirmed for oleic acid. This meant that the particle extraction process could be estimated as a 1st order reaction only for oleic acid (Fig. 19a). Therefore, the dissolution of oleic acid from the organic into the aqueous phase did not influence the process kinetics, since it was quite small in its extent. For ricinoleic acid, in contrast (Fig. 19b), another approximation by a sigmoid function in terms of a dose-response curve had to be applied [28]. Therefore, the mass transport of the ricinoleic acid surfactant by dissolution in the aqueous phase strongly influenced the kinetics of the particle extraction process within the column. This could be described as the dosing rate for the process, and was especially prevalent in the first minutes of the extraction process. This was the case if the equilibrium of ricinoleic acid concentration in either phase was not reached. Furthermore, the response was represented by the functionalization of the particles, resulting in their subsequent extraction. Therefore, it can be assumed

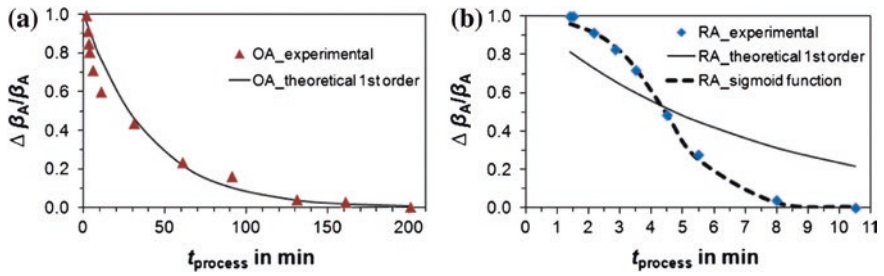

Fig. 19 Depiction of the experimental and theoretical calculated relative changes in mass concentration as a function of the process time, with oleic acid (OA) (**a**) and ricinoleic acid (RA) (**b**) as well as approximations using sigmoid functions

that the particle extraction process with ricinoleic acid as surfactant was controlled by process imbalances. However, in steady-state operation, the influence of the sigmoid function decreased considerably.

For process engineering applications, the particle extraction process is developed as a continuous operation. This means that both phases are in circulation and that within the column a countercurrent flow occurs, such that the product (i.e. organosol) and the waste (i.e. the particle-free used aqueous phase) can be produced continuously into separate tanks, as already presented in Fig. 16b. Therefore, ricinoleic acid is used as a surfactant due to its advantageous process behavior and short processing times. As shown in Fig. 20a, transferred magnetite yields of about 90 % are achieved with a stable process behavior.

Independent of the operating method, a transferred magnetite yield of 100 % cannot be achieved due to the experimental setup of the miniplant, with inefficiencies caused by ubiquitous deposition of particles. Such inefficiencies are unavoidable and, as evaluation of the yields shows, are relatively acceptable.

Moreover, until now the miniplant was utilized for the selective flotation processing of magnetite and quartz particles in a discontinuous operational mode. In Fig. 20b, the recovery of transferred magnetite is demonstrated as a function of processing time [29]. The so-called recovery R in mineral processing is defined as the yield of transferred magnetite $\varphi_{\mathrm{magn,trans}}$ [28]. Thus, the recovery of transferred magnetite $R_{\mathrm{magn,trans}}$ is calculated by means of the ratio of the time-dependent corrected magnetite mass concentration in the receiver tank $\beta_{\mathrm{magn,rt}}(t)$ to the theoretical applied magnetite mass concentration for the phase transfer $\beta_{\mathrm{magn,PT,theor}}$, as shown in Eq. (11).

$$R_{\mathrm{magn,trans}} = \frac{\beta_{\mathrm{magn,rt}}(t)}{\beta_{\mathrm{magn,PT,theor}}} \tag{11}$$

Including the transferred particles of the interfacial layer (IL), a recovery of extracted magnetite particles of 76 % as limit value could be achieved (dashed line in Fig. 20b).

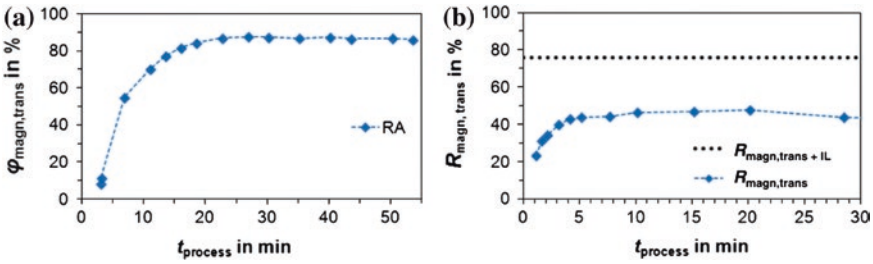

Fig. 20 Depiction of the time-dependent process yield of transferred magnetite in continuous circulation of both phases using ricinoleic acid (RA) as surfactant (**a**), and the recovery of transferred magnetite by the implementation of a separation process using a partial recirculation operational mode for the miniplant (**b**)

3.2.1 Comparison of the Experimental Results from the Laboratory Centrifuge and Drop Column Transfer Devices with the Theoretical Model by Hansen

The colloidal stability of the produced organosols from the laboratory centrifuge and drop column transfer devices was investigated using the calculation of the solubility distances $D_{FA-solvent}$ between the surfactant and the solvent in Eq. (12) by determination of the Hildebrandt parameter δ_t [25] in Eq. (13).

$$D_{FA-solvent} = \sqrt{4 \cdot (\delta_{d,FA} - \delta_{d,solvent})^2 + (\delta_{p,FA} - \delta_{p,solvent})^2 + (\delta_{h,FA} - \delta_{h,solvent})^2} \tag{12}$$

$$\delta_t = \sqrt{\delta_d^2 + \delta_p^2 + \delta_h^2} \tag{13}$$

The Hildebrandt parameter δ_t can be calculated with the three Hansen solubility parameters in consideration of the dispersive δ_d, polar δ_p, and hydrogen δ_h bonding components. Thus, the interaction between the fatty acids (FA) used as pure substances and bonded onto the magnetite surface (FA@Fe_3O_4) could be characterized [15, 22]. The calculated values are presented in Table 1 and the following correlation applies: The smaller the value, the more soluble is the surfactant in the solvent.

Ricinoleic acid (RA) has a lower solubility in iso-octane due to the polar and hydrogen bonding parameters and, therefore, exhibits better dissolution into the aqueous phase, resulting in a more rapid particle extraction process. In contrast, oleic acid (OA) is more soluble in iso-octane, whereby more stable drops are formed during the phase transfer process. Therefore, the colloidal stability of the organosol (OA@Fe_3O_4) is increased. Compared with the organosols produced in the laboratory centrifuge transfer device using the solvent dichloromethane (DCM), the colloidal stability with ricinoleic acid increased (RA@Fe_3O_4). Due to

Table 1 Summary of the calculated Hansen solubility parameters and solubility distances

Substance	δ_t in $MPa^{0.5}$	δ_d in $MPa^{0.5}$	δ_p in $MPa^{0.5}$	δ_h in $MPa^{0.5}$	$D_{FA\text{-}iOCT}$ in $MPa^{0.5}$	$D_{FA\text{-}DCM}$ in $MPa^{0.5}$
Iso-octane	14.30	14.30	0	0	–	–
DCM	20.20	18.20	6.30	6.10	–	–
RA	19.68	16.84	8.32	5.89	11.39	3.39
OA	18.31	17.30	5.73	1.78	8.49	4.71
RA@Fe_3O_4	19.40	17.27	6.89	5.55	10.66	2.03
OA@Fe_3O_4	17.90	17.68	2.81	0	7.02	7.11

the very good solubility of ricinoleic acid in dichloromethane, all surfactant molecules were rapidly available at the phase interface to disintegrate the agglomerates into primary particles. Therefore, the result was a stable colloidal organosol.

In addition, for the analysis of the product stability, a dispersion analyzer (LUMiSizer) was applied, whereby the integral transmission as a function of time could be determined [30]. The smaller the increase in integral transmission, the better was the colloidal stability. For dichloromethane as the solvent, as shown in Fig. 21a, the organosol produced with ricinoleic acid exhibits no increase in integral transmission, in contrast to that produced with oleic acid. Therefore, the result is a stable colloidal organosol. In contrast to the solvent iso-octane as shown in Fig. 21b, oleic acid exhibits no increase in integral transmission, resulting in a stable organosol with oleic acid as the surfactant. These experimental observations were confirmed with the calculated solubility distances using the Hansen solubility parameters.

3.2.2 Single-Drop Transfer Column

The primary idea behind the use of a single-drop transfer column was to investigate the dependency of the magnetite transfer from the magnitude of the interfaces

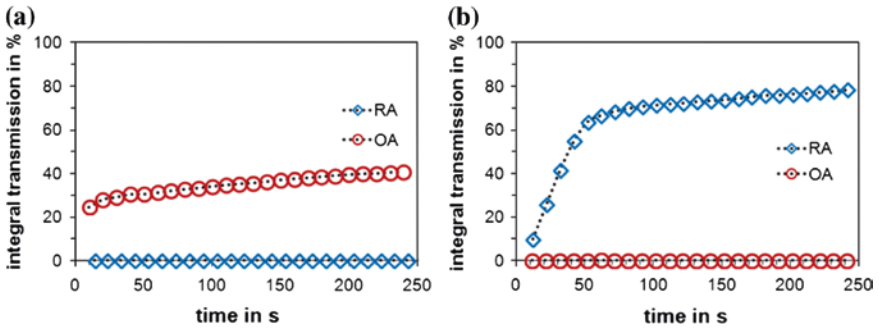

Fig. 21 Depiction of the product stability of RA@Fe_3O_4 and OA@Fe_3O_4 by the integral transmission plotted against time for DCM (**a**) and iso-octane (**b**) as the solvents used

between the two liquids, which is required to obtain a preferred efficient transfer of magnetite particles. The transferable mass flow of magnetite particles should depend on this size, so it was inferred that there could have been a linear correlation between them. To investigate the available transfer interface, it was necessary to produce single drops and to find a way to measure the diameter of the drops, along with how fast they rose in the aqueous phase. With this diameter, it was possible to calculate the interface of one drop (with a simplification based on a perfect sphere), while with its velocity, it was possible to calculate how long the interface would exist. The total interface between the aqueous and organic phases was, therefore, the sum of the interfaces of the individual drops. At the beginning of the experimental investigations, a simple mathematical model was devised which contained all relevant influences for phase transfer, as described in Eq. (14).

$$\dot{m}_{\mathrm{P,transfer}} = \beta \cdot I_{\mathrm{eff,aP-oP}} \cdot dc_{\mathrm{ap-oP}} \tag{14}$$

In this model, $\dot{m}_{\mathrm{P,transfer}}$ is the particle mass transfer, $I_{\mathrm{eff,aP-oP}}$ the effective interface between the aqueous and organic phases as calculated by drop size and velocity, $dc_{\mathrm{ap-oP}}$ is the concentration difference of magnetite between both phases, while β is a coefficient that describes the dependence of particle mass transfer on other parameters of suspension and the organic fluid. This coefficient takes into account, for example, the concentration of surfactant in the fresh organic phase, the ion concentration and pH value in the aqueous phase, and the frequency and size of drops, which influences the Sherwood number[2] [31].

Figure 22 shows the design of the single-drop transfer column. The main component is the 600 mm-high transfer column. At its bottom there is a capillary where drops are generated. Their size depended on the concentration of surfactant in organic fluid (which was dosed using a syringe pump), the concentration of specific ions in the aqueous phase, the diameter of the capillary used, and the volumetric flow. Velocity and formation time of the drops about the surface age were measured with a physical measurement setup that consisted of a source for X-Ray radiation, an X-Ray luminescence film (which emits green light when illuminated by X-Rays), and a lens array, which generated a 1:1 image from the luminescence film on the CCD-line detector behind the set-up. The intensity measured on the detector increased when a drop crossed the optical path.

Research continues on mass transfer and the factors affecting the process. The experiments are executed with the solvent iso-octane and the surfactant ricinoleic acid. Initial results on the behavior of the size of generated drops are shown in Fig. 23. These drops are generated in a clear aqueous phase in the transfer column. To obtain stable single drops, very low concentrations of ions—in particular ammonia—are needed. With more than 0.5 m% of ions resulting from the salts ammonium chloride and ammonium sulfate, stable drop generation cannot be achieved for concentrations of ricinoleic acid of 3.0 m% with capillary diameters

[2] The Sherwood number is a non-dimensional parameter to describe the ratio between diffusive and convective mass transport.

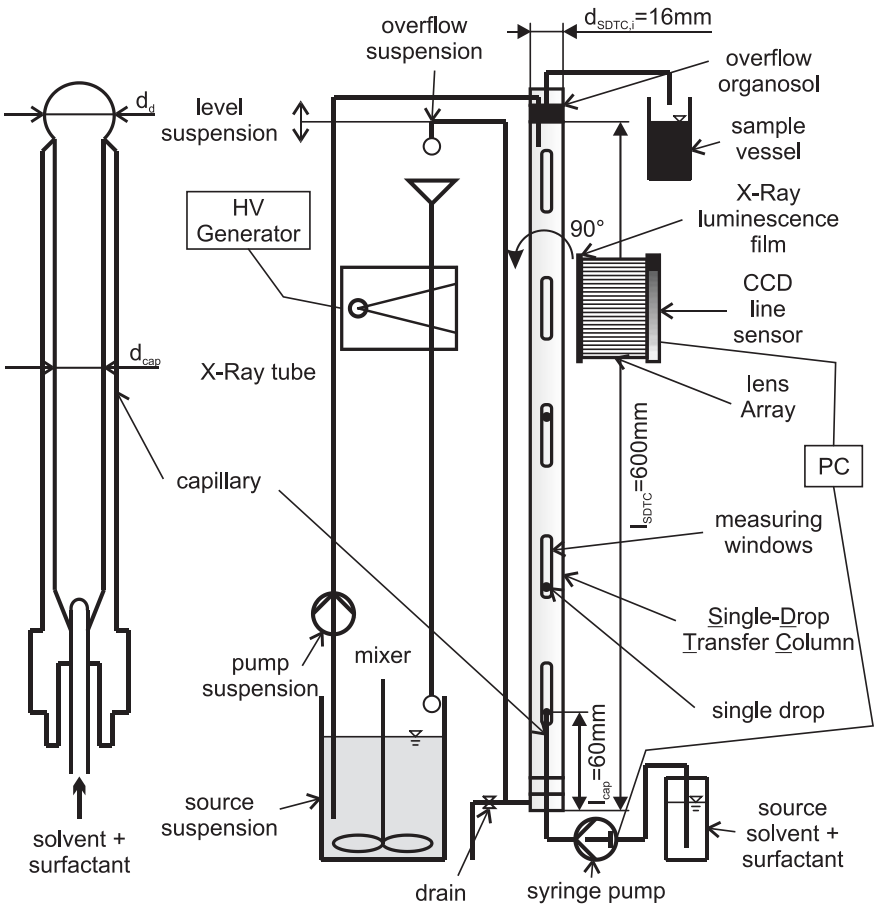

Fig. 22 Single-drop transfer column with drop generation in a capillary and measurement of drop size and velocity

of over 3.0 mm due to the formation of ammonium ricinoleate. If the concentration is higher, the interface where the drop is formed becomes excessively deformed, and water enters the capillary.

The Eq. (15) describes the equilibrium of weight force, buoyancy, and interfacial force, as characterized by the surface tension γ [32]. While dosing the drop, the diameter d_d increases and the drop leaves the capillary when the force equilibrium is exceeded.

$$\gamma \cdot \pi \cdot d_{cap} = \frac{\pi}{6} \cdot d_d^3 \cdot \left(\rho_{cont} - \rho_{disp}\right) \cdot g \tag{15}$$

Table 2 provides an explanation of results, as shown in Fig. 23, with reference to the force equilibrium.

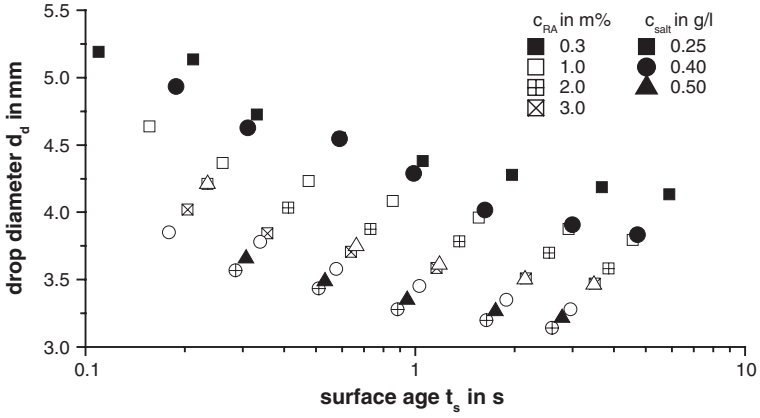

Fig. 23 Behavior of drop sizes as a function of aqueous and organic phase parameters for a 4.0 mm capillary at a pH value of 9

Table 2 Behavior of drop sizes as a function of different parameters and effects

Parameter	d_d	Explanation
$c_{surfactant,o.P.}$ ↑	↓	Increase of interfacial tension
$c_{ammonia,a.P.}$ ↑	↓	Formation of ammonium ricinoleate (higher interfacial activity)
d_{cap} ↑	↑	Larger interface at the capillary
t_S ↑	↓	More time for diffusion of surfactant to the interface

With the selection of different capillary diameters, the effects on drop size (as described in Table 2) may be compensated for in such a way that, for example, with different concentrations of surfactant, the same drop size may be generated. In this way, parameters of suspension and organic phase can be changed individually without changing the drop size and the effective interface between the liquid phases.

Initial experiments have shown that a reproducible phase transfer can only be guaranteed if the aqueous suspension is continually exchanged to prevent sedimentation of the particle agglomerates in the transfer column and a decrease of ammonium concentration in the liquid phase. Agglomerate sedimentation is recognizable by an increase in the medium signal level at the detector while carrying out a phase transfer when the suspension is not circulated. Decreasing ammonium concentration is evidenced by an increase in drop diameters with process time, which suggests the creation of less ammonium ricinoleate at the drop interfaces with increasing time.

4 Conclusions

This study presents the development of a process for liquid-liquid phase transfer of colloidal particles in the production of high-quality organosols. This means that the particle extraction process could be performed in different transfer devices directly through the liquid-liquid interface. As a result, a deeper understanding of the elementary processes was developed to describe the whole process chain, which consisted of particle synthesis, conditioning, and transfer in a miniplant to produce the organosol continuously.

Thus, the study demonstrated that the magnetite nanoparticles could be synthesized in a continuous precipitation reactor with a primary particle size of 15 nm. Furthermore, the capacity of the filtration process for conditioning of the aqueous phase could be confirmed. Due to the quantification and identification of the material process parameters, the particle extraction process could be performed efficiently and in a reproducible manner. Therefore, it was possible to adjust the electrolyte and particle concentrations during the conditioning step, allowing systematic investigations of the filter as well as simulations for the miniplant.

The phase transfer process was performed in a laboratory-scale centrifuge, a single-drop transfer column, and a drop column using different operational methods for the development of a continuous extraction process. The determination of drop sizes, formation times of the drops about the surface age, as well as the formation process of the drops was verified in the single-drop column transfer device. Due to the varying transfer devices, two different solvents were used, and the adsorption mechanism at the interface of the two liquids was investigated. For the production of stable functionalized colloids, saturated surfactants with different carbon chain lengths as well as unsaturated C18 surfactants with different molecule structures were applied. The capacity for the disintegration of agglomerated magnetite particles at the phase boundary was defined by the primary particle concentration. It could be verified that the deagglomeration was a function of the carbon chain length of the surfactant used. This meant that the stabilizing effect of the organosols produced was better with the C18 unsaturated surfactants, and decreased with lower carbon chain length. The highest capacity for the production of stable colloids in the solvent dichloromethane was achieved with ricinoleic acid as a C18 unsaturated surfactant. Due to its additional hydroxyl group in the molecule structure, the impact of its excellent steric stabilization could be explained using the deagglomeration model. The resulting variable repulsive pressures for the disjoining force led to variable adsorption equilibriums of the surfactants. As a consequence, the resulting differences in transfer behavior could be verified in the transfer kinetics of the system. Therefore, the particle extraction process could be assumed to be a reaction of the 1st order when using oleic acid as a surfactant. In contrast, with ricinoleic acid, another approximation using a sigmoid function had to be applied. As a result, the interactions of the surfactants with both phases had to be considered with respect to the process behavior and colloidal stability of the organosol. In combination with the solubility of the surfactant in the solvent

used, the Hansen model could be applied for the determination of the theoretical colloidal stability. The comparison with the experimental colloidal stability of the organosols produced was confirmed. Moreover, the process engineering application of the miniplant for a selective separation process (a two liquid flotation) was verified.

Acknowledgements The authors would like to thank the German Research Foundation (DFG) for its financial support. Additionally, many thanks go to Prof. Rehage (TU Dortmund), Prof. Garnweitner (TU Braunschweig), Prof. Schmidt (University of Paderborn), Prof. Peukert (University of Erlangen), and Prof. Landfester (MPIP Mainz) for their collaboration and advice in carrying out a range of measurements.

References

1. Lange A (2003) Instabilitäten magnetischer Flüssigkeiten in statischen Magnetfeldern. Universität Magdeburg
2. Machunsky S, Peuker UA (2007) Liquid-liquid interfacial transport of nanoparticles. Physical Separation in Science and Engineering, Article ID 34832
3. Lai RWM, Fuerstenau DW (1968) Liquid-liquid extraction of ultrafine particles. Trans Am Inst Min Metall Petrol Eng 241:549–556
4. Banert T, Peuker UA (2006) Preparation of highly filled super-paramagnetic PMMA-magnetite nano composites using the solution method. J Mater Sci 41:3051–3056
5. Kirchberg S, Rudolph M, Ziegmann G, Peuker UA (2011) Nanocomposites based on technical polymers and sterically functionalized soft magnetic magnetite nanoparticles: synthesis, processing and characterization. J Nanomater, Article ID 670531
6. Rudolph M, Peuker UA (2011) Coagulation and stabilization of sterically functionalized magnetite nanoparticles in an organic solvent with different technical polymers. J Colloid Interface Sci 357:292–299
7. Scherer M, Figueiredo Neto AM (2005) Ferrofluids: properties and application. Braz J Phys 35:718–727
8. Hurlebaus S, Gaul L (2006) Smart structure dynamics. Mech Syst Signal Process 20:255–281
9. Dallas P, Georgakilas V, Niarchos D, Komminou P, Kehagias T, Petridis D (2006) Synthesis, characterization and thermal properties of polymer/magnetite nanocomposites. Nanotechnology 17:2046–2053
10. Teja AS, Koh P-Y (2009) Synthesis, properties and applications of magnetic iron oxide nanoparticles. Prog Cryst Growth Charact Mater 55:22–45
11. Hickstein B, Peuker UA (2009) Modular process for the flexible synthesis of magnetic beads—process and product validation. J Appl Polym Sci 112:2366–2373
12. Banert T, Peuker UA (2007) Synthesis of magnetic beads for bio-separation using the solution method. Chem Eng Commun 194:707–719
13. Laurent S, Forge D, Port M, Roch A, Robic C, Vander Elst L, Muller RN (2008) Magnetic iron oxide nanoparticles: synthesis, stabilization, vectorization, physicochemical characterization and biological application. Chem Rev 108:2064–2110
14. Mahmoudi M, Sant S, Wang B, Laurent S, Sen T (2011) Superparamagnetic iron oxide nanoparticles (SPIONs): development, surface modification and applications in chemotherapy. Adv Drug Deliv Rev 63:24–46
15. Rudolph M, Peuker UA (2012) Phase transfer of agglomerated nanoparticles: deagglomeration by adsorbing grafted molecules and colloidal stability in polymer solutions. J Nanopart Res 14:990

16. Erler J, Manchunsky S, Grimm P, Schmid H-J, Peuker UA (2013) Liquid–liquid phase transfer of magnetite nanoparticles—evaluation of surfactants. Powder Technol 247:265–269
17. Cornell R, Schwertmann U (2003) The iron oxides: structure, properties, reactions, occurrences and uses. Wiley-VCH, Weinheim
18. Zhang L, He R, Gu H (2006) Oleic acid coating on the monodisperse magnetite nanoparticles. Appl Surf Sci 253:2611–2617
19. Schwarzer H, Schwertfirm F, Manhart M, Schmid H-J, Peukert W (2006) Predictive simulation of nanoparticle precipitation based on the population balance equation. Chem Eng Sci 61:167–181
20. Machunsky S (2013) Flüssig-Flüssig-Phasentransfer von Nanopartikeln zur Herstellung von Organosolen – Stoffliche Parameter und Prozessparameter, Technische Universität Bergakademie Freiberg
21. Rautenbach R, Melin T (2007) Membranverfahren: Grundlagen der Modul- und Anlagenauslegung, vol 3–7, Springer, Berlin, pp 319-321
22. Hansen CM (2007) A user´s handbook, 2nd edn. CRC Press, Boca Raton
23. Machunsky S, Grimm P, Schmid H-J, Peuker UA (2009) Liquid–liquid phase transfer of magnetite nanoparticles. Colloids Surf A 348:186–190
24. De Gennes PG (1987) Polymers at an interface: a simplified view. Adv Colloid Interface Sci 27:189–209
25. Rudolph M (2013) Nanoparticle-polymer-composites: the solution and spray drying process with an emphasis on colloidal interactions, Technische Universität Bergakademie Freiberg
26. Rudolph M, Erler J, Peuker UA (2012) A TGA-FTIR perspective of fatty acid adsorbed on magnetite nanoparticles—decomposition steps and magnetite reduction. Colloids Surf A 397:16–23
27. Blaß E (1988) Bildung und Koaleszenz von Blasen und Tropfen. Chem Ing Tech 60:935–947
28. Erler JV, Leistner T, Peuker UA (2014) Application of a particle extraction process at the interface of two liquids in a drop column—consideration of the process behavior and kinetic approach. Adv Chem Eng Sci 4:149–160
29. Leistner T, Müller M, Erler JV, Rudolph M, Peuker UA (2014) Selektive Trennung sehr feiner Partikelsysteme mittels Flüssig-Flüssig Flotation (Two Liquid Flotation). Chem Ing Tech 86(6):1–10
30. Sobisch T, Lerche D (2008) Thickener performance traced by multisample analytical centrifugation. Colloids Surf A 331:144–118
31. Carbonell RG (1975) Mass transfer coefficients in coiled tubes. Biotechnol Bioeng 17:1383–1385
32. Dörfler H (2002) Grenzflächen und kolloid-disperse Systeme, Springer, Berlin